wip-A6r08-version-of-CU-PhD-dissertation.docx

EMPIRICAL REASSESSMENTS OF LATTICE DEFECT PROPERTIES IN HIGH-PURITY GOLD

A Dissertation

Presented to the Faculty of the Graduate School of Cornell University

in Partial Fulfillment of the Requirements for the Degree of

Doctor of Philosophy

by

Raymond John Sonoff

December 2019

© 2019 Raymond John Sonoff

ABSTRACT

Analyses of extensive sets of quenched-in resistance data obtained over wide ranges in elevated temperature, quench rate, and isothermal annealing time for multiple specimens have led to establishment of the following determinations:

1. Confirmation of the reliability of a graphical back extrapolation technique (B.E.T.) for ascertaining no-loss equilibrium vacancy concentrations over the temperature range from 400^{o}C through 925^{o}C.

2. In general, for straight downquench treatments involving quench temperatures ranging from 750^{o}C to 925^{o}C and/or moderate to large sink density specimens, diffusion-limited models appear to be required to describe the annealing kinetics, whereas chemical rate equation models appear to be required when low sink density specimens and/or quench temperatures ranging from 400^{o}C to 700^{o}C are involved wherein losses are found to be proportional to an effective time-of-quench parameter.

3. Estimates for the vacancy formation energy and vacancy formation entropy over the temperature range from 400^{o}C to 925^{o}C.

4. An estimate for the heat of solution of helium in pure gold ascertained over the temperature range from 400^{o}C to 550^{o}C.

5. Graphically-represented insights that reveal the nature of isothermal annealing kinetics for many of the elevated temperature Q&A series treatments to be essentially diffusion-limited, exhibiting losses that generally reflect $t_A^{2/3}$ or $t_A^{1/2}$ dependencies during the decay period down to at least 1/e of the fraction remaining of Normalized Quenched-In Resistance.

6. Evidence that metastable residual resistance (MRR) levels result when elevated temperature Q&A series treatments involving $T_Q \geq 700^oC$, $T_A \leq 500^oC$, and isothermal annealing times beyond one hour are performed.

7. Determinations of parameters, such as vacancy defect chemical potential, effective vacancy migration energies, mean relaxation times, instantaneous vacancy activation energies, and absolute macroscopic sink efficiency.

8. Graphically-represented insights regarding the influence of vacancy defect chemical potential upon a) absolute macroscopic sink efficiency, and b) values for instantaneous vacancy activation energies, especially as annealing temperatures approached the associated quench temperature.

9. Insight as to the nature, density, and associated vacancy concentration of secondary defects considered responsible for metastable residual resistance levels was accomplished via Transmission Electron Microscopy (TEM) observations of two gold ribbon foils previously subjected to Q&A's involving T_Q at 800^oC and 900^oC, respectively, followed by contiguous, prolonged anneals for one hour at 385^oC and 340^oC, respectively, and subsequent preparation for TEM methods.

10. An estimate for sink structure recovery activation energy at 950^oC was obtained from analyses of monitored straight downquench ΔR_{QN} (also referred to NQIR) magnitudes associated with quenches from 800^oC performed on specimens that had been initially subjected to direct deformation followed by a series of several extended HTA treatments at 950^oC each lasting for a number of hours and followed by an 800^oC straight downquench to assess what changes occurred in NQIR values.

Extensive sets of data involving five-mil diameter pure 99.9999 weight percent (6N) pure gold wires maintained in situ during subjection to thermal treatments and subsequent lattice defect electrical resistance determinations at liquid helium temperatures have been analyzed. As a consequence of these studies, quantitative estimates for numerous lattice defect parameters were made possible, and insights into the interrelationships among many of these parameters were revealed.

From analyses of data associated with various sets of elevated temperature treatments that were performed, quantitative determinations for each of the following parameters were achieved:

1. Melting Point Resistance Ratio for Gold
2. Establishment of a temperature-time profile[1] defined as a Long-Term Anneal (LTA) treatment to asymptotically approach "vacancy-free" residual resistance levels for potentiometric resistance measurements conducted at $4.2^{o}K$.
3. "No Loss" Normalized Quenched-In Resistance NQIR(T) Ξ QIR(T)/R($40^{o}C$)
4. "No Loss" Vacancy resistivity $\Delta\boldsymbol{\rho}_{V}(T)$
5. "No Loss" equilibrium vacancy concentration $C_{V}(T)$ [2]
6. Vacancy formation energy (E^{F}_{V})
7. Vacancy formation entropy (S^{F}_{V})
8. Heat of solution of helium in pure gold

---

[1] An LTA treatment incorporates a “pre-cleansing annealing” treatment (see sub-section 6.4.2 for details) that is intended to serve as a means to remove entirely or at least minimize whatever lattice defect “histories” that might be present that were associated with prior thermal treatments.

[2] Calculated by converting "No Loss" Normalized Quenched-In Resistance NQIR(T) Ξ QIR(T)/R($40^{o}C$) values using a scattering cross-section for vacancies of 1.5 micro-ohms per one atomic percent vacancies [1, 36, 63].

9. Effective vacancy migration energy $E^{M}_{V}(eff)$
10. Remaining Vacancy Supersaturation Ratios $VSR(T_Q, T_A, t_A)$ defined as

    $\equiv [C_v(T_Q,T_A, t_A) - C_v(T_A, t_A)]/C_v(T_A, t_A \rightarrow \infty)$
11. Vacancy defect chemical potential $\mu_v(T_Q, T_A, t_A)$
12. Absolute macroscopic sink efficiency € [3]
13. Variations in time exponent (m) during $NQIR(T_Q, T_A, t_A)$ Q&A series treatments
14. Metastable Residual Resistance (MRR) Levels for Q&A series treatments
15. Initial annealing rates (IARs) defined as

    $\{[NQIR(T_Q, T_A, t_A = 0) - NQIR(T_Q, T_A, \Delta t_{A(initial)})] / (\Delta t_{A(initial)}) \}$, wherein $\Delta t_{A(initial)}$ is the duration time of the shortest isothermal anneal (hence the added descriptor *initial*) for the overall $NQIR(T_Q, T_A, \Delta t_A)$ series treatment.
16. Mean relaxation times t_{mean} defined as

    $NQIR(T_Q, T_A, t_A = 0) / \{[NQIR(T_Q, T_A, t_A = 0) - NQIR(T_Q, T_A, (\Delta t_{A(initial)})] / (\Delta t_{A(initial)}) \}$
17. Instantaneous Vacancy Activation energy $E^{M}_{V}(act)$
18. Post-direct deformation sink structure recovery activation energy

---

[3] Defined (graphically, in a segment of an overall curve) as the "Observed Rate" ÷ "Maximum Rate"

BIOGRAPHICAL SKETCH

Raymond Sonoff was born in Barberton, Ohio, on April 18, 1941. He attended the University of Akron, Akron, Ohio and obtained a BSEE degree in 1964. He next attended Northeastern University, Boston, Massachusetts and obtained an MSEE degree in 1966.

While enrolled at Cornell University, Raymond met Miss Elisabeth Pettersen, and they were married in December 1967.

DEDICATED TO THE MEMORY OF MY PARENTS:

GEORGE AND THERESA SONOFF

ACKNOWLEDGEMENTS

The author gratefully acknowledges the assistance, patience, and cooperation of his advisor Professor Robert W. Balluffi during all phases of this research work performed at Cornell University. He also wishes to thank Professors David N. Seidman and Dieter C. Ast for their helpful discussions during various phases of data acquisition and initial analyses.

Additionally, Ed Ryan and Y. Komem are to be thanked for their assistance in providing Transmission Electron Microscopy (TEM) results involving several 0.5 mil thick 6N (99.9999 weight percent) pure gold ribbon foils. Prior to their conducting the requested supplementary TEM activities and supplying of photographic images that were examined and which appear within this document, these foils had been subjected to specific thermal treatments and macroscopic resistance measurements.

This work was supported in part by contract E74-2103.

List of Tables

List of Figures

1 INTRODUCTION

1.1 PURPOSE OF INVESTIGATION

The purpose of this research investigation was to obtain extensive sets of experimental data from which numerous elevated temperature lattice defect properties for pure gold could be reliably assessed.

1.2 SCOPE OF INVESTIGATION

The scope of this research investigation centered upon obtaining potentiometric resistance data involving in-situ gas quenched five-mil diameter 6N-(99.9999 weight percent pure) gold wires. These sets of data were associated with conducting highly-controlled elevated temperature treatments referred to as follows: Straight Downquench (ST DQ), Quench-and-Isothermal-Anneal (Q&A), Pre-Quench Anneal (PQA) [4], Long-Term Anneal (LTA), Thermal Cycling (TC), and prolonged High Temperature Anneal (HTA). Additionally, some form of thermal-mechanical treatments involving direct deformation (DD) within a specimen's gauge length followed by execution of any or all of the above thermal treatments were performed on a limited number of specimens.

Among the numerous parameters sought or investigated were energies of vacancy formation and migration, associated annealing kinetics for both straight downquench and for quench-and-isothermal annealing thermal histories, recovery

---

[4] A "cleansing anneal" treatment has as its primary objective the removal of prior thermal histories' remnants from a given specimen. By so doing, the subsequently measured quenched-in resistance values for specific thermal treatments can be found to yield highly reproducible results -- even over the course of conducting many runs involving wide ranges in both quench and isothermal anneal treatments.

activation energy of induced-by-direct-deformation sink structures, and the influence of vacancy defect chemical potential upon any or all of the aforementioned parameters.

To support both the breadth and depth of topics covered within this document, approximately 200 Figures segmented into numerous specific categories for the reader's benefit, have been included. Moreover, a descriptive label has been assigned to each Figure to assist the reader to quickly locate relevant graphical representations that support discussions presented regarding each distinct topic.

1.3 ABBREVIATIONS

This section contains listings of abbreviations, definitions, nomenclature, and notations that appear throughout this document.

5N	99.999 weight percent pure
6N	99.9999 weight percent pure
B.E.T.	Back Extrapolation Technique
DD	Direct Deformation
HTA	High-Temperature Anneal
IAR	Initial Annealing Rate
IQR	Initial Quench Rate
LTA	Long-Term Anneal
MRR	Metastable Residual Resistance
NQIR	Normalized Quenched-In Resistance
NIAR	Normalized Initial Annealing Rate
NIQR	Normalized Initial Quench Rate
O-O-R	Order of Reaction
PQA	Pre-quench Anneal
Q&A	Quench-and-Anneal

QIR	Quenched-in Resistance
QMSD	Quench/Measurement System Design
QMU	Quench/Measurement Unit
SFT	Stacking Fault Tetrahedra
ST DQ	Straight Downquench
TC	Thermal Cycling
TEM	Transmission Electron Microscopy
TEV	Time Exponent Variation
VSR	Vacancy Supersaturation Ratio

1.4 DEFINITIONS AND SYMBOLS

R_Q ≡ actual resistance measured at 4.2^{o}K for a ST DQ thermal treatment.

R_{QA} ≡ actual resistance measured at 4.2^{o}K for a Q&A thermal treatment.

R_{LTA} ≡ residual resistance measured at 4.2^{o}K following completion of a Long Term Anneal (LTA) treatment (see sub-section 6.4.1 for more details). An LTA consists of a series of ten well-defined set of staircase anneals that begin at 700°C for a specified duration time followed by lowering of the temperature to the next isothermal level, held there for the corresponding isothermal anneal time interval, and eventually terminating the treatment after completion of the tenth and final isothermal anneal at 250^{o}C down to room temperature followed by a potentiometric measurement at 4.2^{o}K. The value obtained for R_{LTA} is taken to represent that of a "vacancy free" specimen [5].

IQR ≡ Initial Quench Rate ($dT/dt_{initial}$) determined from plots of recorded straight downquench (ST DQ) thermal histories.

---

[5] A "vacancy free" condition as used here corresponds to having reached the potentiometric measurement resolution limit of resistance of 0.01 μohm for specimens subjected to the adopted LTA treatment (see sub-section 6.4.1).

RIQR ≡ $(dT/dt_{initial})^{-1}$ = Reciprocal Initial Quench Rate

ΔR_Q ≡ resistance quenched-in following a straight downquench (ST DQ) treatment, measured at 4.2°K, and equal to R_Q minus R_{LTA}.

ΔR_{QA} ≡ resistance quenched-in following a quench and isothermal anneal treatment, measured at 4.2°K, and equal to R_{QA} minus R_{LTA}.

NQIR(T_Q) ≡ ΔR_Q ÷ specimen's R(40°C) value = ΔR_{QN}.

NQIR(T_Q, T_A, t_A) ≡ ΔR_{QA} ÷ specimen's R(40°C) value = ΔR_{QAN}.

NIAR(T_Q, T_A, Δt_A) ≡ d{[NQIR(T_Q, T_A, t_A = 0) - NQIR(T_Q, T_A, $\Delta t_{A(initial)}$)]/NQIR(T_Q, T_A, t_A=0)}/dt

wherein $\Delta t_{A(initial)}$ is the duration time of the shortest isothermal anneal (hence the added descriptor (*initial*) for the overall NQIR(T_Q, T_A, Δt_A) series treatment.

$\tau_{initial}$ ≡ T_Q x $[dt/dT]_{initial}$ (determined graphically) associated with the onset of a ST DQ treatment

τ_q ≡ effective time of quench -- for a straight downquench from T_Q involving a given specimen and an associated thermal history -- to reach a temperature (often cited as T* [20]) such that the NQIR (T*) magnitude subsequently measured potentiometrically at liquid helium temperatures will equal the "No Loss" NQIR (T*) value. Calculations of the actual time temperatures (where $T_Q \geq 700°C$) to reach 500°C were used as an alternative definition for the effective time of quench τ_q [6].

---

[6] See sub-section 7.2.2 for a graphical representation of the composite range in τ_q.

m ≡ Exponent value determined from the dynamic slope established for each Time Exponent Variation (TEV) plot [7] of the respective annealing kinetics behavior obtained for each Q&A Series treatment and specific specimen.

t_{mean} = Mean Relaxation Time defined as

$NQIR(T_Q, T_A, t_A = 0) / \{[NQIR(T_Q, T_A, t_A = 0) - NQIR(T_Q, T_A, \Delta t_{A(initial)})] / \Delta t_{A(initial)}\}$

$t_A/t_{1/2}$ ≡ Reduced Annealing Time Variable

1.5 NOTATIONS AND TERMINOLOGY

$NQIR \equiv [(R_{total} - R_{LTA})/R(40^oC)] = QIR/R(40^oC)$

"No Loss" $NQIR(T_Q)$ ≡ "B.E.T." $[NQIR(T_Q, (dT/dt)_{initial}^{-1} \rightarrow 0])$ [8]

VSR ≡ Vacancy Supersaturation Ratio is ideally defined as

$= [C_v(T_Q,T_A, t_A)$ - "No Loss" $C_v(T_A)] /$ "No Loss" $C_v(T_A)$

$= [NQIR(T_Q,T_A, t_A)$ - "No Loss" $NQIR(T_A)] /$ ["No Loss" $NQIR(T_A)]$

μ_v ≡ vacancy defect chemical potential = $kT_A \ln (1 + VSR)$

€(μ_v) ≡ absolute macroscopic sink efficiency defined (graphically) as the

"Observed Rate" ÷ "Maximum Rate" (in an overall curve)

---

[7] See sub-section 8.3.11 for examples of TEV plots with indications of how slope values are illustrated.

[8] B.E.T. is used as a shorthand representation for Back Extrapolation Technique which is the name assigned to the method for graphically extrapolating $NQIR[T_Q, (dT/dt)_{initial}^{-1}]$ values -- obtained for several independent specimens over the range in selected quench temperatures -- to an infinite quench rate, thereby establishing what are then referred to as a set of "No Loss" $NQIR[T_Q]$ reference values.

1.6 LATTICE DEFECT INVESTIGATION METHODS

Much research, both theoretical and experimental, has been reported on lattice defects [18, 22, 32, 35, 38, 64, 77, 80, 87, 95, 139-143, 166-170, 175-208, 213], especially in quenched metals [3, 5, 12, 16, 18, 23, 53, 61, 64, 68, 98]. Gold has received the majority of attention [8-11, 24, 25, 29, 32, 34, 35, 37-52, 55, 56, 60, 62, 63, 65-67, 69, 76, 165, 212] and techniques such as tracer self-diffusion [27,30, 46, 142, 235], internal friction [37, 100, 111, 171-172, 211], transmission electron microscopy [13-15, 52, 57], positron annihilation spectroscopy (PSA) [109, 136], and Zener relaxation studies [80, 201] have proven capable of supplementing the most commonly employed technique of monitoring of electrical resistivity of quenched-in lattice defects via conventional potentiometric measurement methods. Refer to Chapter 2, entitled REVIEW OF LITERATURE, for more specifics.

1.7 STATEMENT OF PROBLEM

To provide significant additional insight regarding lattice defect properties and their interdependencies requires that highly reproducible quenched-in resistance data experiments be performed that collectively span extensive ranges in quench rate, quench temperature, annealing temperatures, and specimen sink densities.

Examples of relationships that will be revealed from analyses of such sets of data include the influence of vacancy defect chemical potential upon such parameters as effective vacancy migration energy, fractional annealing times for excess vacancies, and absolute macroscopic sink efficiency.

1.8 THESIS STATEMENT

Reliable determinations of numerous elevated temperature lattice defect properties can be obtained - provided that an appropriate quench/measurement system design is employed - when an extensive series of well-defined, controlled, and documented thermal treatments is coupled with subsequent determinations of the associated lattice defect electrical resistance changes monitored at liquid helium temperatures.

Specifically, it is the thesis of this document that analyses of sets of quenched-in lattice defect resistance data for five-mil diameter 6N (99.9999 weight percent) pure gold specimens subjected to wide ranges in elevated temperature thermal history profiles, namely straight downquenches and quench-and-isothermal anneals, and performed on specimens having a collectively wide range in pre-existing sink densities can and do provide reliable quantitative estimates for several lattice defect energies and annealing kinetics-related parameters, as well as insight into the nature of dominant pre-existing sinks for excess vacancies in pure gold.

2 REVIEW OF LITERATURE

This chapter presents a brief survey of literature on quenched gold and investigations that employed lattice defect resistance measurement methods.

2.1 INTRODUCTION

2.1.1 Books, Monographs, and Reviews of Lattice Defects

The literature on lattice defects is extensive, and among the publications cited in this document are books [22, 61, 93, 210, 233, and 234], monographs [18, 53, 98, 119, and 120], and reviews [3, 5, 16, 64, 104, 109, 142, 143, 167, 168, 185, 188, 189, 228, and 231].

2.1.2 Categories of Experimental Studies and Methods on Gold

Experimental studies performed on pure gold using electrical resistivity [3-9, 11, 17, 18, 21, 22, 24, 25, 28, 29, 34, 35, 38, 39, 40, 42-44], lattice dilatometry [58, 213], Transmission Electron Microscopy (TEM) [13-15,19, 114], as well as other methods, such as internal friction [37, 100, 111, 171, 172] and tracer self-diffusion experiments [27, 30, 46, 142, 216, 235], provide convincing evidence to support theories that 1) vacancies are the dominant point defect present in thermal equilibrium at elevated temperatures and 2) vacancies are the phenomenological defect responsible for mass transport in metals quenched from elevated temperatures. A tabulation of *Properties of Vacancy Type Defects in Gold* by A. Seeger and D. Schumacher [55] cites associated references regarding each property listed therein.

2.1.3 Additional References on Metals, Alloys, and Elements

Additional references besides those for gold are cited in this document regarding both the theory and experimentally obtained properties of lattice defects [86, 87, 147, 166, 168, 171, 179, 187, 188, 189, 191-193, 202, 206, 208, 209, 210, 212, 214], other metals [18, 73, 74, 75, 84, 94, 107, 110, 112, 114, 116, 144, 145, 146, 148, 163, 169-170, 180, 183, 185, 186, 200, 205, 215], alloys [83, 99, 111, 113, 150, 151, 152, 155, 156, 160, 162, 175-177, 182, 195, 201, 213, 217], and elements [161, 194, 203, 207].

2.1.4 Annealing Kinetics and Precipitation Formulas

Many researchers have reported on precipitation in metals and alloys [37, 56, 70, 80-83, 105,106, 150, 156, 157, 160, 186, 187, 217, 227] and may have made use of various precipitation formulas [70, 90, 105, 106, 107, 164, 186, 187,191] to analyze their respective sets of experimental data to obtain specific values for the time exponent **m** [9].

Ham [105, 106] proposed a simple theory for diffusion-limited general precipitation from a supersaturated solution that provided useful information about the rate-limiting process involved and the size, shape, and density of the precipitate particles, and Burke [81, 82] investigated the kinetics of vacancy precipitation and growth of precipitates from solid solutions.

---

[9] The time exponent **m** is defined in section 1.4 of this document.

In particular, Wintenberger [163] found that annealing kinetics in systems containing excess vacancies and dislocations could be described approximately by a relation of the form

$c(t)/c_o = \exp(-kt^m)$ Eqn. (1-1)

where c(t) is the average concentration at time t, c_o is the equilibrium concentration, k is a constant, and the time exponent m is equal to 2/3 when the interaction energy[10] E varies as 1/r and m=1/2 when E varies as $1/r^2$.

However, Balluffi and Seidman [4] stated that there was no theoretical justification for Eqn. (1-1) and discussed its questionable derivation by stating that nowhere were both the concentration gradient and the drift force taken into account. They went on to show that the annealing data of these investigators with m=1/2 cannot be due to a vacancy-dislocation interaction which varies as $1/r^2$. Balluffi and Seidman stated that correct approximate solutions under various particular conditions had been obtained by Ham [187] and Bullough and Newman [188].

Based on their making two assumptions, namely that a) the concentration gradient term is first neglected entirely (see footnote below) and b) if the interaction is of the form $E_n = -(A_n/r^n)$, two alternative equations were considered to be acceptable approximate solutions for the underlying diffusion processes.

$c(t)/c_o = 1 - \pi N_D[\{n(n+2) A_n D t\}/kT]^{[2/(n+2)]}$ applicable for short times Eqn. (1-2)

$c(t)/c_o = \exp\{ - \pi N_D[\{n(n+2) A_n D t\}/kT]^{[2/(n+2)]}$ applicable for long times Eqn. (1-3)

---

[10] The vacancy current at any point around a dislocation is represented in reference [4] by the equation $j = -(\nabla c + c\nabla E/kT)$. The first term represents the flux due to the concentration gradient, and the second term represents the flux doe to the drift force ($c\nabla E$) which biases the vacancy jumps toward the dislocations.

where c(t) is the average concentration at time t, c_o is the equilibrium concentration, N_D is specimen sink density, A_n is a constant, D equals the diffusivity, t is the annealing time, T is the annealing temperature, n equals 0, 1, or 2 depending upon interaction conditions that are in effect during the annealing kinetics, and k is a constant.

Balluffi and Seidman concluded that the deviation from first-order kinetics as were predicted by Ham [187] and Flynn [86, 87] was caused by other effects and listed specific factors which may have played a role in complicating the kinetics. The five possible factors which they suggested for further consideration are listed below.

1) The formation of debris and the subsequent precipitation of vacancies on this debris;
2) Macroscopically non-uniform dislocation distributions;
3) Changes in the dislocation sink geometry as a result of massive annealing;
4) Changes in the efficiency with which dislocations absorb vacancies;
5) Participation of more than one type of vacancy defect in various stages of the annealing.

Resolving which factors are responsible for the complicated annealing kinetics demands 1) acquisition of extensive sets of annealing kinetics data; 2) subsequent detailed quantitative analyses that will a) result in establishment of comprehensive assessments of the overall behavior and b) provide confirmation as to the validity of precipitation formulas that can account for the observed sets of overall annealing kinetics.

To this end Chapter 8 of this document focuses on precisely these matters and contains specific findings from detailed plots of dynamic time exponent **m** behaviors (see sub-section 8.3.11) that were obtained from analyses of extensive sets of data obtained for many specimens subjected to elevated temperature quench-and-isothermal annealing treatments.

2.2 ELECTRICAL RESISTIVITY MONITORING

Numerous electrical resistivity measurements which macroscopically monitor lattice defect concentrations have been reported for high-purity gold specimens that were quenched, quenched and subsequently annealed, or contiguously quench-and-annealed.

Collectively, such investigations [4-19, 21-25, 28-30, 32, 34, 35, 38-44, 47-56, 60-63, 65-69, 71-76, 78, 79, 84-89, 91, 92, 94-98, 101-104] have sought to establish lattice defect properties ranging from estimates for vacancy formation and migration energies to discernment of the nature of the annealing kinetics, and the associated dominant sink structures. Additionally, relationships of specimen pre-existing sink density and specimen purity upon annealing rates, kinetics, and migration energy magnitudes have also been investigated.

2.2.1 Scattering Resistivity Value Adopted for Vacancies

Lattice defect electrical resistance determinations performed using standard potentiometric techniques with specimens cooled to liquid helium temperatures constitute a sensitive, reliable, and accepted method for monitoring lattice defect concentrations. When in-situ gas media quenches from elevated temperatures are

performed involving quench rates that do not result in plastic deformation of (or thermal strain [33, 60] within) a specimen, it is generally accepted that only vacancy-type defects will be created [23].

If vacancies are widely separated within a specimen, they can be considered to constitute isolated scattering sites for conduction electrons [2 and 54]. Thus, a basic assumption generally adopted by researchers using this method is to consider the associated quenched-in electrical resistance determined potentiometrically to be directly proportional to the mean vacancy concentration retained following the actual quench.

Estimates for the scattering resistivity associated with vacancies have been calculated [2 and 36] and experimentally established [21]. For gold, a value of 1.5 x 10^{-6} ohm-cm per one atomic percent vacancies [1, 36, and 63] is generally considered to represent the most reliable value.

2.2.2 Estimates for the Scattering Resistivity of Vacancy Clusters

The scattering power of vacancy clusters comprised of n vacancies, however, is not presently well-established. A divacancy is generally assumed to scatter with an efficiency of no less than 90 percent of that associated with two isolated mono-vacancies that comprise it [2, 26, 54]. The scattering power of any vacancy cluster must certainly involve the geometrical shape of the cluster in addition to the number of vacancies comprising the cluster shape, e.g., a loop, polyhedral void, and stacking fault tetrahedra. Calculations made by Asdente and Friedel [2], Dexter [26], and Seeger and Bross [54] appear to support a rather slow drop, on a percent basis, in scattering power with increasing cluster size.

2.3 REPORTED ENERGY DETERMINATIONS FOR VACANCIES

Tables 1 and 2 list a number of vacancy formation and migration energy determinations obtained by others from analyses of electrical resistivity data for pure gold subjected to the indicated temperature ranges.

2.3.1 Vacancy Formation Energies

Results of several workers who accounted for losses of vacancies to sinks during elevated temperature quenches are shown in Figure 1 [11] excerpted from C. G. Wang's PhD thesis [62]. Most of the formation energies listed in Table 1 are those based upon correction for losses during any real quench by some form of graphical extrapolation to infinite quench rate [8, 9, 29, 38, 39, 42, 43, 49-51]. These formation energy values, generally near one electron volt, are attributed to mono-vacancies.

[11] The four data points associated with the simultaneous lattice parameter change and length change measurements of Simmons and Balluffi [58] involved lattice dilatometry and specimen length changes, not electrical resistivity measurements.

Table 1. Determinations of Vacancy Formation Energy Values

Investigators [12]	Quench Temperature Range (^{o}C)	Final Bath Temperature(s) (^{o}C)	E^{F}_{V} Value (eV.)
Bauerle and Koehler (1957) [8]	450 - 1000	20	0.98 ± 0.03 [13]
Bradshaw and Pearson (1957a) [9]	900	2	0.92 - 0.98
Flynn, Bass, and Lazarus (1965) [29]	470 - 1030		0.98 ± 0.02
Kauffman and Koehler (1955) [38]	690 - 900	20	1.28 ± 0.03
Kino and Koehler (1967) [42]	400 - 800	2	0.95 ± 0.02
Koehler, Seitz, and Bauerle (1957) [43]	500 - 900	-190	0.98 ± 0.04
Lazarev and Ovcharenko (1959) [44]	600 - 1000	20	0.82
Mori, Meshii, and Kauffman (1962) [49]	$700 \leq T_Q \leq 1030$	0	0.97
Simmons and Balluffi (1962) [58]	$900 \leq T \leq 1060$	-	0.94 ± 0.09
Wang, Seidman, and Balluffi (1968) [63]	450 - 700	-195	0.94

Wang, et al. [63] reviewed the many considerations and attendant difficulties associated with each of several approaches for determining formation energy and concentrations of vacancy defects using quenching experiments. Influences of a finite quench rate, the effects of quenching stresses upon both vacancy concentration and sink density, especially for quenches into liquids, and the importance of repeatability, reproducibility, and control of experimental parameters were discussed.

---

[12] Simmons and Balluffi [58] performed lattice dilatometry studies involving equilibrium measurements. All other research workers listed in Table 1 employed quench rate-based resistivity measurements.

[13] After accounting for insufficiently slow cooling to correct for overestimation in Bauerle and Koehler's reported value, this value was corrected by Flynn, Bass, and Lazarus [28] to be 0.93 ± 0.03.

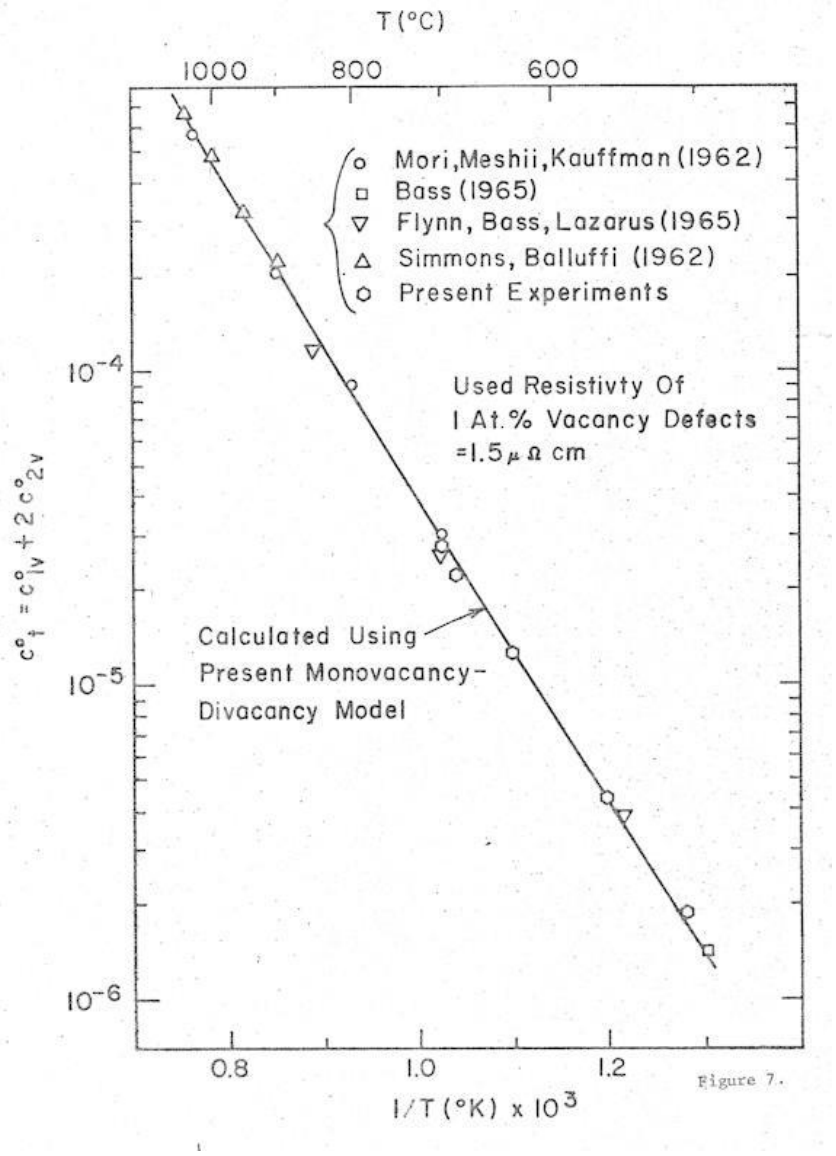

Figure 1. C.G. Wang's Composite Arrhenius Plot of Vacancy Concentration Values based on results reported for five research investigations

2.3.2 Vacancy Migration Energies

Vacancy Migration energies are listed in Table 2.

Table 2. Determinations of Vacancy Migration Energy Values

Investigators	Quench Temperature (^{o}C)	Anneal Temperature (^{o}C)	E^{M}_{V}(eff) Value
Bauerle and Koehler (1957) [8]	700 1000	40 30 and 40	0.82 ± 0.05 0.60 ± 0.06
Bradshaw and Pearson (1957a) [9]	900		0.68
Flynn, Bass, and Lazarus (1965) [29]	$470 \leq T_Q \leq 1030$		0.83 ± 0.04
Kauffman and Koehler (1955) [38]	690 - 900		0.68 ± 0.03
Kauffman and Meshii (1965) [39]	$600 \leq T_Q \leq 1030$	--	0.71 ± 0.03
Kino and Koehler (1967) [42]	$489 \leq T_Q \leq 800$ $600 \leq T_Q \leq 900$	$40 \leq T_A \leq 150$ 30, 40, 140, 150	0.94 ± 0.05 0.90; 0.78
Koehler, Seitz, and Bauerle (1957) [43]	500 - 900		0.78 ± 0.065
Lazarev and Ovcharenko (1959 [44]	600 - 1000	--	0.52
Mori, Meshii, and Kauffman (1962) [49]	$700 \leq T_Q \leq 1030$	--	0.7
Wang, Seidman, and Balluffi (1968) [63]	700	$180 \leq T_A \leq 670$	0.694

Some research workers have obtained results that support effective vacancy migration energies that appear to be essentially independent of specimen purity [43]. Effective vacancy migration energies have also been noted to exhibit dependencies upon excess vacancy concentration, generally diminishing with higher initial excess vacancy concentrations [8, 42, 43, 67]. Such concentration-dependent characteristics nearly always give rise to questions as to whether quasi- or non-equilibrium vacancy defect population conditions are present. Moreover, reduction in absolute macroscopic sink efficiency when diminished initial vacancy supersaturation conditions are present [103, 104, 125, 159, 167] could also prove be a contributing factor.

2.4 MODELS PROPOSED BY OTHER RESEARCHERS

Because the sum of vacancy formation and effective vacancy migration energies is often determined to be less than the self-diffusion energy obtained for pure gold using tracer self-diffusion experiments [27, 30, 46, 142, 235], it is generally contended that a point defect larger than a mono-vacancy, such as a divacancy, trivacancy, or a tightly bound cluster dominates elevated temperature annealing kinetics [2, 28, 29, 31, 57, 63, 76, 100, 101].

Additionally, even though there may be general agreement that a divacancy would likely have a lower migration energy than a single vacancy [28, 100], much controversy still remains as to the magnitude for the divacancy binding energy and associated entropy in pure gold [3, 10-11, 16, 18, 100, 101,and 235]. Consequently, multiple sets of parameters for various models have been forwarded to account for collective sets of data for equilibrium vacancy concentrations [228], effective vacancy migration energies associated with isothermal annealing kinetics [8, 9, 29, 38, 39, 42-44, 49, and 63], and self-diffusion in pure gold [5, 18, 28, 29, 40 - 43, and 101].

2.5 PROPOSED SINK STRUCTURES FOR EXCESS VACANCIES

Among the types of vacancy sinks cited in the literature [5, 18, 61, 63, 167, 169] are free dislocation lines [4, 18, 22, 125, 166], grain boundaries [159, 233] and subgrain boundaries [63], and additional vacancy self-sinks, such as vacancy clusters [5, 94, 96, 108, 120, 129, 131, 132-134. 137, 175], stacking fault tetrahedra [12-15, 21, 35, 52, 56, 57, 81, 89, 92, 96, 97, 103, 104, 127, 148, 189, 196], black spots [28, 118], prismatic dislocation loops [73, 144], dislocations formed from collapsed vacancy discs [71], and the surface of the specimen [18, 31].

Determinations of the dominant sink structure via electrical resistivity measurements for any particular thermal treatment have proven difficult to achieve for many reasons.

For example, not only will several types of sinks always be present, but concepts such as vacancy sink efficiencies [103, 104] and dislocation climb efficiencies [125] arise in interpreting annealing loss kinetics [24, 25, 38-43, 48].

When elevated temperature thermal treatments result in the creation of vacancy supersaturations, specific TEM examinations of stacking fault tetrahedra have been performed to determine estimates of the associated vacancy sink efficiencies [103, 104].

Additionally, it is generally observed that the magnitude of pre-existing dislocation densities plays a prominent role in both the degree and type of precipitation phenomena that occur not only in gold [37, 56, 70, 139-141] but in other metals and alloys [80, 83, 217, 227].

2.6 TRANSMISSION ELECTRON MICROSCOPY INVESTIGATIONS

Investigations aimed at establishment of sink structures for excess vacancies have employed Transmission Electron Microscopy (TEM) techniques [32]. Much of the work has centered on establishing whether pre-existing sink structures or secondary defects can account for the associated annealing kinetics for any one or more types of thermal histories. These studies have encompassed various ranges in quench and/or quench-and-anneal temperatures.

In particular, numerous TEM studies that involve elevated temperature thermal treatments that result in excess vacancy concentrations have been conducted to

investigate the effects of quenching rates [40, 49 -51], quenching atmospheres [34, 66], ranges in specimen sink densities [88, 95, 96], and impurities [19, 23, 34, 94] on both the nature and densities of the observed vacancy defect precipitate structures and annealing behaviors in the vicinity of various defect sink structures [13-16, 21, 31, 35, 37, 52, 56, 57].

2.7 CRITIQUE OF PREVIOUS RESEARCH

2.7.1 Limited Ranges in Acquired Sets of Experimental Data

Although numerous experimental investigations and theoretical models have been reported concerning lattice defect energy determinations and annealing kinetics for quenched metals, the need has remained to acquire reliable defect electrical resistivity data associated with elevated temperature thermal treatments which collectively incorporate wider ranges in initial quench rate, quench and quench-and-anneal temperatures, isothermal annealing times, pre-existing sink densities, and specimen purity ratios. Collective acquisitions of extensive sets of such data have eluded attainment, primarily because of numerous experimental difficulties [18].

2.7.2 Examples of Experimental Problems Encountered

Problems encountered range from specimen burnout to severe temperature gradients and temperature instabilities along specimen gauge lengths [62], and other combinations of conditions that have prevented attainment of wide ranges either in quench rate, temperature, number of quenches, or reproducibility of quenched-in resistance values (e.g., in association with anomalous shifts in specimen residual resistance during a specimen's lifetime). Moreover, for configurations not involving in situ conditions, specimens may likely undergo thermal or mechanical strain during

quenching and subsequent handling that likely result in increases in specimen sink densities [13, 20, 33, 39, 60-61].

2.7.3 What needs to be achieved experimentally?

A primary and fundamental prerequisite for a successful investigation of elevated temperature lattice defect properties is the establishment of a quench/measurement system design (QMSD) capable of eliminating, or at least minimizing, the numerous difficulties highlighted above that have prevented attainment of controlled, reproducible, and extensive sets of quenched-in defect electrical resistance data upon which detailed analyses can be made. Only then would reliable determinations be made possible as to the nature, magnitude, and interrelationships among lattice defect properties, including further insights as to the parametric interrelationships that might subsequently be revealed.

3 OVERVIEW OF RESEARCH INVESTIGATIONS PERFORMED

3.1 GENERAL METHOD AND PLAN OF ATTACK

If a quench/measurement systems design could be achieved that would provide reproducible quenched-in defect electrical resistance data and do so over wide ranges in thermal treatment parameters, such as quench temperature, initial quench rate, and combinations of quench-and-isothermal anneal temperatures and annealing times, subsequent analyses of associated annealing kinetics data should be able to provide reliable quantitative assessments of parameters, such as vacancy formation energy, effective vacancy migration energy, instantaneous vacancy activation energies, absolute macroscopic sink efficiency, as well as insights as to interrelationships between vacancy defect chemical potential and sink efficiency.

Additionally, performing identical thermal treatments on a specimen both before and after subjection to direct deformation [14] mechanically introduced within the specimen's gauge length would likely provide insights as to the nature of dominant sinks for excess vacancies during elevated temperature conditions.

In short, only when sets of reliable, reproducible data have been both obtained and subsequently analyzed will critical assessments of the validity and extension of present models for equilibrium vacancy concentration, straight downquench and isothermal annealing kinetics, lattice defect energies, and numerous related parameters be realized.

---

[14] Refer to sub-section 9.3.1 for details about Direct Deformation treatments conducted during this research.

3.2 HIGH-LEVEL FLOWCHARTS OF RESEARCH INVESTIGATIONS

Graphical summaries are presented here which indicate specific objectives of feasibility studies [15] and primary investigations involving elevated temperature thermal treatments, supplementary thermal and thermal-mechanical treatments [16], and TEM investigations [17].

Presented in the following sub-sections are representative flowcharts of primary investigation data acquisition and data analyses associated with this research investigation.

3.2.1 Flowchart of Overall Research

Refer to Figure 2 -- which consists of twenty-two numbered boxes that highlight what objectives, associated treatments, analyses, findings, assessments, and parameter determinations were pursued during this specific research investigation.

3.2.2 Flowcharts of Elevated Temperature Thermal Treatments

Five principal categories of thermal treatments -- ST DQ, Q&A, LTA, HTA, and TC -- were performed on numerous high-purity 5-mil diameter gold wire specimens, and each of these thermal treatments is detailed somewhere within this document.

The flowchart of Figure 2 (with its 22 numbered boxes) indicates the natural sequence of experimental activities and associated assessments for each thermal treatment and extended thermal treatment included in the overall data acquisition program.

---

[15] See Chapter 4 for details.
[16] See Chapter 9 for details.
[17] See Chapter 10 for details.

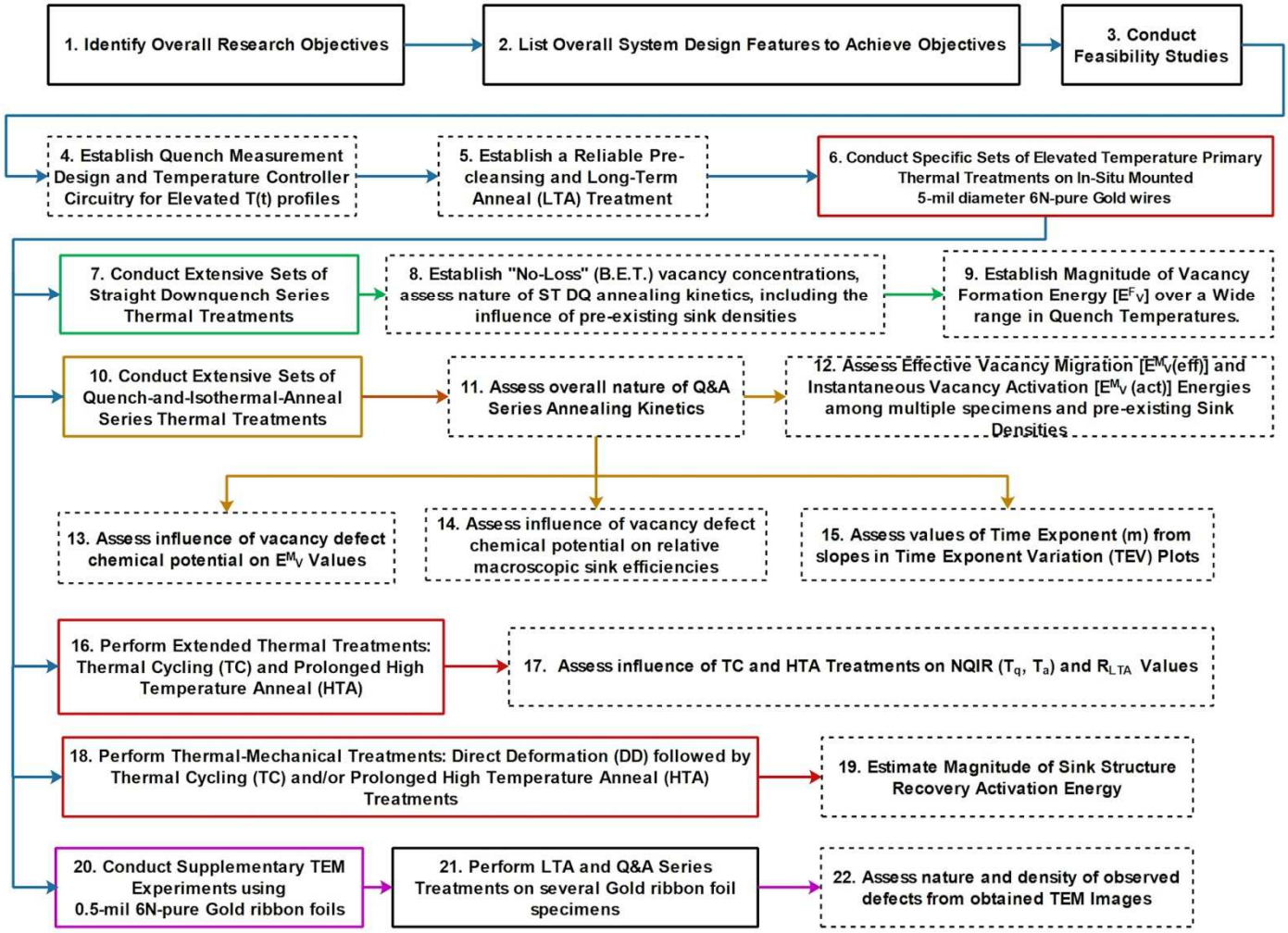

Figure 2. Overall Flowchart of Research Data Acquisition and Assessments

3.2.3 Flowcharts of ST DQ, Q&A, LTA, HTA, TC, and DD Treatments, Analyses, and Findings

Figure 3 shows the sequence for straight downquench treatments, Figure 4 provides a flowchart of ST DQ series treatments, Analyses, and Findings, and Figure 5 provides a high-level illustration of analyses made of data acquired from ST DQ series treatments.

Figure 6 is a flowchart of the overall procedure for specimen creation and resistance measurements.

Figure 7 provides a detailed flowchart of procedures associated with Q&A treatments.

Figure 8 provides a high-level flowchart of data analyses performed on data obtained from numerous Q&A series treatments performed on numerous 5-mil diameter 6N-pure gold wire specimens, including TEM-based examinations subsequently performed on 0.5-mil thick 6N-pure gold foils.

Figure 9 is a flowchart of LTA, TC, HTA, and DD Treatments and Analyses.

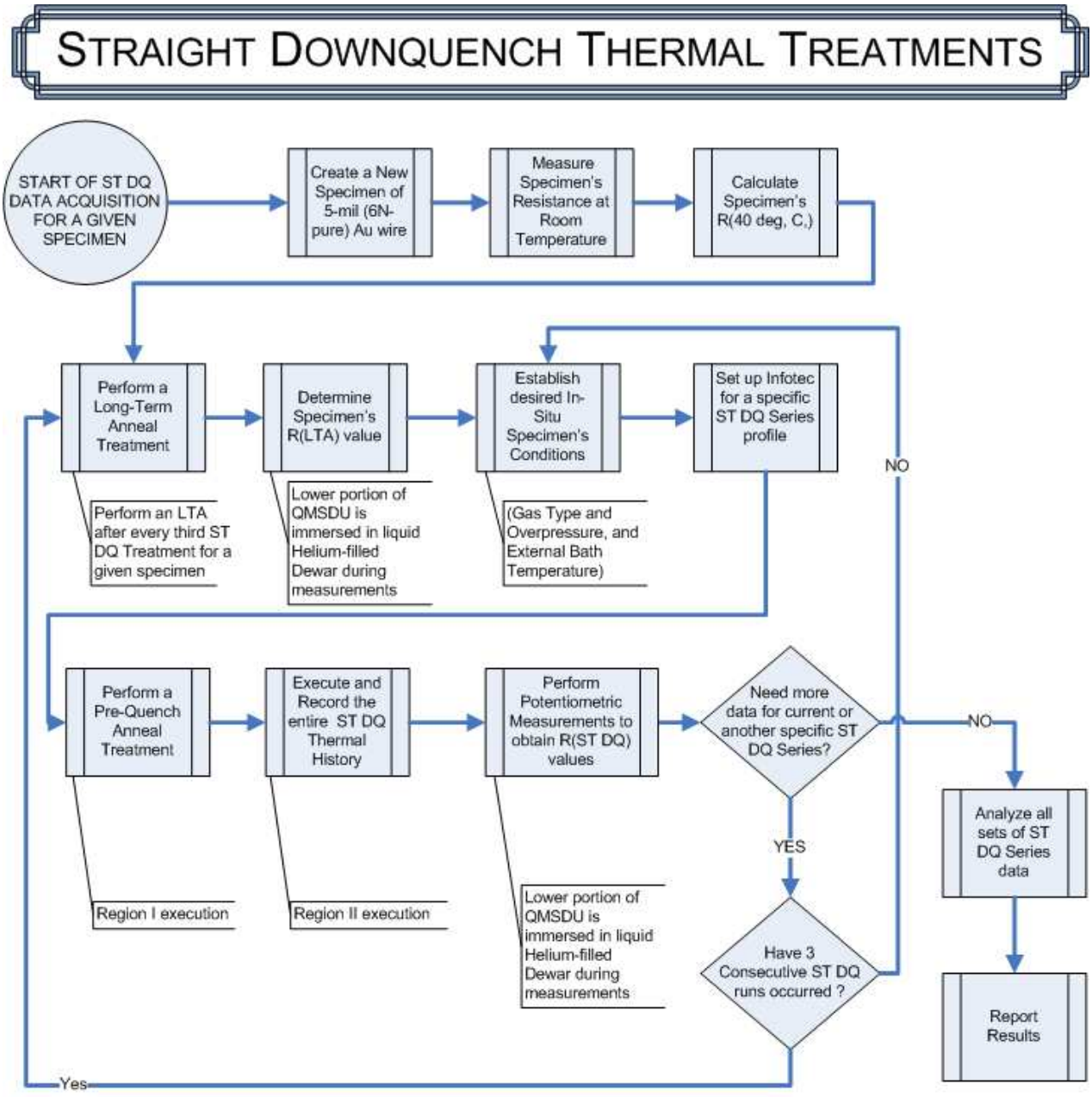

Figure 3. Flowchart for Straight Downquench Treatments

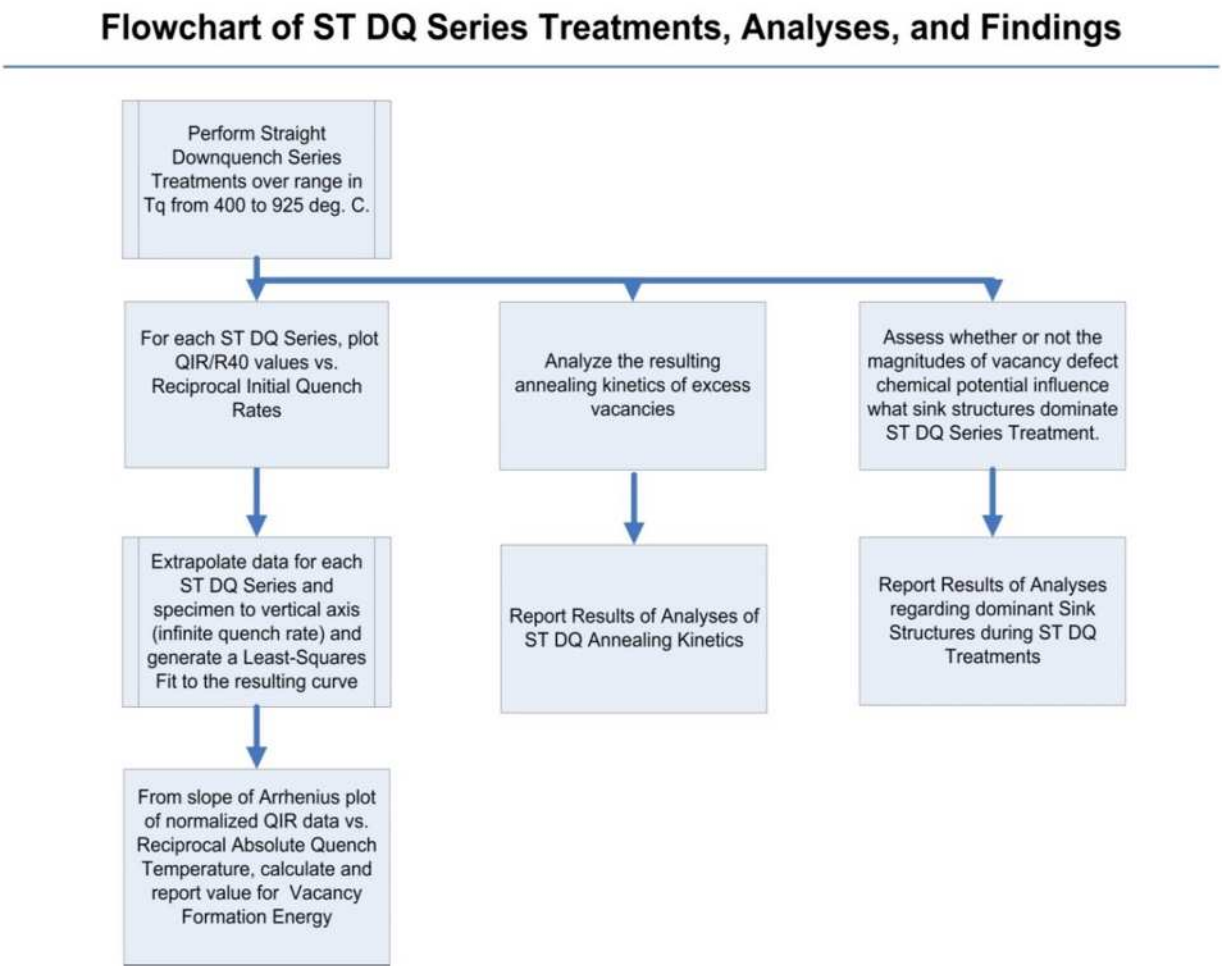

Figure 4. Flowchart of ST DQ Series Treatments, Analyses, and Findings

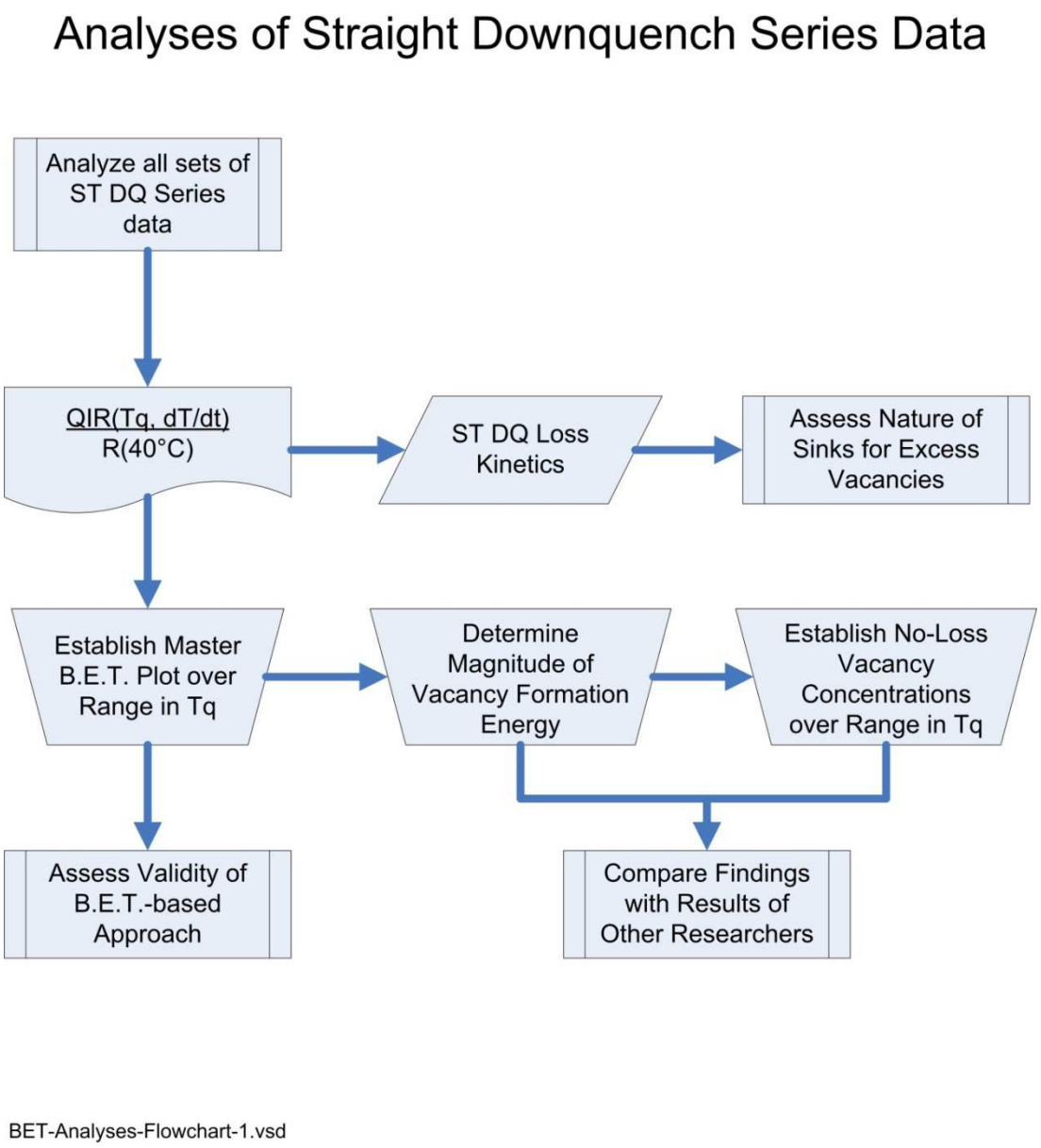

Figure 5. Flowchart for Analyses of Straight Downquench Data

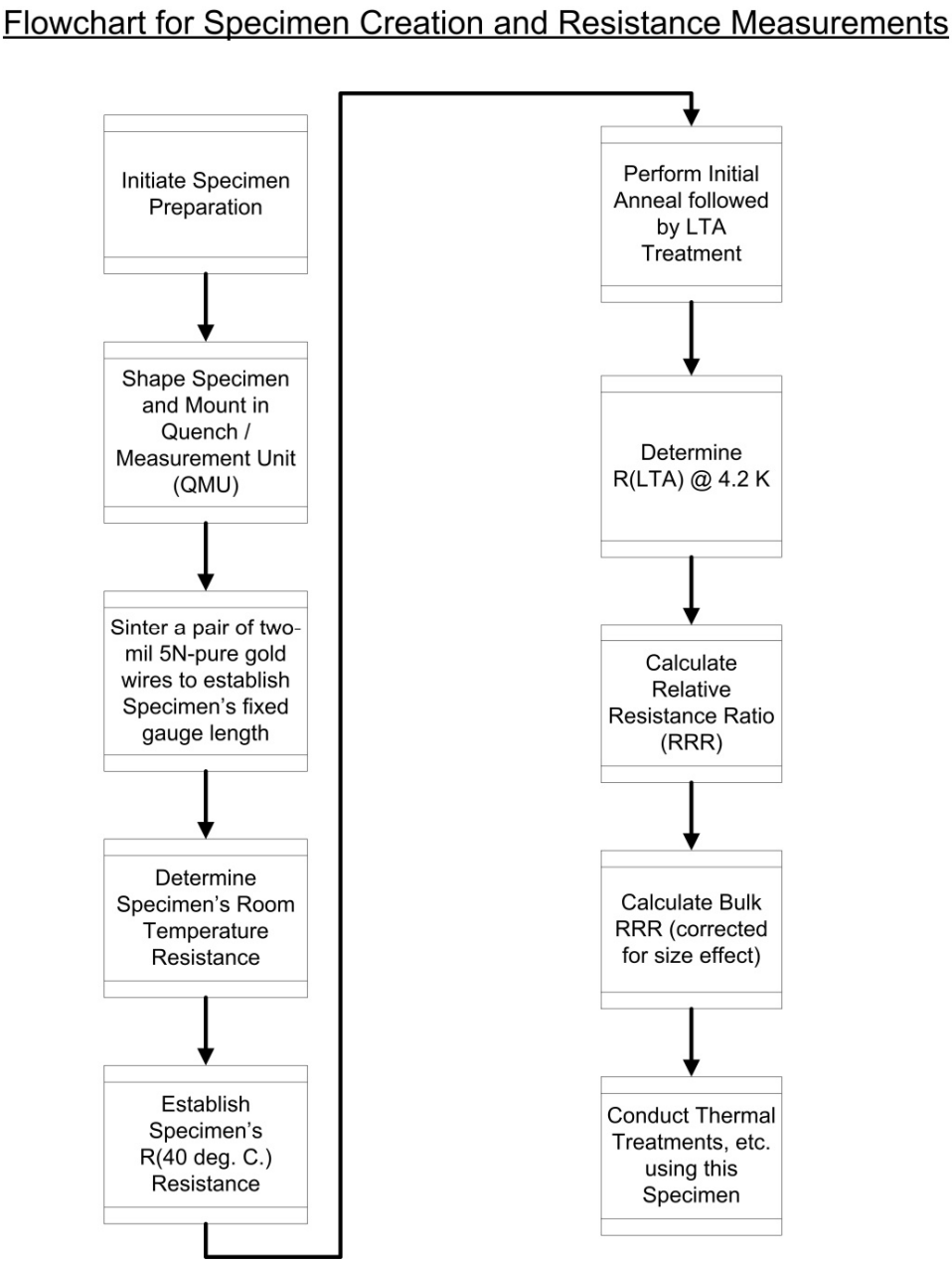

Figure 6. Flowchart for Specimen Creation and Resistance Measurements

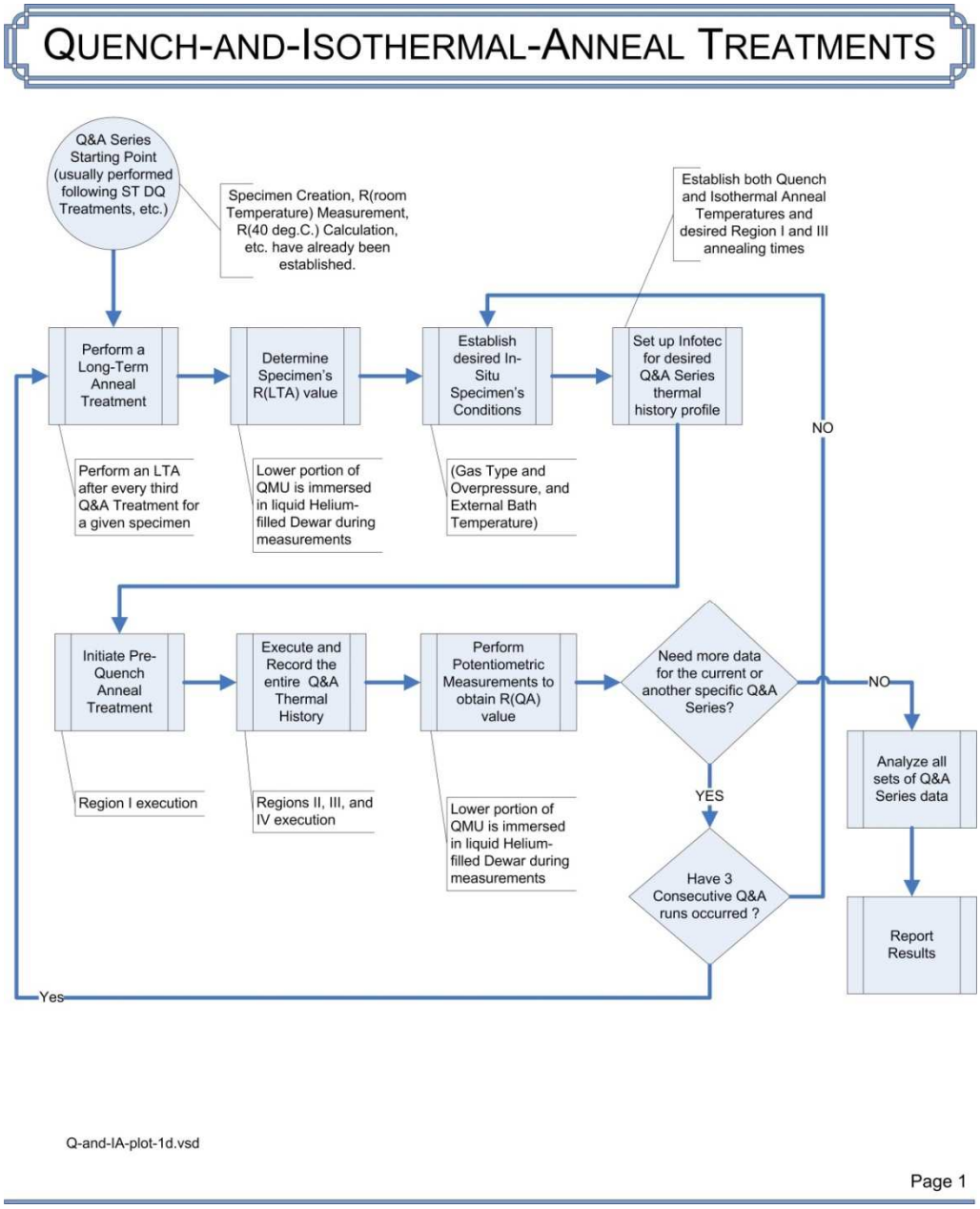

Figure 7. Flowchart for Quench-and-Isothermal-Anneal Treatments

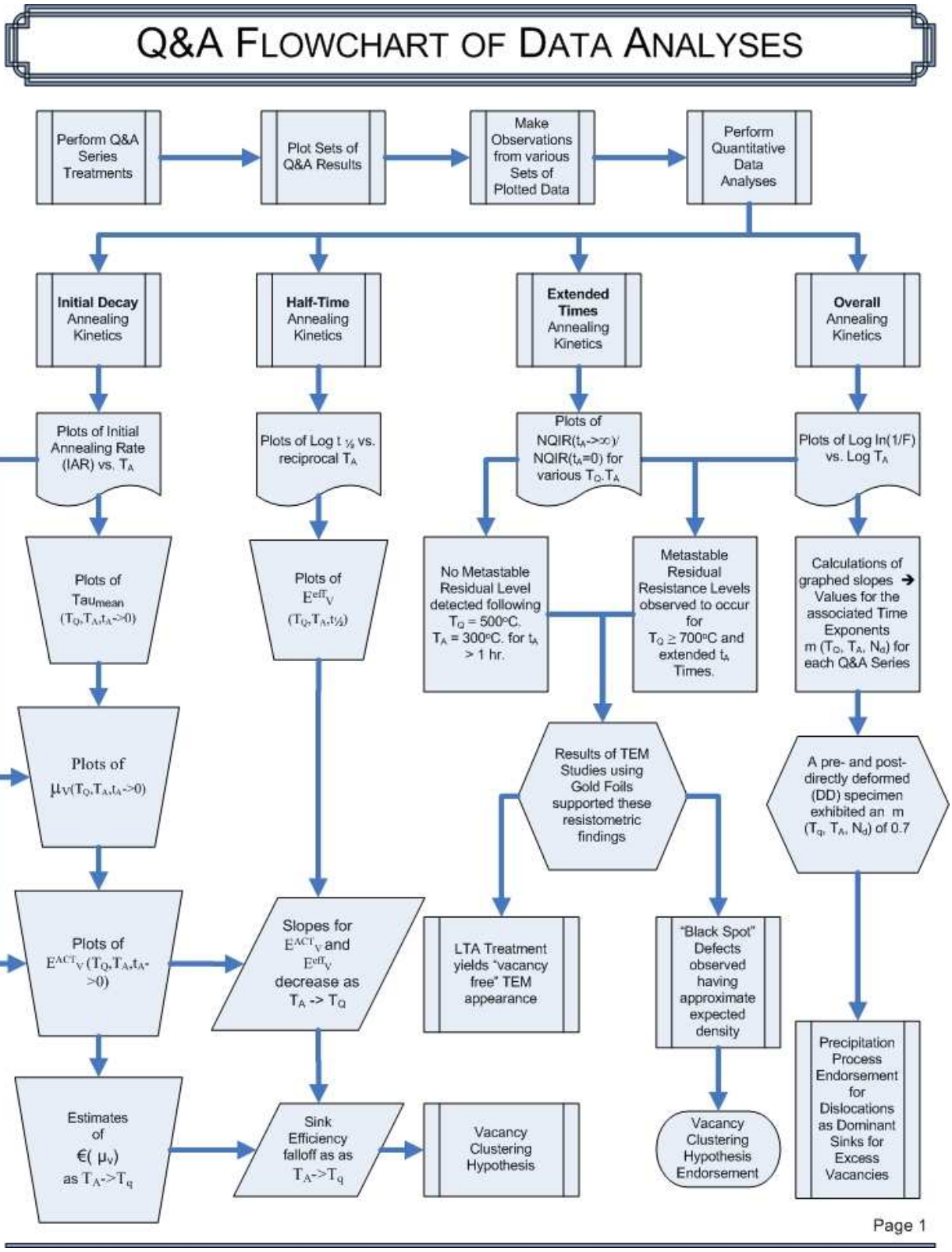

Figure 8. Flowchart of Analyses of Isothermal Annealing Kinetics

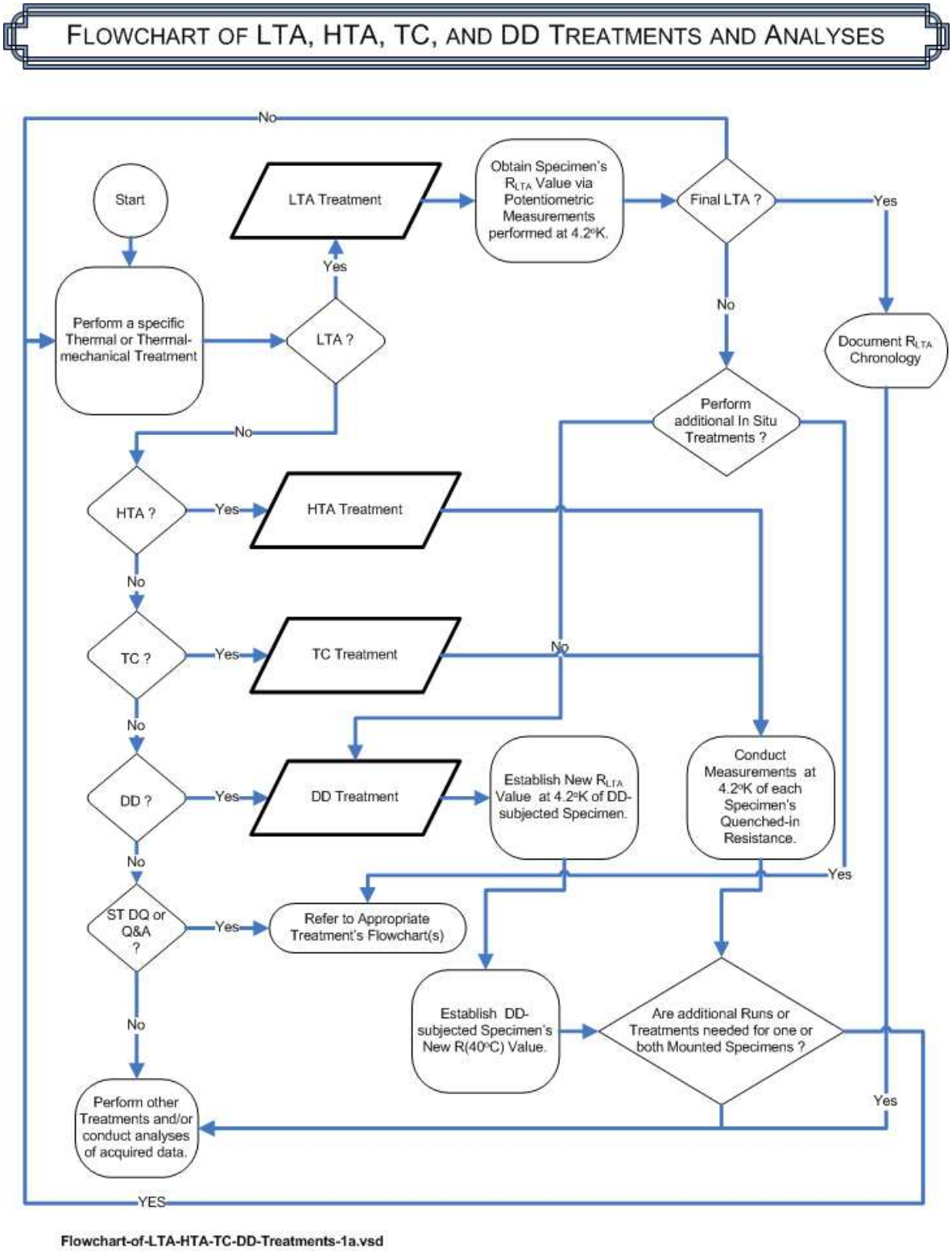

Figure 9. Flowchart of LTA, TC, HTA, and DD Treatments and Analyses

3.3 FOUR DISTINCT PHASES OF RESEARCH INVESTIGATIONS

As stated earlier, Figure 2 provides a simplified flowchart of the overall research data acquisition phases and associated assessments that comprised this research investigation.

The fundamental goal of assessing various lattice defect properties for pure gold was divided into four distinct phases of research that are summarized below.

3.3.1 Phase 1: Feasibility Studies

Feasibility studies (detailed in Chapter 4) were conducted to achieve the twelve specific objectives listed in Table 3.

The Quench/Measurement System Design (QMSD) Units were deemed essential for performing subsequent primary investigations. Figures 10 through 15 provide several views of construction details for what are referred to as QMSD Units #3 and #4.

Table 3. Twelve Goals and Specific Objectives of Feasibility Studies

Goal	Specific Objectives	Associated Achievement(s) and/or Comments
1	Uniform T(x,p) distributions for two different specimen shapes	Adoption of hairpin- and catenary-shaped shapes to allow for widest range in T_Q
2	Reliable Elevated Temperature Scale for gold	Adoption of Meechan and Eggleston R(T) scale for temperatures up to 941.2^{o}C
3	Stable T_Q (p,T_{bath})	Precision power supply selections and design of solid-state control circuitry combined with QMSD Units' design features.
4	Extension of adopted Resistance Thermometry Scale beyond 941.2^{o}C to melting point for gold	1.) Determination of melting point resistance ratio of 5.57 ± 0.01; 2.) Prolonged HTA thermal treatments as high as 1045^{o}C were made possible.
5	Negligible thermal strains of specimens during quenching	Use of 5-mil diameter gold wires and in-situ gas quenching assured negligible strain-induced vacancy contributions [13].
6	Wide range of quench temperatures	T_Q ranged from 400^{o}C to 925^{o}C with T_F values of either 0^{o}C or 78^{o}K, depending on the associated gas quench medium used.
7	Wide range of initial quench rates as a function of chosen quench environments	1. QMSD overpressures from 10 to 500 psig; 2. Final QMSD shell (bath) temperature T_F of 0^{o}C for nitrogen and 77^{o}K for helium gas quench media, respectively.
8	Wide ranges in Q&A series Treatments	From 925^{o}C down to 400^{o}C for T_Q; from 700^{o}C down to 20^{o}C for $T_{Q\&A}$; annealing times from 0.2 msec. to several hundred hours.
9	Establishment of reliable residual resistance values	Established and adopted a Long-Term Anneal (LTA) Treatment that exhibited reproducible R_{LTA}(4.2^{o}K) values per specimen
10	Elevated temperature In situ thermal treatments followed by potentiometric measurements	Creation of two QMSD units (#3 and #4) whose design, construction, associated wiring, and means for sealing met this objective
11	Reproducible quenched-in resistance values for each specimen and associated thermal histories	1) High-purity (6N) 5-mil diameter gold wire specimens are quenched in situ to minimize changes in sink density; 2) Low drift and magnitudes of thermal EMFs achieved as a consequence of employing longer lengths of external wiring for both QMSD units to assure wiring terminations at electrical connectors remained at room temperature. 3) Adoption of QMSD Unit's bath temperatures of 0^{o}C and 78^{o}K to assure that no post-run annealing occurs during preparing for potentiometric measurements that are performed at 4.2^{o}K.
12	Significant ranges in specimen sink densities	Created independent pairs of in situ specimens per QMSD unit that were subjected to differing degrees of mechanical handling either prior to mounting or post-completion of numerous ST DQ and/or Q&A series treatments.

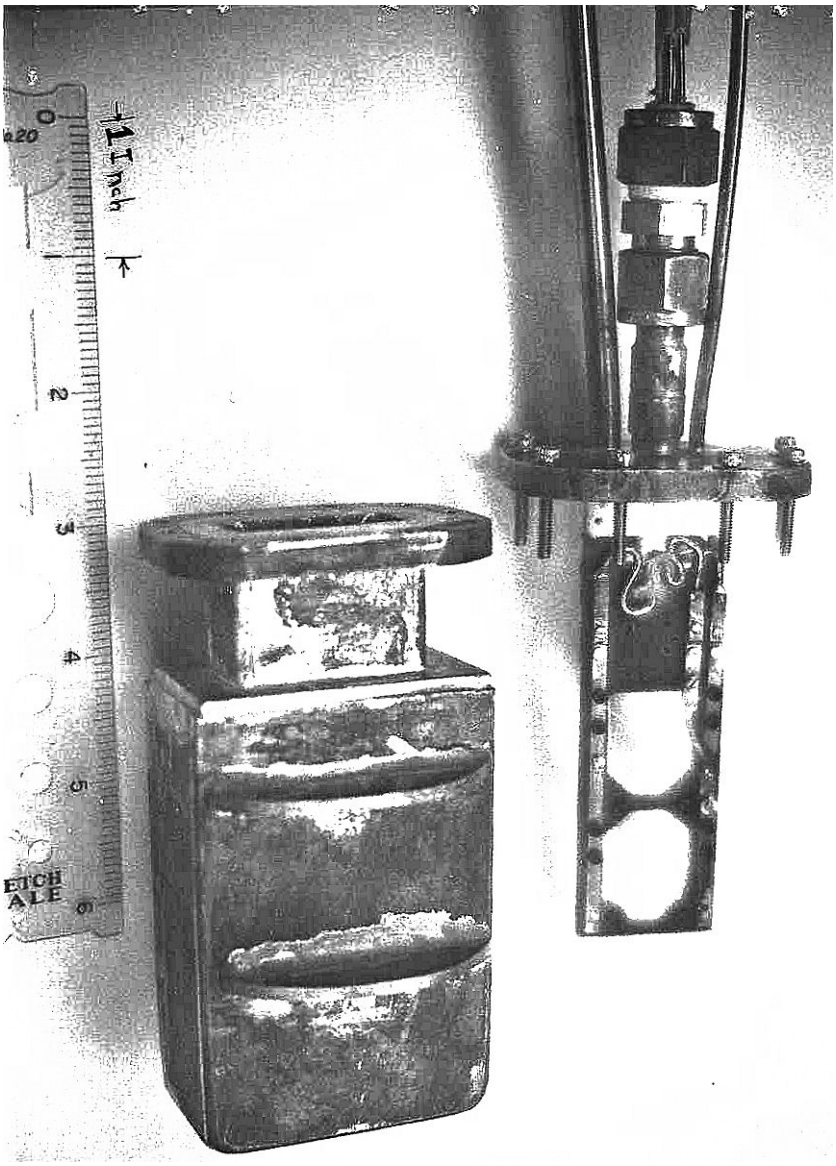

Figure 10. View of Quench/Measurement System Design Unit #4

Figure 11. Hand-held View of the Outer Shell of a QMSD Unit

Figure 12. Front and Back Views of QMSD Unit #4's Mounting Frame and Connections

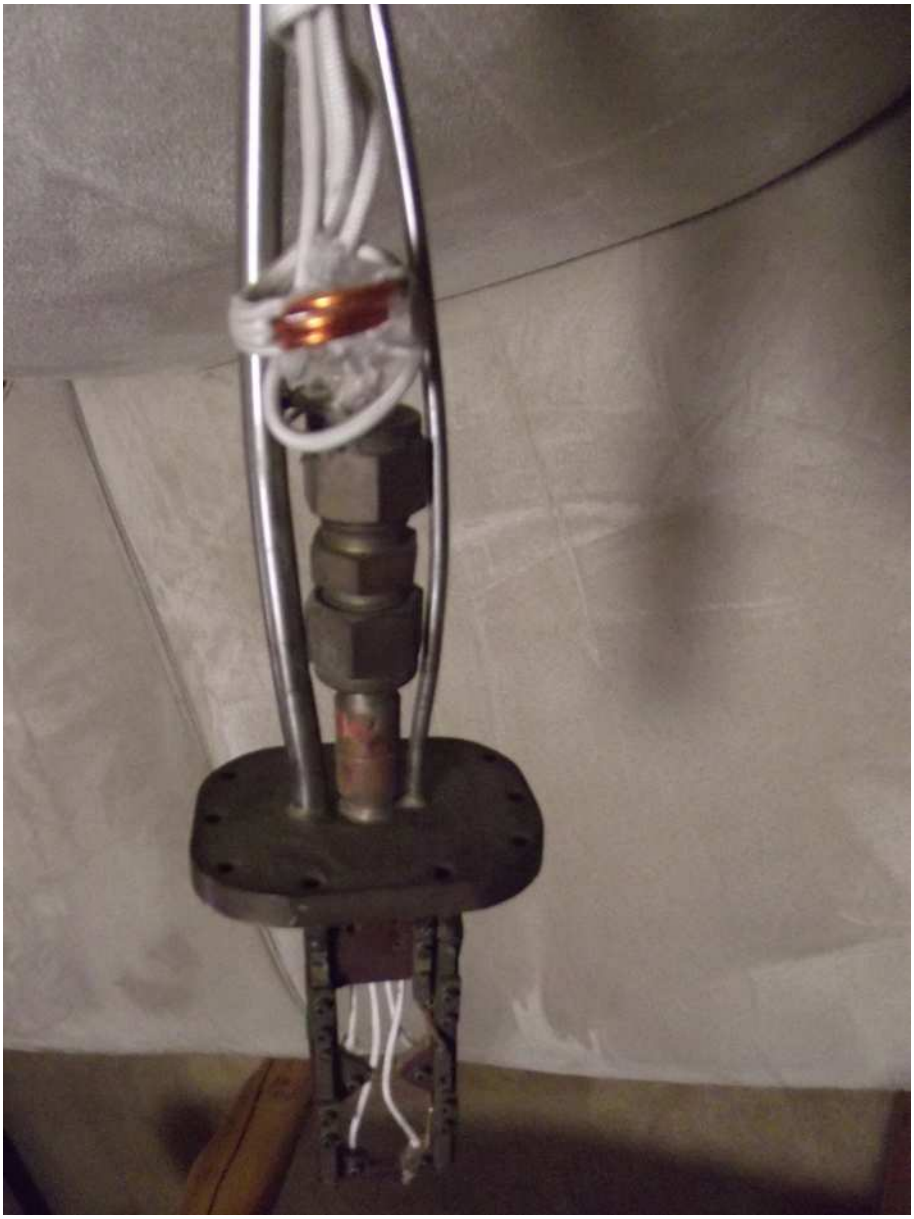

Figure 13. Heat Trap Loop above the QMSD Unit's Mounting Flange

Figure 14. QMSD Unit's Gas Supply Lines with Inlet and Outlet Valves and Electrical Wiring

Figure 15. Second View of QMSD Unit's External Wiring including its termination within a seven-conductor Amphenol Connector

3.3.2 Phase 2: Primary Data Acquisition via ST DQ, Q&A, and LTA Thermal Treatments

Extensive sets of quenched-in resistance data were obtained for 5-mil 6N-pure gold wire specimens for specific thermal treatments involving wide ranges in elevated quench temperatures, isothermal anneal temperatures, initial quench rates, and isothermal annealing times. Figure 3 and Figure 7 indicate the respective activities used for gathering, analyzing, and reporting of the acquired ST DQ and Q&A thermal treatment data.

Notably, as a prerequisite for assuring that reliable determinations of quenched in resistance values were made, an investigation was conducted that led to what is referred to herein as a Long-Term Anneal (LTA) thermal treatment that accomplishes two specific objectives, namely:

1) serves as a "cleansing anneal" intended to remove or at least minimize the retention and associated magnitudes of prior thermal treatment histories, such as secondary defects and clusters of vacancies, (refer to sub-section 4.4.4 for more details.) and

2) ideally would also result in achievement of "vacancy-free" residual resistance levels in specimens so treated. (Refer to Chapter 11 for more details.)

3.3.3 Phase 3: Two additional Thermal Treatments (HTA and TC), Thermal-Mechanical Treatments (DD + HTA and/or TC), and Supplementary TEM Examinations

These four supplementary investigations involved the following:

1. Five-mil diameter 6N-pure gold wires were subjected to prolonged High-Temperature Anneal treatments (see sub-section 9.3.3.1 for associated details).

2. Five-mil diameter 6N-pure gold wires were subjected to Thermal Cycling (TC) treatments (see sub-section 9.3.1.3.2 for associated details).
3. Five-mil diameter 6N-pure gold wires were subjected to Thermal-Mechanical treatments involving Direct Deformation (DD) (see sub-section 9.3.1).
4. Following completion of numerous sets of Long-Term Anneal treatments (see sub-section 6.4.1), Straight Downquench (ST DQ) treatments (see sub-section 6.4.3), and Q&A series treatments (see sub-section 6.4.4) -- all performed on five-mil diameter 6N-pure gold wires, a small number of half-mil thick 6N-pure gold ribbon foils were subjected to a few specific elevated temperature thermal treatments after mounting them in QMSD Unit #3 and performing LTA or specific Q&A thermal treatments which were followed by preparation for and submittal to supplementary Transmission Electron Microscopy examinations (for details, see Chapter 10).

3.3.4 Phase 4: Data Analyses, Observations, Findings, and Conclusions

Analyses were made of the extensive sets of data to obtain insights as to specific interrelationships among the associated parameters and variables.

Chapter 7 covers the Straight Downquench (ST DQ) experiments, Chapter 8 covers the Quench-and-Isothermal-Anneal (Q&A) experiments, Chapter 9 covers the thermal-mechanical (DD + HTA/TC) treatments, Chapter 10 covers the supplementary TEM experiments, Chapter 11 covers the LTA treatments, and Chapter 12 provides a summary of research investigation findings.

4 FEASIBILITY STUDIES

4.1 INTRODUCTION

Information presented in this chapter provides specific information relating to preliminary research activities that preceded the primary investigations outlined above and described in detail in subsequent chapters of this document.

These preliminary investigations were performed to establish a suitable quench/measurement system design employing resistometric monitoring of lattice defects via conventional potentiometric measurement techniques.

4.2 ESSENTIAL OBJECTIVE OF FEASIBILITY STUDIES

In advance of attempting to carry out any extensive sets of primary data acquisition involving either straight downquench (ST DQ) or quench-and-isothermal anneal (Q&A) treatments, it was deemed essential to conduct feasibility studies that would result in the establishment of QMSD designs (see sub-section 4.4.3 for details) that would collectively satisfy a number of specific goals and requirements. Refer to Table 3 for a listing of what was sought and ultimately achieved.

The two adopted QMSD Units (referred to as Units #3 and #4) [18] that evolved from these feasibility studies were subsequently employed for all primary studies involving straight downquenches, isothermal anneals, and supplementary thermal and thermal-mechanical treatments.

---

[18] The only distinction between the construction of these two QMSD Units is in the employment of a pair of stainless steel mounting arms that connect each of the smaller (#3000 series) specimen's leads to the pair of current-carrying bus bars (located along each side of Unit 3's Micarta frame as shown in Figure 17.)

4.3 CHARACTERISTICS ATTAINED FOR QMSD UNITS

The set of characteristics and associated feasibility studies that were pursued are enumerated below as well as listed in Table 3.

1. Uniform temperature profiles for a wide range in gas overpressures (see sub-section 4.4.1 for details) for each of two distinctly different specimen shapes (see sub-section 4.4.1.4 for details).
2. Selection of a reliable elevated temperature scale for gold [47]
3. Stable T_Q and T_A thermal history profiles (typically within ± 0.1°C)
4. Determination of melting point resistance ratio R(1063^{o}C)/R(40^{o}C) for gold (see sub-section 4.4.2 for details) and extension of Meechan and Eggleston's resistance thermometry scale from 941.2^{o}C to 1063^{o}C.
5. Assurance of negligible thermal strains during quenching [60]
6. Wide ranges in quench and isothermal annealing temperatures
7. Wide ranges in initial quench rates $(dT/dt)_{initial}$ (see sub-section 4.4.3.4).
8. Wide ranges in both quench and isothermal annealing temperatures
9. Reliable residual resistance determinations via an LTA treatment (see sub-section 4.4.4 for details).
10. Generated elevated thermal treatments that had reproducible quenched-in resistance data (determined from potentiometric measurements at 4.2^{o}K) for all specimens
11. Reproducible quenched-in resistance data were obtained for each specimen for associated thermal histories.

12. A significant range in specimen pre-existing sink densities was achieved over wide ranges in ST DQ and/or Q&A series treatments and based on observed NQIR losses.

4.4 SUMMARY OF RESULTS OF FEASIBILITY STUDIES

Summarized below are the principal findings from the feasibility studies conducted as a prerequisite to performing any in-depth experiments involving specific thermal and thermal-mechanical treatments.

Range in and reproducibility of quench conditions and quenched-in resistance data were achieved as a combined result of the following: 1) unique specimen shapes, 2) high resistance ratio specimens, 3) use of high-speed, high-accuracy thermal history data recording equipment, 4) design, creation, and employment of solid-state circuitry that served as a stable specimen elevated temperature controller, and 5) use of two pressurizable QMSD Units -- each constructed to allow for a) in situ gas quenching, b) achievement of a wide range in quench rates using helium and nitrogen gas media and gas overpressures of up to 500 psig, and c) exhibiting minimal drifts in and magnitudes of thermal EMF values even when either QMSD unit was immersed in a liquid helium-filled Dewar.

4.4.1 Uniform Specimen Temperature Distribution Requirement

4.4.1.1 Necessity for Establishing Optimal Specimen Shapes

The temperature distribution over the specimen gauge length, regardless of specimen size or shape, should be uniform in order to assure a uniform vacancy concentration. Since vacancy concentration varies exponentially with temperature, a non-uniform temperature distribution either prior to or during a quench would create

substantial vacancy concentration gradients. Moreover, any thermal gradients that might occur during a quench from elevated temperatures could possibly result in thermal stresses that might also increase the sink density within the specimen. Additionally, the retained vacancy concentration could be skewed because of temperature distribution non-uniformities established during a quench, and the monitored resistometric contributions might not reflect the mean vacancy concentration.

4.4.1.2 Addressing Temperature Distribution Shifts

To achieve a wider range in initial quench rates for a given specimen necessitated incorporation of increased gas overpressures for the QMSD units (which are discussed in sub-section 4.4.3) and also the adoption of two primary shapes (discussed in sub-section 4.4.1.4) that were found capable of maintaining a uniform temperature distribution over the gauge length portion for all combinations of gas overpressures.

4.4.1.3 Specimen Shapes Ruled Out

Specimens shaped as shown in Figure 16 [19] approximated what had been adopted by Wang, et al. [63] for their research in this same area. Unfortunately, those specimens were observed to undergo severe temperature profile shifts and redistributions even with gas overpressure values of less than 50 psig.

[19] Figure 16 was excerpted from Reference [62].

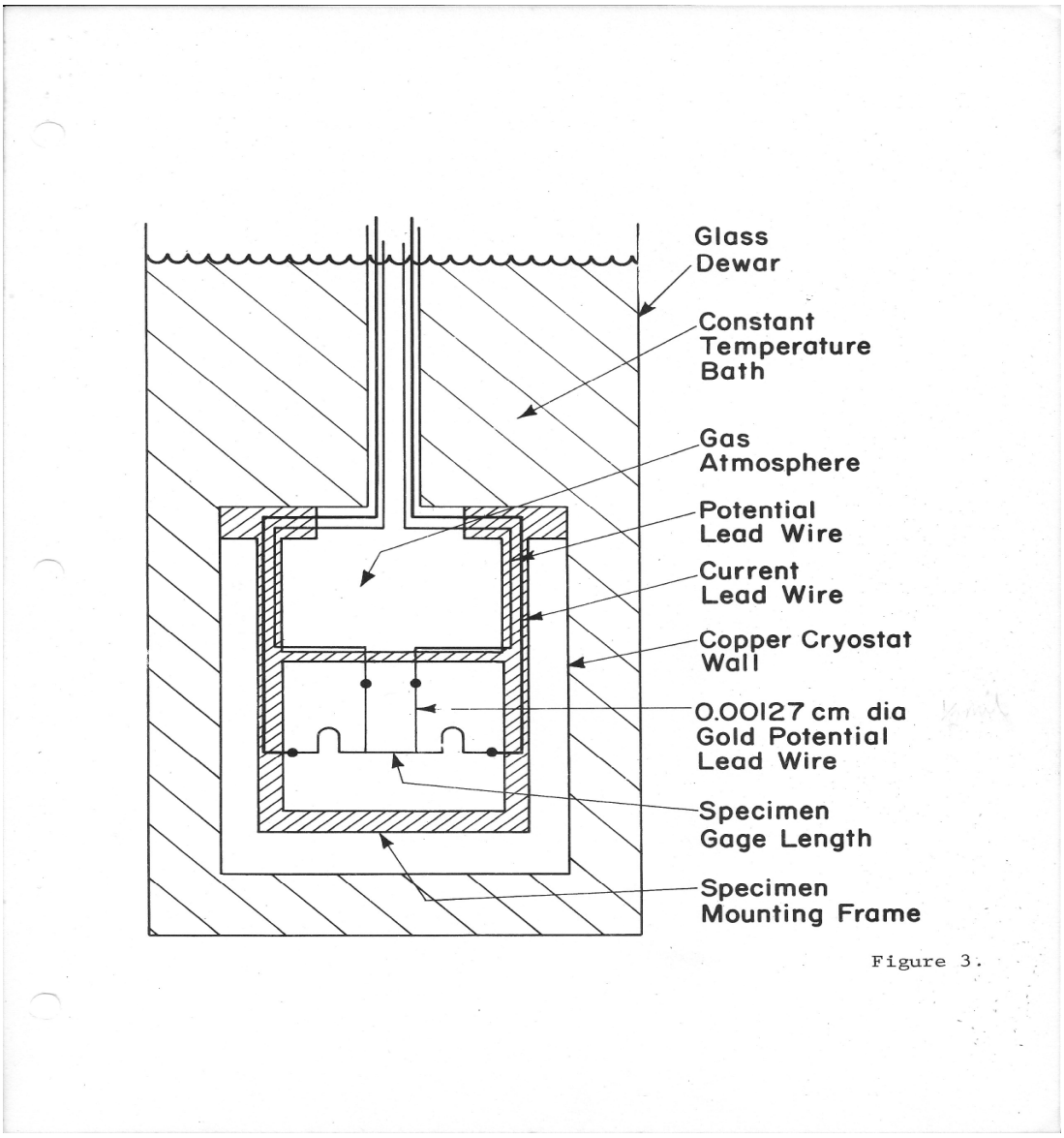

Figure 16. Schematic Representation of Specimen Shape and Quenching Cryostat's Design (cited as Figure 3 in Wang, et al. [63])

Unfortunately, the central portion of these specimens became cooler relative to the vertical segments located closest to the central portion of the overall shape [20].

[20] A specimen of the shape in Figure 16 was first established to have a uniform temperature distribution under free-air conditions. Next, the already mounted specimen was placed within the outer shell of a QMSD unit, sealed and pressurized to 120 psig with helium gas, lowered into a Dewar filled

In one case involving a 100 psig overpressure condition was in effect and an average temperature of 750^{o}C existed within the central portion of the wire, temperature differences of as much as 100°C were noted to be present [21].

Also, gold ribbon foils of from one-half to two mils thickness and one-eighth to three-eighths inches in width were separately subjected to quenches in air. Here, too, although initially uniform temperature distributions were established (by careful shaping near the current bus bar terminations) prior to quenching, severe temperature non-uniformities were observed to occur during the actual quenches and the associated quench rate was estimated to be moderately slow (about 800^{o}C/sec.). As a consequence of such observations, both of these specimen shapes were dropped from further consideration.

4.4.1.4 Adopted Hairpin- and Catenary-shaped Specimen Shapes

Figure 17 illustrates the two distinct shapes that proved capable of maintaining uniform temperature distributions over the range of gas overpressures employed during the various elevated temperature thermal treatments.

---

with liquid nitrogen gas, and slowly heated. The gauge length average temperature was calculated in the normal resistance thermometry manner during this time, and the specimen burned out at an average temperature of but 527 degrees C indicating that a significant shift in temperature distribution must have taken place. Subsequent examination of the specimen revealed that burnout had occurred at a distance of more than 1/4 inch outside the specimen's gauge length.

[21] Optical pyrometry methods were used to view the heated specimen which was kept inside a pressurizable Pyrex vessel whose outer shell was simply left at room temperature.

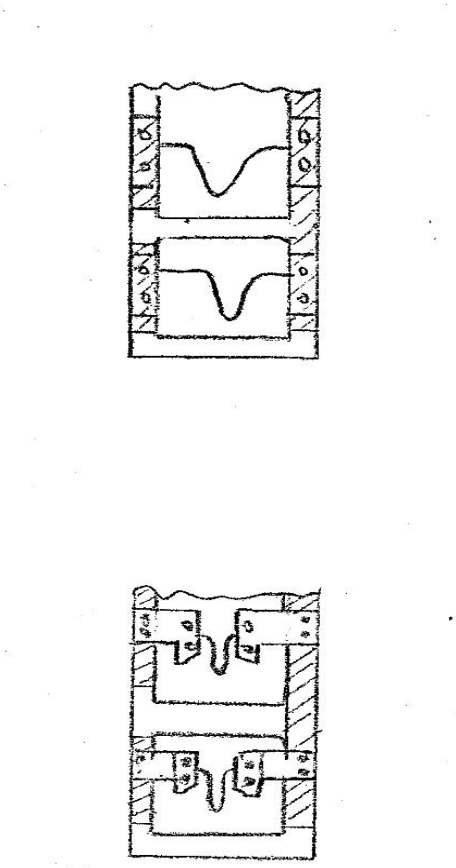

Figure 17. Sketches of Catenary-shaped and Hairpin-shaped Specimens mounted in their Micarta Frames for QMSD Units #4 and #3, respectively.

4.4.1.4.1 Detailed Descriptions of each Adopted Specimen Shape

1. CATENARY-SHAPED: Each specimen was mounted between a pair of bus bars attached to the Micarta frame incorporated within QMSD Unit #4. The principal application for this geometry was for the lower range in quench temperatures where maximal sensitivity to quenched-in vacancies would be essential to achieve. Gauge lengths of catenary-shaped specimens were as much as one centimeter, and only specimens exhibiting extremely uniform temperature distributions could be safely heated to temperatures of over 900^{o}C within the specimens' gauge lengths.

NOTE: With but one exception, namely that of specimen 4005[22], only catenary-shaped specimens were mounted in Quench/Measurement System Design (QMSD) Unit #4 and used throughout this research investigation.

2. HAIRPIN-SHAPED: This specimen shape was selected especially for use at the high-end of quench temperatures, namely 925^{o}C, although thermal treatments from lower quench temperatures were also performed. Each of two hairpin-shaped specimen were mounted between a pair of stainless steel arms connected to a pair of bus bars attached to the Micarta frame incorporated within QMSD Unit #3.

Specimen gauge lengths were selected to be small (nominally less than 0.25") for two reasons: First, to minimize the chance of burnout within the gauge length due to a hot spot; second, to keep the specimen's maximum voltage drop at the highest quench temperatures less than 0.6 volt in order to meet input voltage restrictions imposed by the Infotec data acquisition system's input voltage circuitry design.

Note that by comparison with the catenary-shaped specimens, hairpin-shaped specimens were of much smaller overall size, had smaller gauge lengths, and had significantly improved heat sink capability because of the stainless steel arms being clamped within a centimeter of the potential leads.

4.4.1.4.2 Temperature Distributions of Adopted Specimen Shapes

Direct visual observations of the temperature profiles associated with either adopted specimen shape were made periodically on a number of separate occasions. No noticeable temperature gradients were observed in either the radial or

[22] After specimen 4003 had burned out, a pair of stainless steel extension arms were created and mounted to the lower pair of buss bars within QMSD Unit #4 and specimen 4005 was created to be hairpin-shaped and subsequently was mounted in that location within the overall Micarta frame.

longitudinal directions upon quench initiation in order to assure that uniform (macroscopic) excess vacancy concentrations throughout the entire specimen gauge length would be maximized.

4.4.2 Determination of Melting Point Resistance Ratio for Gold

4.4.2.1 Reasoning underlying achievement of this specific objective

Because employment of elevated temperatures above 941.2^{o}C would be required to conduct either High Temperature Annealing (HTA) and Thermal Cycling (TC) treatments on specimens yet avoid the possibility of specimen burnout during such thermal treatments, it became necessary to conduct a feasibility study that would accurately determine experimentally an actual value for the melting point resistance ratio, R(1063^{o}C)/R(40^{o}C), for gold [23]. To achieve this objective involved creation and sacrificing due to eventual burnout (ideally somewhere with a specimen's gauge length) of a number of five-mil diameter gold wire specimens.

4.4.2.2 Achievement of Temperature Scale Extension to 1063^{o}C

Thirteen specimens were created and sacrificed as part of one specific feasibility study that was focused on establishing a value for the melting point resistance ratio for gold.

Results obtained for these thirteen specimens that were each gradually heated until undergoing burnout are listed in Table 4. Several specimens yielded close agreement, and it was noted that those specimens had melted somewhere within

---

23 Refer to Table 3 which cites Objectives 1 and 2 in regard to this matter.

their respective gauge lengths during this series of tests. Moreover, in most cases, spheroidization was clearly observed to have occurred as well. See Figure 18.

Table 4. Specimen Melting Point (Burnout) Resistance Ratio Determinations

Specimen Numbers	R(Burnout)/R(40°C) Ratios [24]
3005A	4.753
3005B	5.262
3005C	5.0055
3005D	5.3763
3005F	5.5578 (*)
3005P	5.566 (*)
3006A	4.797
3006B	5.403
3006C	5.1936
3006E	5.581 (*)
3006F	5.186
3006P	4.9656
3014	5.574 (*)

Table 4 lists the thirteen values obtained and from which a melting point resistance ratio R(1063°C)/R(40°C) equal to 5.57 ± 0.01 was established.

NOTE: A calculation made using a wholly independent equation established by Laubitz [232] in a study of transport properties in gold resulted in a value for the melting point resistivity ratio for gold of 5.71 which is within 3% of this research finding of 5.57.

[24] Starred (*) values correspond to acceptable criteria, namely: melting or spheroidization occurred somewhere within that five-mil diameter gold wire specimen's gauge length. Unstarred values were associated with specimens that had burned out somewhere outside their respective gauge lengths.

Figure 18. Example of Spheroidization of one specimen during the Melting Point Resistance Ratio Determination Investigation

The experimentally determined melting point value was subsequently used to extend Meechan and Eggleston's [47] well-established resistance thermometry scale for gold from its end point of 941.2^{o}C up to gold's melting point of 1063^{o}C.

4.4.2.3 Curve Fitting of Temperature Scale from 941.2^{o}C to 1063^{o}C

Generation of a curve that closely represents the desired R(T)/R(40^{o}C) extension for temperatures ranging from 941.2^{o}C to 1063^{o}C was pursued. Incorporation of both an additional T^3 component and a vacancy contribution to the resistance ratio values beyond Meechan and Eggleston's elevated temperature resistance scale ratios [25] was deemed essential to achieving this objective.

Provided below is the resulting Eqn. (4-1) with its respective coefficients and vacancy component contribution that was found to closely represent the desired

---

25 A least-squares fit for this extension of the Meechan and Eggleston scale yielded a value for the vacancy formation energy E^{F}_{V} of 0.9744 eV.

curve for normalized resistance ratio R(T)/R(40^{o}C) extensions from 941.2^{o}C (1214.36^{o}K) to 1063^{o}C (1336.16^{o}K). Note that it presumes the specimen's gauge length temperature is both uniform and restricted to the range from 1214.36^{o}K to 1336.16^{o}K.

$$R(T)/R(40^{o}C) = 4.70 + B' T + C' T^{2} + D' T^{3} + 227.06 \exp(-0.9744/kT) \quad \text{Eqn. (4-1)}$$

where $B' = (3.41 * 10^{-6})/^{o}K$; $C' = (1.88 * 10^{-7})/(^{o}K)^{2}$; $D' = (2.2 * 10^{-10})/(^{o}K)^{3}$; and k is equal to Boltzmann's constant ($8.6167 * 10^{-5}$ eV/^{o}K).

Table 5 lists a number of respective resistance ratios that were calculated using Eqn. (4-1), and Figure 19 illustrates graphically the associated extension of Meechan and Eggleston's data beyond 941.2^{o}C up to the melting point (1063^{o}C) for gold [26].

The values associated with Figure 19 over the temperature range from 700^{o}C to 1063^{o}C are provided in Table 5.

[26] Extension of Meechan and Eggleston's results to 1063^{o}C proved crucially important for being able to conduct prolonged High Temperature Annealing (HTA) treatments (see Section 9.2 for specifics) involving temperatures around 950^{o}C or higher. In actuality, only one instance of specimen burnout occurred during an HTA treatment.

Table 5. Extension of Meechan and Eggleston's Temperature Scale for Gold from 941.2°C to 1063°C

Temperature (°C)	R(T)/R(40°C)
700	3.503
750	3.733
800	3.973
825	4.097
850	4.2215
875	4.3505
900	4.480
925	4.616
941.2	4.7042
950	4.75
975	4.88
1000	5.03
1025	5.21
1040	5.34
1050	5.43
1063	5.57

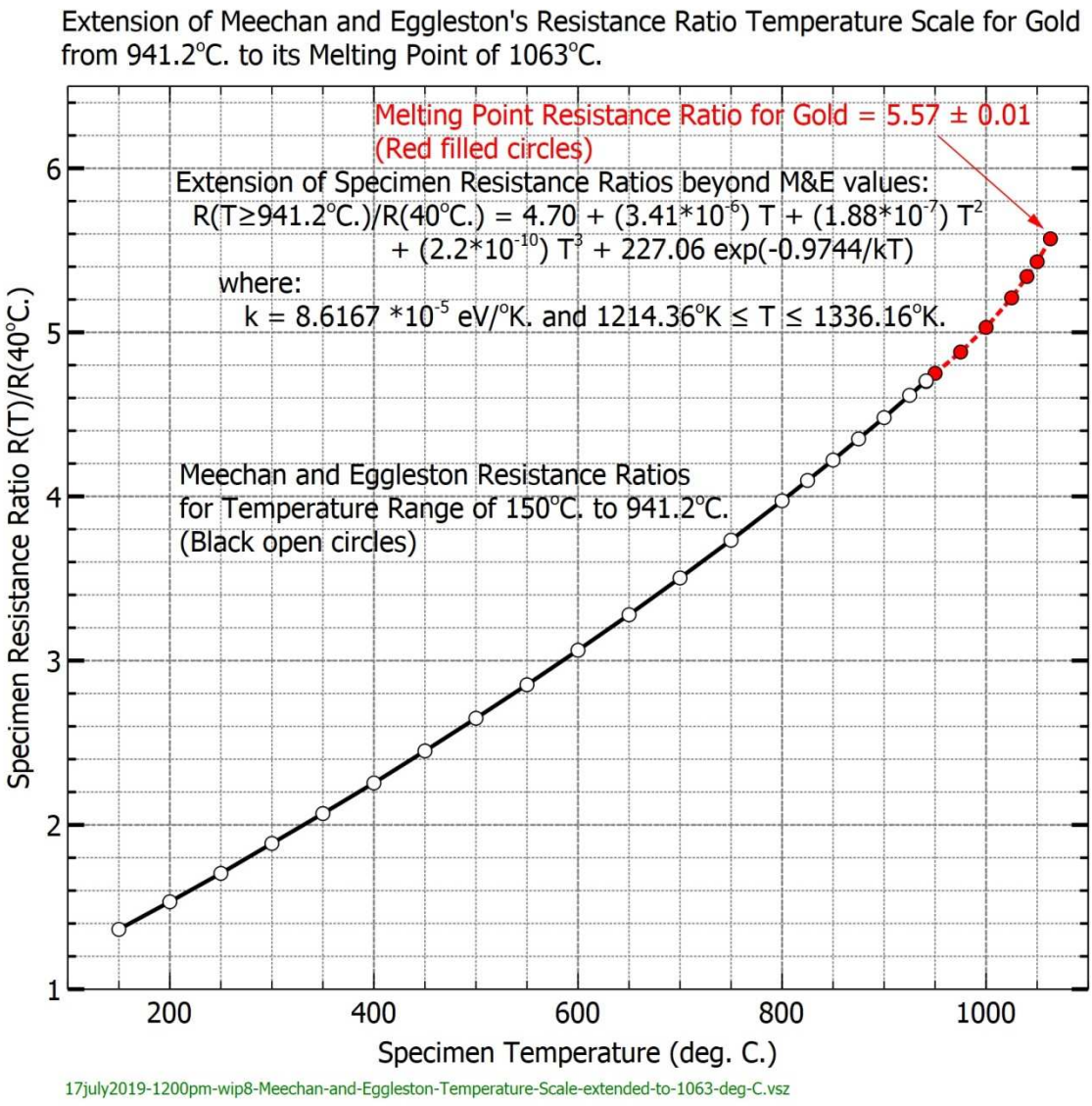

Figure 19. Extension of Meechan and Eggleston's Temperature Scale for Gold from 941.2°C to its Melting Point of 1063°C

4.4.3 Quench/Measurement System Design Highlights

4.4.3.1 Introduction

A primary and fundamental prerequisite for successful investigation of elevated temperature lattice defect properties was the establishment of two Quench/Measurement System Design (QMSD) units capable of either eliminating or at least reducing problem areas that have prevented attainment of controlled, reproducible, and extensive sets of quenched-in defect electrical resistance data.

4.4.3.2 QMSD Construction Details

As cited earlier, Figures 10 through 15 illustrate the general design and construction details associated with two QMSD units that were used for in situ gas quenching of five-mil diameter gold wires (See Figure 20) [27].

4.4.3.2.1 QMSD Shell, Pressure Seal, and Electrical Feedthrough

The shell was made from 0.093 inch yellow brass stock joined by hard solder to form the outlined shape. Reinforcement ribs of the same stock material were hard-soldered on the sides to prevent buckling under sealed high pressure (up to 500 psig) gas quench media during elevated temperature ST DQ and Q&A series thermal treatments.

---

[27] This wire size was selected based on the cited Figure (excerpted from Reference [13]) which illustrates how 5-mil diameter gold wires quenched in situ using gas quench media satisfies the criterion for negligible contributions from strain-induced vacancies.

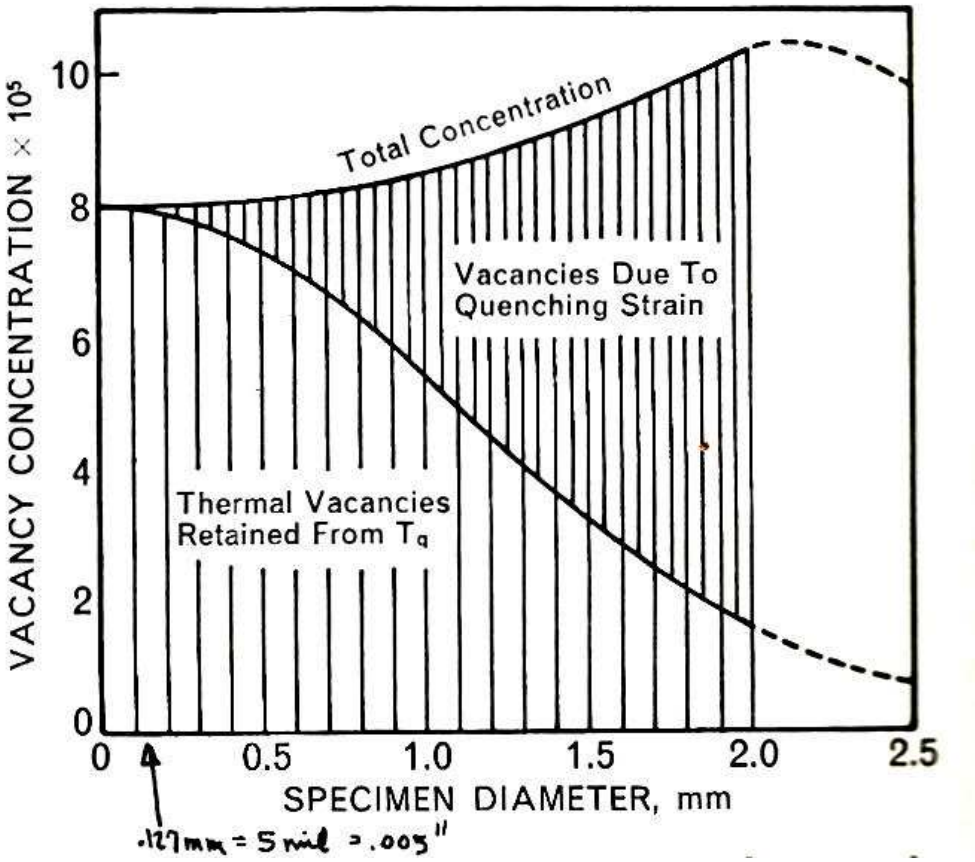

Figure 20. Avoidance of Generation of Vacancies due to Quenching Strain

To construct the apparatus such that electrical connections could be made to the two specimens that would be mounted inside the QMSD unit's outer shell required establishment of a combination pressure seal/electrical feedthrough.

Figure 13 shows the design adopted for this critically important portion of each quench unit. Seven enamel-coated copper wires pass through the cylindrical section of 1/4 inch diameter Teflon material. Three #14 AWG size wires are used for current-carrying purposes, and four #24 AWG size wires are used in pairs to monitor the voltages across the two specimens' gauge lengths. The three #14 AWG wires were used to supply current to the two gold wire specimens, one current lead being

common to the two specimens. These heavy copper current wires were hard-soldered to the ends of three current bus bars between which the specimens were clamped (see Figure 17 [28]). The four #24 wires were terminated at ten-mil gold wires that connected to two pairs of potential leads of two-mil 5N-pure gold wires. All seven wires were electrically insulated from both the quench unit's shell and its upper flange. A Micarta mounting frame for the specimens provided convenient mechanical support for terminations of all wiring within the quench unit.

Finally, a Swagelok® fitting served as the primary seal for the Teflon insulator-feedthrough. Stycast 2850GT epoxy [29] was also incorporated within the Swagelok assembly as an additional sealing agent for the gas overpressures of up to 500 psig.

A seal between the two flanges joining the shell body to the upper portion of the QMSD Unit was created by tightening uniformly the ten #4-40 steel machine screws following placement of a closed ring of fifty-mil diameter Indium wire in the area between the ring of screw holes and the shell opening.

4.4.3.2.2 Gas Quench Media and Overpressure Selections

Ten-mil thick stainless steel thin-wall tubing served as the inlet and outlet channels for gas flow during purging operations of a sealed QMSD Unit. After connecting the desired gas pressure tank supply to the inlet valve and initiating a low-pressure flow of the selected gas to begin passing through the now-assembled

---

28 The two QMSD units (referred to as #3 and #4) created were distinguished by one difference, namely: Unit #3 employed two pairs of stainless steel mounting arms which served as extensions of the current bus bars to accommodate the smaller hairpin-shaped (3XXX-numbered and specimen #4005) gold wire specimens, whereas in Unit #4 the larger catenary-shaped (4XXX-numbered except for specimen #4005) gold wire specimens were mounted directly to the current bus bars. Refer to Figure 17 for sketches of these respective mounting differences.

29 Supplied by Emerson-Cummings, Canton, Massachusetts.

QMSD Unit, the outlet valve was closed, and the pressure tank regulator was adjusted until the desired overpressure was reached [30].

4.4.3.2.3 Factors taken into account to address Thermal EMF-related Matters

Both the drift in and magnitude of thermal emfs associated with potentiometric measurements performed at liquid helium temperatures were minimized by 1) using identical materials for the potential leads and large heat sink current bus bars within the quench unit and 2) incorporating a heat trap loop above the Swagelok feedthrough that exited above the top of the QMSD unit, and 3) employing a six-foot-long length of electrical wiring contained within a heavy duty plastic sleeve that is terminated at a seven-pin Amphenol connector (see Figure 15). The long length was adopted in order to avoid any possibility for altering the temperature of the wire terminations within the connector (particularly during the act of immersion of the QMSD unit into a double-walled Dewar filled with liquid helium for subsequent potentiometric measurements).

As a consequence of these design factors being in place, stable values between 0.1 and 0.4 microvolts were encountered for all specimens during potentiometric measurements at liquid helium temperatures, and these thermal emf magnitudes were found to remain nearly constant (generally constant to within 0.02 μV).

A 9-pin external Amphenol connector served as the termination for the electrical wiring that exited the uppermost portion of the stainless steel tubing housing. The wiring was chosen to be several feet in length to avoid any possibility for introducing

---

[30] By design, gas overpressures of at least 500 psig could be employed safely for the adopted system construction.

thermal EMFs when the QMSD unit is lowered into the liquid helium-filled Dewar for subsequent potentiometric measurements [[31]].

4.4.3.3 Assuring Negligible Joule Heating of Specimens

Determination of any given specimen's quenched-in resistance must be assured in part by making certain that a given specimen's actual temperature during the potentiometric measurements were kept at 4.2^{o}K while the associated potentiometric measurements were performed.

To accomplish this, the measuring current chosen to pass through any specimen was set to a value of one-third of whatever had previously been established to result in Joule heating when that specimen had been mounted within a sealed QMSD kept immersed in liquid helium contained within a large Dewar.

4.4.3.4 Initial Quench Rates for In-situ Gas Quenches

The following characteristics were noted for Initial Quench Rates (IQRs):

1. An upper limit of 500 psig was chosen when plotted data revealed a power law dependency of initial quench rates upon gas quench media overpressure (see Figure 21) that would require a 10,000 psig helium gas overpressure to achieve a doubling of the IQR(500 psig) value.

2. A linear relationship was found to apply between calculated initial quench rates and the pre-quench power dissipation for a given quench temperature. (see Figure 22.)

---

[31] Reason: A five-foot length of external wiring harness served to prevent any temperature changes from occurring at the Amphenol-socketed termination to which the 6-dial Leeds & Northrup potentiometer and power supply were connected.

3. IQRs ranged from less than 10^3 degrees Celsius per second for catenary-shaped specimens of much larger overall size were used and exceeded more than 2 x 10^4 degrees Celsius per second when the smaller hairpin-shaped specimens were used. See Figure 22.

4. IQRs were reproducible to within ± five percent for all ST DQ runs performed for all specimens.

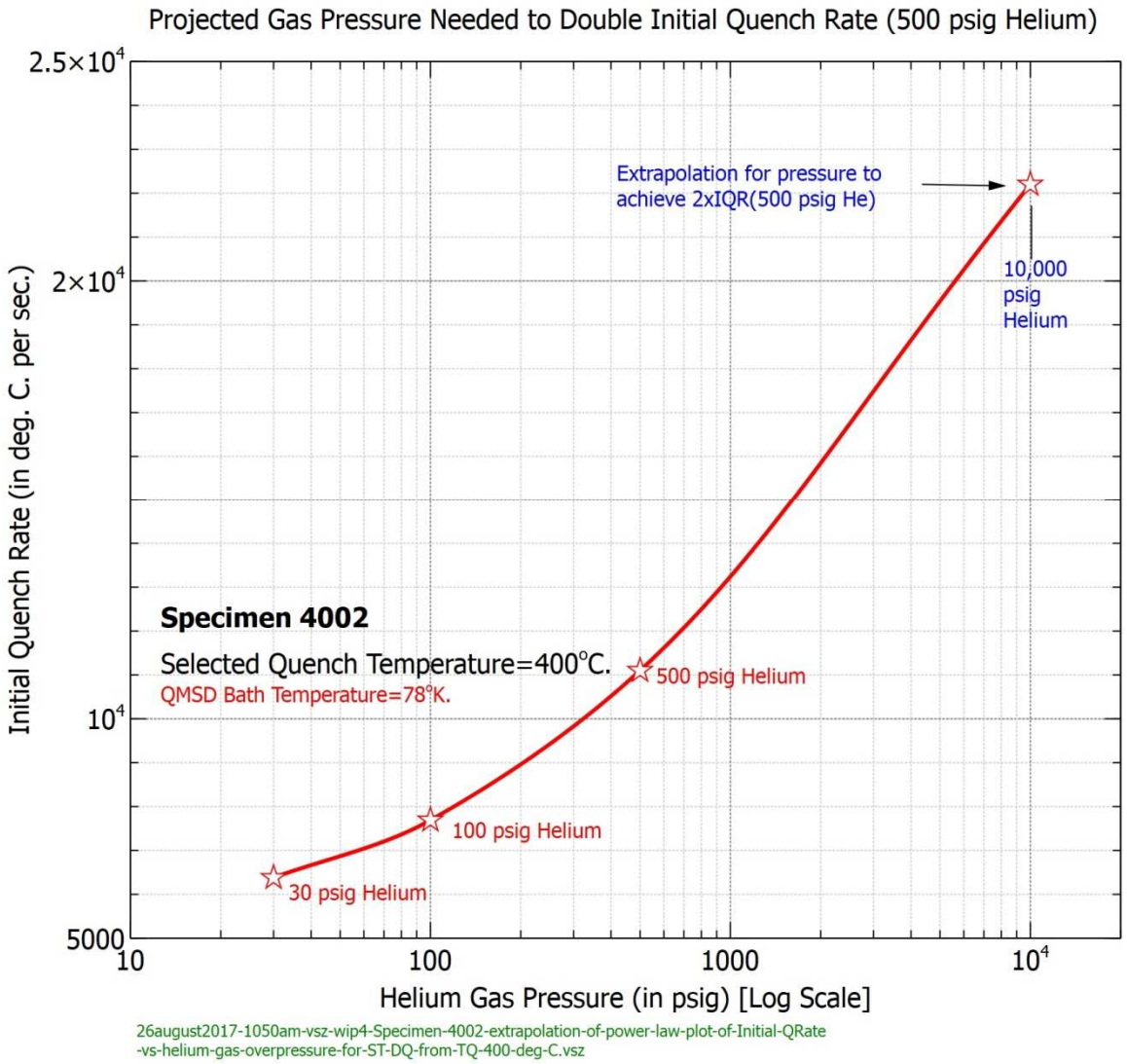

Figure 21. Specimen 4002: Projected Estimate of Gas Overpressure Required to Double the Initial Quench Rate obtained with 500 psig helium

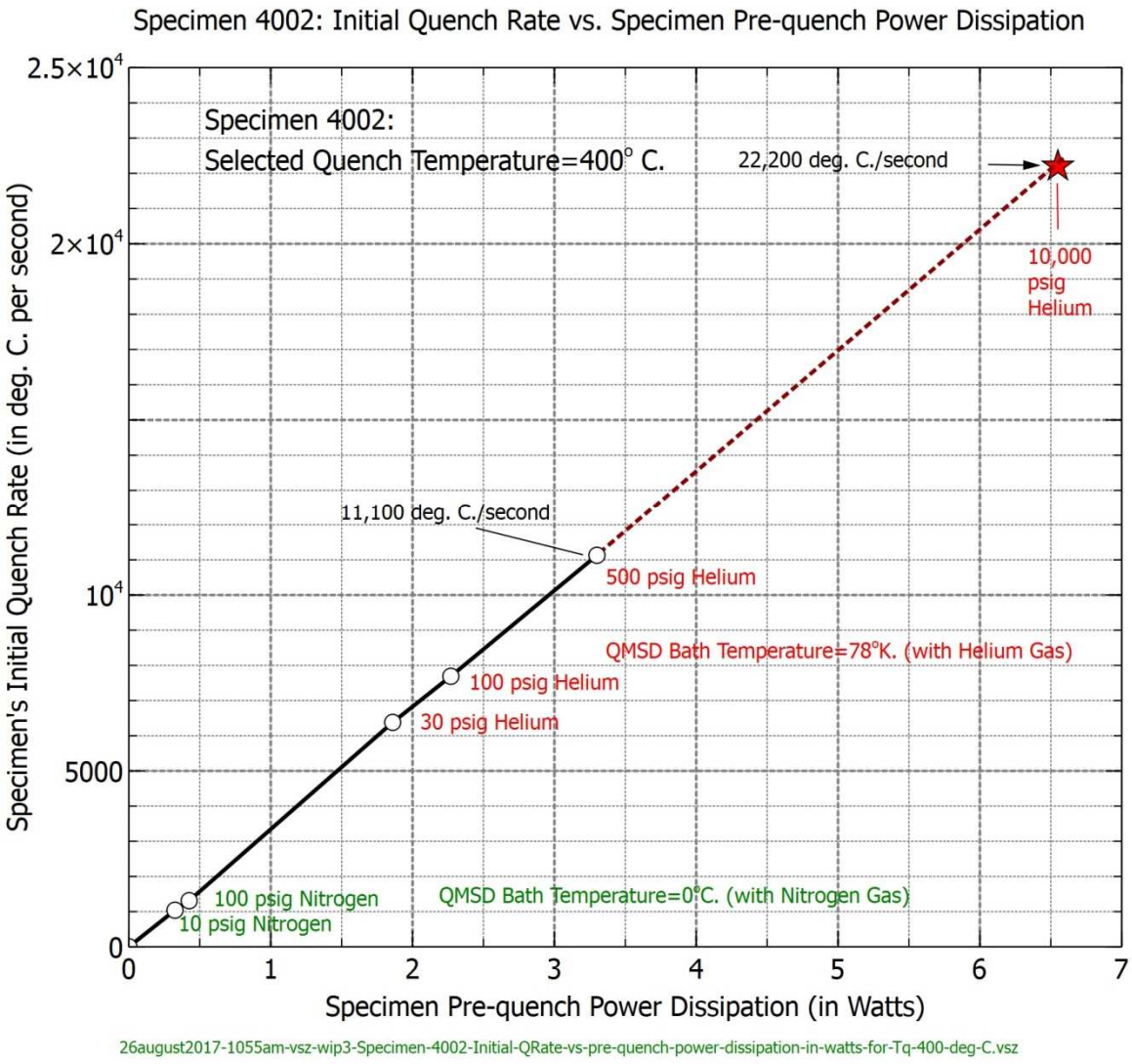

Figure 22. Specimen 4002: Projected Pre-quench Power Dissipation Required to Double Initial Quench Rate (500 psig helium)

4.4.3.5 Thermal EMF Magnitudes

During potentiometric measurements at liquid helium temperatures, stable thermal EMF magnitudes, generally between 0.1 and 0.4 microvolts, were measured. Achievement of both low and stable thermal EMF values assisted greatly in achieving reliable magnitudes of quenched-in resistance, especially for lower quench temperature thermal histories.

Notably, such stable and low EMFs were achieved by allowing for any escaping helium gas that came up from around the stainless steel tubing that housed the set of seven wires to not be propagated into the remaining length of external wiring that stretched for several feet so that the external connector (where the seven wires were terminated) was always well removed from the opening at the top of the Dewar.

This modification served to avoid experiencing any temperature shifts in the connector terminations during transfers of the QMSD Unit's shell with its stainless steel tubing while being directly lowered into the liquid helium contained within the Dewar.

4.4.4 Requirement for Establishing a Reliable Cleansing Anneal Treatment

Crucial to accurate determinations of quenched-in resistance values associated with documentable thermal histories is the establishment of a vacancy-free [32] residual resistance for each and every specimen. Refer to sub-section 6.4.1 for more

---

32 "Vacancy-free" is defined here as being below the threshold of detection using conventional potentiometric methods. For the 5-mil 6N-pure gold wire specimens used throughout this research, quench temperatures of 400^{o}C or higher were determined to be the threshold necessary for obtaining reliable quenched-in resistance changes measured at 4.2^{o}K using the adopted Leeds & Northrup six-dial potentiometer-based circuitry configuration having a potentiometric measurement resolution of 10^{-8} ohms.

details on what will be referred to as a Long-Term Anneal (LTA) thermal treatment that was adopted as a reliable cleansing anneal treatment applied throughout all primary data acquisition experiments.

Table 6 and Table 7 illustrate, respectively, what became the adopted LTA profile and an example of an unsatisfactory LTA-like profile that were established during feasibility studies into this particular matter.

A "vacancy-free residual resistance" is defined hereafter as the resistance value associated with a specimen subjected to a thermal treatment that results in a reduction of the excess vacancy concentration to a magnitude such that no measureable contribution to electrical resistance can be detected using standard potentiometric methods of measurement when performed with the specimen's temperature kept at 4.2^{o}K.

In effect, the residual resistance that remains can then be attributed entirely to impurities and other defect structures (such as dislocation lines, grain- and sub-grain boundaries) present within the specimen's gauge length.

This residual resistance served as the baseline value from which to calculate quenched-in resistance magnitudes associated with any selected elevated temperature thermal treatment that results in producing detectable quenched-in lattice vacancy concentrations.

Since quenched-in lattice defect resistance values are to be monitored, it becomes essential to establish confidence that reliable values for specimen residual resistances are being achieved and that these conditions are reproducible for a selected thermal treatment. The LTA treatment that has been adopted based upon

reproducible quenched-in resistance data for a given thermal treatment, even after numerous straight downquench thermal treatments, is considered to satisfactorily meet this condition.

Table 6. Adopted Long-Term Anneal (LTA) Treatment

T_A (^oC)	Annealing Time T_A (in minutes)
700	5
650	15
600	30
550	15
500	20
450	40
400	20
350	100
300	100
250	410

Quenched-in lattice defect resistance values are expressed by the symbol ΔR_{QN} and were calculated by subtracting the residual resistance value R_{LTA} from the measured total quenched-in resistance value R_{total}. When normalized by the respective specimen's R(40^oC) value, this dimensionless parameter is referred to symbolically as NQIR. These values of NQIR thereafter are considered to reliably reflect a direct proportionality to the retained mean vacancy concentration within a given specimen's gauge length, as well as to the change in resistivity associated with the retained mean vacancy concentration.

Table 7. An unsatisfactory "Long-Term-Anneal-like" Thermal Treatment

T_A (^oC)	Annealing Time @ T_A (in minutes)
700	3
650	1
600	1
550	1
500	2
450	4
400	4
350	6
300	10
250	300

NOTE: The term "unsatisfactory" is defined here to indicate that the resistance value obtained proves to be higher, e.g. by about 0.2 μΩ, when compared with the reliable LTA treatment (as cited in Table 6). This is believed to be indicative of insufficient step-annealing time(s) being allotted for quasi-equilibrium vacancy concentrations to be attained compared with what occurs when the adopted LTA treatment step-annealing sequences are followed. See Figure 23 for a graphical representation for a "Long-Term-Anneal-like" thermal treatment profile.

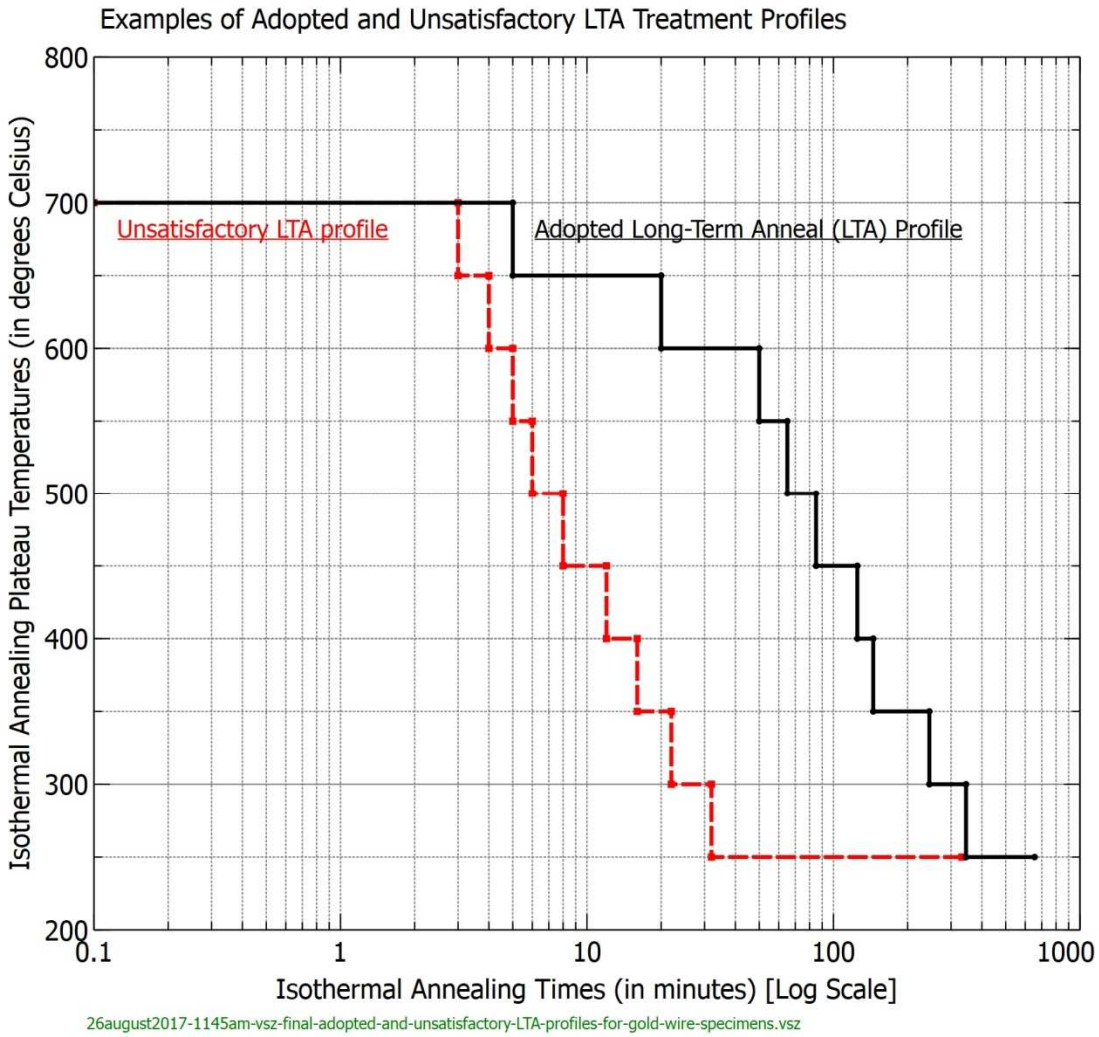

Figure 23. Adopted LTA Treatment Profile and an Example of an Unsatisfactory "LTA-like" Profile[33]

Examinations of the relative magnitudes of residual resistance values obtained for specific LTA thermal histories served as the principal means for determining the reliability of a particular LTA treatment. For, as a satisfactory LTA treatment is approached, the associated residual resistance values should remain fairly close to

[33] Refer to Tables 6 and 7 for the respective temperatures and isothermal annealing times represented in Figure 23.

one another, thereby indicating that a truly reliable residual resistance containing no detectable vacancy contributions has been achieved.

4.4.4.1 Details regarding LTA Treatment Results and Conclusions

Because LTA treatments were performed throughout the lifetimes of numerous specimens, further discussions about the related findings from analyses of sets of LTA treatments and associated LTA chronologies for specific specimens are presented later (see Chapter 11).

4.4.4.2 Concept of Gradual Step-Annealing: LTA Treatment

It is well accepted that vacancy clustering may occur whenever an abrupt elevated temperature reduction occurs within metals such as gold. So, it was judged essential to pursue establishment of a suitable thermal treatment that would ideally reach or at least closely approach quasi-equilibrium conditions for excess vacancies as the elevated temperature was lowered to the lowest step-level annealing temperature in the overall LTA profile. By establishing this LTA treatment whatever vacancy defect contribution associated with the remaining excess vacancies should become negligible, i.e., reduced to or below the detection threshold limit obtainable via potentiometric measurements conducted at liquid helium temperatures.

For example, a sequence of stepped isothermal anneals using a specific set of intermediate temperatures with ever longer isothermal annealing times at each temperature should, in principle at least, result in the attainment of thermal equilibrium vacancy concentrations at each intermediate temperature, thereby minimizing the likelihood of vacancy clustering following completion of the lowest isothermal anneal step in the overall Long-Term Anneal (LTA) treatment.

Stated in a simpler way, a "vacancy free" residual resistance would be achieved when a specimen's associated impurity scattering completely dominates over that made by whatever vacancy concentration remains within the specimen material's gauge length.

4.4.4.3 Selection of Initial Temperature for LTA Treatments

Based on findings made known by other researchers that are outlined in the next several paragraphs, an elevated temperature of 700^{o}C was selected for the initial annealing temperature for each Long-Term Anneal (LTA).

Meshii and Kauffman [198] conducted an investigation of the effects on mechanical properties of quenching 99.999% pure gold wires in the range 500^{o}C-1050^{o}C over the range of cooling rates from 1000 to 60,000^{o}C/sec. Subsequent aging reflected a re-softening behavior that was observed above 600^{o}C for anneals of 1 hour (see their Figure 9: Ratio of Yield Stress Before and after Annealing for one hour at elevated temperatures between 100^{o}C and 700^{o}C).

In a subsequent study, Meshii and Kauffman [69] noted that recovery of quenched-in resistivity exhibited two recovery regions: The first region (see Figure 1 in [69]) of this remaining resistivity was within a wide temperature range from 200^{o}C to 630^{o}C; the second region was within a very narrow temperature range of about 630^{o}C. The recovery in the 200^{o}C to 630^{o}C (see Figure 2 in reference [69]) had no observable effect on the yield stress, whereas the second step of the resistivity recovery observed in a narrow range about 600^{o}C corresponded to the resoftening of quench hardening.

In another independent study, Cotterill [21] monitored changes in electrical resistivity of stacking faults and lattice vacancies in gold and established the temperature dependence of residual resistivity in a specimen quenched from 1000^{o}C, fully annealed at 100^{o}C, and then annealed for one hour at temperatures of 100^{o}C, 200^{o}C, 300^{o}C, 400^{o}C, 500^{o}C, 600^{o}C, and 700^{o}C (see Figure 5 in [21]) supported the conclusion that secondary defects would anneal out at temperatures above 650^{o}C,

That reported observation served as the basis for selecting 700^{o}C as the initial elevated isothermal annealing temperature for LTA treatments that attempt to remove whatever histories, such as vacancy clusters or secondary defects [19] associated with any excess vacancies that may have been retained from previous thermal treatments.

In addition, Cotterill and Segall [59] performed TEM investigations on gold specimens and determined the following:

1) for T_Q>850^{o}C followed by annealing at 100^{o}C only stacking fault tetrahedra are observed and the concentration of those defects increases with increasing T_Q; and in the same temperature range, the mean tetrahedron size decreases with increasing T_Q; and

2) for T_Q < 800^{o}C, only black-spot defects are observed (thought to be clusters of vacancies); and

3) for T_Q between 800^{o}C and 850^{o}C, a mixture of tetrahedra and black spots is observed.

Given the above findings reported by those researchers, it was especially important that the adopted LTA treatment serve as a "cleansing anneal" that would remove all traces of vacancy clusters and secondary defects created during prior thermal treatments as well as assure quasi-equilibrium vacancy concentrations would be achieved for sufficiently low temperatures such that no detectable levels of excess vacancy contributions would be detectable via potentiometric measurements, even for high-purity material having $R(40^oC)/R_{LTA}(4.2^oK)$ ratios typically above 1000.

The next sub-section presents the initial experimental results obtained based on applying the above argument which led to adoption of the Long-Term Anneal (LTA) thermal treatment used throughout subsequent research investigations.

4.4.4.4 Description of the Adopted LTA Procedure

Table 6 indicates what was established as an acceptable LTA treatment for the five-mil 6N-pure gold wire specimens. For comparison purposes, Table 7 provides an example of what proved to be an inadequate "LTA-like" step-annealing profile [34].

Figure 23 illustrates the temperature-time profiles that are listed in Tables 6 and 7. The annealing plateaus are manually established by adjustment of a power supply rheostat. Figure 24 illustrates four actual LTA-like treatment profiles that were performed over a period of several months and indicates the resulting R_{LTA} values obtained for the respective LTA-like treatment profiles.

---

[34] An unsatisfactory "LTA-like" treatment is defined here as one that results in an R_{LTA} value that proves to be detectably higher than what would be measured following the adopted LTA treatment. Why? A few tenths of a μohm difference between the results obtained for each of these measurements can lead to significantly different calculated NQIR values, particularly when associated with lower quench temperatures,

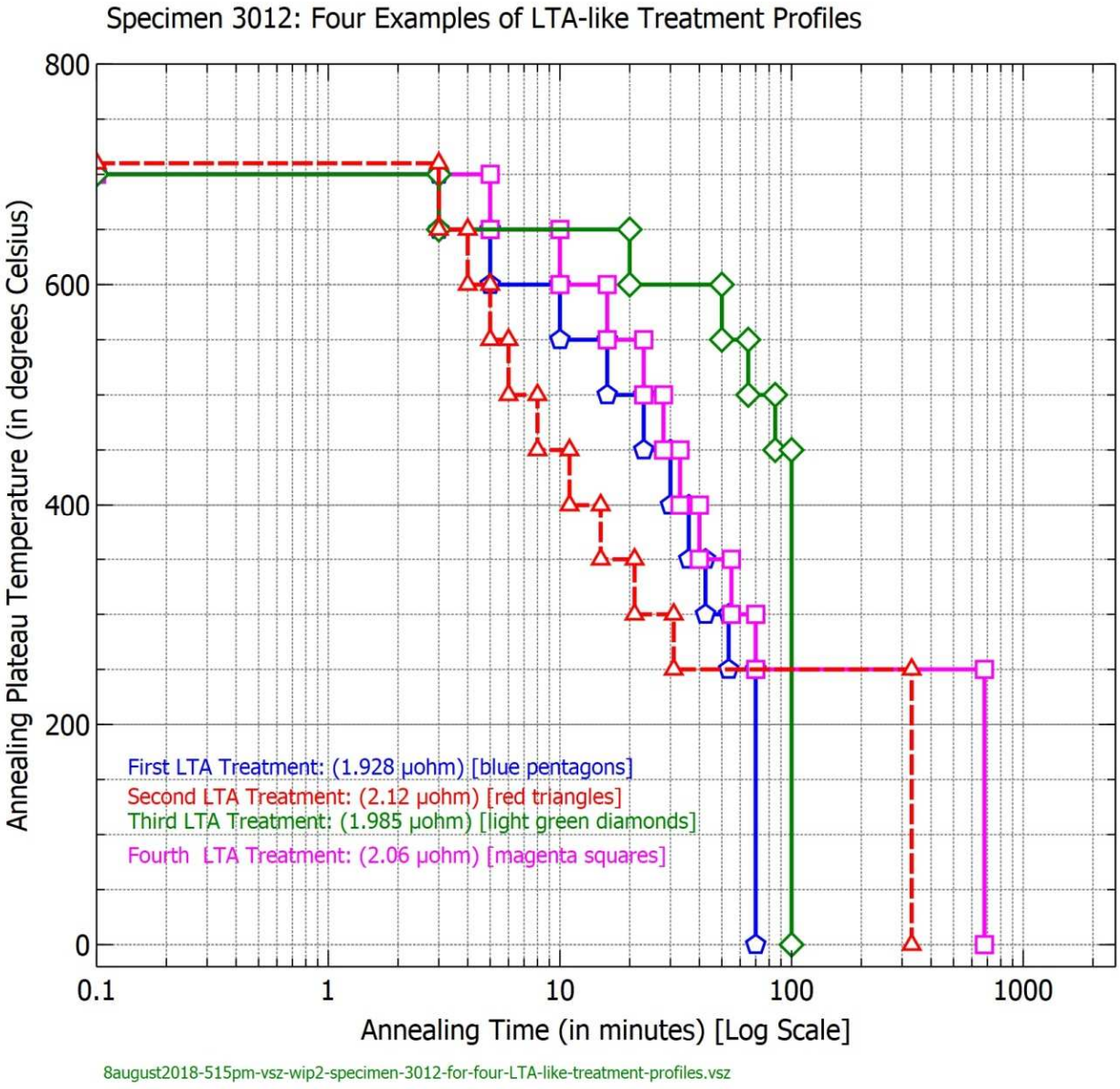

Figure 24. Specimen 3012: Four Actual LTA-like Treatment Profiles to illustrate resulting R_{LTA} Values

It should also be noted that these LTA treatments were specifically performed with the quench/measurement unit's valves opened to the atmosphere. This was done to avoid any possibility for the occurrence of helium solubility in gold discerned following observation of an anomaly in ST DQ NQIR data levels (see sub-section 7.4.2 for specific details and analyses) associated with quenches made from quench temperatures ≤ 550^{o}C that employed helium gas compared with nitrogen gas quench environments.

5 MATERIALS, METHODS, EQUIPMENT, AND PROCEDURES

5.1 INTRODUCTION

This chapter describes the adopted materials, methods, equipment, and procedures used for primary data acquisition. The sets of flowcharts of data acquisition sequences and subsequent analyses already referenced are intended to serve as convenient visual aids for each specific investigation presented in this document.

5.2 SPECIMENS-RELATED DETAILS

The following sub-sections describe and detail specimen preparation, shaping, mounting, and various specimen-related initialization procedures.

5.2.1 Five-mil diameter Gold Wires and 0.5-mil Gold Ribbon Foils

Nominally pure 99.9999 weight per cent pure (6N) ingots were drawn by Cominco American, Incorporated of Spokane, Washington, to form the five-mil diameter wire used as specimen material throughout this research. Two-mil diameter 99.999 weight percent pure (5N) wires were supplied by Sigmund Cohn Corporation of Mount Vernon, New York.

Five-mil diameter 6N (99.9999 weight percent) pure gold wires were used for the in-situ specimens, and a pair of two-mil diameter gold wires were sintered in place to establish a specimen gauge length and allow for performing all subsequent potentiometric measurements across the established gauge length of each in-situ mounted five-mil diameter gold wire specimen.

Later, when it came to for performing supplementary thermal-mechanical treatments (as described in Chapter 9), one-half mil thick 6N (99.9999 weight percent) pure gold ribbon foils were used for the in-situ specimens. As described above, two-mil diameter 5N (99.999 weight percent) pure gold wires were sintered to establish specimen gauge lengths for subsequent electrical measurements on each in-situ mounted gold foil specimen. Finally, each of these ribbon foils was subsequently subjected to Transmission Electron Microscopy examinations (see Chapter 10).

5.2.2 Specimen Preparation Sequence

Listed below and illustrated in Figure 6 are the sequential steps for preparing and creating 5-mil diameter gold wire specimens [35] that are executed only after chemical cleaning as described below in sub-section 5.2.3 has been performed.

1. Initiate specimen preparation.
2. Shape and mount specimen on frame of QMSD Unit (#3 or #4).
3. Establish a specimen gauge length and sinter potential leads.
4. Determine specimen's room temperature resistance.
5. Establish specimen's R(40^{o}C) resistance.
6. Perform high temperature stabilization of microstructure followed by performing a Long-Term Anneal (LTA) Treatment.
7. Determine specimen's residual resistance at liquid helium temperature.

---

[35] Similar procedures were used for the 0.5-mil thick gold foil ribbons used for subsequent TEM investigations that are detailed in Chapter 10.

8. Assess purity and establish size-effect-corrected Relative Resistance Ratio (RRR) values for each newly-created specimen.

9. Conduct thermal treatments using this specimen.

5.2.3 Specimen Cleaning Procedures

Prior to specimen creation and subsequent experimentation, specimen and potential lead materials were subjected to a cleaning treatment that began with a two-hour immersion in nitric acid of Reagent grade combined with triply-distilled water.

Handling of the wires was accomplished using stainless steel forceps. Momentary removal each half hour from the nitric acid served to remove any buildup of bubbles that may have formed on the wires. Following flush-rinsing with triply-distilled water, the wires were placed into a 95 per cent absolute ethanol solution, covered, and kept there for 30 minutes. Finally, the wires were flushed with triply-distilled water for one minute and placed on clean filter paper to permit evaporation of the remaining water droplets from the surface of the wires. Once dry, the two wire sizes were separated, transferred to covered Petri dishes, and kept under cover until selected for use in creating specimens.

5.2.4 Specimen Shaping and Mounting

All specimen shapes were produced using two pairs of stainless steel forceps to manipulate the overall specimen in any region except the central portion, and rubber gloves were worn to avoid possible surface contamination during any stage of this

shaping process. In most cases, direct deformation of the central portion of any specimen during its initial creation was avoided [36] for two reasons:

First, contamination associated with particles of dirt, metal, or other foreign substances that may be present on the forceps will not be deposited within the region not directly handled.

Second, additional dislocations would be introduced besides those created by the inevitable overall bending of the specimen material during the shaping process.

Once created and shaped, each specimen was mounted within the space between the current-carrying bus connections attached to a Micarta mounting frame of the quench unit (see Figure 17).

Clamping of the ends of each specimen required holding of the specimen near the portion to be clamped so as to prevent creation of residual torque during the actual tightening of the machine screws on the bus terminations.

Two sets of stainless steel current arms were used in one of the quench units (Unit #3) to connect the hairpin-shaped specimens to their respective pair of current bus bars.

Whenever catenary-shaped specimens were created, unit #4 was used with its current-carrying bus bars serving as the terminations for each specimen. Figure 17

---

[36] Exceptions to this statement were made when intentional Direct Deformation (DD) experiments were conducted (see Section 9.3 for details) or where multiple flexures (x4 to x10) were made to introduce additional dislocations. This specimen handling procedure was done for the purpose of investigating the effects on the magnitudes of losses, the associated annealing kinetics, and possible magnitude changes of parameters determined from analyses of subsequent ST DQ and/or Q&A Series Treatments

shows sketches (not drawn to scale) of the mounting frame constructions used for the hairpin- and catenary-shaped five-mil gold wire specimens.

5.2.5 Establishment of each Specimen's Gauge Length

For each now-mounted specimen two 5N gold wires of two-mil diameter and previously cleaned as described above, were mechanically connected near the central portion of each of the specimens. To accomplish this, each potential lead wire was separately manipulated using two pairs of stainless steel forceps until a single-turn mechanical contact was established around the five-mil diameter 6N (99.9999 weight percent) pure gold wire.

An initial and prolonged high-temperature anneal (HTA) treatment at temperatures above 900^{o}C was performed following the mechanical placement of potential lead wires. This was done to sinter the pair of potential leads for each specimen permanently into position and thereby define a unique gauge length for that specimen. The sintering operation was carried through to completion only if a uniform temperature distribution was observed to well beyond the gauge length portion of the specimen [37]. If not so, an entirely new specimen was created as a replacement specimen.

Intimate electrical connections resulted from these sintering treatments, and achieving a fixed gauge length per specimen was deemed essential given the fact that 1) elevated temperature treatments (ST DQ, Q&A, HTA, and TC) had to be made, and 2) subsequent potentiometric measurements with the outer shell of each

---

[37] The potential leads were noted as not being significant heat sinks at their points of attachment to the five-mil wire no matter what temperatures were involved.

sealed QMSD unit lowered into a Dewar filled with liquid helium had to follow at some point following almost every elevated temperature treatment.

5.2.6 Comments regarding Adopted Range in Specimen Gauge Lengths

Specimen gauge lengths ranging from 0.2 to 1.5 centimeters were used. The smaller gauge lengths were adopted for the smaller overall specimen geometry design associated with quench unit #3; the larger, with catenary-shaped specimens that were mounted in quench unit #4.

The voltage drop across the specimen gauge length at elevated quench temperatures was required to be less than 0.63 volts so as to remain below saturation limits of the Infotec differential amplifiers whose gain was set to 16 throughout most of the straight downquench experimentation.

For the higher quench temperatures the quenched-in resistance values were substantially greater than the $R_{LTA}(4.2^{o}K)$ residual resistance values, thus permitting very small gauge length specimens to be used. For example, residual resistances of about one micro-ohm were associated with specimens having gauge length $R(40^{o}C)$ resistances of from two to four milliohms, and quenched-in resistances of tens of micro-ohms were obtained when quenches from above $800^{o}C$ were performed.

Under ideal conditions following an LTA treatment, a specimen's residual resistance would remain constant and reproducible, and the potentiometric measurement circuitry's thermal EMF values would be negligibly small compared to the product of the measuring current and specimen resistance, $I_{meas} \times R_{specimen}$. Specimen gauge lengths generally did not exceed one centimeter, the associated room temperature resistances were less than 20 milliohms, and potentiometric

measurements at liquid helium temperatures could resolve resistance changes down to 0.01 µohm. So, the threshold sensitivity limit of 5×10^{-7} (that is, 0.01 µohm/20 milliohm) would correspond to a "no-loss" QIR/R(40°C) value associated with a quench from approximately 300°C.[38] However, for smaller gauge length specimens having a room temperature resistance of about 4 milliohms, the threshold sensitivity limit would be about 2.5×10^{-6}, and this would correspond to a "no-loss" QIR/R(40°C) value associated with a quench from 350°C. See Table 9.

5.2.7 Attachment and Sintering of Potential Leads

Following mounting of the shaped specimen between the current-carrying arms of a quench/measurement unit's mounting frame, a pair of 5N (99.999 weight per cent pure) gold wires, two mils in diameter, (mechanically wrapped) are carefully attached.

Sintering of the potential leads was accompanied by examination for temperature uniformity to well beyond the specimen gauge length using optical pyrometry equipment and temperatures of from 750°C to 900°C. During this examination, the specimen was kept inside a covered glass chamber to minimize thermal fluctuations due to drafts. Only if a specimen had no discernible temperature non-uniformities to well beyond its gauge length was it considered acceptable. Otherwise, it was removed and the entire procedure repeated until a satisfactory specimen temperature distribution was achieved. Note that two independent specimens were mounted within each QMSD unit.

[38] See Table 9 presented in sub-section 7.4.7.1 of this document for tabulations of numerous "No Loss" NQIR(T) values established during this research investigation for temperatures ranging from 40°C to 1063°C.

5.2.8 Objectives for Performing Specimen Stabilization Anneals

Each newly-created specimen was subjected to a stabilization anneal at temperatures between 950^{o}C and 1000^{o}C [39] for one hour for three reasons:

1. Attainment of a truly fixed specimen gauge length was assured by the process of sintering of the potential leads to the specimen.

2. Internal stresses introduced during mechanical handling, shaping, and mounting of the specimen can be reduced by such annealing. Polygonization and formation of stable microstructures [93, 152, 153] are two examples of stress-reduction phenomena that are associated with high temperature annealing treatments.

3. Grain growth was encouraged. This would result in a lowered overall sink density within the specimen and, as a consequence, produce specimen material with lower losses during quenches from elevated temperatures.

5.2.9 Establishment of a Reliable Long-Term Anneal Treatment

Upon the completion of a prolonged elevated High Temperature Anneal (HTA treatment) to promote grain growth and to stabilize the existing sink structures, each specimen was subjected to a Long-Term Anneal (LTA) treatment (see sub-sections 4.4.4 and 6.4.1, and Chapter 11 for additional details) to remove residual vacancies, vacancy clusters, and secondary defects associated with any prior thermal treatments and thereby establish a "vacancy-free" residual resistance state to provide a baseline specimen resistance value. Subsequent elevated temperature quenches

[39] These elevated temperatures (above 941.2^{o}C) were ascertained using the Meechan and Eggleston scale extended to the melting point of 1063^{o}C for gold.

or quench-and-isothermal anneal treatments were performed and followed by determinations via potentiometric measurements made at liquid helium temperatures to establish the associated quenched-in resistance values associated with each specimen's specific thermal treatment.

5.3 MATERIALS, EQUIPMENT, AND METHODS

5.3.1 Quench/Measurement System Design Units, Materials, and Methods

Numerous preliminary feasibility studies (see Chapter 4) were conducted that ultimately led to the two adopted Quench/Measurement System Design Units #3 and #4 (see Section 4.2) used throughout all subsequent primary data acquisition experiments.

5.3.1.1 Desired Features of Quench/Measurement System Design Units

Listed below are features that were deemed essential to have in a QMSD:

1. Wide ranges in quench temperatures, initial quench rates, and contiguous quench-and-anneal temperatures for multiple specimens.

2. Uniform, stable temperatures within each specimen’s gauge length.

3. High specimen resistance ratios [$R(40^{o}C)$] $R_{LTA}(4.2^{o}K)$].

4. Stable, yet minimal, thermal EMF values during potentiometric measurements performed at $4.2^{o}K$.

5. High-speed, high-accuracy thermal history data recording equipment.

6. Reliable high-current solid-state design for specimen thermal history generation and control.

7. Reproducible quenched-in specimen resistance values.

5.3.1.2 Selected Specimen Materials

5.3.1.2.1 Five-mil diameter 6N-pure gold wires

Five-mil diameter gold wire of 99.9999 (6N) weight percent purity was chosen for use as the specimen material for all primary research investigations [40].

5.3.1.3 Two Adopted Shapes for Gold Wire Specimens

Figure 17 schematically indicates the two adopted shapes for five-mil gold wire specimens mounted within each of two Quench/Measurement System Design Units (referred to as QMSDs #3 and #4) for in situ thermal treatments. Smaller "hairpin-shaped" specimens were mounted within QMSD #3 and were assigned 3000-series numbers. Two larger "catenary-shaped" specimens were mounted within QMSD #4 and were assigned 4000-series numbers 4002 and 4003.

5.3.1.4 Specimen Gauge Lengths

Two-mil diameter 5N-purity gold wires [41] were sintered to each 5-mil 6N (99.9999 weight percent) pure gold wire specimen for the purpose of establishing a specimen gauge length and to serve as a means for obtaining potentiometric measurements.

5.3.1.4.1 Five-mil-diameter Gold Wires

All of the "hairpin-shaped" 3000-series specimens (ranging from #3005 through #3018 in assigned numbers during their respective lifetimes) had gauge lengths generally less than 0.3 cm. with corresponding room-temperature resistance values

---

[40] Supplied by Cominco, Incorporated of Spokane, Washington.

[41] Specimen gauge lengths were selected to give a) compatible output voltages at desired quench temperature ranges and b) detectable increments at liquid helium temperature following any given quench history.

less than five milliohms. Only two "catenary-shaped" 4000-series specimens (#4002 and #4003) were created and these each had gauge lengths on the order of one centimeter.

When specimen #4003 eventually burned out, a mounting modification was made to add a pair of stainless steel arms to allow that lower position specimen #4005 to have a hairpin-like shape as was already established for both mounting locations within QMSD #3.

5.3.1.4.2 One-half-mil-thick Gold Ribbon Foils

As part of a supplementary Transmission Electron Microscopy (TEM) investigation detailed in Chapter 10, a total of four 0.0005" thick gold ribbon foil specimens were created from 99.9999 (6N) weight percent purity gold material supplied originally in the form of ribbon of nominal 1.5 mil thickness [42] [43]. Use was made of QMSD Unit #3 for mounting of these specimens as they were needed for specific thermal treatments followed by their removal for preparation for TEM examination and assessment objectives.

---

[42] Supplied by the Sigmund Cohn Corporation, Mount Vernon, New York.

[43] After undergoing the same type of thermal treatments as the five mil diameter wire specimens and subsequent electrical resistance determinations, these ribbon-shaped specimens were subjected to Transmission Electron Microscopy examinations in an attempt to assess specimen microstructures associated with each particular thermal treatment.

5.3.2 Equipment and Methods used for Specimen Data Acquisition

5.3.2.1 Equipment List

The following equipment was employed during elevated temperature thermal treatments and related potentiometric measurements conducted during this research investigation:

- Infotec High-Speed Data Acquisition System
- Regatran Model TO 6-120 Semiconductor DC Power Supply [Load (no load to full load) Regulation: 0.03% or 0.01 volts DC]
- Electronic Measurements Company, Inc. Model 612A Constant Current] Voltage Power Supply (DC Output: 1 uA to 100 mA; 0-100 volts DC)
- Leeds and Northrup (L&N) 7556 six-dial potentiometer with photocell galvanometer amplifier
- Leeds and Northrup K-3 potentiometer
- Standard Resistors (0.01, 0.1, and 1.0 ohms) that were maintained in oil baths kept at room temperature
- HP 3459A digital voltmeter (±0.0001 volts DC resolution; used for ST DQs)
- Vidar 520 digital voltmeter (±0.000001 volts DC resolution; used for Q&As)
- An AC Line Voltage Regulator

Figures 25 through 29 provide photos of some of the laboratory equipment listed above.

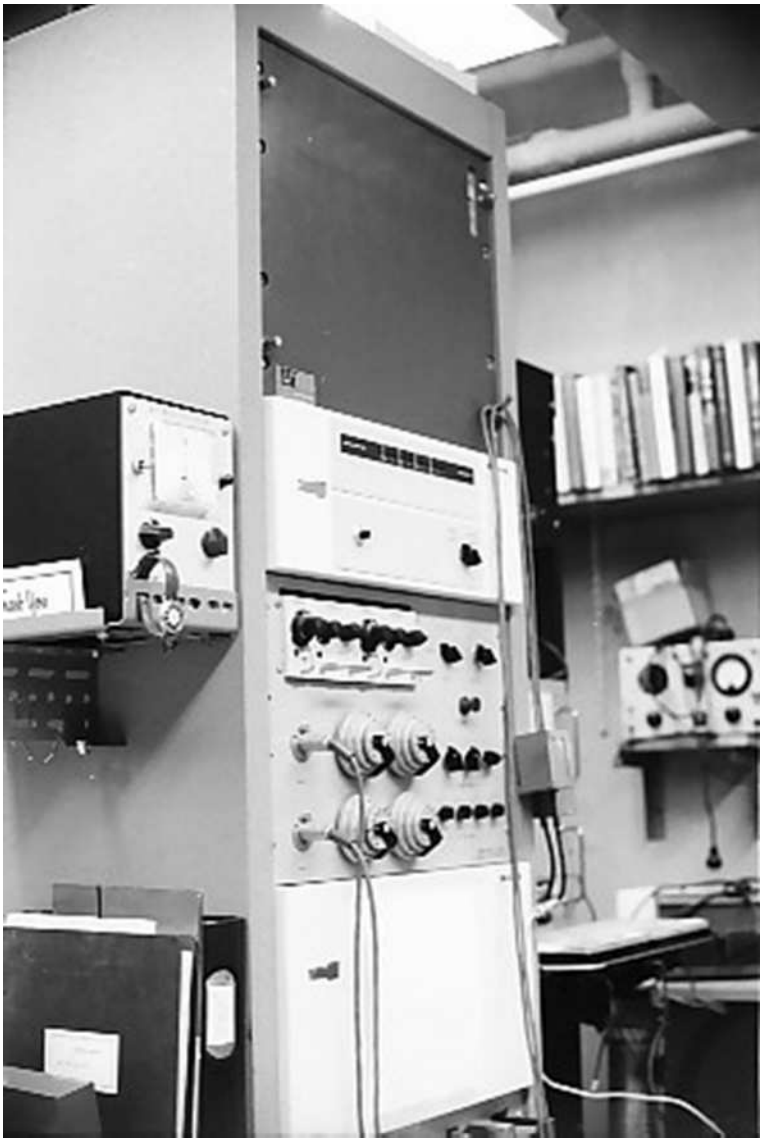

Figure 25. Photo of Infotec Data Acquisition System

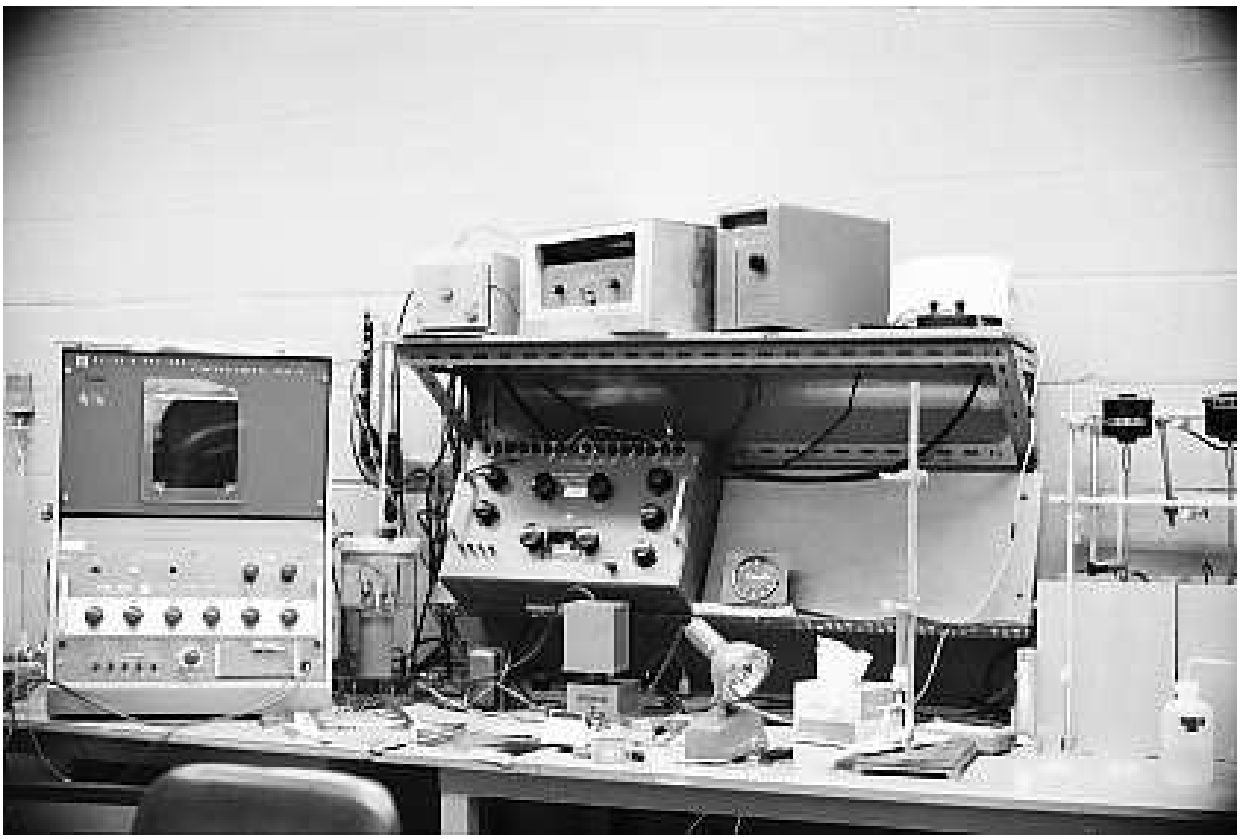

Figure 26. Photo of Bench Layout of Potentiometric Measurements Equipment

Figure 27. Photo of L&N Six-Dial Potentiometer Instrument's Front Panel

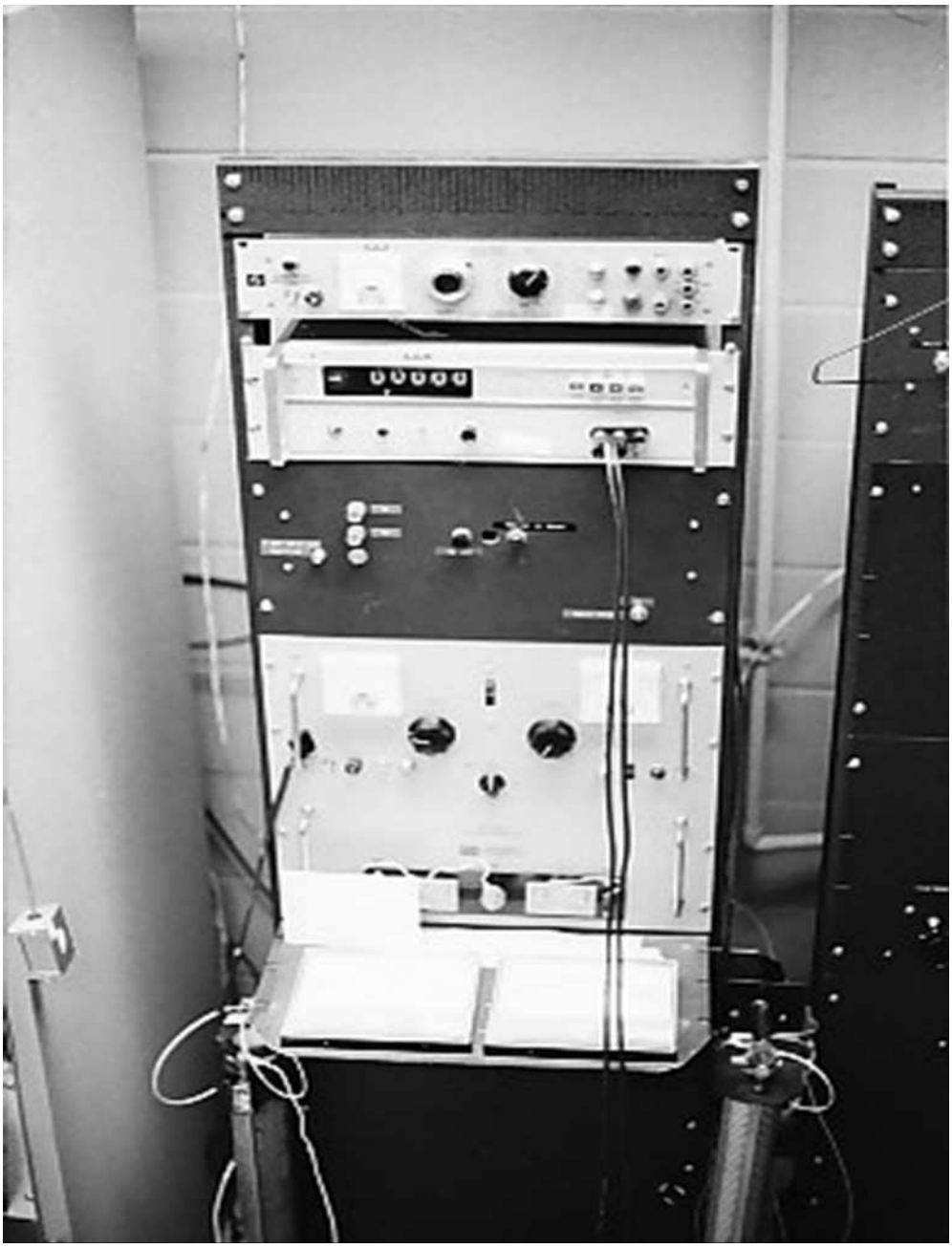

Figure 28. Photo of Rack-mounted EMC Power Supplies and HP DVM

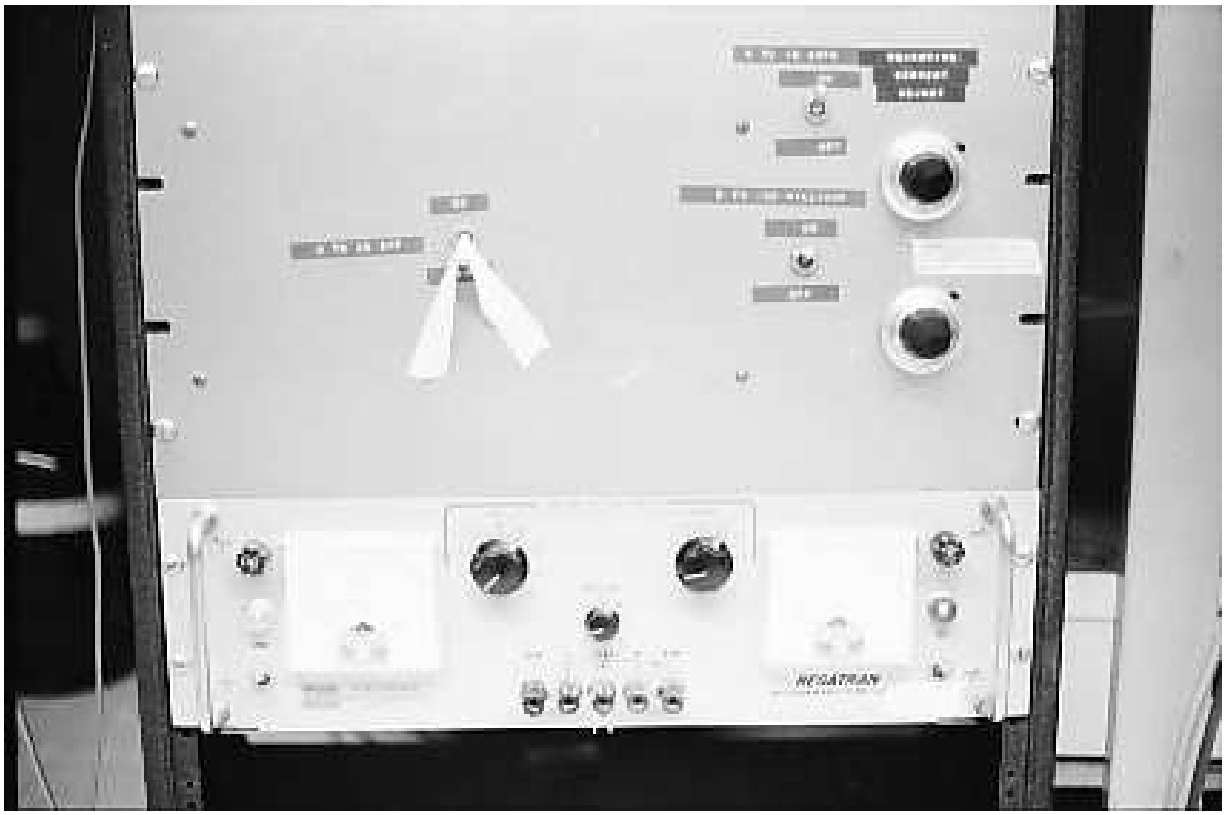

Figure 29. Photo of Rack-mounted Regatran 0-120-amp Power Supply with two 10-turn Potentiometers

5.3.2.2 Elevated Temperature Determinations

Accurate temperature setting, monitoring, and retrieval are essential requirements for reliable determinations of properties associated with lattice defects, especially vacancies. Each specimen was used as its own resistance thermometer based on use of the temperature scale of Meechan and Eggleston [47]. A reference resistance value associated with a specimen's temperature of 40^{o}C was chosen in order to establish specimen temperatures using a normalized resistance ratio, namely, R(T)/R(40^{o}C). The temperature of any specimen could then be established using R(T)/R(40^{o}C) ratios.

5.3.2.3 Potentiometric Measurements

Standard potentiometric measurement techniques were employed throughout this research investigation, and these were conducted with the specimens mounted in the quench/measurement system design/units which evolved from the preliminary feasibility studies described in Chapter 4.

Potentiometric measurements performed to establish a specimen's gauge length resistance were generally conducted at room temperature using a series circuit with a 1-ohm standard resistance to establish the measuring current [**44**]. Occasionally, heating of specimens to 40^{o}C was done as a means to double check on the accuracy of these conversion-from-room-temperature resistance values.

Measurements of both pairs of voltages, namely across the standard resistor and across the specimen gauge length, were performed for each direction of current

---

44 Subsequent calculations of each specimen's resistance value associated with a temperature of 40^{o}C were made using the Meechan and Eggleston scale.

flow as established using a current reversal switch. Such current reversal procedures were deemed essential to minimize errors associated with thermal emf voltages which occur in systems involving junctions of metals having temperature differentials. Because the value of the series circuit current always equals the voltage drop across the standard resistance divided by the standard resistance used, the specimen's resistance at the temperature of interest was computed as being equal to the average of the values obtained for both directions of current flow.

Potentiometric measurements following LTA, ST DQ, Q&A, TC, HTA, and DD treatments of specimens were all made at 4.2^{o}K. Resolution of ± 0.01 μohm is obtained using the Leeds and Northrup Model 7556 six-dial potentiometer that employed a photocell galvanometer amplifier.

Measuring current was monitored [45] to 1.000000 ± 0.00002 amperes using a Leeds & Northrup Model K3 potentiometer connected across a 1-ohm standard resistor connected in series with the specimen. It should also be noted that care was always taken to avoid Joule heating of any of the series circuit components by not using higher measuring currents.

5.3.2.4 Description of Infotec Data Acquisition System

The Infotec data acquisition system (cited in Appendix A of reference [62]) shown in Figure 25 served as the primary means for acquiring all elevated temperature thermal histories. Figure 30 depicts four regions labeled I, II, III, and IV. Thermal histories are distinguished as follows:

---

[45] and simultaneously checked using a Vidar Model 520 6-place DVM also connected across the standard resistor.

1. Region I -- when held for an extended period of time -- represents a Pre-Quench Anneal treatment.
2. Regions I, II, and IV (with Region III reduced to zero time duration) represents a Straight Downquench (ST DQ) treatment.
3. Regions I, II, III, and IV represents a Quench-and-Isothermal Anneal (Q&A) treatment.

All voltage pair data associated with a thermal history were recorded into a 2 KB memory core of the Infotec unit [46]. Actual retrieval of data from memory core was achieved by initiating punch-out of stored data onto paper tape. The voltage pairs as punched out were in binary-coded-decimal (BCD) format and consisted of a total of 1,024 pairs. An assembly language computer program was used to convert these 1,024 pairs of data into each specimen's elevated temperature thermal history for subsequent data analyses in conjunction with the associated potentiometric measurements that had been made for each specimen.

---

46 The sampling "window" between the specimen voltage and the standard resistance voltage was ten microseconds. Thus, uncertainty in the actual temperature was less than $0.2^{o}C$, even for a quench rate of 2×10^{4} deg. C/sec.

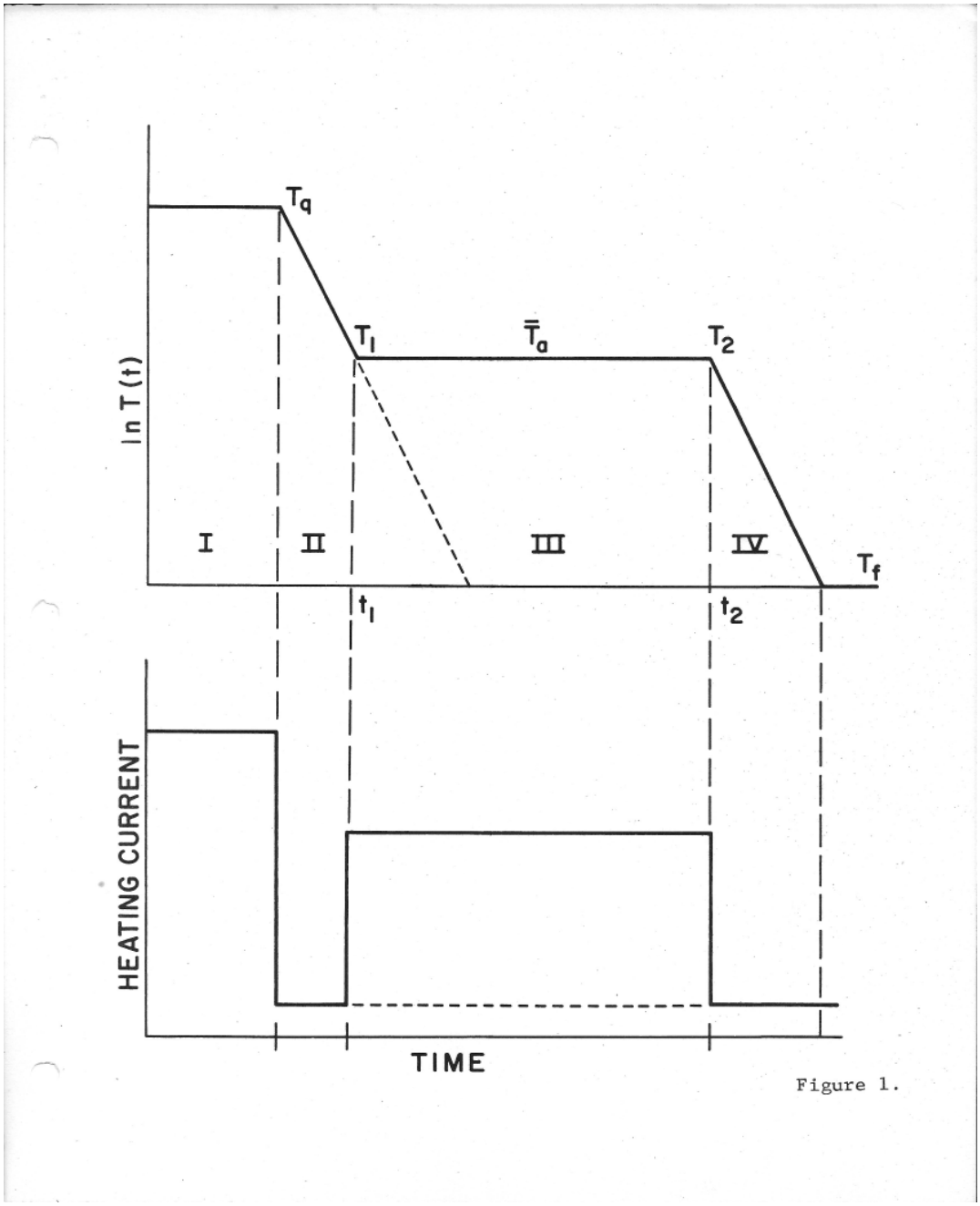

Figure 30. Four Possible Regions of Elevated Temperature Profiles

When only a portion of a paper tape's punched-out data was of interest, manual reading of the paper tape was done. One example of such a situation was the calculation of initial quench rate -- something that only required having to read Region II data which consisted of no more than 64 sets of voltage pairs.

An internal quartz crystal oscillator supplied a stable, precise two kHz calibration frequency. Voltages could be sampled at time intervals of from 0.5, msec. to 1/8 sec. within each of four regions (see Figure 30) of data acquisition: pre-quench, quench, isothermal anneal, and final quench. The maximum oscillator frequency that could be used on the Infotec was four kHz. Time intervals as long as desired, however, were obtained simply by using (instead of the quartz crystal) an external oscillator that could output stable lower frequencies that could be chosen as desired [47].

5.3.2.5 Principle Used to Obtain Thermal Histories

By simply recording the specimen's voltage as a function of time together with the associated current (determinable from the also recorded voltage across the standard resistance in series with the specimen, the specimen's resistance-versus-time profile could be retrieved from processing of the paper tape punch out of these voltage pairs for pre-established time intervals.

Determination of any thermal history, therefore, involves conversion of normalized resistance ratio, $R[T(t)]/R(40^{o}C)$ for each time interval into a complete set

---

[47] Whenever isothermal annealing treatments involving extended annealing times beyond tens of minutes to many hours were to be conducted, control of the duration of the isothermal annealing time was done through simple external circuitry, such as knife switches which were then opened to initiate the end-stage (Region IV) activation of the final downquench from temperature T_A down to the final bath temperature T_F with its associated non-Joule heating of the specimen being subjected to that particular Q&A Series treatment.

of discrete temperature-time data points which, taken as a collective set, yield the thermal history [48] associated with the recorded voltage pairs and given specimen.

5.3.2.6 Setting/Monitoring of Specimen Quench Temperatures

A Vidar 520 DVM having six-digit resolution (± 1 μV) was used to monitor, alternately, the specimen voltage drop and standard resistance voltage drop prior to quench initiation. In this manner, pre-quench temperature determinations to within $0.1^{o}C$ were made possible. Manipulations of specimen current and quench environment overpressure prior to quench initiation permitted nearly identical readings to be obtained for assuring virtually identical quench conditions and quench temperatures for each run.

Figure 31 provides a schematic diagram [49] of the data acquisition circuitry associated with resistance determinations on specimens conducted either at room temperature or with the specimen cooled to liquid helium temperatures. The particular standard resistance inserted into the series circuit was dictated by the measurement situation.

Note: The high temperature annealing experiments employed the 0.01 ohm resistor shown in Figure 31. Associated room temperature resistance measurements employed a one ohm resistor. Both resistors were Leeds and Northrup standard resistors accurate to one part in 10^5.

---

48 A maximum input voltage (specimen voltage drop across its gauge length) of less than 10 volts was dictated by the internal circuitry contained within the Infotec data acquisition system.

49 The schematic diagram of Figure 31 shows DC battery symbols (which had consisted of wet-cell batteries requiring charging) as the source of power for heating of the specimen. In actuality, employment of an all-solid-state controller circuitry was made as a replacement for these batteries in order to achieve more precise control at all times.

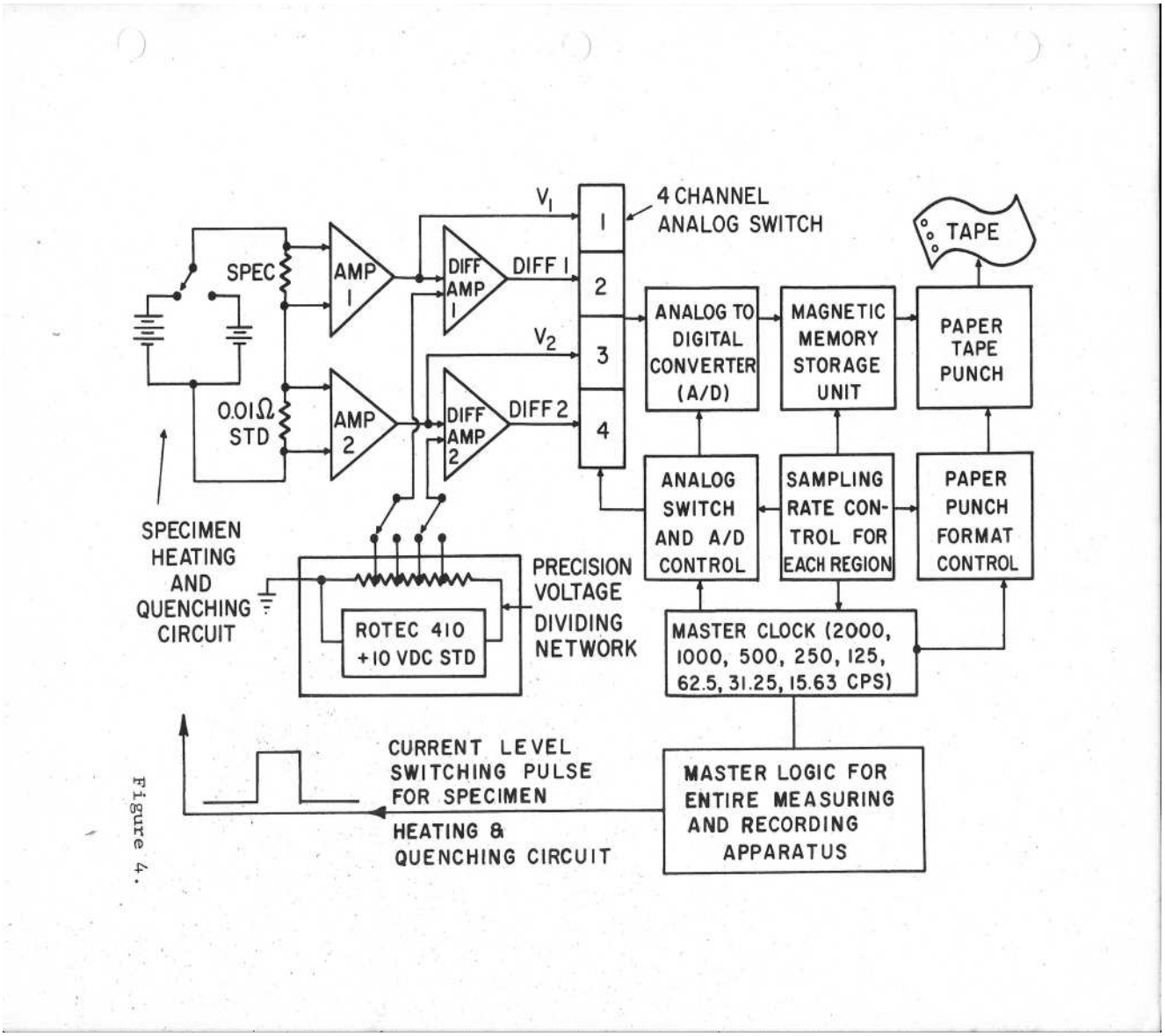

Figure 31. Schematic Diagram of Infotec Data Acquisition Circuitry

Measurements of both pairs of voltages, namely across the standard resistance and across the specimen gauge length, were performed for each direction of current flow established by the current reversal switch. Such current reversal procedures were essential to minimizing offset errors associated with thermal EMF voltages that are always present in systems involving junctions of metals and temperature differentials. Since the values of the current were easily established from the voltage drop across the standard resistance, specimen resistances at the temperature of interest were readily computed.

The residual and quenched-in resistances were measured at 4.2^{o}K by standard potentiometric techniques. Standard resistances were maintained in room temperature oil baths throughout any potentiometric measurement performed on a specimen.

Resolution of ± 0.01 μohm was obtained using a Leeds and Northrup six-dial Model 7556 potentiometer and photocell galvanometer with the measuring current being monitored to 1.00000 ± 0.00002 amperes by use of a Leeds & Northrup Model K3 potentiometer across a 1-ohm standard in series with the specimen [50]. Care was also taken to test for and to assure that no Joule heating of either the standard resistors or the specimen occurred throughout the measurement activity.

For maximal accuracy in quenched-in resistance determinations for 400^{o}C or 450^{o}C straight downquench treatments, Long-Term Anneal (LTA) treatments were always performed (and subsequent R_{LTA} determinations made) both immediately

---

[50] Validated by measurement of the voltage drop across the standard resistor using a six-place digital voltmeter.

before and immediately after 400^{o}C or 450^{o}C straight downquench treatments were conducted.

5.3.2.7 Notable Distinctions from Prior Research

Straight downquench and quench-and-isothermal anneal treatments presented in this research report were patterned after those reported by Wang, Seidman, and Balluffi [63] and the associated data acquisition equipment and procedures have remained essentially unchanged.

However, during feasibility studies two unique Quench/Measurement System Design (QMSD) Units #3 and #4 (see sub-section 4.4.3 for details) each housing two specially shaped specimens were created, together with an all-solid-state temperature profile controller circuitry.

Taken together, these enhancements produced the following benefits:

1) reduced temperature instabilities across each specimen's gauge length [51],

2) contributed significantly to an increased breadth of data acquisition,

3) significantly extended ranges in quench temperatures, initial quench rates, annealing temperatures, and isothermal annealing times,

4) ability to reproduce results of specific thermal treatments, and

5) accomplish extended data analyses involving both thermal and thermal-mechanical treatments.

[51] This was a specific problem noted in the research of Wang [62].

5.3.2.8 Quench/Measurement System Designs

Two Quench/Measurement System Design (QMSD) units were adopted for subsequent in situ gas quenching and potentiometric measurements of specially shaped specimens. Figure 17 illustrates the two adopted shapes, hairpin and catenary-shaped, for the five-mil gold wire specimens. A mounting frame that extended into the quench/measurement unit's shell was employed to hold two specimens per quench/measurement unit.

The mounting frame for QMSD Unit #3 incorporated pairs of stainless steel extension arms between which each hairpin-shaped specimen was mounted. QMSD Unit #4 did not have stainless steel extension arms on its mounting frame, and the two catenary-shaped specimens were mounted on that frame. These two particular shapes were adopted once they proved to exhibit uniform temperature distributions along their entire specimen gauge lengths when subjected to various combinations of elevated temperatures, overpressures, and gas quench media.

Either helium or nitrogen gas served as the quench medium within the quench/measurement unit. When helium gas was used, liquid nitrogen served as the external bath temperature of 77^{o}K for the QMSD unit's shell. When nitrogen gas was used, ice water served as the external bath temperature surrounding the QMSD unit's shell [52]. Gas overpressures of up to 500 psig were maintained by direct

---

[52] From the outset a bath temperature of $T_F \leq 0^{o}$C was specifically chosen to minimize any possibility for losses occurring in quenched-in resistance values associated with ST DQ, Q&A, or other thermal treatments between the time of completion of such elevated temperature runs and transfer of the QMSD unit into the liquid helium-filled Dewar for subsequent potentiometric measurements to be performed on each in situ-mounted specimen.

connection of copper tubing to a pressure-regulated supply tank of the selected gas quench medium for each particular thermal treatment.

Wire specimens were heated for quenching by passing a current through the wire while the specimens were enclosed within the sealed quench/measurement unit. Quenching was accomplished by abruptly reducing the current supplied to a low residual (non-heating) magnitude that remained sufficient to allow for monitoring of the voltage across the specimen's gauge length throughout each chosen thermal treatment.

5.3.2.8.1 Uniqueness of the Adopted QMSD Units' Designs

As stated earlier, with but a few modifications, the thermal history data acquisition system and techniques used are essentially identical to that used by Wang, Seidman, and Balluffi (WSB) [63] and described in detail in Appendix A of their publication.

However, among the more noteworthy changes or additions incorporated in this research investigation were the following:

1. Some of the high-temperature annealing experiments employed two 0.01 ohm Standard resistors connected in parallel to avoid Joule heating of these Leeds and Northrup resistances when heating currents above ten amperes were required to achieve desired elevated temperatures for the five-mil diameter gold wire specimens.

2. An external oscillator (Tektronix Type 114 square wave oscillator) was used in conjunction with the Infotec apparatus to achieve a basic clock frequency of four kHz for temporal spacing of but 0.25 milliseconds when desired combined with clock

frequencies of 100 Hz to allow for extended anneals of tens of minutes when so desired.

Example: 2,000/100 = 20; 20 times 30 seconds = 10 minutes.

3. Q&A treatments that necessitated many hours of annealing at elevated temperatures were performed by employing manual pushbutton tripping from Region III to Region IV thereby bypassing any direct control via the Infotec system. When periodic readings of digital voltmeter readings were used to monitor the average isothermal annealing temperature, generation of paper tape thermal histories was deemed unnecessary.

4. An all-solid-state temperature profile controller was designed and employed in order to achieve both higher heating currents and greater temperature stability [53] either during pre-quench or isothermal annealing stages of thermal treatments.

5. The particular design of the quench/measurement unit and the associated specimens differed substantially from that used by Wang. A few of the principal features which distinguish the present apparatus from Wang's are described in the sub-section below.

5.3.2.8.2 Advantages of the Adopted QMSD Units' Designs

Among the advantages of the adopted Quench/Measurement System Design Units (QMSDs) were the following:

1 A constant specimen shape and associated sink density could be maintained for in situ gas quenching conditions,

---

[53] Stable elevated temperatures having values for ΔT of ±0.2^{o}C were typically achieved.

2. Negligible thermal strains [54] are introduced during quenching,

3. Having two completely independent specimens contained within each QMSD permitted nearly identical quench environment data comparisons (when so desired) and minimal separation between each pair of thermal treatments and associated potentiometric measurements,

4. Reproducible, repeatable, and highly accurate quenched-in resistance determinations were obtainable in association with documented thermal histories.

Additional advantages to be noted besides those listed above are highlighted in Table 3.

[54] See Figure 20 (excerpted from Reference [13]) which indicates that 5-mil diameter gold wires satisfied this criterion.

6 OVERVIEW OF DATA ACQUISITION PROCEDURES

6.1 INTRODUCTION

Specimens are subjected to in situ thermal treatments (described in Section 6.4) during which each specimen serves as its own resistance thermometer [55]. A high-speed high-accuracy data acquisition and recording system manufactured by Infotec and described in [63] was employed for documenting all thermal treatments involving rapid quenches or quench-and-isothermal anneals.

Upon completion of each thermal history profile, lattice defect resistance magnitudes were ascertained using conventional potentiometric measurement techniques [56] that are performed with the quench/measurement unit fully immersed in liquid helium contained within a glass Dewar. Thus, the entire Infotec system-based data acquisition procedure employed in situ conditions. Once a set of measurements had been recorded, the sequence was repeated for whatever thermal treatment and related set of temperatures, initial quench rate, annealing time (if any), or other conditions were desired.

6.2 INFOTEC DATA ACQUISITION SYSTEM

The Infotec Data Acquisition System was described in detail in Chia-Gee Wang's PhD. thesis [62] entitled, Annealing Kinetics of Vacancy Defects in Quenched Gold at Elevated Temperatures.

---

[55] The resistance thermometry scale of Meechan and Eggleston [47] was employed. See sub-section 4.4.2 for additional findings that served to extend this adopted temperature scale to the melting point of gold, namely 1063^{o}C.

[56] A six-dial Leeds & Northrup potentiometer coupled to a photocell galvanometer was employed for all resistometric measurements.

An all-solid-state temperature controller was designed and employed in conjunction with the Infotec data acquisition system. See Figures 26 through 29 for photos of the associated equipment used throughout the data acquisition phases of this research investigation.

6.2.1 Data Acquisition Procedures

Figure 31 illustrates schematically the data acquisition circuitry arrangement. When desired, the temperature regions I and III (see Figure 30) could be manually rather than electronically initiated, for example when checking what quench and isothermal anneal temperatures would be prior to any actual ST DQ or Q&A treatment and subsequent data recording via the Infotec data acquisition system. If only a straight downquench were desired, only pulse # 2 cable from the Infotec would be connected to the controller. Otherwise, pulses 2, 3, and 4 would be employed, and for both cases the pre-quench anneal temperature (corresponding to pulse #1) would be set manually in advance to allow for thermal equilibration.

A solid-state temperature controller comprised of a Regatran zero-to-120-ampere D.C. power supply and high current-switching transistors configured to allow for setting of the current levels associated with Regions I through IV of a Q&A thermal treatment was used in place of wet-cell acid batteries, slide resistors, and mercury-wetted relays used in the research of Wang, et al. [62].

Moreover, front panel manual override circuitry was designed and implemented so that it could be employed in addition to using electronic signals from the Infotec system. This override functionality allowed for convenient checking of both quench and anneal temperatures prior to committing to initiating an ST DQ or Q&A treatment

and the associated data recording actions that would be performed via the Infotec system's circuitry. The principles and features of the Infotec system have been adequately described in references [62] and [63]. Q&A treatments involving times longer than about 30 seconds were made possible by substantially reducing the clock frequency within the Infotec combined with manual execution of Region IV initiation. By these combined means elevated temperature isothermal annealing times of many hours were achieved whenever so desired.

6.2.2 Establishing Elevated Temperatures

Both quench and isothermal annealing temperatures were independently adjusted using the all-solid-state temperature controller triggered during an actual thermal history by pulses from the Infotec apparatus. A Vidar Model 520 six-digit Digital Volt Meter (DVM) was used to establish these temperatures in conjunction with the resistance thermometry scale of Meechan and Eggleston [47] and knowledge of a specimen's gauge length resistance at 40^{o}C.

Adjustment of gas overpressure was coupled with prior knowledge of Q&A voltage settings in order to achieve identical voltage pair settings (i.e., voltage drop across the specimen gauge length and across the selected standard resistance). This method assured as nearly identical initial quench rates between sets of Q&A treatments wherein only the annealing time t_A was to be changed. Each such span of annealing temperatures is referred to as a Q&A series throughout this document.

Since vacancies exhibit increased mobility with increasing temperature [8], the greatest rate of vacancy migration to sinks can be expected to occur during the initial portion of a straight downquench; namely, the first several hundred degrees of

temperature decay. For this reason, initial quench rate (or its reciprocal, defined or represented by the Greek symbol β when used herein) was selected as the independent variable against which to plot monitored quenched-in resistance values for each Straight Downquench (ST DQ) series.

6.3 THERMAL TREATMENTS DATA ACQUISITION PROCEDURES

6.3.1 Outline of In Situ Gas Quenching Procedures

A specimen of pre-determined shape and mounted within a pressurizable Quench/Measurement System Design (QMSD) unit was heated to an elevated temperature by passing direct current through a series circuit incorporating a standard resistor for determining the current levels by measuring the voltage drop across the standard resistor. A gaseous medium of either helium or nitrogen physically surrounded both specimens. The walls of the QMSD were maintained at a bath temperature of 0^{o}C when nitrogen gas was inside the QMSD. When helium gas was inside the QMSD, a bath temperature of 78^{o}K was used. The gas overpressure was supplied and maintained using pressure regulators on the selected supply tank (either nitrogen or helium) connected to an inlet valve that is an integral part of the QMSD unit's design. A second valve served as an outlet valve to allow for purging the internal atmosphere of any prior gas quench medium. When desired, the inlet valve could be disconnected from the supply tank, left open, and the outlet valve opened to the atmosphere so that air could flow freely into and out of the otherwise sealed QMSD unit.

A quench was initiated by reducing the heating current abruptly. Opening of a shunting switch placed across a load resistor that was also part of the overall series

circuit resulted in an abrupt current reduction and permitted only a small non-Joule heating measuring current to remain flowing through the connected specimen. The final temperature of the specimen would then decrease until it reached the bath temperature, either 0^{o}C or 78^{o}K depending upon the selected quench media and bath temperature.

After the respective quench was completed for each of the specimens mounted therein, the QMSD unit was prepared for immersion into a liquid helium Dewar. If the quench had been performed with nitrogen as the quench medium, purging of the quench unit's atmosphere using helium was performed and included setting and maintaining a gas overpressure of 50 psi followed by immersion of the QMSD unit in a liquid nitrogen-filled Dewar for some time prior to transferring the QMSD unit into the liquid helium Dewar. This setting of an overpressure of 50 psig helium served to provide additional heat transfer, to cool the specimen(s) and reduce the chance for any Joule heating occurring during subsequent potentiometric measurements at liquid helium temperatures.

6.3.2 ST DQ and Q&A Treatments of In-Situ Mounted Specimens

6.3.2.1 Steps for Setting up a ST DQ Series Run

Take the following steps for each ST DQ series run on a given specimen mounted within its QMSD Unit.

1. Configure the gas quench medium (helium or nitrogen), gas overpressure (two to 500 psig), and associated bath temperature (0^{o}C or 78^{o}K) environment for the QMSD unit.

2. Connect the selected specimen's heating and quenching circuit to the Infotec Data Acquisition System.

3. Adjust the specimen's elevated temperature resistance ratio, $R(T_Q)/R(40^oC)$ to equal the Pre-quench Anneal (Region I) value for temperature T_Q.

4. Perform a Pre-quench anneal (PQA) treatment (see sub-section 6.4.2 for details) that lasts for at least five minutes and as long as 30 minutes [57].

5. Initiate a ST DQ run for the selected specimen [58] and obtain the associated Regions I and II thermal history (voltage pairs vs. time) values for that were recorded by the Infotec Data Acquisition System and punched out onto paper tape for subsequent examination and further processing.

6. Remove all power from the specimen by opening the power supply current lead circuitry.

After this point, continue with the steps enumerated in sub-section 6.3.3.

6.3.2.2 Steps for Setting Up a Q&A Series Run

The following steps were performed for each run that contributes one data point to a specific Q&A series treatment involving a given specimen mounted within its associated QMSD Unit:

---

[57] A Pre-quench anneal (PQA) treatment was adopted as a means to either remove or at least to minimize whatever pre-existing secondary defects that might have formed as a consequence of previous thermal ST DQ or Q&A treatments involving that specimen.

[58] A ST DQ was accomplished by abruptly reducing the current supplied in the series circuit down to a low residual (non-heating) magnitude that remained sufficient to allow for monitoring of the voltage across the specimen's gauge length throughout the (Region II) downquench phase.

1. Configure the desired gas quench medium (helium or nitrogen), gas overpressure (usually set at10 psig), and associated bath temperature (0^oC or 78^oK) environment for the QMSD unit.

2. Connect the selected specimen's heating and quenching circuit to the Infotec Data Acquisition System.

3. Adjust the specimen's elevated temperature resistance ratio, $R(T_Q)/R(40^oC)$ to equal the Pre-quench Anneal (Region I) value for temperature T_Q.

4. Select the appropriate combination of sampling frequency and number of voltage pairs for Region II) that will result in an ideal transition [59] from T_Q down to the desired isothermal anneal temperature T_A.

5. Perform a Pre-quench anneal (PQA) treatment that lasts for at least five minutes and oftentimes for as long as 30 minutes [60].

6. Initiate a Q&A run of the selected specimen and obtain the associated Regions I through IV thermal history (voltage pairs vs. time) values recorded by the Infotec Data Acquisition System and punched out onto paper tape for subsequent examination and further processing.

7. Remove all power from the specimen by opening the power supply current lead.

---

[59] Only those Q&A histories that exhibited acceptable transitions were pursued to the NQIR determination stage. A quick examination of the transition portion of the thermal history by examination of the paper tape punch-out provided a quick means for this screening to be accomplished.

[60] This treatment was adopted as a means to either remove or at least to minimize whatever pre-existing secondary defects that might have formed as a consequence of previous thermal ST DQ or Q&A treatments involving that specimen.

6.3.3 Potentiometric Measurements at Liquid Helium Temperatures

1. Immediately after completing either step 6 (in sub-section 6.3.2.1) of the ST DQ run or step 7 of the Q&A run (enumerated in sub-section 6.3.2.2 above), purge the QMSD unit with helium (if nitrogen gas had been used during the ST DQ or Q&A run) and pressurize the QMSD Unit to 50 psig.

2. Immerse the pressurized QMSD Unit into a liquid nitrogen-filled Dewar.

3. Calibrate the six-dial potentiometer equipment.

4. Fill an outer Dewar with liquid nitrogen and then transfer liquid helium into an inner three-liter Dewar.

5. Close off the valves to the QMSD unit, carefully remove the unit from the liquid nitrogen bath and slowly lower it into the inner Dewar filled with liquid helium.

NOTE 1: Seek to minimize the boil off of helium by performing this lowering of the QMSD unit very slowly, thereby allowing the QMSD unit's outer shell temperature to approach closely to that of the surrounding liquid helium.

NOTE 2: Within ten minutes after the QMSD unit's immersion, only a slow boil-off of liquid helium would occur. After that time, stable thermal EMFs were attained and associated potentiometric calibrations could be initiated [61]. Within the next twenty minutes, potentiometric measurements for each of the two specimens were performed [62] as described in the remaining steps below.

---

[61] Thermal EMFs were both measured under open-circuit conditions and calculated from the two sets of specimen voltage measurements and were always found to be in close agreement (typically within 0.05 µV of each other, even when the thermal EMF was on the order of 0.5 µV.

[62] Usually, once this amount of immersion time was reached, the liquid helium level in the Dewar proved too low to permit stable EMF readings. If any unavoidable delays were incurred before completion of the sets of measurements, additional liquid helium was transferred into the inner Dewar

6. Recalibrate the six-dial equipment.

7. Using the standardized series circuitry, pass a pre-established non-Joule heating current through the first specimen selected for potentiometric measurements. Usually, the upper specimen was measured first to assure that an adequate liquid helium level remained for subsequent potentiometric measurements of the second specimen.

8. Perform the potentiometric measurements on the first selected specimen, recording all data including voltage drop across the standard resistance selected [63].

9. Disconnect the current lead from the external Amphenol connector that is wired to the upper specimen and connect the current lead from the lower specimen in series with the standard resistance.

10. Recalibrate the six-dial potentiometer.

11. Repeat step 8 above.

12. Visually check for what the remaining liquid helium level is inside the inner Dewar.

13. If a sufficient level of liquid helium remains in the inner Dewar, perform additional readings if deemed desirable, repeating as necessary these potentiometric measurements (including recalibrations).

14. Remove all power from quench unit specimens and carefully raise the QMSD unit assembly from the inner Dewar and immerse it in the appropriate

---

so that quenched-in resistance measurements could be completed. In general, this was not encountered.

[63] This standard resistance used was nearly always the 1.00000 ohm unit kept at constant temperature in an oil bath.

temperature bath (ice water or liquid nitrogen) if another ST DQ run is scheduled for the specimens mounted within that QMSD unit.

16. Calculate quenched-in resistance values of both specimens by taking the difference between the just-determined resistance values and the respective specimen's residual resistance values [64].

6.4 DESCRIPTIONS OF PRIMARY THERMAL TREATMENTS

The data acquisition phase of this research investigation focused on conducting thermal treatments on in situ mounted five-mil diameter 99.9999 weight percent pure gold wire specimens.

Definitions, concepts, and objectives associated with each of four primary thermal treatments -- LTA, Pre-Quench Anneal, ST DQ, and Q&A -- that were extensively employed for data acquisition are outlined in this section.

The collective purpose of these elevated temperature thermal treatments was to obtain resistometric data from which reliable, quantitative assessments of lattice defect energies, kinetics, and dominant sink structures and their respective densities might be estimated or calculated.

6.4.1 Long-Term Anneal (LTA) Treatments

An LTA treatment is simply a thermal treatment performed initially on each newly-created specimen while it is kept mounted within its Quench/Measurement

---

[64] The residual resistance values are defined here to be the R_{LTA} values obtained after performing Long-term Anneal (LTA) treatments as defined in sub-section 6.4.1.1 of this document.

System Design (QMSD) unit[65]. The fundamental purpose of performing an LTA treatment is to achieve a “vacancy free” residual resistance magnitude that will serve as a baseline from which to calculate subsequent quenched-in resistance values that are introduced after performing any elevated temperature quench or quench-and-anneal thermal treatments on each specimen.

For potentiometric resistance measurements to be as reliable as possible, it was deemed essential to establish and employ a thermal treatment of each specimen that would result in achievement of "vacancy-free" residual resistance values when measured at liquid helium temperatures following such thermal treatments. Long-Term Anneal (LTA) was chosen as the phrase to associate with this specific thermal treatment. The idea that led to its establishment was that of performing a gradual stepped sequence of reduction in each specimen's elevated temperature with the end objective of having whatever excess vacancy concentration that may be present eventually anneal out until (for the lowest annealing temperature) the resulting excess vacancy concentration would prove to fall below a resistometrically detectable level.

[65] Before conducting any given LTA treatment, the QMSD unit's inlet valve is disconnected from the gas source (helium or nitrogen), and both the inlet and outlet valves were opened to the air in the laboratory room.

6.4.1.1 Definition of a Long-Term Anneal (LTA) Treatment

The thermal treatment associated with establishment of vacancy-free residual resistance for any given specimen cooled to 4.2^{o}K is referred to throughout this document as a Long-Term Anneal (LTA) [66].

The specific step-annealing temperature-time profile that was found to result in reliable residual resistance values for all specimens is illustrated in Table 6 (see sub-section 4.4.4).

This Long-Term Anneal (LTA) treatment was adopted throughout this research and served to establish residual resistance chronologies (for details, see Section 11.2) for each of many specimens subjected to all types of thermal and thermal-mechanical treatments.

6.4.1.2 Objectives of LTA Treatments

LTA treatments represent a fundamental requirement performed for all subsequent types of elevated thermal treatments, be they ST DQ, or Q&A.

For every specimen created and subjected to an LTA treatment, the associated uncorrected for size effect specimen purity ratios, $R(40^{o}C)/R_{LTA}(4.2^{o}K)$, were calculated [67].

Once determined, the R_{LTA} values were considered to represent attainment of "vacancy-free" conditions insofar as potentiometric measurements could resolve. With that perspective, such results were equated to achieving a $\Delta R_{QN}=0$ condition

---

[66] Refer to Chapter 11 for subsequent data analyses of the results obtained for collective sets of specimen-specific Long-Term Anneal treatments.

[67] In addition, corrections for size effect [59] were made established using the curve shown in Figure 33. Table 8 lists the respective corrected RRR ratios for a number of five-mil gold wire specimens that were used throughout this research investigation.

that established the baseline from which any subsequent ST DQ, Q&A, or whatever thermal treatments' respective ΔR_{QN} values would be calculated in the short term. After usually no more than three elevated temperature thermal treatments have been conducted for a given specimen, an LTA treatment was repeated, and the resulting R_{LTA} value applied in subsequent NQIR determinations for the next series of elevated temperature thermal treatments. Such recording of R_{LTA} values led to the generation of R_{LTA} chronologies (see Figure 32 for three specific examples of such monitoring) which were analyzed and are discussed in Section 11.2 of this document.

6.4.1.3 Achievement of the Adopted LTA Step-Annealing Profile

Table 6 details a step-anneal sequence referred to herein as a Long-Term Anneal (LTA) treatment that was found to produce reliable, reproducible [68] residual resistance values for each specimen so treated, regardless of prior thermal history [69].

This specific annealing sequence was performed periodically between several sets of thermal treatments in order to assure that a reliable vacancy-free residual resistance value (labeled as R_{LTA}) would be established that would contribute significantly to establishing accurate determinations of quenched-in resistance values for any subsequent ST DQ or Q&A series elevated temperature thermal treatments.

---

68 The residual resistance shift between quenches was calculated to be about 0.01×10^{-6} ohms, whereas most quenched-in resistance magnitudes were typically tens of micro-ohms.

69 Figure 24 illustrates four different LTA profiles performed on Specimen 3012 over several months and the resulting R_{LTA} values obtained following each of the four LTA treatments.

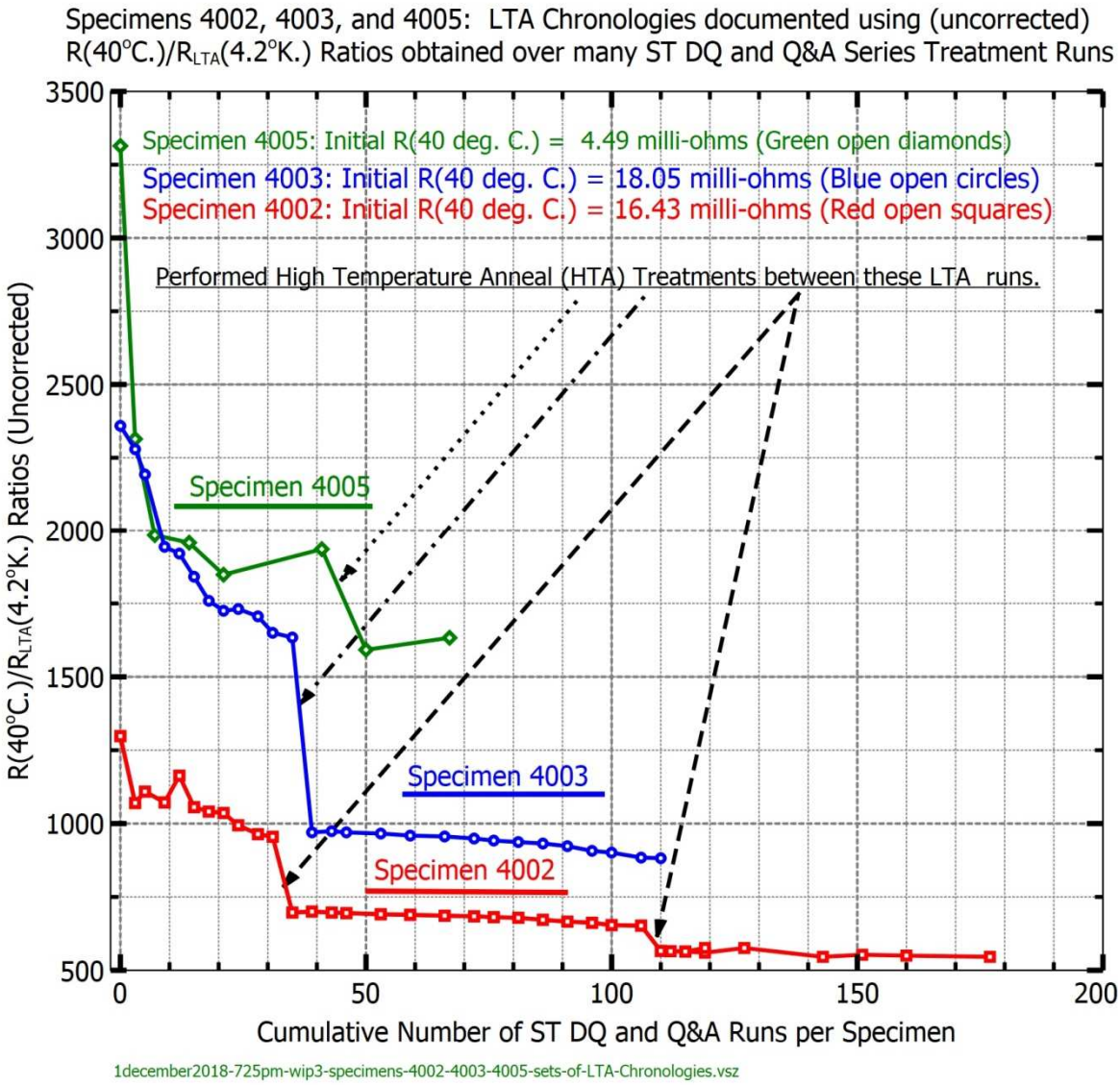

Figure 32. Specimens 4002, 4003, and 4005: LTA Chronologies documented using (uncorrected) $R(40^{o}C)/R_{LTA}(4.2^{o}K)$ Ratios over many ST DQ and Q&A Series Treatment Runs.

6.4.1.3.1 Residual Resistance Determinations

The objective of an LTA treatment is to allow vacancies to maintain quasi-equilibrium to low enough temperatures so that whatever impurities and other pre-existing lattice defects that may be present within the specimen will completely mask out any remaining vacancy contributions when subsequent potentiometric measurements of electrical resistance are made at liquid helium temperatures.

In principle if a specimen is slowly cooled from elevated temperatures, a condition is approached at the lower temperatures such that the vacancy concentration becomes negligible compared with the impurity concentration. For this research investigation, this condition should occur in 6N gold for temperatures at or below 250^{o}C.

6.4.1.3.2 Specimen Relative Resistance Ratio (RRR) Results

Table 8 indicates the calculated resistance ratios, $R(40^{o}C)/R_{LTA}(4.2^{o}K)$, for a number of specimens. Specimen residual resistance values, labeled R_{LTA} $(4.2^{o}K)$, are those obtained following a specific Long-Term Anneal (LTA) step-annealing profile illustrated in Table 6.

Table 8. Determinations of R(40°C), R_{LTA}, and Size-Effect-Corrected RRR Values for Fifteen 5-mil Diameter (6N-pure) Gold Wire Specimens

Specimen Numbers	R(40°C) x 10^{-3} ohms	R_{LTA}(4.2°K) x 10^{-6} ohms	RRR	Size Effect Correction	RRR (corrected [70])
3005	1.904	0.56	3,400	6.32	21,477
3006	2.637	0.705	3,740	11.5	42,954
3007	4.125	1.255	3,287	5.75	18,900
3008	3.357	1.235	2,718	3.1	8,438
3009	2.59	1.365	1,904	1.88	3,580
3010	3.815	1.32	2,890	3.72	10,737
3011	2.59	0.82	3,158	4.7	14,845
3012	3.19	0.96	3,319	5.93	19,688
3013	4.04	1.76	2,295	2.45	5,625
3014	4.772	2.92	1,634	1.45	2,362
3016	3.154	1.00	3,154	4.68	14,761
3018	3.866	1.04	3,717	11.5	42,779
4002	16.43	12.66	1,298	1.4	1,817
4003	18.08	7.65	2,359	2.44	5,762
4005	4.53	1.355	3,343	6.31	21,062

6.4.1.4 Corrections for Size Effect in 5-mil Diameter Gold Specimens

Each 5-mil diameter gold wire specimen's initial Relative Resistance Ratio, RRR(uncorrected) = R(40°C)/R_{LTA}(4.2°K), was corrected for size effect using the size effect correction curve of Figure 33 patterned after Sondheimer [59].

[70] This column lists values that have been corrected for size effect as indicated in Figure 33. RRR (corrected).

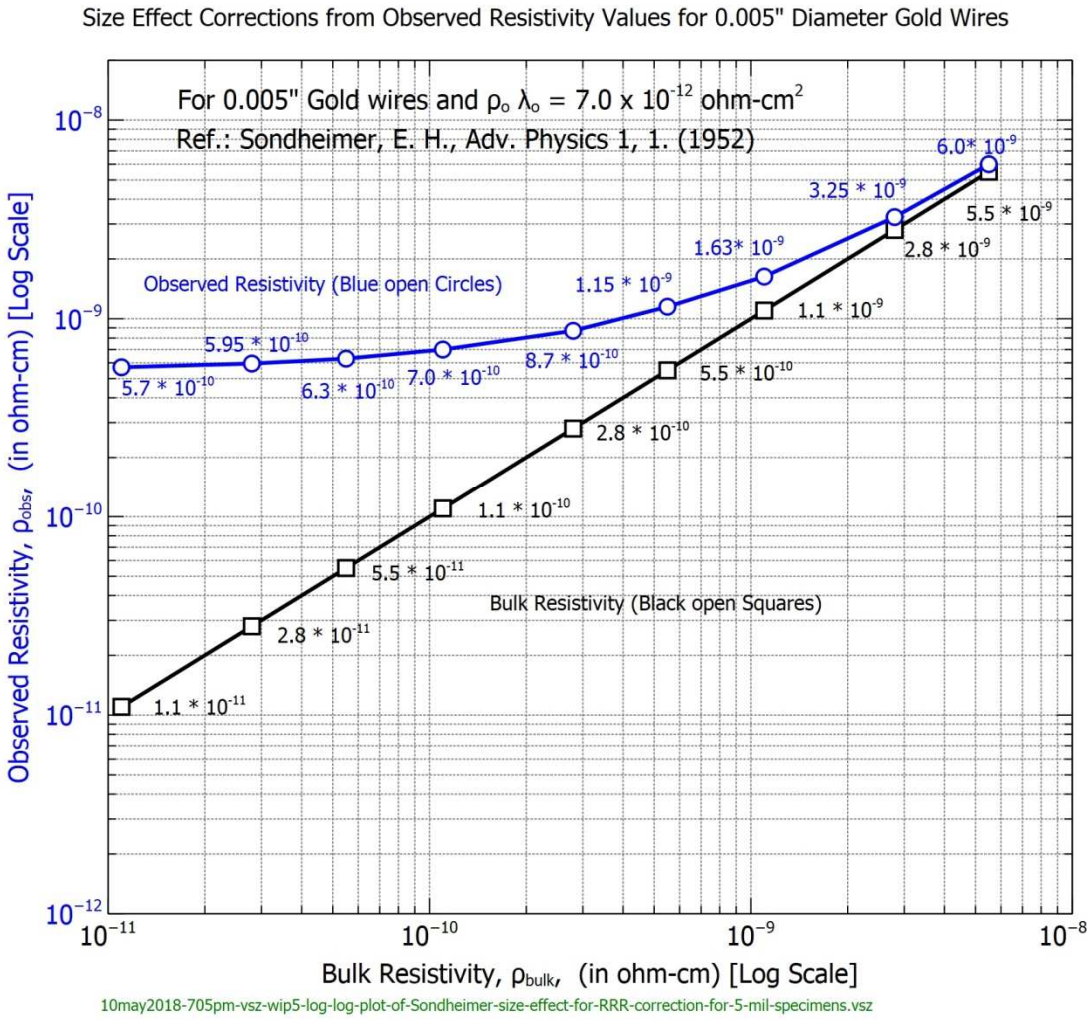

Figure 33. Relative Resistance Ratio (RRR) Correction for Size Effect in 5-mil Diameter Gold Wires.

As Table 8 shows, the RRR (uncorrected) values for specimens used throughout this research before correction for size effect ranged from 1267 to 3740. Following correcting for size effect, the values for RRR (corrected) were calculated to range from 1,817 to 42,954. In fact, a representative RRR (uncorrected) value associated with many of the specimens used throughout this research investigation was 3300 ± 400 that corresponded to RRR(corrected) values of between 11,000 and 28,000.

6.4.1.5 Results of "LTA-like" Step-Annealing Profiles

For comparison purposes, Table 7 provides an example of what proves to be an unsatisfactory step-annealing sequence for achieving a vacancy-free residual resistance value for gold specimens, particularly when ST DQ or Q&A runs with quench temperatures in the range from 400^{o}C to 600^{o}C are involved.

A lowest quench temperature of 400^{o}C was chosen due to limits of detection sensitivity of quenched-in vacancies above residual resistance levels in the 6N (99.9999 weight percent)-pure gold 5-mil diameter wire specimens. For this reason, the values listed in Table 6 were used for LTA treatments performed on nearly all specimens.

Figure 23 provides graphical representations for the adopted LTA profile and an unsatisfactory "LTA-like" profile.

From an examination of the values obtained for the treatments shown in Figure 23 it is readily observed that a foreshortened (shorter annealing times for any of the steps) or abbreviated (fewer overall step anneals) "LTA-like" treatment resulted in a higher, and hence inaccurate, residual resistance value.

By comparison, the adopted LTA treatment with its longer, more gradual temperature reduction sequence, was found to yield consistently reproducible quenched-in resistance values throughout the thermal histories associated with numerous specimens [71].

6.4.1.6 Endorsement of the Adopted LTA Step-Annealing Treatment Profile as a Cleansing Anneal Treatment

Establishment of vacancy-free residual resistance conditions must actively be sought in order to assure accurate and precise determinations of vacancy formation energy magnitudes from quenched-in lattice vacancy concentrations. At lower quench temperatures, for example, any foreshortened or abbreviated "LTA-like" treatment was found to result in "quasi-residual resistance values" that were higher than what was obtained when the adopted LTA treatment was performed on the same specimen.

6.4.1.7 Establishing Uncorrected and Corrected RRR Values

Table 8 provides tabulations of respective R(40^{o}C.), R_{LTA}, RRR (uncorrected), and RRR (corrected) [72] values for fifteen (15) gold wire specimens used throughout the primary investigations that followed completion of feasibility studies. Figure 33 represents the Size Effect Correction Curve created and used based on the work of E. H. Sonderheimer [59].

---

[71] The reproducibility was obtained even in spite of gradual upward shifts in the residual resistance values that were noted to occur throughout every specimen's R_{LTA} chronology (see Chapter 11 for more details).

[72] See sub-section 6.4.1.4 for details on RRR corrections for size effect [59].

6.4.2 Pre-quench Anneal (PQA) Treatments

6.4.2.1 Definition of a Pre-quench Anneal (PQA) Treatment

With Figure 30 as a reference, what is labeled as Region I represents what served as a pre-quench anneal (PQA) treatment [73] generally lasting anywhere from five to 30 or more minutes that with but a few exceptions always preceded each and every ST DQ or Q&A series [74] treatment data acquisition activity which was then followed by potentiometric measurements at liquid helium temperatures to determine quenched-in resistance values that resulted from each specific thermal treatment history.

6.4.2.2 Objectives of a Pre-quench Anneal (PQA) Treatment

The two primary objectives of a pre-quench anneal were 1) to establish a thermal equilibrium vacancy concentration at temperature T_Q prior to any subsequent thermal treatment and 2) to serve as a "cleansing anneal" that would assure removal of or at least significant reduction in the number of secondary defects that may have

---

73 The phrase "cleansing anneal" consists of the elevated temperature treatment that was performed before each series of quenches in order to ensure satisfactory reproducibility of a specimen's quenched-in resistance value measured at liquid helium temperature of 4.2^{o}K. In this research investigation, moreover, performing an LTA treatment was established as the method to achieve precisely that objective throughout a specimen's lifetime.

74 Some Q&A Series runs involved what are referred to as Extended Anneals. Such Extended Anneals were initiated after a ST DQ from T_Q was performed and followed by a potentiometric measurement at 4.2^{o}K). In short, the specimen was subsequently heated to and held at a chosen isothermal annealing temperature T_A for whatever "extended period of annealing time" was desired, and subsequently quenched to the QMSD shell's bath temperature followed by a potentiometric measurement at 4.2^{o}K. For graphing-related purposes, each such Extended Anneal run was distinguished by appending an (A), (B), (C),and so on notation to the associated run number in order to reflect the fact that the nature of the associated measurement result was the consequence of having performed what is referred to here as an Extended Anneal treatment.

been formed as a consequence of prior thermal treatments performed on every in situ mounted specimen [75].

6.4.3 Straight Downquench (ST DQ) Treatments

6.4.3.1 Definition of ST DQ Treatments

Each thermal treatment labeled throughout this document as a straight downquench (ST DQ) treatment (refer to Figure 30) consisted of a pre-quench anneal (Region I) treatment (as described in sub-section 6.4.2) followed by an in situ gas quench (Region II) directly from the pre-quench anneal temperature T_Q down to a final bath temperature T_F (selected to be either 0^oC or 78^oK, depending on the gas quench medium being used for that specific run) at which the pressurized QMSD unit's outer walls were kept using ice water or liquid nitrogen, respectively.

6.4.3.2 Objectives of ST DQ Treatments

The fundamental objective of straight downquench treatments was to obtain sets of quenched-in lattice defect electrical resistance data as a function of both quench temperature and initial quench rate.

A second objective was to perform detailed analyses of the acquired sets of data to determine the value for the effective formation energy of vacancies, examine the associated ST DQ annealing kinetics, and reveal insights into the nature of sinks for excess vacancies during straight downquenches from elevated temperatures.

More details about this topic are provided in Chapter 7 of this document.

---

[75] Jeannotte and Machlin [34] have noted that monitored annealing kinetics of excess vacancies in gold specimens were significantly influenced by pre-quench annealing histories.

6.4.4 Quench-and-Isothermal Anneal (Q&A) Treatments

6.4.4.1 Definition of Q&A Treatments

Four distinct regions comprise a Q&A thermal history. Using Figure 30 as a reference, a Q&A thermal treatment becomes established when a stable plateau [76] (Region III) is inserted into what would otherwise have been a ST DQ treatment.

During the duration of Region III, an isothermal temperature T_A would be maintained for a pre-set annealing time t_A (ranging anywhere from as short as 180 milliseconds to as long as hundreds of hours) and is subsequently terminated when Region IV which is defined as a final straight downquench of the specimen from the isothermal temperature T_A down to the final bath temperature T_F (either 0^oC or 78^oK, according to the gas quench medium being used) is completed. This overall four-region temperature profile sequence is defined as a Quench-and-Isothermal Anneal (Q&A) treatment.

Ideally, the final downquench (Region IV) would result in retention of the excess vacancy concentration remaining at the end of Region III. However, some additional losses can be expected to occur, particularly whenever isothermal annealing temperatures (T_A values) are at or above what can be referred to as the associated specimen's T* temperature. Notably, if the value for t_A (associated with Region III) were set equal to zero seconds, the thermal treatment would no longer be a Q&A

---

[76] A smooth transition from a Region I quench to a Region III isothermal anneal was achieved by programming the duration of Region II to minimize either under- or over-shooting of the desired isothermal annealing temperature. This task was accomplished programmatically within the Infotec data acquisition system by selecting appropriate combinations of clock speed and number of pairs of data to be recorded associated with Region II and also involved prior examinations of the respective ST DQ thermal histories for the associated quench environments to establish the relevant transition times.

treatment but would become a straight downquench (ST DQ) treatment that proceeds directly from the temperature T_Q down to the final bath temperature T_F [77].

6.4.4.2 Objectives of Q&A Treatments

The fundamental objective of Q&A treatments was to acquire sufficiently extensive data of quenched-in resistance as functions of quench temperature, annealing temperature, and annealing time.

A second objective was to perform subsequent analyses of various sets of Q&A series data obtained during isothermal anneals involving elevated temperatures in order to 1) establish magnitudes for effective vacancy migration energy for vacancies, E^M_V(eff), 2) assess annealing kinetics and what may be the nature of sinks for excess vacancies, and 3) employ parameters, such as Initial Annealing Rates (IARs) and Normalized Initial Annealing Rates (NIARs), to determine values for what will be referred to as mean relaxation times, (t_{mean}),[78] and the Instantaneous Vacancy Activation Energy, E^M_V(act).

More details about each of these topics are provided in Chapter 8 of this document.

---

77 Current levels associated with Regions II and IV of every Q&A thermal history were pre-set to low levels (e.g., 10 milliamps) to assure that no Joule heating of specimens would ever occur.

78 Mean relaxation times are defined and calculated by dividing a specimen's associated straight downquench NQIR(T_Q, T_A, t_A = 0) value by the quantity {[NQIR(T_Q, T_A, t_A = 0) - NQIR(T_Q, T_A, $\Delta t_A)_{initial}$] / $(\Delta t_A)_{initial}$}. As a consequence of this definition, a "normalized" time parameter generally referred to as "mean relaxation time (t_{mean})" can be obtained that is wholly independent of a specimen's geometry. As a result, direct comparisons of results among specimens are made possible when such a parameter is used, for example, in Arrhenius plots.

7 STRAIGHT DOWNQUENCH (ST DQ) EXPERIMENTS

7.1 INTRODUCTION

This chapter details the purpose, results, parameter determinations, associated discussions of results, and conclusions arising from analyses of data obtained from straight downquench treatments.

7.2 ST DQ DATA ACQUISITION

Following completion of feasibility studies, experiments were undertaken involving numerous sets of Straight Downquench (ST DQ) series thermal treatments (See Figure 3 cited earlier).

Each of two Quench/Measurement System Design (QMSD) units, referred to as Unit #3 and Unit #4, respectively, were employed with each unit having two specimens mounted independently of one another inside each unit. This allowed for performing LTA treatments on one specimen, say in QMSD Unit #3, while allowing for conducting concurrently either a ST DQ or Q&A treatment on one of the two specimens mounted in QMSD Unit #4.

Notably, QMSD Unit #3's internal framework was designed to give uniform temperature profiles to 3000-numbered specimens having overall smaller gauge lengths and hairpin-like shapes, whereas QMSD Unit #4 was used for the 4000-numbered specimens [[79]] having larger gauge lengths and catenary-like shapes.

[79] Specimen #4005 was the sole notable exception to this numbering system. It had the smaller hairpin shape that involved addition of a pair of stainless steel mounting arms as indicated in the lower sketch of Figure 17 (see section 4.4.1.4).

7.3 ST DQ SERIES TREATMENT RESULTS AND OBSERVATIONS

7.3.1 Straight Downquench Thermal Histories

Most specimens exhibited ST DQ thermal histories that closely obeyed (for the first two hundred degrees of decay) a relationship of the form $T(t) = (T_Q - T_F)\exp(-t/\tau) + T_F$ where τ would equal the amount of time associated with reaching e^{-1} of the quantity $(T_Q - T_F)$ where T_Q is the quench temperature, t is the time since quench initiation, and T_F equals the final bath temperature (being either 0^oC or 78^oK for nitrogen or helium gas quench media, respectively).

See Figures 34 through 38 for some plotted examples of thermal histories associated with Straight Downquench (ST DQ) treatments.

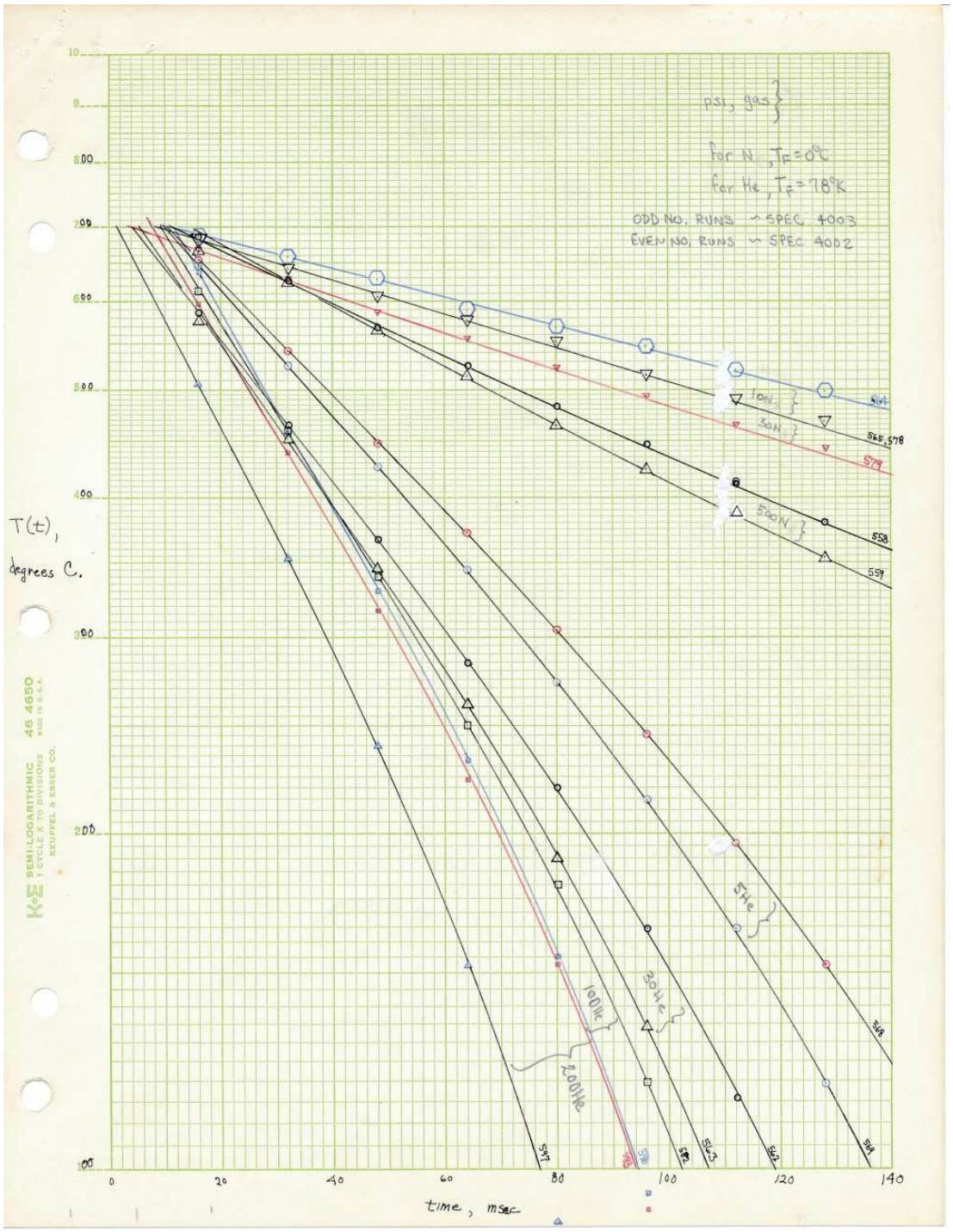

Figure 34. Specimens 4002 and 4003: Thirteen examples of 700°C ST DQ Thermal Histories

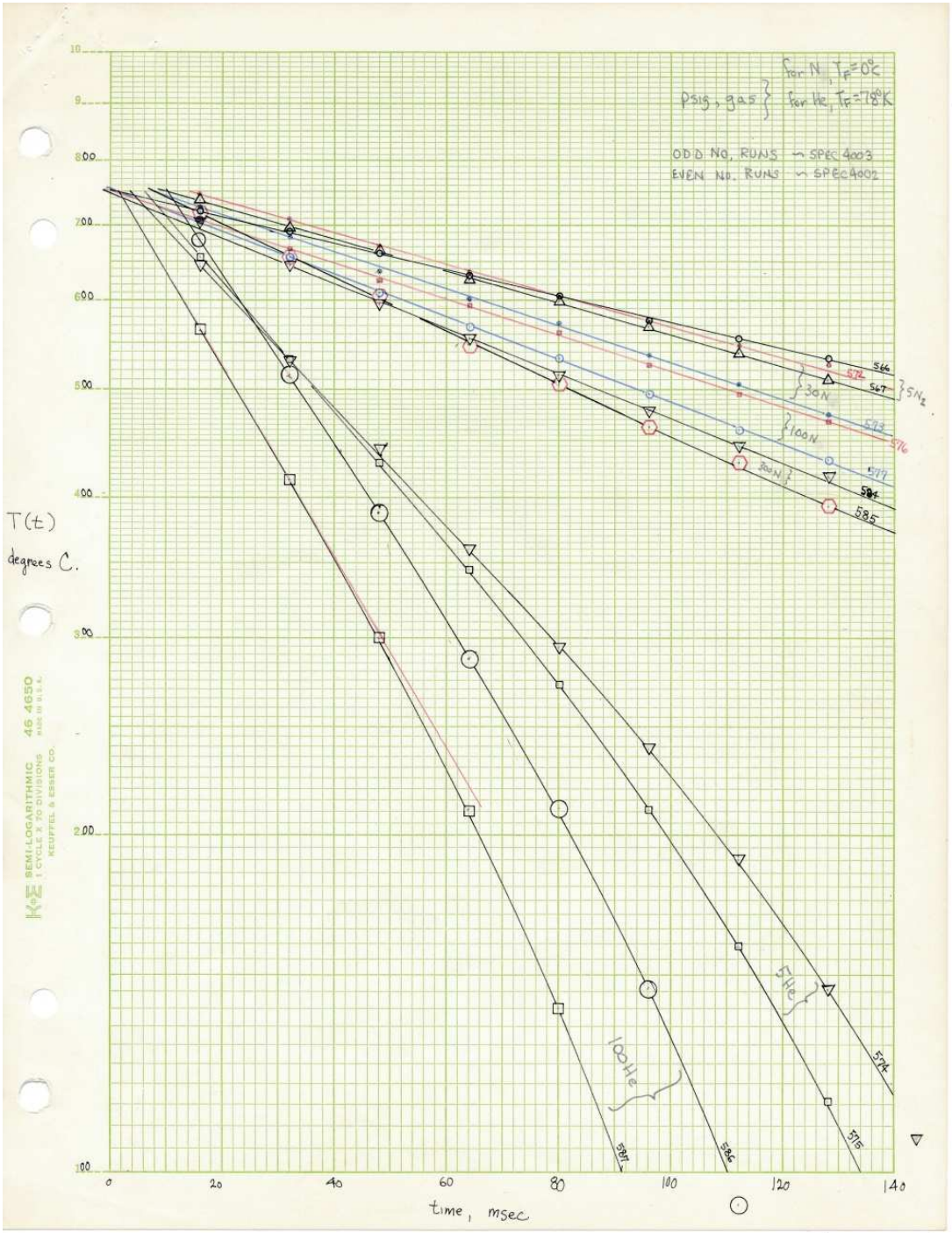

Figure 35. Specimens 4002 and 4003: Twelve examples of 750°C ST DQ Thermal Histories

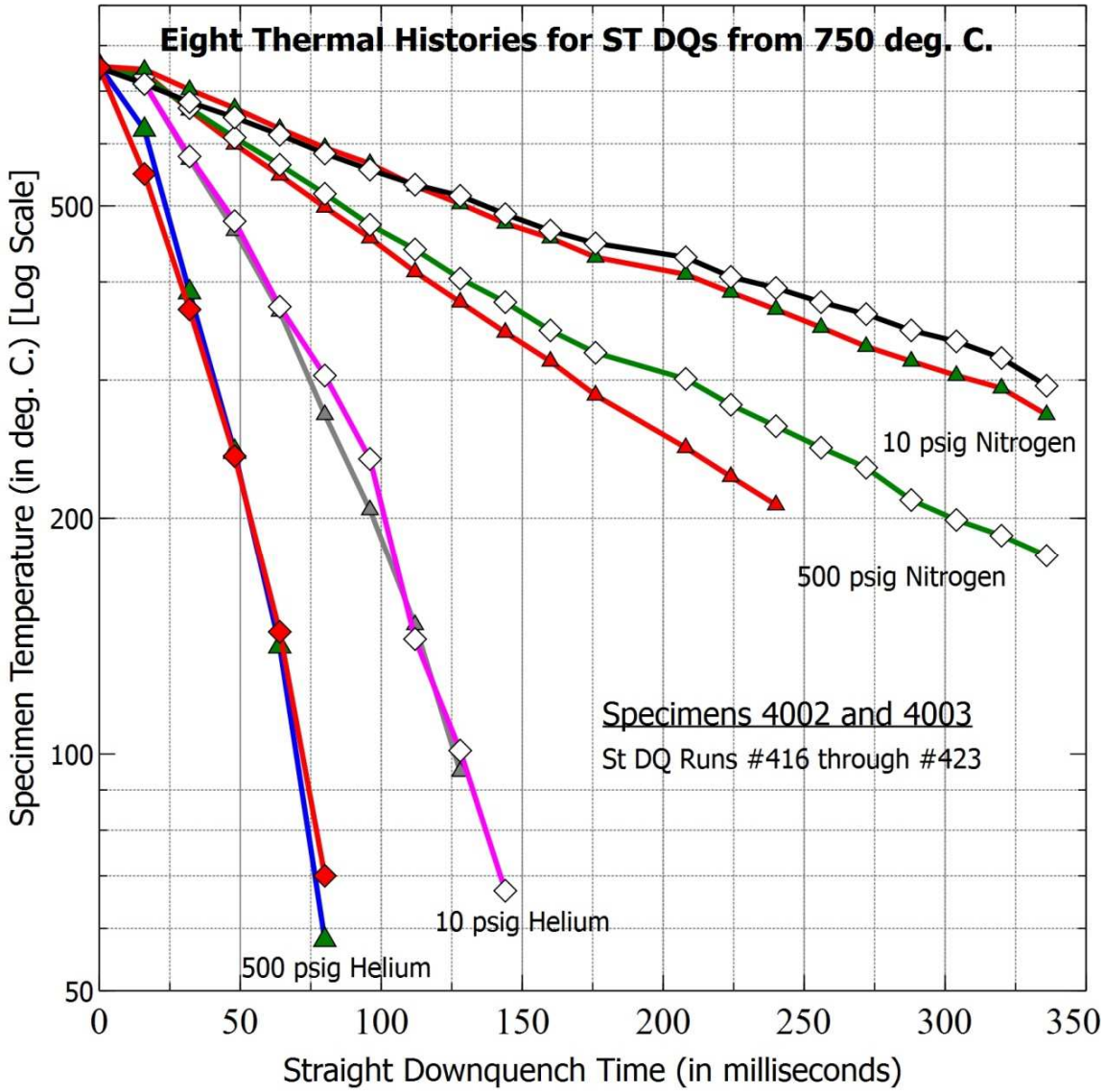

Figure 36. Specimens 4002 and 4005: Eight Examples of 750°C ST DQ Thermal Histories

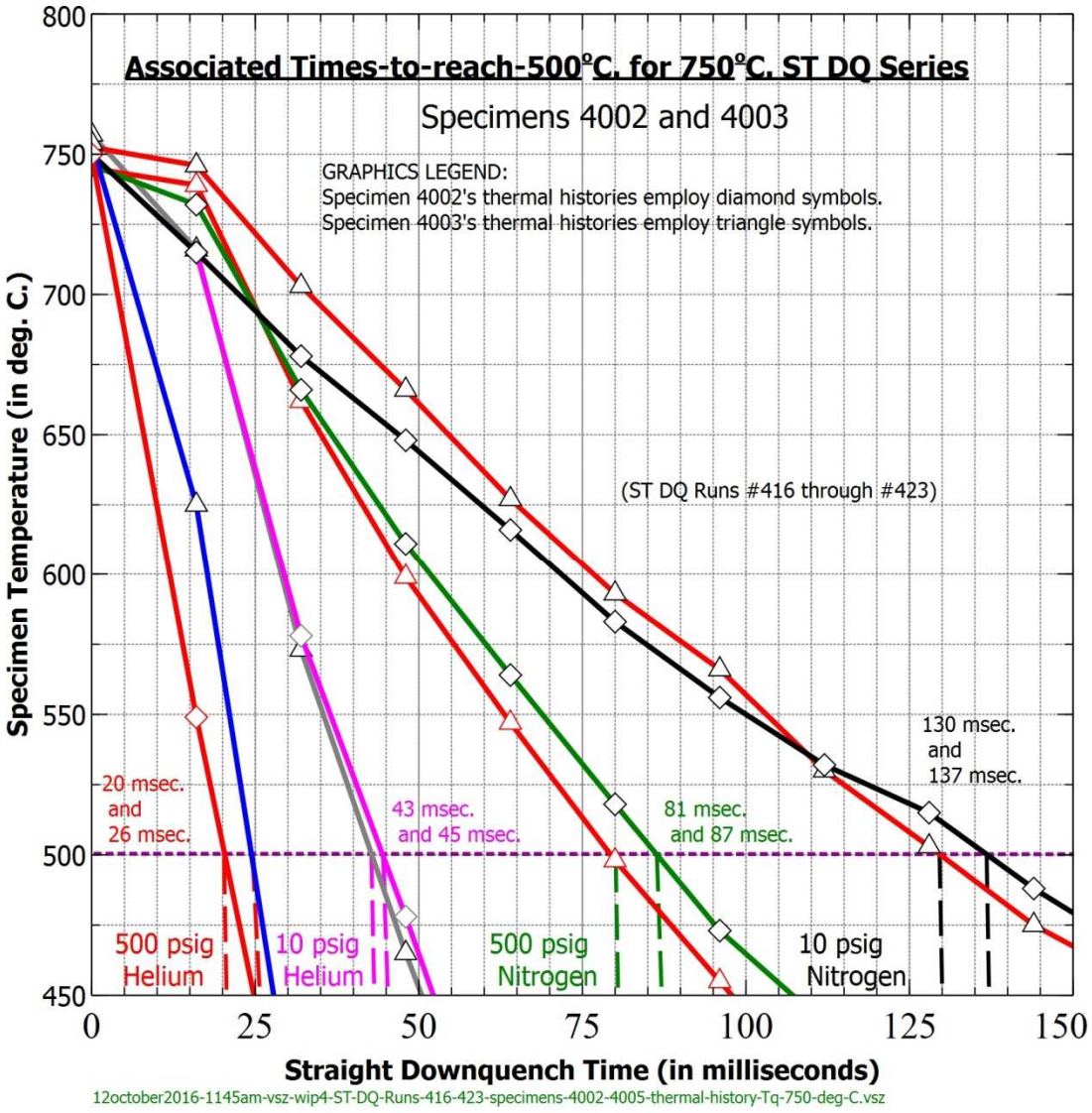

Figure 37. Associated Times-to-Reach-500°C for eight 750°C ST DQ Thermal Histories [80]

[80] NOTE: In some instances, occurrences of delays of up to 20 msec. before the onset of ST DQ thermal histories were encountered, and these occasional delays were attributed to the use of electro-mechanical relays associated with the Infotec Data Acquisition's control circuitry.

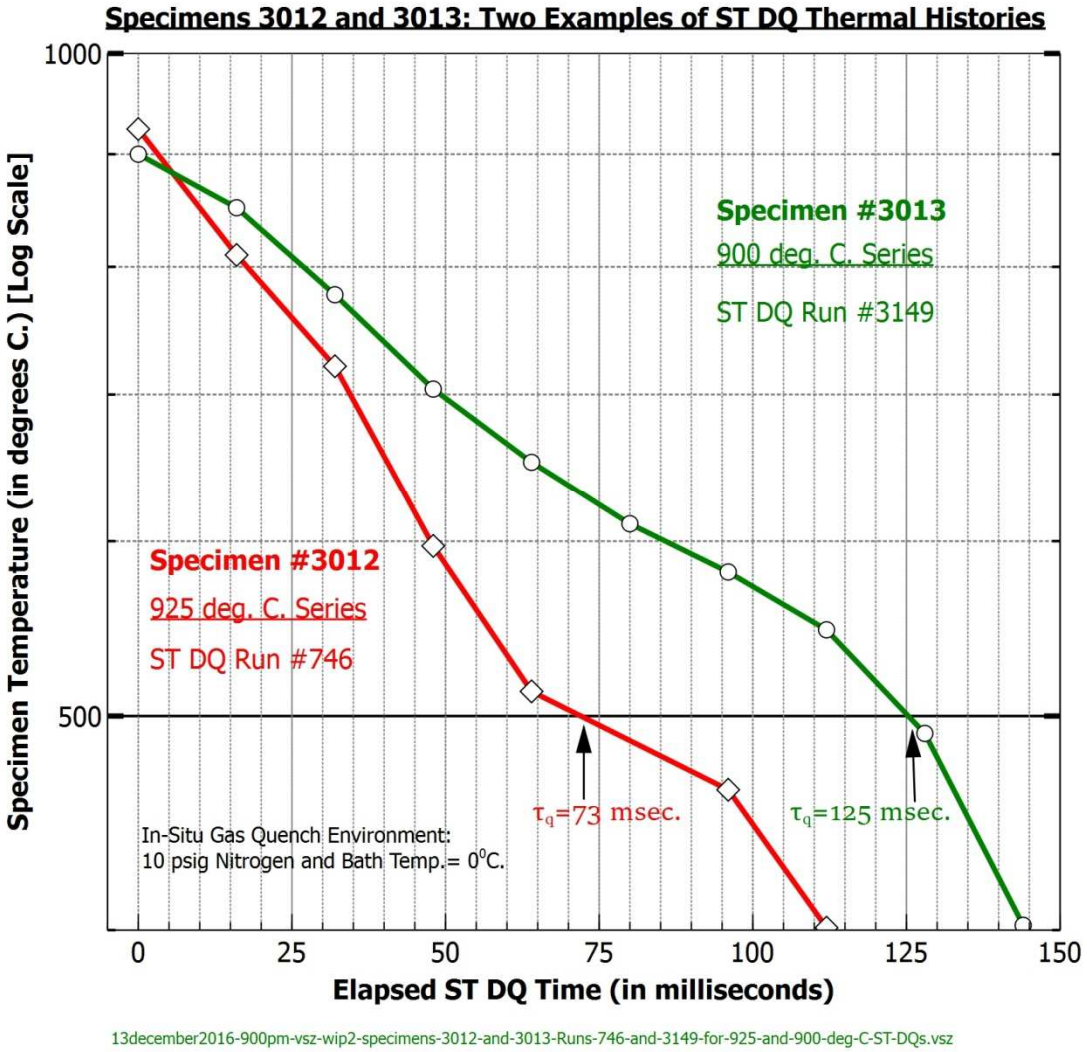

Figure 38. Specimens 3012 and 3013: Examples of 925°C and 900°C ST DQ Thermal Histories

7.3.2 Representative Ranges in Effective Time of Quench

Figure 39 illustrates a typical range in effective time of quench (τ_q) values calculated from straight downquench thermal histories involving $T_Q \geq 700^oC$.

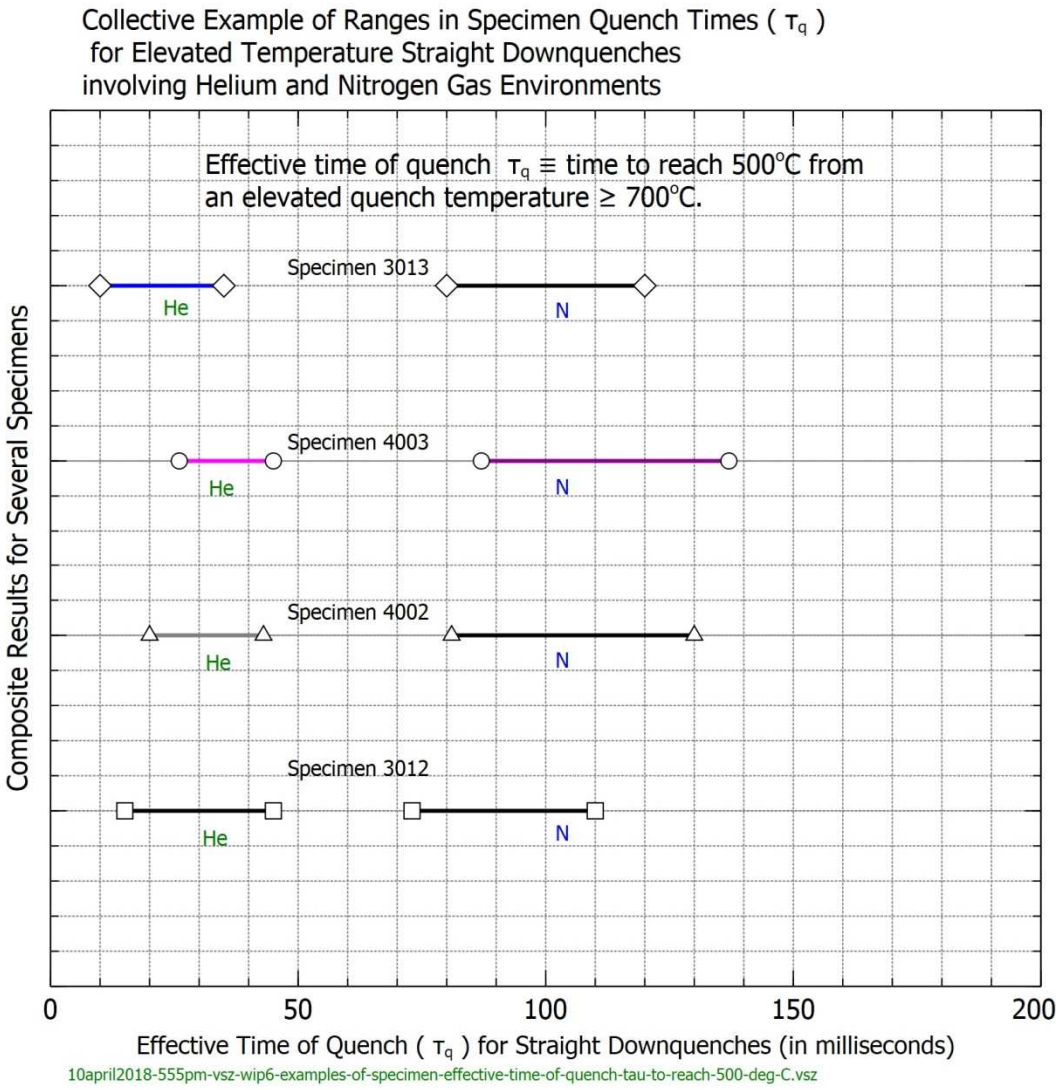

Figure 39. Example of Overall Composite Range of Effective Time of Quench (τ_q) for Straight Downquenches involving $T_Q \geq 700^oC$

7.3.3 Representative Sets of B.E.T. Plots

Figure 40 provides representative examples of initial hand-drafted BET plots obtained for seven five-mil diameter 6N-pure gold wire specimens involving 925, 800, 750, and 700^{o}C ST DQ Series Treatments

Initial quench rates associated with the selected in situ gas quench apparatus were selectively variable for each specimen.

Final bath temperature (T_F), quench medium (helium or nitrogen), and gas overpressure (10 to 500 psig) determined the initial quench rate for any particular specimen. The highest initial quench rates were obtained with the smallest overall specimens quenched in helium at 500 psig with the specimen's QMSD unit's outer shell immersed in a Dewar filled with liquid nitrogen.

Normalized quenched-in resistance values were used in order to permit graphical comparison of data for several different specimens on a single graph. The selected independent variable, namely reciprocal initial quench rate, eliminated any requirement for either knowing or idealizing the entire thermal history associated with any given straight downquench.

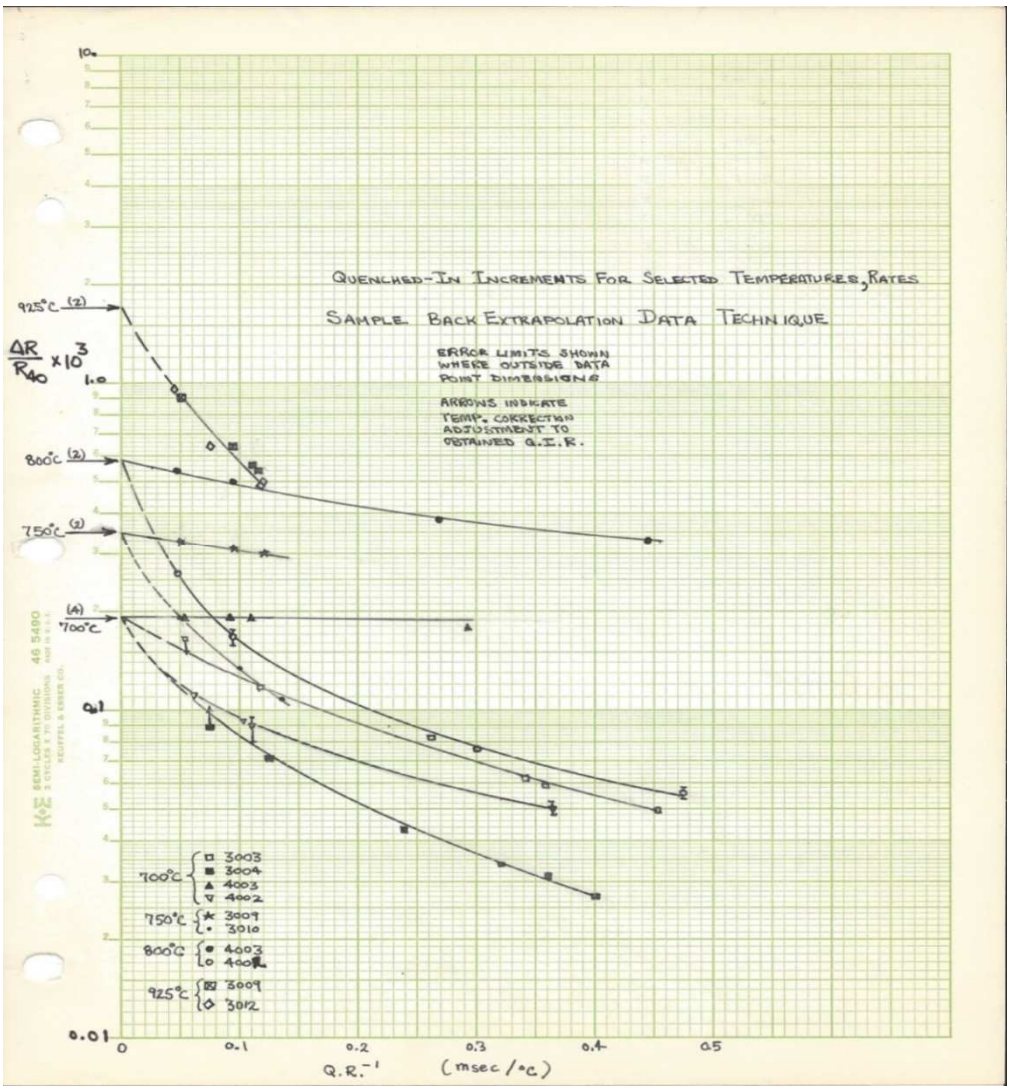

Figure 40. Ten "No-Loss" B.E.T. Plots of NQIR [T_Q, $(dt/dT_{initial})^{-1}$] Data for 925, 800, 750, and 700°C ST DQ Series for seven 5-mil diameter 6N-pure Gold Wire Specimens

7.3.4 Observations made from numerous sets of B.E.T. Plots

Analyses of back-extrapolated data for each specimen and quench temperature are detailed later in Section 7.4 of this document, but several points concerning the graphed data can be made at this time.

1. Reproducibility of ΔR_{QN} values endorses achievement of repeatable ΔR_{QN} thermal histories and constant specimen sink densities.

2. The observed monotonic increase in ΔR_{QN} values with increasing initial quench rate combined with the smooth merger for the two quench media's associated data sets graphically supports the reasonableness of the adopted quench system and independent variable selection for subsequent graphical back extrapolation analyses.

3. Attainment of a range in specimen sink densities should provide a means for checking of the reliability of extrapolating the acquired data to obtain no-loss, sink density-independent equilibrium vacancy concentrations associated with each quench temperature.

4. That the selected in situ gas quench systems design for producing vacancy supersaturations introduced no significant increases in sink densities for any of the specimens is evidenced by highly reproducible straight downquench data obtained when repeated for the same ST DQ series and environmental conditions, as well as over wide ranges in quench temperature, initial quench rate, pre-existing sink density, and runs well separated in time. This observation supports the conclusion that any forms of handling of the QMSD, including transfer and preparation from actual quench conditions to liquid helium potentiometric measurement conditions apparently

did not result in creation of additional sink structures within any of the in situ mounted five-mil gold wire specimens.

7.3.5 General Findings drawn from Examinations of plotted ST DQ Data

1. Although use of smaller overall specimens resulted in a reduction in range of initial quench rates, this was offset by attainment of increased maximum quench rates for a given set of environmental conditions.

2. The range in initial quench rates proved adequate for reliable back extrapolation to be performed, especially when only small-to-moderate losses (as exhibited within B.E.T. data plots by modest-to-minimal slopes) occurred during straight downquenching involving selected sets of elevated temperatures.

3. As Figure 40 clearly illustrates, differing specimen pre-existing sink densities significantly impact the normalized quenched-in resistance values obtained for a given quench temperature series and associated range in reciprocal initial quench rates.

4. In general, the dependence of QIR/R40 values upon reciprocal initial quench rate was neither exponential nor linear. However, for specimens having lower pre-existing sink density specimens such that calculated losses were noticeably smaller, approximately exponential decay with reciprocal initial quench rate was observed.

7.3.6 Reliability Assessments of In Situ ST DQ Data

Several observations are especially worthy of note as to the reliability of the experimental data:

1. Ability to repeat LTA treatments on any specimen after every three or four ST DQ and/or Q&A series treatments and in most cases obtain essentially unchanged magnitudes for that specimen's R_{LTA} value.

2. Reproducibility of calculated quenched-in resistance values, ΔR_{QN} for each specimen for a given quench temperature and thermal history even when substantial changes may have occurred in R_{LTA} following an HTA treatment.

3. Ability to reproduce ΔR_{QN} values on a given specimen even after perhaps tens of runs between the repeated quench histories. This supports high confidence levels in the recorded data throughout the entire data accumulation sequence and minimizes the concern for significant drift effects or trends.

4. Close agreement between normalized quenched-in resistance ΔR_{QN} (which is labeled NQIR in most Figures and Tables) values for a number of independent specimens of varying gauge length offers an endorsement of uniformity of temperature with either gas medium or gas overpressures, or overall specimen size or shape.

5. Quenched-in resistance values were found to be highly reproducible for all in-situ specimens not subjected to direct deformation once annealed.

7.4 DETERMINATIONS OF "NO-LOSS" NQIR(T_Q) VALUES FROM ST DQ SERIES DATA SETS

In this section analyses of the results of extensive sets of straight downquench experiments are presented (see Figures 4 and 5 cited earlier). Specifically, estimates for a number of parameters, including vacancy formation energy, vacancy formation entropy, and heat of solution of helium in pure gold are forwarded.

Independent sets of normalized quenched-in resistance data reflecting retained non-equilibrium excess vacancy concentrations are analyzed as a function of quench temperature and initial quench rate for each quench temperature series.

Achievement of no-loss equilibrium vacancy concentration magnitudes using ΔR_{QN} data involving real, finite quench rate quenches requires some form of extrapolation of these data to establish these no-loss values. Extrapolations of these sets of ST DQ series data to infinite quench rate were performed using graphical methods.

As quench rates are increased, pre-existing sink density becomes less of a factor in determining losses during a quench. In principle, the retained equilibrium vacancy concentration for a quench rate sufficient to have negligible losses of excess vacancies would equal in magnitude the equilibrium vacancy concentration at the temperature of quench.

Ideally, each specimen should be used over the entire quench temperature range and for all achievable initial quench rates, thereby supplying a more complete set of Quenched-In Resistance (QIR) data [81] for each specimen. Such resistance determinations were then normalized for a given specimen by dividing by the specimen's gauge length resistance established at a measurement temperature of 40^oC, resulting in a set of QIR/R(40^oC) determinations, which proves especially useful for subsequent plotting and gauge length-independent analyses. Such normalization of data (using values for QIR/R40) allows all 5-mil gold wire specimens

---

[81] Clearly, obtained values of QIR data are functions not only of the associated thermal history but also of each specimen's pre-existing sink density (N_D).

to be compared with each other on a single plot for the specified thermal histories $[T_Q(t), T_{QA}(t)]$.

Figure 40 indicates the data analysis scheme which led to an estimate for the magnitude for the vacancy formation energy E^F_V involving straight downquenches. Note that for each quench temperature series two or more specimens were employed each involving a wide range in initial quench rates.

In some instances, specific specimens were found to exhibit high loss rates, i.e., slopes of QIR versus reciprocal initial quench rate that would not prove acceptable for B.E.T.-related purposes use at or above certain elevated temperatures. For those cases, in order to justify use of the Back Extrapolation Technique outlined in sub-section 7.2.3, those specimens were restricted to the associated ranges in lower quench temperature series treatments wherein only modest slopes were found to occur.

Both the larger overall catenary-like shaped specimens and the smaller overall hairpin-shaped specimens were used for quench temperatures up to 925^{o}C. Sets of normalized QIR [referred to as NQIR ≡ QIR/R(40^{o}C)] were thereby obtained as a function of initial quench rate for the associated temperature ranges.

Quenched-in resistance values associated with quenches from quench temperatures of 450^{o}C or lower for any given specimen were nearly always determined both immediately before and immediately after each LTA treatment. This was done in order to maximize accuracy of QIR determinations. Moreover, LTA's were generally performed after every three ST DQ's on a given specimen. This practice also established a chronology of residual resistance for each specimen.

Examinations of these sets of R_{LTA} chronologies (for details, see Section 11.2) revealed close reproducibility of a specimen's residual resistance values throughout many thermal treatments and thereby confirmed the overall reliability of the adopted R_{LTA} treatment.

Analyses and discussions as to the nature of the associated straight downquench annealing kinetics are deferred to Section 7.5 where these matters are discussed and comparisons are made with models proposed in the literature. The influence of direct deformation upon losses associated with quenches from several temperatures will be examined and developed further in Section 9.3.

7.4.1 Back Extrapolation Technique

7.4.1.1 Back Extrapolation Technique Description

The technique adopted and applied to the ΔR_{QN} data already obtained involved graphical extension of the curves of ΔR_{QN} as a function of reciprocal initial quench rate to obtain the intercept value for zero reciprocal initial quench rate to thereby define the no-loss normalized quenched-in resistance value for each specimen for that particular quench temperature series.

The adoption of semi-log scales was made both to accommodate the wide range in ΔR_{QN} (T_Q, $dT/dt_{initial}$) and to minimize the uncertainty of the resultant extrapolation. Moreover, placement of normalized ΔR_Q data, referred to symbolically as ΔR_{QN} or NQIR(T_Q), on a single graph for each quench temperature series permitted ready comparison between specimens for the influence of specimen pre-existing sink density. Additionally, a visible indication of the general agreement for the extrapolated values for the particular quench temperature series could be observed.

7.4.1.2 Back Extrapolation Technique Procedure

The overall procedure followed to obtain no-loss ΔR_{QN} values was as follows:

1. Plot on semi-log coordinates the ΔR_{QN} data for each quench temperature series as a function of reciprocal initial quench rate for each thermal history.

2. Back extrapolate graphically each of the sets of ΔR_{QN} (T_Q, $dT/dt_{initial}$) data to determine the no-loss value for each straight downquench temperature series.

3. Determine the energy of vacancy formation energy E^F_V from the slope of the least squares fit to the composite sets of no-loss ΔR_{QN} magnitudes [82].

7.4.1.3 T* Temperature Determinations

One definition for T* is that it is the temperature associated with a quench involving an acknowledged finite quench rate from temperature T_Q which, if employed as a quench temperature from temperature T* on that specimen at the same quench rate, would result in no loss of excess vacancies [20, 24, 25].

Figure 41 suggests one graphical technique for estimating T* for specimens based upon using "no-loss" NQIR(T), $\Delta\rho_V(T)$, or $C_V(T)$ values provided in Tables 9, 10, and 11, respectively.

NOTE: An alternative graphical example that illustrates how T* values arose from gathered ST DQ data for specimen 3009 is illustrated in Figure 43.

Looking back at plotted data for specimens 3009 and 4003 (see Figure 40) suggests that these two specimens had associated T* values near 700°C for

---

[82] Further details are deferred to sub-section 7.4.5 regarding the results of analyses of the acquired data sets leading to establishment of an equation (7-1) for the Master B.E.T. Arrhenius plot of "No Loss" Normalized Quenched-in Resistance (NQIR) over the temperature range from 400°C to 925°C.

associated quench rates (obtained from respective thermal histories) of no more than 10^3 degrees Celsius/second.

This deduction is based upon the essentially flat (i.e., quench-rate independent) values of ΔR_{QN} for $T_Q = 700^oC$ with specimen 4003 as shown in Figure 40. Data shown for Specimen 3009 for straight downquenches from $T_Q = 750^oC$ suggest that for $T_Q = 700^oC$ the associated slope might also be nearly the same as shown for specimen 4003.

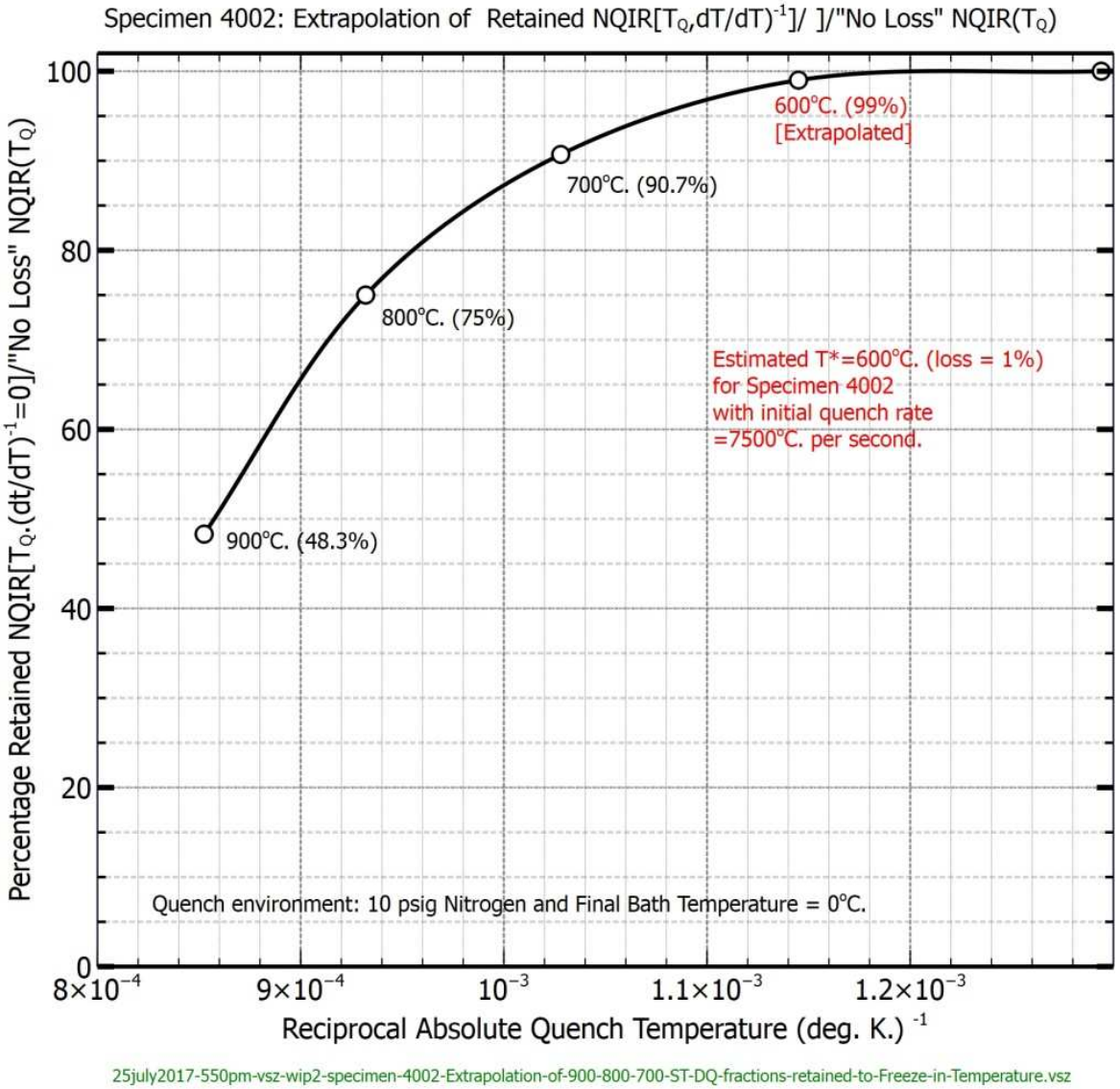

Figure 41. Specimen 4002: Temperature (T*) Estimation from Extrapolation of Plot of Fraction Retained NQIR(ST DQ)/["No Loss" (T_Q)] vs. Reciprocal Absolute Quench Temperature

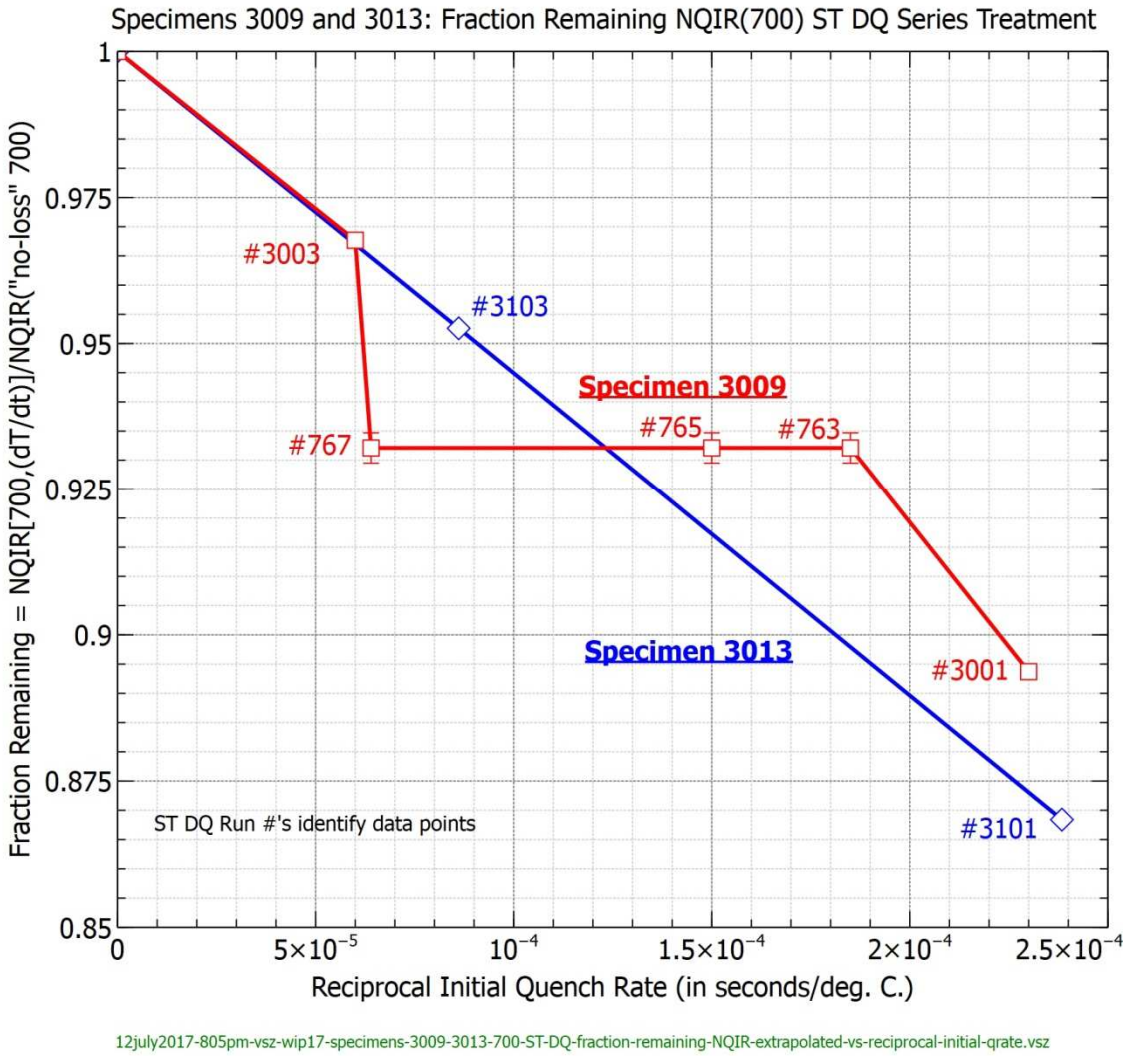

Figure 42. Specimens 3009 and 3013: Extensions for 700°C ST DQ Treatments to "No-Loss" B.E.T. Levels of Fraction Remaining NQIR Plots

The Fraction Remaining plot in Figure 42 for specimen 3009's 700°C ST DQ treatment illustrates the occurrence of a T* plateau that is manifested only over a limited range in RIQR values.

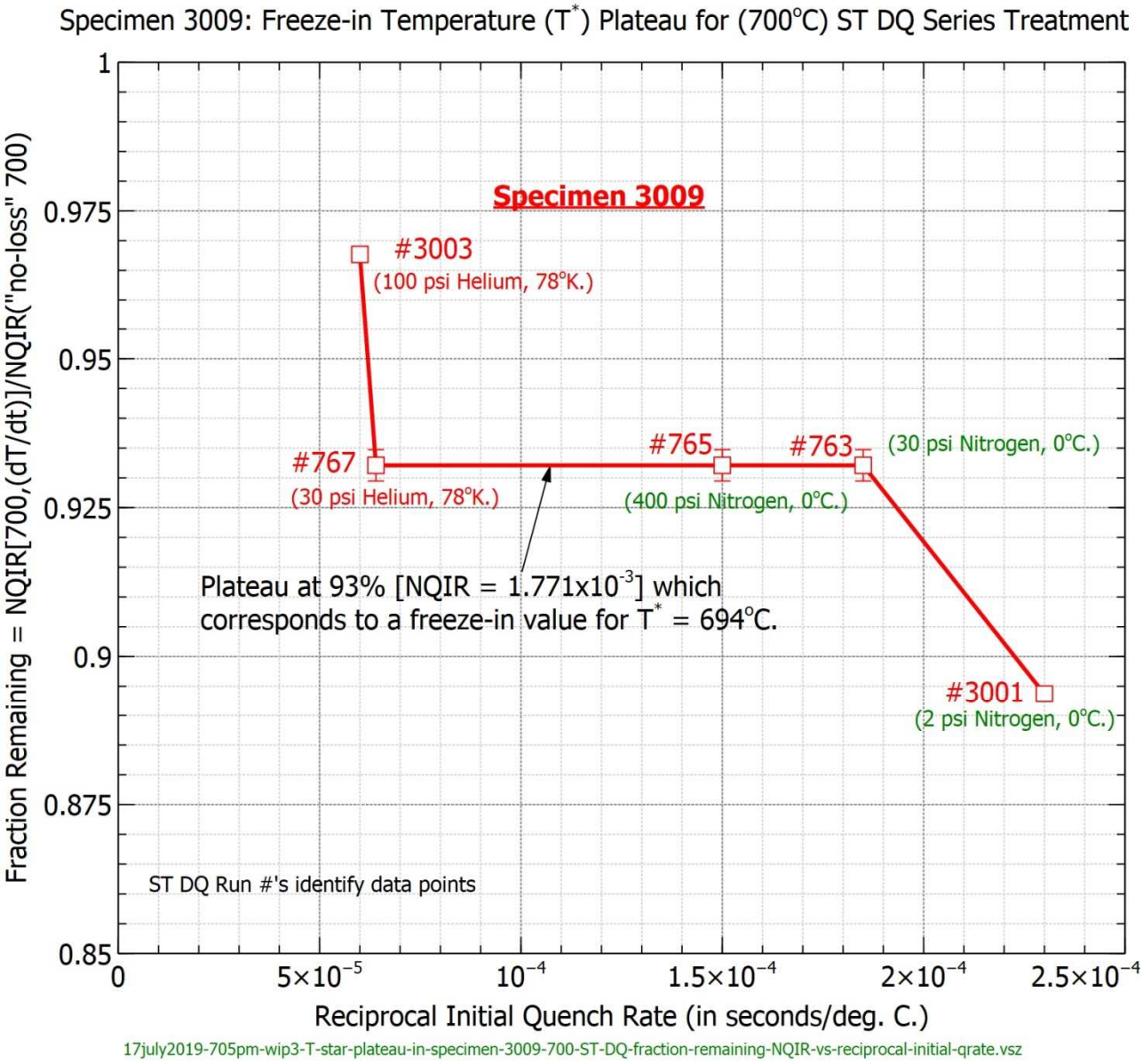

Figure 43. Specimen 3009: T* Estimate from noted Plateau in a Plot of Fraction Remaining NQIR(700°C) ST DQ Series Treatment vs. RIQR.

Figure 43 quantifies the associated freeze-in temperature T* of the plateau to be 694°C for an NQIR(700°C) ST DQ series treatment with RIQRs involving the indicated helium and nitrogen gas pressure and bath temperature environments.

Applying the knowledge of calculable losses to specimen 4002 as shown by the graphical technique of Figure 41, it is estimated that the associated temperature T* for specimen 4002 would be 600^{o}C (based on the associated initial quench rate of 7500^{o}C per second calculated from its recorded thermal history).

Thus, all quenches for specimen 4002 for temperatures below 600^{o}C at comparable (or faster) initial quench rates should result in total retention of the pre-quench (referred to as the "no loss") vacancy concentration.

As Figure 40 illustrates, a T* temperature near 700^{o}C was obtained for specimen 4003, as well as for specimen 3009. Such high values of T* [20] infer that specimens having low pre-existing sink density were associated with at least some of these elevated temperature thermal treatments and subsequent data acquisition activities.

Such values of T* proved vital in establishing reliable extrapolated (no-loss) values of ΔR_{QN} leading to achievement of a Master BET Curve of no-loss equilibrium vacancy concentrations in gold and an estimate for the associated energy of vacancy formation.

Specimens that were either cold-worked prior to final shaping or deformed following initial potential lead sintering were always noted to have much lower T* values.

Values of T* can thus serve to generally indicate relative magnitudes of pre-existing sink density among specimens. Specimens having low T* values cannot be considered for use in BET plotting except perhaps for ST DQ runs involving the lower range in quench temperatures. As Figure 41 clearly reveals, when a $T_Q = 800^oC$ BET is undertaken for specimen 4002 (which has a T* value of 600^oC), the reliability for an accurate extrapolation becomes more prone to reduced accuracy upon extrapolation.

Similarly, even for specimens 3009 and 3012 which have associated T* values near 700^oC were noted to exhibit losses of about 50 per cent for 925^oC ST DQ treatments even for the fastest initial quench rates associated with these two specimens.

Conversely, several benefits of having high T* specimens can be cited as they relate to the present task of performing BET operations on data for a number of specimens that, perhaps, have much lower T* values:

1. Back extrapolations for all quench temperature series at or below T_Q can be made without requiring a high density of ΔR_{QN} (T_Q, quench rate) data.

2. Margins of error in extrapolation to obtain no-loss ΔR_{QN} magnitudes are minimized when the actual ΔR_{QN} data are highly reproducible when quench temperature at or below T* are employed. A flat-line projection under such ST DQ treatments becomes expected as a result.

3. Also, because the final no-loss magnitude of ΔR_{QN} should be truly independent of specimen pre-existing sink density (and specimen T* values for any finite quench rate), if a high T* specimen is included on a common graph (such as is done in Figure 40) with other specimens having even much lower T* values, a "built-

in (visual, at least) check" on the reliability of the extrapolation for these other specimens can be made.

With all of the above-stated T*-related information in mind coupled with an apparent manifestation of “extra increments” [83] of quenched-in defect resistance associated with lower temperature quenches when helium gas is used as the quench medium -- detailed in sub-section 7.4.2 which follows -- compared to those values obtained when nitrogen gas is used as the quench medium, the distinct possibility that helium might be permeating the gold wire specimens at elevated temperatures was deemed necessary to pursue further as part of this overall research investigation.

7.4.2 Observed Anomalies in ST DQ NQIR Data for $T_Q \leq 550^oC$

For these lower ST DQ series treatments the associated ΔR_{QN} data plotted over the associated range in initial quench rate involving use of a helium gas quench medium readily approached a flat (that is, essentially constant) value for each ST DQ series between 400^oC through 550^oC. Similarly, data plotted over the associated range in initial quench rate involving use of nitrogen gas quench medium did so as well.

However, an unanticipated anomaly became apparent upon comparing the helium and nitrogen gas quench media results for $\Delta R_{QN}(T_Q \leq 550^oC)$ sets over their respective ranges in initial quench rates. Although essentially "flat plateaus" in data

---

[83] The term “extra increments” as used here is defined as the quantitative differences that were revealed in the associated quench rate- and gas overpressure-independent flat “plateaus” determined from the respective sets of plots of NQIR(T) values that were discerned over the quench temperatures ranging from 400^oC to 550^oC for the corresponding helium and nitrogen gas environments involving two distinct specimens, namely 4002 and 4003.

values for each quench temperature were noted for each of the two gas quench media environments when examined alone, it became apparent that each pair of plateaus (helium and nitrogen) exhibited increasing offsets in ΔR_{QN} magnitudes when lower quench temperatures were involved.

Looking ahead for a moment, an Arrhenius plot (see Figure 44 in sub-section 7.4.3 below) provides graphic illustrations of the ever-widening offsets in ΔR_{QN} magnitudes among several sets of plateaus.

Moreover, when these data were plotted and examined graphically, applicability of the Back Extrapolation Technique itself would be brought into question unless a reasonable explanation could be found to account for the anomaly.

In addition, upon making visual comparisons it became evident that the sets of NQIR [T_Q, $(dT/dt)_{initial}^{-1}$] data for helium environment quenches always exhibited higher plateau levels for each respective ST DQ series from 400^{o}C through 550^{o}C than those obtained when conducted under nitrogen gas environment conditions for the same quench temperature. Also, the disparities between the two (helium and nitrogen gas) environment's levels were clearly noted to increase exponentially for lower quench temperature runs.

7.4.3 Estimated Value for Heat of Solution of Helium in Gold

Before an assessment of the magnitude for the vacancy formation energy E^F_V was made, an explanation for the observation of this anomaly that was noted in NQIR(T_Q) data over the range in quench temperatures between 400^{o}C and 550^{o}C had to be pursued. This led to hypothesizing that helium might be soluble in pure gold. In fact, an estimate for what might prove to be the heat of solution of helium in gold equal to 0.357 ± 0.003 eV was determined from an analysis over that range in straight downquench temperatures wherein discernible differences between the respective plateaus in NQIR(T_Q) values became obvious when sets of straight downquenches that involved use of a helium gas quench environment were compared with those made using nitrogen gas.

An Arrhenius plot of the graphical representation of this apparent anomaly was made (see Figure 44). Analyses of the plotted data over the temperature range from 400^{o}C through 550^{o}C yielded evidence (see Figures 45 through 47) for hypothesizing that helium is soluble in 6N-pure gold wire specimens.

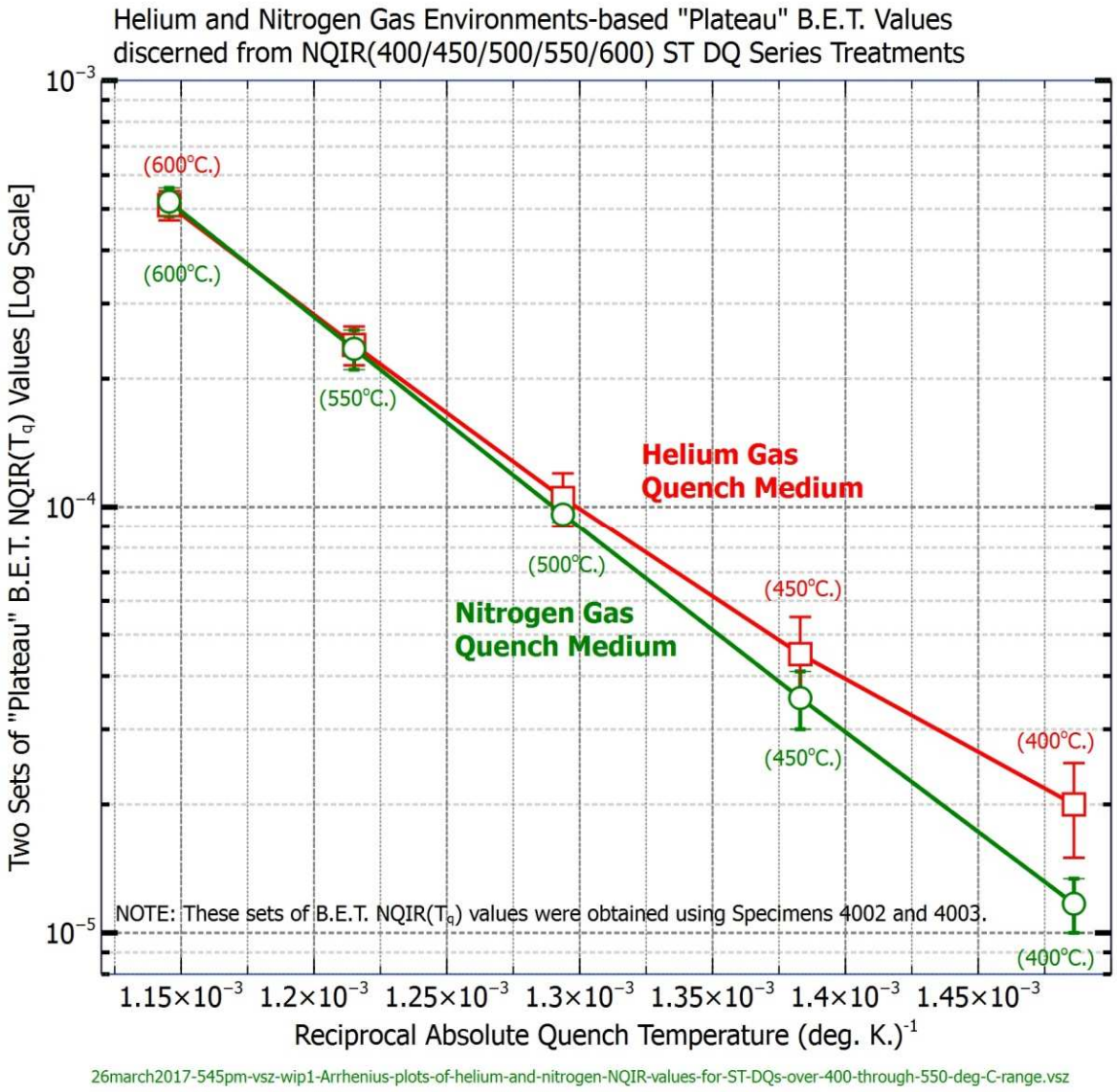

Figure 44. Helium and Nitrogen Gas Environments-based "Plateau" B.E.T. Values discerned from NQIR(400/450/500/550/600) ST DQ Series Treatments of Specimens 4002 and 4003

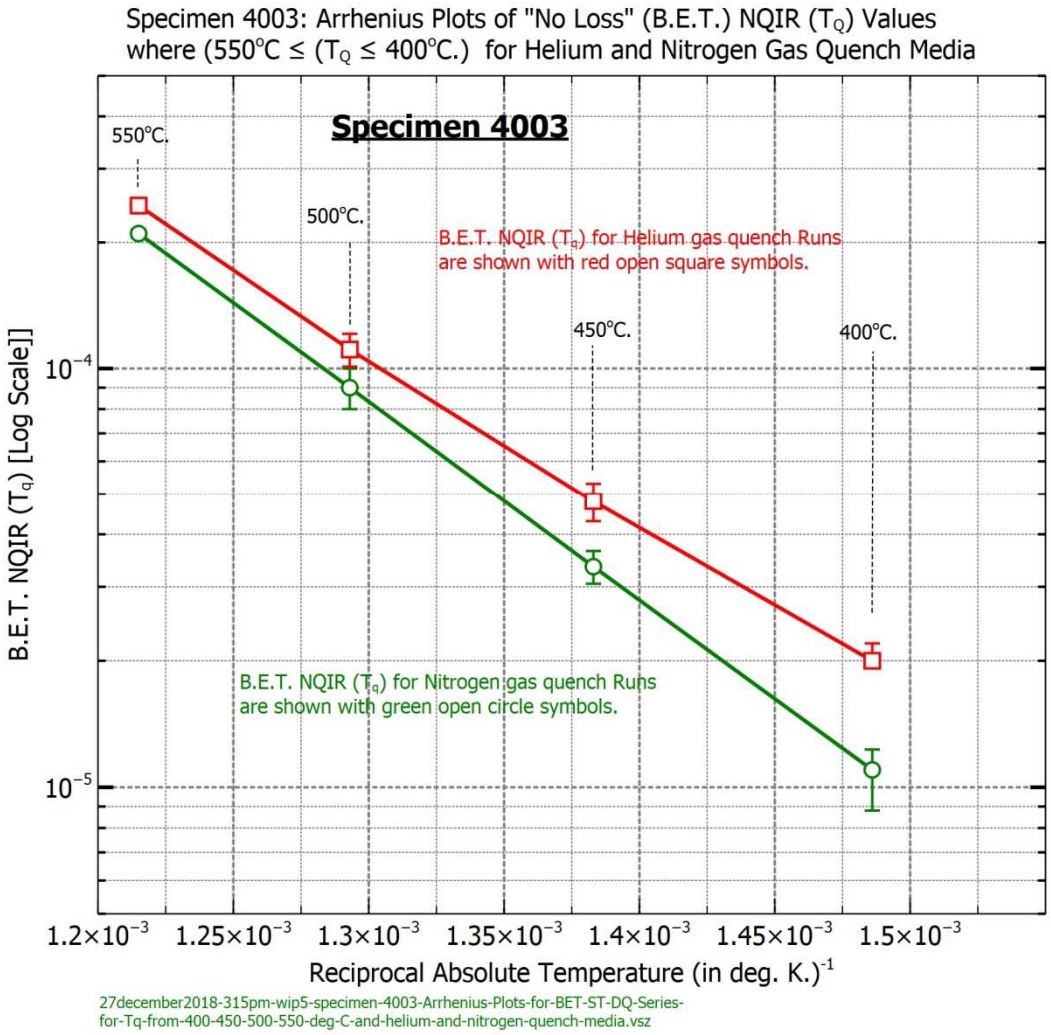

Figure 45. Specimen 4003: Discernible Evidence of Helium Solubility in Gold over the Temperature Range 400°C ≤ T_Q ≤ 550°C

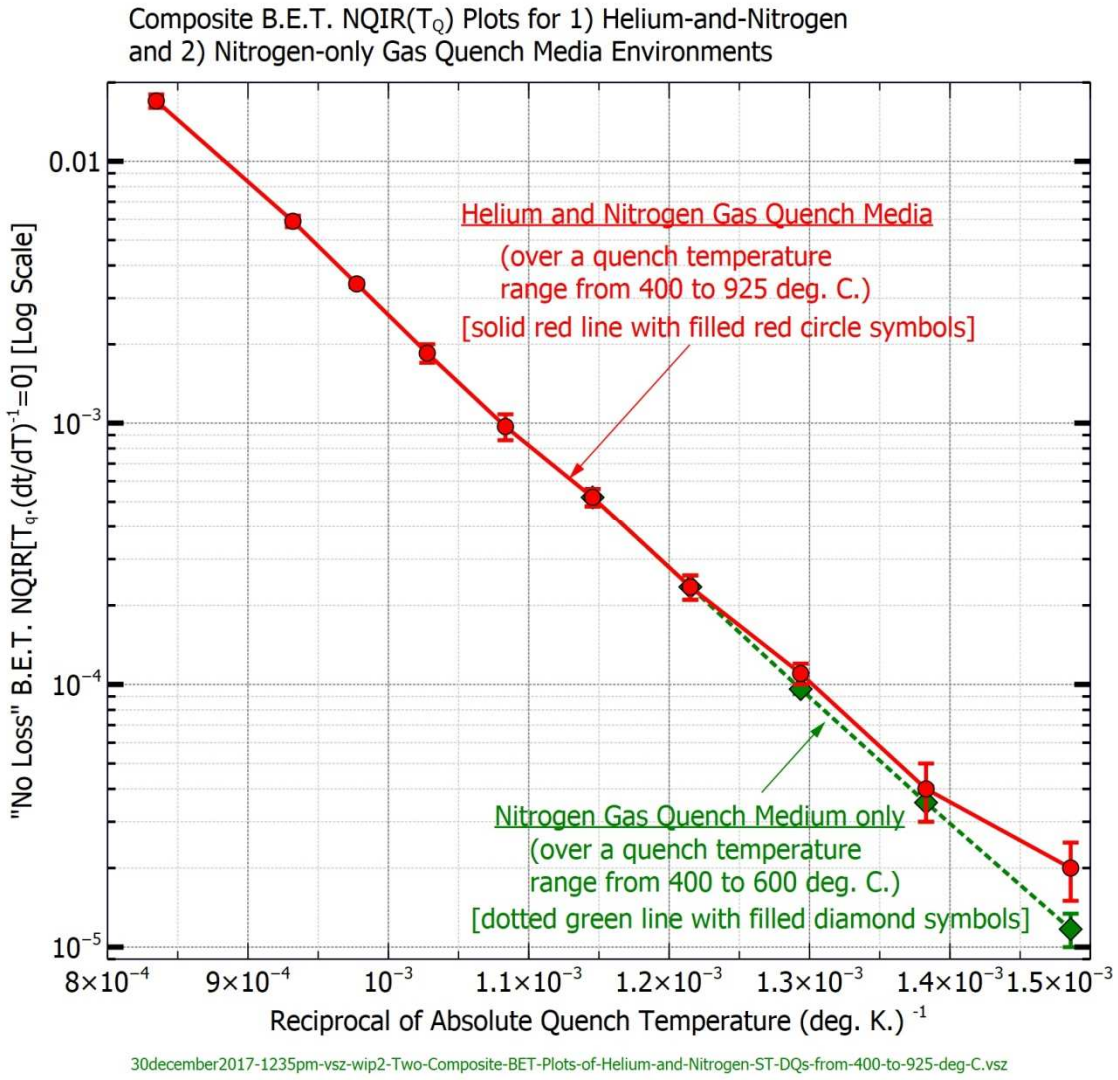

Figure 46. Two Composite B.E.T. Plots that support a hypothesis for Helium Solubility (discernible over the temperature range from 400°C to 550°C) in Gold

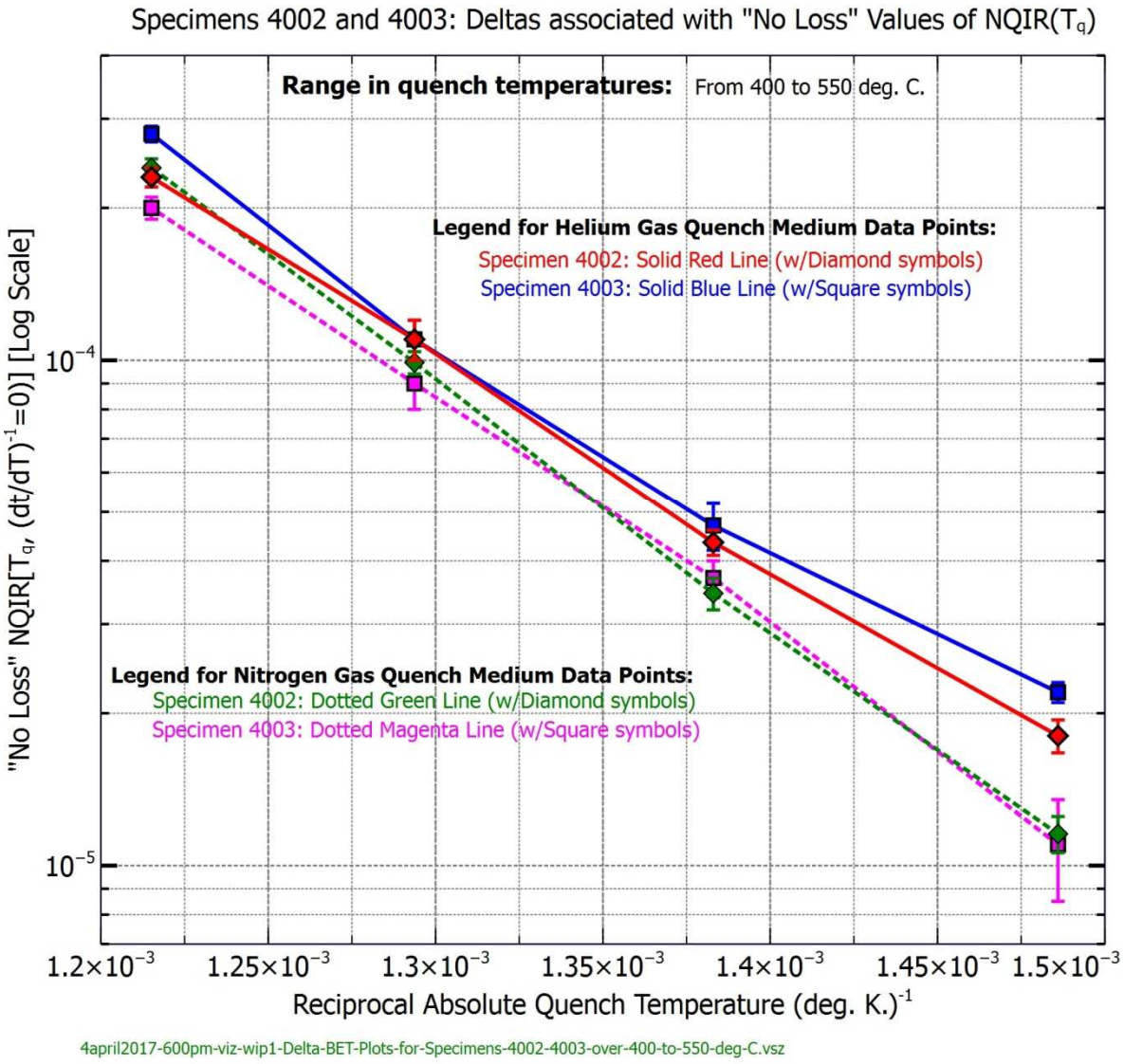

Figure 47. Arrhenius Plots of "Delta" Back Extrapolation Results over the quench temperature range from 400°C to 550°C

7.4.4 Summary of Helium Solubility Evidence and Analyses

Figures 44 through 47 illustrate a proposed resolution for what is the source of the anomaly discerned in quenched-in resistance values over the temperature range $400^{o}C \leq T_{Q} \leq 550^{o}C$.

Two specific observations made from the plotted data were that 1) the respective quenched-in resistance values obtained for both the helium and nitrogen gas quench media for a given ST DQ series were essentially flat across their respective quench rates, and 2) each respective plateau level was clearly evident even for the lowest quench temperatures of $400^{o}C$. These two observations led to determinations of the plateau level differences between helium and nitrogen gas quenches for each ST DQ series from $400^{o}C$ through $550^{o}C$ and subsequently using an Arrhenius plot to see whether or not a straightforward explanation could be found that might explain what was the source for the "deltas" (differences) associated with the observed anomalies. See Figure 47.

7.4.4.1 Comparing Helium vs. Nitrogen Gas Quench Results

From examinations of these graphed results came the hypothesis that the discerned anomaly was most likely attributable to the presence of helium gas which served as the source for the noted disparities detectable over the temperature range from $400^{o}C$ through $550^{o}C$.

7.4.4.2 Hypothesis of Helium Solubility in Gold

To account for these anomalies, a hypothesis of helium solubility in pure gold was forwarded, and an estimate for the heat of solution of helium in gold was deduced from analyses of data over the range in quench temperatures from $400^{o}C$ to

550^{o}C. The result of doing so yielded a least-squares fit straight line having a slope of 0.357 ± 0.003 eV.

Specifically, Arrhenius plots (see Figure 48) of the respective differences involving two completely independent specimens were created and resulted in straight line plots having slopes of 0.360 eV for specimen 4002 and 0.354 eV for specimen 4003.

Subsequent calculations using the respective slopes for two specimens (4002 and 4003) resulted in a value of 0.357 ± 0.003 eV for the heat of solution of helium in gold (see Figure 48) of the associated sets of data when the differences in plateau levels were examined using an Arrhenius plot of the pairs of data obtained from potentiometric measurements at liquid helium temperatures for ST DQ runs involving two independent specimens (4002 and 4003) that were made following downquenches wherein 550 ≤ T_Q ≥ 400 deg. C.

Moreover, extensions of the respective slopes for specimens 4002 and 4003 to 1063^{o}C (see Figure 48) suggest negligible contributions are made to the vacancy formation energy curve or its slope.

Additionally, the continued adoption of BET analyses for quench temperatures at or below 550^{o}C was deemed reasonable to employ using just the values for ΔR_{QN} obtained for ST DQ runs performed with the nitrogen gas quench medium. This decision was based upon the observation that the ΔR_{QN} values obtained could clearly be noted as being independent of quench rate.

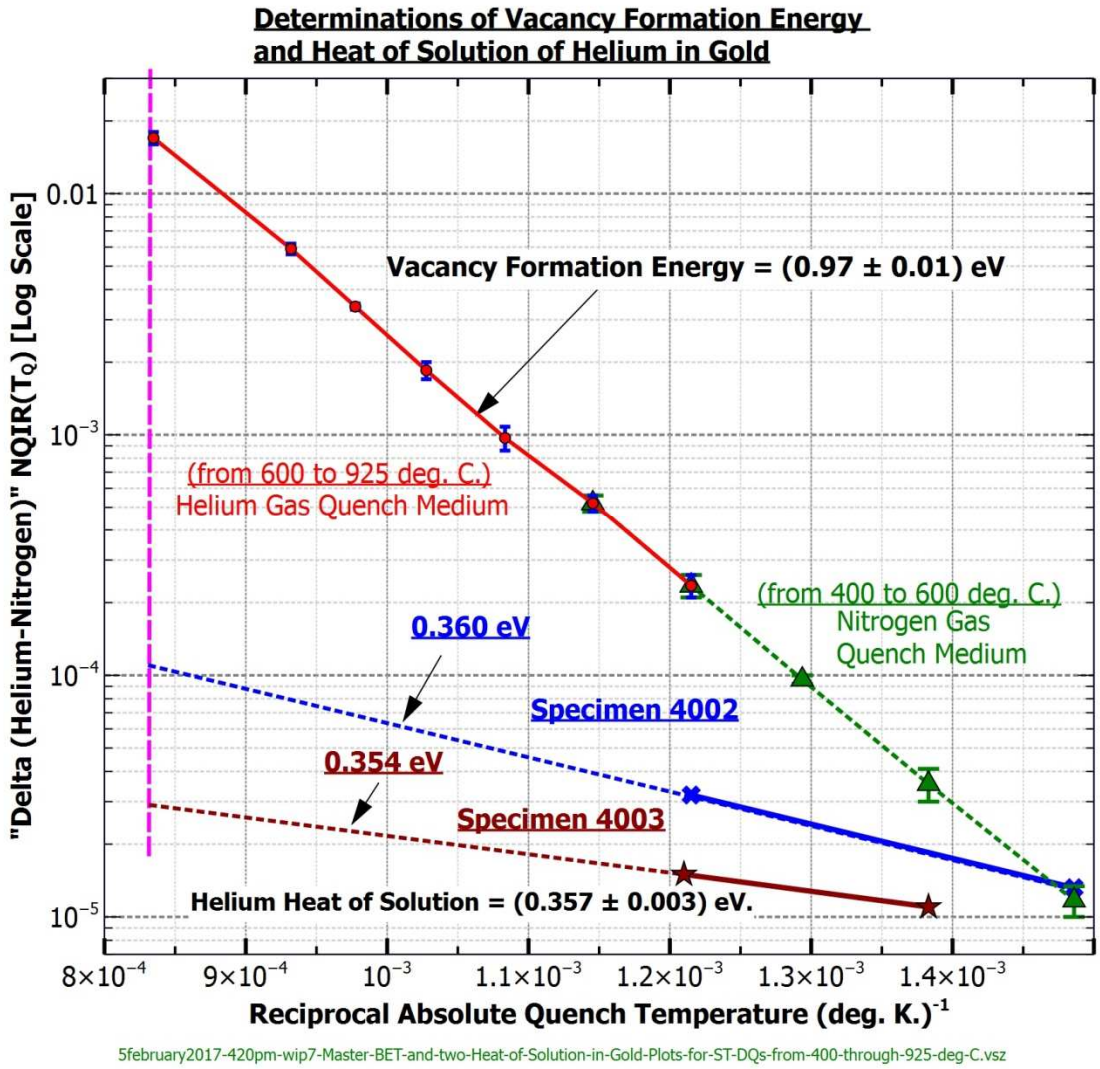

Figure 48. Determinations of Vacancy Formation Energy and Heat of Solution of Helium in Gold

7.4.4.3 Discussion and Conclusions regarding Helium Solubility in Gold

Laakmann, et al. [204] investigated helium solubility in gold associated with irradiation treatments and concluded that a lower limit of 2.2 eV was obtained for the formation energy of helium on interstitial sites in gold. Such a value is far higher than the value of 0.357 ± 0.003 eV determined during this research investigation, but this

is not unexpected since interstitial sites associated with irradiation treatments were involved in that analysis rather than vacancy sites associated with elevated temperature straight downquench treatments as was the situation described herein.

Since no other independent investigations were found in the literature with which to make comparisons that would serve to test this hypothesis of helium solubility in gold, its verification or refutation remains unconfirmed at this time.

7.4.5 Back Extrapolation Technique (A Graphical Analysis)

Figure 40 (see sub-section 7.3.3) indicates the data analysis scheme which ultimately led to an estimate for the magnitude for the vacancy formation energy E^F_V involving straight downquenches [84].

The overall set of B.E.T. values were graphically established for each ST DQ series by extrapolating the acquired data that involved several specimens to the intersection with the vertical axis where the value reached for each quench temperature turns out to be common for all specimens. In principle, each such extrapolated B.E.T. point corresponds to having achieved a reciprocal initial quench rate equal to zero.

The Master B.E.T. plot of Figure 49 shows values for the Normalized Quenched-in Resistance (NQIR), defined as $\Delta R_{QN} = \Delta R(T_Q)/R(40^oC)$, plotted as a function of reciprocal absolute quench temperatures ranging from 400^oC through 925^oC and involving the use of both helium and nitrogen gases as the surrounding quench media. Figure 50 represents the Master B.E.T. plot for vacancy resistivity

---

[84] Note that for each ST DQ Series a number of specimens and a range in initial quench rates were employed.

$\Delta\boldsymbol{\rho}_V(T_Q)$, and Figure 51 represents the Master B.E.T. plot for vacancy concentration

$C_V(T)$ for the same range of temperatures,

7.4.5.1 Master "Composite" B.E.T. ("No Loss") Arrhenius Plot of NQIR(T) for Gold over the temperature range from 400°C to 925°C

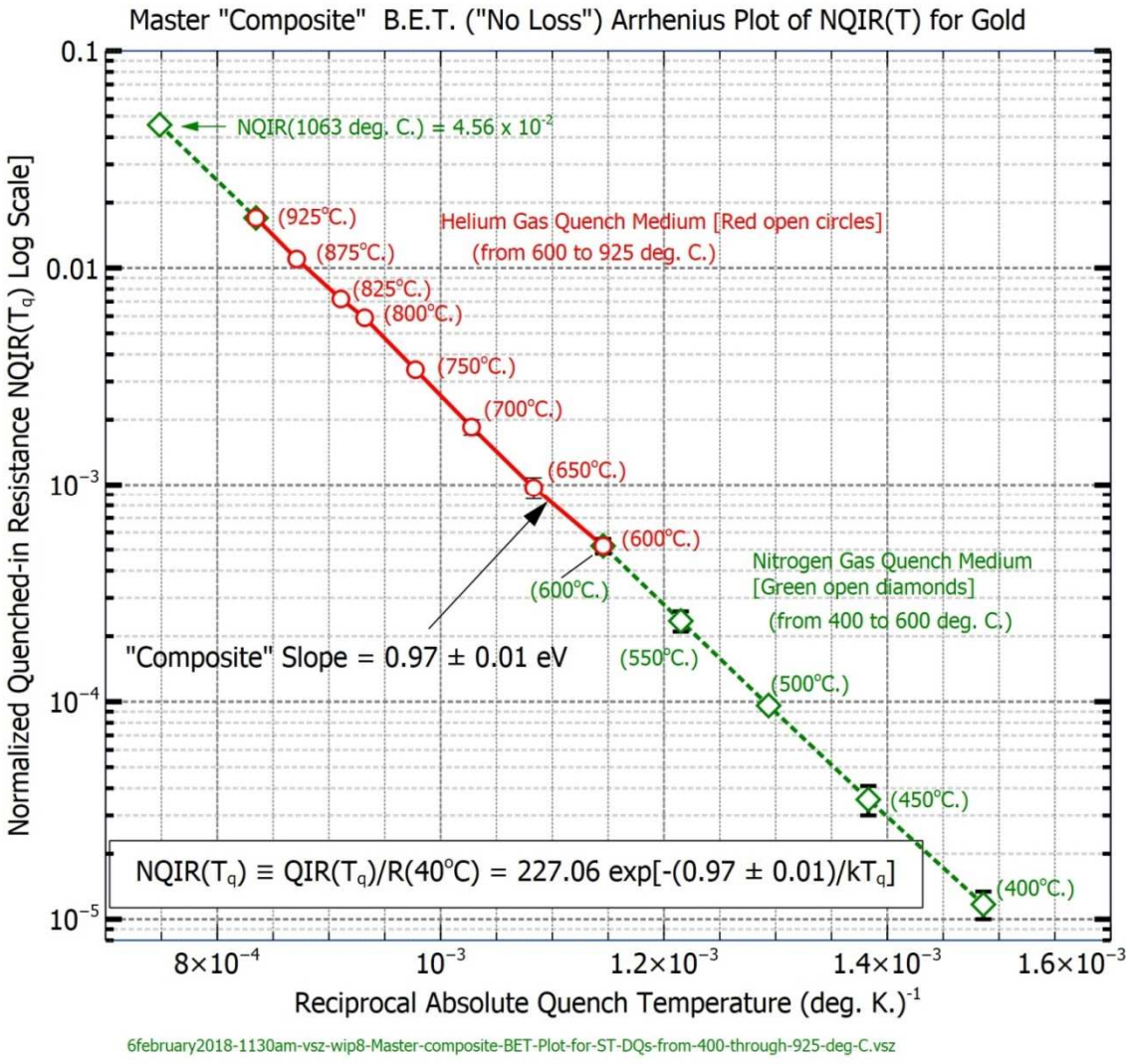

Figure 49. Master "Composite" B.E.T. ("No Loss") Arrhenius Plot of NQIR(T) for Gold over the temperature range from 400°C to 925°C

7.4.5.2 Master B.E.T. ("No Loss") Arrhenius Plot of Vacancy Resistivity $\Delta\boldsymbol{\rho}_V(T)$ over the temperature range from 400°C to 925°C

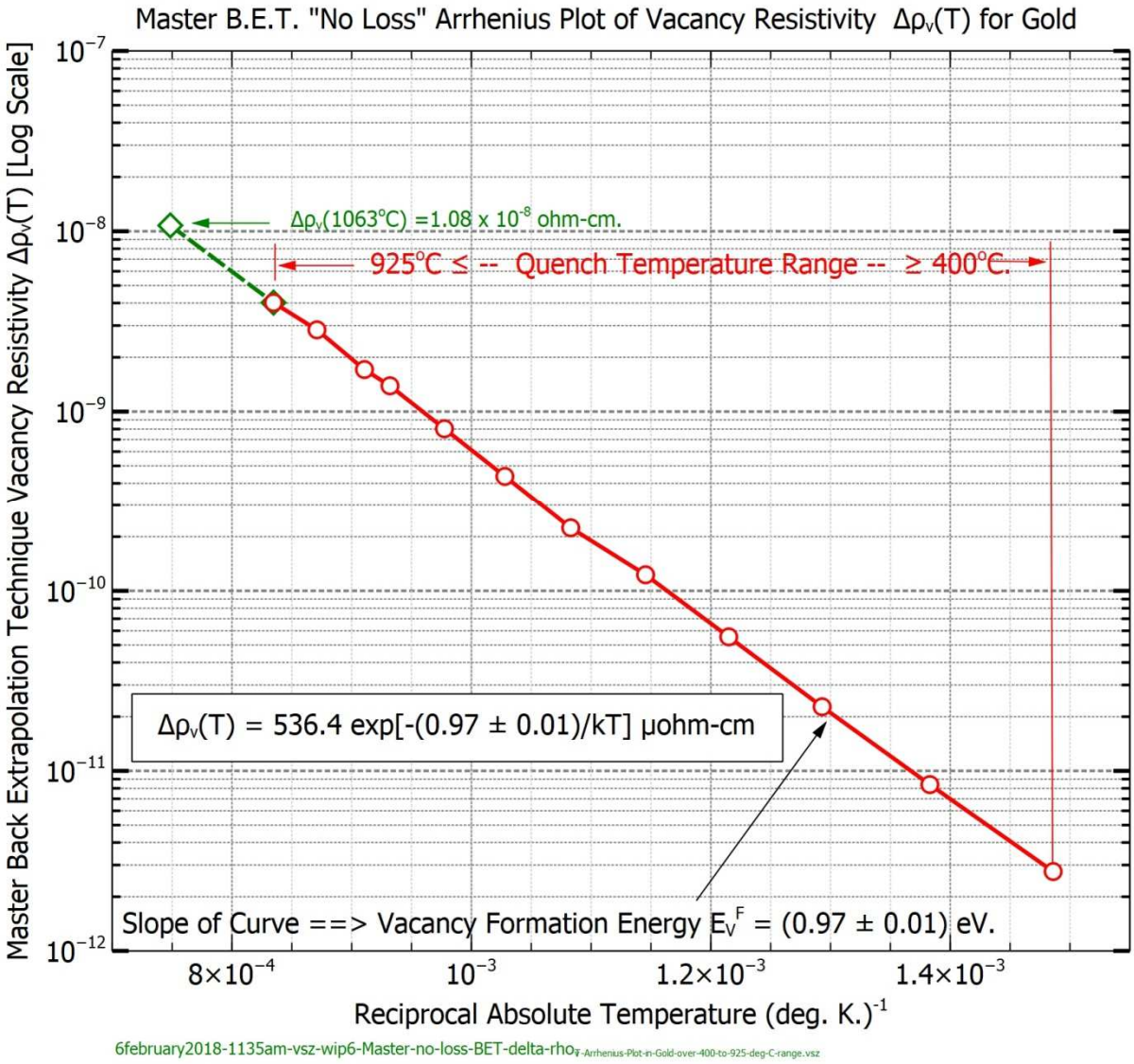

Figure 50. Master B.E.T. ("No Loss") Arrhenius Plot of Vacancy Resistivity $\Delta\boldsymbol{\rho}_V(T)$ over the temperature range from 400°C to 925°C

7.4.5.3 Master B.E.T. ("No Loss") Arrhenius Plot of Vacancy Concentration $C_v(T)$ in Gold (from 400°C to 925°C)

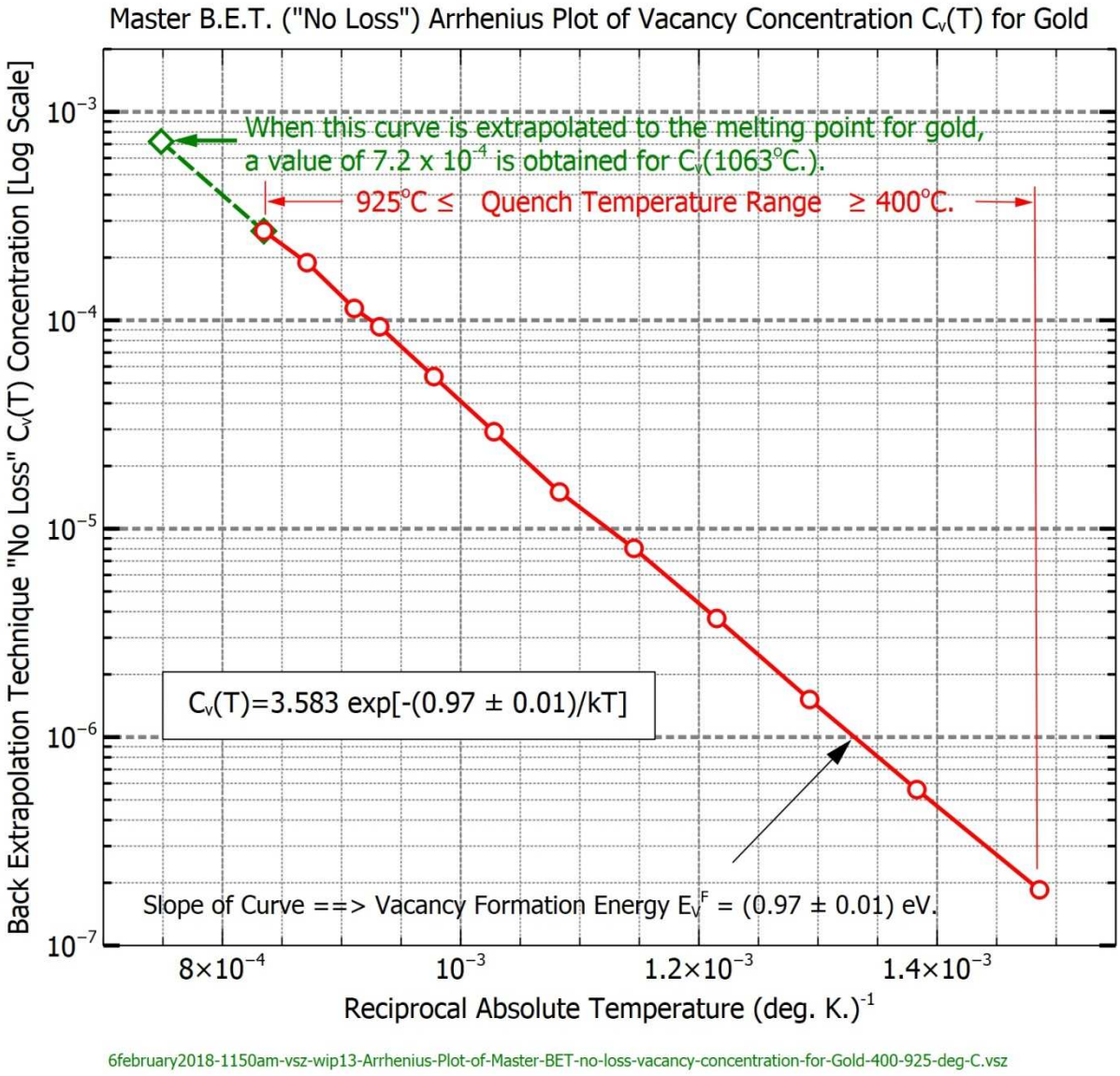

Figure 51. Master B.E.T. ("No Loss") Arrhenius Plot of Vacancy Concentration $C_v(T)$ in Gold (from 400°C to 925°C)

These sets of B.E.T. values are thereby presumed to reasonably correspond to what would have been attained if an infinitely fast in situ gas quench from each respective quench temperature were to have been possible to perform.

A Master B.E.T. Arrhenius Plot through the extrapolated sets of data for ST DQ temperatures from 600^{o}C through 925^{o}C resulted in Eqn. (7-1):

$$\Delta R_{QN} (T_Q) = 227.06 \exp [-(0.97 \pm 0.01) / kT_Q] \qquad \text{Eqn. (7-1)}$$

7.4.6 Back Extrapolation Technique-based Assessments, Findings, and Conclusions

7.4.6.1 Error Limits on Back Extrapolation Values

From the uncertainty limits associated with each quench maximum temperature series extrapolation, the maximum Back Extrapolation uncertainties for each temperature can be estimated. Corresponding values for the no-loss normalized quenched-in resistance values are indicated in the Master Back Extrapolation plot of Figure 49. For example, uncertainty in the 925°C no-loss normalized quenched-in resistance value is approximately (1.7 ± 0.1)/1.7, or seven per cent; at 650°C about 10 per cent; and at 400°C (using the nitrogen data only), about 17 per cent.

7.4.6.2 Equations associated with Master B.E.T. Plots

Since the Master B.E.T. plot is based upon normalized quenched-in resistance data, and the slope of the curve reflects the associated vacancy formation energy E^F_V, a straightforward conversion from normalized quenched-in resistance (NQIR) to either quenched-in resistivity or quenched-in vacancy concentration can readily be performed whenever desired.

When expressed in terms of resistivity (symbolized by **ρ**, the Greek letter for RHO), the associated equation becomes:

$\Delta\rho_V(T_Q) = 536.4 \exp [-(0.97\pm0.01) / kT_Q]$ μohm-cm [85] Eqn. (7-2)

Similarly, the total vacancy concentration can be represented [86] by the equation

$C_v(T_Q) = 3.583 \exp [-(0.97\pm0.01) / kT_Q]$ Eqn. (7-3)

In this equation the coefficient 3.583 represents $\exp(S_V/k)$, so the value for S_V/k equals ln(3.583), yielding a value of 1.276.[87]

7.4.6.3 B.E.T. Plot for Nitrogen-only Medium for $T_Q \leq 550°C$

The slope of the nitrogen-only (the dashed green-colored line segment) no-loss B.E.T. plot in Figure 49 yielded a value for the vacancy formation energy of 0.965 ± 0.015 eV over the temperature range from 400°C through 550°C. Notably, this value is very close to the value of 0.97 ± 0.01 eV obtained for the combined helium and nitrogen gas quench media B.E.T. graphical analyses conducted over the upper quench temperature range from 600°C through 925°C.

7.4.6.4 Discussion of Back Extrapolation Magnitude Scatter

Quenched-in resistance values obtained for any specific ST DQ series undoubtedly vary to some extent. Variations are expected to be manifested, for example, when the actual quench temperatures prove to be either above or below the nominal T_Q value associated with any specific ST DQ series. In addition, each of these sets of ST DQ series involves differing gas quench media and gas overpressures. Collectively, all such variations are expected to influence to some

---

85 Based on using $\rho(25^oC) = (2.25 \pm 0.05) \times 10^{-6}$ ohm-cm (Bass [7]) and $R(20^oC)/R(40^oC)=0.9506$ (Meechan and Eggleston [47]) to yield a value for $\rho(40^oC) = 2.3625 \times 10^{-6}$.

86 Using 1.5×10^{-6} ohm-cm/atomic per cent vacancies [17, 39, 23] as a scattering factor.

87 Note that this value falls within the range of 1.2 ± 0.2 reported by Simmons [212].

degree the precision obtained using a graphical Back Extrapolation Technique (B.E.T.) method to determine "no loss" NQIR(T_Q) values.

Even for specimens exhibiting moderate losses at the highest initial quench rates, it is reasonable to expect larger uncertainties to be present in the Back Extrapolation values.

Another consideration is the following: If large numbers of vacancies agglomerate during the quench to form larger clusters, the total (cluster) resistivity may not be equal to the sum of the resistivities of the vacancies under completely isolated vacancy conditions. That is, the composite scattering of an n-vacancy size cluster, where n is the total number of vacancies comprising the cluster, may not be equal to n times the scattering of a single, isolated vacancy.

7.4.6.5 Back Extrapolation Technique Results

For the collective graphical back extrapolations of NQIR(T_Q, $[dT/dt]_{initial}^{-1}$) ST DQ series data sets associated with quench temperatures ranging from 400^{o}C to 925^{o}C, application of a least-squares fit to graphical back extrapolation data yielded a value for the vacancy formation energy of 0.97±0.01 eV. This overall result lends credence to the following conclusions:

1. Both the validity of the acquired sets of ST DQ data and the adopted graphical extrapolation technique applied to the experimental data gathered for each ST DQ temperature series are endorsed.

2. Attainment of low pre-existing sink densities for the majority of in situ quenched specimens when coupled with a wide range in initial quench rates permits

reliable graphical extrapolations of semi-log plots of normalized quenched-in resistance data toward pre-quench (no-loss) equilibrium magnitudes to be justified.

3. Reproducible quenched-in lattice defect resistance values are obtained coupled with the establishment of an associated formation energy near one electron volt endorses the assumption that the defects quenched in are indeed vacancies and that the defects are thermodynamically stable at the quench temperatures and pre-quench anneal times chosen prior to quench initiation.

4. For cases involving specimens of lower sink densities the technique of performing graphical back extrapolations of the acquired NQIR [T_Q, $(dT/dt)_{initial}^{-1}$] values as a function of reciprocal initial quench rate does appear to result in the establishment of reliable no-loss magnitudes of normalized quenched-in defect electrical resistance.

5. Because the extrapolation technique and the underlying potentiometric measurements that yield data which B.E.T. plots make use of data that are macroscopic in nature, it is obviously not possible to distinguish between mono- and di-vacancy concentrations through potentiometric measurement techniques alone.

Moreover, it is readily acknowledged that both mono- and mono-divacancy models of equilibrium concentrations could be proposed to fit the acquired B.E.T. NQIR(T) sets of data.

A least-squares fit to the acquired B.E.T. “No-Loss” NQIR(T) sets of data over the associated temperature range from 400^{o}C to 925^{o}C resulted in the generation of Arrhenius plots for NQIR(T_Q), $\Delta\rho_V(T_Q)$, and $C_V(T_Q)$ presented in Figures 49, 50, and 51, respectively.

6. Creation of specimens having a range in pre-existing sink density [88] coupled with a wide range in initial quench rates for each specimen, obtainable by using two adopted Quench/Measurement System Design Units (QMSDs) simply by gas, overpressure, and bath temperature selections, permitted reliable determinations of no-loss $\Delta R_{QN}(T_Q)$ values for quenches from temperatures as high as 925^{o}C.

7. Because the adopted designs for the five-mil gold wire specimens resulted in gauge lengths that exhibited residual resistances near 1 μohm and thermal EMF magnitudes encountered generally near 0.4 μV during potentiometric measurements at 4.2^{o}K, a detection sensitivity of 0.01 μohm for a measurement current of one ampere effectively ruled out performing ST DQ treatments below a quench temperature of 400^{o}C if quenched-in resistance values were to be detectable with any significant degree of reliability and reproducibility

8. Straight downquench losses much above fifty per cent were not considered to allow reliable back extrapolations to be graphically endorsed and 925^{o}C was judged to be the highest allowable quench temperature that would still permit graphical techniques to be applied with a moderate degree of confidence in the resulting no-loss values.

7.4.6.6 Values for No-Loss Equilibrium Vacancy Concentration

Magnitudes of no-loss equilibrium vacancy concentration over the range of temperatures from 400°C through 925°C are assumed to be directly proportional to

---

[88] Several particularly low pre-existing sink density specimens (3009, 3012 [before direct deformations were performed], 3016, and 4003) were the consequence of careful preparation, handling, and shaping. By comparison, cold-worked specimens (such as 3011, 4002, and 4005) exhibited greater losses, and it seems reasonable to associate these observations with higher pre-existing sink densities.

the normalized quenched-in resistance values ΔR_{QN} (T_Q) obtained during this research investigation. So, a Master Back Extrapolation plot can serve as a means for assessment of vacancy defect losses for any thermal treatment.

Rather than using the time actually taken to reach the final bath temperature T_F for ST DQ series treatments, losses can be examined either as a function of initial quench rate or the time to reach the associated temperature T*.

7.4.6.7 Usefulness of Master “No Loss” B.E.T. Values

The Master Back Extrapolation NQIR(T) plot provides the researcher with an indicator of no-loss normalized quenched-in resistance values [89] associated with elevated temperatures ranging from 400°C to 925°C.

Calculations of specific losses associated with a specimen and thermal treatment can readily be made simply by subtracting the obtained normalized QIR(T_Q)/R(40^{o}C) value from the no-loss NQIR(T_Q) value.

Looking ahead for a moment [90], when subsequent quench-and-isothermal anneal (Q&A) treatments are performed, acquired NQIR(T_Q, T_A, t_A) data can all be normalized by the associated NQIR(T_Q, T_A, $t_A = 0$) ST DQ value to determine what the excess fraction remaining value (labeled as $\mathbf{f_r}$ but referred to as $\mathbf{f_{QA}}$ in general) is as a function of annealing time at the isothermal annealing temperature T_A. See Figures 105 through 114.

---

89 If vacancy concentration is chosen for the ordinate scale parameter, use of a conversion factor of 63.37 can be applied to the no-loss QIR(T_Q)/R(40^{o}C) values to obtain the associated vacancy concentration values.

90 See sub-section 8.2.3 for typical examples of plots using Fraction Remaining NQIR(T_Q, T_A, t_A) / NQIR(T_Q, T_A, $t_A = 0$) as the dependent parameter.

Moreover, metastable residual resistance (MRR) levels are manifested after extended isothermal annealing times represent the fraction remaining that are above the equilibrium concentrations associated with the respective isothermal annealing temperatures. Quantified values for these resulting MRR levels for various Q&A series treatments are graphically estimated using the labeled right-hand side axes of two-axes plots, such as those included in sub-sections 8.3.2.2 through 8.3.13.5 of this document.

7.4.6.8 Conclusions drawn from Master "Composite" B.E.T. ("No-Loss") NQIR(T) Plot

The composite sets of back extrapolation values for quench series between 400^{o}C and 925^{o}C are shown in Figures 49 through 51, and these support two principal conclusions:

1) The least-squares fit yields a slope of 0.97 eV ± 0.01 eV [91] that is proposed to represent the vacancy formation energy E^{F}_{V}.
2) Insofar as to what might be the magnitude for the binding energy E^{B}_{2V} for divacancies in pure gold [3, 16, 18, 235] at elevated temperatures, examination of the Master Composite B.E.T. "No-Loss" Arrhenius plot provides no discernible upward curvature even for temperatures as high as 925^{o}C. This observation suggests that the magnitude of E^{B}_{2V} is likely to be somewhat less than 0.4 eV.

---

[91] Langeler [Ref. 135] reported a value of 0.97 ±0.03 eV for his work involving 1 mm diameter gold single crystals with dislocation densities lower than 2000/cm^{2}. Additionally, Triftshäuser and McGervey [Ref. 136] from their work using Positron Annihilation techniques involving gold established a value of 0.97±0.01 eV for the monovacancy formation energy (E^{F}_{1v}).

7.4.7 Tabulations of "No Loss" NQIR(T), $\Delta\rho_v(T)$, and $C_v(T)$ Values

Table 9 lists NQIR(T) values for the temperature range from 40^{o}C to 1063^{o}C that were established from analyses of data involving numerous elevated temperature ST DQ treatments [92].

For gold of 6N (99.9999 weight per cent) purity, the comparable $\Delta\rho_V(T)$ resistivity value associated with an elevated temperature of around 400^{o}C would be about 2.36 x 10^{-11} (see Table 10), and the corresponding $C_V(T)$ vacancy concentration would be about 1.58 x 10^{-7} (see Table 11).

---

92 Refer to Section 7.5 for the relevant plots that illustrate how knowledge of the associated values for "No Loss" NQIR(T) Ξ QIR(T)/R(40^{o}C) contributed to establishing what the nature of the ST DQ annealing kinetics was with respect to a specimen's pre-existing sink density.

7.4.7.1 Tabulations of "No Loss" QIR(T)/R(40^{o}C) Values

Table 9. "No Loss" QIR(T)/R(40^{o}C) Values for 40^{o}C ≤ T ≤ 1063^{o}C

T (^{o}C)	T(^{o}K)$^{-1}$	NQIR(T) Ξ QIR(T)/R(40^{o}C) Values [93]	NQIR(T) / NQIR(400^{o}C)
1063	0.000748	4.56 x10^{-2}	4560
925	0.000835	1.7 x 10^{-2}	1700
900	0.000852	1.4 x10^{-2}	1400
875	0.000871	1.1 x10^{-2}	1100
850	0.000890	9.1 x 10^{-3}	910
825	0.000911	7.2 x 10^{-3}	720
800	0.000932	5.7 x 10^{-3}	570
750	0.000977	3.4 x 10^{-3}	340
700	0.001028	1.9 x 10^{-3}	190
650	0.001083	1.0 x 10^{-3}	100
600	0.001145	5 x 10^{-4}	50
550	0.001215	2.3 x 10^{-4}	23
500	0.001293	9.2 x 10^{-5}	9.2
450	0.001383	3.3 x 10^{-5}	3.3
400	0.001486	1 x 10^{-5}	1
350	0.001605	3 x 10^{-6}	0.3
300	0.001745	7 x 10^{-7}	7 x 10^{-2}
200	0.002113	1 x 10^{-8}	10^{-3}
150	0.002363	8.4 x 10^{-10}	8.4 x 10^{-5}
100	0.002680	1 x 10^{-11}	10^{-6}
40	0.003193	4 x 10^{-14}	4 x 10^{-9}

[93] "No loss" values listed in Table 9 are intended to serve only as approximate values.

7.4.7.2 Tabulations of "No Loss" $\Delta\rho_V(T)$ Values

Table 10. "No Loss" $\Delta\rho_V(T)$ Values for $40^oC \leq T \leq 1063^oC$

T (^{o}C)	$\Delta\rho_V(T)$ Values [94] (in Ω-cm)
1063	1.08×10^{-7}
925	4.02×10^{-8}
900	3.31×10^{-8}
875	2.60×10^{-8}
850	2.15×10^{-8}
825	1.70×10^{-8}
800	1.35×10^{-8}
750	8.03×10^{-9}
700	4.49×10^{-9}
650	2.24×10^{-9}
600	1.18×10^{-9}
550	5.43×10^{-10}
500	2.17×10^{-10}
450	7.80×10^{-11}
400	2.36×10^{-11}
350	7.1×10^{-12}
300	1.65×10^{-12}
200	2.36×10^{-14}
150	1.98×10^{-15}
100	2.36×10^{-17}
40	9.444×10^{-20}

[94] The "no loss" values listed in Table 10 are intended to serve as approximate values.

7.4.7.3 Tabulations of "No Loss" $C_V(T)$ Values

Table 11. "No Loss" $C_V(T)$ Values for $40^oC \leq T \leq 1063^oC$

T (^oC)	$C_V(T)$ Values [95]
1063	7.20×10^{-4}
925	2.70×10^{-4}
900	2.20×10^{-4}
875	1.74×10^{-4}
850	1.44×10^{-4}
800	8.99×10^{-5}
750	5.37×10^{-5}
700	3.00×10^{-5}
650	1.58×10^{-5}
600	7.89×10^{-6}
550	3.63×10^{-6}
500	1.45×10^{-6}
450	5.21×10^{-7}
400	1.58×10^{-7}
350	4.73×10^{-8}
300	7×10^{-9}
200	1.10×10^{-9}
100	1.58×10^{-13}
40	6.31×10^{-16}

Table 12 provides an easy-to-use reference for comparing or converting between "No Loss" values listed in various plots presented throughout this document.

[95] The "no loss" values listed in Table 11 are intended to serve as approximate values.

7.4.7.4 Tabulations of "No Loss" NQIR(T), $\Delta\rho_V(T)$, and $C_V(T)$ Values

Table 12. "No Loss" NQIR(T), $\Delta\rho_V(T)$, and $C_V(T)$ for $40^oC \leq T \leq 1063^oC$

T (^oC)	NQIR(T) Ξ QIR(T)/R(40^oC) [96] Values	$\Delta\rho_V(T)$ Values (in Ω-cm)	$C_V(T)$ Values
1063	4.56×10^{-2}	1.08×10^{-7}	7.20×10^{-4}
925	1.7×10^{-2}	4.02×10^{-8}	2.70×10^{-4}
900	1.4×10^{-2}	3.31×10^{-8}	2.20×10^{-4}
875	1.1×10^{-2}	2.60×10^{-8}	1.74×10^{-4}
850	9.1×10^{-3}	2.15×10^{-8}	1.44×10^{-4}
825	7.2×10^{-3}	1.70×10^{-8}	1.14×10^{-4}
800	5.7×10^{-3}	1.35×10^{-8}	8.99×10^{-5}
750	3.4×10^{-3}	8.03×10^{-9}	5.37×10^{-5}
700	1.9×10^{-3}	4.49×10^{-9}	3.00×10^{-5}
650	1.0×10^{-3}	2.24×10^{-9}	1.58×10^{-5}
600	5×10^{-4}	1.18×10^{-9}	7.89×10^{-6}
550	2.3×10^{-4}	5.43×10^{-10}	3.63×10^{-6}
500	9.2×10^{-5}	2.17×10^{-10}	1.45×10^{-6}
450	3.3×10^{-5}	7.80×10^{-11}	5.21×10^{-7}
400	1×10^{-5}	2.36×10^{-11}	1.58×10^{-7}
350	3×10^{-6}	$7.1x\ 10^{-12}$	4.73×10^{-8}
300	7×10^{-7}	1.65×10^{-12}	7×10^{-9}
200	1×10^{-8}	2.36×10^{-14}	1.10×10^{-9}
150	8.4×10^{-10}	1.98×10^{-15}	1.33×10^{-11}
100	1×10^{-11}	2.36×10^{-17}	1.58×10^{-13}
40	4×10^{-14}	9.444×10^{-20}	6.31×10^{-16}

[96] "No loss" values listed in Table 12 are intended to serve only as approximate values.

7.5 SEGMENTED ANALYSES OF ST DQ ANNEALING KINETICS

Having achieved establishment of an overall set of No-Loss NQIR(T_Q) values from the acquired data presented in Section 7.4, analyses were made of the associated ST DQ annealing kinetics from T_Q from as high as 925^{o}C down to 700^{o}C.

7.5.1 Adoption of Reciprocal Initial Quench Rate as an Independent Parameter

Reciprocal initial quench rate (RIQR) is labeled $(dT/dt_{initial})^{-1}$ and was chosen as the independent parameter for most of the subsequent analyses performed on the acquired sets of ST DQ data.

7.5.2 Specific Series of Plots Chosen for Analyzing the Nature of Straight Downquench Data Annealing Kinetics

As sets of QIR(T_Q)/R(40^{o}C) data were obtained over the quench temperature range from 925^{o}C down to 700^{o}C, numerous plots were generated.

7.5.2.1 Plots with Reciprocal Initial Quench Rate (RIQR) or its Square Root as the Independent Parameter

Figures 52 through 74 provide five variations in the plotting of each of these sets of ST DQ series treatment data, namely:

1) NQIR[T_Q, $(dT/dt)_{initial}^{-1}$] data obtained over the range of initial quench rates;

2) NQIR[T_Q, $(dT/dt)_{initial}^{-1}$] extended to infinite quench rate to thereby reach "No Loss" NQIR[T_Q, $(dT/dt)_{initial}^{-1}$=0] levels; and

3) Semi-Log plots of NQIR[T_Q, $(dT/dt)_{initial}^{-1}$] data extended to infinite quench rate, thereby reaching "No Loss" NQIR[T_Q, $(dT/dt)_{initial}^{-1}$=0] levels.

4) Plots of NQIR[T_Q, $(dT/dt)_{initial}^{-1}$] with square root of RIQR as the independent parameter

5) Semi-Log plots of NQIR[T_Q, $(dT/dt)_{initial}^{-1}$] with square root of RIQR as the independent parameter.

Examinations of the 925°C ST DQ series treatments data encompass five separate plots (Figures 52 through 56) to allow for incremental insights leading up to several conclusions regarding the underlying annealing kinetics.

Figure 52 presents ST DQ series data sets for two specimens (3009 and 3012).

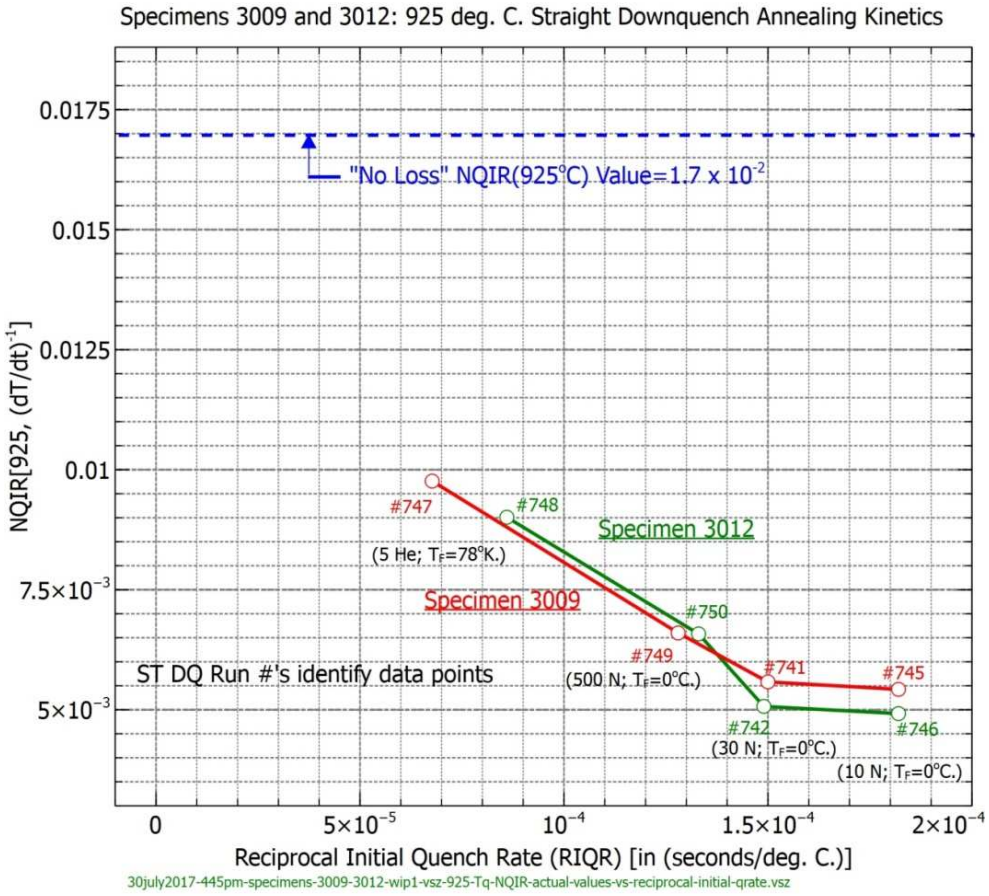

Figure 52. Specimens 3009 and 3012: Plots of NQIR [925°C, $(dT/dt)_{initial}^{-1}$] vs. Reciprocal Initial Quench Rate (RIQR)

Figure 53 illustrates the results of linear extensions and extensions to No-Loss values associated with an infinite quench rate.

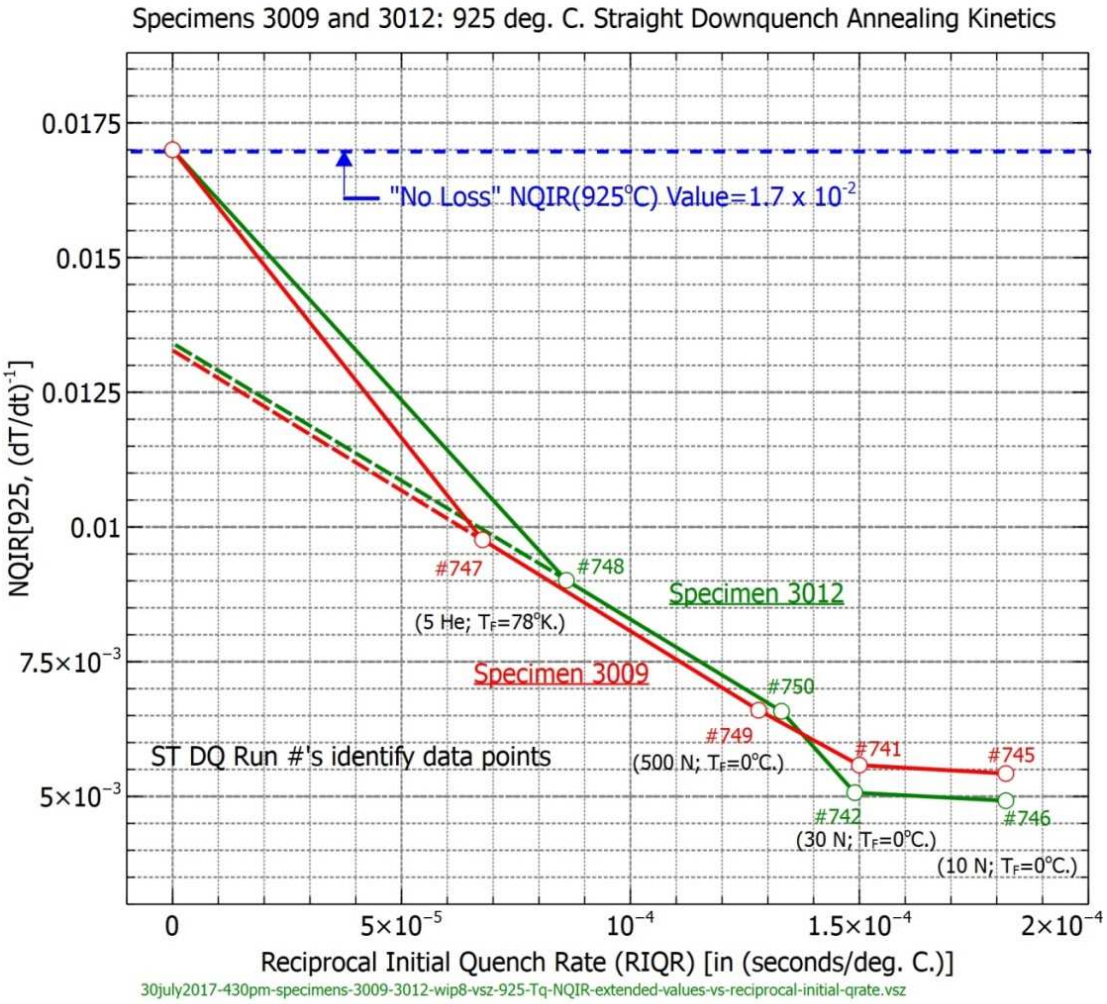

Figure 53. Specimens 3009 and 3012: Plots of NQIR [925°C, $(dT/dt)_{initial}^{-1}$] vs. Reciprocal Initial Quench Rate (RIQR) extended to infinite quench rate

Figure 54 reveals a reasonable extension to a "No Loss" NQIR value when a semi-log plot is used. However, the occurrence of a crossover of values for slower quenches (higher RIQR values) was noted as a concern to be examined further.

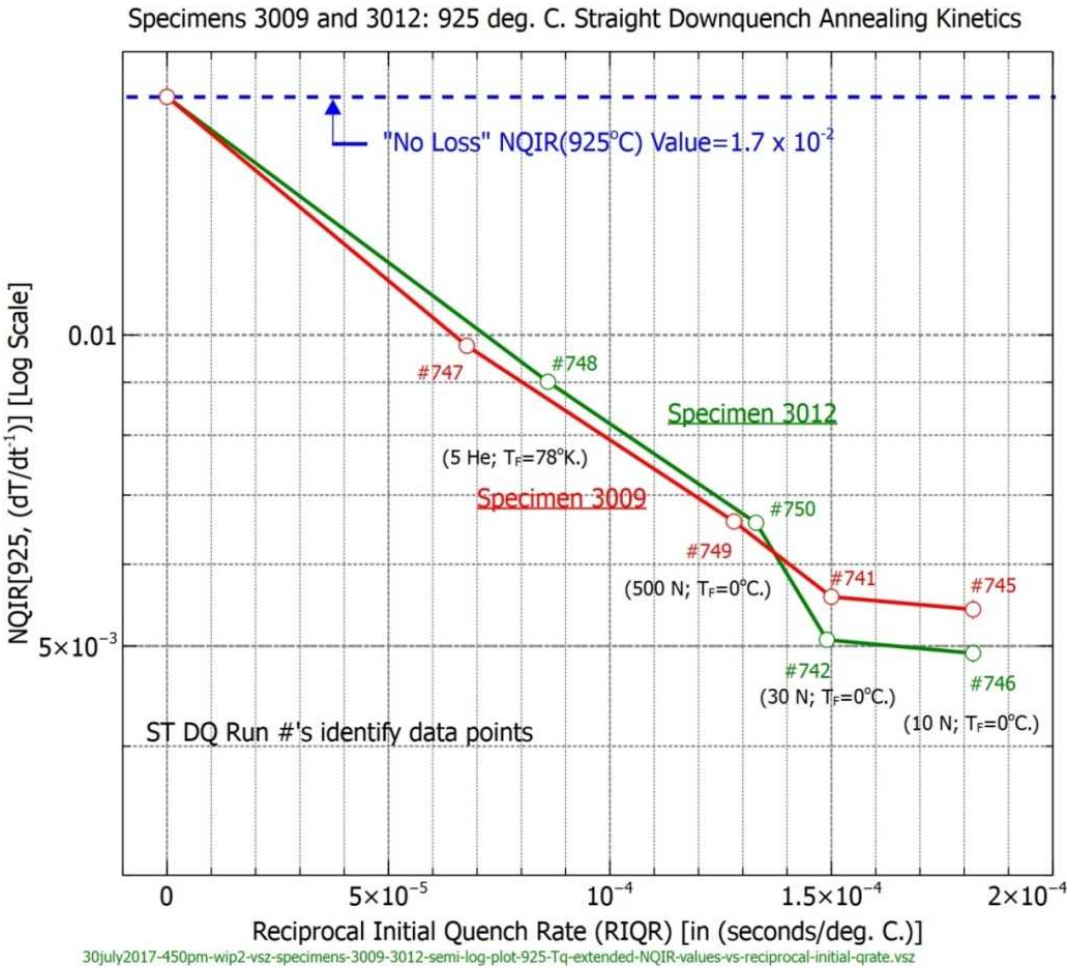

Figure 54. Specimens 3009 and 3012: Semi-Log plots of NQIR [925°C, $(dT/dt)_{initial}^{-1}$] vs. Reciprocal Initial Quench Rate (RIQR) extended to infinite quench rate

Specifically, the appearance of a crossover region between two sets of data points associated with the slowest initial quench rates led to making use of a different independent parameter, namely the square root of RIQR. As Figure 55 indicates, this choice did result in the removal of crossovers that were noted in the prior three Figures.

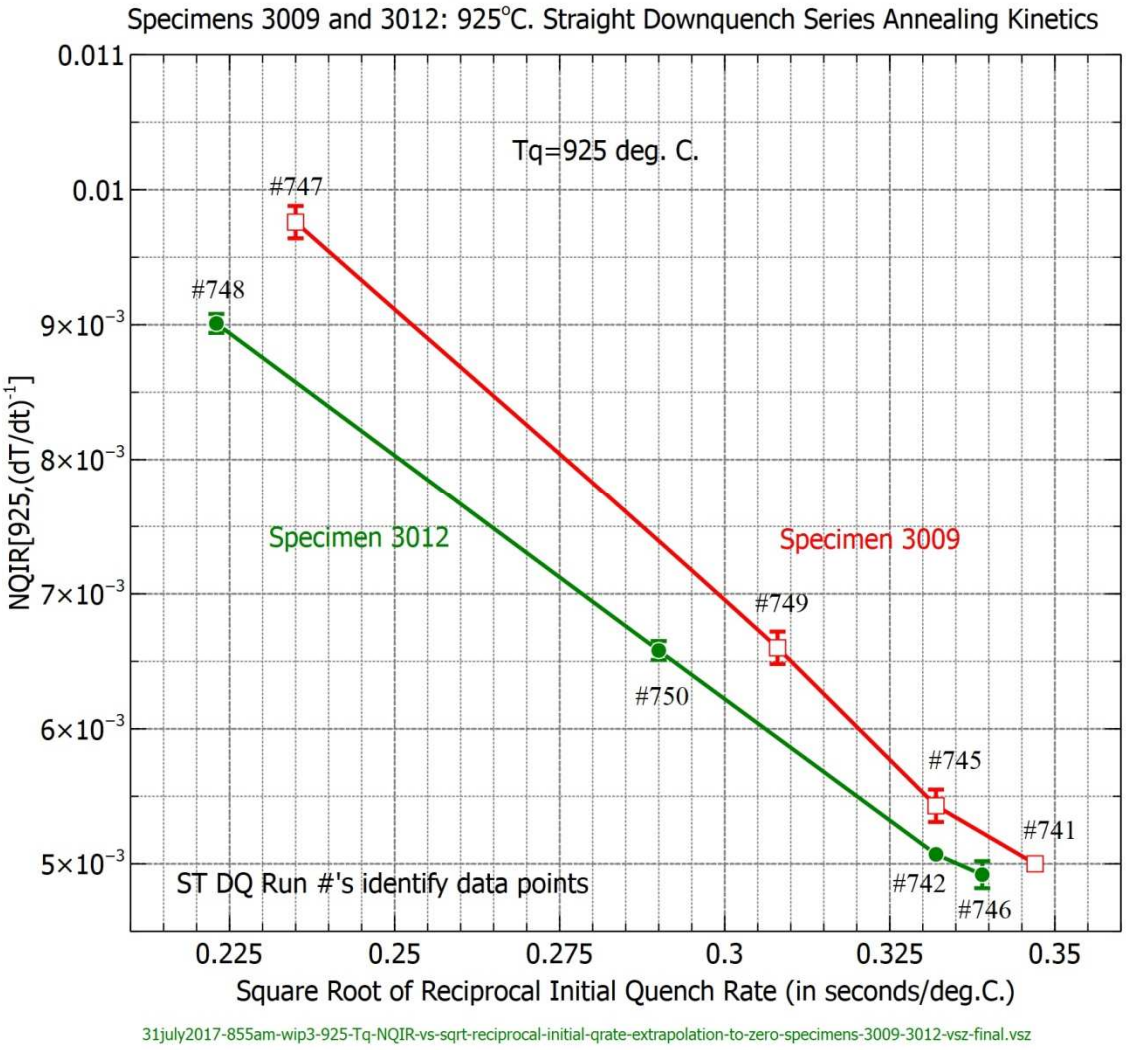

Figure 55. Specimens 3009 and 3012: Plots of NQIR [925°C, $(dT/dt)_{initial}^{-1}$] vs. Square Root of Reciprocal Initial Quench Rate (RIQR)

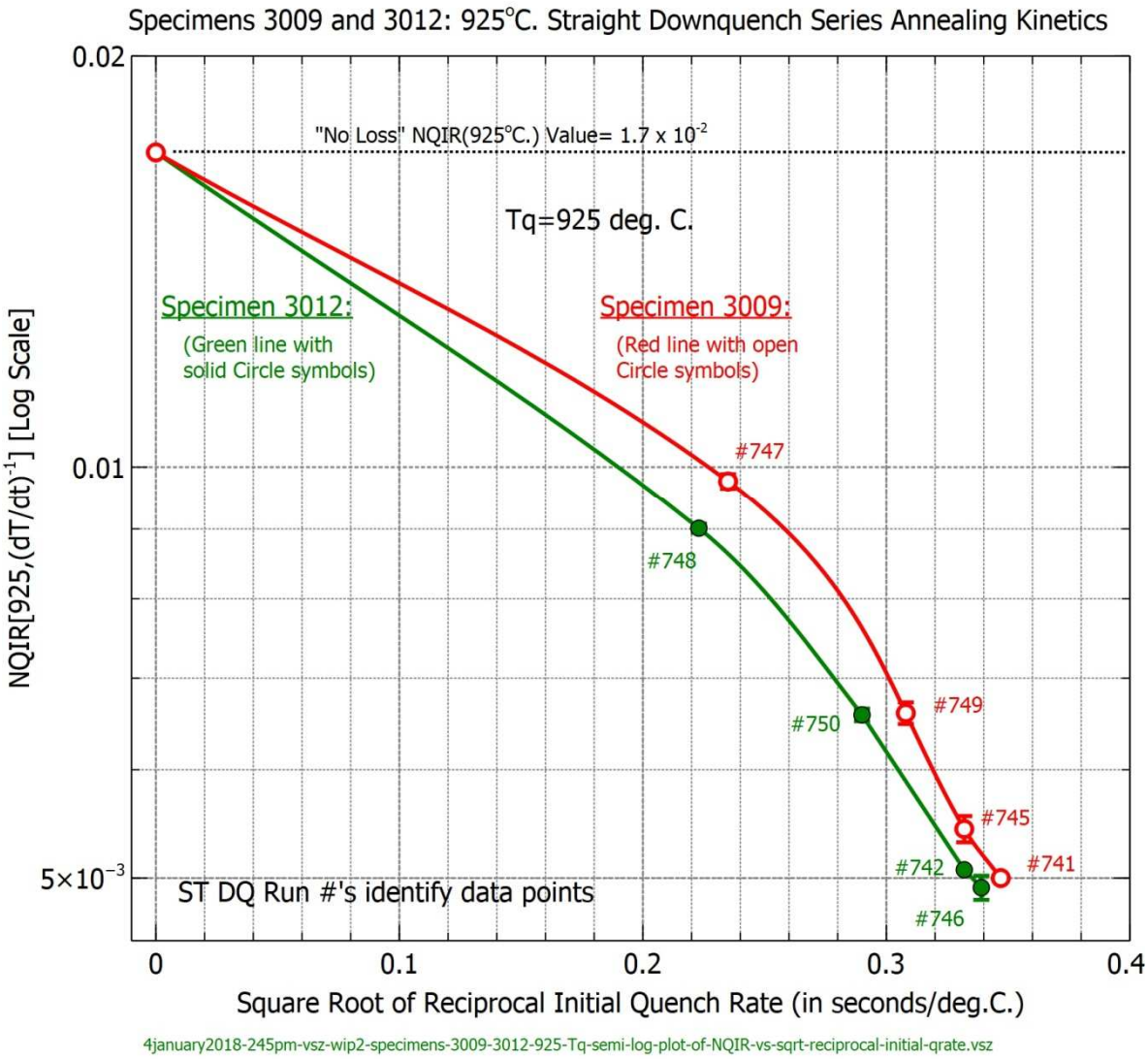

Figure 56. Specimens 3009 and 3012: Semi-Log plots of NQIR [925°C, $(dT/dt)_{initial}^{-1}$] vs. Square Root of Reciprocal Initial Quench Rate (RIQR) extended to infinite quench rate

Moreover, the semi-log plot shown in Figure 56 reveals two distinct slopes that appear to more reasonably reflect diffusion-limited ST DQ annealing kinetics that would be expected to occur during straight downquenches from 925°C.

Figures 57 through 79 illustrate sets of plots of NQIR [T_Q, $(dT/dt)_{initial}^{-1}$] ST DQ annealing kinetics involving quench temperatures of 875°C, 825°C, 800°C, 750°C, and 700°C. In similar fashion several combinations of independent and dependent parameters were chosen as deemed appropriate for illustrating the discernible nature of each particular set of annealing kinetics.

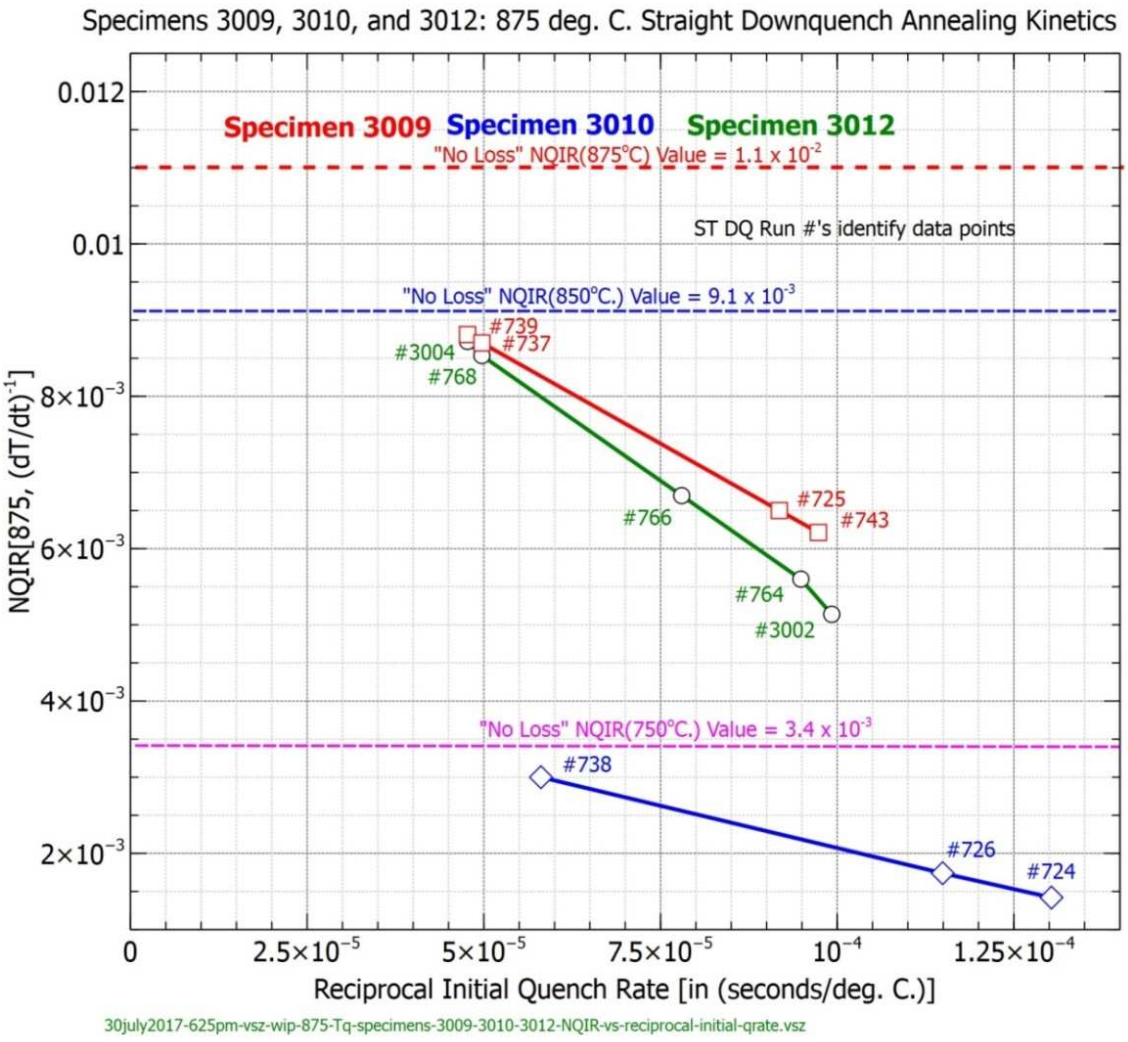

Figure 57. Specimens 3009, 3010, and 3012: Plots of NQIR[875°C, $(dT/dt)_{initial}^{-1}$] vs. Reciprocal Initial Quench Rate (RIQR)

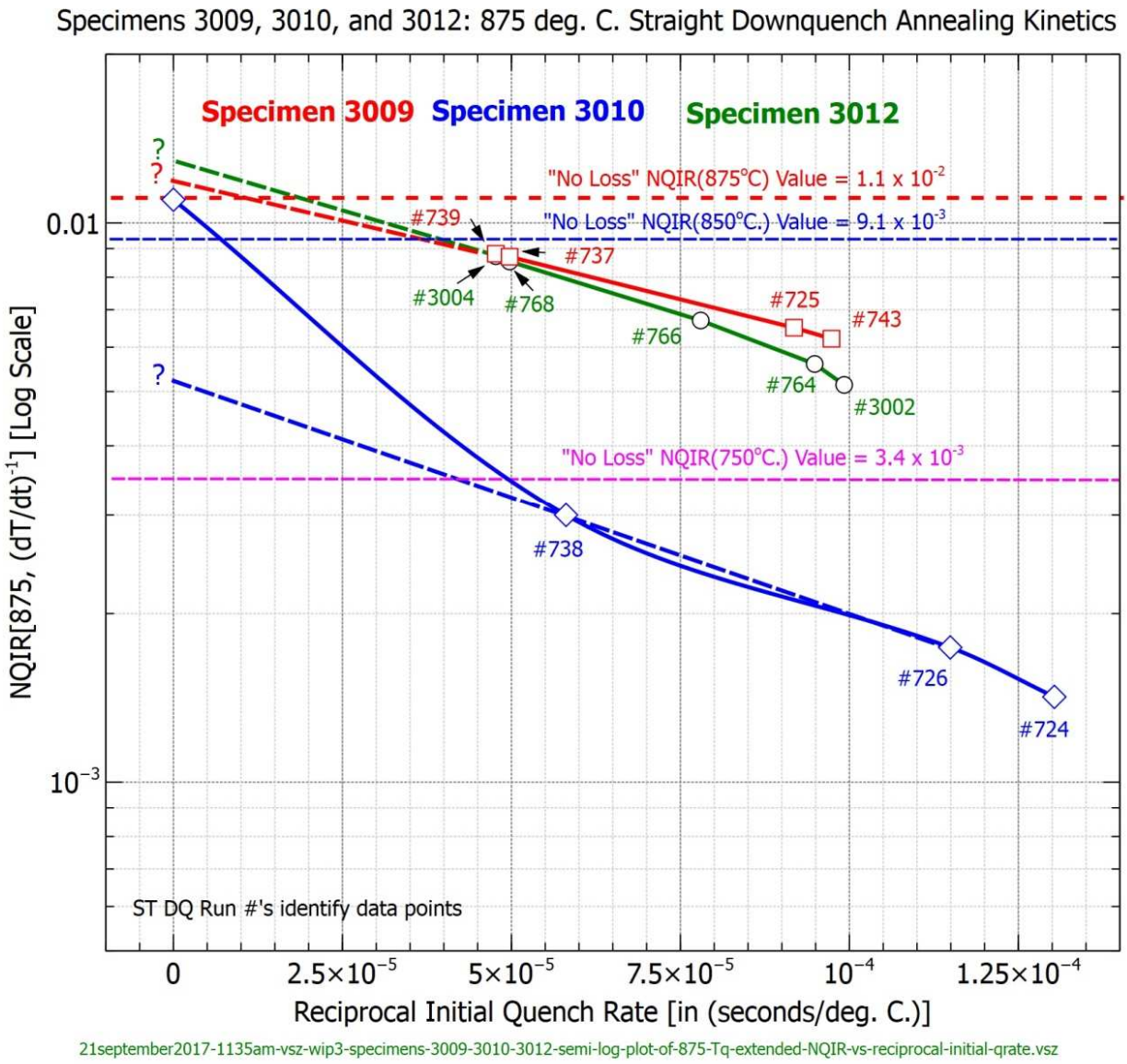

Figure 58. Specimens 3009, 3010, and 3012: Semi-Log Plots of logarithmic extrapolation of NQIR [875°C, $(dT/dt)_{initial}^{-1}$] Values vs. Reciprocal Initial Quench Rate (RIQR)

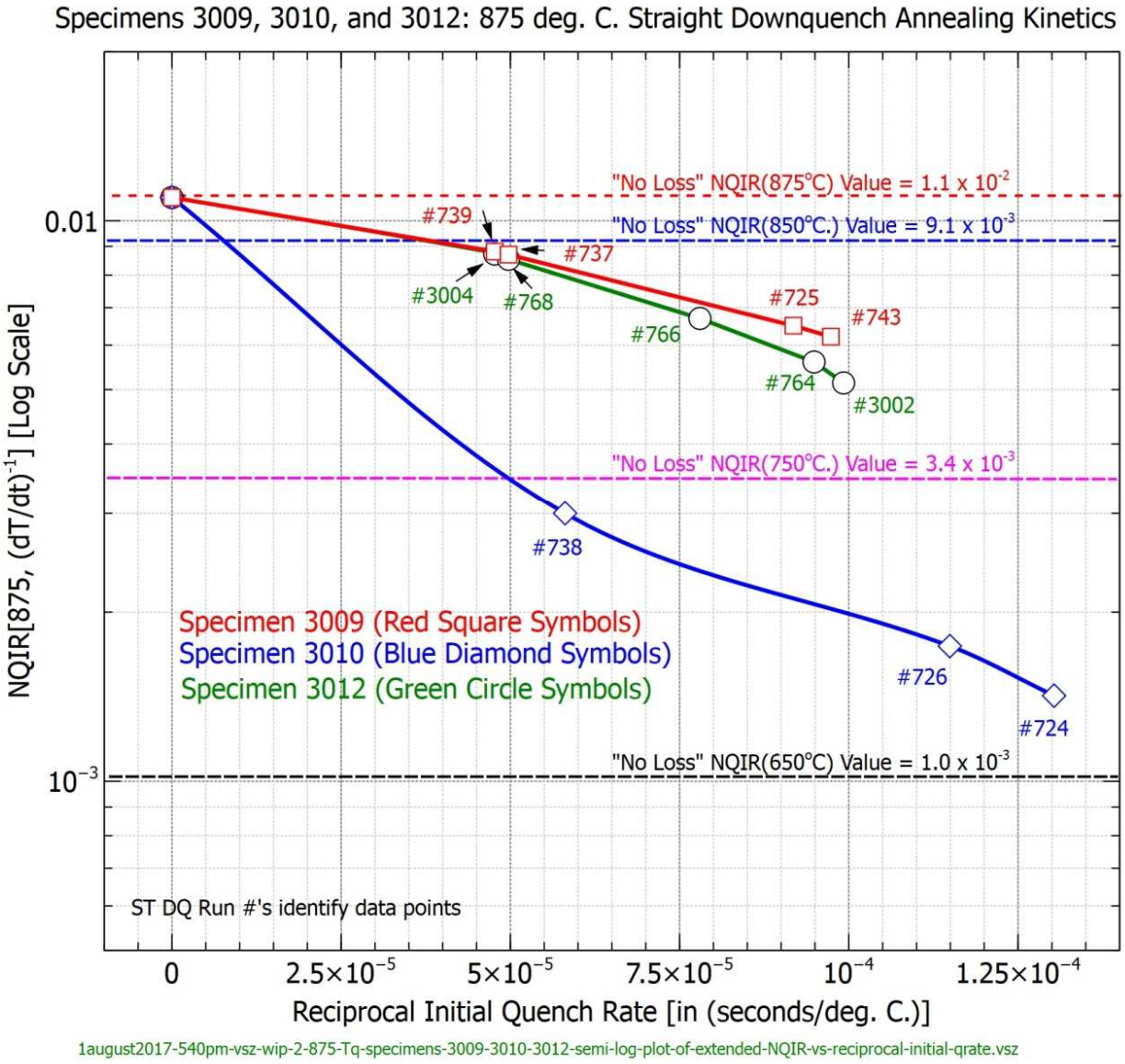

Figure 59. Specimens 3009, 3010, and 3012: Semi-Log plots of NQIR [875°C, $(dT/dt)_{initial}^{-1}$] data extended to "No Loss" NQIR[875°C, (B.E.T.)] Values vs. Reciprocal Initial Quench Rate (RIQR)

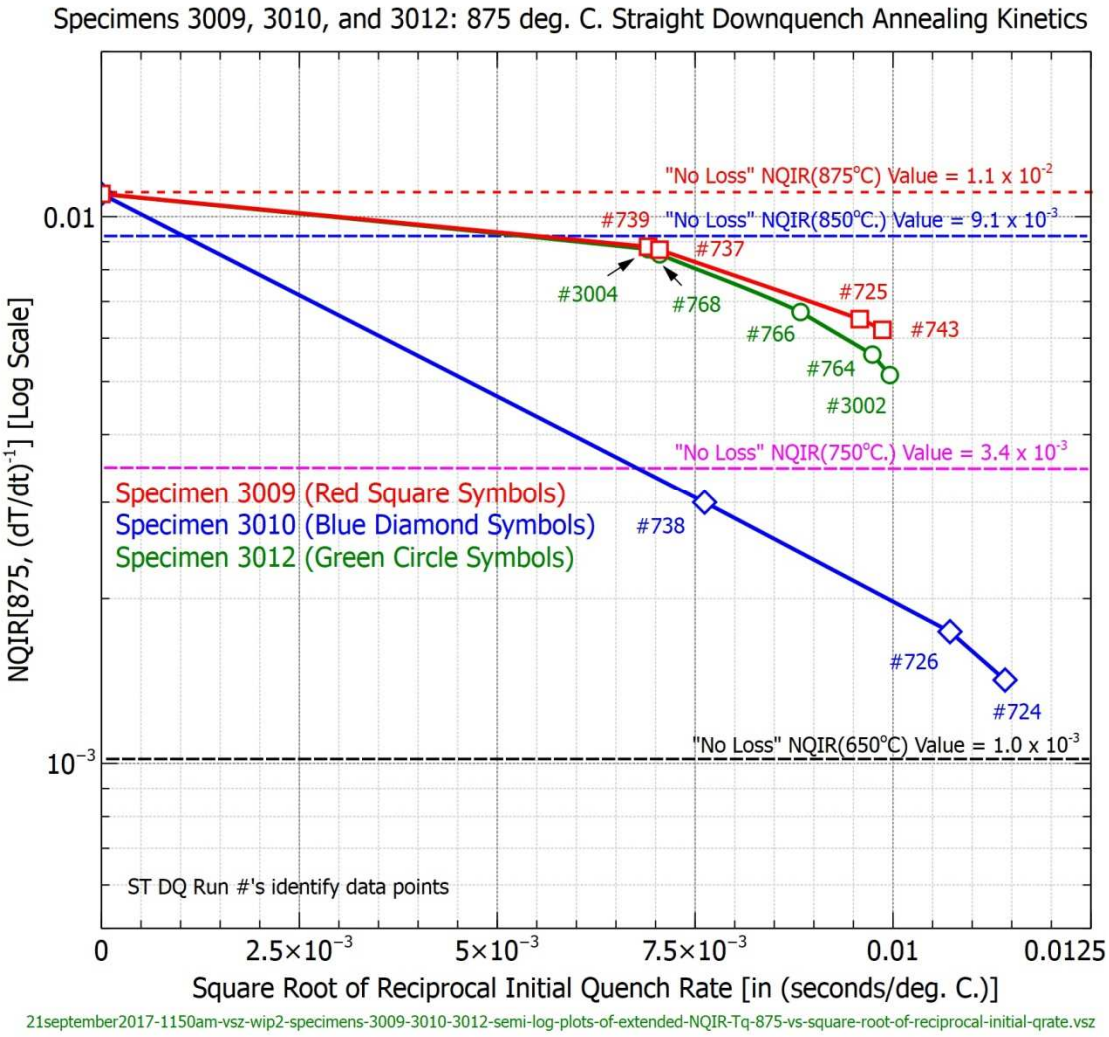

Figure 60. Specimens 3009, 3010, and 3012: Semi-Log plots of extended NQIR [875°C, $(dT/dt)_{initial}^{-1}$] Values vs. Square Root of Reciprocal Initial Quench Rate (RIQR)

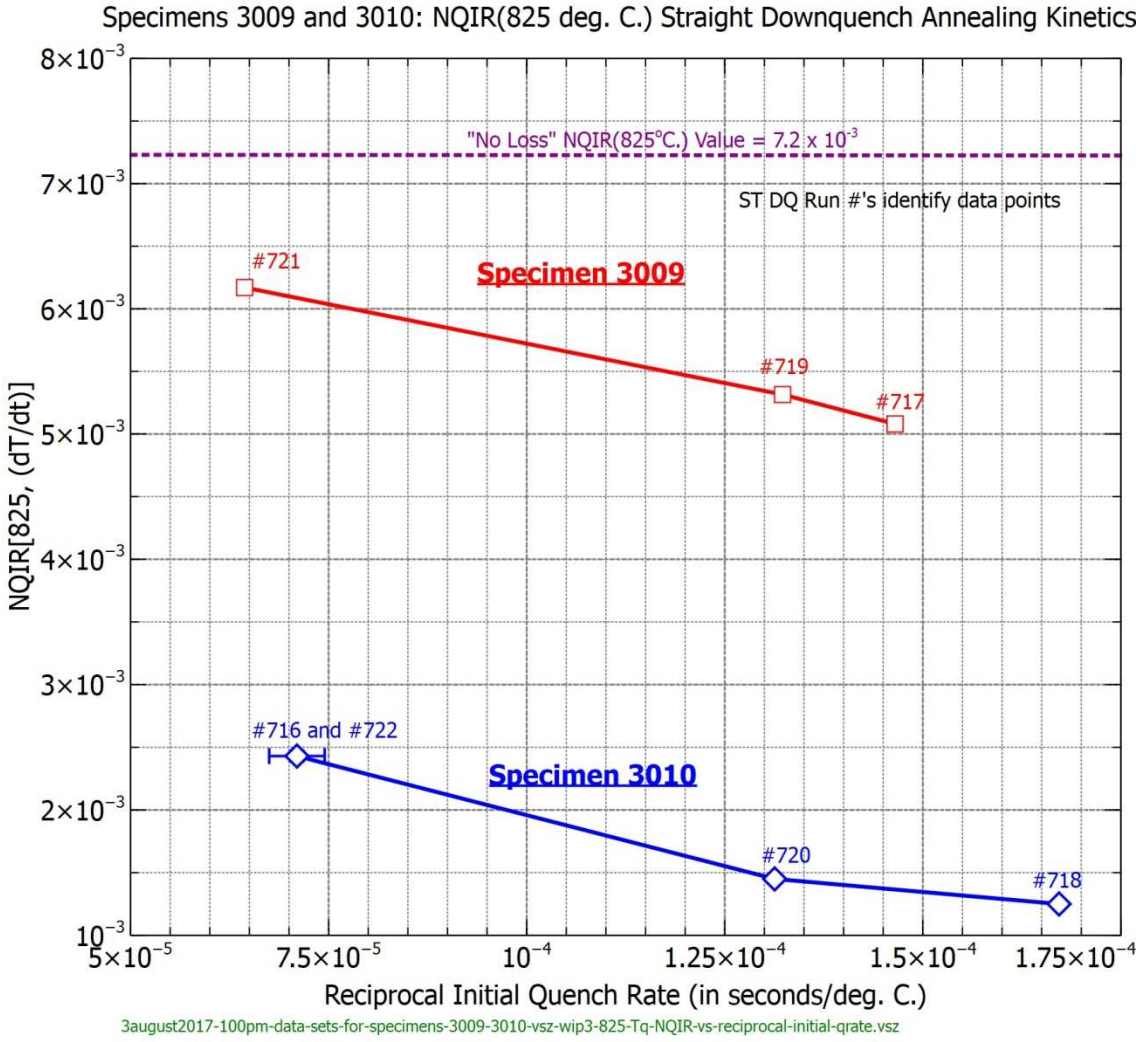

Figure 61. Specimens 3009 and 3010: Plots of NQIR [825°C, $(dT/dt)_{initial}^{-1}$] vs. Reciprocal Initial Quench Rate (RIQR)

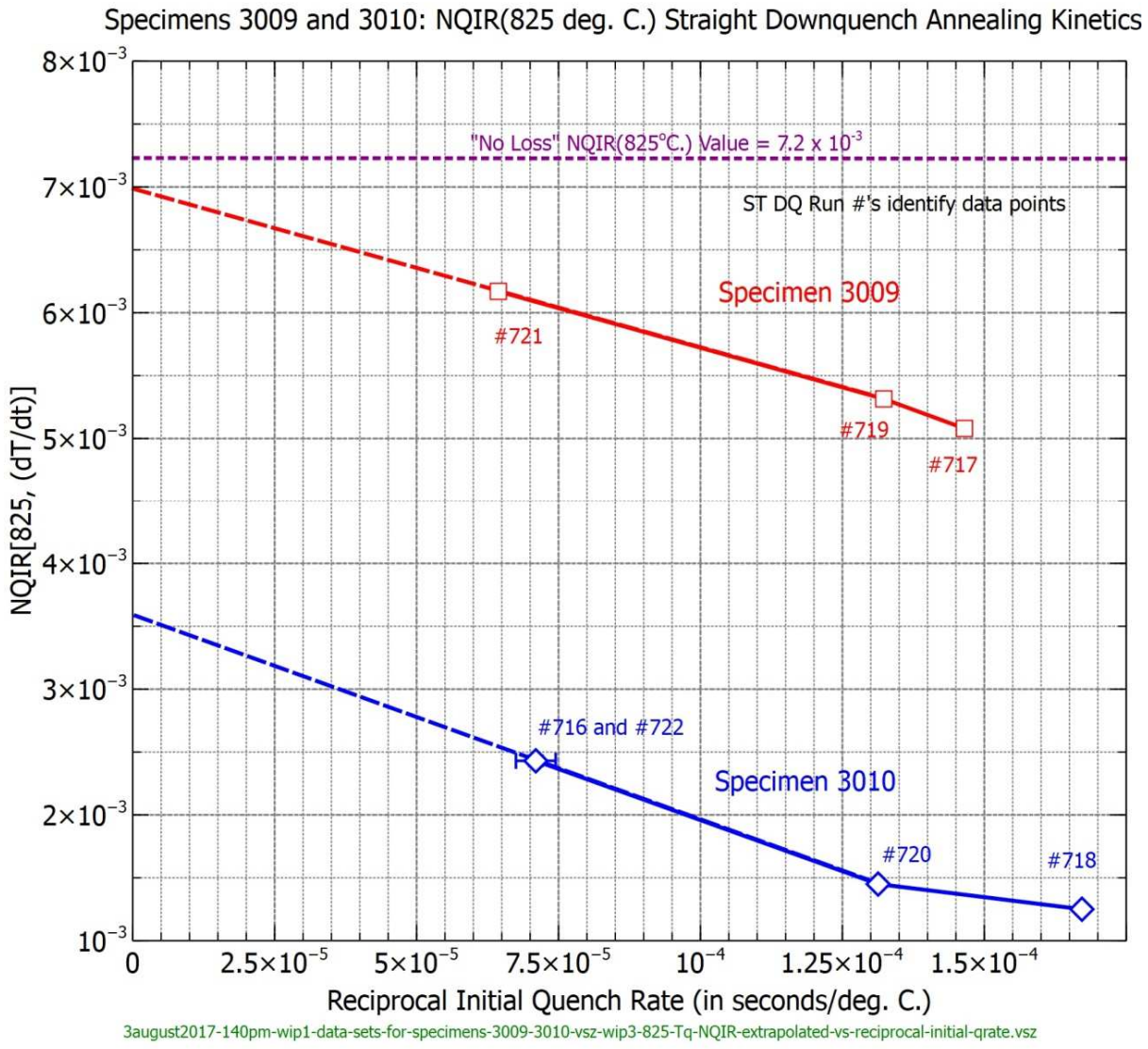

Figure 62. Specimens 3009 and 3010: Plots of NQIR [825°C, $(dT/dt)_{initial}^{-1}$] vs. Reciprocal Initial Quench Rate (RIQR) extended to infinite quench rate

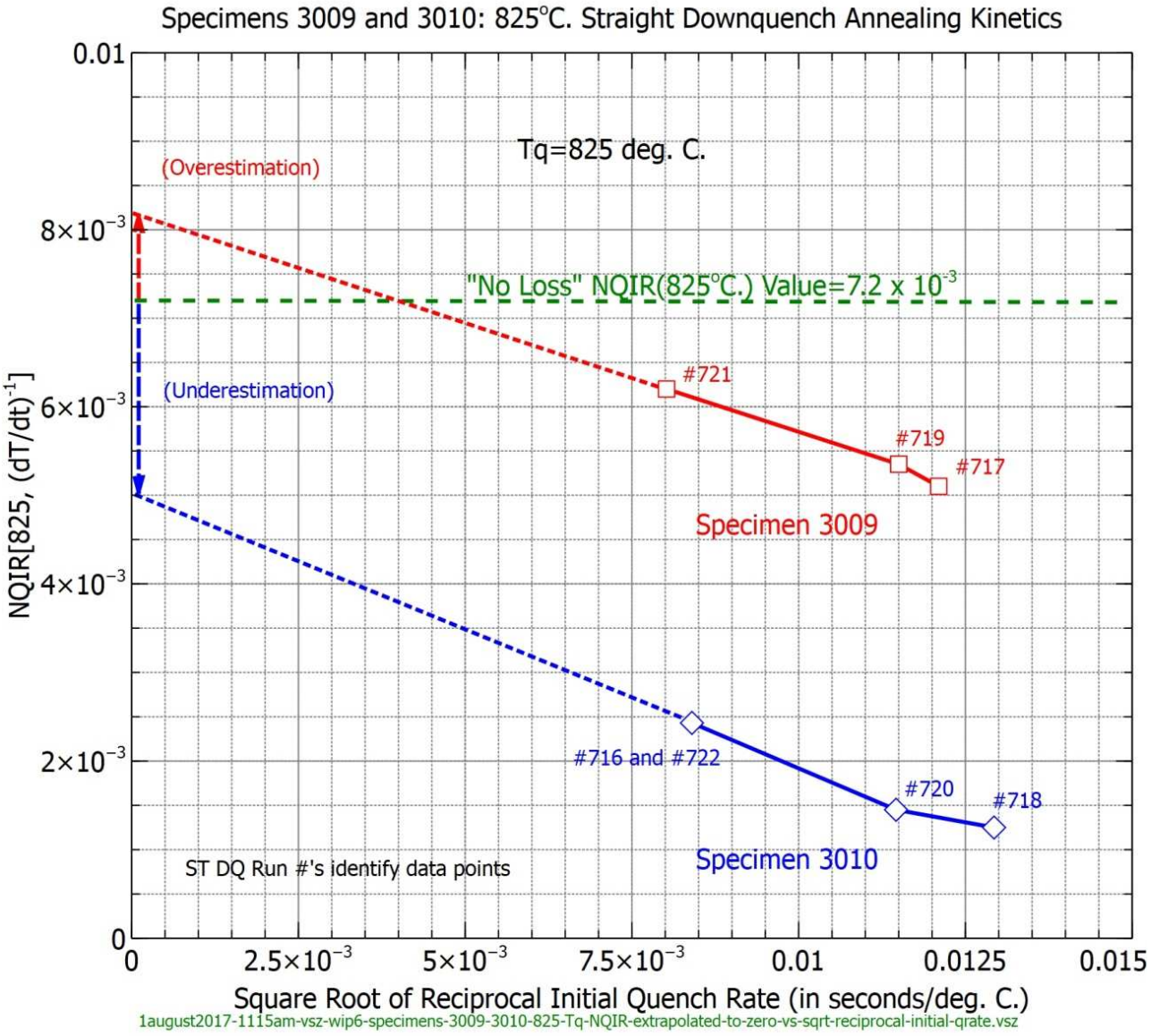

Figure 63. Specimens 3009 and 3010: Plots of extended NQIR [825°C, $(dT/dt)_{initial}^{-1}$] vs. Square Root of Reciprocal Initial Quench Rate (RIQR)

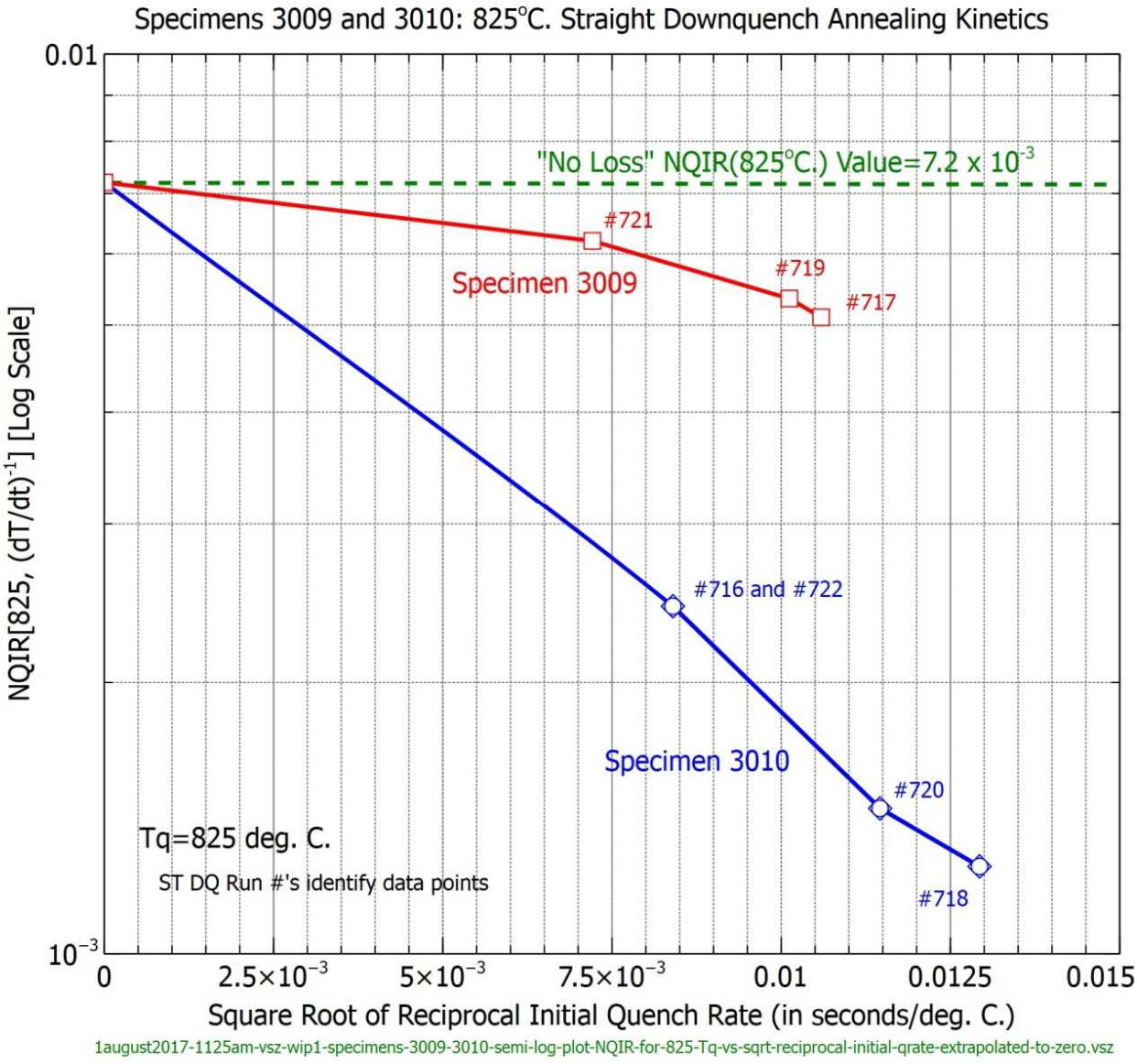

Figure 64. Specimens 3009 and 3010: Semi-Log Plots of extended NQIR [825°C, $(dT/dt)_{initial}^{-1}$] vs. Square Root of RIQR

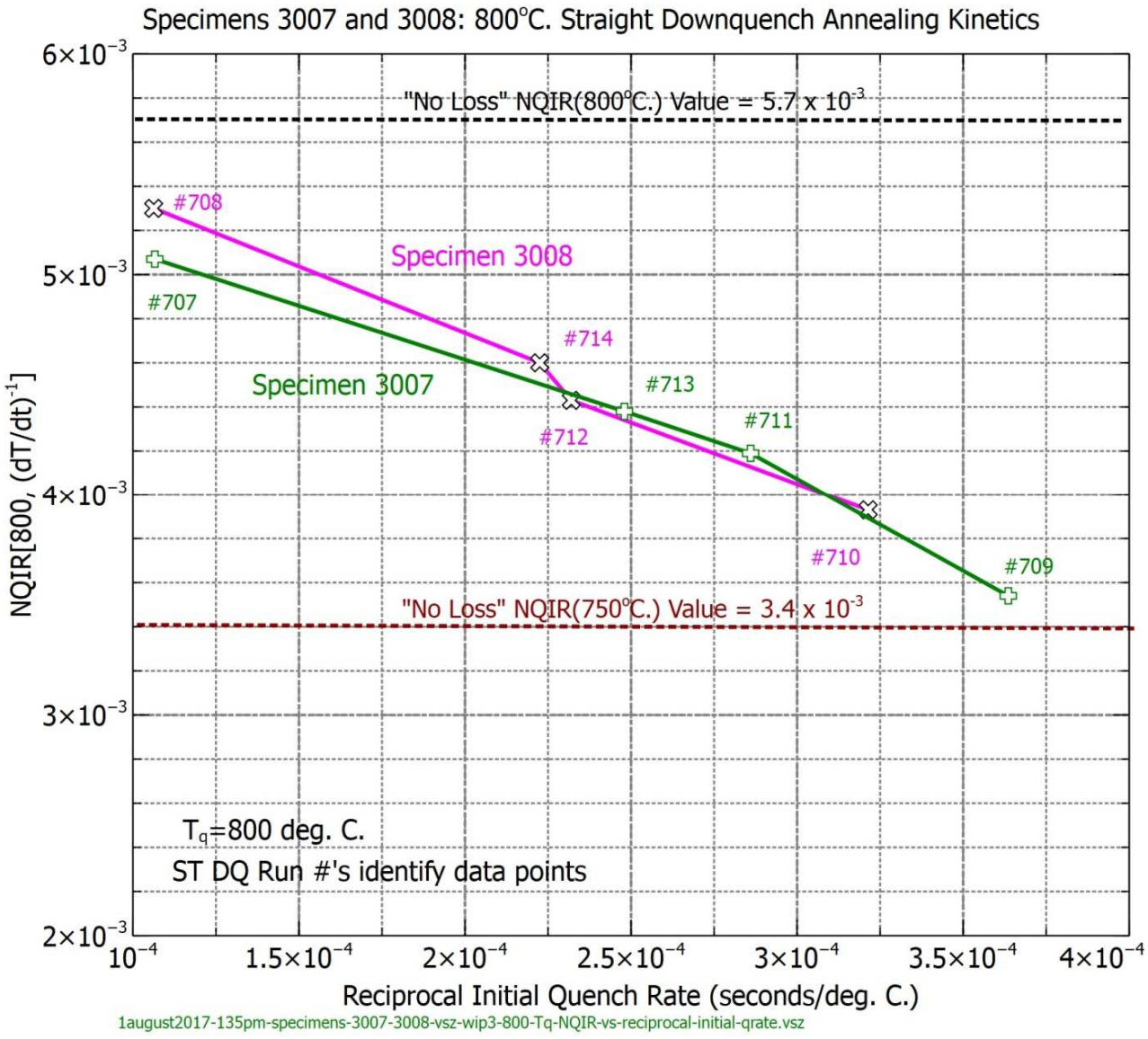

Figure 65. Specimens 3007 and 3008: Plots of NQIR [800°C, $(dT/dt)_{initial}^{-1}$] vs. Reciprocal Initial Quench Rate (RIQR)

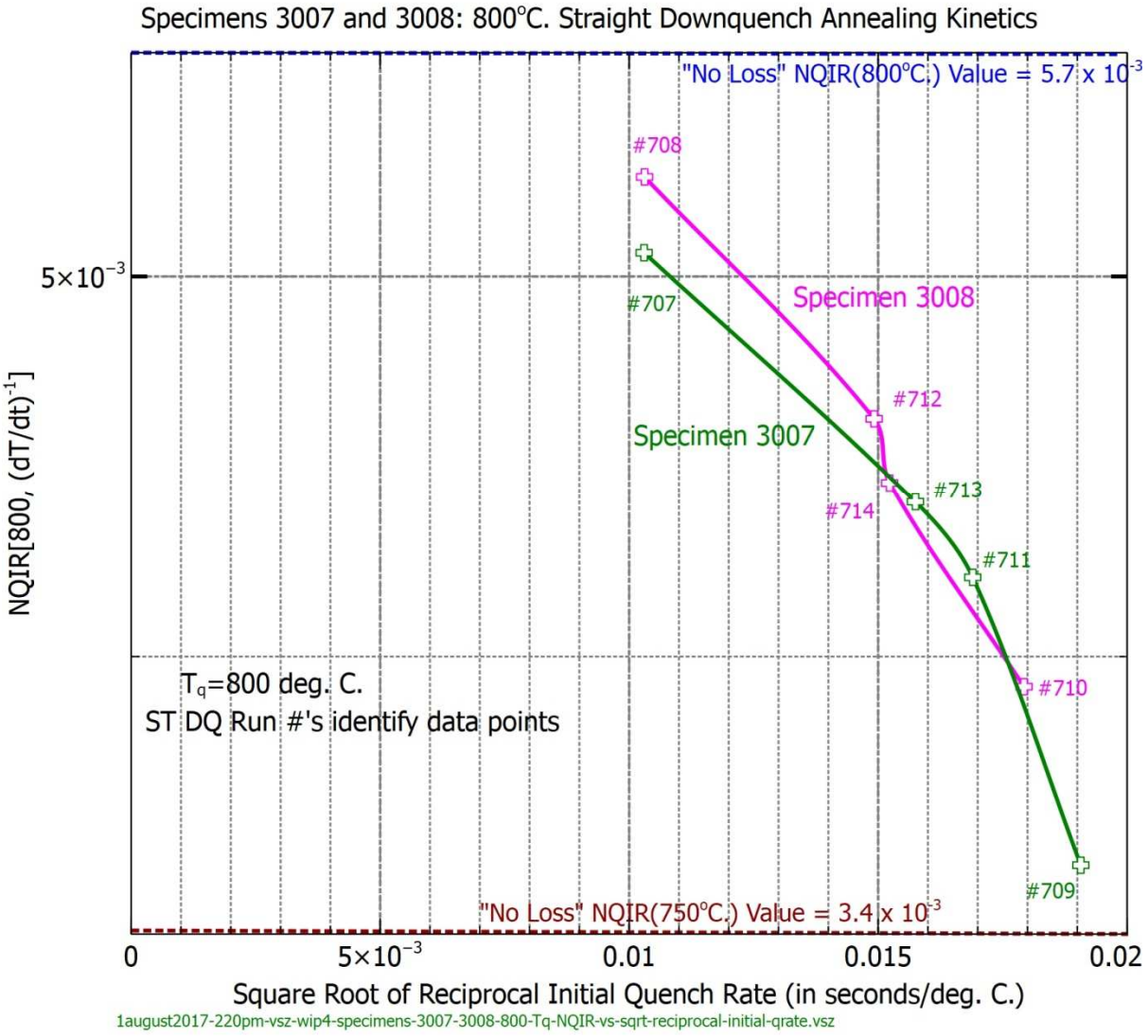

Figure 66. Specimens 3007 and 3008: Plots of NQIR [800°C, $(dT/dt)_{initial}^{-1}$] vs. Square Root of Reciprocal Initial Quench Rate (RIQR)

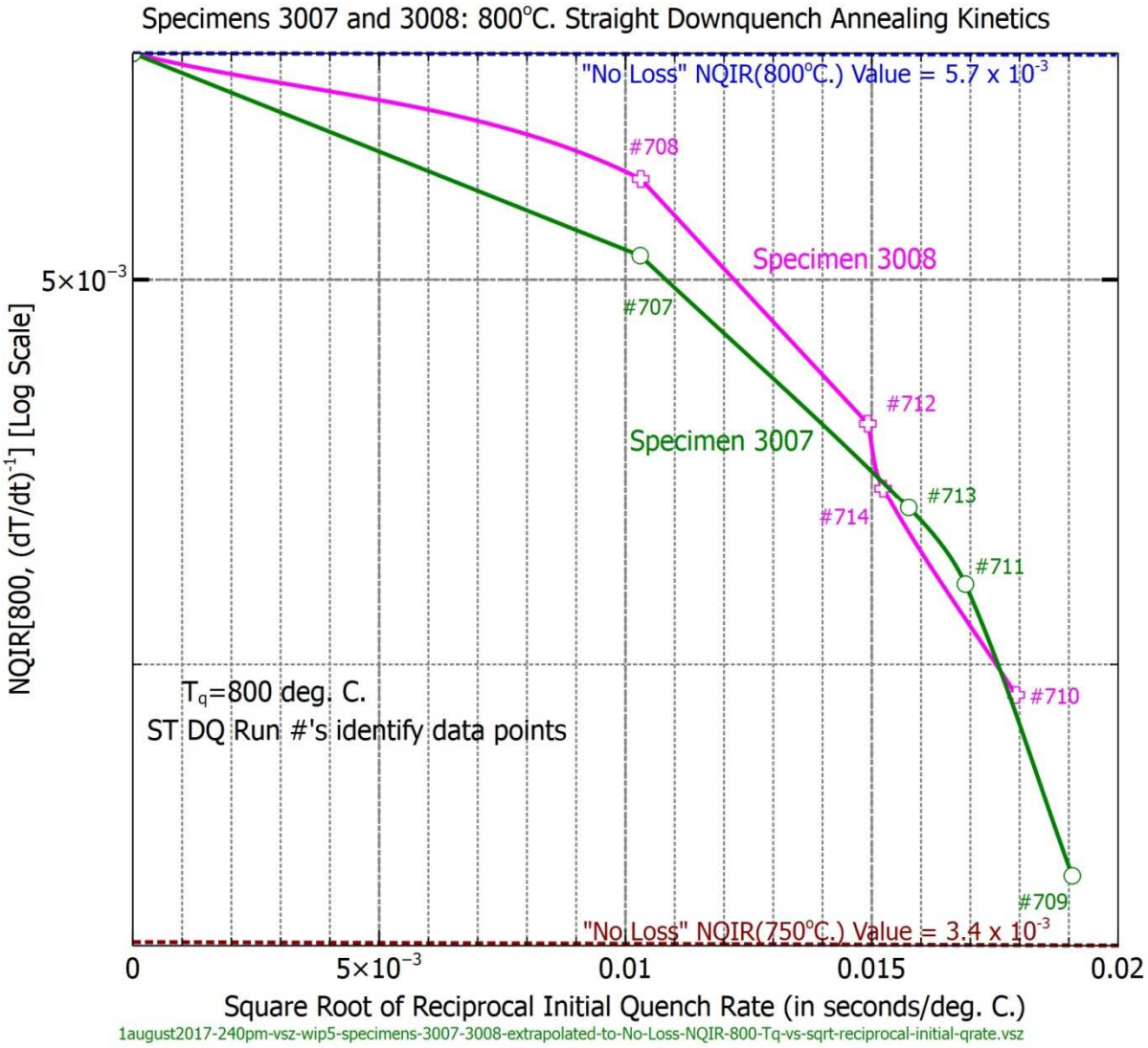

Figure 67. Specimens 3007 and 3008: Semi-Log Plots of extended NQIR [800°C, $(dT/dt)_{initial}^{-1}$] Values vs. Square Root of Reciprocal Initial Quench Rate (RIQR)

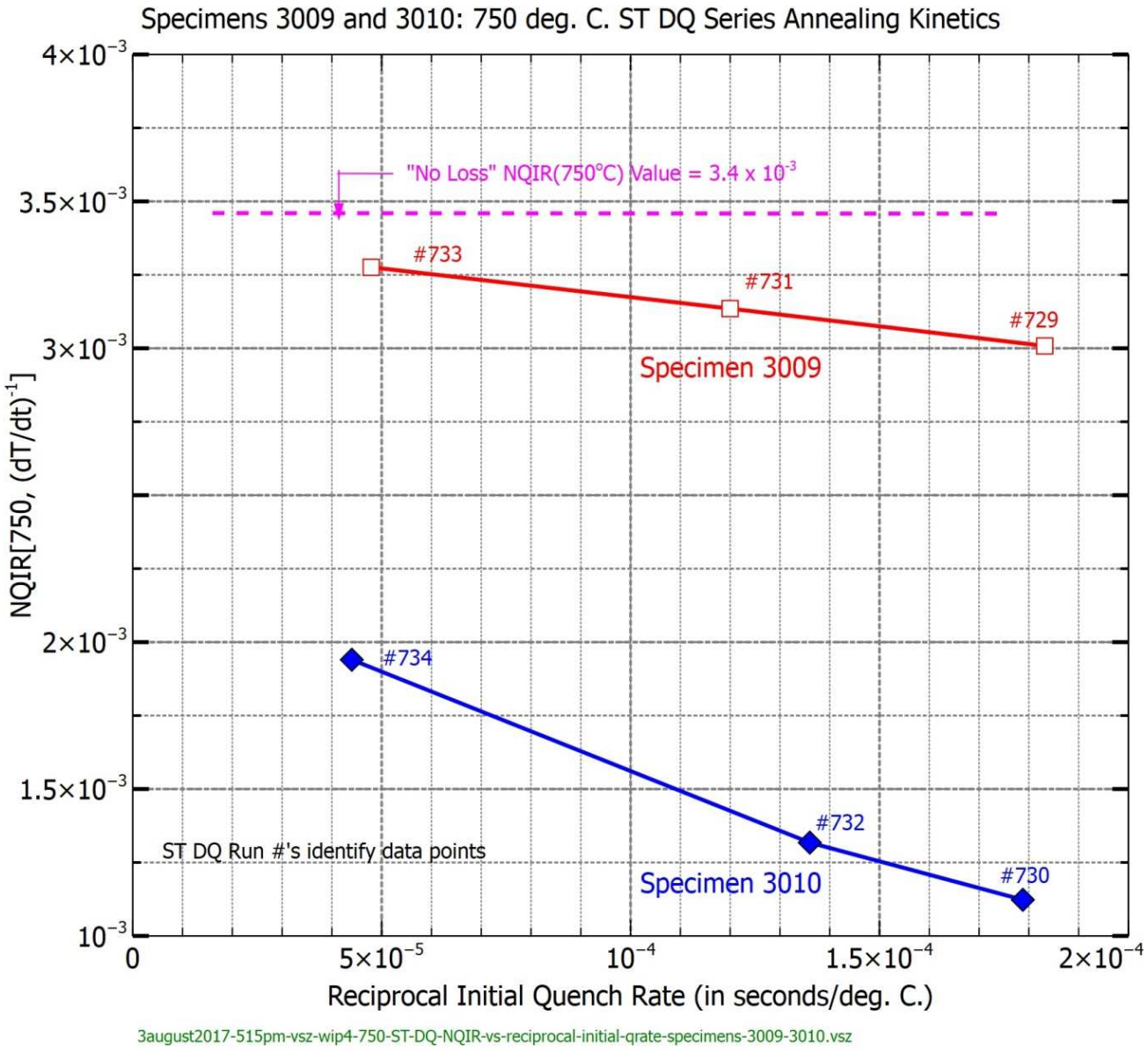

Figure 68. Specimens 3009 and 3010: Plots of NQIR [750°C, $(dT/dt)_{initial}^{-1}$] vs. Reciprocal Initial Quench Rate (RIQR)

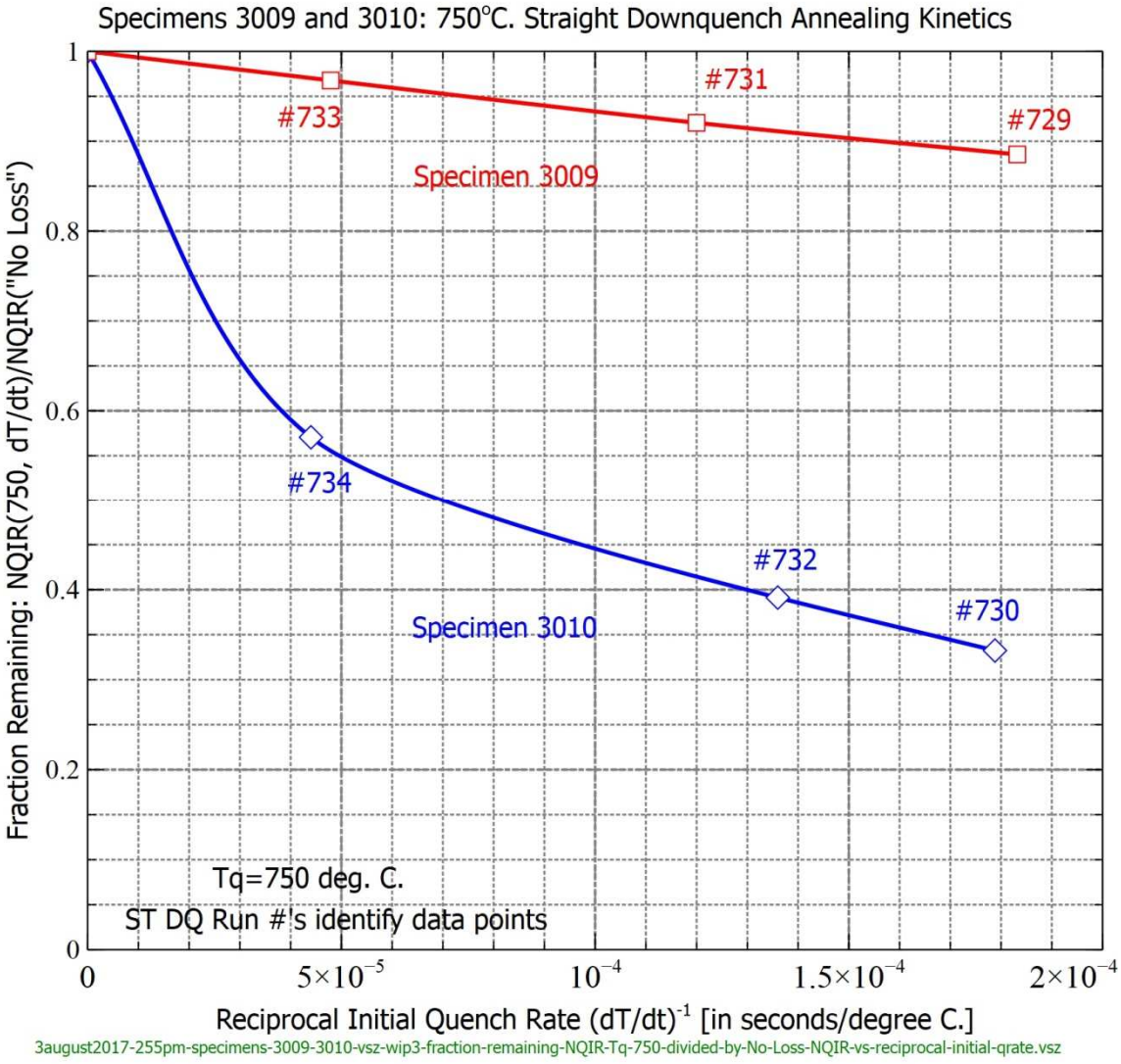

Figure 69. Specimens 3009 and 3010: Plots of Fraction Remaining NQIR[750°C, $(dT/dt)_{initial}^{-1}$]/["No Loss" NQIR(750°C)] vs. Reciprocal Initial Quench Rate (RIQR)

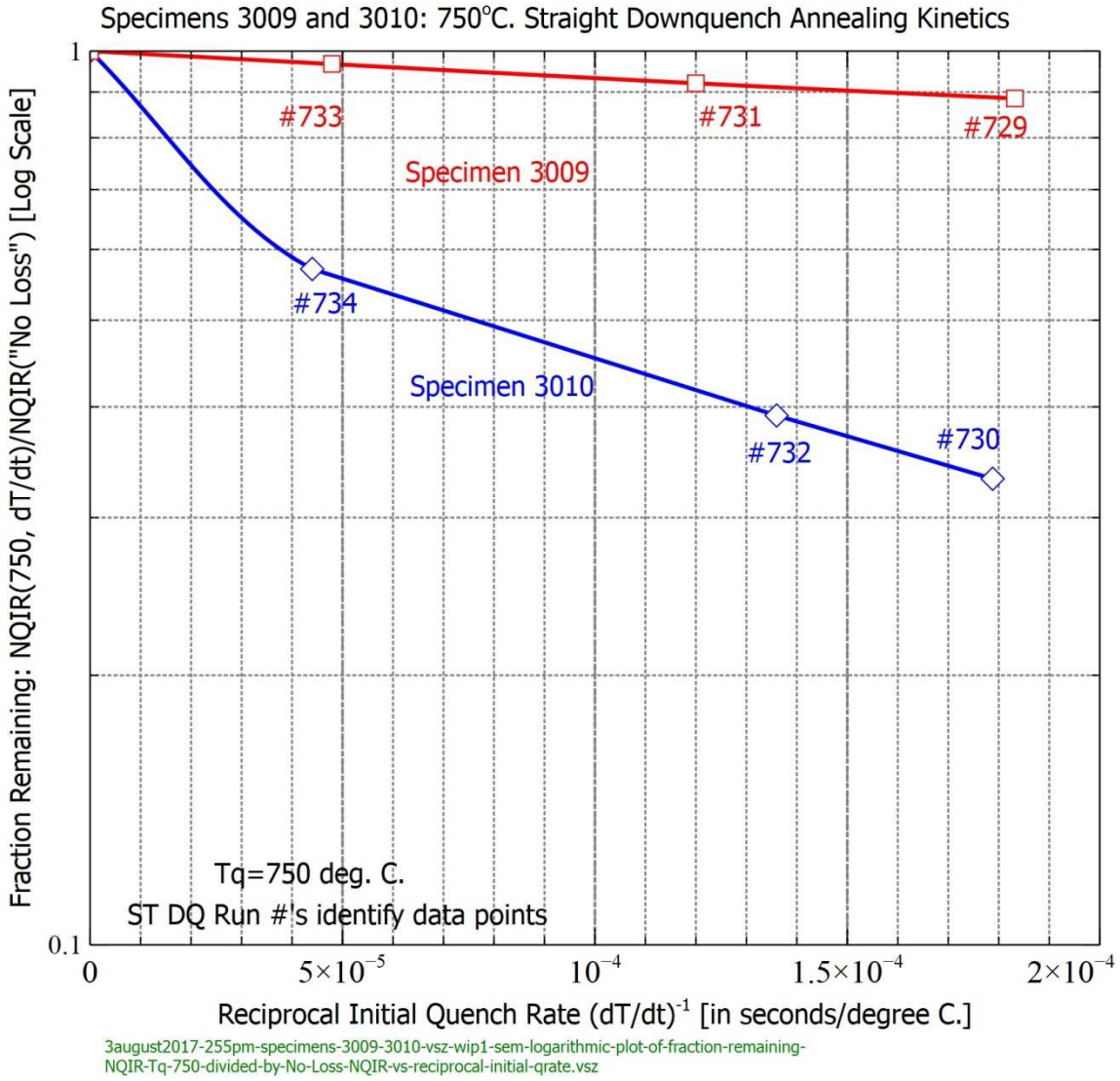

Figure 70. Specimens 3009 and 3010: Semi-Log Plots of Fraction Remaining NQIR[750°C, $(dT/dt)_{initial}^{-1}$]/["No Loss" NQIR(750°C)] vs. Reciprocal Initial Quench Rate (RIQR)

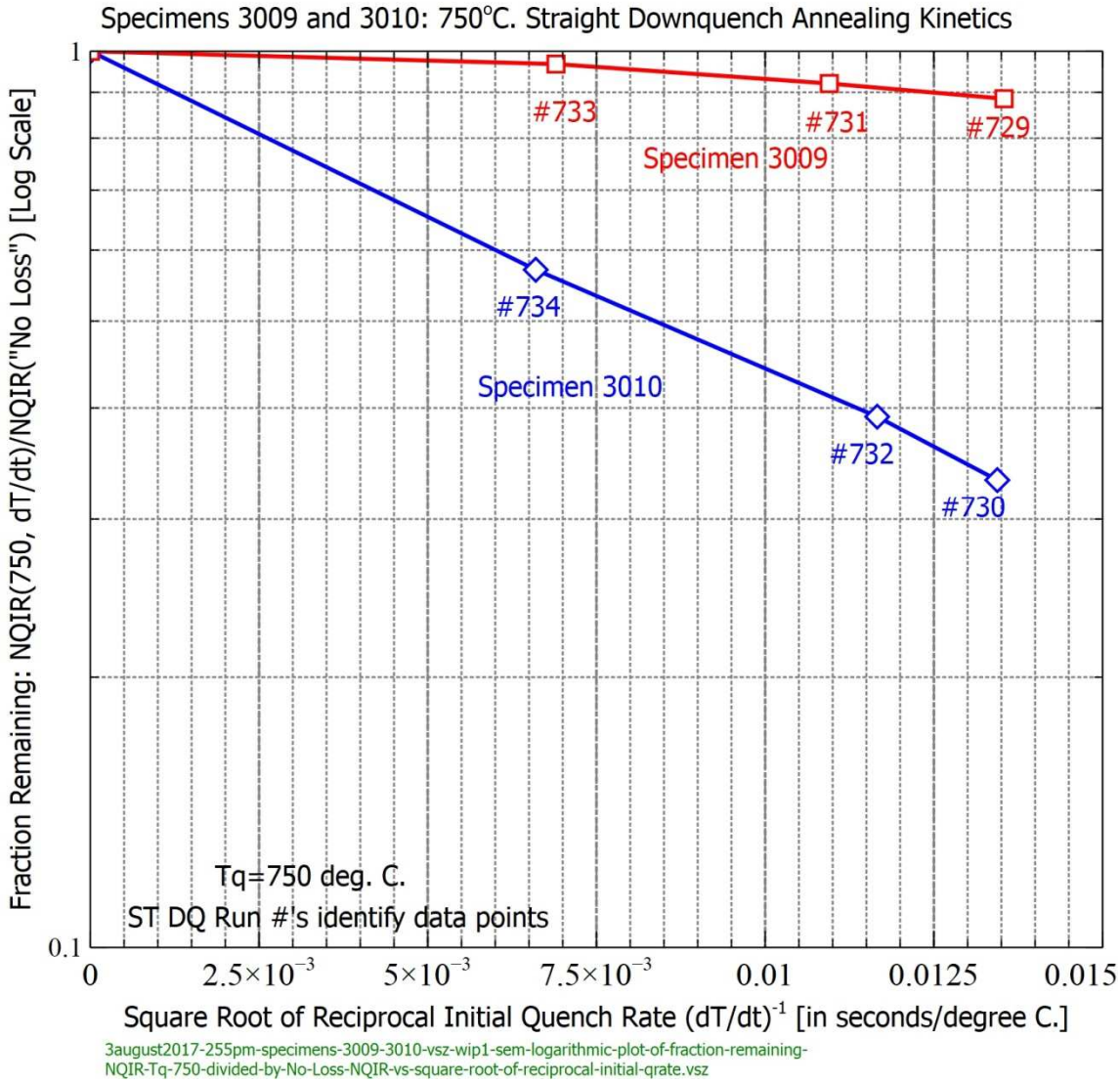

Figure 71. Specimens 3009 and 3010: Semi-Log Plots of Fraction Remaining NQIR[750°C, $(dT/dt)_{initial}^{-1}$]/["No Loss" NQIR(750°C)] vs. Square Root of Reciprocal Initial Quench Rate (RIQR)

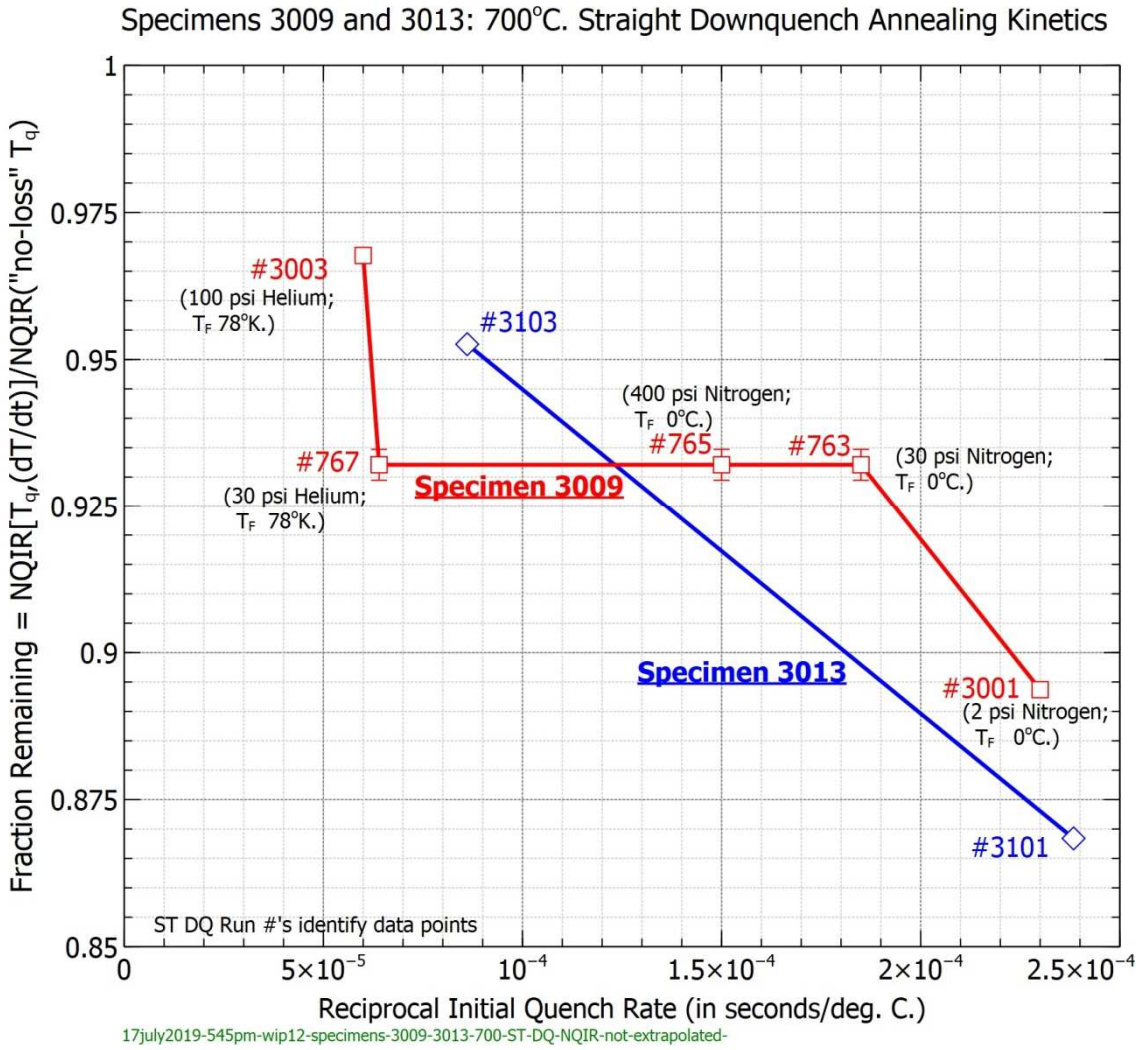

Figure 72. Specimens 3009 and 3013: Plots of Fraction Remaining NQIR[700°C, $(dT/dt)_{initial}^{-1}$]/["No Loss" NQIR(700°C)] vs. Reciprocal Initial Quench Rate (RIQR)

Figure 72 illustrates the occurrence of a demonstrable T* temperature plateau over a specific range in initial quench rates during an NQIR(700) ST DQ series treatment involving specimen 3009.

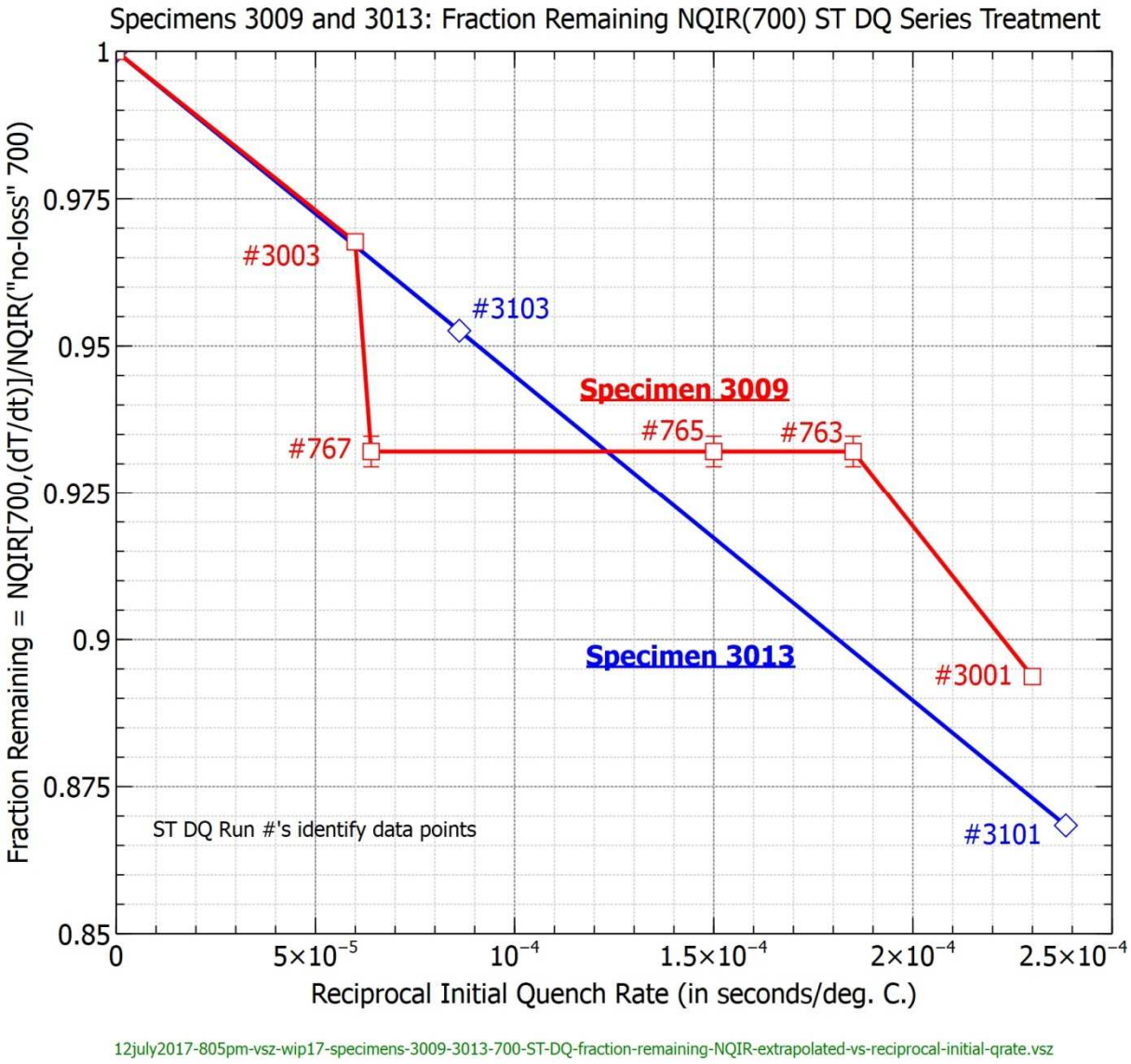

Figure 73. Specimens 3009 and 3013: Plots of extensions of NQIR [700°C, $(dT/dt)_{initial}^{-1}$] vs. Reciprocal Initial Quench Rate (RIQR)

Figure 73 includes straight line extensions of each of the two specimen's data to what would be an infinitely fast straight downquench "No Loss" NQIR(700°C) Fraction Remaining value.

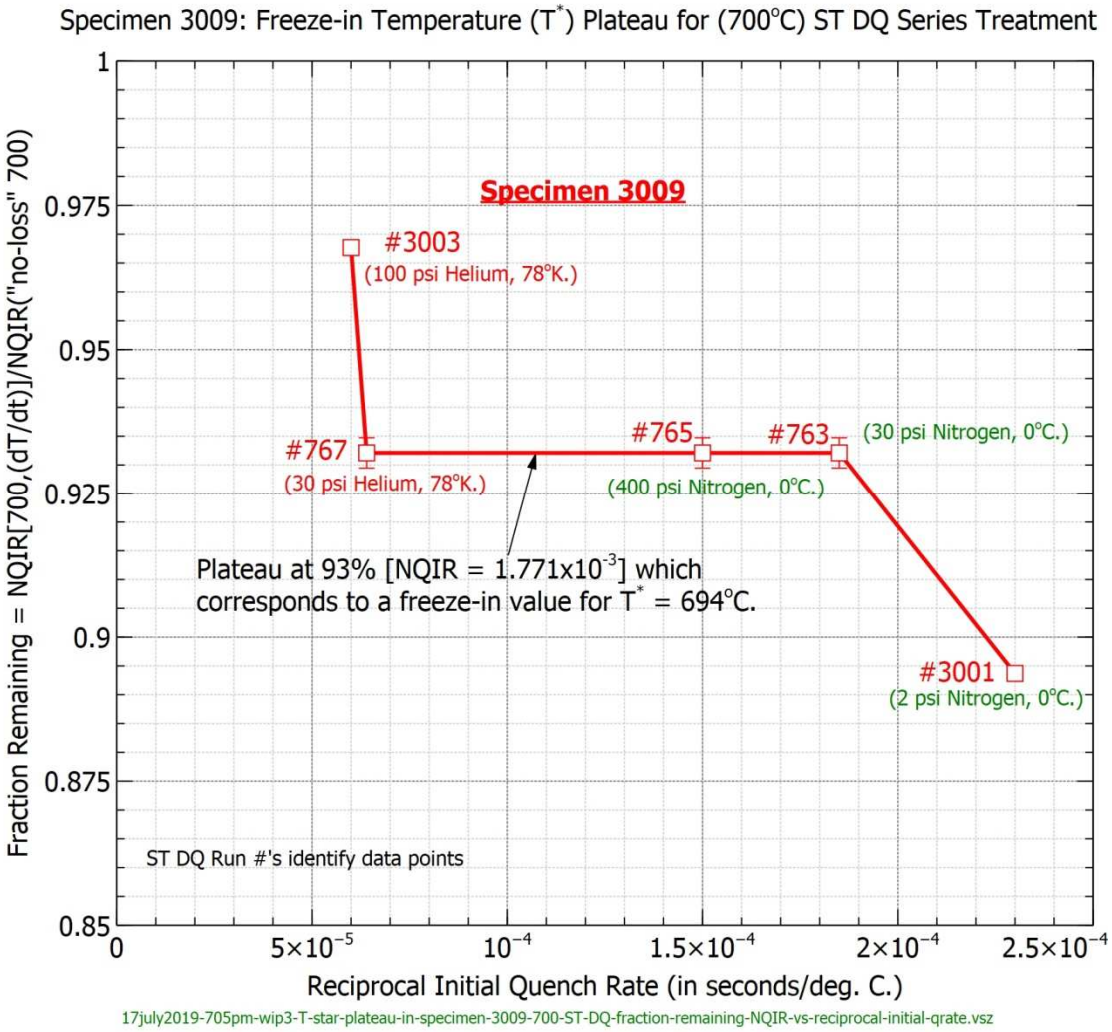

Figure 74. Specimen 3009: Plot of NQIR [700°C, $(dT/dt)_{initial}^{-1}$] vs. Reciprocal Initial Quench Rate (RIQR) with an indicated T* temperature of 694°C

7.5.2.2 Plots with Effective Time of Quench or its Square Root as the Independent Parameter

For comparison purposes, Figures 75 through 79 make use either of Effective Time of Quench ($\boldsymbol{\tau}_q$) or its square root value as the independent parameter.

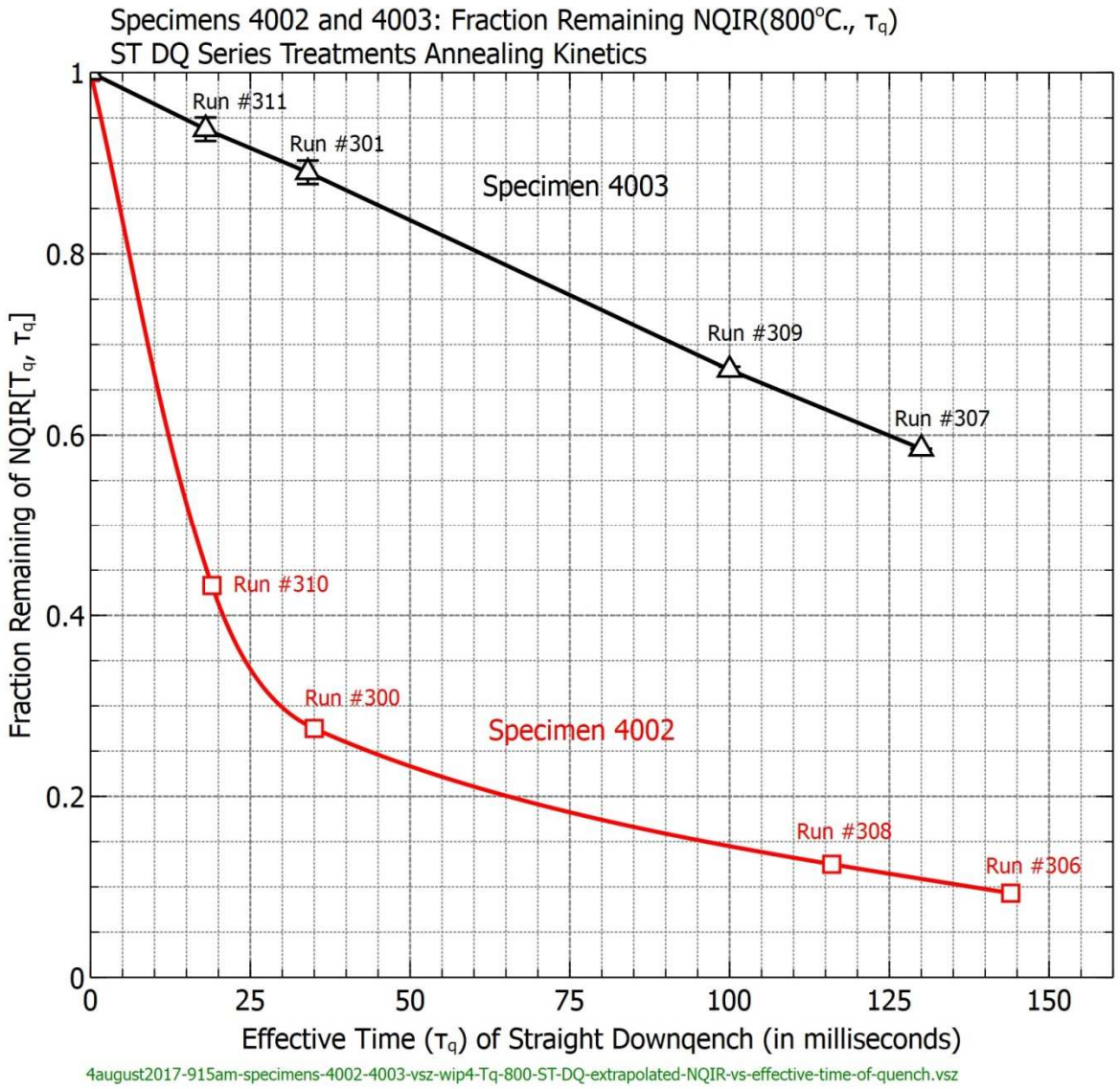

Figure 75. Specimens 4002 and 4003: Plots of Fraction Remaining of NQIR [800°C, $\boldsymbol{\tau}_q$] vs. Effective Time of Quench ($\boldsymbol{\tau}_q$)

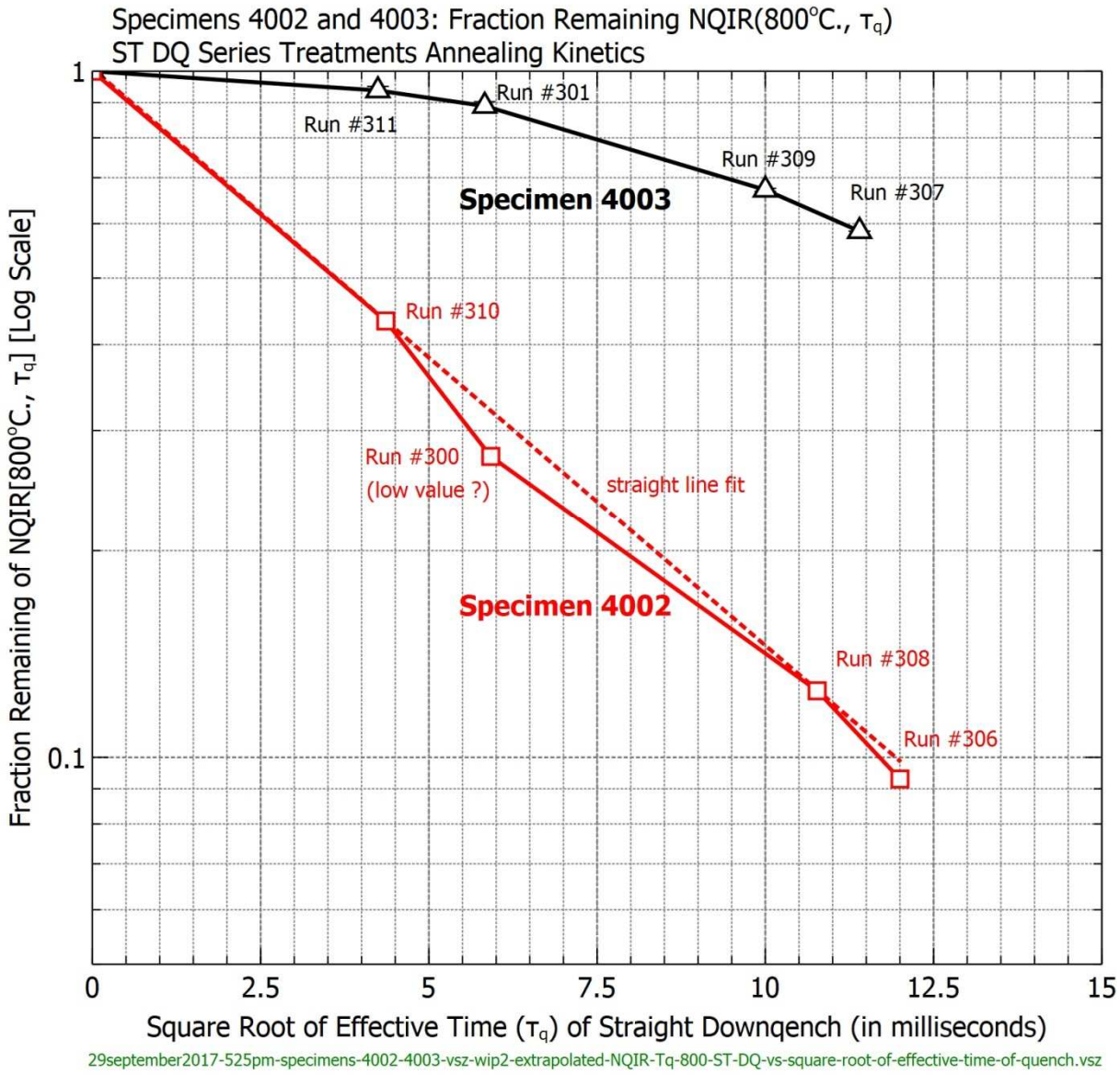

Figure 76. Specimens 4002 and 4003: Semi-Log Plots of Fraction Remaining of NQIR [800°C, $\boldsymbol{\tau}_q$] vs. Square Root of Effective Time of Quench ($\boldsymbol{\tau}_q$).

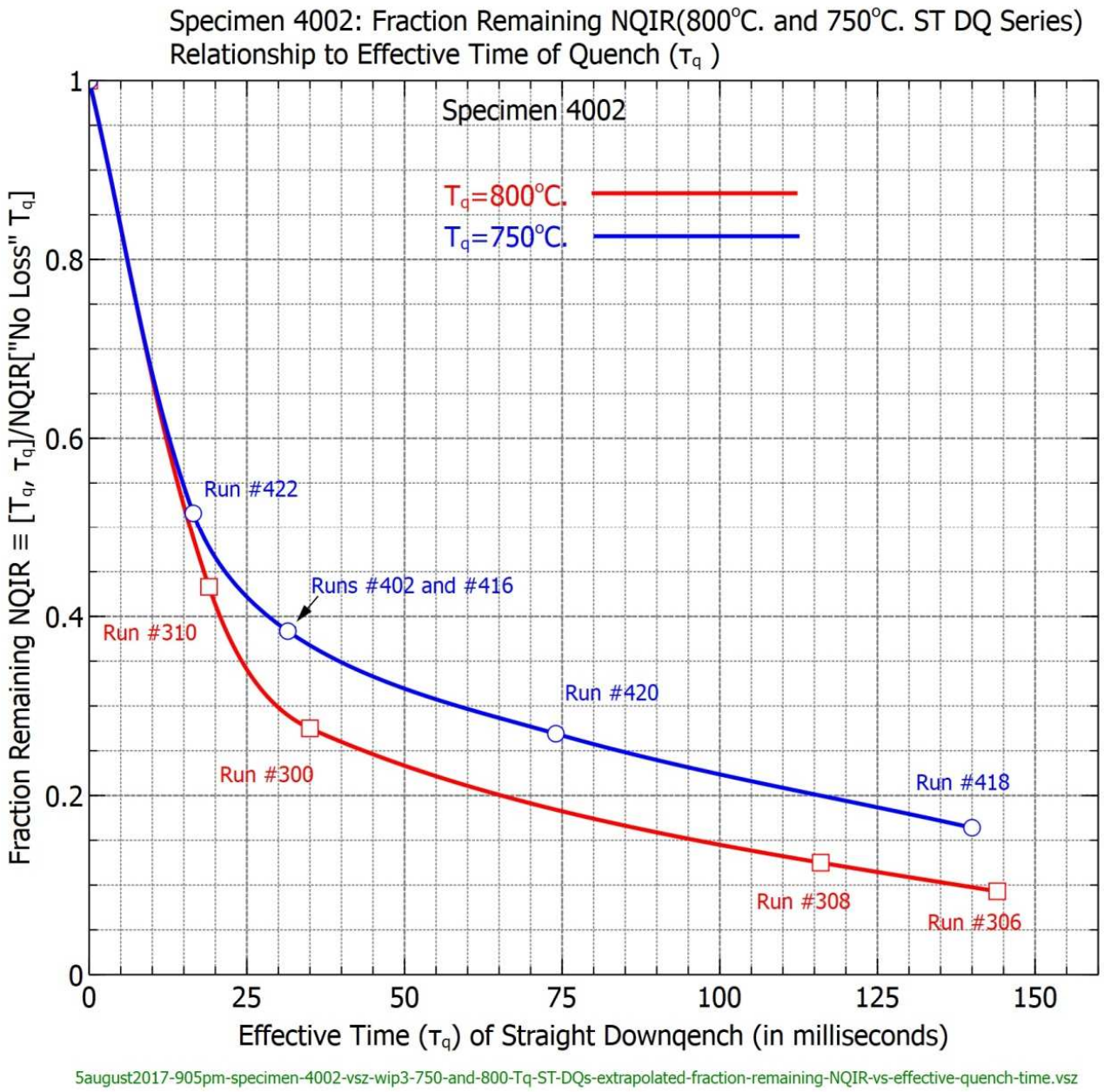

Figure 77. Specimen 4002: Plots for 800°C and 750°C ST DQ Series of Fraction Remaining NQIR vs. Effective Time of Quench ($\boldsymbol{\tau}_q$)

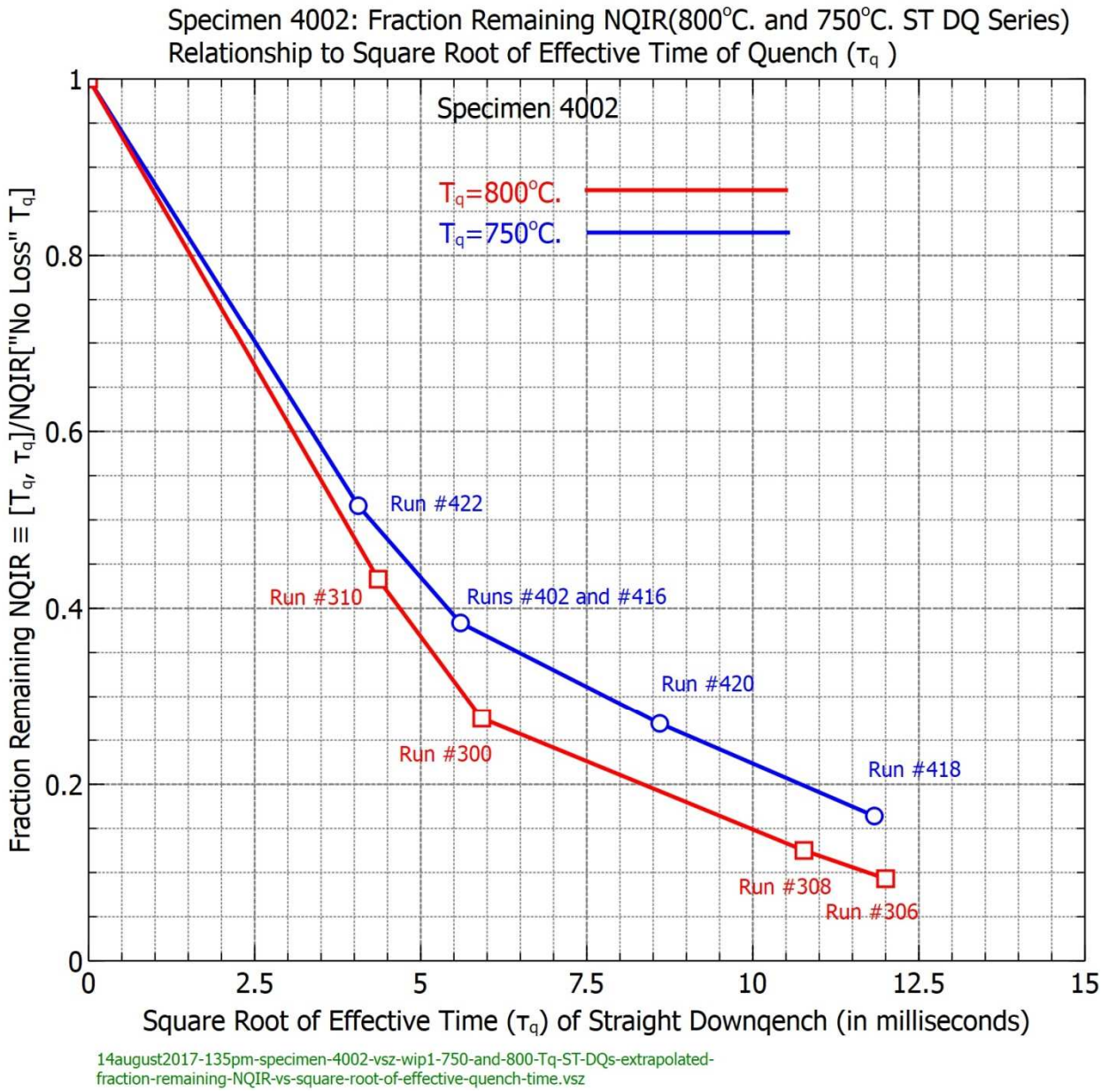

Figure 78. Specimen 4002: Plots for 800°C and 750°C ST DQ Series Treatments of Fraction Remaining NQIR vs. Square Root of Effective Time of Quench ($\boldsymbol{\tau}_q$).

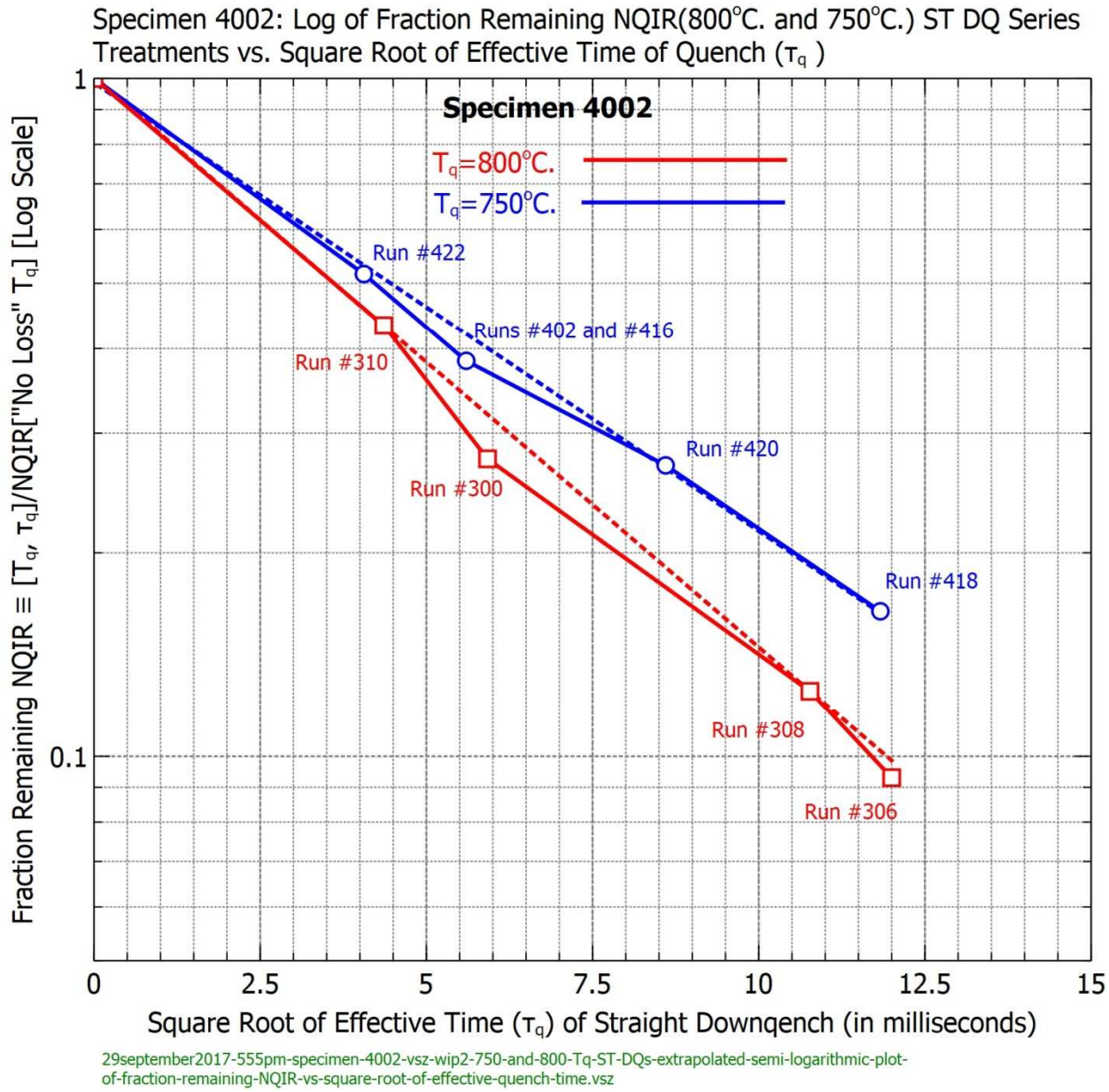

Figure 79. Specimen 4002: Semi-Log Plots for 800°C and 750°C ST DQ Series Treatments of Fraction Remaining NQIR vs. Square Root of Effective Time of Quench ($\boldsymbol{\tau}_q$)

7.5.3 ST DQ Loss Observations and Findings

Figures 52 through 79 reveal the nature of NQIR(925/875/825/800/750/700) ST DQ annealing kinetics vs. RIQR for the indicated ST DQ series thermal treatment runs involving quench temperatures ranging from 925^{o}C down to 700^{o}C.

7.5.3.1 Straight Downquenches from 925^{o}C

For specimens 3012 and 3013 Figures 52 through 54 reveal the nature of NQIR(925^{o}C) ST DQ annealing kinetics vs. RIQR, and Figures 55 and 56 reveal the nature of NQIR(925^{o}C) ST DQ annealing kinetics vs. the square root of RIQR.

7.5.3.2 Straight Downquenches from 875^{o}C

Figures 57 through 60 reveal the nature of NQIR(875^{o}C) ST DQ annealing kinetics vs. RIQR for specimens 3009, 3010, and 3012.

7.5.3.3 Straight Downquenches from 825^{o}C

Figures 61 and 62 reveal the nature of NQIR(825^{o}C) ST DQ annealing kinetics vs. RIQR for specimens 3009 and 3010, and Figures 63 and 64 reveal the nature of NQIR(825^{o}C) ST DQ annealing kinetics vs. the square root of RIQR.

7.5.3.4 Straight Downquenches from 800^{o}C

For specimens 3007 and 3008 Figure 65 reveals the nature of NQIR(800^{o}C) ST DQ annealing kinetics vs. RIQR, and Figures 66 and 67 reveal the nature of NQIR(800^{o}C) ST DQ annealing kinetics vs. the square root of RIQR.

For specimens 4002 and 4003 Figure 75 reveals the nature of Fraction Remaining NQIR(800^{o}C) ST DQ annealing kinetics vs. effective time of quench ($\boldsymbol{\tau}_{q}$),

and Figure 76 reveals the nature of NQIR(800^{o}C) ST DQ annealing kinetics vs. the square root of effective time of quench ($\boldsymbol{\tau}_{q}$).

7.5.3.5 Straight Downquenches from 800^{o}C and 750^{o}C

For specimen 4002 Figure 77 shows plots of fraction remaining NQIR(800^{o}C and 750^{o}C) ST DQ annealing kinetics vs. effective time of quench ($\boldsymbol{\tau}_{q}$), Figure 78 shows plots of fraction remaining NQIR(800^{o}C and 750^{o}C) ST DQ annealing kinetics vs. the square root of effective time of quench ($\boldsymbol{\tau}_{q}$), and Figure 79 shows for specimen 4002 Semi-Log plots of fraction remaining NQIR(800^{o}C and 750^{o}C) ST DQ annealing kinetics vs. the square root of effective time of quench ($\boldsymbol{\tau}_{q}$).

7.5.3.6 Straight Downquenches from 750^{o}C

For specimens 3009 and 3010 Figures 68 through 70 reveal the nature of NQIR(750^{o}C) ST DQ annealing kinetics vs. RIQR, and Figure 71 reveals the nature of NQIR(750^{o}C) ST DQ annealing kinetics vs. the square root of RIQR.

7.5.3.7 Straight Downquenches from 700^{o}C

For specimens 3009 and 3013 Figures 72 and 73 show plots of fraction remaining NQIR(700^{o}C) ST DQ annealing kinetics vs. RIQR, and Figure 74 shows for specimen 3009's NQIR(700^{o}C) ST DQ annealing kinetics vs. RIQR an estimate of T* value of 694^{o}C for the associated plateau in the plotted data during the indicated span of runs #763, #765, and #767.

7.5.4 Discussion of ST DQ Losses

Most specimens' straight downquench losses appear to be of diffusion-limited type for the higher quench temperatures series, as Figure 56 for specimens 3009 and 3012, Figure 60 for specimens 3009, 3010, and 3012, Figure 64 for specimens 3009 and 3010, and Figure 76 for specimen 4002 suggest, whereas Figure 75 for specimen 4003 appears to closely adhere to a linear proportionality between the fraction remaining straight downquench data and effective time of quench.

Moreover, for specimens having T* values significantly below the associated ST DQ series quench temperature, Figures 53, 58, 62, 63, and 68 clearly indicate that straight line extensions of the ST DQ annealing kinetics data plotted as a function of $(dT/dt_{initial})^{-1}$ fall considerably below the associated Master B.E.T. "no-loss" graphical values for normalized quenched- in resistance (NQIR) values.

Three additional observations were noted to apply for certain of these Figures:

1) It appears that for specimens having higher NQIR(T_Q, dT/dt) values (associated with lower sink density) straight line extensions made of the corresponding specimen's data plotted as a function of $(dT/dt_{initial})^{-1}$ would yield overestimates of "no loss" NQIR(T_Q) values; and

2) For specimens having lower NQIR(T_Q, dT/dt) values (associated with higher sink densities) straight line extensions made of the corresponding specimen's data plotted as a function of $(dT/dt_{initial})^{-1}$ would yield underestimates for "No Loss" NQIR(T_Q).

3) Figure 59 illustrates the use of curved line extensions -- beyond the finite reciprocal quench rates obtained experimentally for three specimens (3009, 3010,

and 3012) having differing loss values when slower initial quench rates are involved -- that do converge at the "no loss" NQIR(875^{o}C) value.

7.5.5 ST DQ Annealing Kinetics

7.5.5.1 Overall Observations

Plots of data obtained for straight downquenches performed during this research revealed to some degree the nature of the kinetics that occurred during these treatments.

1. ST DQ losses occurring during the onset of quenches made from 925^{o}C (see Figures 52 through 56) even when lower sink density specimens (#3009 and #3012 pre-direct-deformation) were involved do appear to follow fractional power of reciprocal initial quench rate dependencies during the ST DQ initiation. This behavior is also observed for lower temperature quenches involving specimens that exhibited substantial losses from those quench temperatures. This observation suggests diffusion-limited annealing processes dominate the early stages of annealing to sinks. A subsequent linear annealing rate suggests a chemical rate equation behavior taking place thereafter that ends with a leveling off at an NQIR value associated with a T* somewhat above 750^{o}C.

2. When either lower quench temperatures and/or specimens having especially low pre-existing sink densities are subjected to elevated ST DQ treatments, they tend to exhibit annealing losses that are directly proportional to the effective time of quench. This finding suggests that chemical rate-type equations may likely be appropriate to describe the associated annealing kinetics.

7.5.5.2 Categories of Plots employed for ST DQ Annealing Kinetics Analyses

From the graphed quenched-in resistance data versus reciprocal initial quench rate presented in the above sub-sections, it is to be noted that higher sink density specimens exhibit the following behavior: As quench temperatures increase, the initial rate of decay begins to approach infinity, indicative of an annealing process that is proportional to some fractional power in time.

For the specific case of a straight downquench, the independent parameter is the reciprocal initial quench rate, and this quantity can reasonably be considered to be directly proportional to the time of quench.

Based on this relationship, if the annealing kinetics were found to be proportional to the square root of the quenching time, then the time rate of change of annealing would be proportional to $t^{1/2}$. Figure 79 illustrates for specimen 4002 semi-log plots of fraction remaining NQIR for straight downquenches from 800^{o}C and 750^{o}C vs. square root of the effective time of quench ($\boldsymbol{\tau}_{q}$).

Notably, both the 800^{o}C and 750^{o}C annealing kinetics associated with specimen 4002 do appear to closely follow a $t^{1/2}$ diffusion-limited behavior.

In contrast to what is observed for specimen 4002, Figures 75 and 76 illustrate for specimen 4003 plots of fraction remaining NQIR for straight downquenches from 800^{o}C that are directly proportional to the square root of $\boldsymbol{\tau}_{q}$.

Because the initial rate of decay of quenched-in resistance as a function of reciprocal initial quench rate exhibited a finite, nearly constant slope for lower sink

density specimens, a chemical rate equation involving time to an integer power should constitute a reasonable approximation for the annealing process.

It should be noted that graphing straight downquench data for a number of specimens for common quench temperatures permitted assessments of the generality of the annealing kinetics and examination of losses in terms of different pre-existing sink densities. In fact, use of the independent parameter effective time of quench ($\boldsymbol{\tau}_q$) tends to draw increased focus on the behavior of the fractional losses associated with relative specimen sink densities without requiring actual specimen sink densities to be known or determined.

Figure 75 suggests that losses appear to be approximately proportional to time of quench only for low sink density specimens or for much lower quench temperatures. Thus, as a generalization, chemical rate descriptions appear to be applicable only for lower quench temperature and/or low sink density specimens. For higher quench temperatures or for moderate to large sink density material, diffusion-limited models appear to be required.

For quenches made from 700^{o}C or lower, losses are closely approximated by a modified first-order chemical rate expression that incorporates a sink density function in it to account for the observed general dependence of quenched-in resistance upon pre-existing specimen sink densities. Losses are observed to be proportional to the reciprocal initial quench rate, reflecting a direct proportionality to the quench time required to reach T* temperatures. For low sink density specimens negligible losses are obtained even for quenches from as high as 600^{o}C. When quench temperatures

are lowered and approach 400^{o}C, losses tend to become negligible even for specimens having the largest sink densities.

Figures 70, 71, and 75 provide examples that imply -- at least for specimens such as specimen 4003 and 3009 which have reduced losses (implying lower pre-existing sink densities) or for quenches performed from much lower quench temperatures -- losses may be approximated by a linear quench time expression [97]. This behavior was proposed by Flynn, Bass, and Lazarus [28, 29] wherein losses were expressed as being directly proportional to the term DTτ.

However, from present data the expression DTτ has limited applicability since it does not account for the influence of increased magnitudes of pre-existing sink density upon losses (such as are associated with specimens 3010 and 4002) for the higher straight downquench treatments just cited for specimens 3009 and 4003, nor does it exhibit an obvious upward curvature for short quench times, higher quench temperatures, or for high sink density specimens that demands a relationship involving time raised to a fractional power less than unity to be dominant.

Moreover, further examination of Figures 53, 58, and 60 (for specimens 3009 and 3012), Figure 62 (especially for specimen 3010), and Figure 63 (for both specimen 3009 and 3010) clearly reveal the fact that straight line extrapolations of actual data plotted versus reciprocal initial quench rate (in seconds/deg. C.) do not converge to common (sink density independent) no-loss normalized quenched-in

---

[97] Note, however, that even for just these two sets of plots, the "extrapolated to zero time of quench" values fall below the established "No Loss" NQIR(T_Q) values obtained through use of a graphical B.E.T. approach.

resistance values for any of these elevated (≥ 700^{o}C) temperature ST DQ series thermal treatments.

Additionally, for the higher loss specimens, semi-log plots vs. square root of reciprocal initial quench rate (RIQR) do appear to provide more acceptable extrapolations that more closely converge on the respective “No Loss” NQIR(T_Q) levels established during the B.E.T. portion of this research presented in Section 7.4 of this document.

Looking back, the graphically-based extrapolations of semi-log plots of normalized quenched-in resistance values versus reciprocal initial quench rate (as were shown in Figure 40) collectively illustrate achievement of convergence values for the “No Loss” NQIR(T_Q) levels for each of four quench temperature series, namely 700^{o}C, 750^{o}C, 800^{o}C, and 925^{o}C.

So, for most of these cited plots it becomes obvious that a linear extension of the curves to what would be an infinitely fast quench condition will result in NQIR [T_Q, $(dT/dt)_{initial}^{-1} = 0$) values that would be somewhat or even significantly below the associated "No Loss" NQIR(T_Q) values established and represented by the Master B.E.T. plots (see Figures 49 through 51).

Observations of a nearly semi-log relationship for moderate-to-high-loss specimens (having $T^* \ll T_Q$), straight downquench annealing kinetics for quenches from $T_Q \geq 700^{o}$C are indicative of a diffusion-limited relationship wherein measureable losses [98] do appear to be proportional to the square root of the

---

[98] The term "measureable" as used here refers to ST DQs having finite initial quench rates and are not based on extrapolations or extensions to a reciprocal initial quench rate of zero.

effective time of quench τ_q. Figure 79 serves as a good example of such a relationship revealed for straight downquenches from 800^{o}C and from 750^{o}C that were conducted on specimen 4002.

In addition, in nearly all cases, extensions of linear dependence of fraction retained versus reciprocal square root of initial quench rate did not converge on a common value for the "no-loss" magnitudes of quenched-in concentrations corresponding to the NQIR(T_Q) that were obtained using the adopted graphical Back Extrapolation Technique (B.E.T.) method.

In general, straight downquench losses exhibit a $(\tau_q)^{1/2}$ [99] dependence for moderate-to-high loss conditions (i.e., $T^* << T_Q$) and a linear dependence upon τ_q for low-loss conditions (i.e., as $T^* \rightarrow \approx T_Q$).

7.5.5.3 Single, Dual, and Multiple Slopes in specific Plots

Possible additional insights into the underlying types of point defects associated with straight downquench annealing kinetics may be garnered by examining the behaviors exhibited by the slopes revealed in two specific sets of plots, namely Figures 56, 60, 64, 67, 71 and Figures 76 and 79. The first grouping of semi-log plots employs the square root of RIQR as the independent parameter, whereas the second set employs the square root of effective time of quench τ_q as the independent parameter. Here are the basic observations regarding these specific Figures:

---

[99] The time-of-quench parameter τ_q is defined here as the time it took to reach 500^{o}C from that particular ST DQ series quench temperature T_Q.

1) In Figure 56 which displays the semi-log plots of 925^{o}C ST DQ series annealing kinetics as a function of the square root of RIQR, two regions of nearly identical slopes are clearly evident. The increased slopes associated with the slower quench rates may be an indication that divacancies have had sufficient time to form in increased numbers, thereby resulting in such steeper slopes that are associated with slower initial quench rates.
2) In a similar manner, Figure 60 displays three semi-log plots of 875^{o}C ST DQ series annealing kinetics for specimens 3009, 3010, and 3012 as a function of the square root of RIQR and exhibits multiple slopes for each specimen that become steeper for slower initial quench rates.
3) As a third example, Figure 64 displays two semi-log plots of 825^{o}C ST DQ series annealing kinetics for specimens 3009 and 3010 as a function of the square root of RIQR and exhibits multiple slopes for each specimen that become steeper for slower initial quench rates.
4) Figure 71 displays two semi-log plots of 750^{o}C ST DQ series annealing kinetics for specimens 3009 and 3010 as a function of the square root of RIQR and appears to exhibit a single slope for each specimen even for slower initial quench rates.
5) Figure 76 displays two semi-log plots of 800^{o}C ST DQ series annealing kinetics for specimens 4002 and 4003 as a function of the square root of effective time of quench $\boldsymbol{\tau}_q$ in which specimen 4003 exhibits multiple slopes for each specimen that slowly become steeper for slower initial quench rates whereas specimen 4002 appears to exhibit an essentially constant single

slope over the entire set of values for the square root of effective time of quench.

6) Figure 79 displays two semi-log plots (one for a 800^{o}C ST DQ series and a second for a 700^{o}C ST DQ series) for specimen 4002 of the respective annealing kinetics graphed as a function of the square root of effective time of quench τ_q in which nearly constant slopes are obtained over the entire set of values for the square root of effective time of quench.
7) As an overall trend, observed slope variations appear to be more evident for higher quench temperature treatments and tend to be less severe or even become nearly constant for lower quench temperature series treatments and/or for specimens that likely have lower sink densities.

7.5.5.4 Summary of ST DQ Annealing Kinetics

The associated shapes of the straight downquench experimental data of quenched-in resistance versus reciprocal initial quench rate (RIQR) indicated that diffusion-limited annealing occurs for higher quench temperature series that involve higher sink density specimens whereas a modified first-order chemical rate expression appears to approximate the majority of the annealing kinetics for lower quench temperature series performed using lower sink density specimens.

7.6 PARAMETER DETERMINATIONS MADE FROM ST DQ SERIES DATA ANALYSES

Among the parameter determinations made from analyses of the ST DQ series thermal treatments were the following:

1. "No Loss" Master B.E.T. plots for $NQIR_V(T)$, $C_V(T)$, and $\rho_V(T)$

a. Composite [100] B.E.T. equation from 400°C thru 925°C;

b. B.E.T. Equation (for Nitrogen only) from 400°C thru 550°C;

c. B.E.T. Equation (for Helium and Nitrogen) over 700°C thru 925°C range;

2. Heat of Solution of Helium in Gold (over 400 thru 550°C range)

3. Straight downquench annealing kinetics were generally observed to be: 1) proportional to the square root of effective time of quench for ST DQs from 700°C or higher for higher sink density specimens or 2) directly proportional to the effective time of quench for ST DQs from 700°C for lower sink density specimens.

7.7 COMPARISONS WITH OTHER REPORTED ST DQ RESEARCH

Tables 1 and 2 provide a summary of the results obtained by other researchers. Their results can be compared with the results of this research which were obtained using the graphically-based B.E.T. technique discussed in sub-section 7.4.5 which reveals that the no-loss values of ΔR_{QN} (T_Q) for all ST DQ treatments are in close agreement over the temperature range from 400°C through 925°C for all specimens, regardless of pre-existing sink densities or purity ratios associated with the specimens.

Additionally, the overall agreement of the MASTER B.E.T. plot when compared with data obtained by other researchers endorses the reliability of the selected quench/measurement systems design and associated measurements of resistance and temperature.

---

[100] Figures 46, 48, and 49 illustrate what are referred to herein as "composite" plots.

The least-squares-fit Master B.E.T. plot's slope of 0.97±0.01 eV agrees favorably with the generally accepted value of 0.98 eV often cited as the mono-vacancy formation energy in gold [29, 43].

Furthermore, a melting point concentration of vacancies of 7.2×10^{-4} was calculated by extrapolating the least-squares-fit Master B.E.T. plot expressed by Eqn. (7-1) above established from the data obtained for quenches from 700^{o}C through 925^{o}C. That value correlates well with a ΔR_{QN} of 4.56×10^{-2} obtained by extrapolating the least-squares-fit Master B.E.T. plot given by Eqn. (7-1).

Notable is the fact that previously reported lattice parameter change and length change measurements on gold performed by Simmons and Balluffi [58] involving temperatures near the melting point predicted an essentially identical value for Cv (T_{melt} = 1063^{o}C) equal to 7.2×10^{-4}.

7.8 SUMMARY OF FINDINGS FROM ST DQ EXPERIMENTS

Numerous series of straight downquench experiments were performed with a primary objective of establishing a Master Curve of no-loss equilibrium vacancy concentration over a wide range in quench temperatures. Such no-loss values would thereafter serve as the basis from which annealing losses during isothermal anneal treatments could be calculated. The nature of the straight downquench annealing kinetics was also examined. Finally, the observation of an anomalous slope in low quench temperature quenched-in resistance data was investigated and is hypothesized to be attributable to helium solubility in pure gold.

7.8.1 No-Loss Absolute Vacancy Concentration

The no-loss absolute vacancy concentration over the temperature range 400^{o}C to 925^{o}C is found to be well represented by the equation:

$$C_v(T_Q) = 3.583 \exp[-(0.97 +/- 0.01)/kT_Q]$$

where the vacancy formation energy value is based upon a least-squares fit to the composite sets of no-loss ΔR_{QN} magnitudes.

7.8.2 Heat of Solution of Helium in Gold

Based upon the observation that the ΔR_{QN} values obtained could clearly be noted as being independent of quench rate followed by a graphical analyses of data presented in Figures 46 and 48, a value of 0.357 +/- 0.003 eV is proposed to represent the heat of solution of helium in pure gold over the temperature range from 400^{o}C to 550^{o}C.

8 QUENCH-AND-ISOTHERMAL ANNEAL (Q&A) EXPERIMENTS

8.1 INTRODUCTION

This chapter details the attained prerequisites, work flow, objectives, extensions beyond prior research results, specific lattice defect properties sought, obtained results, observations, analyses, parameter determinations, and associated discussions of quench-and-isothermal anneal treatments performed during this research investigation.

For any particular Figure presented within this chapter the specific scales, independent parameters, and dependent parameters used were chosen so as to most adequately exemplify and reveal the specific parameter(s) of interest.

8.2 Q&A SERIES TREATMENTS

8.2.1 Summary of Attained Prerequisites

Analyses of data obtained from the straight downquench (ST DQ) series treatments led to quantitative assessments for the vacancy formation energy E^F_V and vacancy formation entropy S^F_V that were made upon establishment of a Master B.E.T. plots of no-loss normalized quenched-in resistance NQIR(T), resistivity $\Delta\boldsymbol{\rho}_V(T)$, and vacancy concentration $C_V(T)$ values over a wide range in elevated temperatures. Insights regarding the associated non-isothermal annealing kinetics and related parameters were also discussed.

Concurrently with the ST DQ-related activities and analyses, extensive sets of quench-and-isothermal annealing (Q&A) series thermal treatments were performed on numerous specimens, and these data will be presented throughout this chapter.

8.2.2 Work Flow for Q&A Series Treatments

Figure 7 provides a flowchart of the adopted sequence of actions followed for gathering data associated with quench-and-isothermal anneal (Q&A) series treatments. All data acquisition-related procedures remained essentially unchanged, except for those details associated with establishing annealing temperatures, the settings for the duration of the initial downquench from elevated temperature T_Q to T_A so that the transition associated with reaching the desired isothermal anneal temperature T_A would occur with minimal over- or under-shoot in temperature, and the desired duration time t_A for any particular Q&A series treatment [**101**].

8.2.3 Objectives of Q&A Series Treatments

The primary reason for conducting these Q&A experimental investigations was to accumulate extensive sets of normalized quenched-in resistance data for wide ranges in quench-and-isothermal-anneal temperatures, annealing times, and specimens having significantly different magnitudes of pre-existing sink densities.

Such accumulated sets of data were sought in order to encompass the spectrum from initial high vacancy supersaturations down to whatever levels remain present after completing extended anneal conditions.

8.2.4 Extensions beyond prior Research Investigations

Although research on elevated temperature annealing kinetics of vacancy defects in pure gold as performed by Wang, Seidman, and Balluffi (WSB) [63] did

---

101 Triggering of these Regions (see Figure 31) was performed automatically using the all-solid-state controller in conjunction with electronic pulses supplied by the Infotec Data Acquisition System [63]. NOTE: Whenever isothermal annealing times longer than about 30 minutes were desired, manual triggering of Region IV was employed.

involve annealing temperatures near 670^{o}C and quench temperatures of 700^{o}C, several extensions seemed highly desirable, including the following:

1). Ranges in both quench and annealing temperatures should be extended.

2). Monitoring of annealing kinetics data toward values well below the 1/e levels should be examined.

3). Effects of direct deformation upon annealing kinetics, annealing rates, and losses should be assessed with data for pre-deformation experiments serving as both a reference and for comparison purposes.

4). Inclusion of Transmission Electron Microscopy (TEM) examinations of high-purity gold ribbon foils after subjection to specific elevated temperature treatments to seek further insight as to what possible correlations might be found relative to the potentiometric resistance results involving comparable thermal treatments.

Thus, to some degree a major portion of this research investigation served as a continuation and extension of the work reported by WSB [63]. Specifically, significant extensions were made regarding data acquisition that involved extending the ranges in elevated temperatures and annealing times, conducting additional thermal treatments (referred to as HTA and TC), adoption of two distinct specimen shapes and creation of unique QMSD unit designs, and various measurements-related improvements (including design of an all-solid-state temperature controller) [**102**].

---

102 Refer to Table 3 for an enumerated list of Major Objectives Achieved through Feasibility Studies.

8.2.5 Specific Lattice Defect Properties Sought via Q&A Treatments

The need has existed for obtaining sufficiently extensive annealing kinetics data to be able to provide further insights that might contribute to answering questions such as those listed below:

1. What might explain why reported magnitudes for the effective vacancy migration energy diminish with increasing vacancy concentration [42, 67, 101]?

2. What might explain the nature and magnitudes for the metastable residual resistance (MRR) levels that are reported (e.g., see Figure 5 in [Ref. 39]) to occur, and do these detected levels tend to have magnitudes that increase for Q&A treatments involving quench temperatures above 500°C?

3. How might elevated temperature isothermal annealing half-times be checked for whether or not they are independent of excess vacancy concentration?

4. How might it be shown whether or not a falloff in absolute macroscopic sink efficiency occurs for Q&A's as isothermal annealing temperatures approach the associated quench temperatures?

5. How might it be determined a) whether or not effective vacancy migration energy values that are generally reported to be around 0.7 eV can be attributed to tightly bound clusters, divacancies, or trivacancies and b) if so, over what range in Q&A series treatment temperatures would such values be noted to occur?

8.3 SEGMENTED ANALYSES OF Q&A ANNEALING KINETICS

This section is comprised of sub-sections 8.3.1 through 8.3.13 which span such topics as the four major categories of analyses, overall sets of plots of NQIR(T_Q, T_A, t_A) Q&A series treatments, plots of fraction remaining NQIR(T_Q, T_A, t_A), isothermal

annealing half-time and effective vacancy migration energy determinations, and much more. As already cited in Chapter 3, Figure 8 provides a high-level flowchart of data analyses performed on data obtained from numerous Q&A series treatments performed on 5-mil diameter 6N-pure gold wire specimens, supplemented by TEM-based examinations subsequently performed on 0.5-mil thick 6N-pure gold foils.

8.3.1 Four Major Categories of Analyses

As Figure 8 indicates, analyses of isothermal annealing kinetics are segmented into four major categories: Initial Decay, Half-time, Extended Times, and Overall.

In some cases a few specific observations are interspersed among the included Figures which follow. However, in most cases detailed discussions of the results, observations, analyses, findings, and conclusions regarding any specific plots of Q&A series treatments are elaborated upon within appropriate sub-sections of this chapter.

8.3.1.1 Multiplicity of Specific Types of Plots and Relevant Parameters

Analyses of various types of plots involving numerous sets of isothermal annealing kinetics data required 1) choosing of appropriate scaling (linear, semi-log, -log-log, and [log ln[$(\mathbf{f_r})^{-1}$ vs. log (t_A)]) and 2) selections of specific parameters, such as quench temperature, isothermal annealing temperature, annealing half-times, reduced annealing time variable $t_A/t_{1/2}$, excess fraction remaining NQIR(T_Q, T_A, t_A)/NQIR(T_Q, t_A=0), effective vacancy migration energy (E^M_V(eff)), initial annealing rate (IAR), mean relaxation time (t_{mean}), instantaneous vacancy activation energy (E^M_V(act)), time exponent **m**, MRR levels, excess vacancy supersaturation ratio (VSR), excess vacancy defect chemical potential (μ_v), and absolute macroscopic sink efficiency (€), among others.

8.3.1.2 Inclusion of Run Numbers and Environmental Settings

Looking ahead for a moment, it is important to note that Figure 80 (presented and discussed in sub-section 8.3.2.1 of this document) serves as an example of inclusion of environmental settings and the respective Run #'s associated with a given specimen's thermal treatment. Such chronologies were included to emphasize the fact that the respective data acquisition activities that resulted in all such plots of graphed NQIR(T_Q, T_A, t_A) values were essentially performed in randomized sequences.

Specifically, the cited run numbers reveal the fact that although only ten Q&A run numbers are listed in Figure 80, thirty-six distinct runs were made involving specimen 3013 before the indicated three sets of Q&A series treatments were completed. This reflects the fact that runs associated with straight downquench and LTA treatments may have been interspersed between any two specific Q&A series treatment runs performed in the course of overall data acquisition. Finally, it is judged to be significant that the resulting plots do appear to exhibit minimal deviations from a smooth fit, and this observation is taken to be indicative of an overall reliable data acquisition methodology.

Sub-sections 8.3.2 through 8.3.13 describe the various categorized sets of plots of annealing kinetics data acquired from numerous specific Q&A series treatments performed during this overall research investigation. Associated analyses are covered in each respective sub-section.

8.3.2 Overall Sets of Plots of NQIR(T_Q, T_A, t_A) Q&A Series Treatments

Listed below are four of more than one dozen specific Q&A series thermal treatments that were performed on one or more specimens, along with descriptions of the intended objectives associated with each specific treatment.

1. Collectively, various T_Q -to-fixed T_A Q&A series treatments were performed to examine the influence of initial excess vacancy concentration upon initial and overall annealing kinetics' rates and shapes. Quench temperatures ranged from 900^{o}C down to 400^{o}C, and isothermal annealing temperatures ranged from 700^{o}C down to room temperature. In many cases, isothermal annealing times ranged from 200 milliseconds to as much as hundreds of hours. Some Q&A series treatments involving anneals with $T_A \leq 100^o$C made use of extended annealing times of several days.

2. 700-to-$T_A \leq 600$, 800-to-$T_A \leq 500$, and 900-to-$T_A \leq 700$ Q&A Series treatments were performed to observe the nature and rate of annealing kinetics for moderate vacancy supersaturations (T_Q-$T_A \geq 100°C$) and possibly discern the role that vacancy defect chemical potential might play under these conditions.

3. 600-to-$T_A \leq 575$ Q&A Series treatments were performed to obtain initial annealing rate data from which assessments of instantaneous vacancy activation energies and absolute macroscopic sink efficiencies can be plotted as a function of vacancy defect chemical potential (see the Figures in sub-sections 8.3.10.1.11 and 8.3.10.1.12, respectively). Selection of 600^{o}C as the quench temperature was made to assure attainment of reasonably high resistometric measurements sensitivity while

minimizing the possibilities of encountering significant vacancy clustering conditions. Values selected for T_A ranged from 575^{o}C down to room temperature.

4. 500-to-$T_A \leq 300$ Q&A Series treatments were performed to examine annealing kinetics at temperatures and initial concentrations that would likely support minimizing of losses involving climbing of dislocations to pre-existing sinks and reductions in possible clustering of vacancies to form secondary defects. Some specific values selected for T_A were 300^{o}C, 150^{o}C, and 65^{o}C.

In summary, extensive sets of categorized plots of quenched-in resistance data associated with various combinations of quench and-isothermal anneals performed during this research are presented throughout the remainder of this chapter.

8.3.2.1 Specimen 3013: Plots of NQIR(900/800/700, 300, t_A) Values

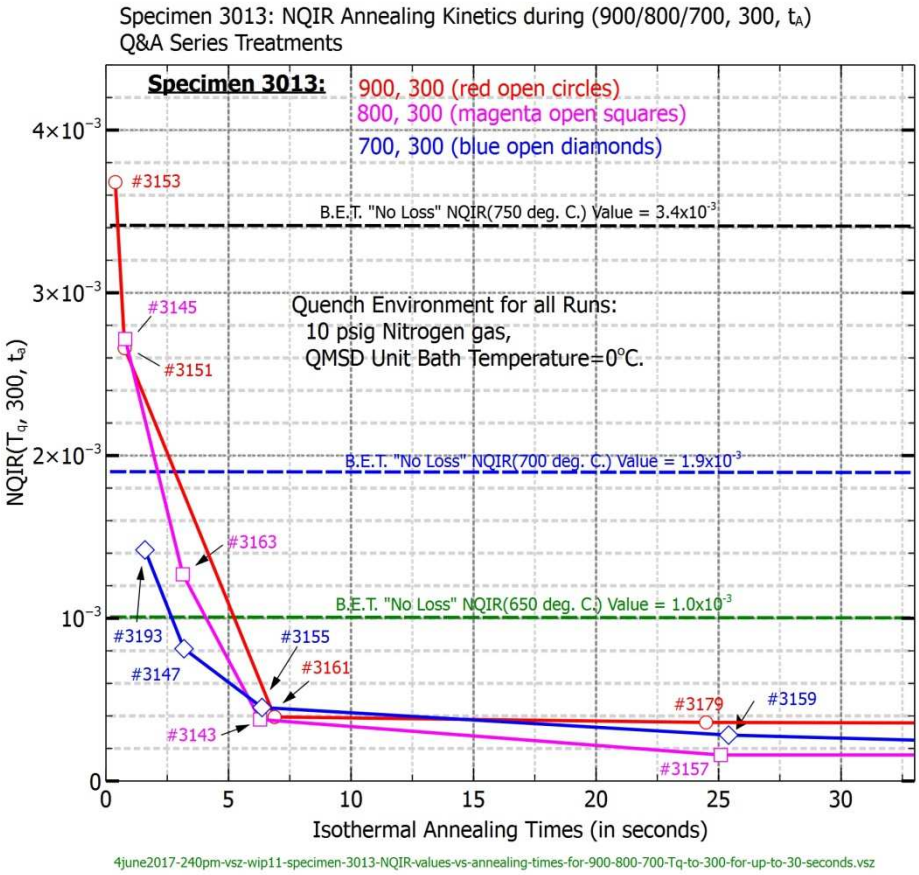

Figure 80. Specimen 3013: Plots of NQIR(900/800/700, 300, t_A) Values vs. Isothermal Annealing Times under 30 seconds

See Figures 81 through 97 for additional plots of NQIR(T_Q, T_A, t_A) Annealing Kinetics vs. Isothermal Annealing Times.

8.3.2.2 Specimen 3013: Log-Log Plots of NQIR(900/800/700, 300, t_A) Values

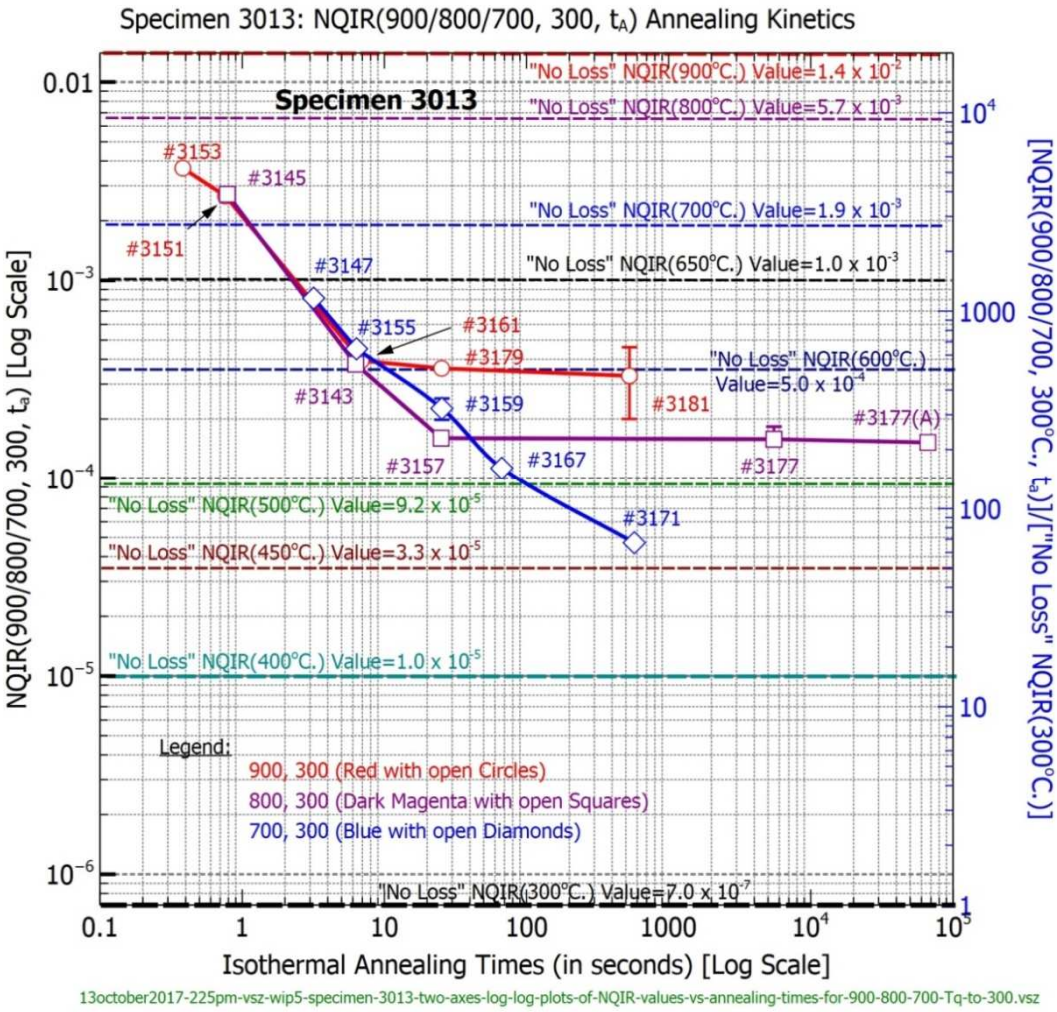

Figure 81. Specimen 3013: Two-Axes Log-Log Comparison Plots of NQIR(900/800/700, 300, t_A) vs. Annealing Times approaching 70,000 seconds

Figure 81 illustrates obvious crossovers in NQIR(T_Q, 300, t_A) annealing kinetics and the subsequent higher MRR levels that tend to be manifested in association with higher quench temperatures.

8.3.2.3 Specimens 4002 and 4005: Semi-Log Plots of NQIR(900,700, t_A) Values

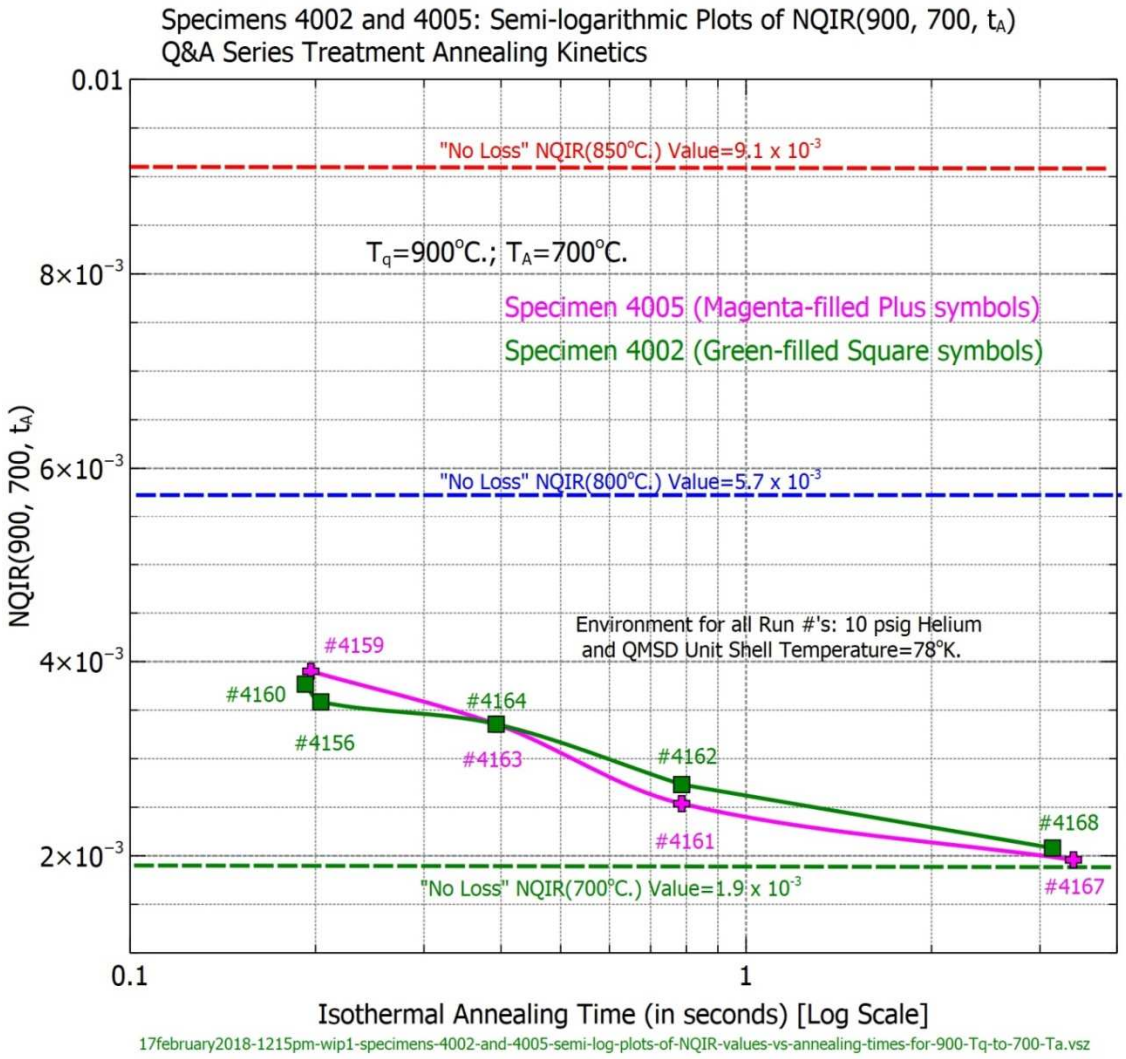

Figure 82. Specimens 4002 and 4005: Semi-Log Plots of NQIR(900,700, t_A) Values

8.3.2.4 Specimen 4002: Two-Axes Semi-Log Plot of Annealing Kinetics during NQIR(900, 500, t_A) Q&A Series Treatments and Half-time Annealing Determination

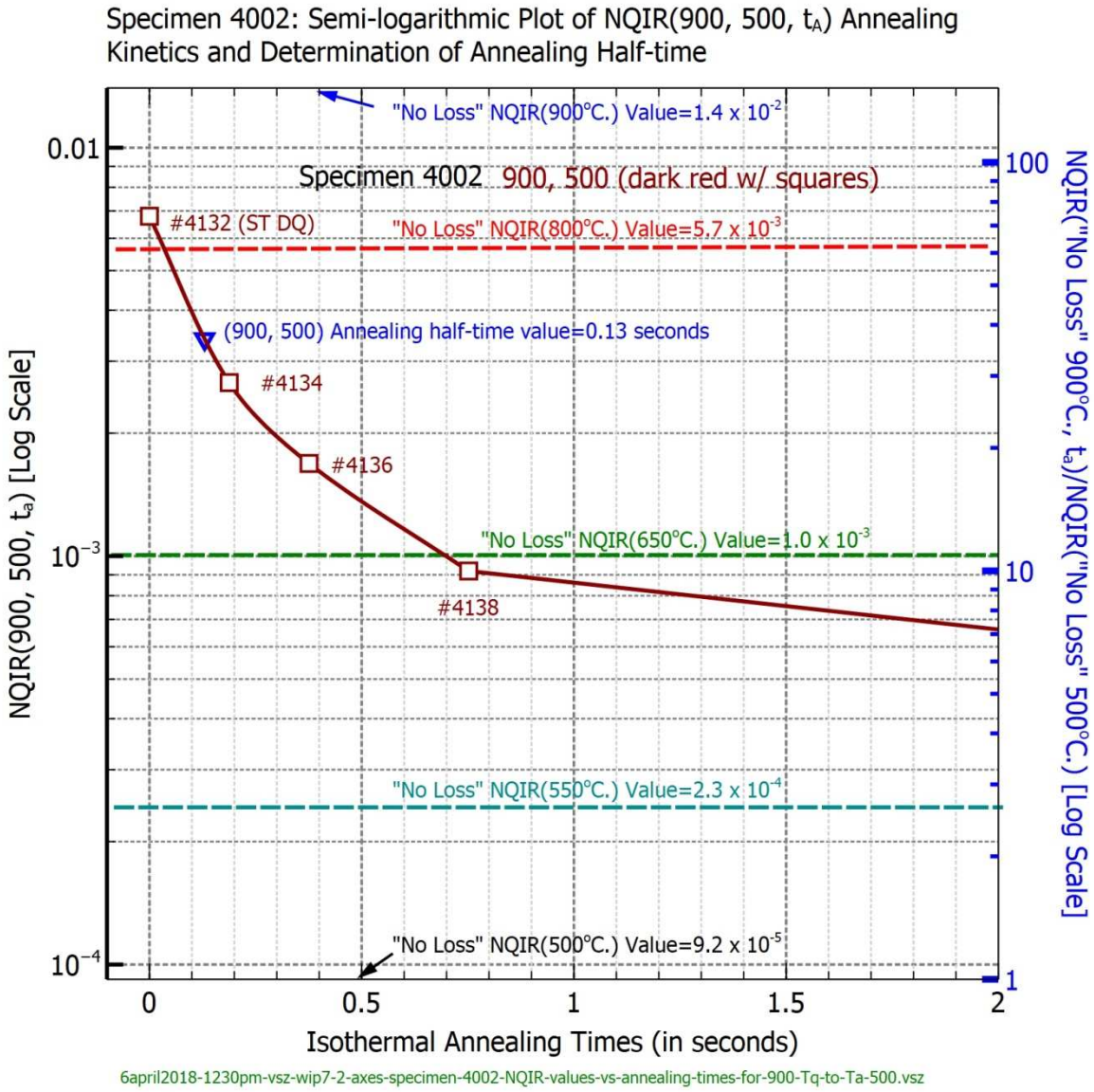

Figure 83. Specimen 4002: Two-Axes Semi-Log Plot of Annealing Kinetics during NQIR(900, 500, t_A) Q&A Series Treatments and Half-time Annealing Determination

8.3.2.5 Specimen 4005: Semi-Log Plots of NQIR(900/800/700, 500, t_A) Values

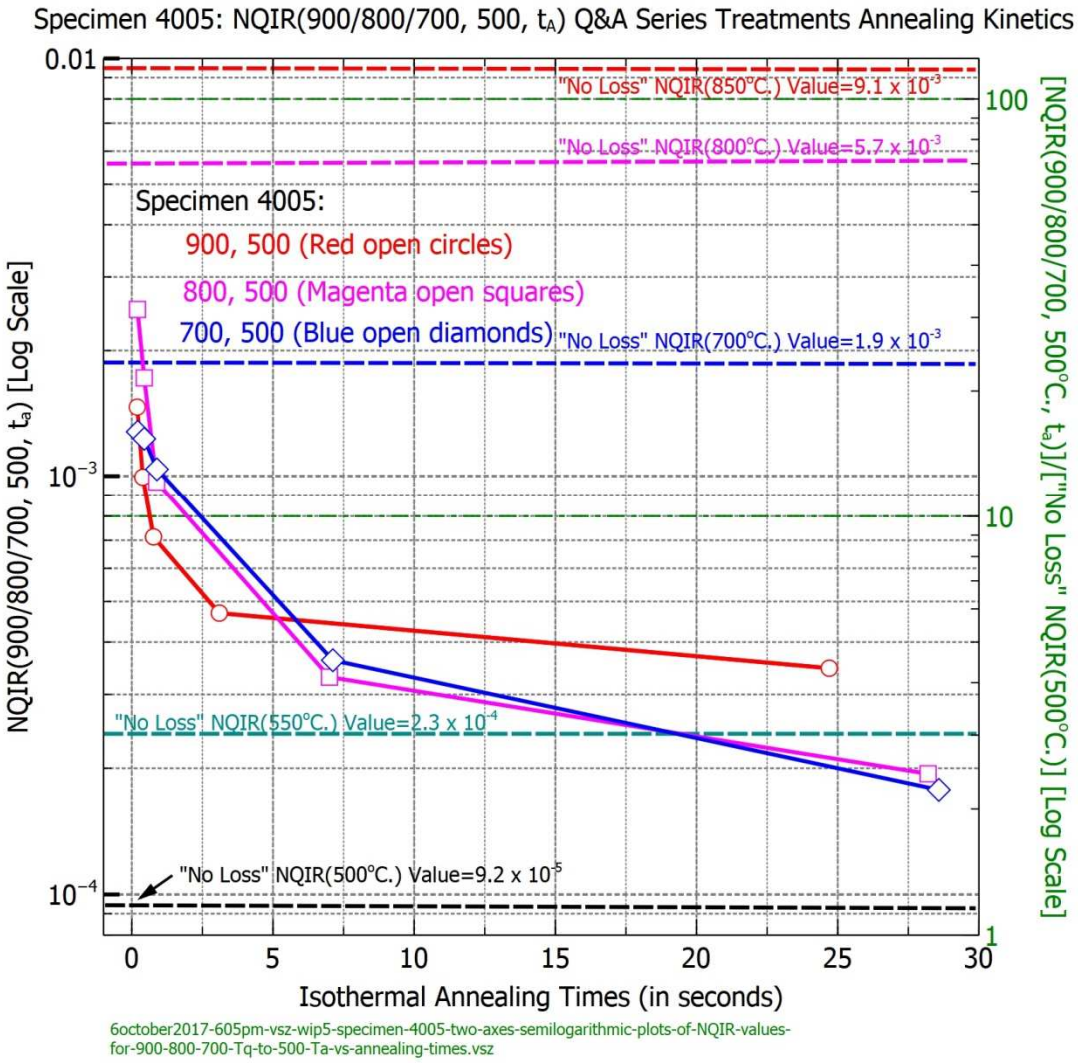

Figure 84. Specimen 4005: Comparison Two-Axes Semi-Log Plots of NQIR(900/800/700, 500, t_A) vs. Annealing Times of up to 30 seconds

Note the obvious crossovers in NQIR(T_Q, 500, t_A) MRR levels revealed in Figure 84.

8.3.2.6 Specimen 3016: Semi-Log Plots of NQIR(900/800/700, 400, t_A) Values

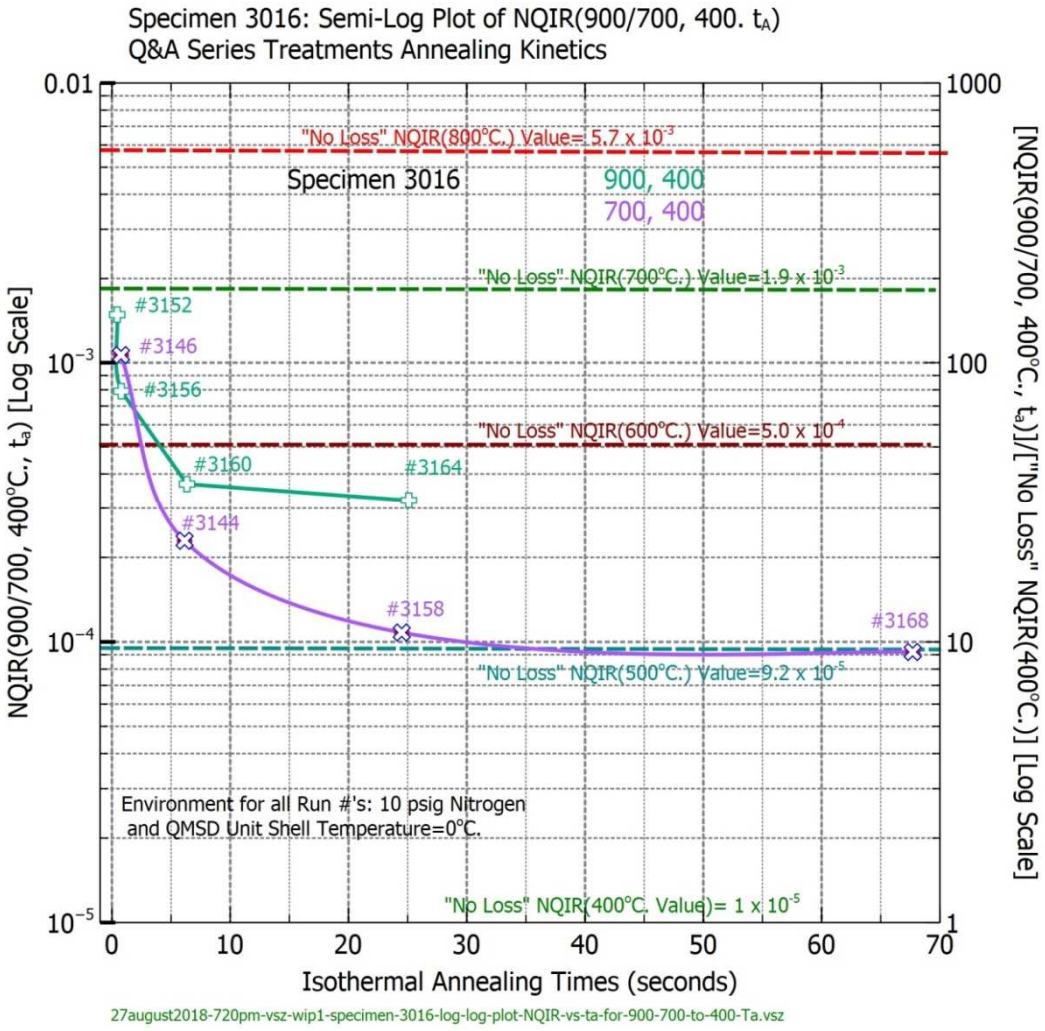

Figure 85. Specimen 3016: Two-Axes Comparison Semi-Log Plots of Annealing Kinetics during NQIR(900/700, 400, t_A) Q&A Series Treatments vs. Annealing Time

Figure 85 illustrates obvious crossovers in NQIR(900/700, 400, t_A) annealing kinetics and the subsequent higher MRR levels associated with increasing quench temperature.

8.3.2.7 Specimen 4002: Semi-Log Plot of NQIR(900,400, t_A) Values

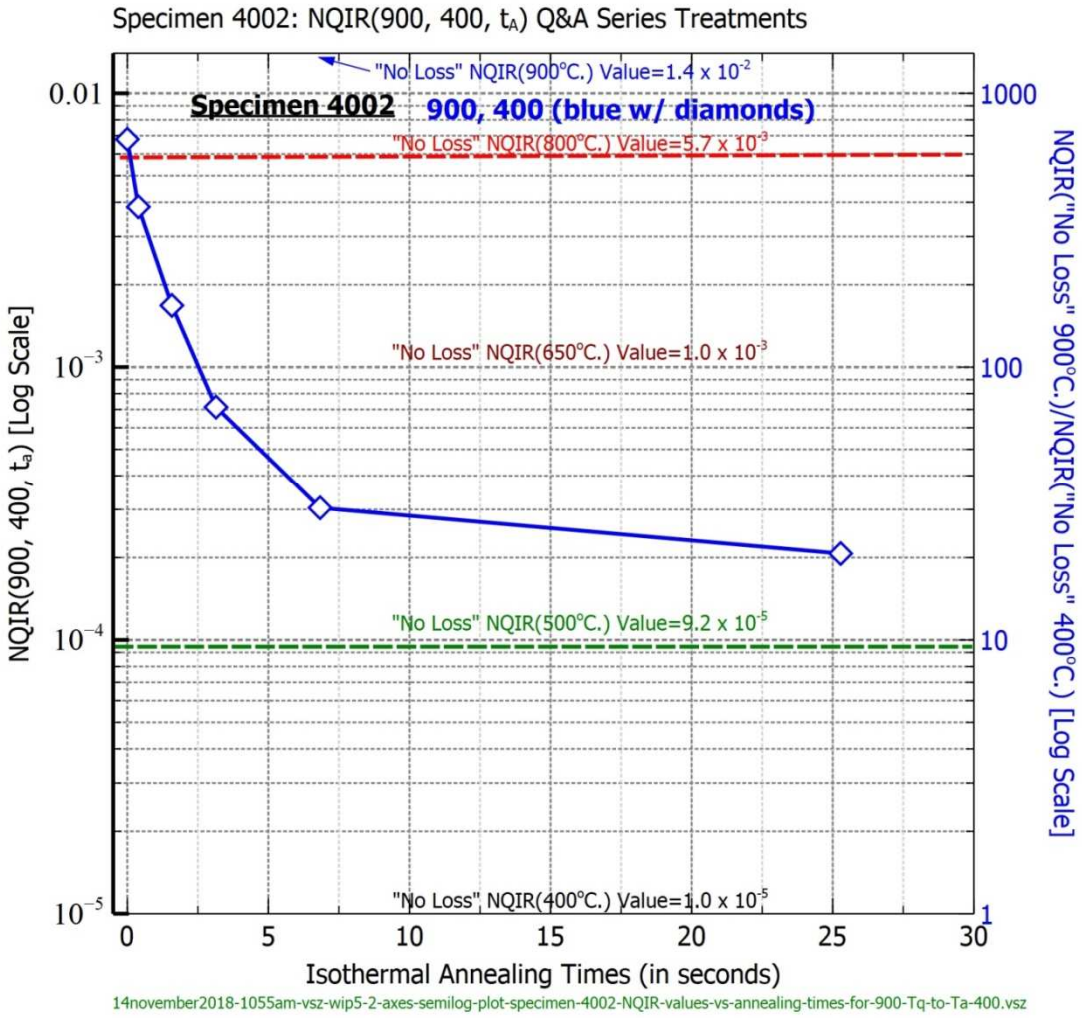

Figure 86. Specimen 4002: Two-Axes Semi-Log Plot of NQIR(900, 400, t_A) vs. Annealing Times under 30 seconds

8.3.2.8 Specimen 4002: Semi-Log Plot of NQIR(900,300, t_A) Values

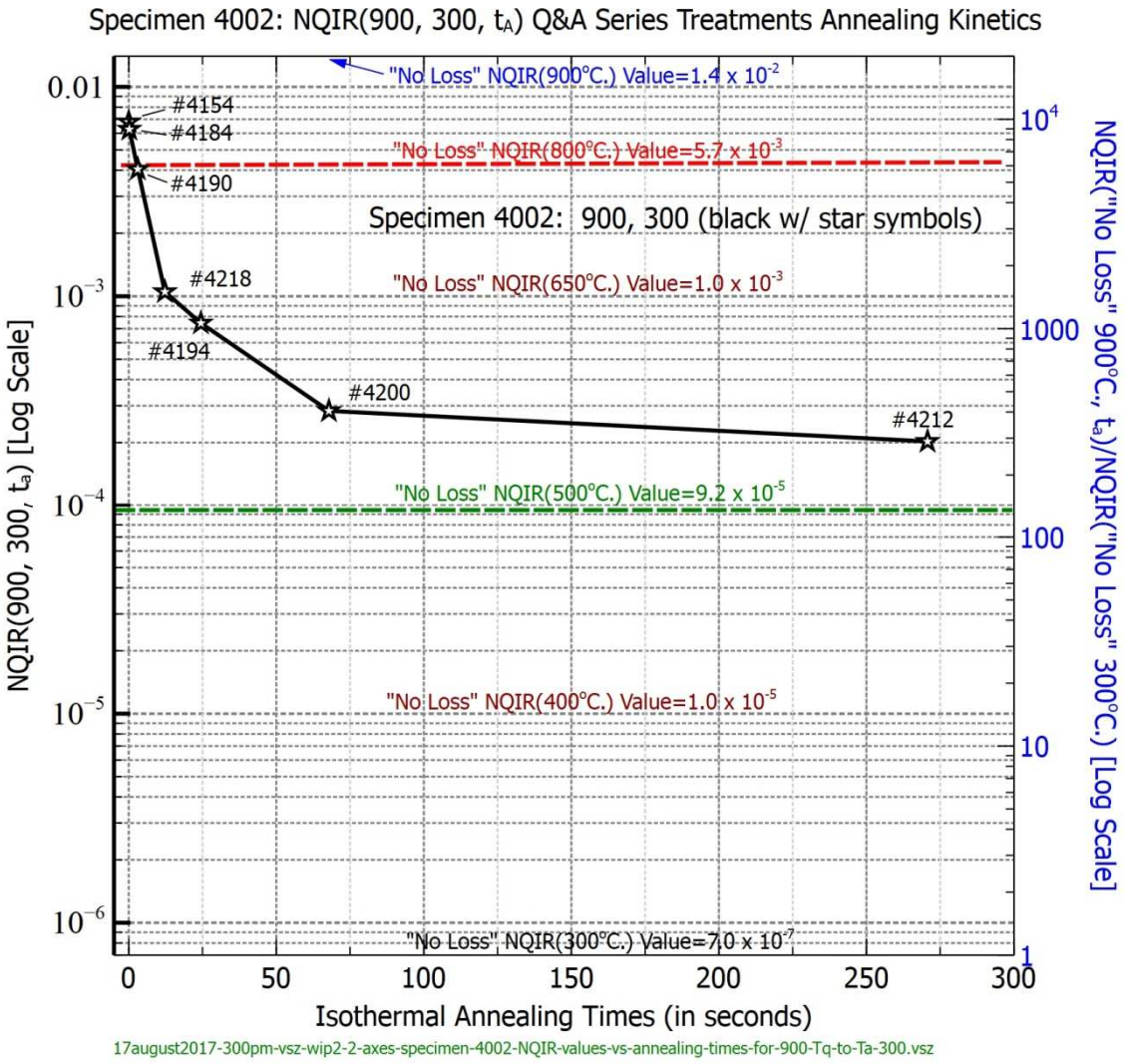

Figure 87. Specimen 4002: Two-Axes Semi-Log Plot of NQIR(900, 300, t_A) vs. Annealing Times under 300 seconds

8.3.2.9 Specimen 4002: Semi-Log Plot of NQIR(800,500, t_A) Values

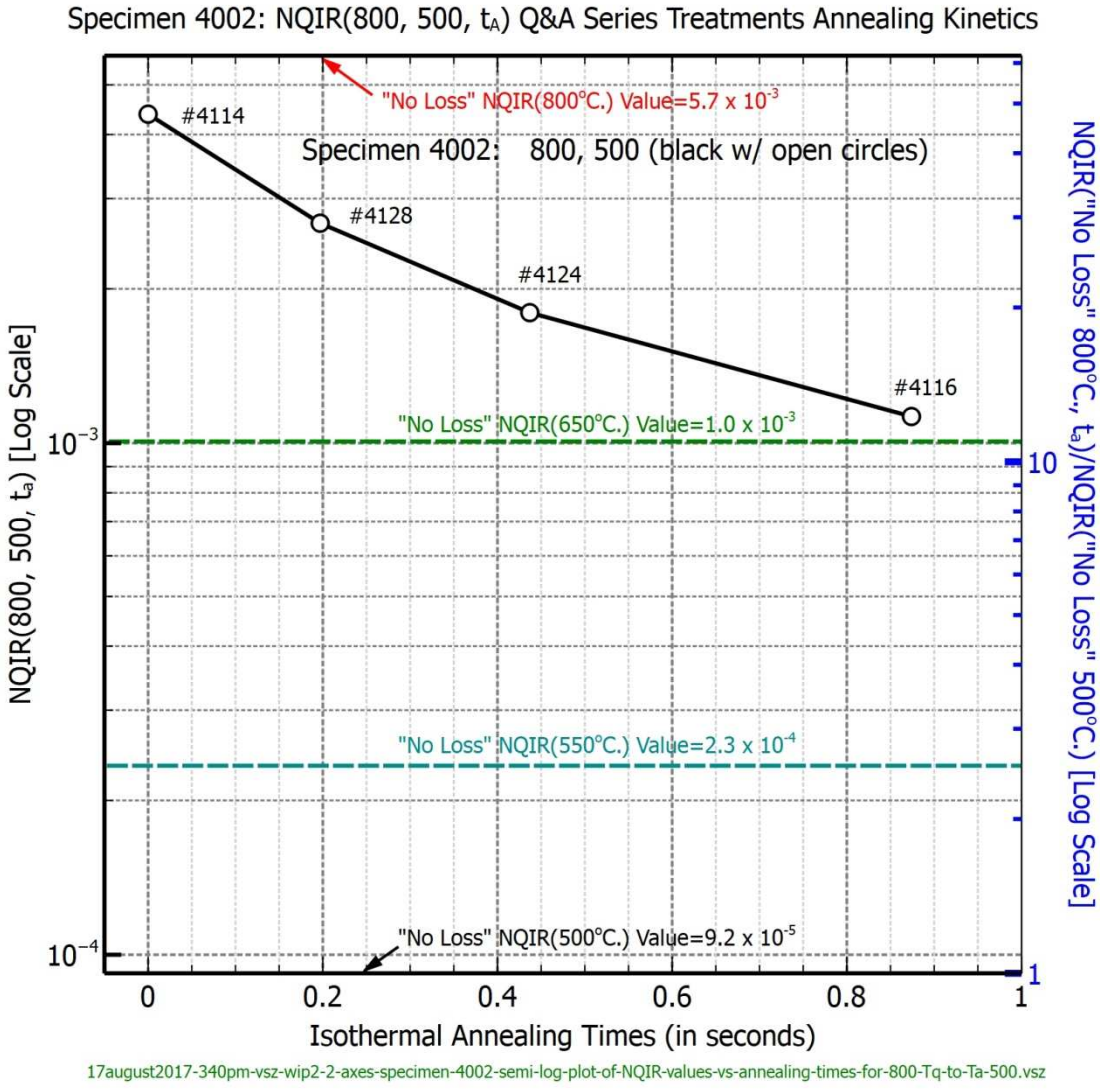

Figure 88. Specimen 4002: Two-Axes Semi-Log Plot of NQIR(800, 500, t_A) vs. Annealing times under one second

8.3.2.10 Specimen 4002: Plot of NQIR(800,300, t_A) Values

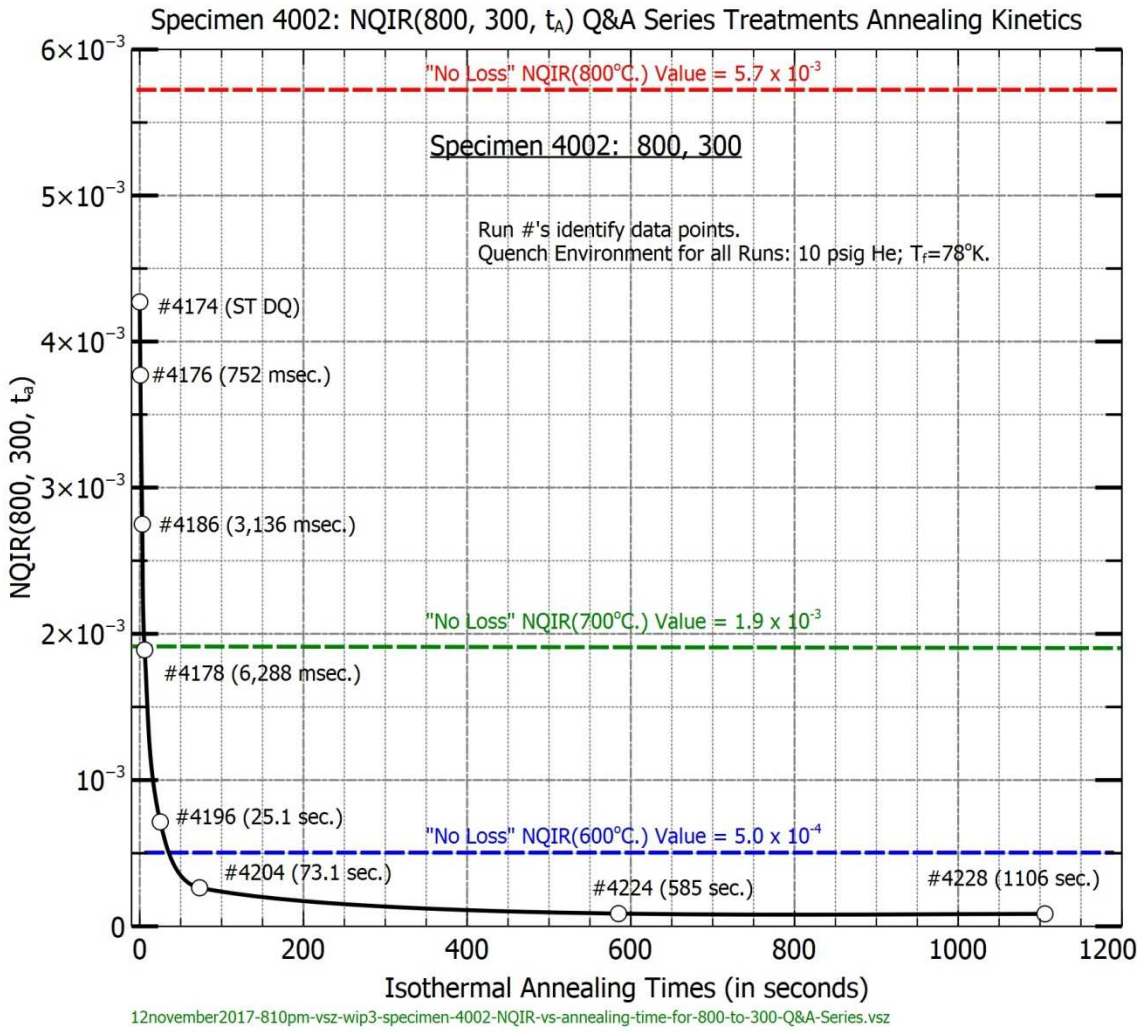

Figure 89. Specimen 4002: Plot of NQIR(800, 300, t_A) vs. Annealing Times up to 1106 seconds

8.3.2.11 Specimen 4002: Semi-Log Plot of NQIR(800,300, t_A) Values

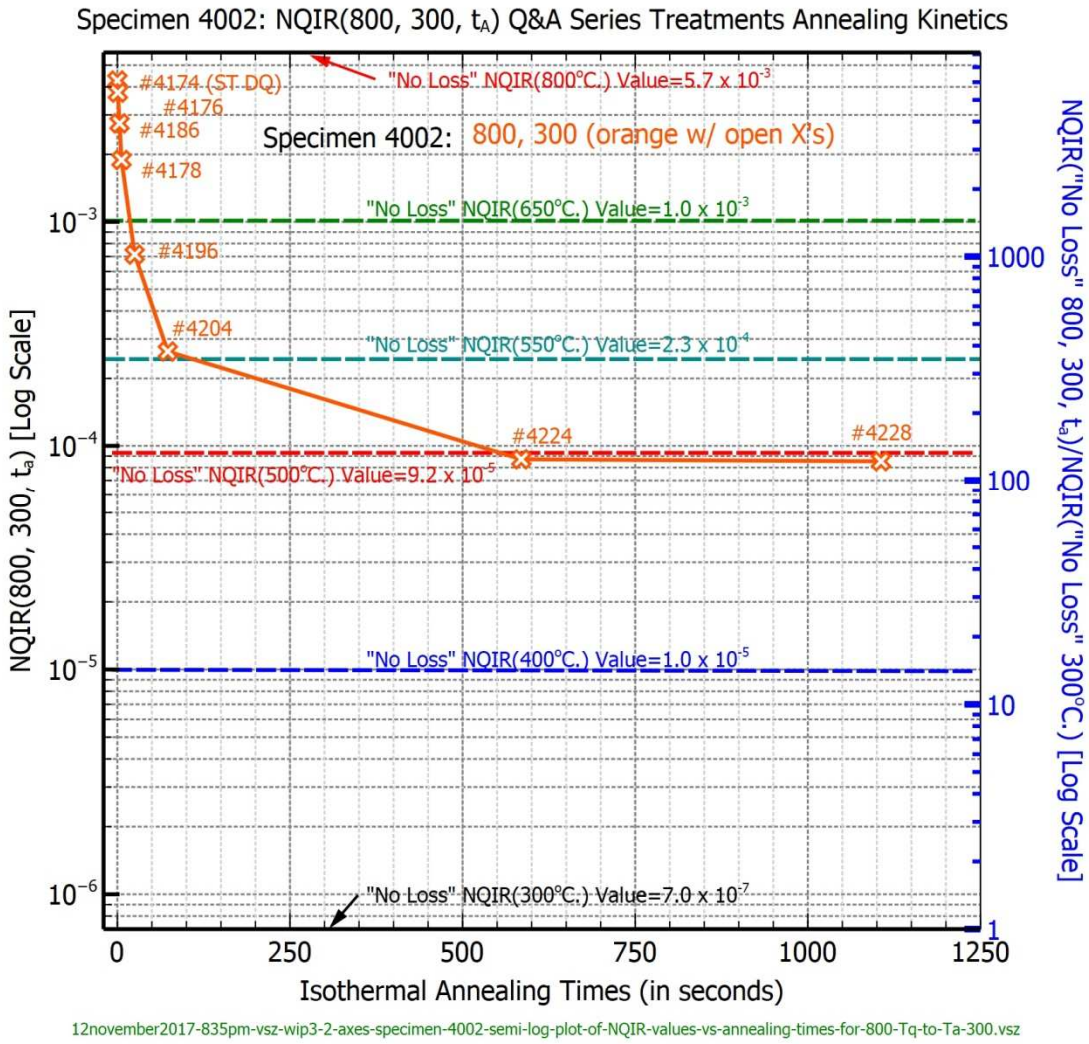

Figure 90. Specimen 4002: Two-Axes Semi-Log Plot of NQIR(800, 300, t_A) vs. Annealing Times up to 1106 seconds

8.3.2.12 Specimen 3013: Plot of NQIR(800,300, t_A) Values

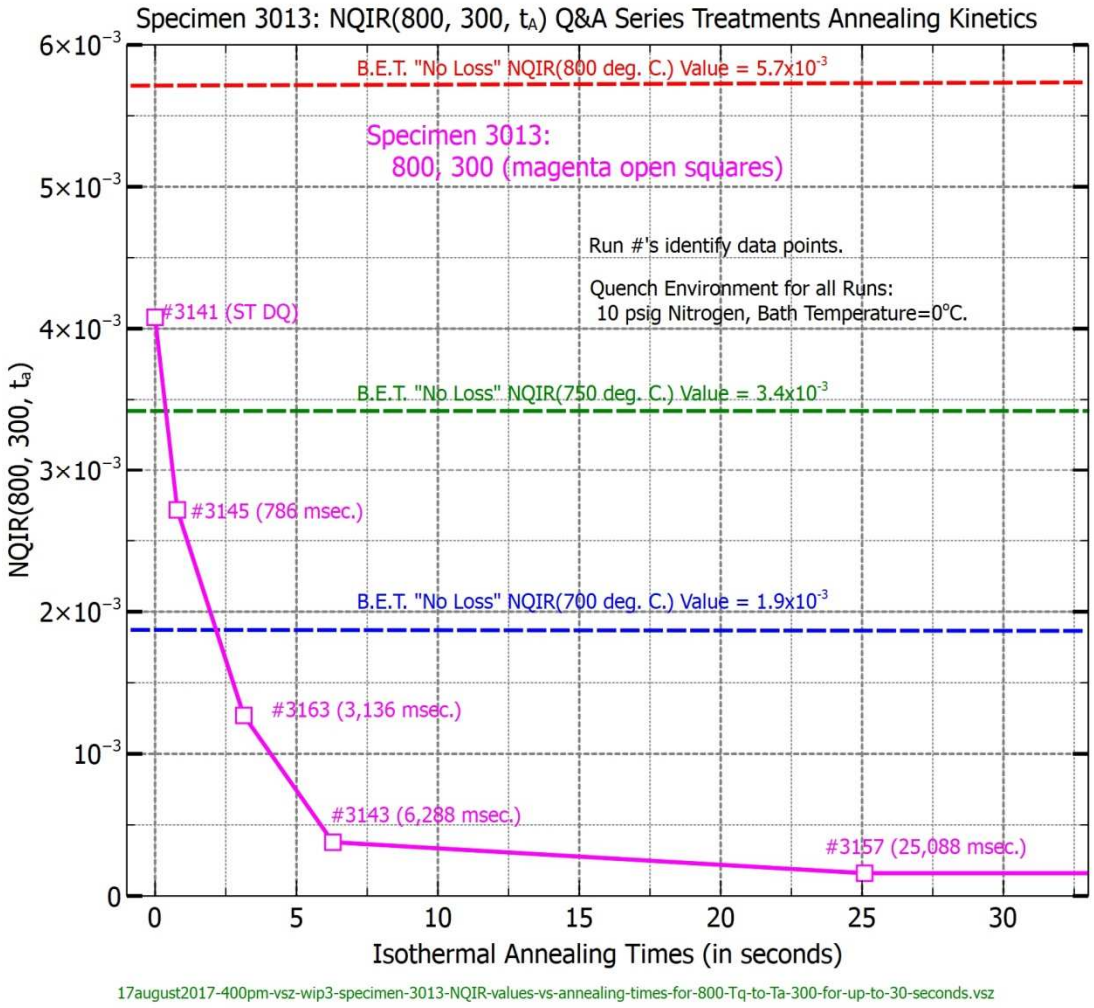

Figure 91. Specimen 3013: Plot of NQIR(800, 300, t_A) vs. Annealing Times less than 30 seconds

8.3.2.13 Specimen 3013: Semi-Log Plot of NQIR(800,300, t_A) Values

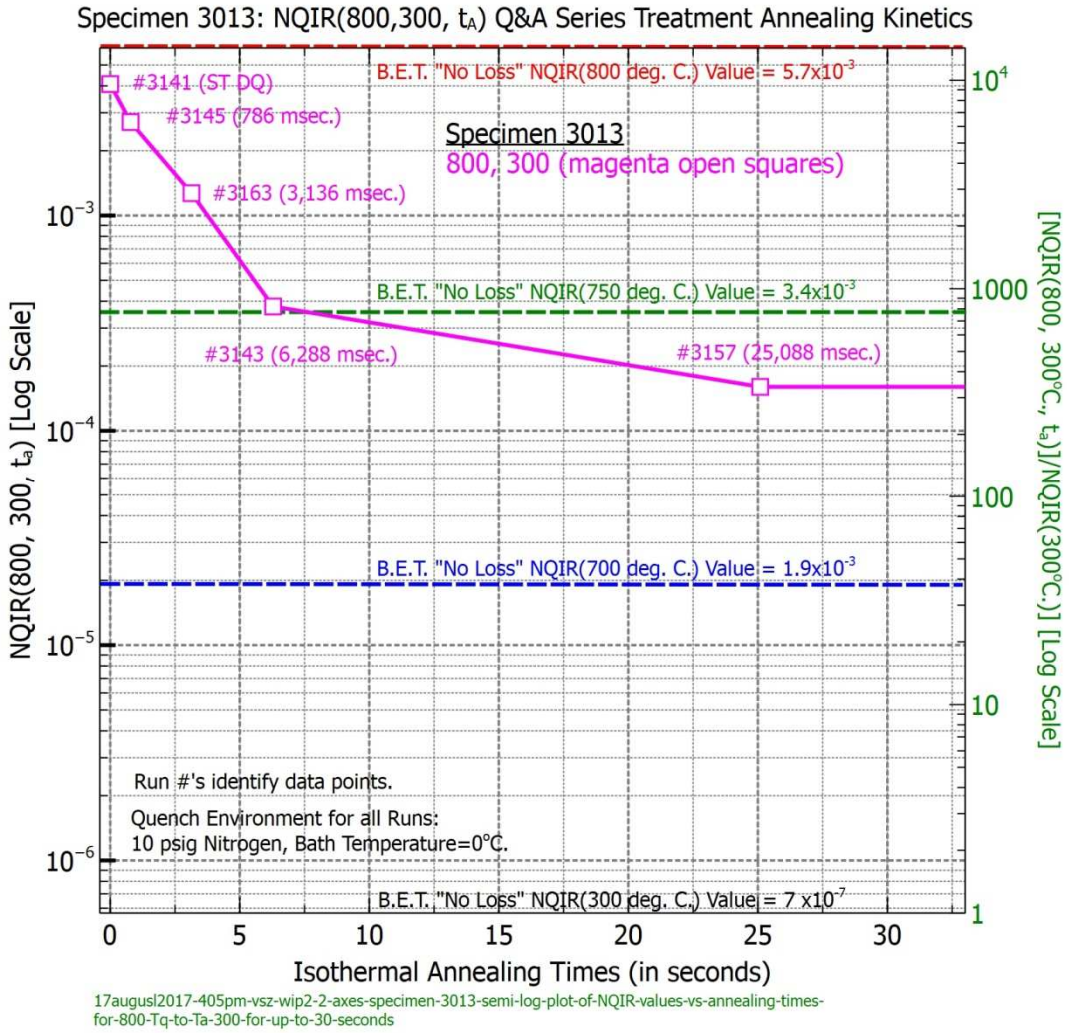

Figure 92. Specimen 3013: Two-Axes Semi-Log Plot of NQIR(800, 300, t_A) vs. Annealing Times less than 30 seconds

8.3.2.14 Specimen 3013: Log-Log Plot of NQIR(800,300, t_A) Values

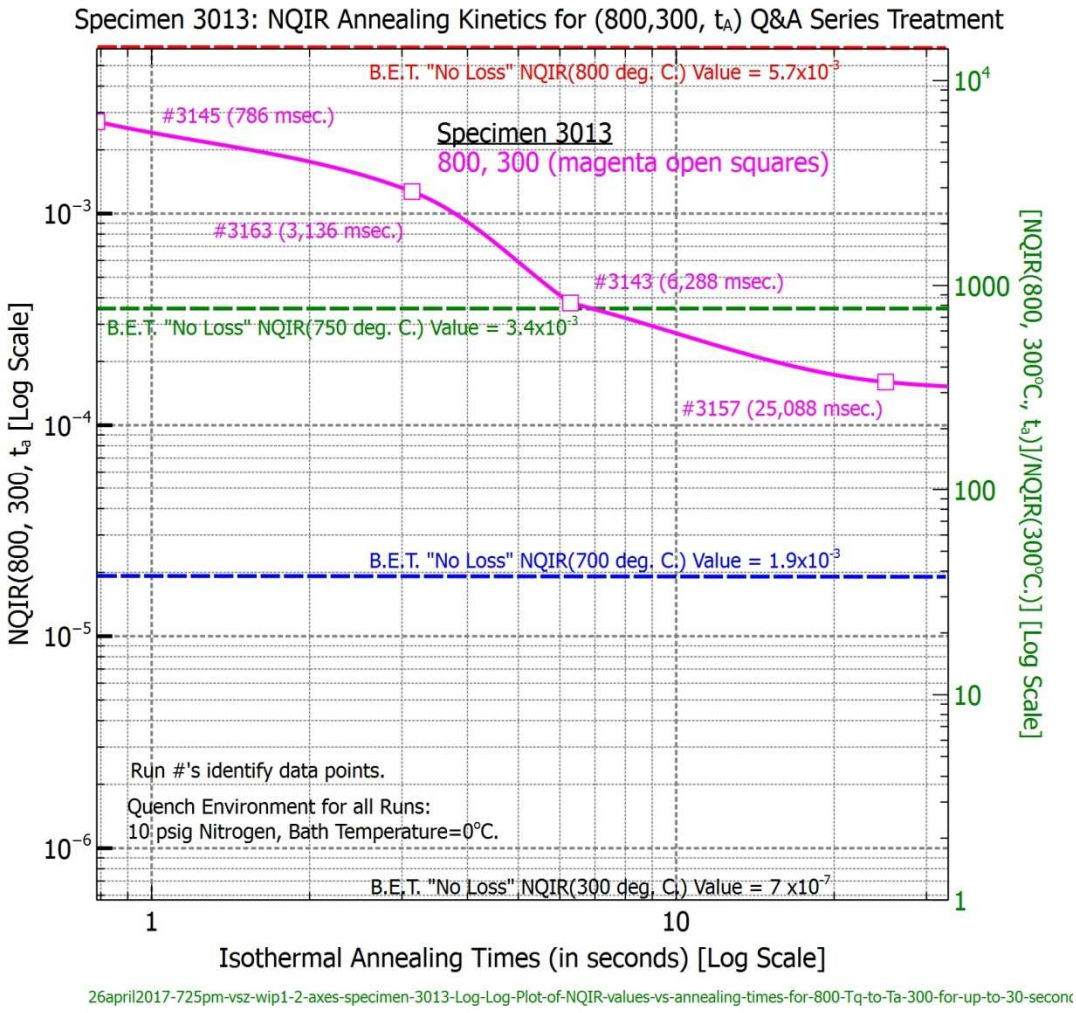

Figure 93. Specimen 3013: Two-Axes Log-Log Plot of NQIR(800, 300, t_A) vs. Annealing Times less than 30 seconds

Note both the sigmoidal shape with its associated inflection point and the MRR level associated with this specific Q&A series treatment.

8.3.2.15 Specimen 3013: Semi-Log Plot of NQIR(700,200, t_A) Values

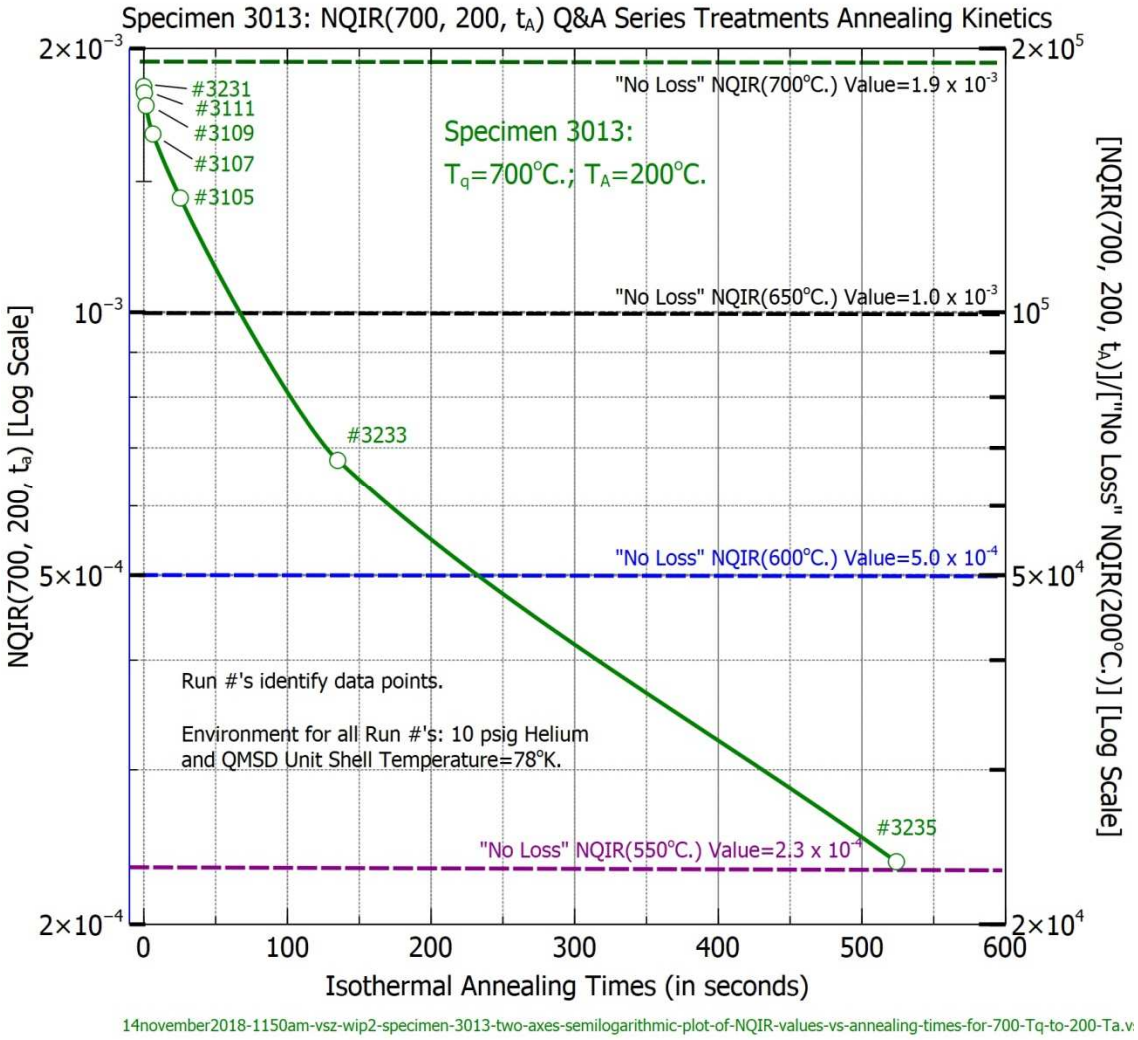

Figure 94. Specimen 3013: Two-Axes Semi-Log Plot of NQIR(700, 200, t_A) vs. Annealing Times up to 524 seconds

Note the large MRR level associated with this NQIR(700, 200, t_A) Q&A series treatment following annealing times up to 525 seconds.

Table 13 provides one set of potentiometric measurements data, namely: R(40°C), R_{LTA}, and associated NQIR values for specimen 4005 that involved NQIR(700, 200, t_A) Q&A series treatments. Figure 94 shows a plot of that NQIR data.

Table 13. Specimen 4005: (700, 200, t_A) Q&A Series Treatments Data

Specimen 4005: (700, 200, t_A) Q&A Series Treatments

R(40°C) (in milli-ohms)	R_{LTA} (in micro-ohms)	Run # & Environment	T_q, T_a	t_{III} (seconds)	NQIR (x 10^{-3})	Fraction remaining (w.r.t. ST DQ value)	$\ln[(f_r)^{-1}]$
4.556	LTA #6: 2.325						
		4173 10 He, 78 K	700 ST DQ	0	1.531	--	N/A
		4201 10 He, 78 K	700 ST DQ	0	1.561	--	N/A
		4229 10 He, 78 K	700 ST DQ	0	1.6433	--	N/A
		4175	700, 200	0.784	1.5858	0.965	0.0356
		4177	700, 200	6.272	1.432	0.8714	0.1376
	LTA #7: 2.82						
		4213	700, 200	25.088	1.302	0.7923	0.2328
		4203	700, 200	73.12	1.0438	0.6352	0.4538
		4195	700, 200	138	0.6805	0.4141	0.8817
		4189	700, 200	271.36	0.44967	0.2736	1.29595
		4215	700, 200	549	0.0711	0.042367	3.14
	LTA #8: 2.75						
		4225	700, 200	1103.8	0.04814	0.02929	3.53

8.3.2.16 Specimen 4005: Comparison Semi-Log Plots of NQIR(900/800/700, 200, t_A) Annealing Kinetics and Half-time Determinations

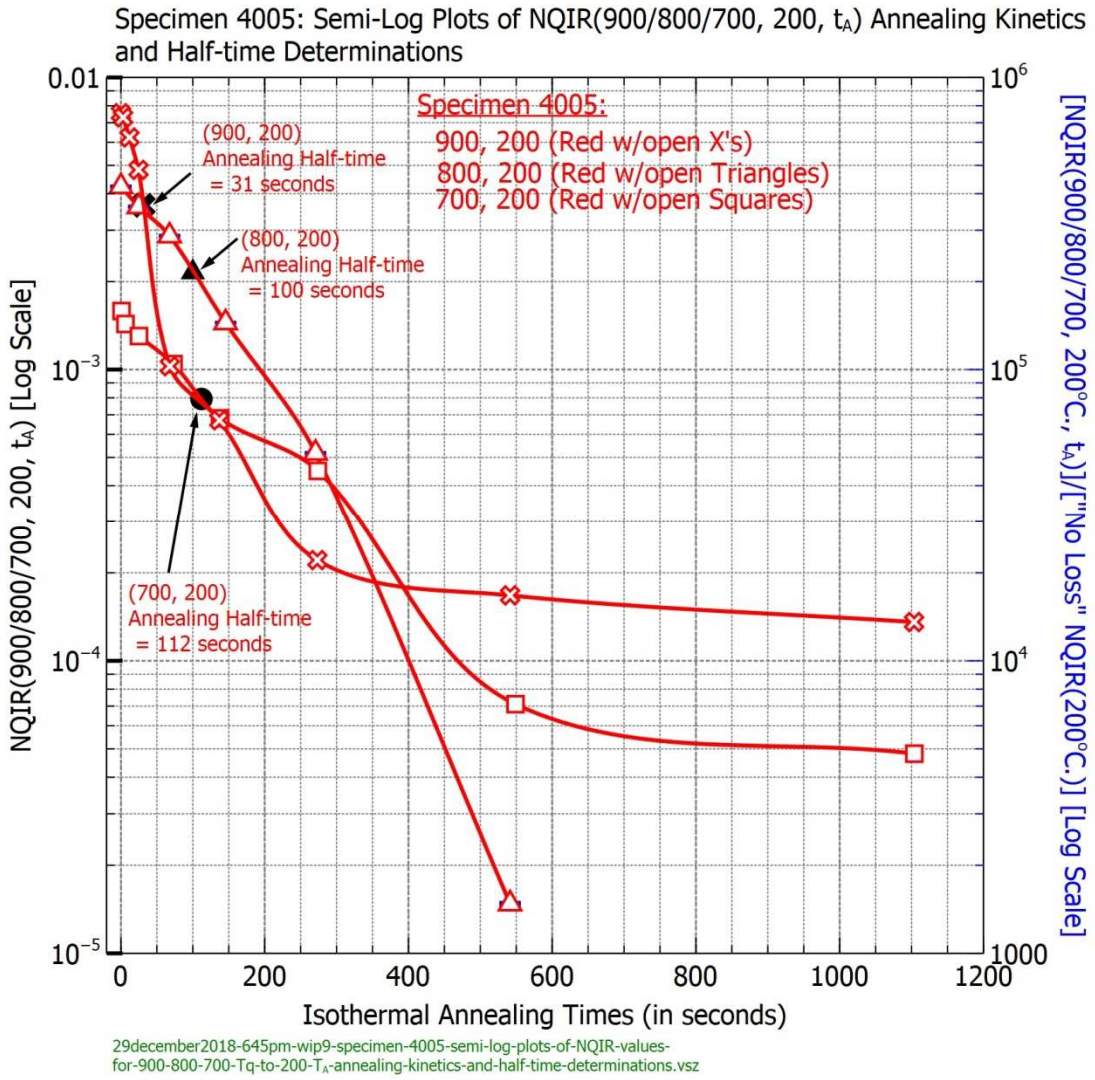

Figure 95. Specimen 4005: Comparison Semi-Log Plots of NQIR(900/800/700, 200, t_A) Annealing Kinetics and Half-time Determinations.

8.3.2.17 Specimens 4002 and 4005: Log-Log Plots of NQIR(900/800/700, 500, t_A) Values

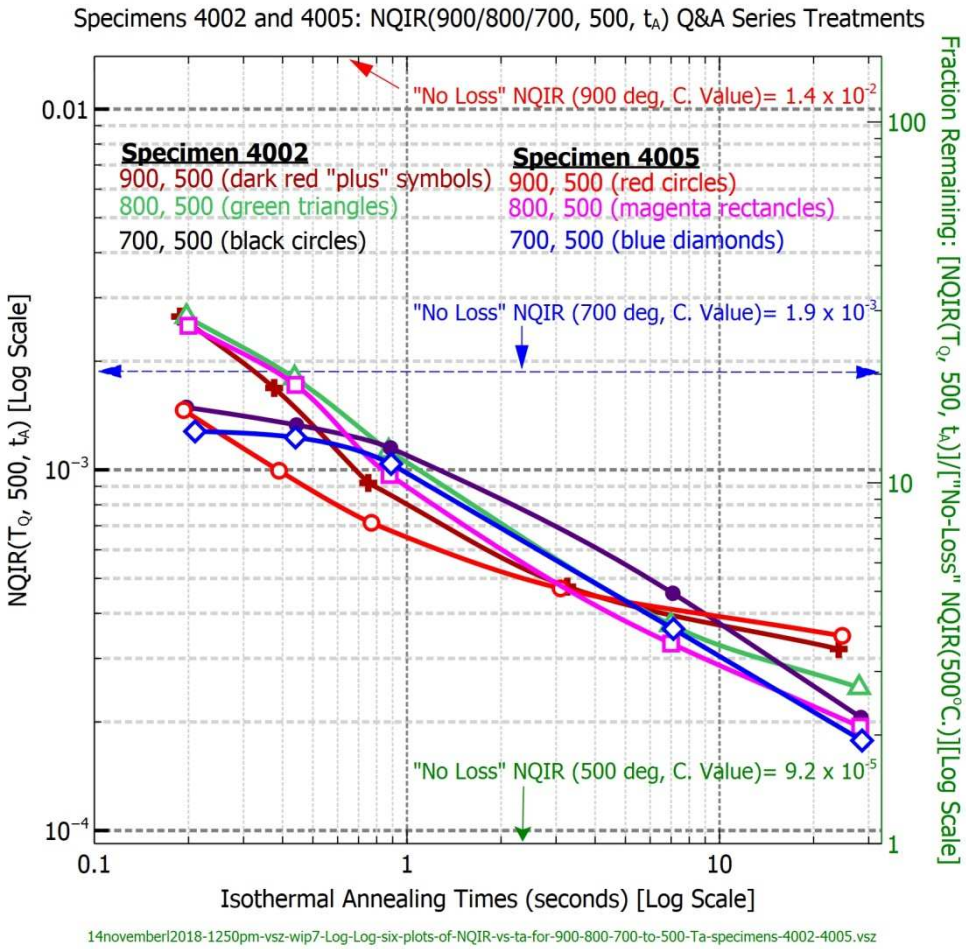

Figure 96. Specimens 4002 and 4005: Two-Axes Comparison Log-Log Plots of NQIR(900/800/700, 500, t_A) vs. Annealing Times up to 30 seconds

Note 1) the significant reductions in sigmoidal shapes that occur for both specimen 4002 and 4005 as the associated quench temperature is increased, 2) the crossovers in NQIR(T_Q, 500, t_A) levels associated with these six sets of Q&A series treatments, and 3) the MRR levels associated with each of these Q&A series treatments.

8.3.2.18 Specimen 3016: Log-Log Plots of NQIR(900/800/700, 400, t_A) Values

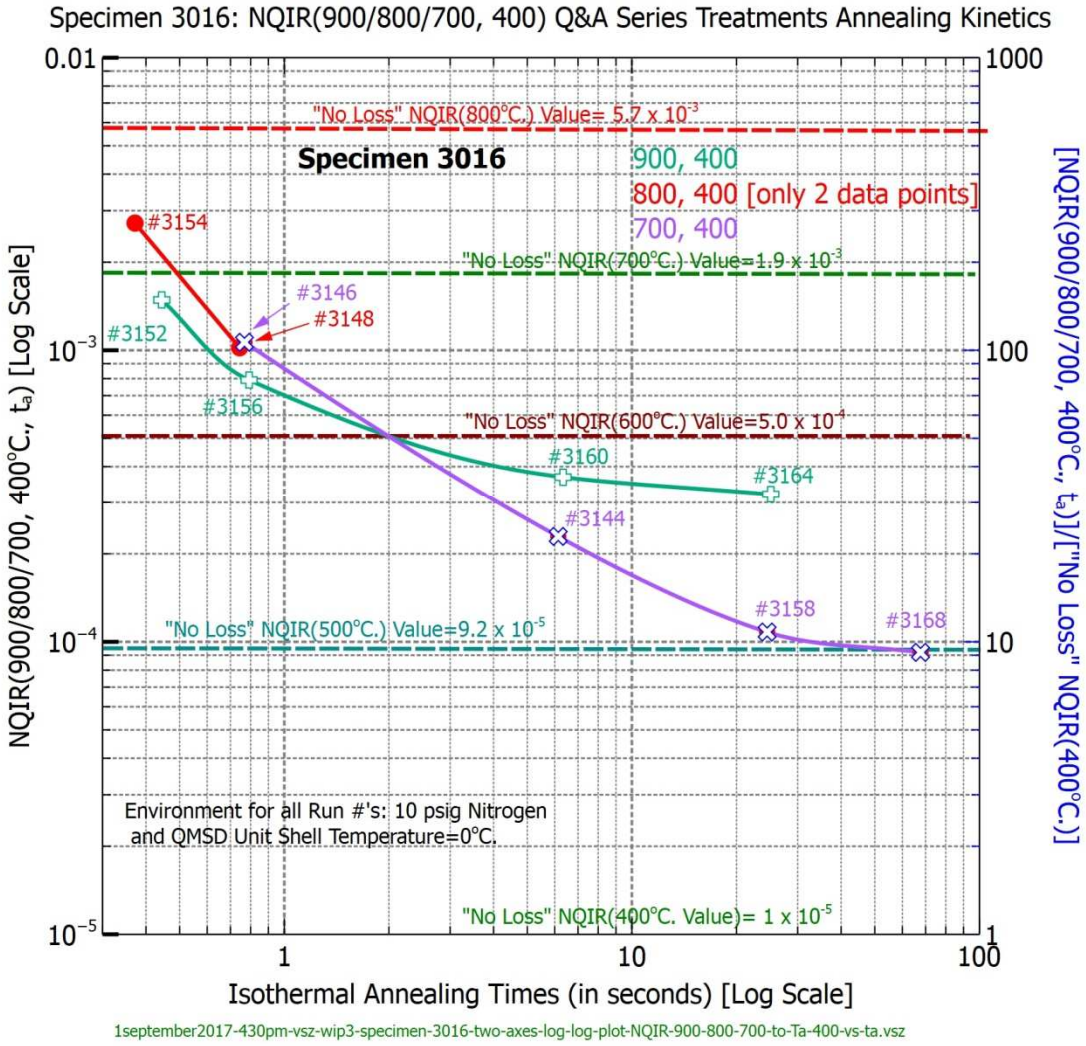

Figure 97. Specimen 3016: Comparison Log-Log Plots of NQIR(900/800/700, 400, t_A) vs. Annealing Times up to 100 seconds

8.3.3 Extensive Sets of Plots of Fraction Remaining NQIR(T_Q, T_A, t_A) during Q&A Series Treatments

It is important to point out that further insights became discernible when plots of Fraction Remaining NQIR(T_Q, T_A, t_A) are made from these same sets of already acquired Q&A series treatments data. See Figures 98 through 114 and note that Figures 109 and 112 employ (Annealing Time)$^{2/3}$ as the independent parameter.

In Figure 99 specimen 4005's annealing kinetics are shown in a Log-Log plot that includes specimen 4002's (700, 300, t_A) Q&A series treatment to illustrate the underlying behaviors for two different annealing temperatures.

Note also in Figure 99 the significant sigmoidal shape for specimen 4005's NQIR(700, 200, t_A) data, whereas specimen 4002's NQIR(700, 300, t_A) Q&A series treatment shows only a slightly sigmoidal shape.

8.3.3.1 Specimens 3012, 3013, and 4005: Plot of Fraction Remaining NQIR(700, 200, t_A) Values and Determinations of Annealing Half-Times

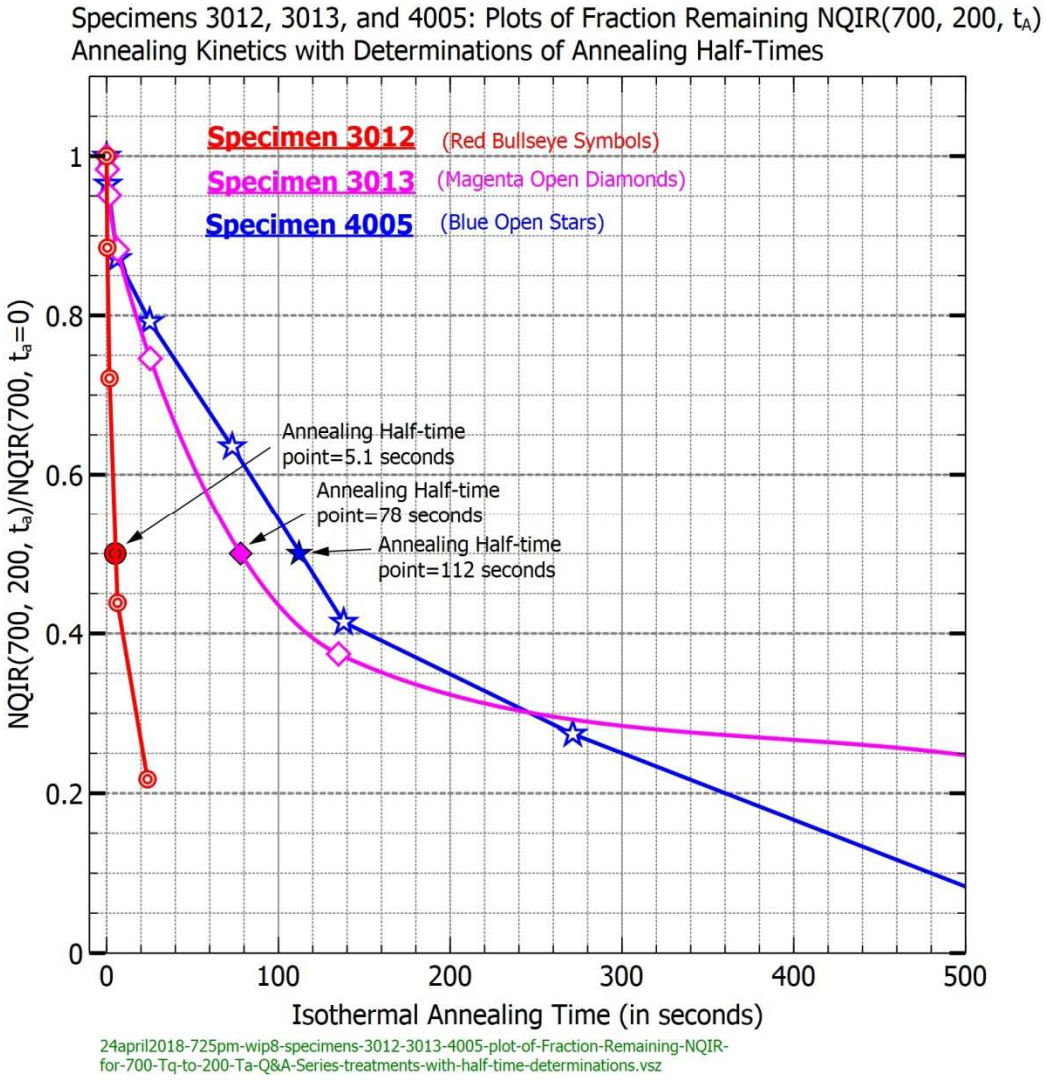

Figure 98. Specimens 3012, 3013, and 4005: Plots of Fraction Remaining NQIR(700, 200, t_A) Annealing Kinetics with Determinations of Annealing Half-times

8.3.3.2 Specimens 4002 and 4005: Log-log Plots of Fraction Remaining of NQIR(700, T_A, t_A) Values, [where T_A =300 and 200, respectively]

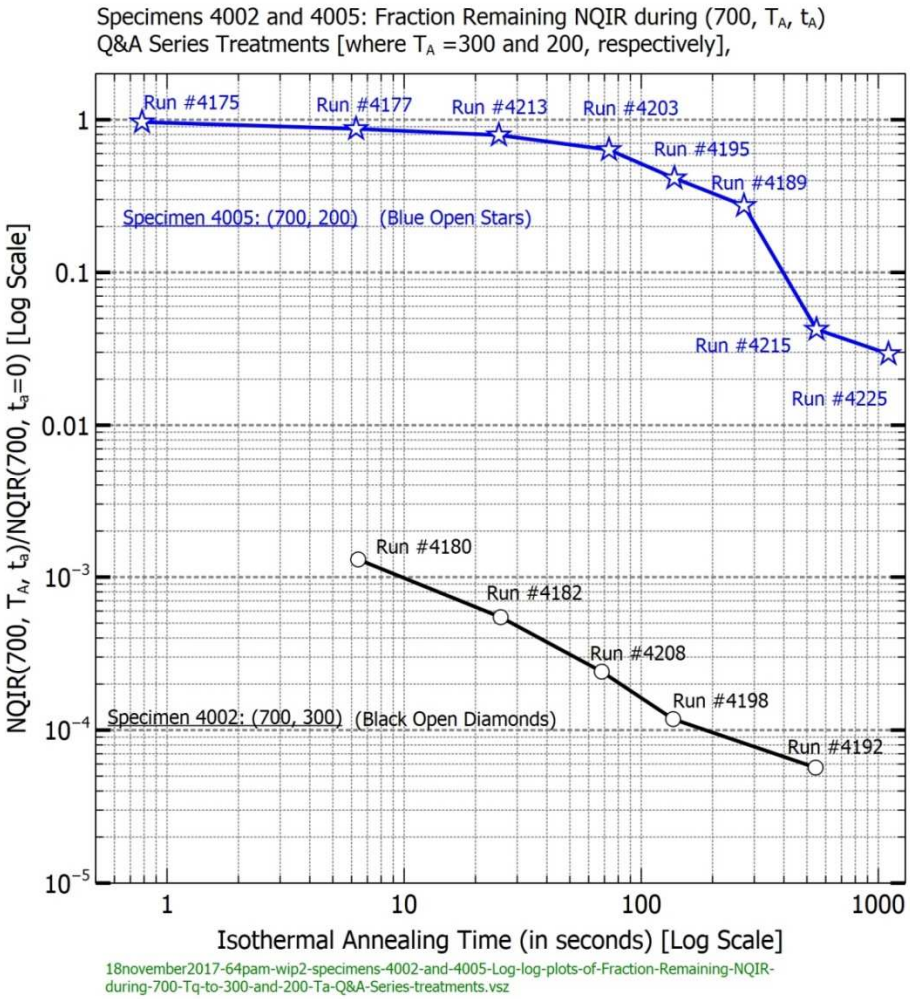

Figure 99. Specimens 4002 and 4005: Log-log Plots of Fraction Remaining of NQIR(700, T_A, t_A), [where T_A =300 and 200, respectively], vs. Annealing Times up to 1104 seconds

8.3.3.3 Specimens 4002 and 4005: Reciprocal of Fraction Remaining during NQIR(900/800/700, 500) and NQIR(700, 600) Q&A Series Treatments vs. Annealing Times under 30 seconds

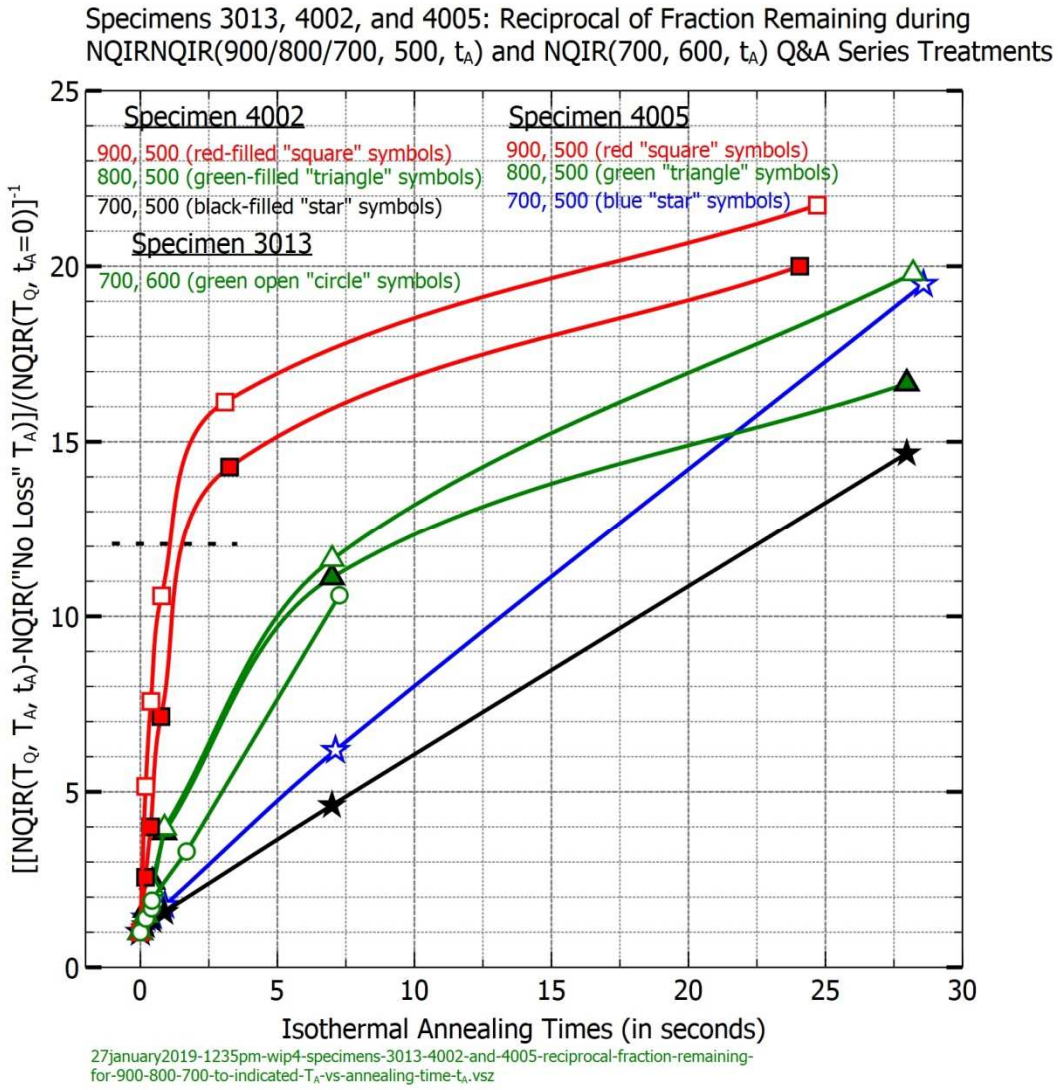

Figure 100. Specimens 3013, 4002 and 4005: Reciprocal of Fraction Remaining during NQIR(900/800/700, 500) and NQIR(700, 600) Q&A Series Treatments vs. Annealing Times under 30 seconds

Straight line segments in such reciprocal fraction remaining NQIR(T_Q, T_A, t_A) plots are indicative of second-order annealing kinetics. In Figure 100 the entire range for the three NQIR(700^{o}C, T_A, t_A) Q&A series treatments as well as the two initial

segments (demarcated by annealing times that are below the dotted line marker) for the two NQIR(900, T_A, t_A) Q&A treatments, could be considered to follow second-order annealing kinetics.

However, significant reductions in the respective fraction-remaining annealing rates are clearly manifested during the longer annealing times (demarcated by annealing times that are above the dotted line marker) associated with all four NQIR(900/800, T_A, t_A) Q&A treatments. One consequence of such complex annealing kinetics that is cited in other sub-sections of this document is the appearance of "crossovers"[103] in the associated sets of NQIR(T_Q, T_A, t_A) plots.

Selection of another independent parameter, namely $t^{2/3}$, was made to examine further what would be the subsequent behaviors manifested in such reciprocal fraction remaining data plots, and the results of this decision are presented in Figure 101.

Now, it is easily noted that the resulting plots for the three NQIR(700^{o}C, T_A, t_A) are no longer straight lines as they were in Figure 100. However, it is easily discerned that dependencies upon $t^{2/3}$ are now clearly revealed to apply to all four NQIR(900/800, 500, t_A) plots over the regions of annealing times from zero up to where the dotted demarcation line has been placed in Figure 101. Finally, in all four NQIR(900/800, 500, t_A) plots significant reductions in isothermal annealing rates are clearly manifested for the longer annealing times.

---

[103] See specimen's 4005 plots of NQIR(900/800/700, 500, t_A) contained in Figure 102 for an obvious example of "crossovers" in annealing kinetics.

8.3.3.4 Specimens 4002 and 4005: Reciprocal of Fraction Remaining during NQIR(900/800/700, 500) and NQIR(700, 600) Q&A Series Treatments vs. Annealing Time [in seconds]$^{2/3}$

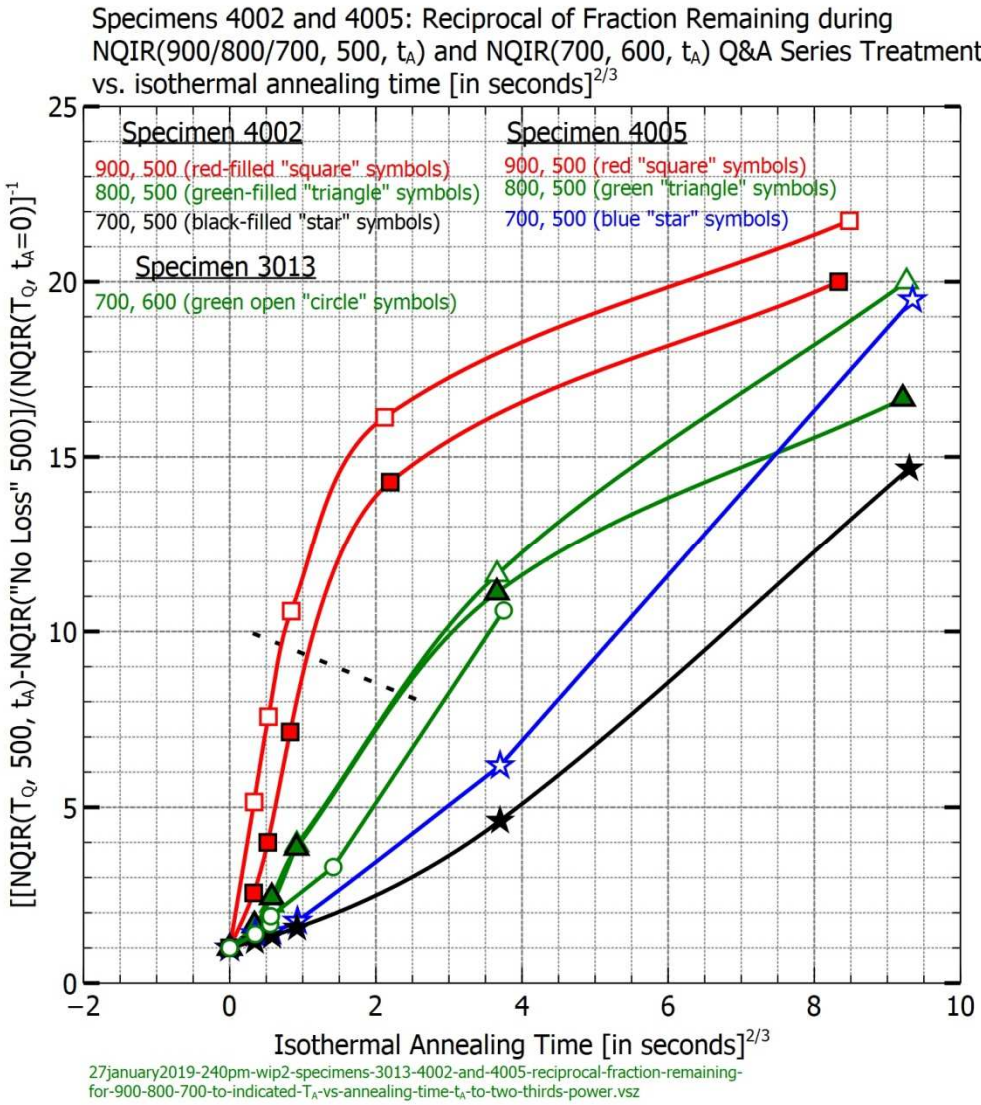

Figure 101. Specimens 4002 and 4005: Reciprocal of Fraction Remaining during NQIR(900/800/700, 500) and NQIR(700, 600) Q&A Series Treatments vs. Annealing Time [in seconds]$^{2/3}$

8.3.3.5 Specimen 4005: Comparison Log-Log Plots of NQIR(900/800/700, 500, t_A) and NQIR(900/800/700, 200, t_A) Values

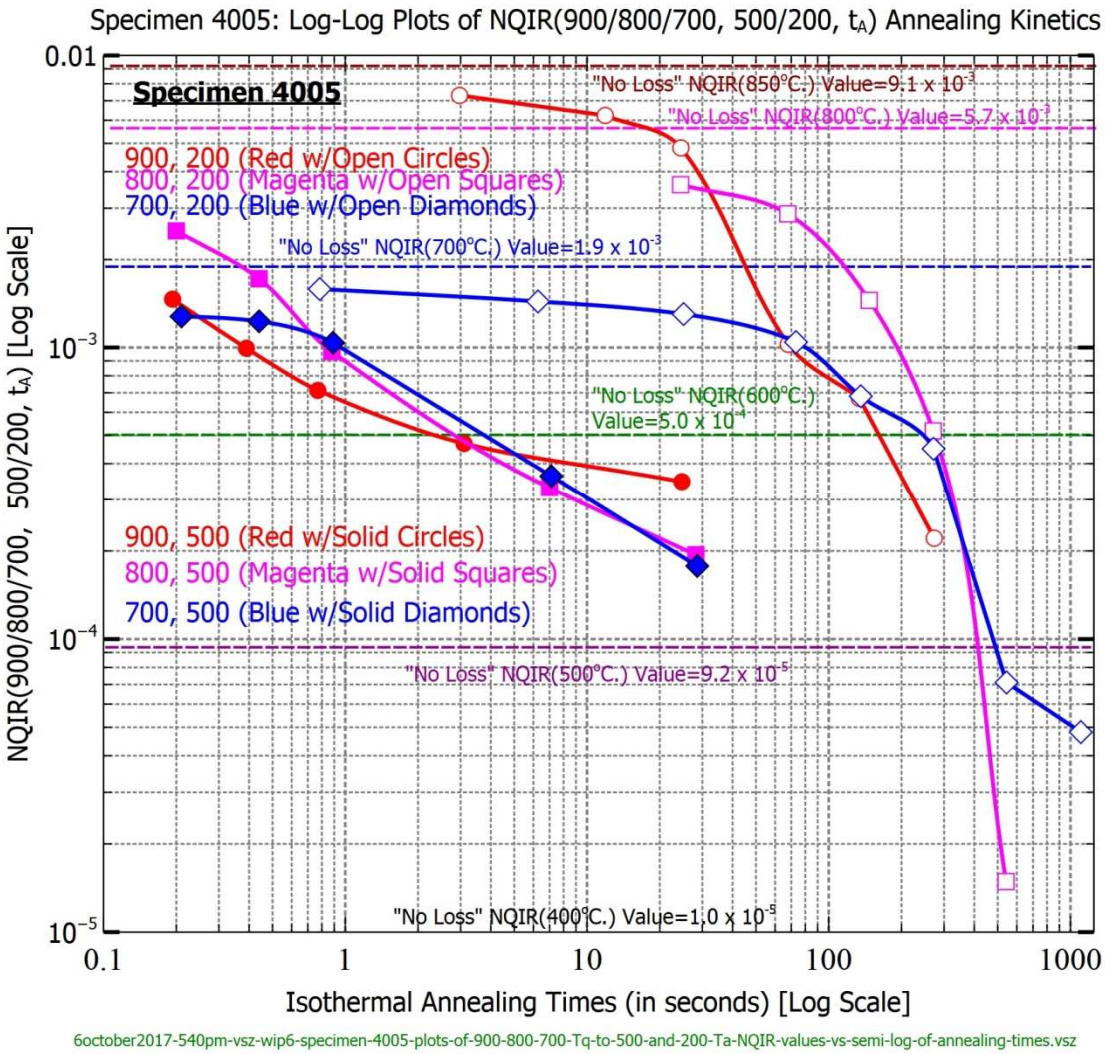

Figure 102. Specimen 4005: Comparison Log-Log Plots of NQIR(900/800/700, 500, t_A) and NQIR(900/800/700, 200, t_A) vs. Annealing Time

Note the sigmoidal shapes associated with the (900/800/700, 200, t_A) Q&A series treatments and the differing MRR levels for these Q&A series treatments.

8.3.3.6 Specimen 4005: Comparison Log-Log Plots of Fraction Remaining NQIR(900/800/700, 500, t_A)/NQIR(ST DQ from T_Q) and NQIR(900/800/700, 200, t_A)/NQIR(ST DQ from T_Q) Values

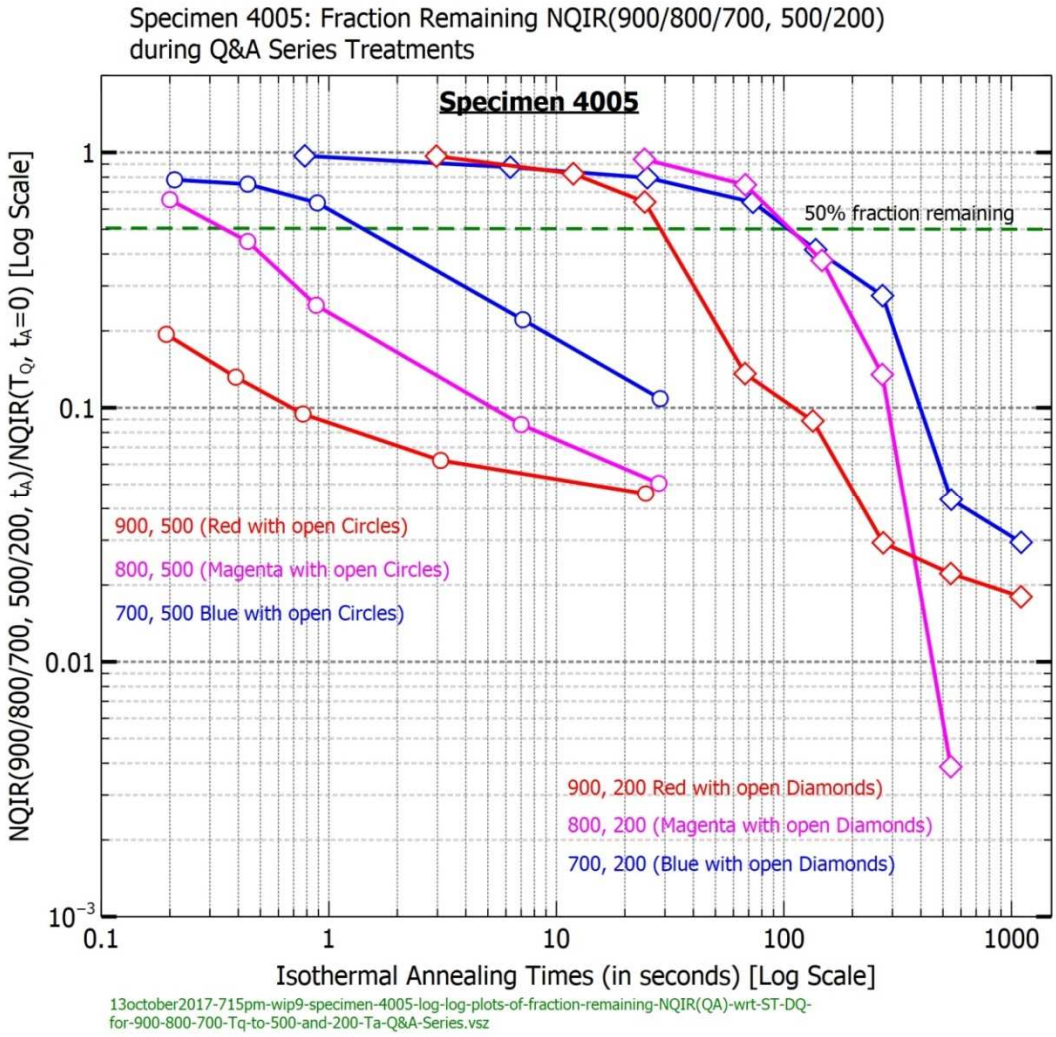

Figure 103. Specimen 4005: Comparison Log-Log Plots of Fraction Remaining NQIR(900/800/700, 500, t_A)/NQIR(ST DQ from T_Q) and NQIR(900/800/700, 200, t_A)/NQIR(ST DQ from T_Q) during Q&A Series Treatments vs. Annealing Times of up to 1106 seconds

Note that for the fraction remaining plots of the (900/800/700, 500, t_A) Q&A series treatments crossovers are either not present or are no longer obvious.

8.3.3.7 Specimen 3013: Plot of Fraction Remaining NQIR(800, 300, t_A)/NQIR(800°C ST DQ) vs. Annealing Times under 30 seconds, along with Determination of Annealing Half-time.

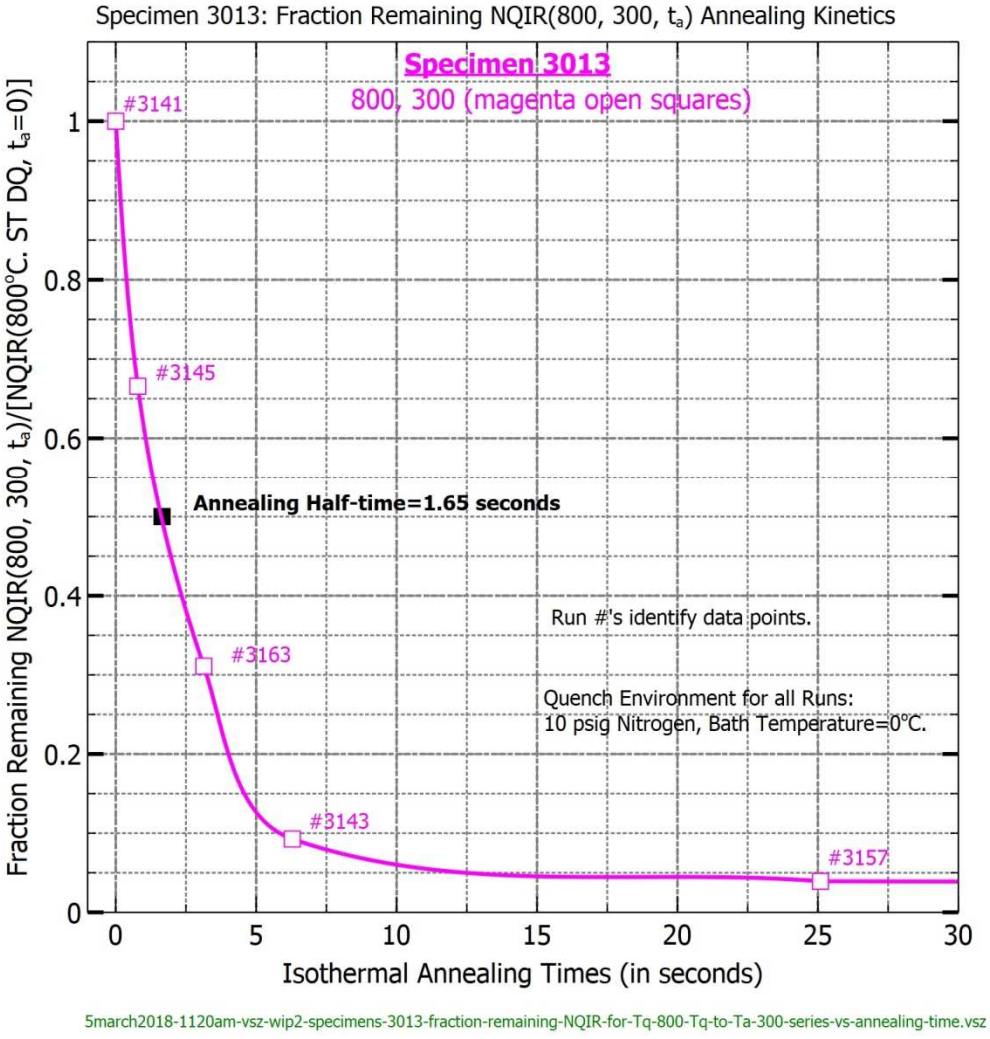

Figure 104. Specimen 3013: Plot of Fraction Remaining NQIR(800, 300, t_A)/NQIR(800°C ST DQ) vs. Annealing Times under 30 seconds, along with Determination of Annealing Half-time

8.3.3.8 Specimens 3013 and 4002: Semi-Log Plots of Fraction Remaining NQIR(800, 300, t_A)/NQIR(800°C ST DQ) Values

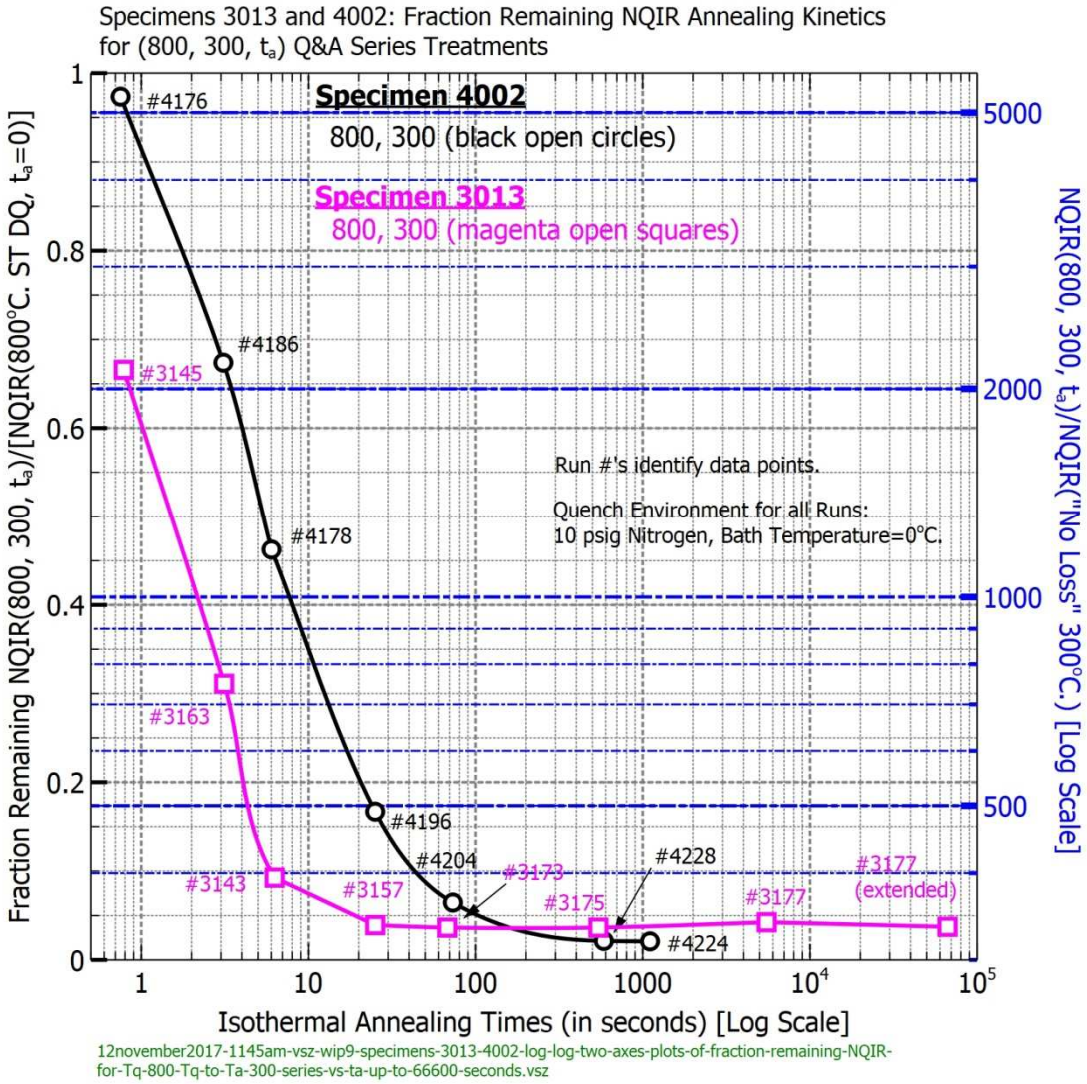

Figure 105. Specimens 3013 and 4002: Two-Axes Comparison Plots of Fraction Remaining NQIR(800, 300, t_A)/NQIR(800°C ST DQ) vs. Log of Annealing Times approaching 70,000 seconds

8.3.3.9 Specimen 4005: Plots of Fraction Remaining NQIR Annealing Kinetics during (900/800/700,500, t_A) Q&A Series Thermal Treatments

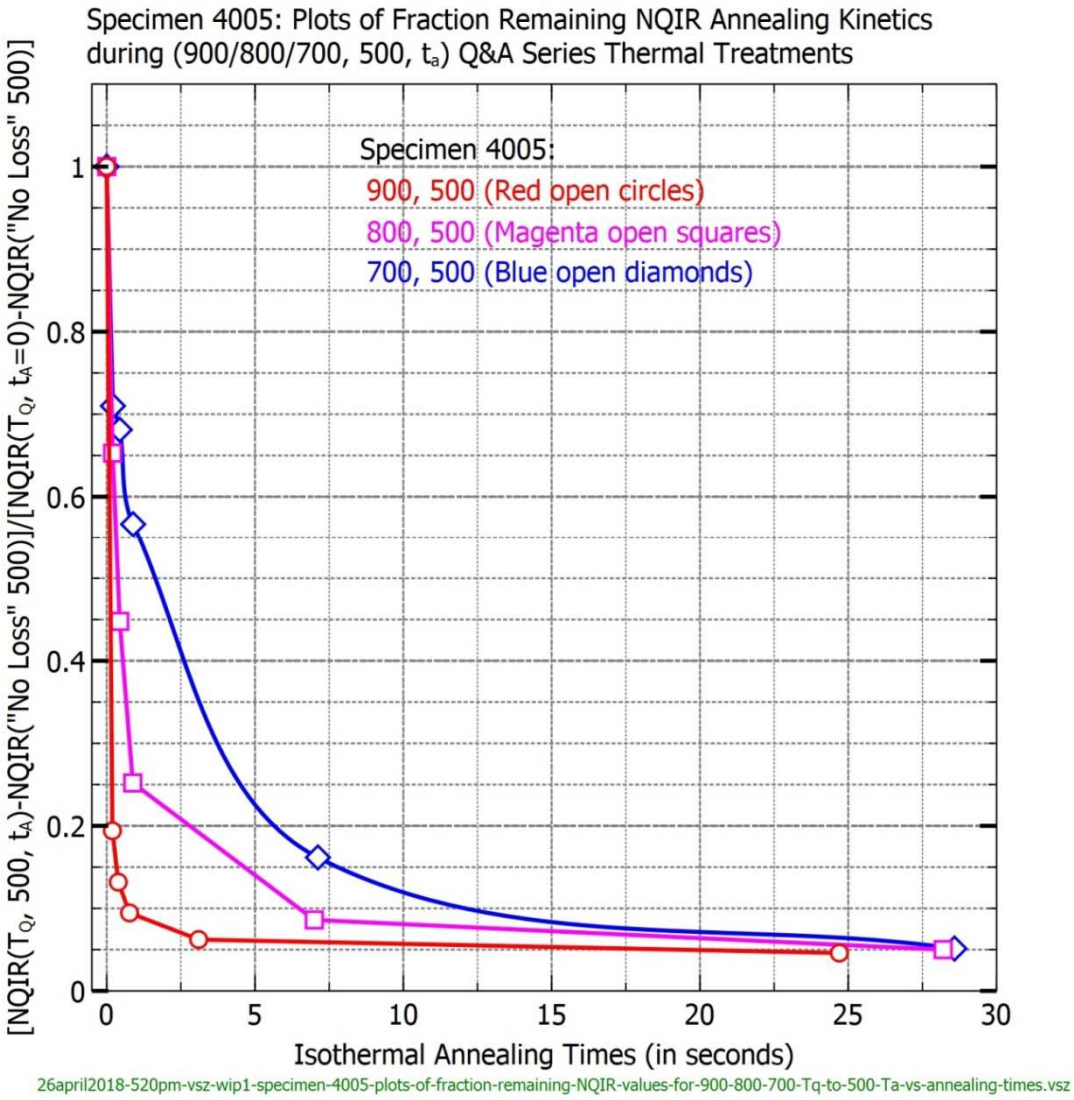

Figure 106. Specimen 4005: Plots of Fraction Remaining NQIR Annealing Kinetics during (900/800/700,500, t_A) Q&A Series Thermal Treatments

8.3.3.10 Specimens 4002 and 4005: Plots of Fraction Remaining NQIR(700, 500, t_A)/NQIR(700°C ST DQ) Values, along with Determinations of Annealing Half-times

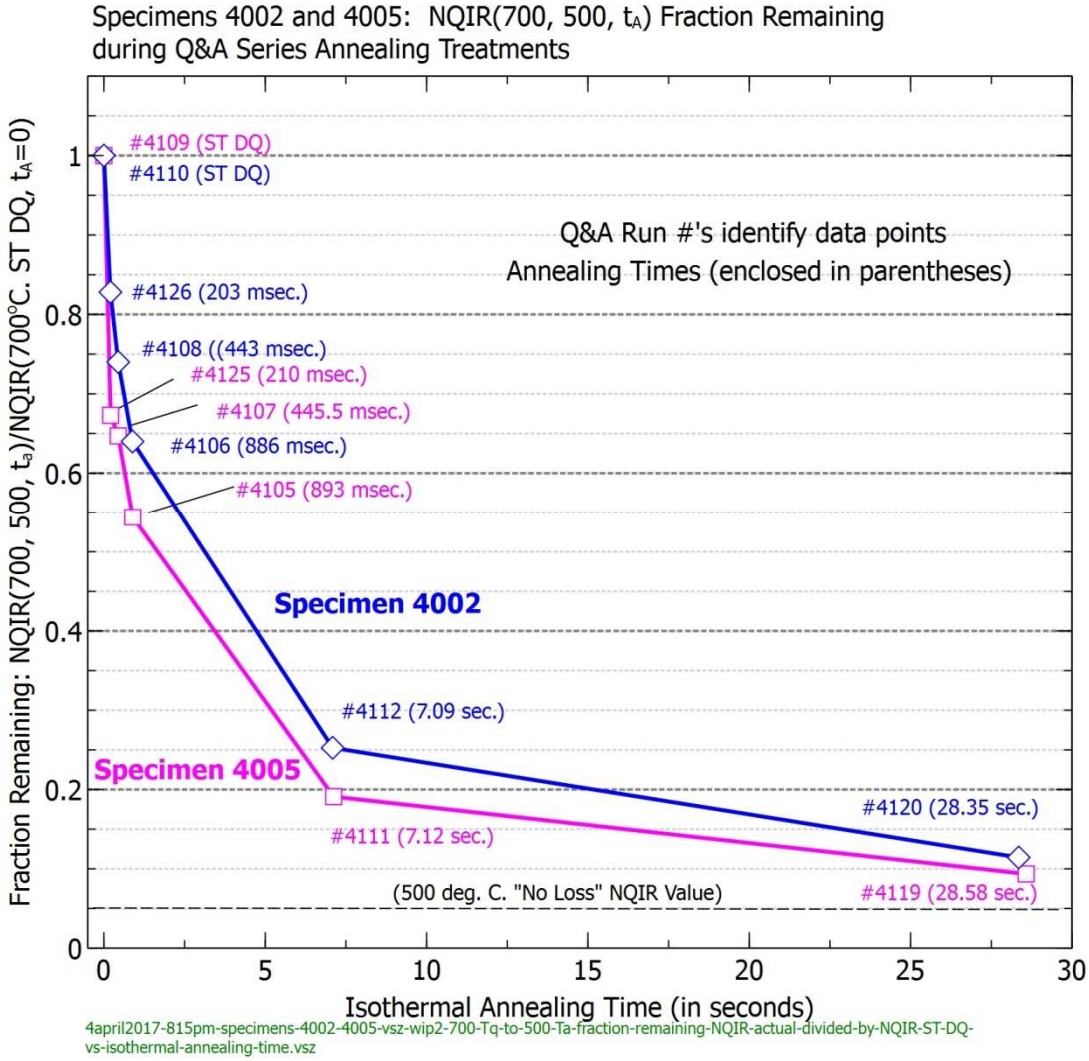

Figure 107. Specimens 4002 and 4005: Plots of Fraction Remaining NQIR(700, 500, t_A)/NQIR(700°C ST DQ) vs. Annealing Times under 30 seconds, along with Determinations of Annealing Half-times

8.3.3.11 Specimens 4002 and 4005: Semi-Log Plots of NQIR Fractions Remaining and Lost during (700, 500, t_A) Q&A Series Treatments

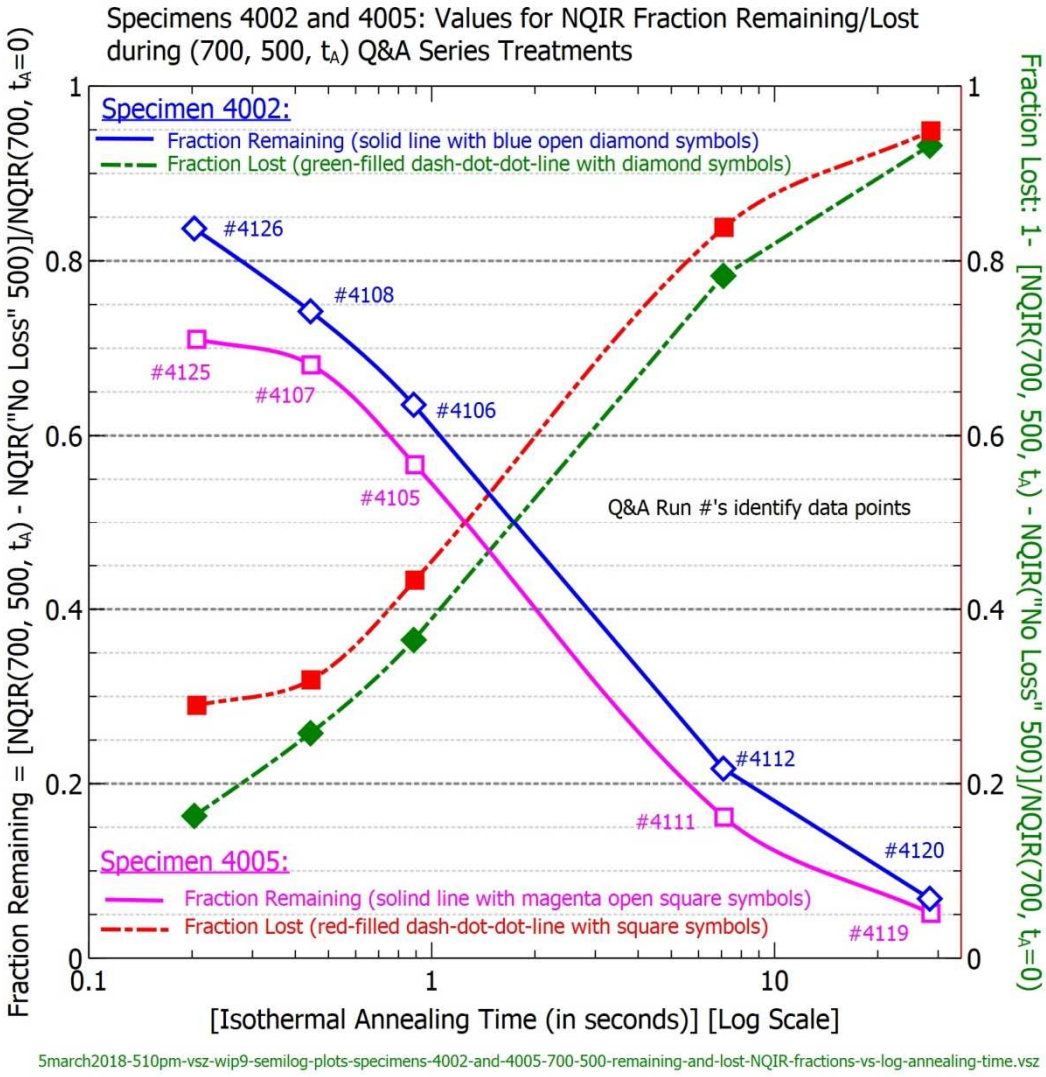

Figure 108. Specimens 4002 and 4005: Two-Axes Plots of NQIR Fractions Remaining and Lost during (700, 500, t_A) Q&A Series Treatments vs. Log of Annealing Time

8.3.3.12 Specimen 3016: Fraction Remaining NQIR(900/700, 400, t_A)/NQIR(ST DQ from T_Q) Values vs. Annealing Time$^{2/3}$

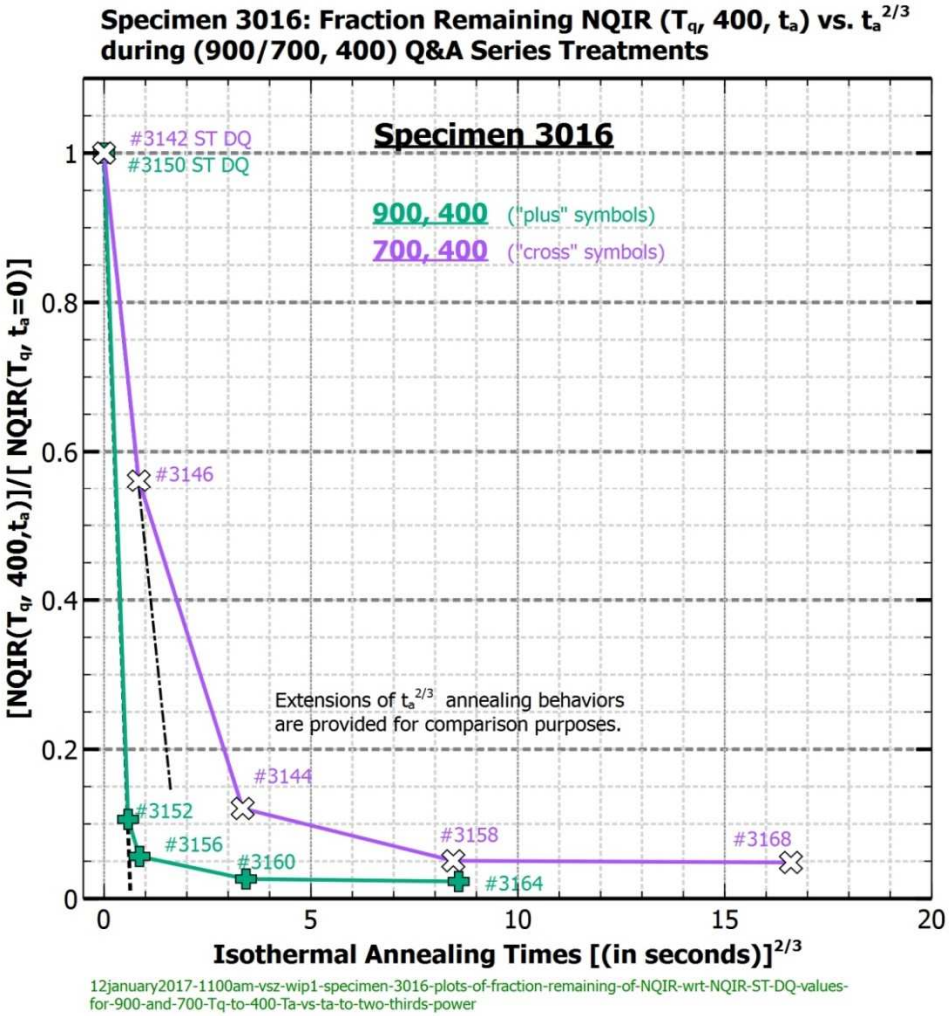

Figure 109. Specimen 3016: Fraction Remaining NQIR(900/700, 400, t_A)/NQIR(ST DQ from T_Q) during Q&A Series Treatments vs. (Annealing Time)$^{2/3}$

8.3.3.13 Specimens 4002 and 4005: Fraction Remaining NQIR(900, 400, t_A)/NQIR(ST DQ from T_Q) Values vs. Annealing Time, along with Determinations of Annealing Half-times

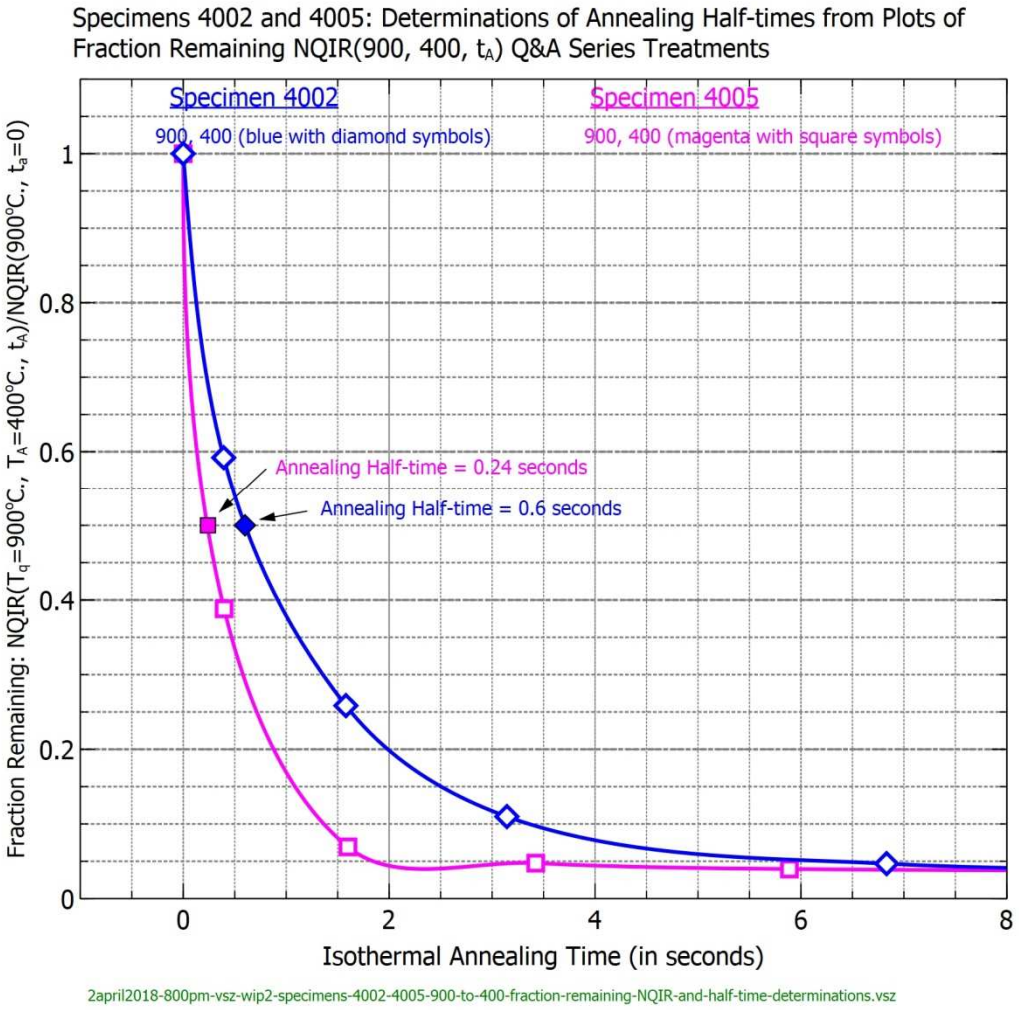

Figure 110. Specimens 4002 and 4005: Fraction Remaining NQIR(900, 400, t_A)/NQIR(ST DQ from T_Q) during Q&A Series Treatments vs. (Annealing Time), along with Determinations of Annealing Half-times

8.3.3.14 Specimens 4002 and 4005: Comparison Log-Log Plots of NQIR(700, 500, t_A)/NQIR(700°C ST DQ) Values

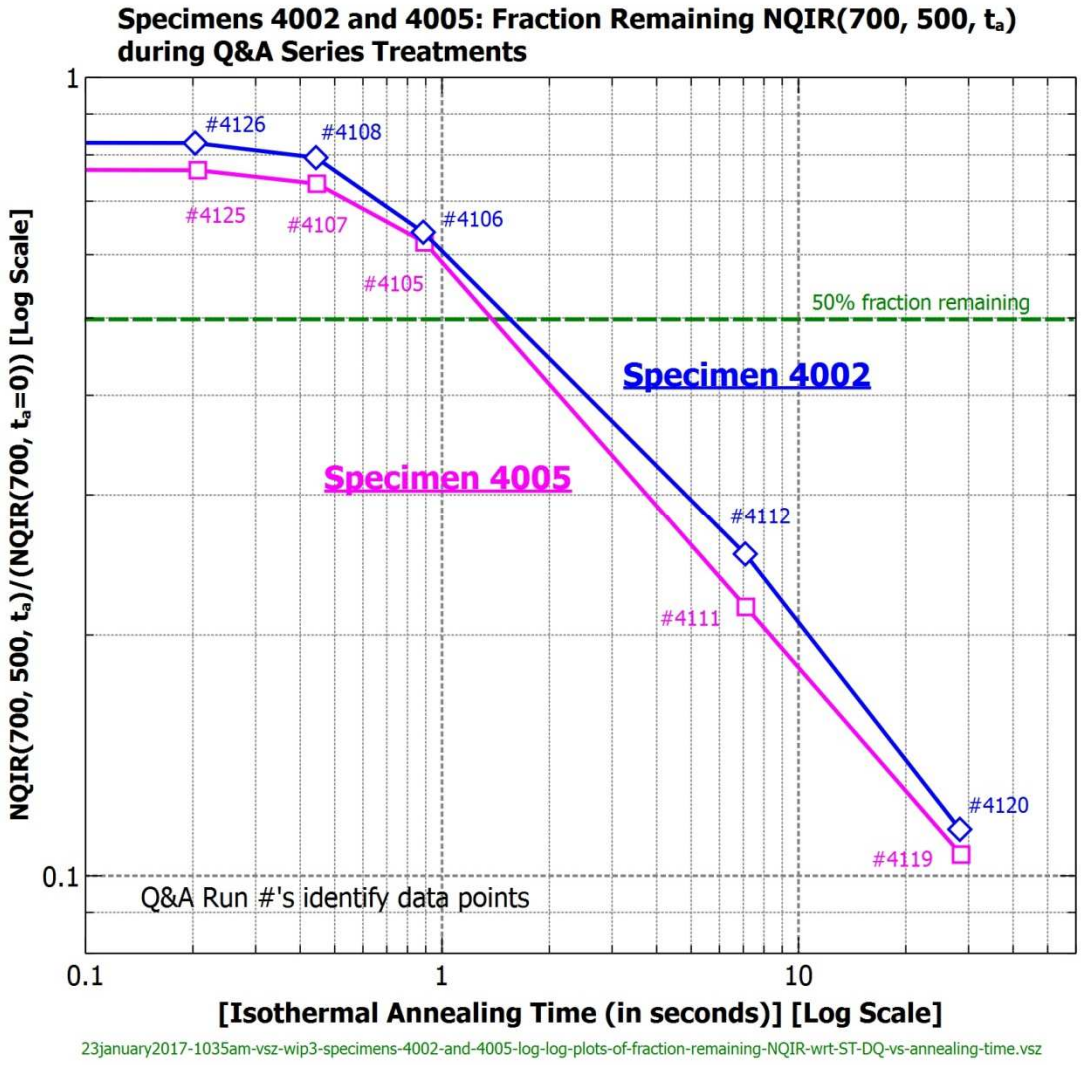

Figure 111. Specimens 4002 and 4005: Comparison Log-Log Plots of NQIR(700, 500, t_A)/NQIR(700°C ST DQ) during Q&A Series Treatments vs. Annealing Times of up to 30 seconds

8.3.3.15 Specimens 4002 and 4005: Comparison Log-Log Plots of NQIR(700, 500, t_A)/NQIR(ST DQ from 700°C) Values vs. (Annealing Time)$^{2/3}$

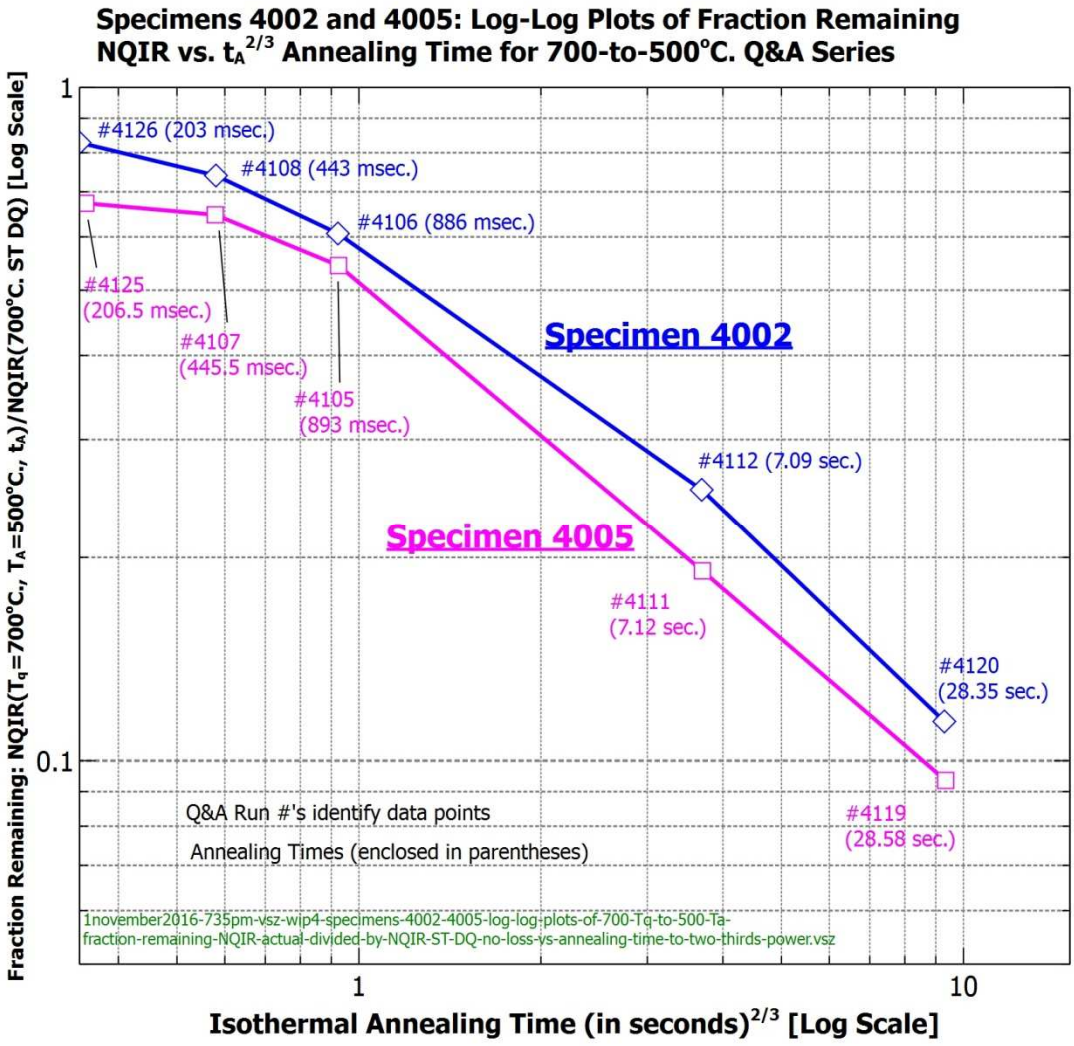

Figure 112. Specimens 4002 and 4005: Comparison Log-Log Plots of NQIR(700, 500, t_A)/NQIR(ST DQ from 700°C) vs. (Annealing Time)$^{2/3}$

8.3.3.16 Semi-log Plots of fraction remaining NQIR(900/800/700, 300, t_A) Values vs. Isothermal Annealing Time

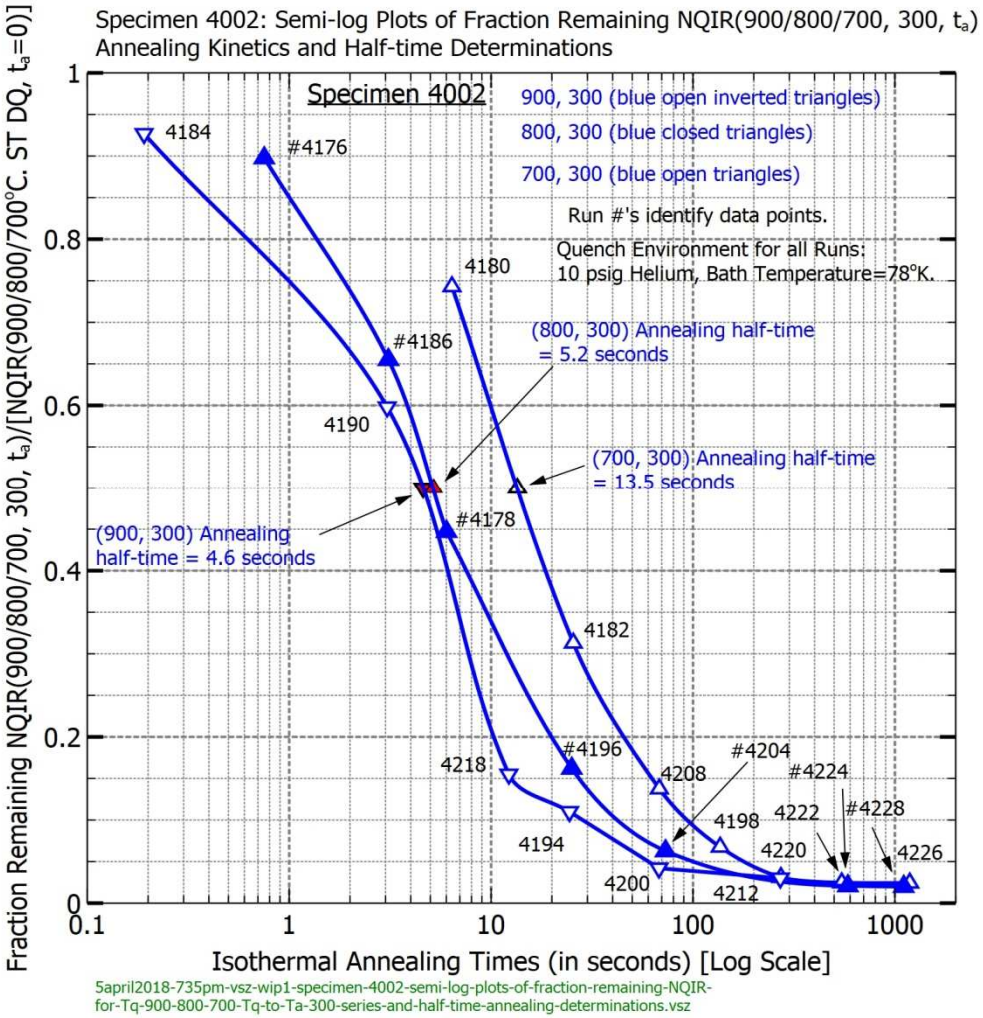

Figure 113. Specimen 4002: Semi-log Plots of fraction remaining NQIR(900/800/700, 300, t_A) Values vs. Isothermal Annealing Time

8.3.3.17 Specimen 4002: Plot of Fraction Remaining NQIR(500, 150, t_A)/NQIR(500°C ST DQ) Values

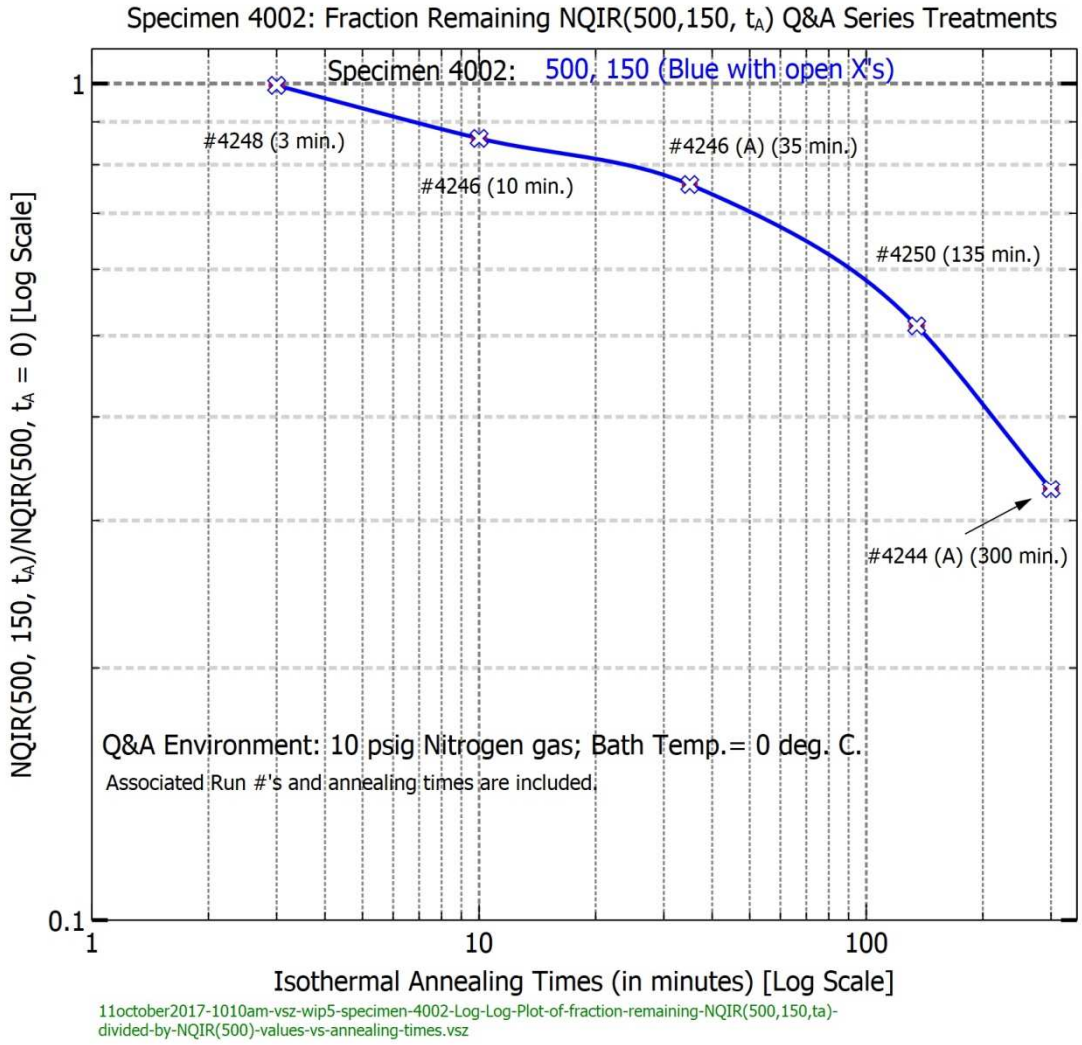

Figure 114. Specimen 4002: Plot of Fraction Remaining NQIR(500, 150, t_A)/NQIR(500°C ST DQ) vs. Annealing Time

8.3.4 Some Specific Determinations made from Analyses of Isothermal Annealing Half-Time Plots

This sub-section presents 17 independent sets of plots that focus on addressing analyses of annealing kinetics that not only establish the half-time annealing points associated with specific Q&A series treatments but also indicate what extended anneals performed to well beyond the respective half-time points reveal for further analyses.

Besides Figures 83, 95, 98, 104, 107, and 110 presented earlier, numerous additional examples of NQIR(T_Q, T_A, t_A) Q&A series plots that yielded the associated annealing half-times are illustrated in Figures 115 through 130.

8.3.4.1 Specimen 4005: Annealing Half-time Determination from a Plot of an NQIR(900, 700, t_A) Q&A Series Treatment

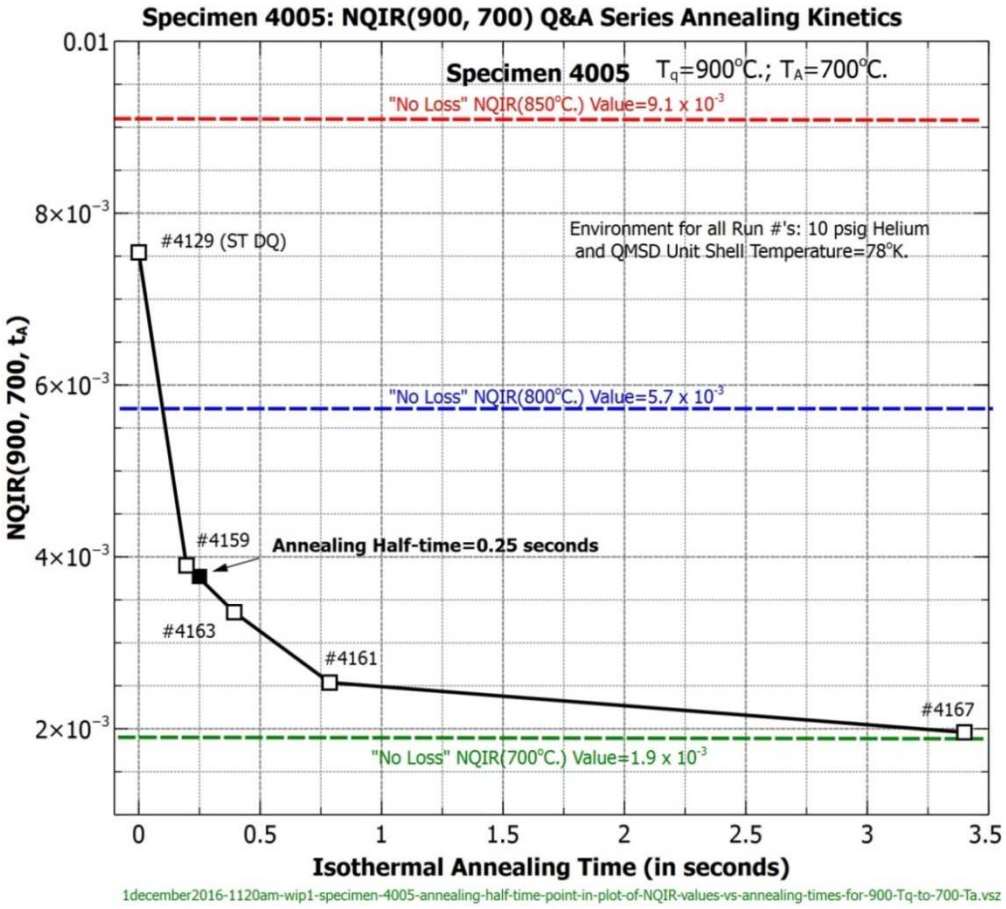

Figure 115. Specimen 4005: Annealing Half-time Determination from Plot of an NQIR(900, 700, t_A) Q&A Series Treatment vs. Annealing Times of less than 4 seconds

Note that the asymptotic value approaches "No Loss" NQIR(700°C) in Figure 115 in less than 3.5 seconds of isothermal annealing time.

8.3.4.2 Specimen 4002: Semi-Log Plot of NQIR(900, 700, t_A) Annealing Kinetics and Determination of Annealing Half Time

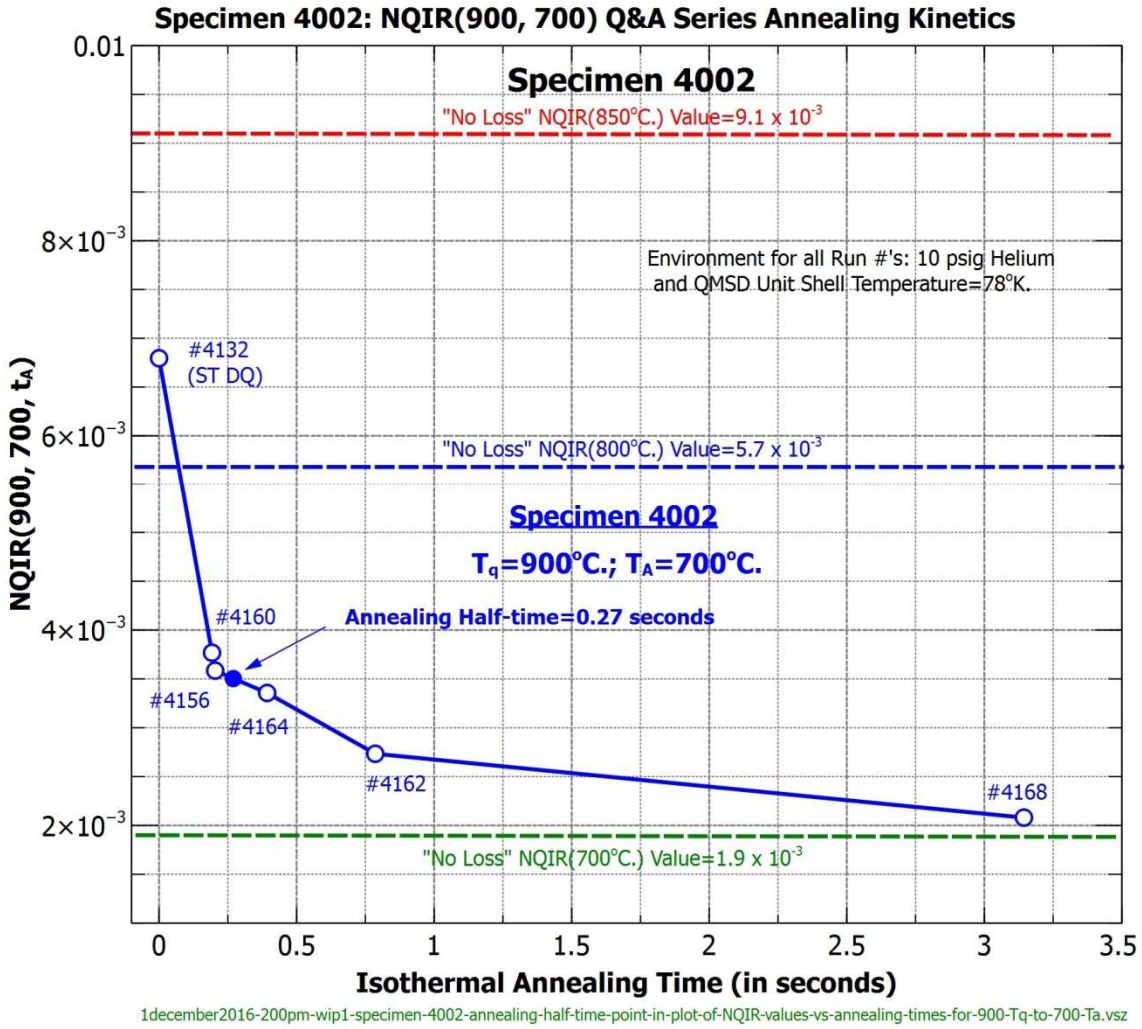

Figure 116. Specimen 4002: Semi-Log Plot of NQIR(900, 700, t_A) Annealing Kinetics and Determination of Annealing Half Time

8.3.4.3 Specimen 3016: Annealing Half-time Determinations from Plots of NQIR(900/700, 400, t_A) Q&A Series Treatments

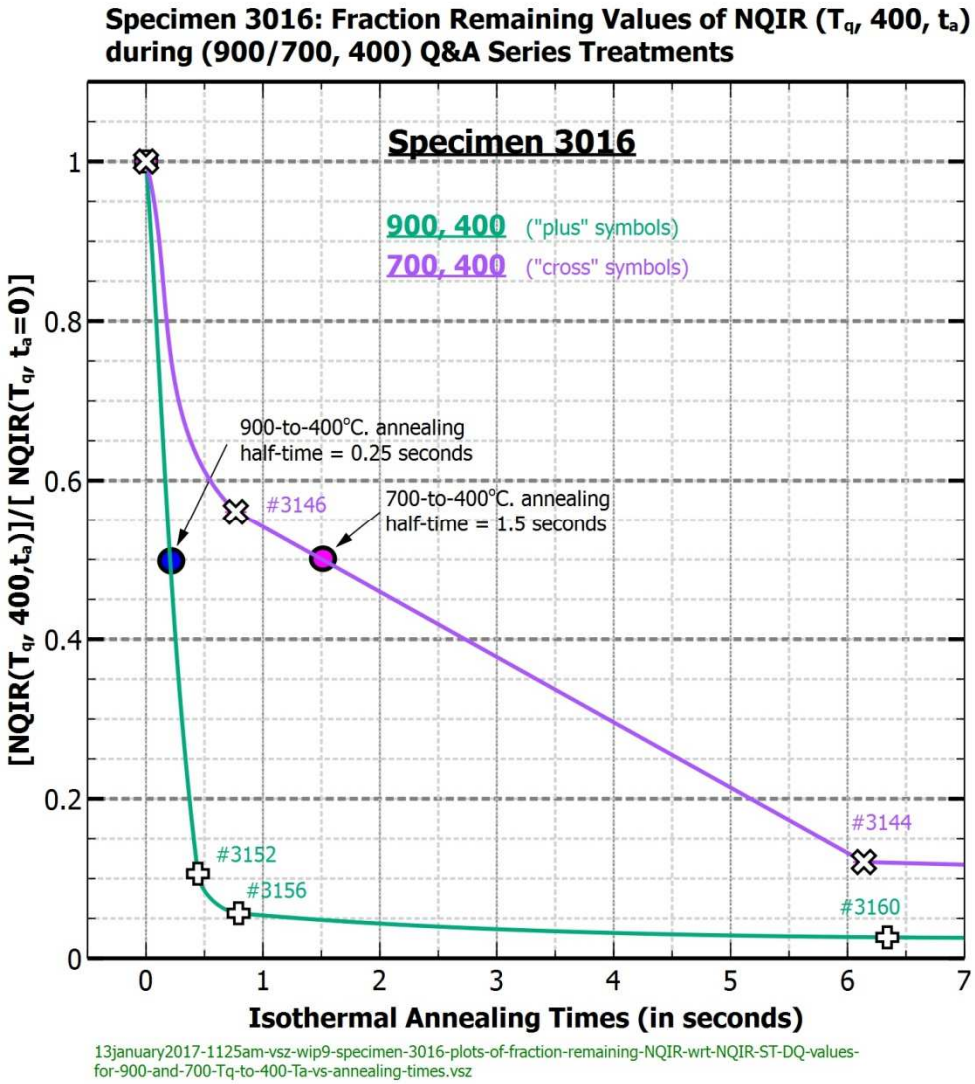

Figure 117. Specimen 3016: Annealing Half-time Determinations from Plots of NQIR(900/700, 400, t_A) Q&A Series Treatments vs. Annealing Times of less than 7 seconds

8.3.4.4 Specimen 4005: Plots of Fraction Remaining NQIR(900/800/700, 500, t_A) and Determinations of Respective Half-time Annealing Values

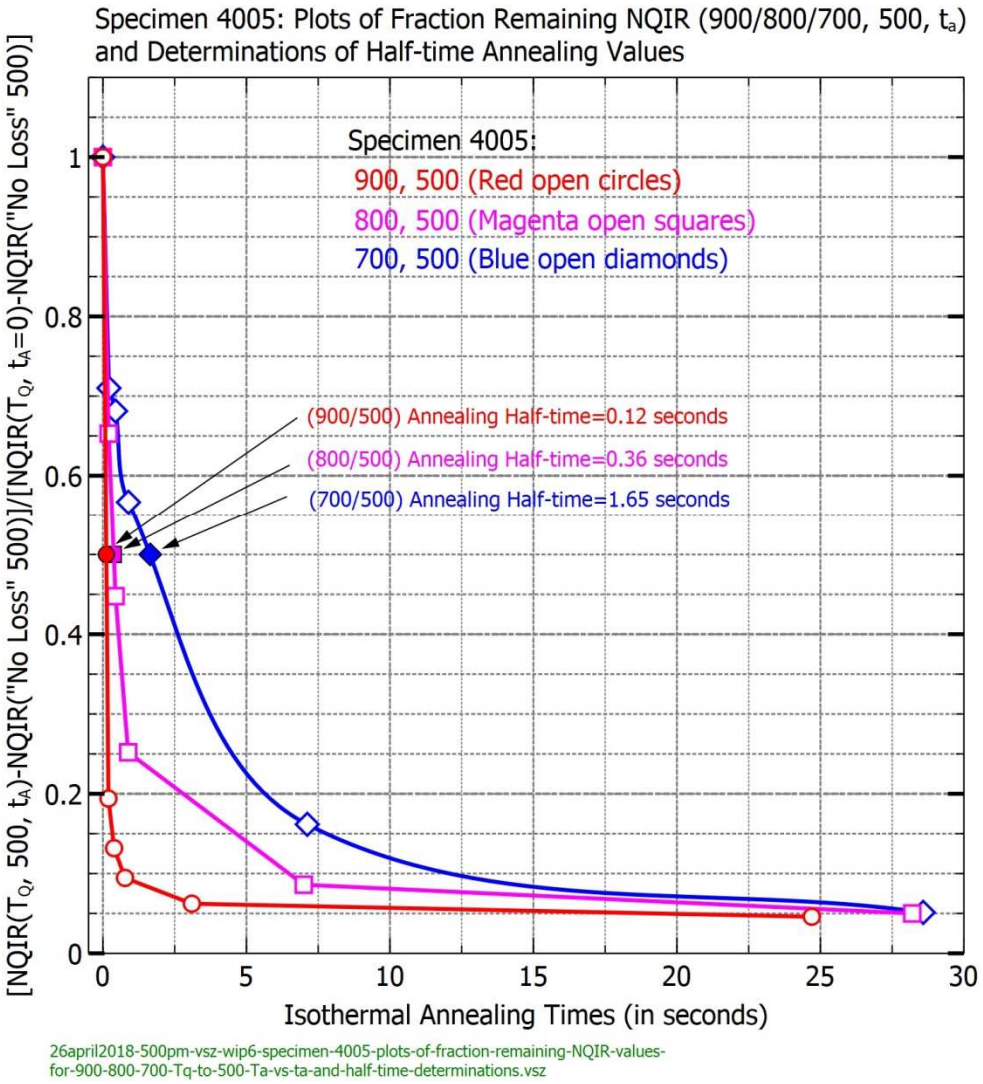

Figure 118. Specimen 4005: Plots of Fraction Remaining NQIR(900/800/700, 500, t_A) and Determinations of Respective Half-time Annealing Values

8.3.4.5 Specimen 3016: Annealing Half-time Determination from a Two-Axes Plot of an NQIR(800, 400, t_A) Q&A Series Treatment vs. Annealing Times of less than one second.

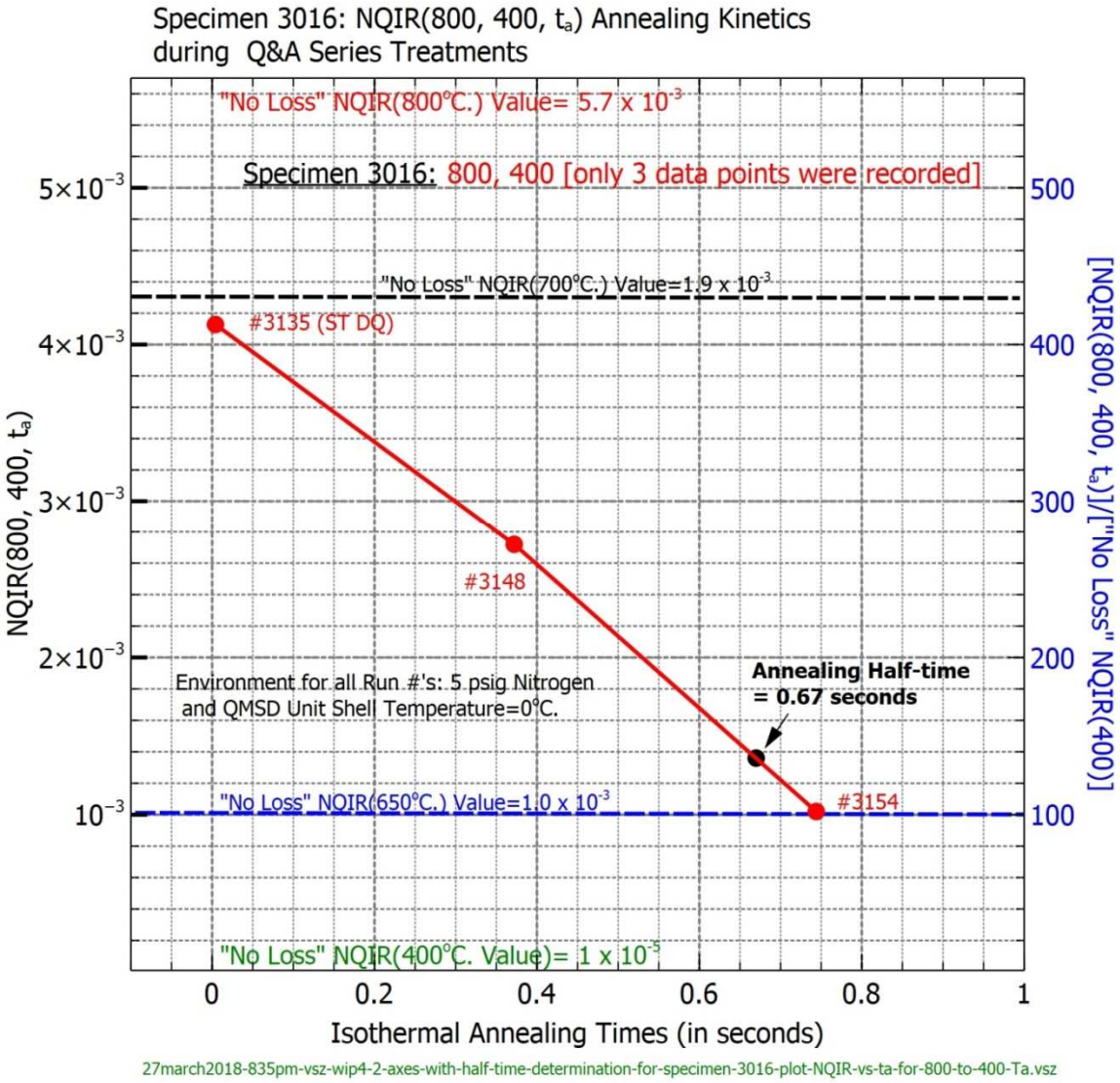

Figure 119. Specimen 3016: Annealing Half-time Determination from a Two-Axes Plot of an NQIR(800, 400, t_A) Q&A Series Treatment vs. Annealing Times of less than one second.

8.3.4.6 Specimen 4002: Annealing Half-time Determination from a Plot of an NQIR(800, 300, t_A) Q&A Series Treatment vs. Annealing Times of up to ten seconds

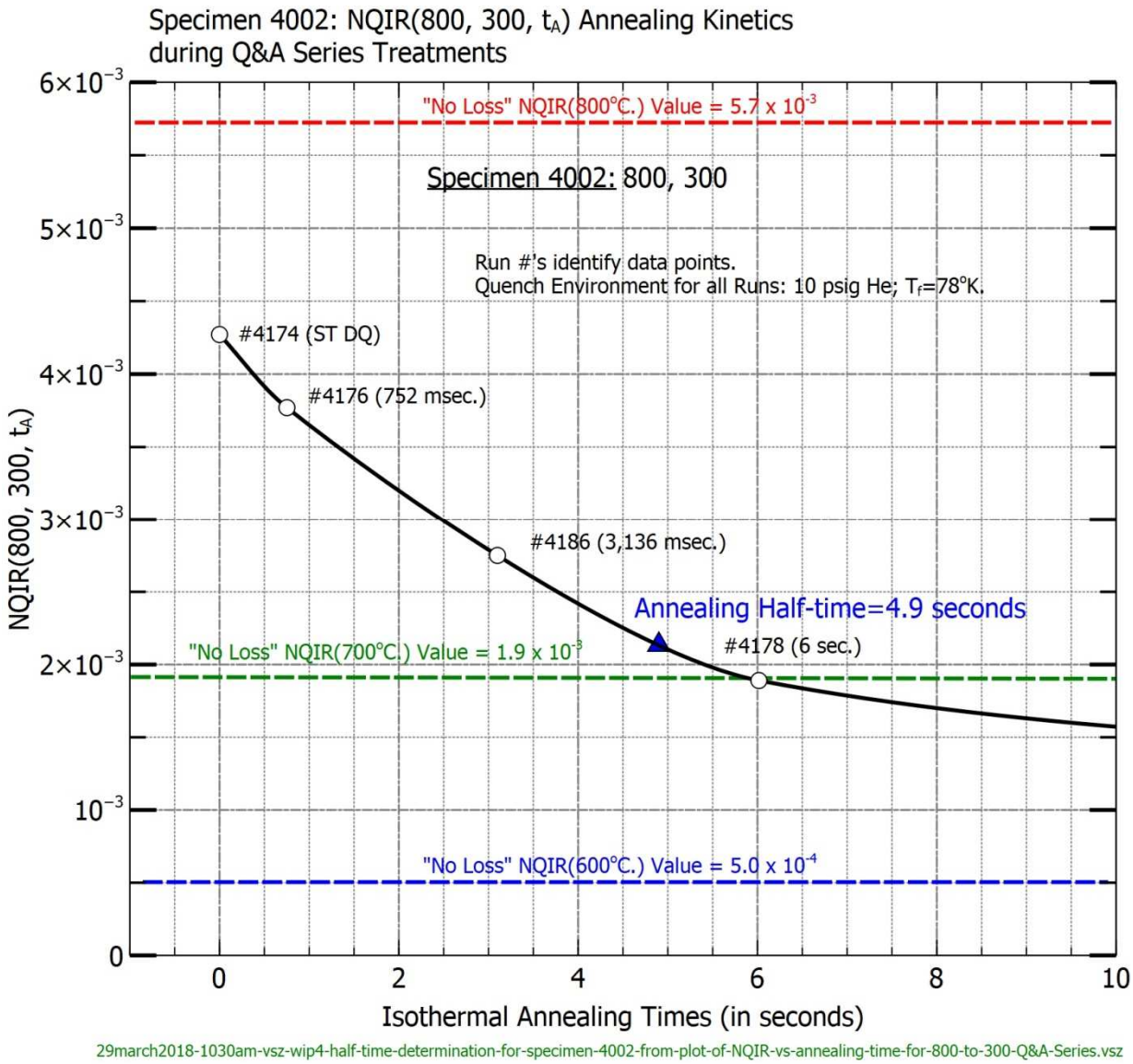

Figure 120. Specimen 4002: Annealing Half-time Determination from a Plot of an NQIR(800, 300, t_A) Q&A Series Treatment vs. Annealing Times of up to ten seconds

8.3.4.7 Specimens 3012 and 3013: Annealing Half-time Determinations from Plots of NQIR(700, 600, t_A) Q&A Series Treatments

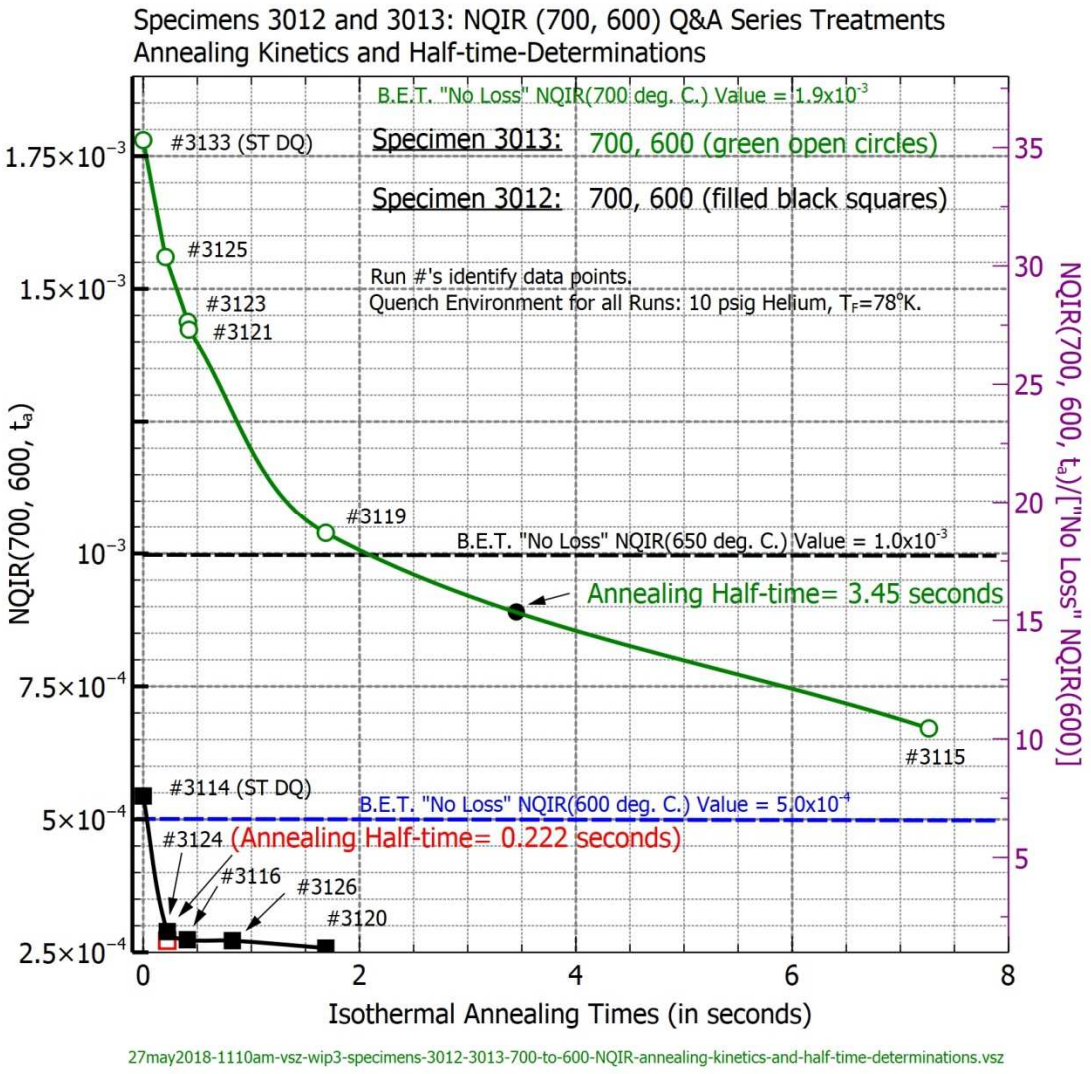

Figure 121. Specimens 3012 and 3013: Annealing Half-time Determinations from Plots of NQIR(700, 600, t_A) Q&A Series Treatments

8.3.4.8 Specimen 3013: Annealing Half-time Determination from a Plot of an NQIR(700, 500, t_A) Q&A Series Treatment

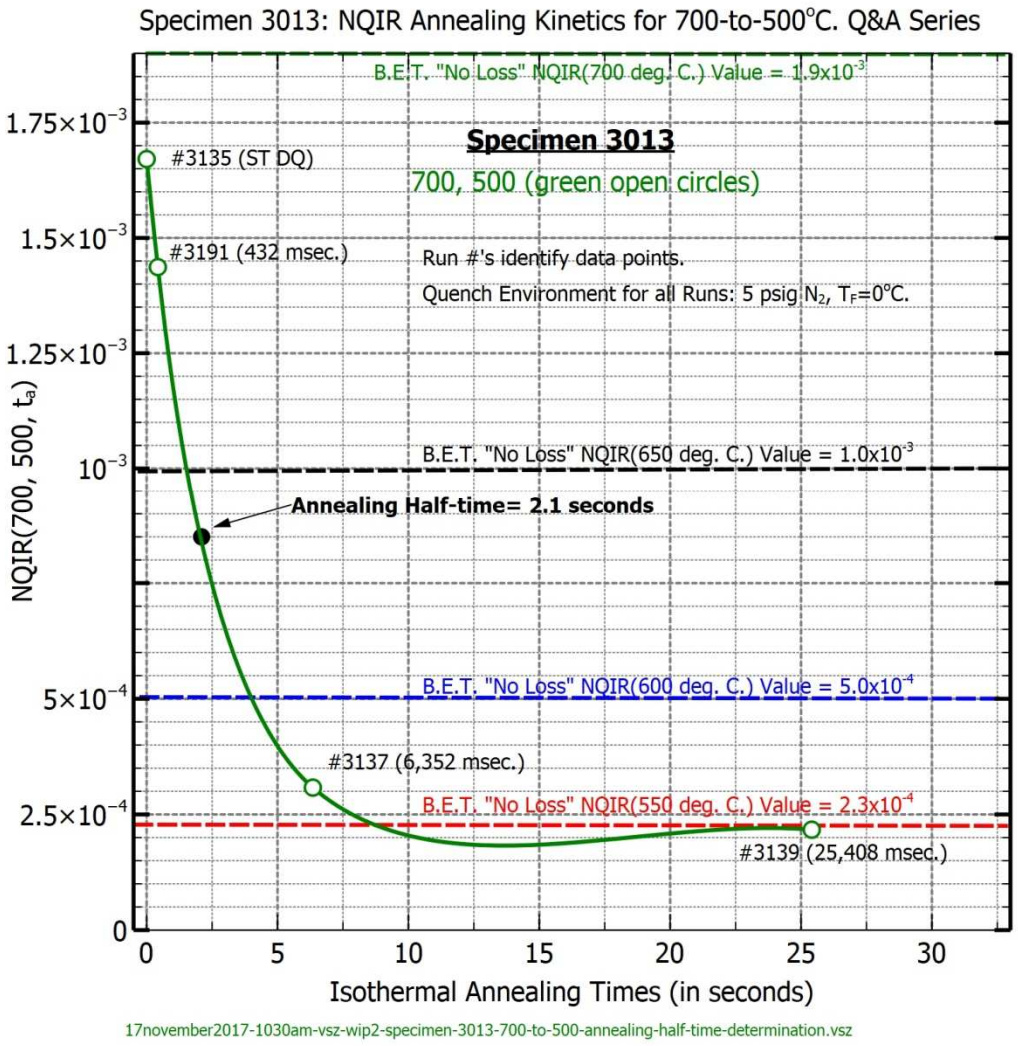

Figure 122. Specimen 3013: Annealing Half-time Determination from a Plot of an NQIR(700, 500, t_A) Q&A Series Treatment vs. Annealing Times of less than 30 seconds

8.3.4.9 Specimens 4002 and 4005: Plots of NQIR(700, 500, t_A) / NQIR(700°C ST DQ) Values vs. (Annealing Time)$^{2/3}$ (with associated half-times for each specimen included)

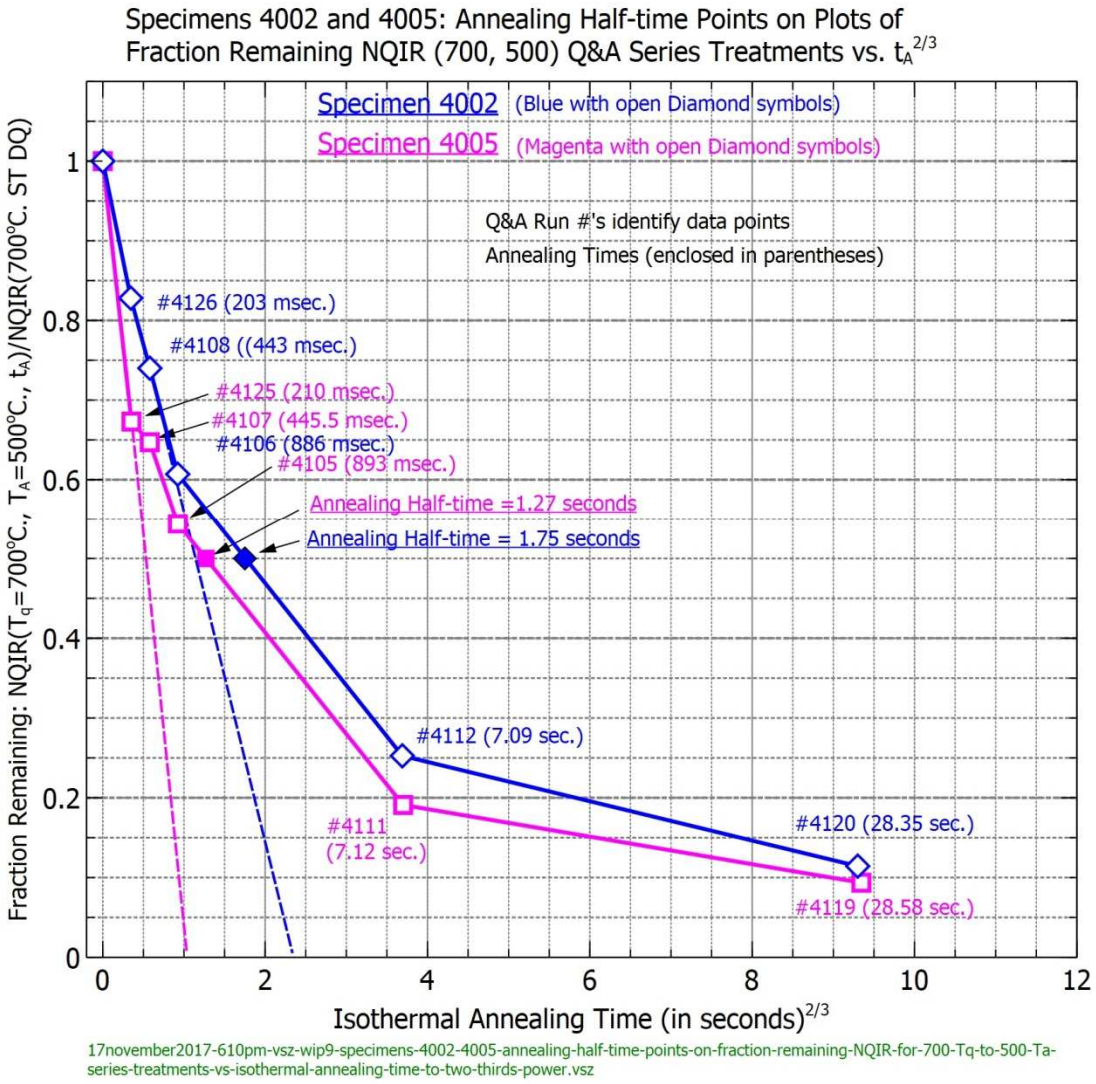

Figure 123. Specimens 4002 and 4005: Plots of NQIR(700, 500, t_A) / NQIR(700°C ST DQ) Values vs. (Annealing Time)$^{2/3}$ (with associated half-times for each specimen included)

8.3.4.10 Specimen 3013: Annealing Half-time Determination from a Plot of NQIR(700, 300, t_A) Q&A Series Treatment

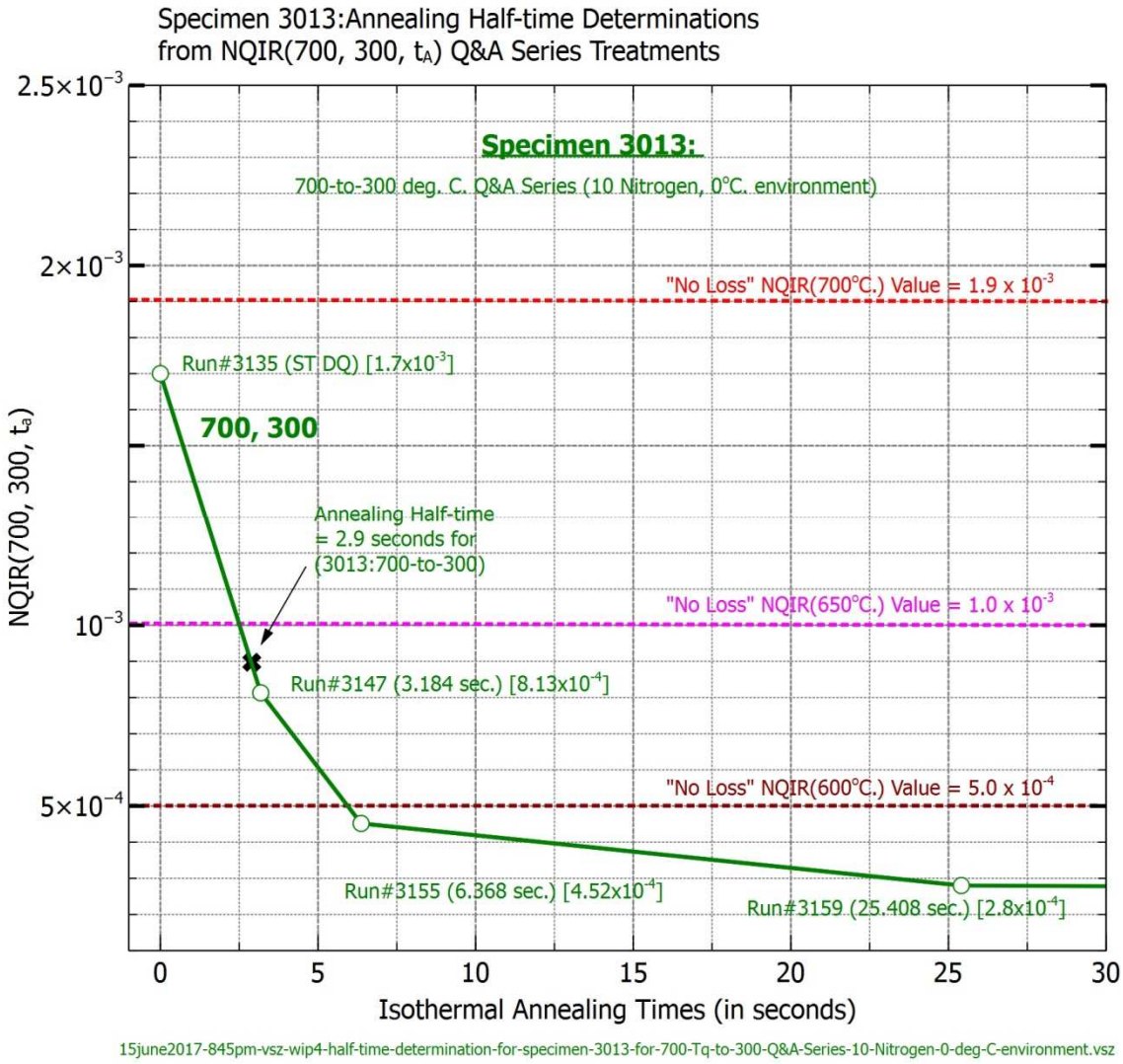

Figure 124. Specimen 3013: Annealing Half-time Determination from a Plot of NQIR(700, 300, t_A) Q&A Series Treatment vs. Annealing Times under 30 seconds

8.3.4.11 Specimen 3016: Annealing Half-time Point Determination from a Plot of an NQIR(700, 400, t_A) Q&A Series Treatment

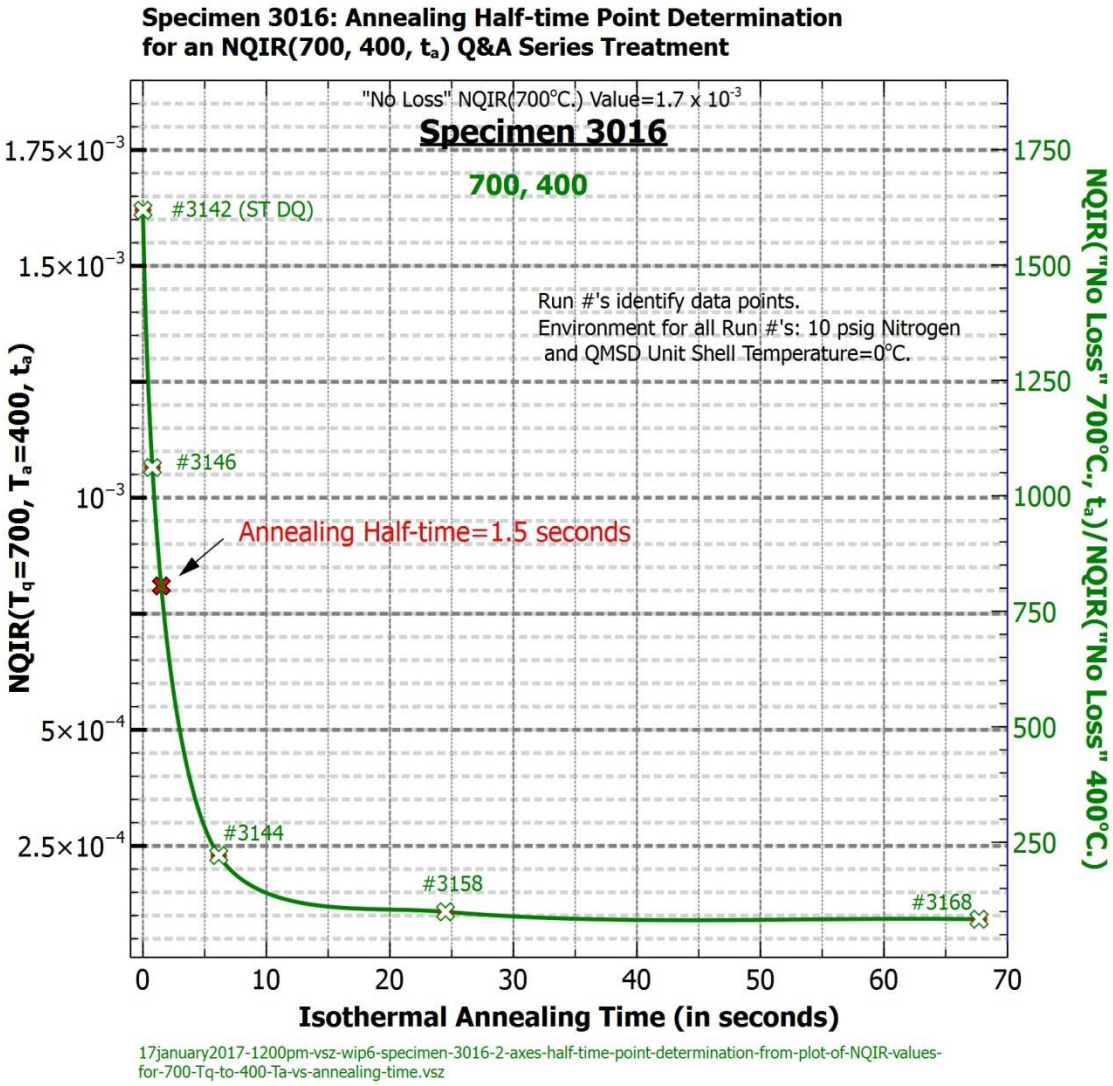

Figure 125. Specimen 3016: Two-Axes Annealing Half-time Point Determination from a Plot of an NQIR(700, 400, t_A) Q&A Series Treatment vs. Annealing Time under 70 seconds

8.3.4.12 Specimens 3012 and 3013: Annealing Half-time Determinations from Plots of NQIR(700, 200, t_A) and NQIR(700, 300, t_A) Q&A Series Treatments

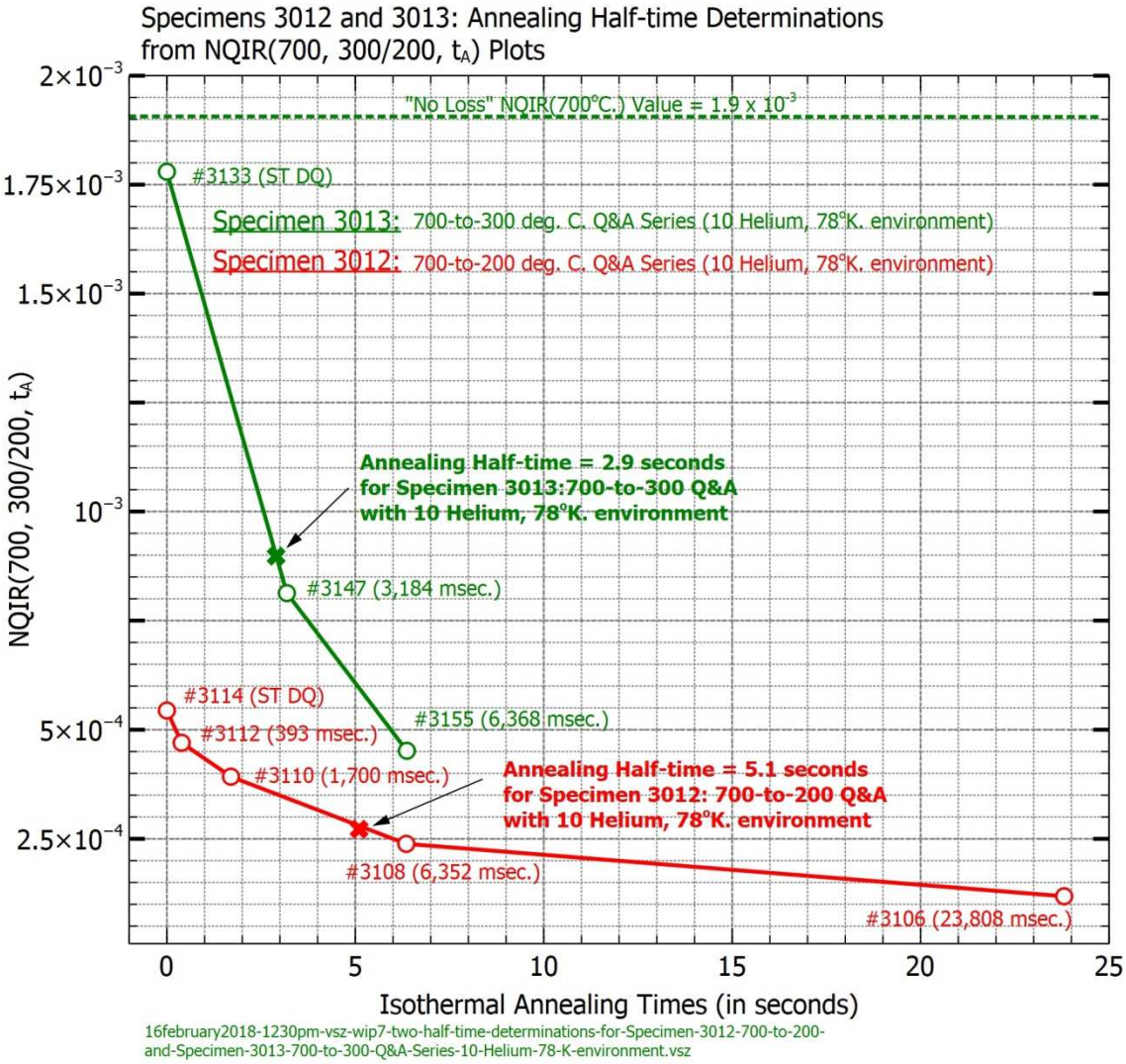

Figure 126. Specimens 3012 and 3013: Annealing Half-time Determinations from Plots of NQIR(700, 200, t_A) and NQIR(700, 300, t_A) during Q&A Series Treatments vs. Annealing Times of less than 25 seconds

8.3.4.13 Specimen 3013: Semi-Log Plot of NQIR(700, 200, t_A) during Q&A Series Treatments

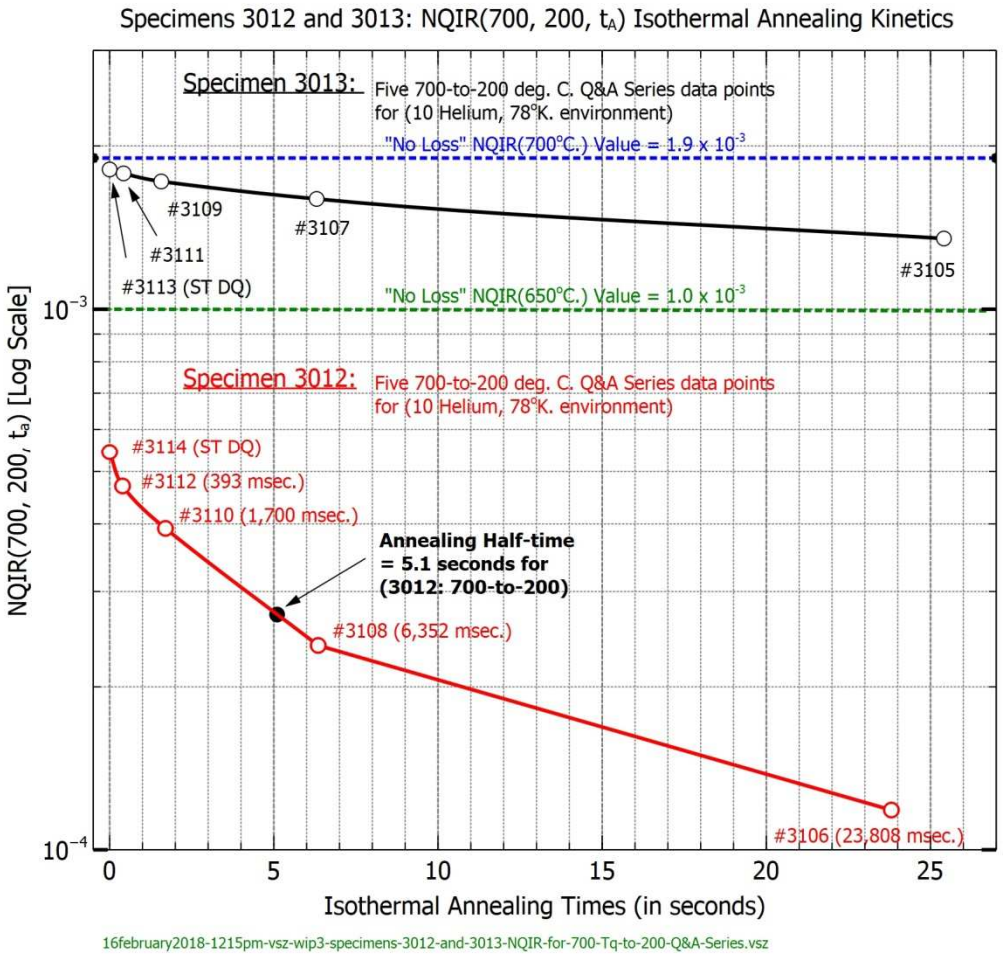

Figure 127. Specimens 3012 and 3013: Plots of NQIR(700, 200, t_A) during Q&A Series Treatments vs. Annealing Times (with an annealing half-time of 5.1 seconds determined for specimen 3012)

Figure 127 reveals an annealing half-time of 5.1 seconds for specimen 3012, whereas for specimen 3013 an annealing half-time was not yet reached even after 25 seconds of isothermal annealing at 200°C.

8.3.4.14 Specimen 3013: Half-time Determination from a Plot of Annealing Kinetics during NQIR(700, 200, t_A) Q&A Series Treatments

In Figure 128 an annealing half-time estimate of 78 seconds for specimen 3013 was established based on a smooth merging of data involving two separate sets of NQIR(700, 200, t_A) treatments (one with helium and the second with nitrogen as the gas quench environment).

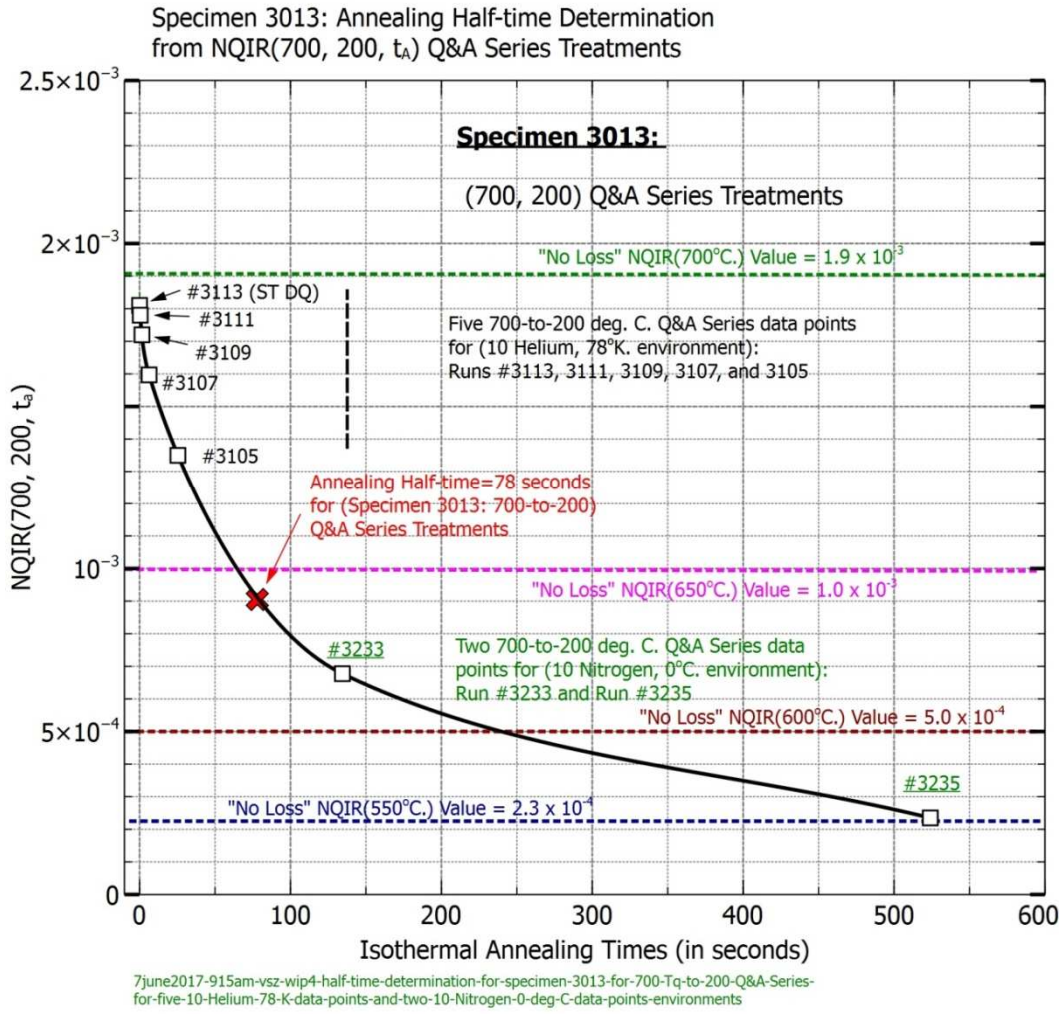

Figure 128. Specimen 3013: Half-time Determination from a Plot of Annealing Kinetics during NQIR(700, 200, t_A) Q&A Series Treatments that involved use of helium and nitrogen gas quench environments.

8.3.4.15 Specimen 3018: Determination of Annealing Half-time from a Plot of an NQIR(500, 300, t_A) Q&A Series Treatment

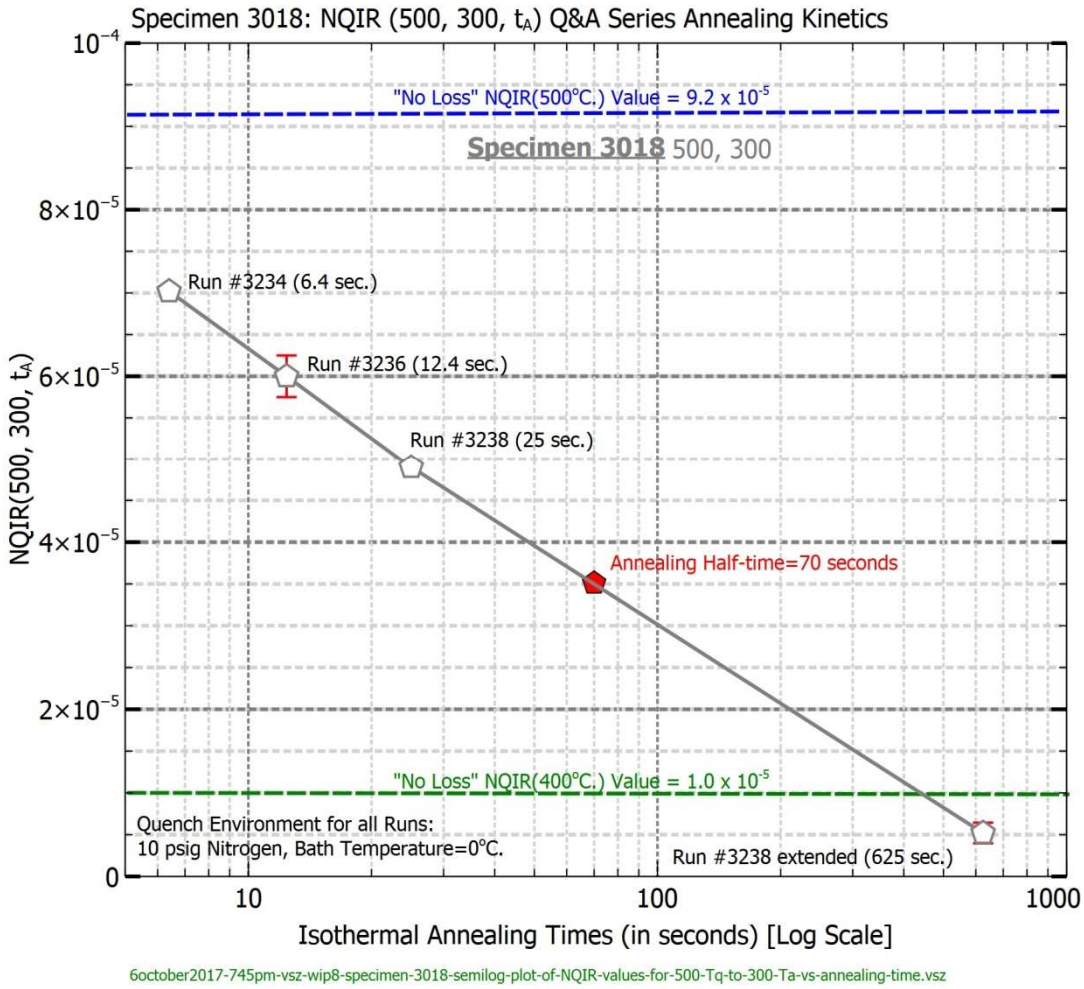

Figure 129. Specimen 3018: Plot of Annealing Kinetics during an NQIR(500, 300, t_A) Q&A Series Treatment vs. Annealing Times up to 625 seconds (with an Annealing Half-time point of 70 seconds)

Figure 129 includes specimen 3018's NQIR(500, 300, t_A=685 sec.) data point whose value was 5.2×10^{-6}. This equates to a "No-Loss" NQIR(375°C) and suggests minimal likelihood for vacancy clustering occurred during this annealing treatment.

.

8.3.4.16 Specimen 4002: Determination of Annealing Half-time from a Plot of an NQIR(500, 150, t_A) Q&A Series Treatment

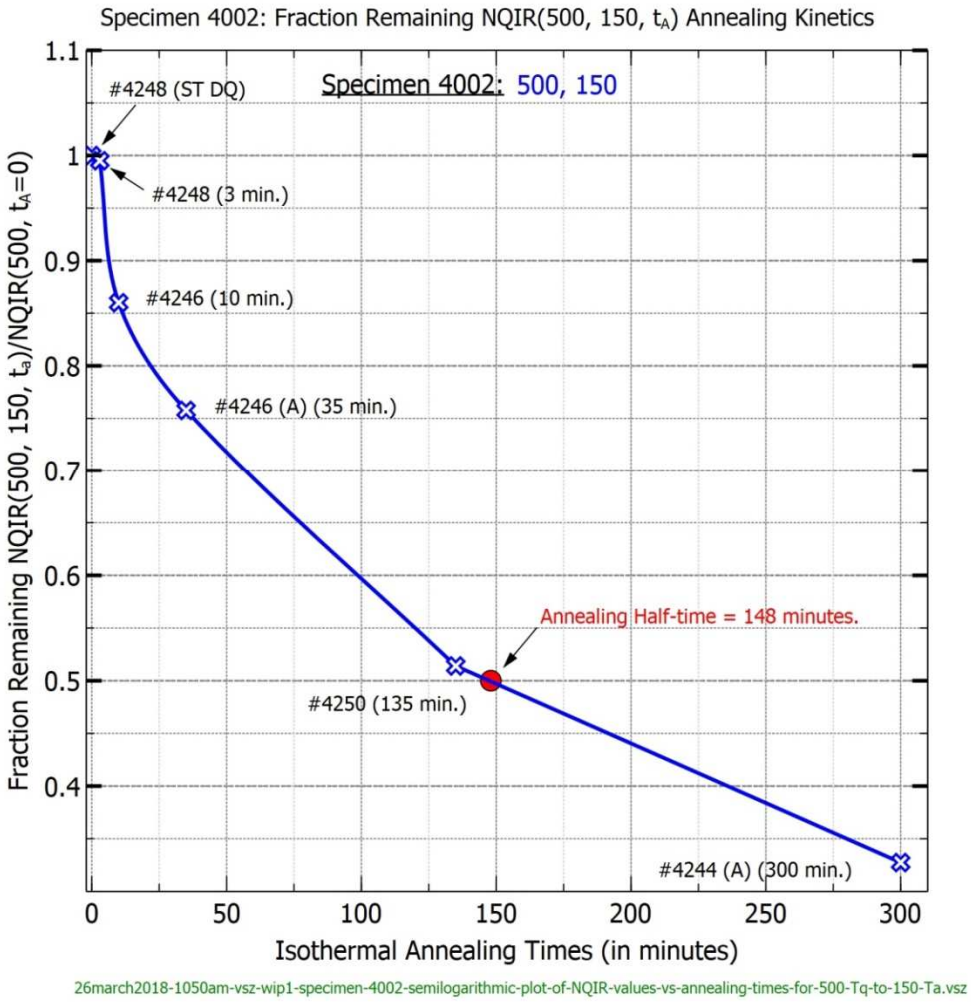

Figure 130. Specimen 4002: Plot of Annealing Kinetics during an NQIR(500, 150, t_A) Q&A Series Treatment vs. Annealing Times of up to 300 minutes (with an annealing half-time data point of 148 minutes).

Figure 130 includes specimen 4002's NQIR(500, 150, t_A=300 min.) data point whose value was 3.2×10^{-6}. This equates to a "No-Loss" NQIR(356^{o}C) and suggests minimal likelihood for vacancy clustering occurred during this annealing treatment.

8.3.4.17 Table of Annealing Half-times for associated Sets of Q&A Series Thermal Treatments involving Six Specimens

Table 14 below provides a collective summary of isothermal annealing half-times obtained from Figures 83, 95, 98, 104, 107, 110, and Figures 115 through 130 involving the indicated specimens for the associated Q&A Series thermal treatments.

Table 14. Specimen Annealing Half-times for Q&A Series Treatments

T_Q (^oC)	T_A (^oC)	4002	4005	3012	3013	3016	3018
900	700	0.27 sec.	0.25 sec.				
900	500	0.13 sec.	0.12 sec.				
900	400	0.6 sec.	0.24 sec.			0.25 sec.	
900	300	4.6 sec.			1.3 sec.		
900	200		31 sec.				
800	500	0.3 sec.	0.36 sec.				
800	400					0.67 sec.	
800	300	5.05 sec.[104]			1.65 sec.		
800	200		121 sec.				
700	600			0.222	3.45 sec.		
700	500	1.75 sec	1.27 sec.		2.1 sec.		
700	400					1.5 sec.	
700	300	13.5 sec.			2.9 sec.		
700	200		100 sec.	5.1 sec.	78 sec.		
700	65	71 hours					
500	300						70 sec.
500	150	148 min.					

[104] This annealing half-time value is the average of the two values, namely 4.9 and 5.2, that were obtained from plots in Figures 120 and 81, respectively.

Graphical assessments of the various sets of annealing half-time determinations that are listed in Table 14 are collectively presented in Figure 131.

8.3.4.18 Specimens 3012, 3013, 3016, 4002, and 4005: Arrhenius Plots of Isothermal Annealing Half-Times associated with 13 Sets of various NQIR(T_Q, T_A, t_A) Q&A Series Treatments

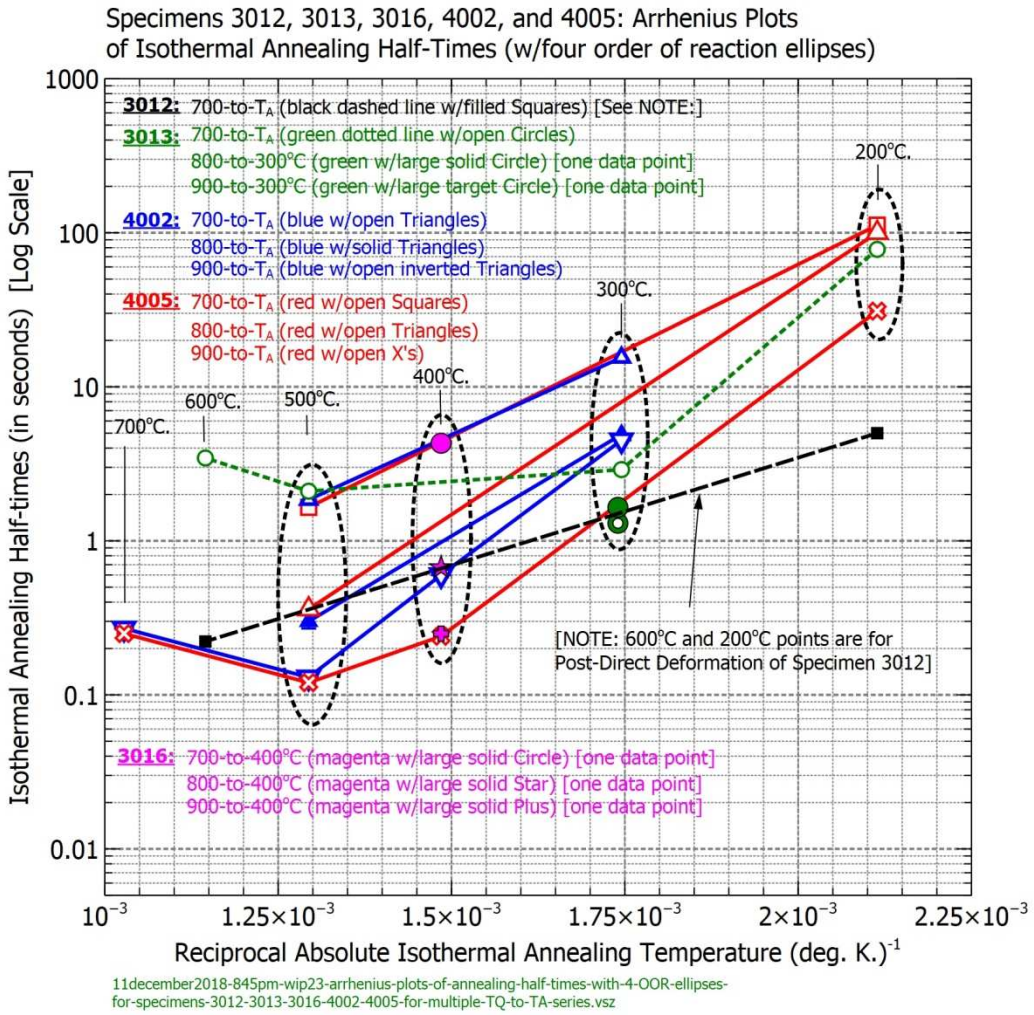

Figure 131. Specimens 3012, 3013, 3016, 4002, and 4005: Arrhenius Plots of Isothermal Annealing Half-Times for 13 Sets of various Q&A Series Treatments.

8.3.4.19 Overall Observations from Examinations of Collective Sets of Half-time Plots

Several important observations become immediately apparent upon closer examination of Figure 131 and are enumerated at this time.

1. For annealing temperatures up to 500^{o}C, all specimens' annealing half-time plots exhibited positive slopes.
2. Negative slopes (labeled N/A to indicate Non-Applicable[105]), however, are noted 1) for specimens 4002 and 4005 for the two (900, 700/500, t_A) Q&A series treatments when annealing temperatures are between 500^{o}C and 700^{o}C, and 2) for specimen 3013 for its (700, 600/500, t_A) Q&A series segment when annealing temperatures are between 500^{o}C and 600^{o}C.
3. Post-direct deformation specimen 3012 exhibits 1) a positive slope throughout its (700, 600/200, t_A) Q&A series treatment, and 2) associated annealing half-times that are certainly much lower in magnitude than those obtained for specimen 3013 which had not been subjected to any direct deformation.
4. Figure 131 also reveals additional information about relationships among annealing half-times for five separate specimens as indicated by the insertion of four order-of-reaction (O-O-R) ellipses[106] (shown with dashed lines) that are included to draw attention to what suggest as underlying reaction-order dependencies for the respective isothermal annealing

[105] The term “Non-Applicable” indicates for any segment labeled N/A in an Arrhenius plot that a negative slope was encountered. Such occurrences rule out use of those segments for establishing meaningful energy values.

[106] NOTE: Five instances are included in Figure 131 where only a single half-time data point for a particular (T_Q, T_A) Q&A series treatment, namely: two for specimen 3013 for T_A=300^{o}C and three for specimen 3016 for T_A=400^{o}C.

temperatures that are influenced by the respective quench temperatures for each Q&A series treatment. These ellipses surrounding the respective sets of data points clearly suggest that concentration-related order-of-reaction dependencies are manifested and are reflected in the associated sets of annealing half-times. Calculations based on comparing annealing half-time ratios to their respective NQIR(ST DQ) values are presented in the following sub-sections to support this tentative interpretation.

8.3.4.20 Order-of-Reaction (O-O-R) Determinations for Specimens 4002 and 4005

For specimen 4005, the respective NQIR(ST DQ) values for quenches from 900, 800, and 700^{o}C were as follows: 7.544 x 10^{-3}, 3.842 x 10^{-3}, and 1.67 x 10^{-3}, respectively.

Selecting the 900^{o}C value as a reference, the respective ratios for NQIR(900)/NQIR(900), NQIR(800)/NQIR(900), NQIR(700)/NQIR(900), are 1.0, 0.51, and 0.22, respectively. Inverting each of these ratios yields 1.0, 1.99, and 4.5 as relative ratios that can be compared with the respective half-time ratios that are plotted in Figure 131.

Selecting the (900, T_A) half-time value as a reference, the respective ratios of annealing half-times for the (900, 500/200) Q&A series treatments are calculated to be as follows:

T_A = 500: 0.12/0.12, 0.36/0.12, and 1.85/0.12 yield 1.0, 3.0, and 15.4 [experimental] versus 1.0, 4.16, and 20.25 [theoretical] in support of a **("quasi-") third-order** reaction.

T_A = 200: 31/31, 100/31, and 112/31 yield 1.0, 3.2, and 3.6 [experimental] versus 1.0, 2.6 and 4.5 [theoretical] in support of a **("quasi-") second-order** reaction which is not independent of concentration as would be the case for first-order reactions.

Similarly, an examination of three sets of half-time ratios for specimen 4002 involving (900, 500/300) Q&A series treatments were made.

For specimen 4002, the respective NQIR(ST DQ) values for quenches from 900, 800, and 700^{o}C were as follows: 7.252 x 10^{-3}, 4.088 x 10^{-3}, and 1.561 x 10^{-3}, respectively.

Selecting the 900^{o}C value as a reference, the respective ratios for NQIR(900)/NQIR(900), NQIR(800)/NQIR(900), NQIR(700)/NQIR(900), are 1.0, 0.564, and 0.215, respectively. Inverting each of these ratios yields 1.0, 1.77, and 4.65 as relative ratios that can be compared with the respective half-time ratios that are plotted in Figure 131.

Selecting the (900, T_A) half-time value as a reference, the respective ratios of annealing half-times for the (900, 500/300) Q&A series treatments are calculated to be as follows:

T_A = 500: 0.13/0.13, 0.30/0.13, and 1.85/0.13 yield 1.0, 2.31, and 14.23 [experimental] versus 1.0, 4.16, and 20.25 [theoretical] in support of a ("quasi-") third-order reaction.

T_A = 300: 4.5/4.5, 4.9/4.5, and 15.85/4.5 yield 1.0, 1.09, and 3.52 [experimental] versus 1.0, 2.0, and 4.5 [theoretical] in support of a (quasi-) second-order reaction.

Additionally, it should be noted that even though no (900/800/700, 200, t_A) Q&A treatments were conducted for specimen 4002 (hence no half-time data points were obtained), graphical projections of the respective half-time plots to that annealing temperature do tend to suggest (quasi-) second-order reactions would most likely be expected to be endorsed.

8.3.4.21 Consistencies among half-time values within all four Order-of-Reaction (O-O-R) Ellipses

Examination of the annealing half-time values obtained for each of the five specimens (3012, 3013, 3016, 4002, and 4005) reveals that with but two exceptions associated with the post-direct deformation specimen 3012's 600^{o}C and 200^{o}C half-time values, an overall consistency is clearly indicated for the respective sets of half-time values contained within each of the four O-O-R ellipses.

8.3.4.22 Conclusions Reached from Analyses of Order-of-Reaction (O-O-R) Findings

Based on the determinations presented in sub-sections 8.3.4.20 and the additional comments made in sub-section 8.3.4.21, it appears reasonable to conclude that the resulting calculations of order-of-reaction ratios do appear to provide an acceptable overall accounting for the actual annealing half-times shown in Figure 131 for annealing temperatures ≤ 500^{o}C.

Specifically, the respective annealing half-times were compared and were found to closely approximate first-, second-, and third-order annealing reactions for the respective annealing temperatures of 200^{o}C (or lower), 300^{o}C, and 500^{o}C based upon comparisons of annealing half-times for a given specimen at each of these annealing temperatures for the associated quenches from 700, 800, and 900^{o}C.

In the next sub-section, determinations of the Effective Vacancy Migration Energy, E^{M}_{V}(eff), will be illustrated graphically based on the obtained isothermal annealing half-times listed in Table 14 provided in sub-section 8.3.4.17.

8.3.5 Effective Vacancy Migration Energy Determinations from Arrhenius Plots of Half-Times for various NQIR(T_Q, T_A, t_A) Q&A Series Treatments

Figures 132 through 135 make use of the slopes in the Arrhenius plots of annealing half-time data points for specimens 3012, 3013, 4002, and 4005, respectively, to determine the E^{M}_{V}(eff) magnitudes over the indicated ranges in annealing temperatures, and Figure 136 shows the collective sets of E^{M}_{V}(eff) values determined for all four specimens.

8.3.5.1 Specimen 3012: Determination of Effective Vacancy Migration Energy from an Arrhenius Plot of Annealing Half-times for NQIR(700, 600/200, t_A) Q&A Series Treatments

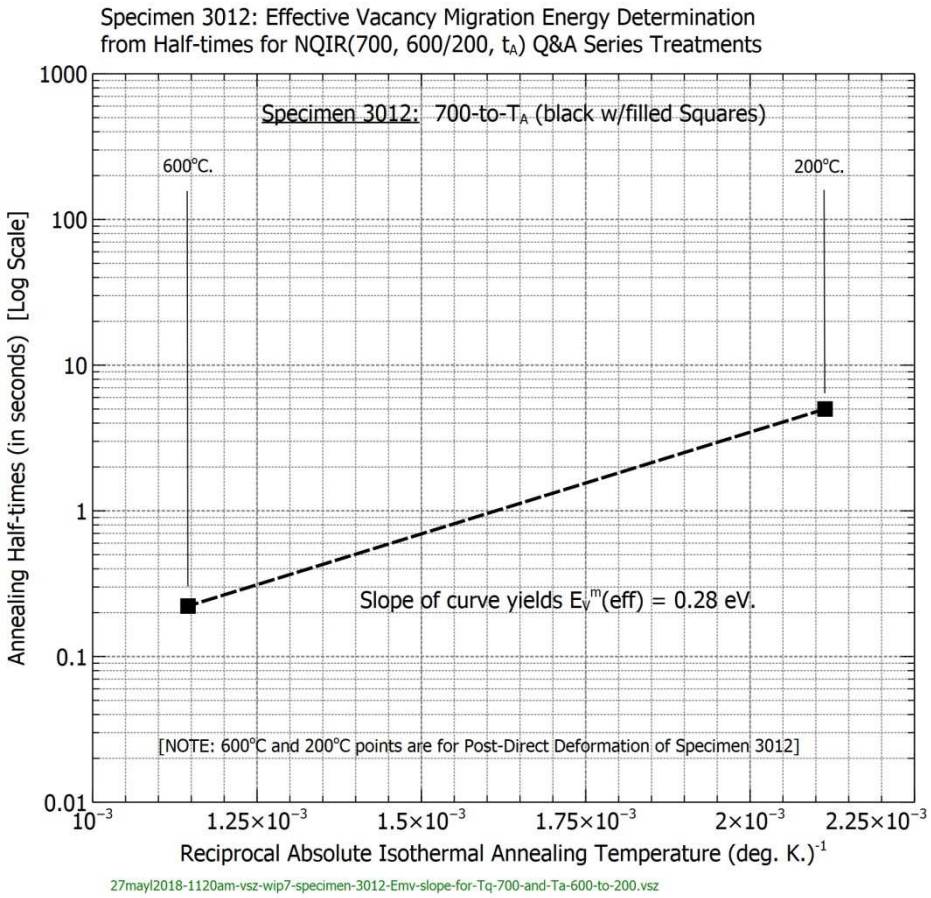

Figure 132. Specimen 3012: Determination of Effective Vacancy Migration Energy from an Arrhenius Plot of Annealing Half-times for NQIR(700, 600/200, t_A) Q&A Series Treatments

8.3.5.2 Specimen 3013: Determination of Effective Vacancy Migration Energies from an Arrhenius Plot of Annealing Half-times for NQIR(T_Q=700, T_A=600/500/300/200, t_A) Q&A Series Treatments

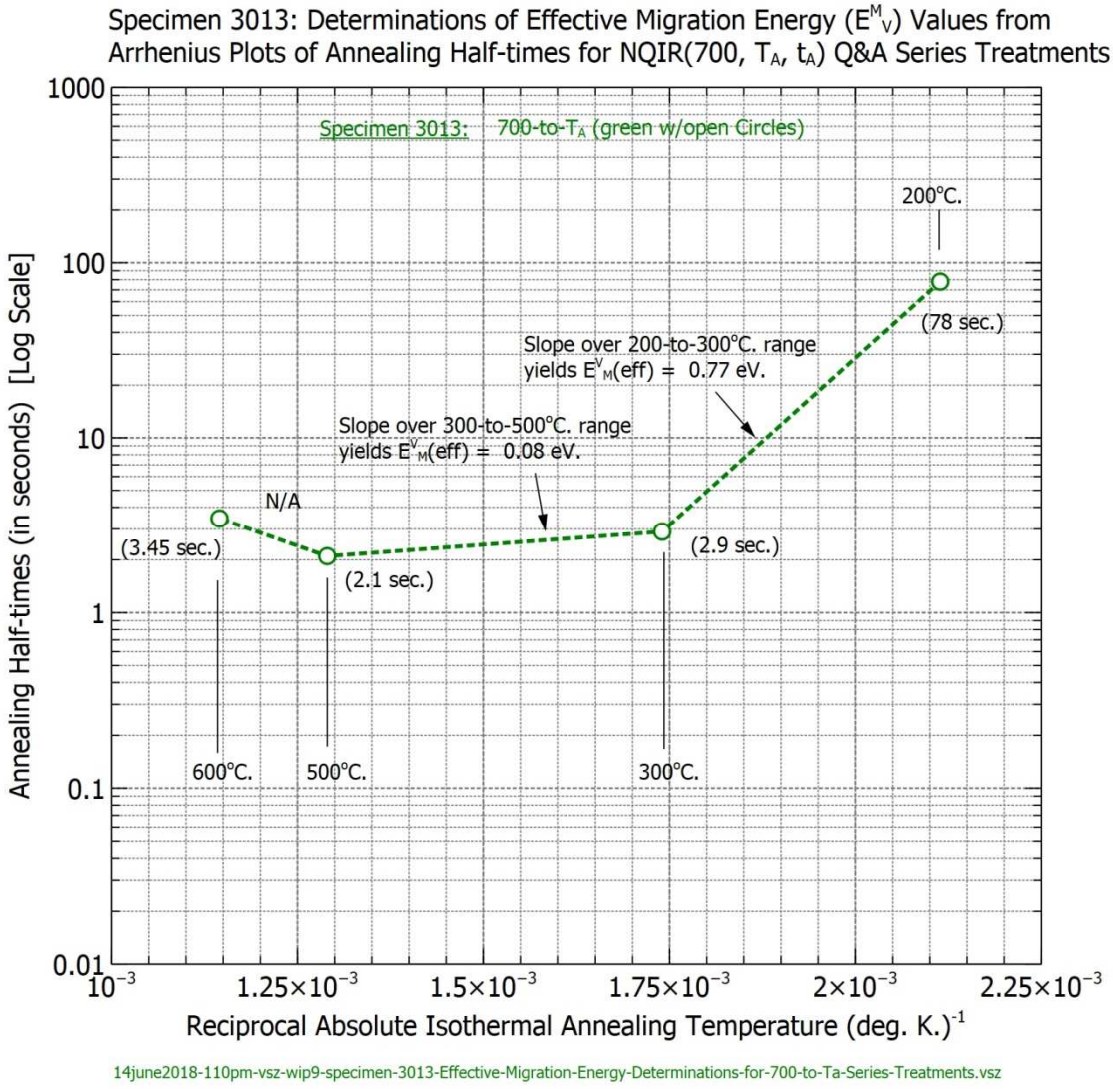

Figure 133. Specimen 3013: Determination of Effective Vacancy Migration Energy from Arrhenius Plot of Annealing Half-times for NQIR(T_Q=700, T_A=600/500/300/200, t_A) Q&A Series Treatments

8.3.5.3 Specimen 4002: Determination of Effective Vacancy Migration Energies from an Arrhenius Plot of Annealing Half-times for NQIR(900/800/700, T_A, t_A) Q&A Series Treatments

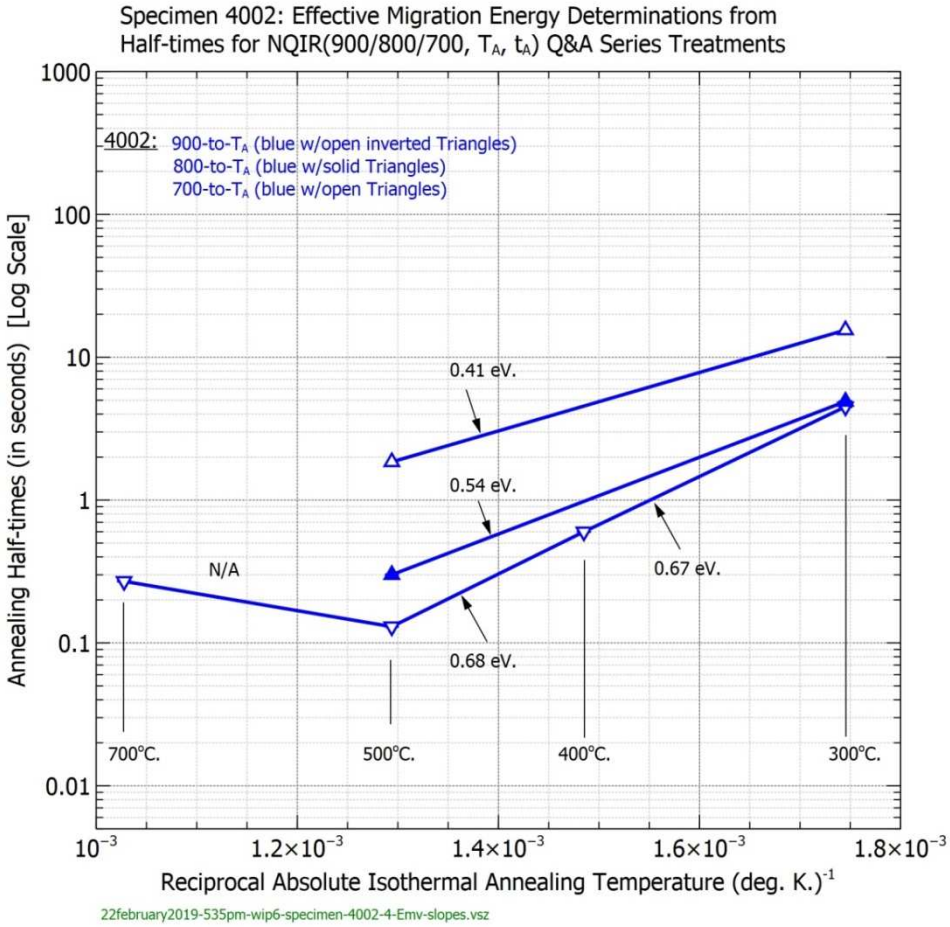

Figure 134. Specimen 4002: Determination of Effective Vacancy Migration Energies from Annealing Half-times for NQIR(900/800/700, T_A, t_A) Q&A Series Treatments

In Figure 134 two things should be noted: 1) increased slopes as the quench temperature T_Q increases and 2) over the annealing temperature range from 500°C to 700°C a negative slope (labeled N/A) is manifested for the T_Q=900°C series Q&A treatment.

8.3.5.4 Specimen 4005: Determination of Effective Vacancy Migration Energies from Arrhenius Plots of Annealing Half-times for NQIR(900/800/700, T_A, t_A) Q&A Series Treatments

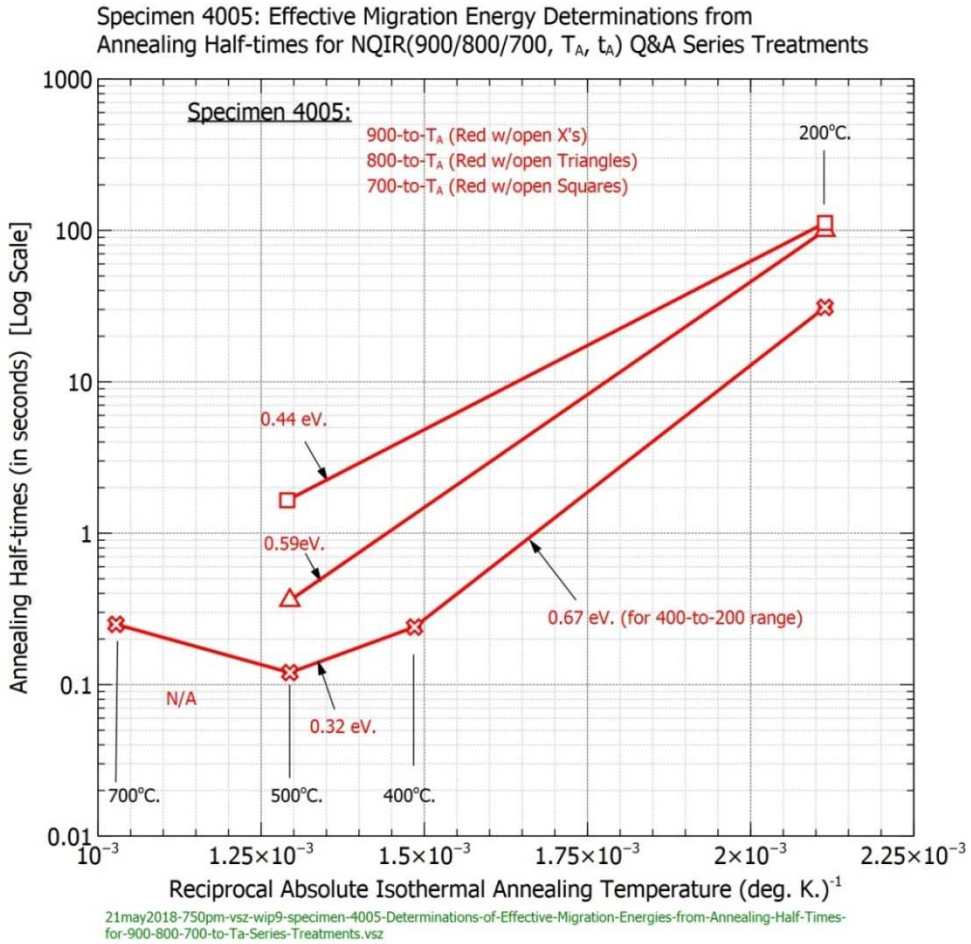

Figure 135. Specimen 4005: Determination of Effective Vacancy Migration Energies from Arrhenius Plots of Annealing Half-times for NQIR(900/800/700, T_A, t_A) Q&A Series Treatments

Figure 135 reveals that the slopes 1) for the 900/800/700-T_A treatments, increase for $T_A \leq 400^oC$ for higher T_Q; 2) for the (900-T_A) treatment's $400^oC \leq T_A \leq 500^oC$ segment, decrease somewhat; and 3) for the (900-T_A) treatment's $500^oC \leq T_A \leq 700^oC$ segment, become negative (labeled N/A to denote such a reversal in slope).

8.3.5.5 Effective Vacancy Migration Energy Determinations for Specimens 3012, 3013, 4002, and 4005 from Arrhenius Plots of Annealing Half-times

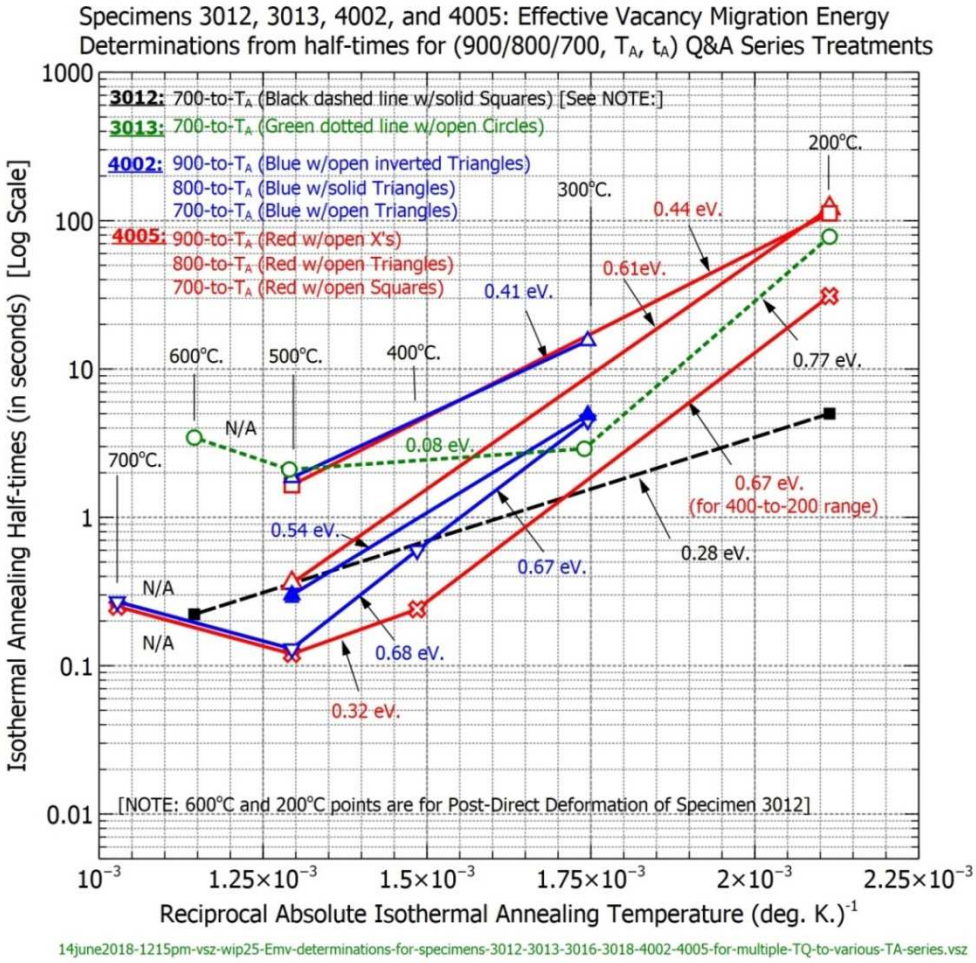

Figure 136. Specimens 3012, 3013, 4002, and 4005: Arrhenius Plots of Effective Vacancy Migration Energies determined from Annealing Half-times associated with eight Sets of NQIR(900/800/700, T_A, t_A) Q&A Series Treatments Annealing Kinetics.

Because no (700, 400, t_A) Q&A series treatments were performed for specimens 3012 and 3013, the two sets of dashed lines in Figure 136 are used to signify that the labeled slopes of 0.28 and 0.08 eV should only be considered as tentative E^M_V(eff) values.

8.3.5.6 Observations of E^{M}_{V}(eff) Values determined from Analyses of Arrhenius Plots of Annealing Half-times for various NQIR(T_Q, T_A, t_A) Q&A Series Treatments

Among the observations that can be discerned from the Arrhenius plots in Figure 136 are the following:

1) For specimens 4002 and 4005, positive values of E^{M}_{V}(eff) were obtained for Q&A series treatments involving annealing temperatures ranging from 200^{o}C up to 500^{o}C.
2) Except for specimen 4005's segment for T_Q = 900^{o}C and 400^{o}C ≤ T_A ≤ 500^{o}C which indicates a reduced value in E^{M}_{V}(eff) equal to 0.32 eV, the sets of determined E^{M}_{V}(eff) values are consistently higher as the associated quench temperatures increases from T_Q = 700^{o}C, then to 800^{o}C, and finally to 900^{o}C. Specifically, for specimen 4002 the E^{M}_{V}(eff) values are indicated to be 0.41 eV, 0.54 eV, and 0.67 eV, and for specimen 4005 the E^{M}_{V}(eff) values are indicated to be 0.44 eV, 0.61 eV, and 0.67 eV, respectively.
3) For specimens 4002 and 4005 essentially identical negative slopes (labeled N/A) were obtained for the two 500^{o}C ≤ T_A ≤ 700^{o}C segments associated with (900,T_A) Q&A series treatments.
4) For specimen 3013's 700-to-T_A Q&A series treatments a) a negative slope (labeled N/A) was obtained for the 500^{o}C ≤ T_A ≤ 600^{o}C segment; b) a value for E^{M}_{V}(eff) equal to 0.08 eV was estimated for the segment where 300^{o}C ≤ T_A ≤ 500^{o}C; and c) an estimated value for E^{M}_{V}(eff) equal to 0.77 eV was estimated for the segment where 200^{o}C ≤ T_A ≤ 300^{o}C.
5) For specimen 3012 which had undergone direct deformation treatments prior to the indicated Q&A series treatments, thereby having a much higher

dislocation sink density than the other specimens included in Figure 136, the dotted line segment where $200^{o}C \leq T_A \leq 600^{o}C$ and involved a (700, T_A) Q&A series treatment has an estimated value for E^{M}_{V}(eff) equal to 0.28 eV.

Observations of negative slopes (labeled N/A) occurring for some specimens as T_A approaches T_Q certainly demand further data analyses in search of a reasonable explanation, and this specific matter will be discussed in detail in sub-section 8.3.9.

However, before tackling whatever might account for the noted occurrences of negative (labeled N/A) slopes for certain regions of Q&A series treatments in several of the Arrhenius plots in Figures 133 through 135, three additional sub-sections follow.

Sub-section 8.3.6 presents several plots of remaining vacancy supersaturation ratio (VSR) and excess vacancy defect chemical potential (μ_v) vs. annealing time, and these parameters are discussed in some detail. Sub-section 8.3.7 presents plots of (700/500-to-65^{o}C) and (500-to-150^{o}C) Q&A series extended anneal treatments. Sub-section 8.3.8 presents several plots of fraction remaining values of NQIR(T_Q, T_A, t_A) vs. reduced annealing time variable $t_A/t_{1/2}$.

8.3.6 Remaining Vacancy Supersaturation Ratios and Excess Vacancy Defect Chemical Potential (μ_v)

8.3.6.1 Vacancy Supersaturation Ratio Determinations for specific Q&A Series Treatments

Expressed in terms of vacancy concentration, the remaining vacancy supersaturation ratio (VSR) can be slightly re-defined using the equation[107]

$$VSR(T_Q, T_A, t_A) \equiv [C_v(T_Q,T_A, t_A) - \text{"No Loss" } C_v(T_A)]/C_v(T_A, t_A \rightarrow \infty) \qquad \text{Eqn. (8-1)}$$

Table 15 provides examples of "No-Loss" $VSR(T_Q, T_A)$ combinations, many of which apply to Q&A series treatments that were performed, and includes the calculated values for the respective vacancy defect chemical potential magnitudes. Figures 137 through 142 are provided as representative examples of the associated annealing kinetics.

[107] This re-definition for VSR is made necessary based on analyses of results obtained for Q&A series treatments that revealed significant MRR levels do remain even after long annealing times. As a consequence, the value for $C_v(T_A, t_A \rightarrow \infty)$ proves to remain larger than what would occur in the ideal situation of complete annealing, namely values equal to "No Loss" $Cv(T_A)$.

Table 15. "No Loss" VSR and Excess Vacancy Defect Chemical Potentials

T_Q (^oC)	T_A (^oC)	"No Loss" $C_V(T_Q)$	"No Loss" $C_V(T_A)$	VSR	Ln (1+VSR)	kT_A	μ_V (eV) [108]
900	40	$2.2x10^{-4}$	$6.31x10^{-16}$	3.5×10^{11}	26.58	0.027	0.718
700	20	$3.0x10^{-5}$	$7.39x10^{-17}$	4.06×10^{11}	26.728	0.02525	0.675
700	40	$3.0x10^{-5}$	$6.31x10^{-16}$	4.75×10^{10}	24.58	0.027	0.664
700	65	$3.0x10^{-5}$	$1.224x10^{-14}$	2.45×10^{9}	21.62	0.0291	0.629
600	40	$7.89x10^{-6}$	$6.31x10^{-16}$	1.25×10^{10}	23.25	0.027	0.629
900	200	$2.2x10^{-4}$	$1.1x10^{-9}$	2.0×10^{6}	14.5	0.04076	0.591
500	65	$1.45x10^{-6}$	$1.224x10^{-14}$	1.18×10^{8}	18.59	0.0291	0.541
900	300	$2.2x10^{-4}$	$7.0x10^{-9}$	3.143×10^{4}	10.364	0.04937	0.511
800	400	$8.99x10^{-5}$	$1.58x10^{-7}$	5.726×10^{3}	8.65	0.058	0.501
800	300	$8.99x10^{-5}$	$7.0x10^{-9}$	1.28×10^{4}	9.46	0.04937	0.467
800	200	$8.99x10^{-5}$	$1.1x10^{-9}$	8.17×10^{4}	11.31	0.04076	0.461
500	150	$1.45x10^{-6}$	$7.5x10^{-12}$	1.95×10^{5}	12.172	0.03645	0.444
900	400	$2.2x10^{-4}$	$1.58x10^{-7}$	1.39×10^{3}	7.239	0.058	0.42
700	200	$3.0x10^{-5}$	$1.1x10^{-9}$	2.727×10^{4}	10.21	0.04076	0.416
700	300	$3.0x10^{-5}$	$7.0x10^{-9}$	4.285×10^{3}	8.363	0.04937	0.413
900	500	$2.2x10^{-4}$	$1.45x10^{-6}$	151.72	5.029	0.0666	0.335
800	500	$8.99x10^{-5}$	$1.45x10^{-6}$	61	4.11	0.0666	0.274
500	300	$1.45x10^{-6}$	$7.0x10^{-9}$	207	5.333	0.04937	0.263
700	500	$3.0x10^{-5}$	$1.45x10^{-6}$	20.69	3.03	0.0666	0.20
800	600	$8.99x10^{-5}$	$7.89x10^{-6}$	10.4	2.43	0.07522	0.183
900	700	$2.2x10^{-4}$	$3.0x10^{5}$	5.286	1.665	0.08384	0.14
600	500	$7.89x10^{-6}$	$1.45x10^{-6}$	5.43	1.86	0.0666	0.124
700	600	$3.0x10^{-5}$	$7.89x10^{-6}$	2.80	1.336	0.07522	0.10
600	575	$7.89x10^{-6}$	5.36×10^{-6}	0.472	0.387	0.07307	0.028

[108] Note that the VSR(T_Q,T_A) combinations are listed in descending order of the associated excess vacancy defect chemical potential values.

8.3.6.2 Specimen 4005: Remaining Vacancy Supersaturation Ratios during NQIR(900/800/700, 500, t_A) Q&A Series Treatments

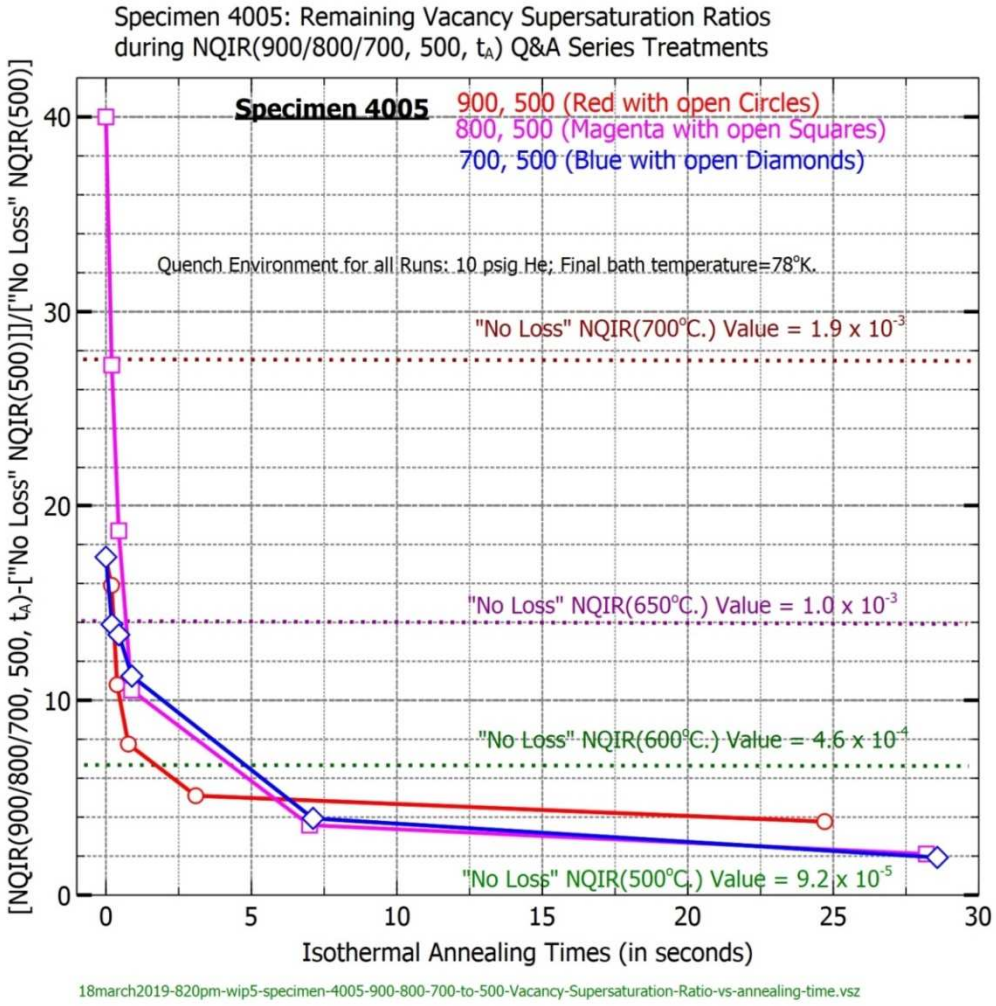

Figure 137. Specimen 4005: Remaining Vacancy Supersaturation Ratios during NQIR(900/800/700, 500, t_A) Q&A Series Treatments vs. Annealing Times under 30 seconds

Abrupt tailing off in rates of annealing are manifested when VSR values fall below 10, and plateaus (MRR levels) are reached when VSR values fall below 4.

8.3.6.3 Specimen 4005: Remaining Vacancy Supersaturation Ratios during NQIR(900/800/700, 200, t_A) Q&A Series Treatments

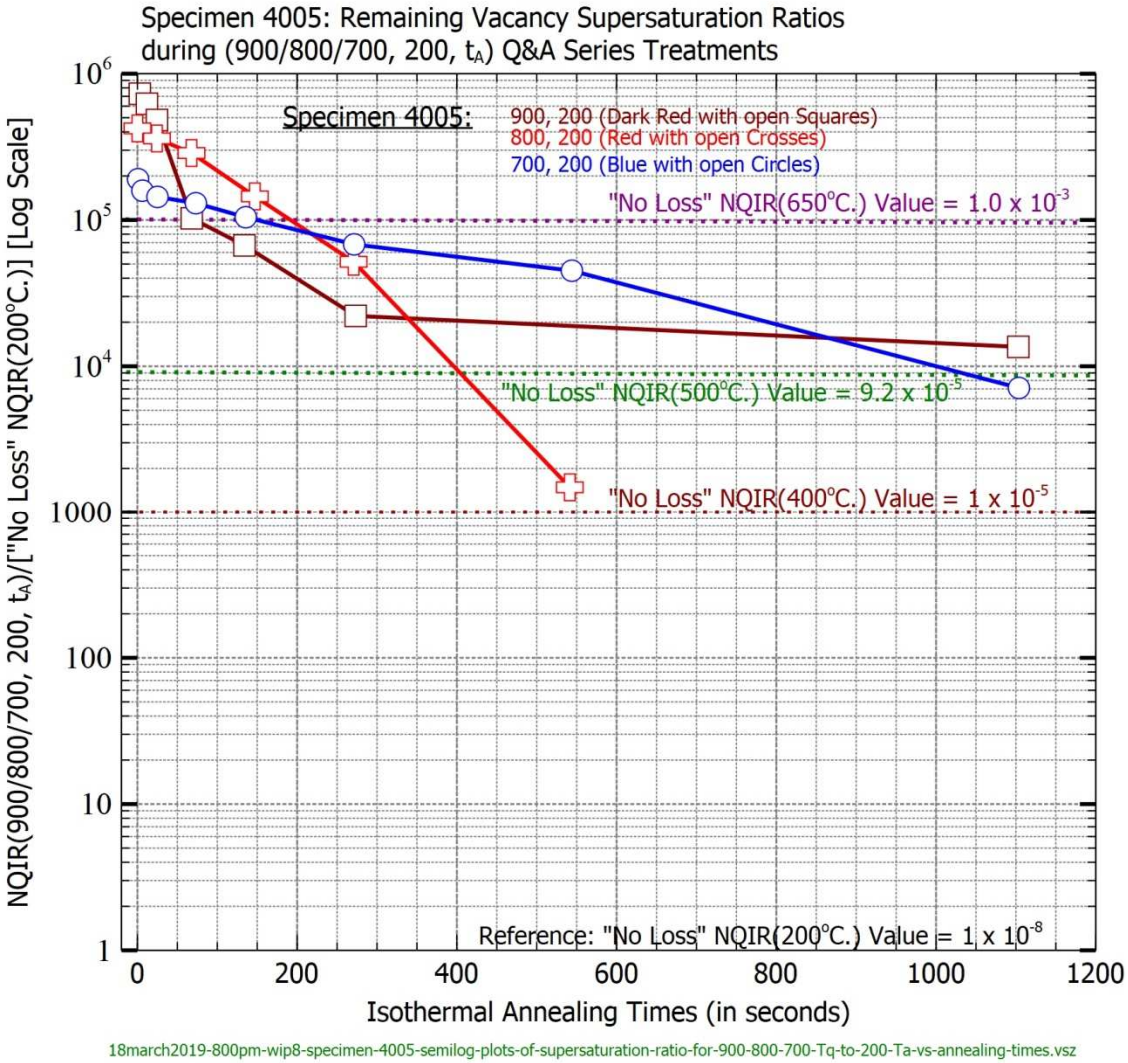

Figure 138. Specimen 4005: Remaining Vacancy Supersaturation Ratios during NQIR(900/800/700, 200, t_A) Q&A Series Treatments vs. Annealing Times up to 1100 seconds

For all three Q&A series treatments, MRR levels suggestive of occurrences of vacancy clustering are manifested for VSR values between 1,000 and 10,000.

8.3.6.4 Specimen 3016: Plots of NQIR(900/700,400, t_A) [with μ_v (in eV.)] Values

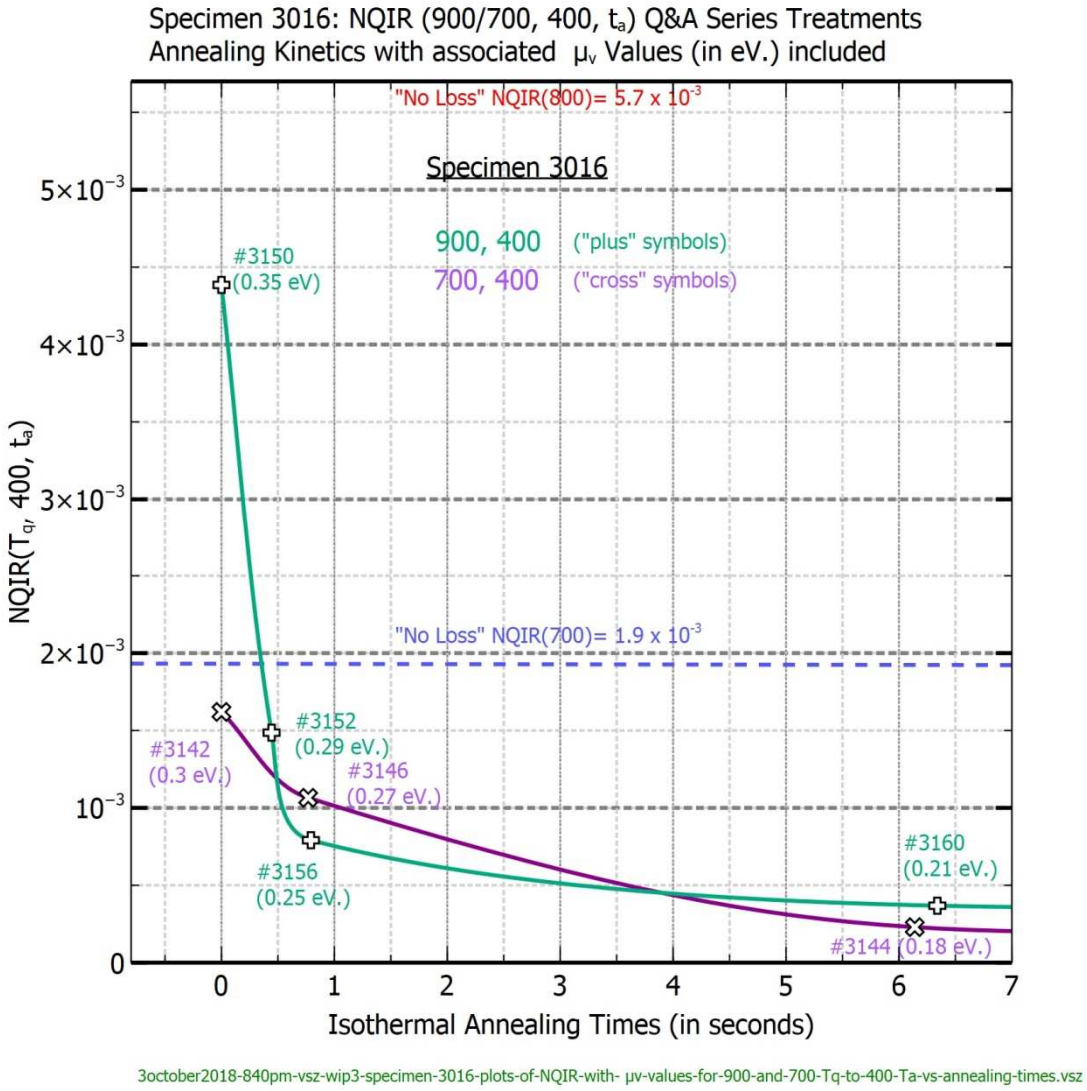

Figure 139. Specimen 3016: Comparison Plots of Annealing Kinetics [with μ_v (in eV.)] during NQIR(900/700, 400, t_A) Q&A Series Treatments vs. Annealing Times of less than seven seconds

Note in Figure 139 the fact that an abrupt reduction in annealing rates occurs when the vacancy defect chemical potential μ_V levels fall below 0.27 eV.

8.3.6.5 Specimen 4005: Plot of Vacancy Defect Chemical Potential μ_V for an NQIR(800, 200, t_A) Q&A Series Treatments

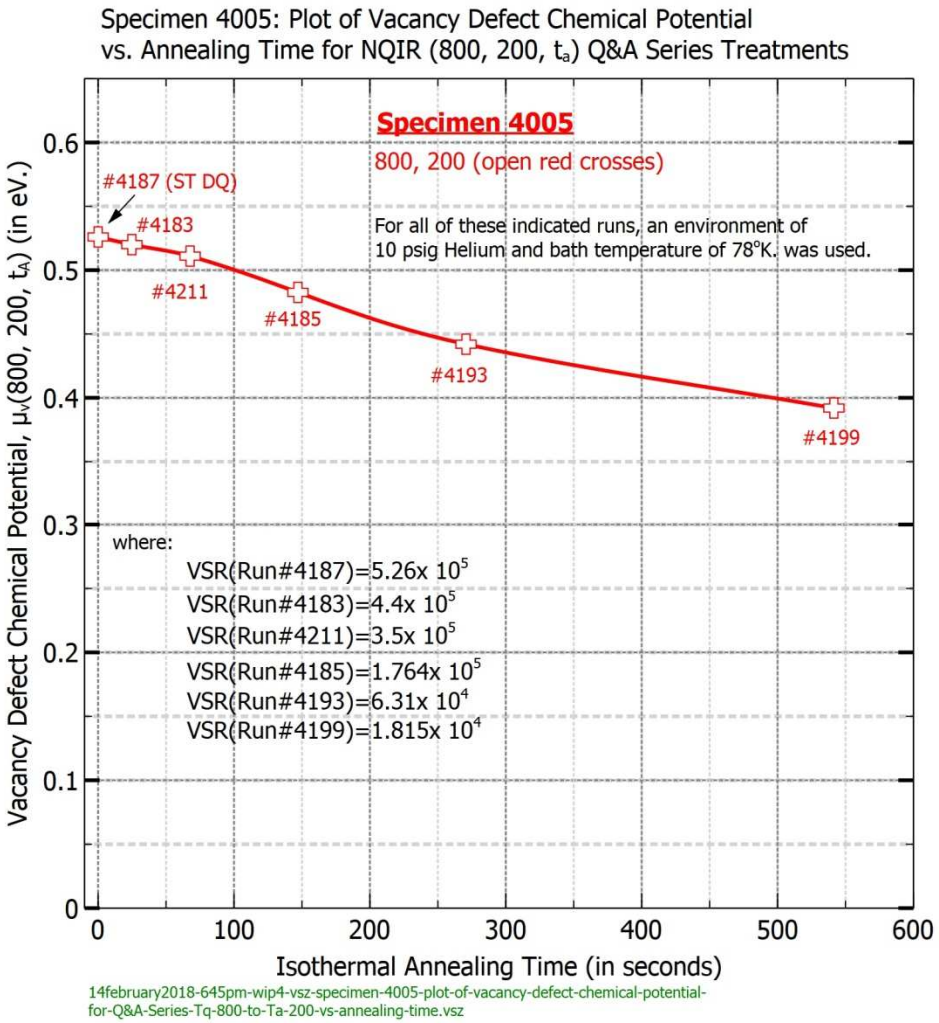

Figure 140. Specimen 4005: Plot of Vacancy Defect Chemical Potential μ_V for NQIR(800, 200, t_A) Q&A Series Treatments vs. Annealing Times of less than 600 seconds

Note in Figure 140 the minimal reduction in annealing rates even though the vacancy defect chemical potential μ_V level remains above 0.4 eV.

8.3.6.6 Specimen 4002: Plots of Vacancy Defect Chemical Potential μ_V for three NQIR(900/800/700, 500, t_A) and one NQIR(900, 700, t_A) Q&A Series Treatments

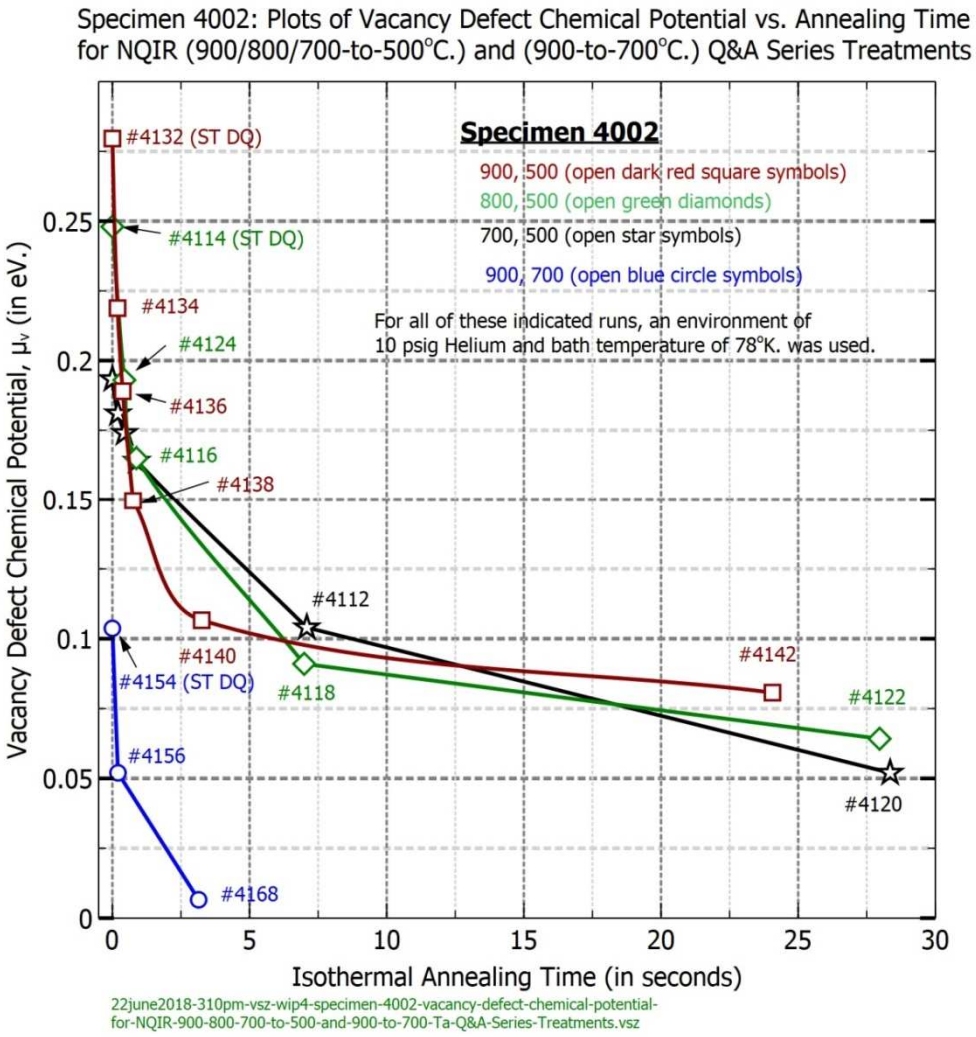

Figure 141. Specimen 4002: Plots of Vacancy Defect Chemical Potential μ_V for three NQIR(900/800/700, 500, t_A) and one NQIR(900, 700, t_A) Q&A Series Treatments vs. Annealing Times of less than 30 seconds

Note that μ_V(Run #4168) - obtained by converting its NQIR value of 2.0×10^{-3} - was calculated to be 0.00656 eV and is close to "No Loss" NQIR(700°C) of 1.9×10^{-3} which is included in Figure 116 for the NQIR(900, 700, t_A) Q&A Series Treatment.

8.3.6.7 Specimen 4002: Plots of Vacancy Defect Chemical Potential μ_V for three NQIR(900/800/700, 500, t_A) and one NQIR(900, 700, t_A) Q&A Series Treatments

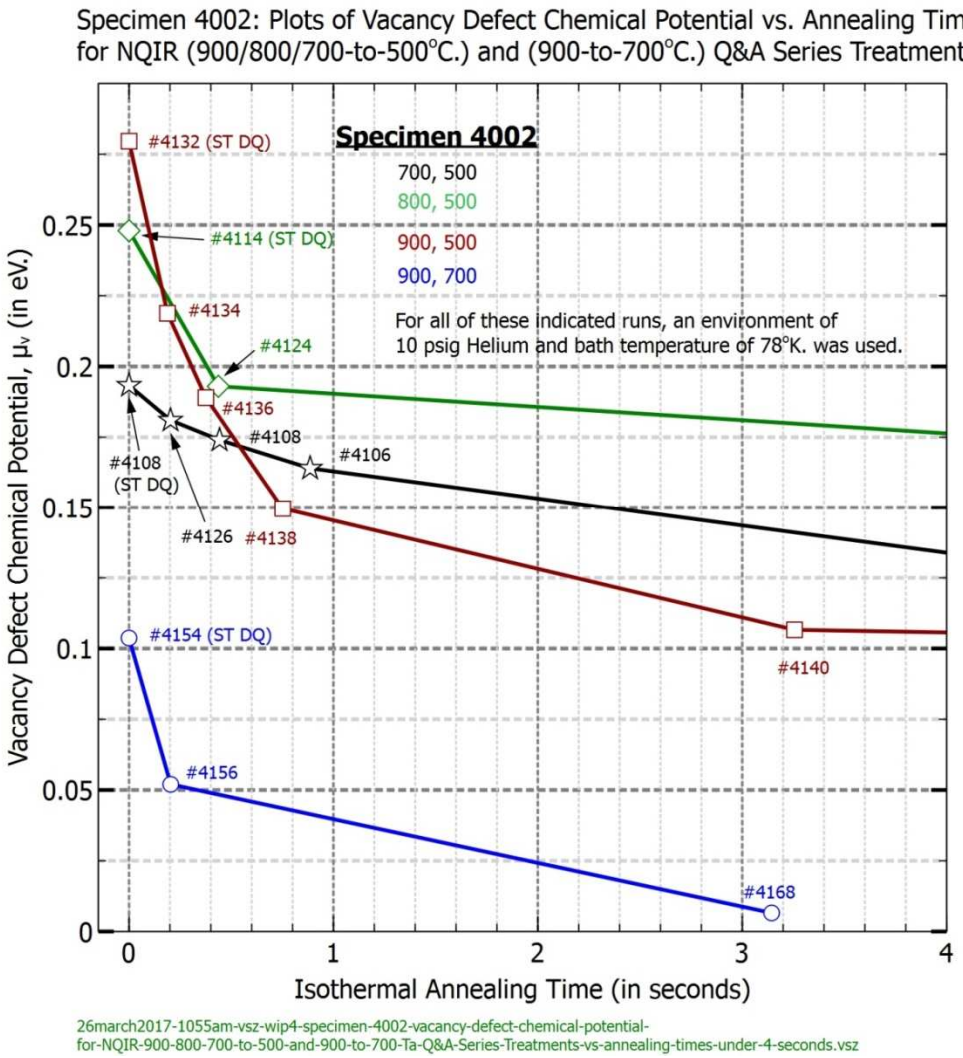

Figure 142. Specimen 4002: Plots of Vacancy Defect Chemical Potential μ_V for three NQIR(900/800/700, 500, t_A) and one NQIR(900, 700, t_A) Q&A Series Treatments vs. Annealing Times of less than four seconds

The influence of the magnitudes of μ_V will become even more obvious when section 8.3.10 presents plots of instantaneous vacancy migration energies, labeled E^M_V(act), which are determined from slopes involving sets of calculated initial annealing rates (IARs) for numerous elevated temperature Q&A series treatments.

In the next sub-section Q&A series treatments involving T_A values of 65^{o}C and 150^{o}C are presented to illustrate the results obtained for three specific Q&A series treatments (700/500-to-65) and 500-to-150 that involve substantially extended annealing times.

8.3.7 700/500-to-65^{o}C and 500-to-150^{o}C Q&A Series Extended Anneal Treatments

Figure 143 illustrates the associated annealing kinetics obtained for specimens 4002 and 4005.

8.3.7.1 Specimens 4002 and 4005: Plots of NQIR(700, 65, t_A) and (500, 65, t_A) Q&A Series Extended Anneals

The observed behavior of the (500, 65) Q&A series treatment showing an initial rise in NQIR (500, 65, t_A) values had not been observed for any other Q&A series treatments and was deemed worthy of further assessment.

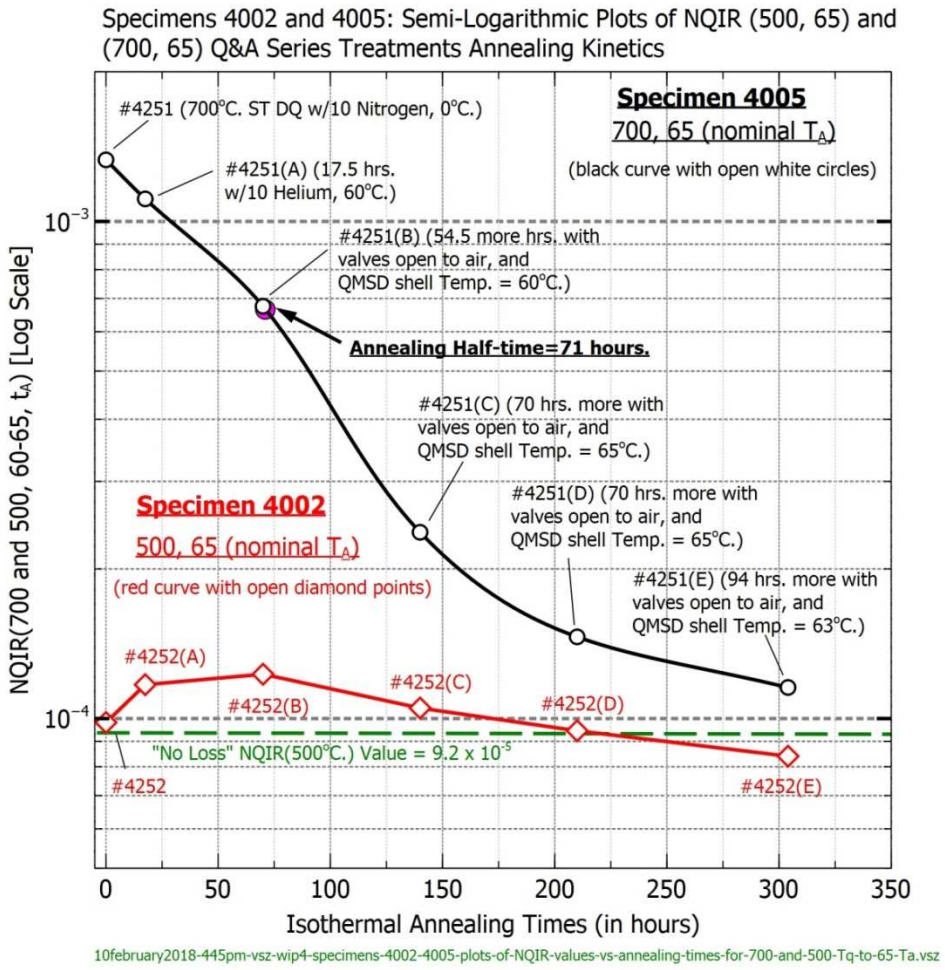

Figure 143. Specimens 4002 and 4005: Semi-Log Plots of NQIR(700, 65, t_A) and (500, 65, t_A) Q&A Series Extended Anneals vs. Annealing Times of up to 306 hours.

8.3.7.2 Specimen 4002: Plot of NQIR(500, 65, t_A) Q&A Series Extended Anneals

Specimen 4002's NQIR(500, 65) data is illustrated in the Figure 144, and it clearly reveals a significant initial rise followed by a gradual decay behavior.

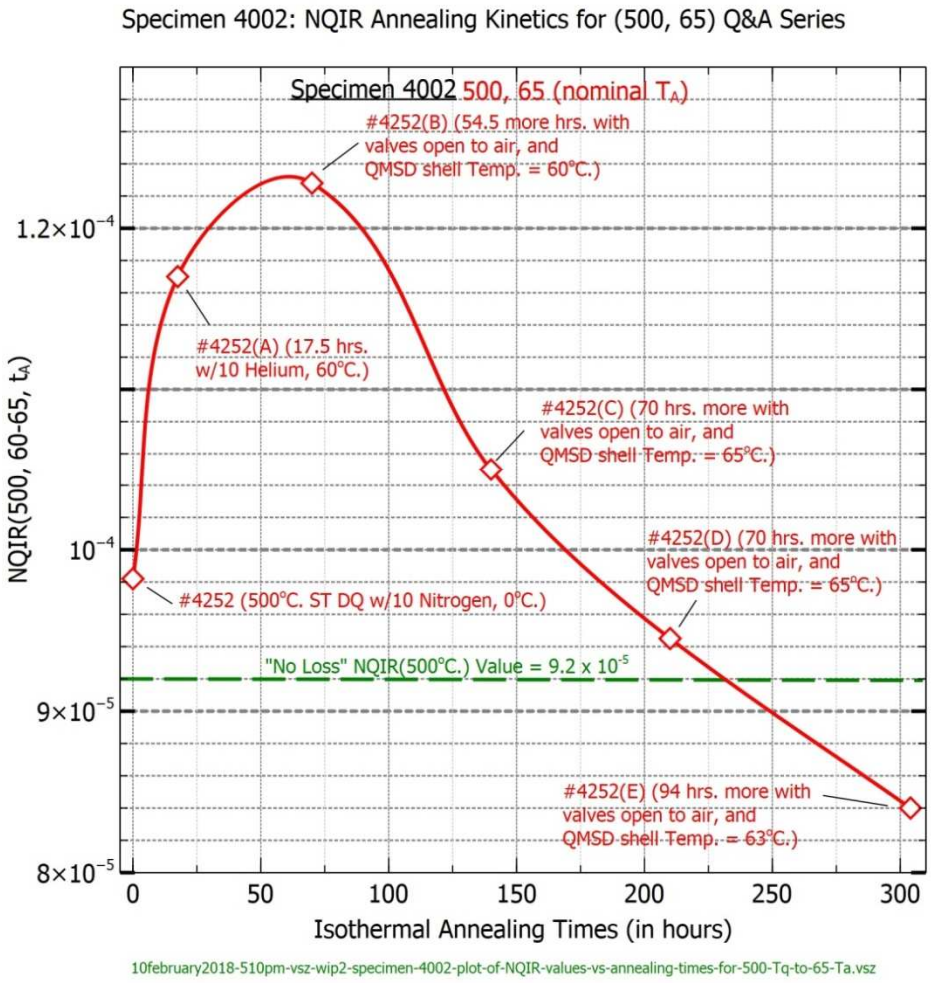

Figure 144. Specimen 4002: Plot of NQIR(500, 65, t_A) Q&A Series Extended Anneals vs. Annealing Times of up to 306 hours

Quantitatively, the peak rise magnitude indicated in Figure 145 represents a value of only 0.4 µ-ohms in quenched in resistance increase, and it took about 175 hours of annealing time for the Delta QIR value just to return to the initial value.

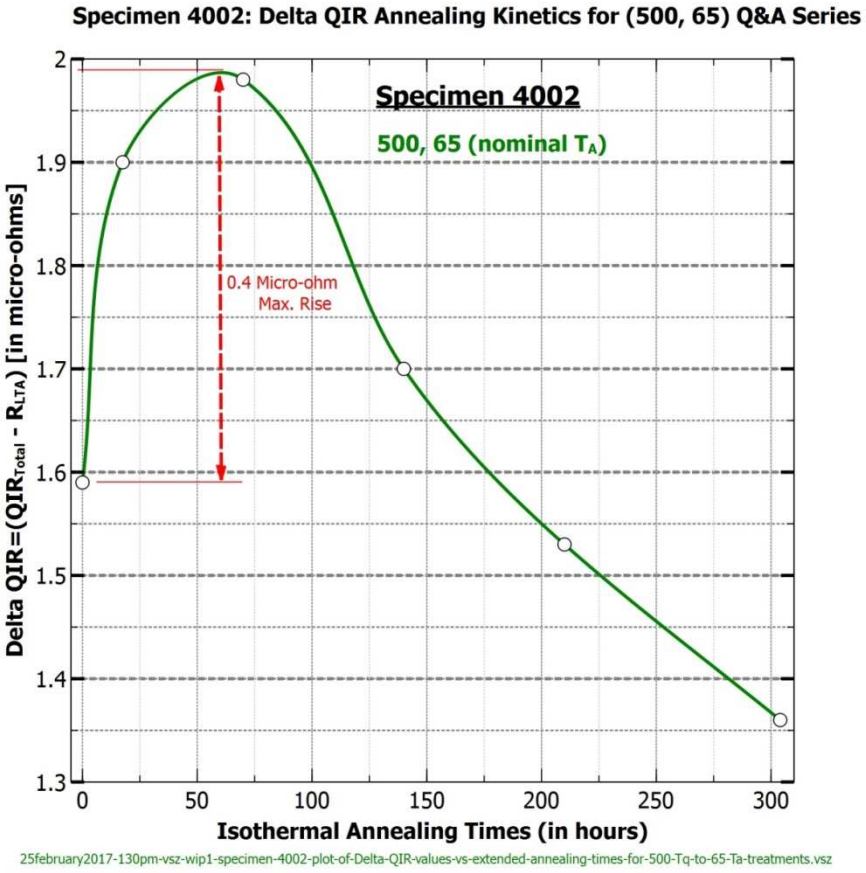

Figure 145. Specimen 4002: Plot of Delta QIR(500, 65, t_A) Q&A Series Extended Anneals vs. Annealing Times of up to 306 hours.

Notably, similar behavior had been reported by 1) Meshii, Mori, and Kauffman [48] for their (500, 65) Q&A treatment, 2) Herman and Cohen [137], 3) Asdente and Friedel [2], 4) Matyas [138], 5) Herman, Cohen, and Fine [182], and 6) Cotterill [21] who suggested that the formation of small vacancy complexes might explain such an observation.

8.3.7.3 Plot of NQIR(500, 150, t_A) Q&A Series Treatment vs. Square Root of Annealing Time

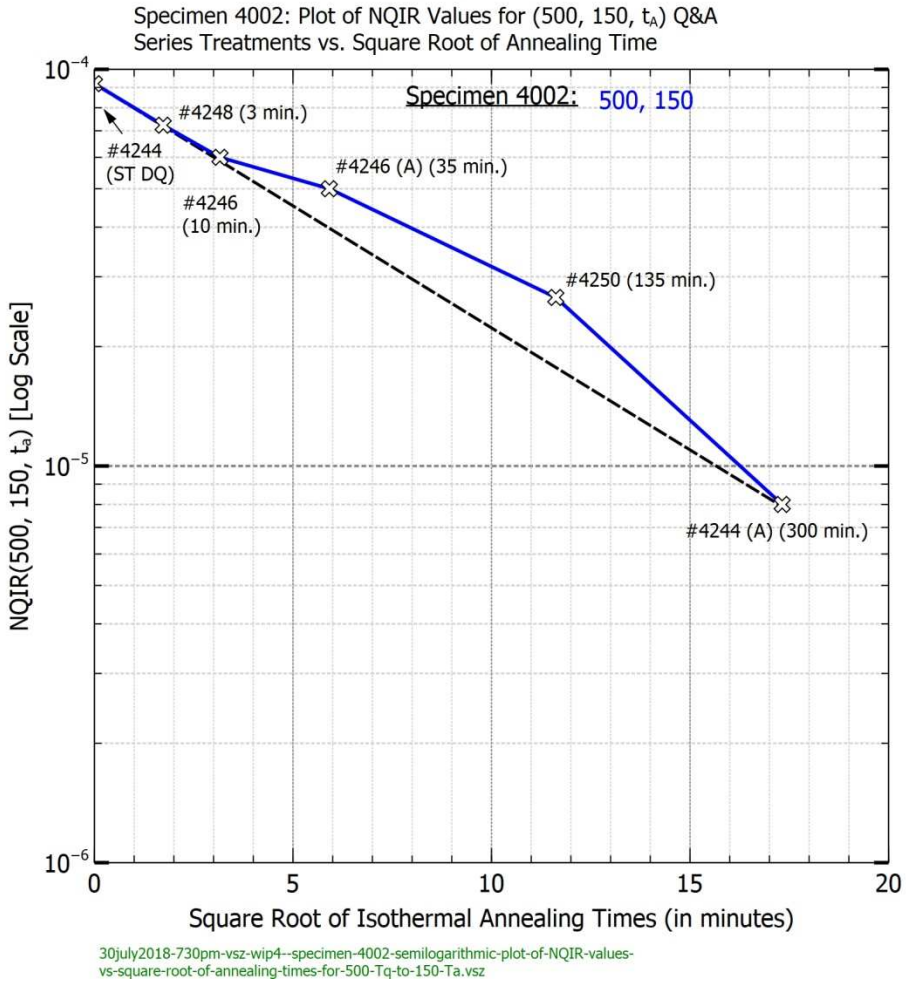

Figure 146. Specimen 4002: Semi-Log Plot of NQIR(500, 150, t_A) vs. Square Root of Annealing Time

A re-examination of the data plotted in Figure 114 in sub-section 8.3.3.17 as a semi-log plot vs. $(t_A)^{1/2}$ is made in Figure 146 to illustrate more clearly the likely time dependency for the (500,150, t_A) Q&A series treatment that reveals a dependency upon time that is clearly not obvious upon examination of Figure 114.

Figure 146 includes a straight line approximation plot that reflects a $t^{1/2}$ annealing kinetics behavior that is exhibited over the entire curve plotted for specimen 4002 for annealing times ranging from zero up to the 300-minute NQIR(500, 150, t_A) Q&A treatment data points.

The next sub-section presents plots that illustrate how the annealing kinetics for eleven sets of Q&A series treatments involving up to five different specimens appear when plotted against the Reduced Annealing Time Variable $t_A/t_{1/2}$ defined as the ratio $t(T_Q, T_A, t_A)/t(T_Q, T_A, t_{1/2})$.[109]

8.3.8 Examinations of Plots of Fraction Remaining Values of NQIR(T_Q, T_A, t_A) vs. Reduced Annealing Time Variable $t_A/t_{1/2}$

Even with all of the various plots of Q&A series treatment annealing kinetics presented to this point, it should prove instructive to examine what can be observed when a number of sets of NQIR(T_Q, T_A, t_A) data are plotted as a function of a reduced annealing time variable $t_A/t_{1/2}$.

Selection was made of five distinct specimens and eleven associated Q&A series treatments. The collective results are graphically presented in Figures 147, 148, and 149. For specific comparison purposes these plots are segmented respectively into three distinct ranges, namely: from zero up to five, from zero up to 20, and from 0.02 up to 250, for the independent parameter labeled as the reduced annealing time variable $t_A/t_{1/2}$.

---

[109] Refer to Table 14 in section 8.3.4.17 for the annealing half-times associated with the indicated specimens and their respective Q&A series treatments.

8.3.8.1 Specimens 3012, 3013, 3016, 4002, and 4005: Eleven Plots for Reduced Annealing Time Variable $t_A/t_{1/2}$ Values ranging from zero up to 5

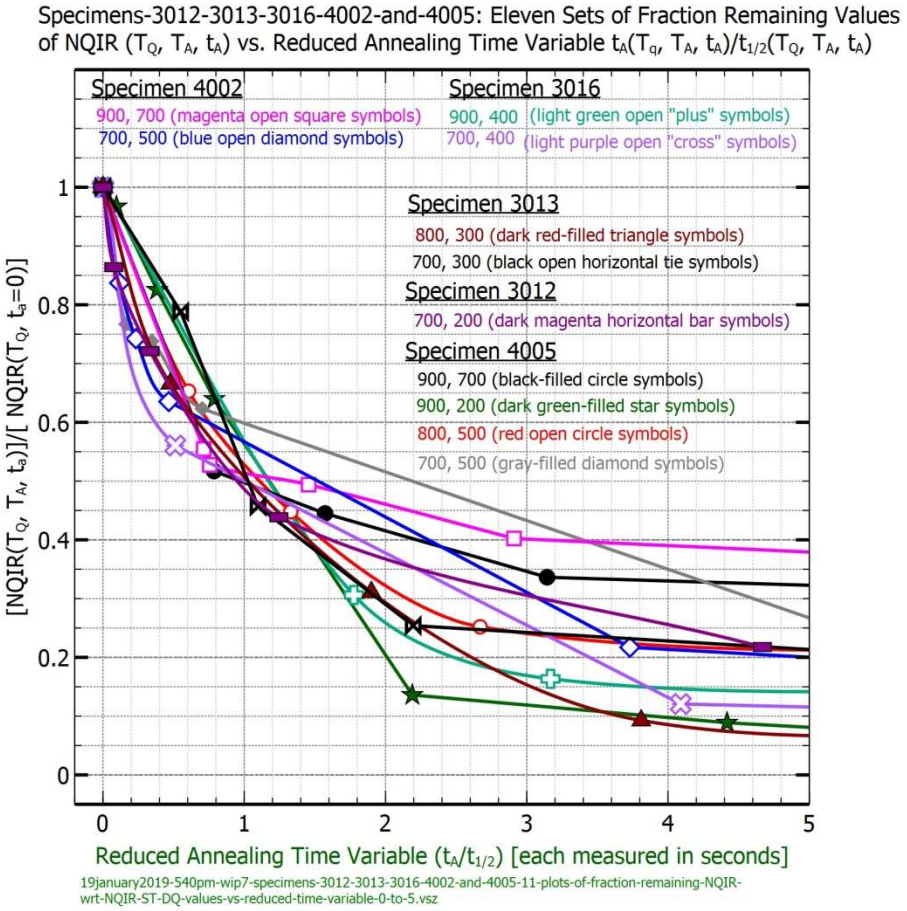

Figure 147. Specimens 3012, 3013, 3016, 4002, and 4005: Eleven Plots of Initial Fraction Remaining Values of NQIR(T_Q, T_A, t_A) where the Reduced Annealing Time Variable $t_A/t_{1/2}$ Values ranging from zero up to 5

8.3.8.2 Specimens 3012, 3013, 3016, 4002, and 4005: Eleven Plots for Reduced Annealing Time Variable $t_A/t_{1/2}$ Values ranging from zero up to 20

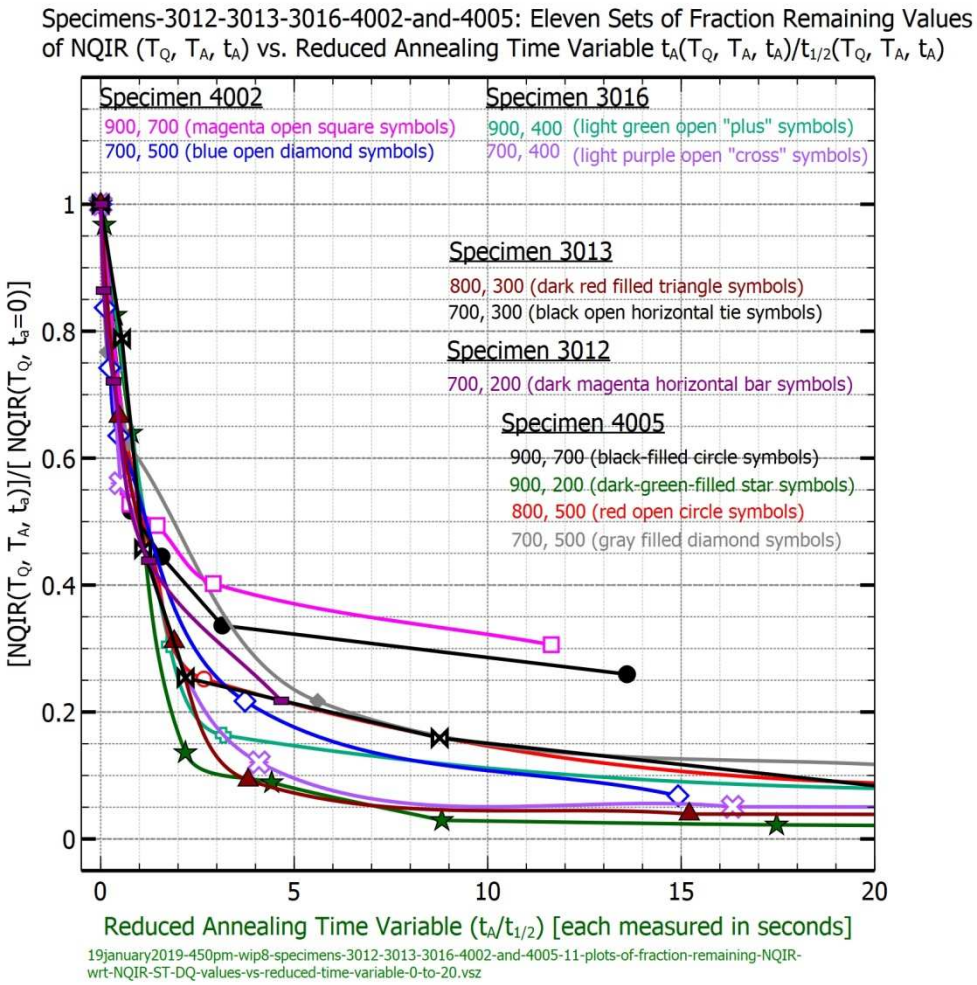

Figure 148. Specimens 3012, 3013, 3016, 4002, and 4005: Eleven Plots of Fraction Remaining Values of NQIR(T_Q, T_A, t_A) where the Reduced Annealing Time Variable $t_A/t_{1/2}$ Values ranging from zero up to 20

8.3.8.3 Specimens 3012, 3013, 3016, 4002, and 4005: Eleven Plots of Fraction Remaining Values of NQIR(T_Q, T_A, t_A) vs. Log of Reduced Annealing Time Variable $t_A/t_{1/2}$ Values ranging from 0.02 up to 250

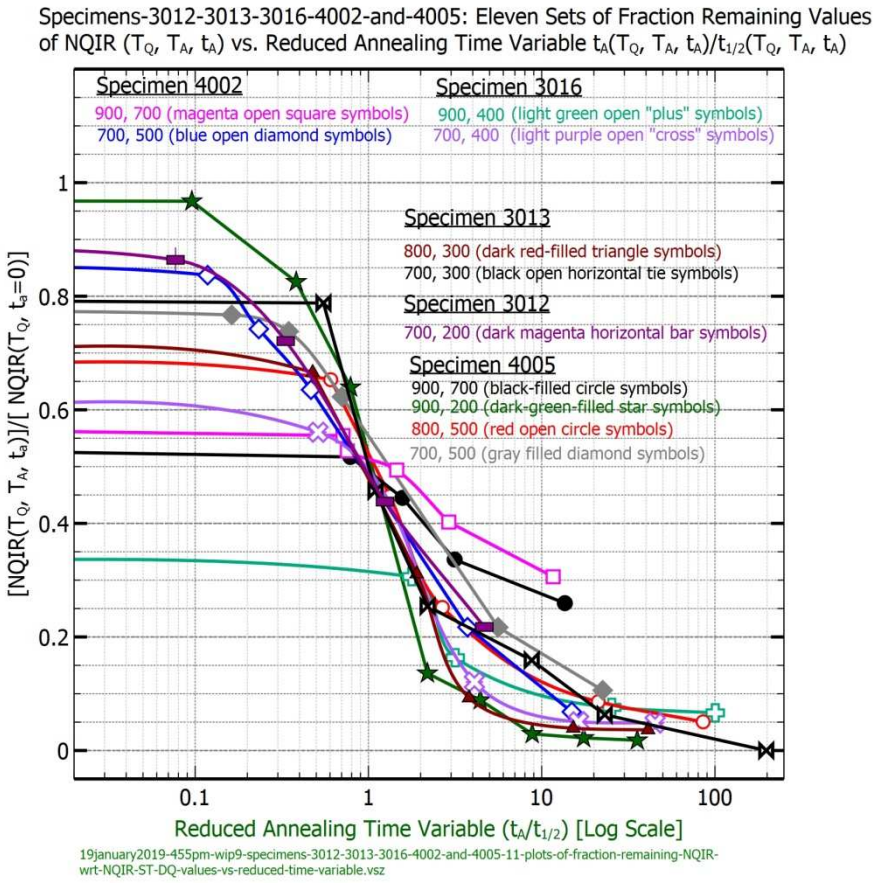

Figure 149. Specimens 3012, 3013, 3016, 4002, and 4005: Eleven Plots of Fraction Remaining Values of NQIR(T_Q, T_A, t_A) vs.Log of Reduced Annealing Time Variable $t_A/t_{1/2}$ Values ranging from 0.02 up to 250

Figures 150 through 152 provide additional illustrations of the respective annealing kinetics when only one of the three quench temperatures is chosen for the indicated sets of specimens in order to a) more clearly distinguish their respective characteristics and b) allow for distinct comparisons to be readily discerned that the collective sets of plots presented in Figure 147 do not show in sufficient detail.

8.3.8.4 Specimens 3012, 3013, 3016, 4002, and 4005: Five Plots of Fraction Remaining Values of NQIR(700, T_A, t_A) vs. Reduced Annealing Time Variable $t_A/t_{1/2}$ Values ranging from zero up to 5

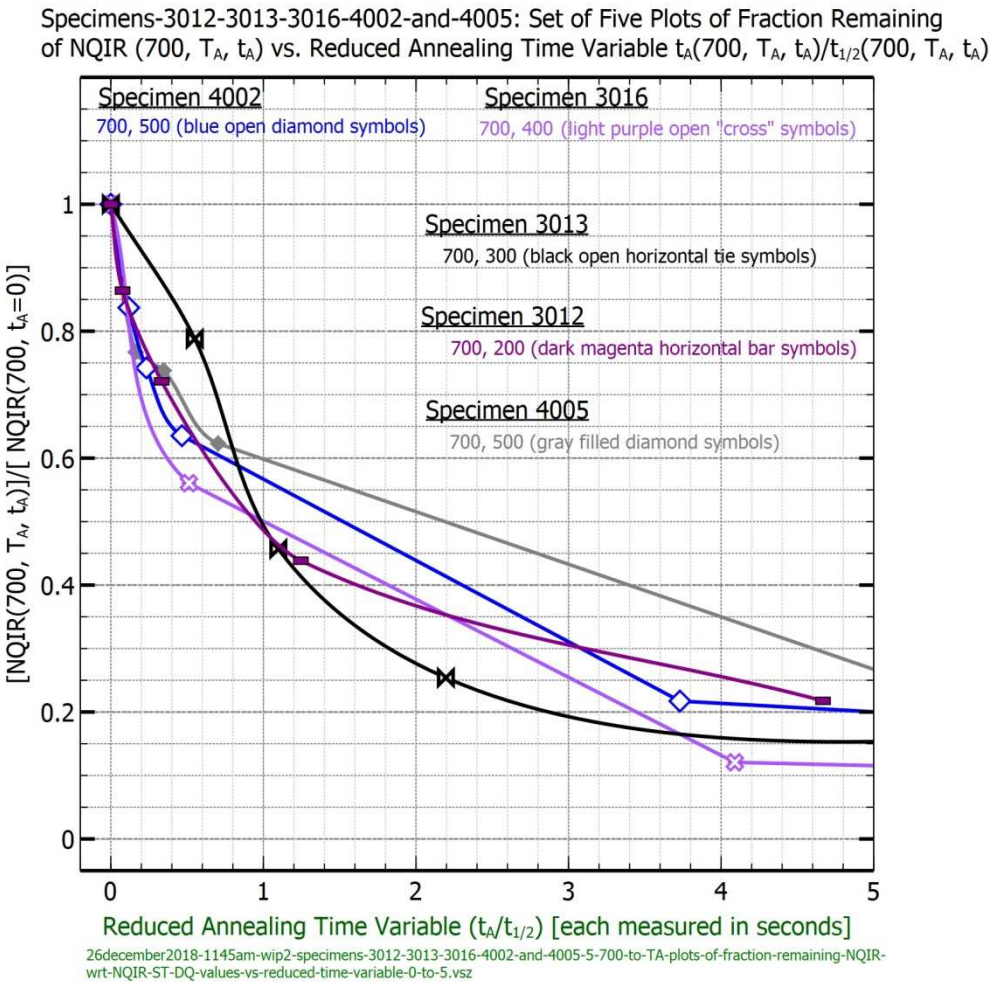

Figure 150. Specimens 3012, 3013, 3016, 4002, and 4005: Five Plots of Fraction Remaining Values of NQIR(700, T_A, t_A) vs. Reduced Annealing Time Variable $t_A/t_{1/2}$ Values ranging from zero up to 5

Note that only the (700, 300) plot for specimen 3013 exhibits any indication of S-shaped annealing kinetics.

8.3.8.5 Specimens 3013 and 4005: Two Plots of NQIR(800, T_A, t_A) vs. Reduced Annealing Time Variable $t_A/t_{1/2}$ Values ranging from zero up to 5

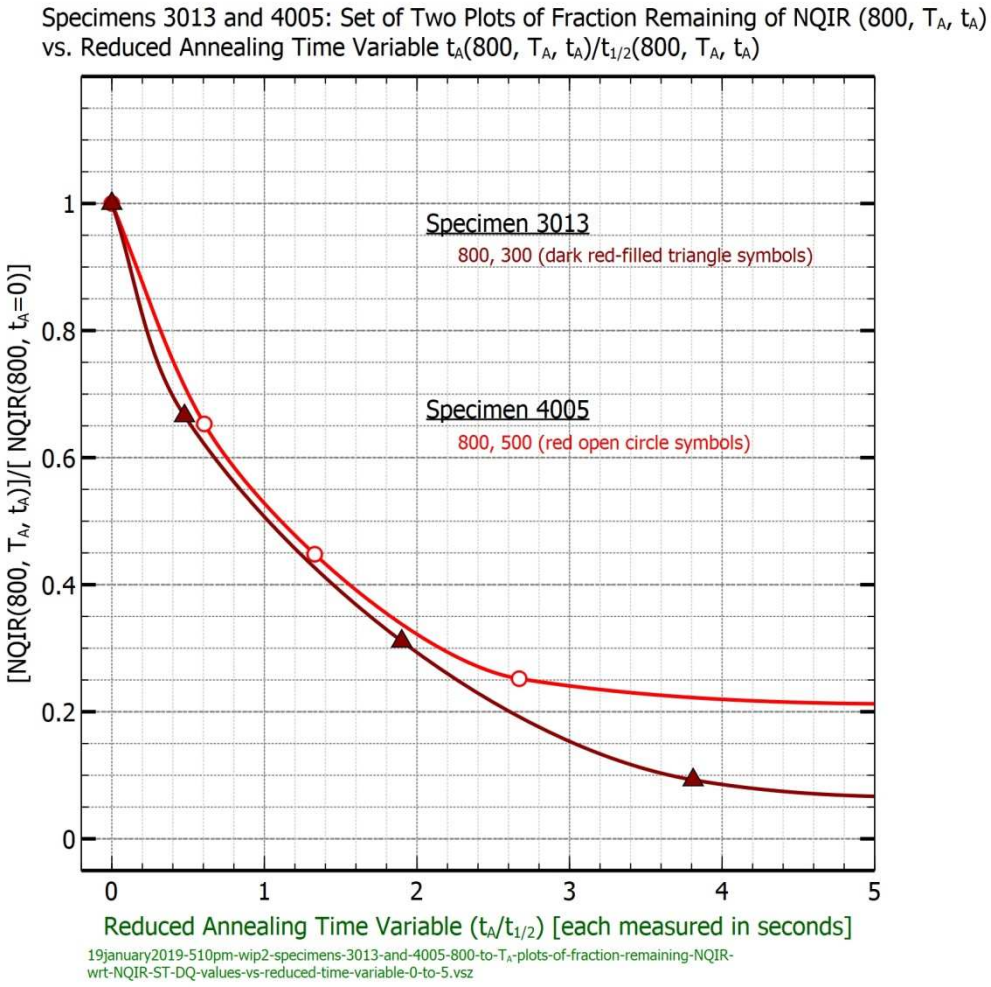

Figure 151. Specimens 3013 and 4005: Two Plots of Fraction Remaining Values of NQIR(T_Q, T_A, t_A) vs. Reduced Annealing Time Variable $t_A/t_{1/2}$ Values ranging from zero up to 5

8.3.8.6 Specimens 3016, 4002, and 4005: Four Plots of NQIR(900, T_A, t_A) vs. Reduced Annealing Time Variable $t_A/t_{1/2}$ Values ranging from zero up to 5

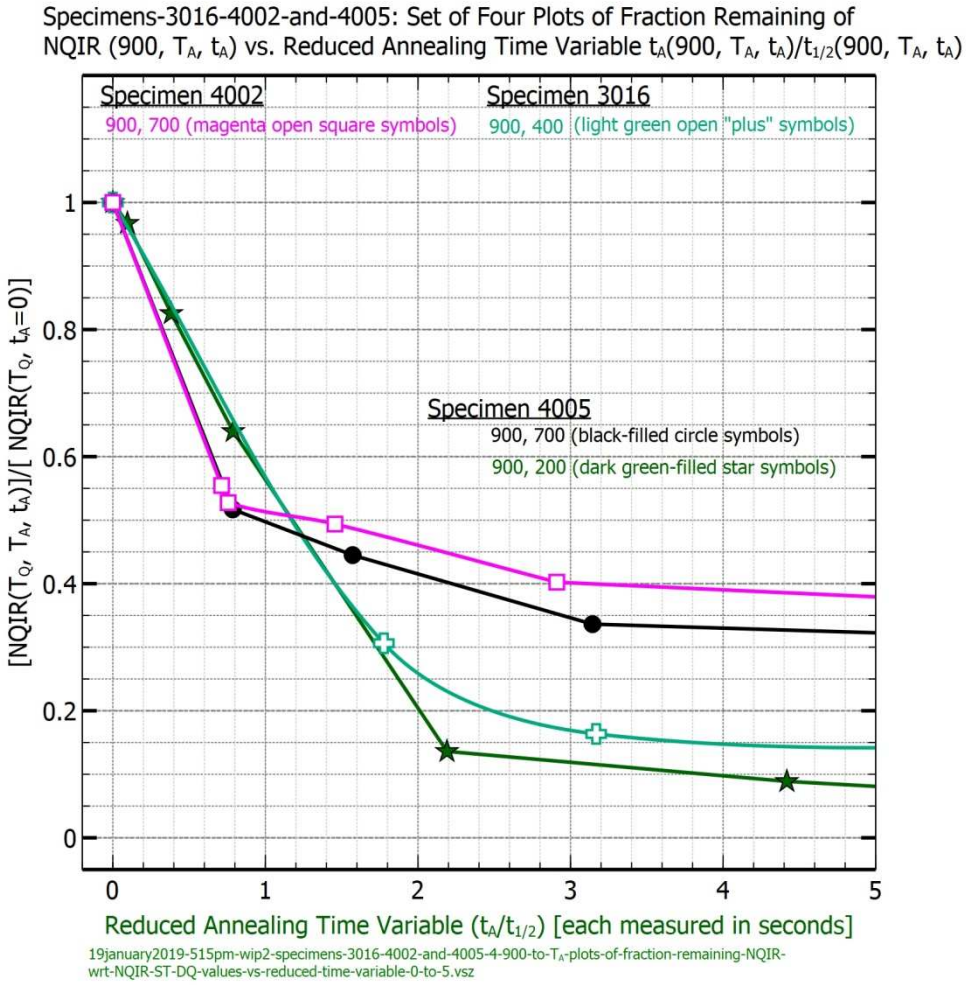

Figure 152. Specimens 3016, 4002, and 4005: Four Plots of Fraction Remaining Values of NQIR(T_Q, T_A, t_A) vs. Reduced Annealing Time Variable $t_A/t_{1/2}$ Values ranging from zero up to 5.

8.3.8.7 Principal Conclusion reached from Examinations of Plots of Fraction Remaining Values of NQIR(T_Q, T_A, t_A) vs. Reduced Annealing Time Variable $t_A/t_{1/2}$.

With the exception of the (700, 300) plot for specimen 3013, all Reduced Annealing Time Variable $t_A/t_{1/2}$ plots exhibited a fast (initial) annealing rate followed by a slower extended annealing rate behavior.

8.3.9 Accounting for Occurrences in some graphed segments where T_A approaches T_Q of Slope Reversals in Arrhenius Plots of NQIR(T_Q, T_A, t_A) Q&A Series Treatments vs. Annealing Half-times

As was stated in sub-section 8.3.5.6, negative slopes (labeled N/A) occurred in Figure 136 for three instances as T_A approaches T_Q. This observation called into play further data analyses directed toward coming up with a reasonable explanation, and an initial interpretation is introduced at this time.

8.3.9.1 How and Why Negative Slopes are related to Excess Vacancy Defect Chemical Potential $\mu_V(T_Q, T_A)$ Magnitudes for Specific Half-time Segments in Arrhenius Plots

Examination of the values listed in Table 15 for “No-Loss” magnitudes for $\mu_V(T_Q, T_A)$ for the corresponding T_Q and T_A combinations associated with each of the negative slope segments shown in Figure 136 reveals the following relative relationships:

1) For specimen 3013: μ_v(700, 600)=0.10 eV; μ_v(700, 500)=0.20 eV;
2) For specimen 4002: μ_v(900, 700)=0.14 eV; μ_v(900, 500)=0.335 eV;
3) For specimen 4005: μ_v(900, 700)=0.14 eV; μ_v(900, 500)=0.335 eV.

Even recognizing the fact that these three sets of relative values may only approximate the actual excess vacancy defect chemical potential (μ_v) values, they might nonetheless tend to infer how and why for each negative slope segment a longer annealing half-time was encountered for that higher T_A value compared to the half-time established for the segment associated with the next lower T_A value.

Figure 142 in sub-section 8.3.6.7 provides a graphical example for specimen 4002 that reveals the influence of differing magnitudes of μ_v upon annealing kinetics for quench temperatures of 900^{o}C and 700^{o}C during anneals at 500^{o}C, and the

respective associated annealing half-times of 0.27 and 0.13 seconds are labeled in Figures 116 and 83 and are listed in Table 14.

One possible hypothesis that might account for such negative slope occurrences in Arrhenius plots of half-time annealing kinetics would be to acknowledge that significant reductions in absolute macroscopic sink efficiency **€** are likely to result as excess vacancy defect chemical potentials diminish to levels ≤ 0.2 eV, particularly for specimens that happen to have low pre-existing sink densities.

8.3.9.2 Influence of Specimen Pre-existing Sink Density Magnitudes upon Annealing Half-times

Examination of results in Figure 131 for post-direct deformation specimen 3012 gives support to considerations of pre-existing sink densities on annealing kinetics. Specifically, it is readily observed that the annealing half-times for specimen 3012 when compared with those for specimen 3013 for (700, 600/200, t_A) Q&A series treatments indicate that specimen 3012 exhibits much higher losses. This result was an expected consequence of the direct deformation which specimen 3012 had been intentionally subjected to following its initial use during the straight downquench data acquisition phase of this research already presented in Chapter 7.

Unfortunately, because only two annealing temperature data points of 600^{o}C and 200^{o}C were associated with this Q&A series treatment of specimen 3012, no additional slope segments were created for further comparisons to be made.

Additional analyses, discussions, and conclusions regarding half-time annealing kinetics are detailed in sub-section 8.4.2.

8.3.10 Extensive Sets of Arrhenius Plots of Initial Annealing Rates (IARs), Normalized Initial Annealing Rates (NIARs), Mean Relaxation Times (t_{mean}), and determinations of Instantaneous Vacancy Activation Energy, $E^M_V(act)$, for various Q&A Series Treatments

Presented in this sub-section are sets of Arrhenius plots that resulted from calculations of initial annealing rates (IARs) for each of three specimens. These plots served as the starting point that would lead to determinations of magnitudes for the parameter defined hereafter as the instantaneous vacancy activation energy[110], $E^M_V(act)$, from the resulting slopes for each segment between two associated isothermal annealing temperatures.

The overall focus of this sub-section will be on presenting the results of having acquired specific sets of resistometric data associated with each specimen's initial annealing region to be able to calculate values for three parameters, namely: Initial Annealing Rate (IAR), Normalized Initial Annealing Rate (NIAR), and Mean Relaxation Time (t_{mean}), in order to achieve the objective of establishing values for the parameter $E^M_V(act)$.

Specifically, analyses of the associated Arrhenius plots were made that involved specimens 3013, 4002, and 4005 subjected to sets of NQIR(600, T_A, Δt_A) , NQIR(700, T_A, Δt_A), and NQIR(900/800/700, T_A, Δt_A) Q&A series treatments wherein T_A covers a wide range in isothermal annealing temperatures for each NQIR(T_Q, T_A, Δt_A) Q&A series treatment and Δt_A is the label used for the parameter $(\Delta t_A)_{initial}$ (defined as the duration time of the shortest isothermal anneal, hence the added

[110]NOTE: This parameter was reported by Chik [12-15] as the nucleation process activation energy for stacking fault tetrahedra (SFT) in gold.

descriptor *initial*), associated with each and every data acquisition point in the respective sets of plots of NQIR(T_Q, T_A, Δt_A) Q&A series treatments.

Sub-sections 8.3.10.1, 8.3.10.2, and 8.3.10.3 present, respectively, the results and analyses of NQIR(600, T_A, Δt_A), NQIR(700, T_A, Δt_A), and NQIR(900/800/700, T_A, Δt_A) Q&A Series treatments which are followed by summaries of data analyses and discussions presented in sub-sections 8.3.10.4, 8.3.10.5, and 8.3.10.6.

Categorized discussions of annealing kinetics and associated data analyses are covered in Section 8.4.

8.3.10.1 NQIR(600, T_A, Δt_A) Q&A Series Treatments Results and Analyses

8.3.10.1.1 Specimen 3013: Arrhenius Plot of Initial Annealing Rates for various NQIR(600°C,T_A, Δt_A) Q&A Series Treatments

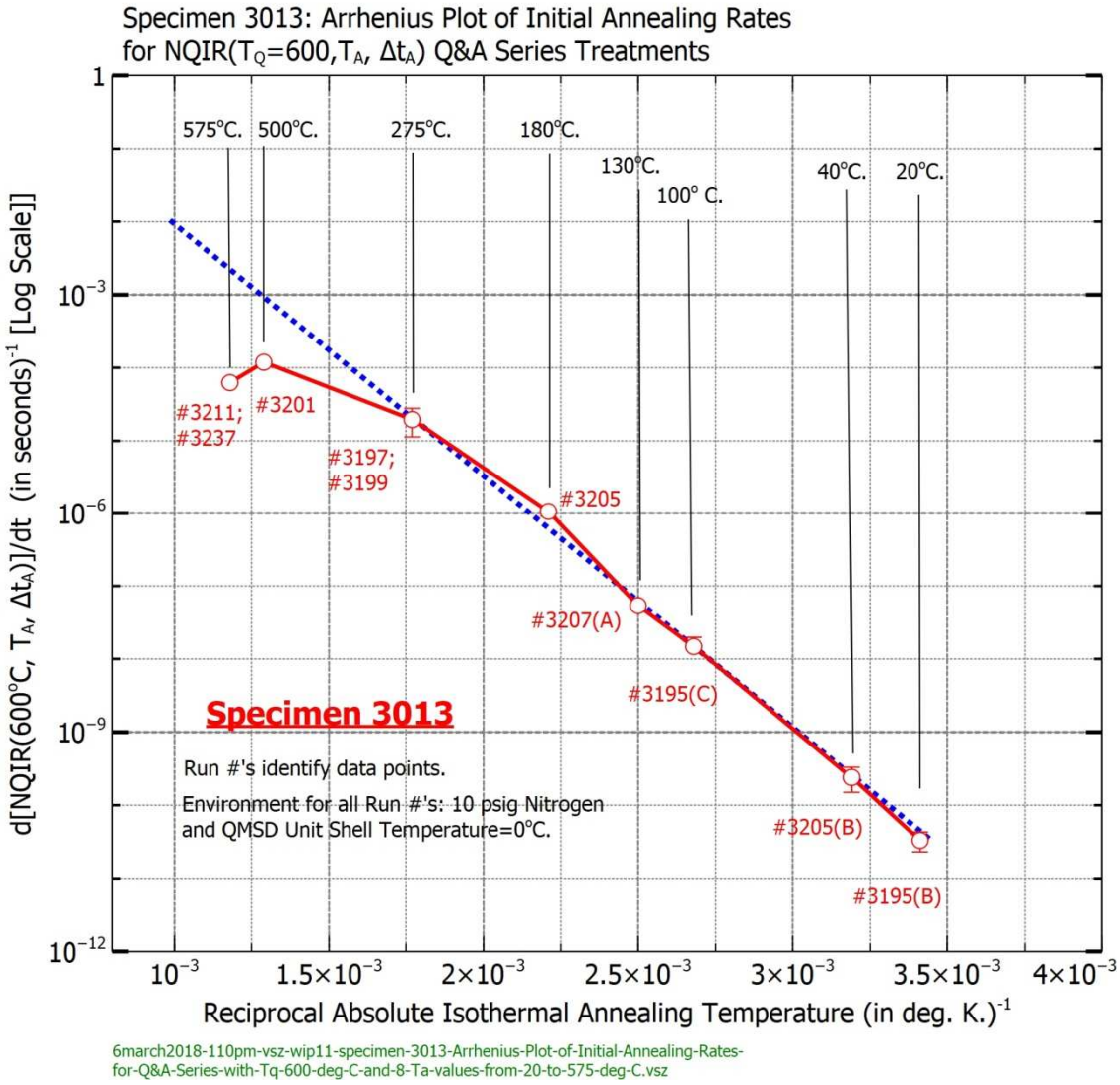

Figure 153. Specimen 3013: Arrhenius Plot of Initial Annealing Rates for various NQIR(600°C,T_A, Δt_A) Q&A Series Treatments

8.3.10.1.2 Specimen 3013: Arrhenius Plot of Normalized Initial Annealing Rate (NIAR) for various NQIR(600°C,T_A, Δt_A) Q&A Series Treatments

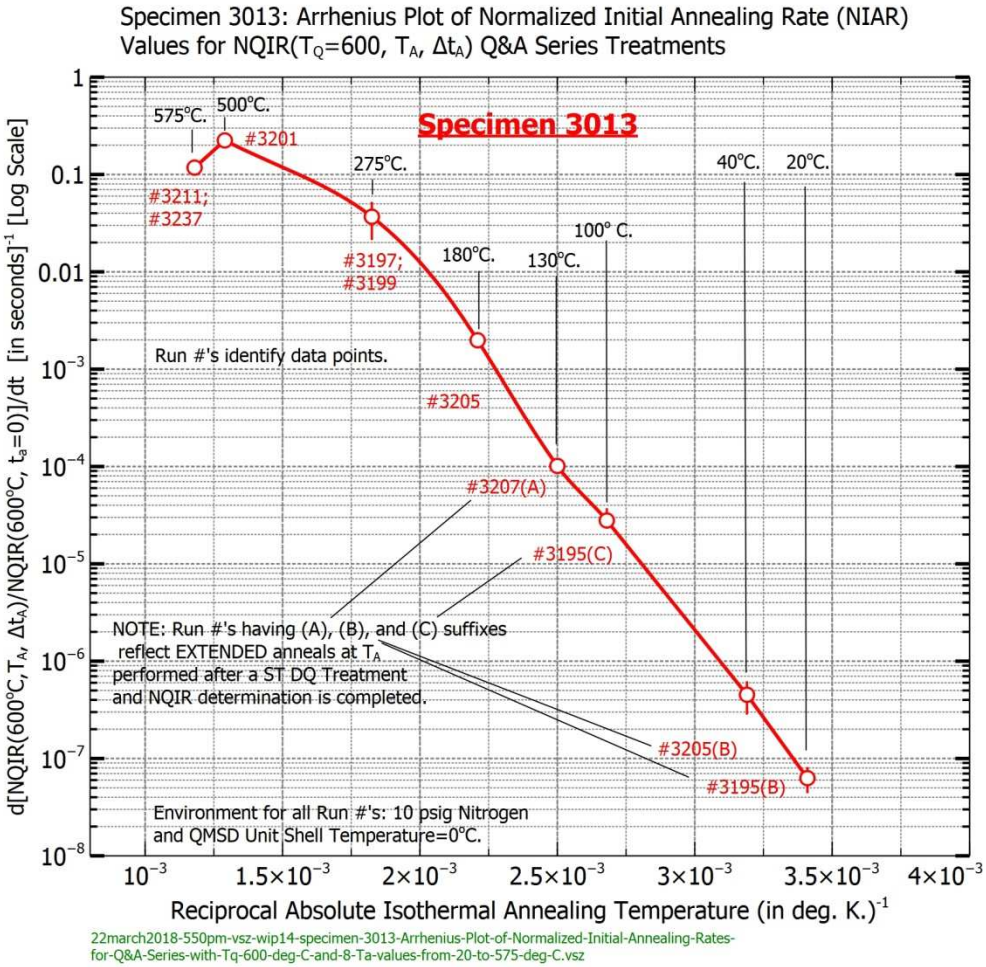

Figure 154. Specimen 3013: Arrhenius Plot of Normalized Initial Annealing Rate (NIAR) for various NQIR(600°C,T_A, Δt_A) Q&A Series Treatments

Figure 154 shows an Arrhenius plot for Specimens 3013 of Normalized Initial Annealing Rate (NIAR) for a NQIR(600,T_A, Δt_A) Q&A series treatment, and Figure 155 shows collective NIAR Arrhenius plots for Specimens 3013, 4002, and 4005 for various NQIR(600°C,T_A, Δt_A) Q&A series treatments.

8.3.10.1.3 Specimens 3013, 4002, and 4005: Arrhenius Plots of NIAR for three independent sets of various NQIR(600°C,T_A, Δt_A) Q&A Series Treatments

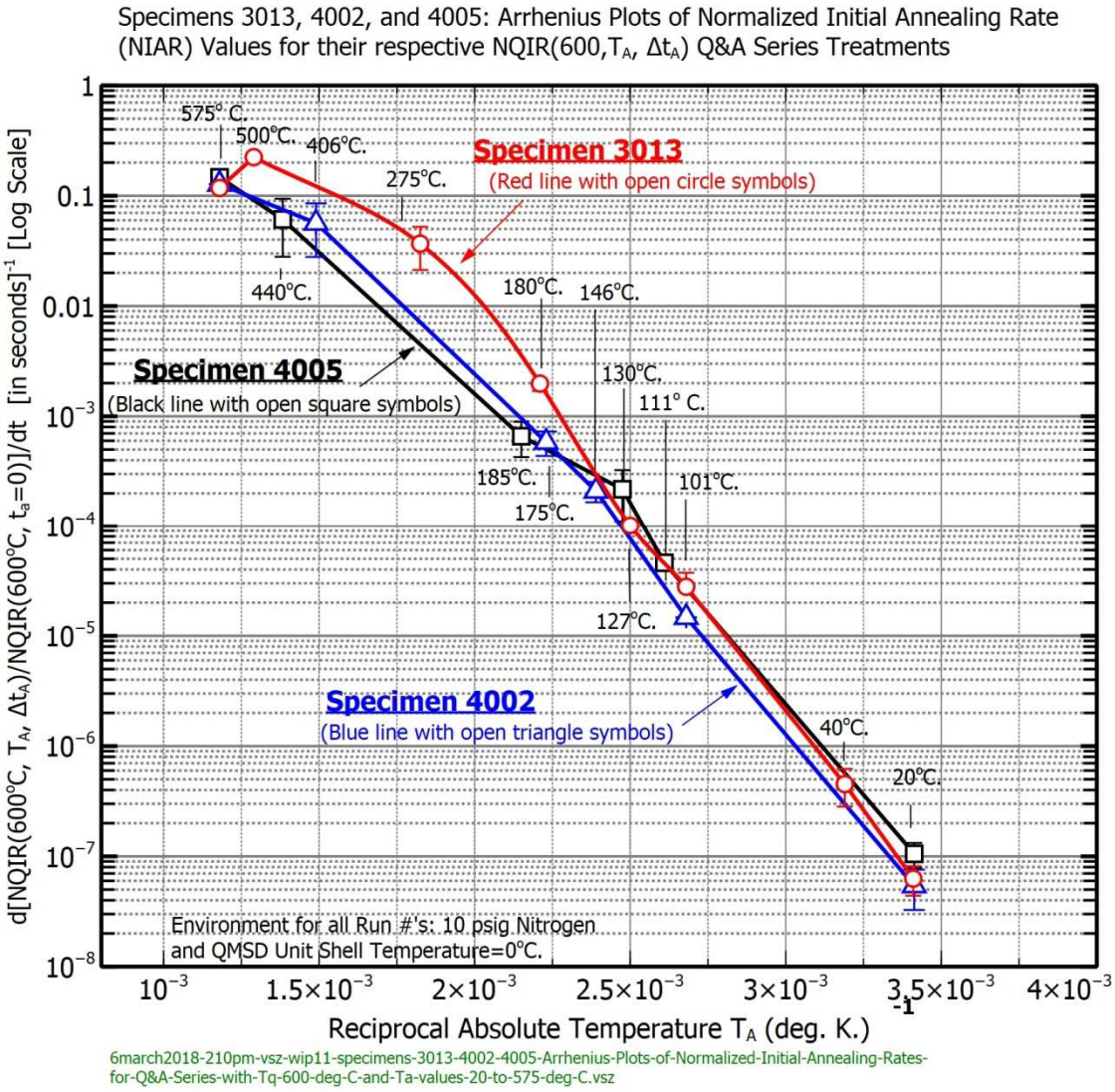

Figure 155. Specimens 3013, 4002, and 4005: Arrhenius Plots of NIAR for three independent sets of various NQIR(600°C,T_A, Δt_A) Q&A Series Treatments

Figures 156 through 162 show Arrhenius plots of the Mean Relaxation Time (t_{mean}) for various NQIR(600°C,T_A, Δt_A) Q&A series treatments.

8.3.10.1.4 Specimen 3013: Arrhenius Plot of Mean Relaxation Time (t_{mean}) for various NQIR(600°C,T_A, Δt_A) Q&A Series Treatments

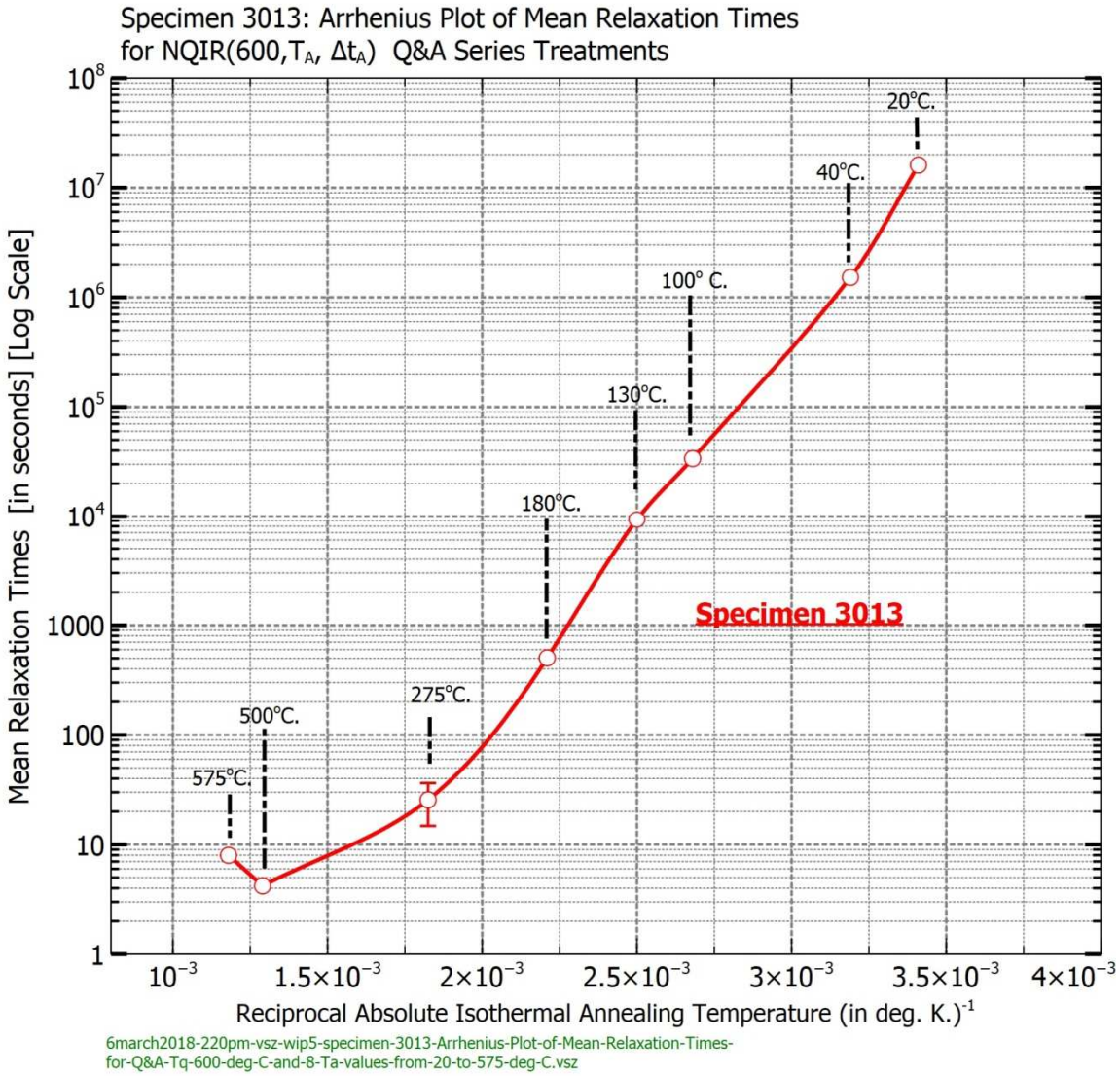

Figure 156. Specimen 3013: Arrhenius Plot of Mean Relaxation Time (t_{mean}) for various NQIR(600°C,T_A, Δt_A) Q&A Series Treatments

8.3.10.1.5 Specimen 4002: Arrhenius Plot of Mean Relaxation Time (t_{mean}) for various NQIR(600°C,T_A, Δt_A) Q&A Series Treatments

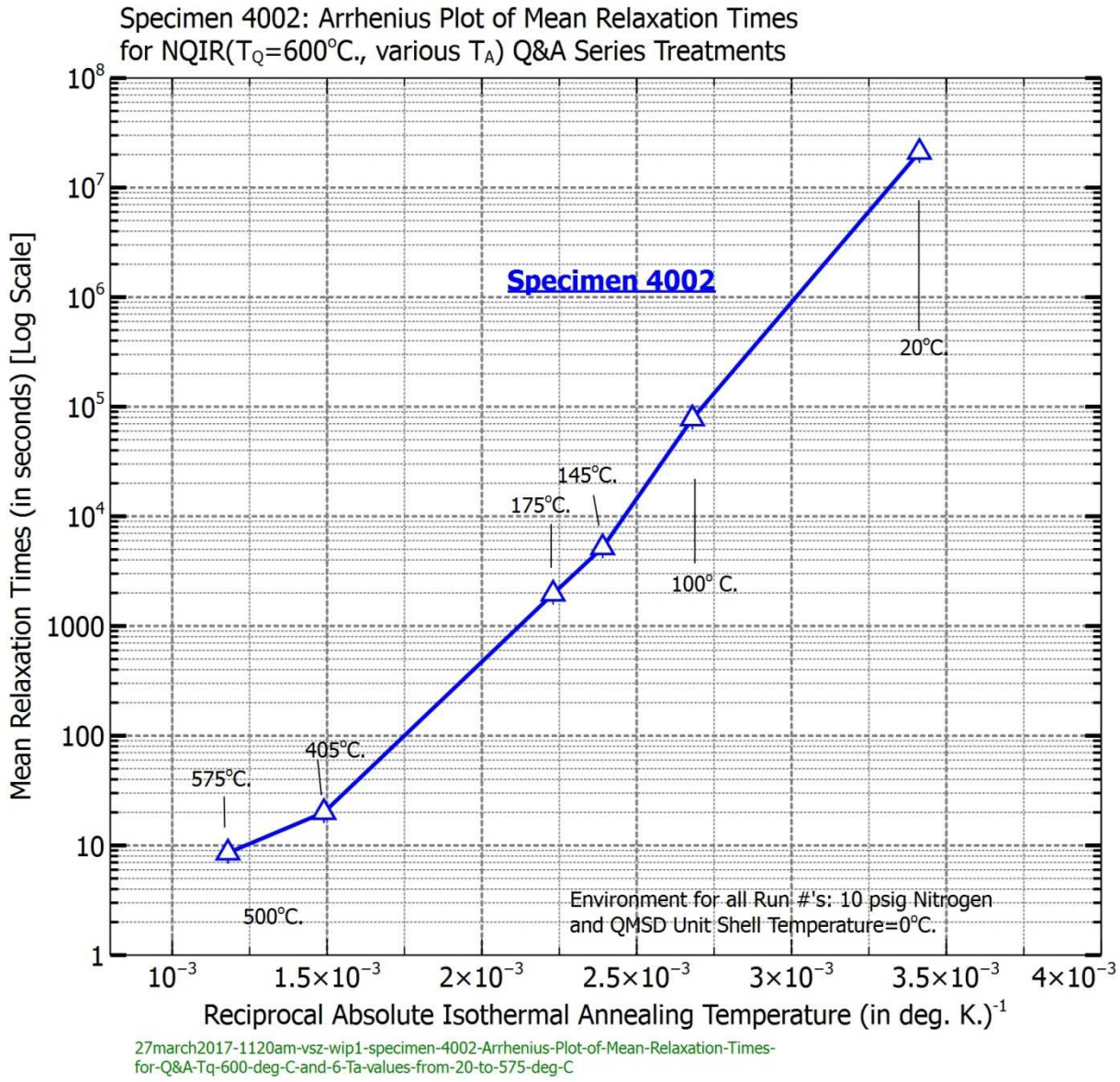

Figure 157. Specimen 4002: Arrhenius Plot of Mean Relaxation Time (t_{mean}) for various NQIR(600°C,T_A, Δt_A) Q&A Series Treatments

8.3.10.1.6 Specimen 4005: Arrhenius Plot of Mean Relaxation Time (t_{mean}) for various NQIR(600°C,T_A, Δt_A) Q&A Series Treatments

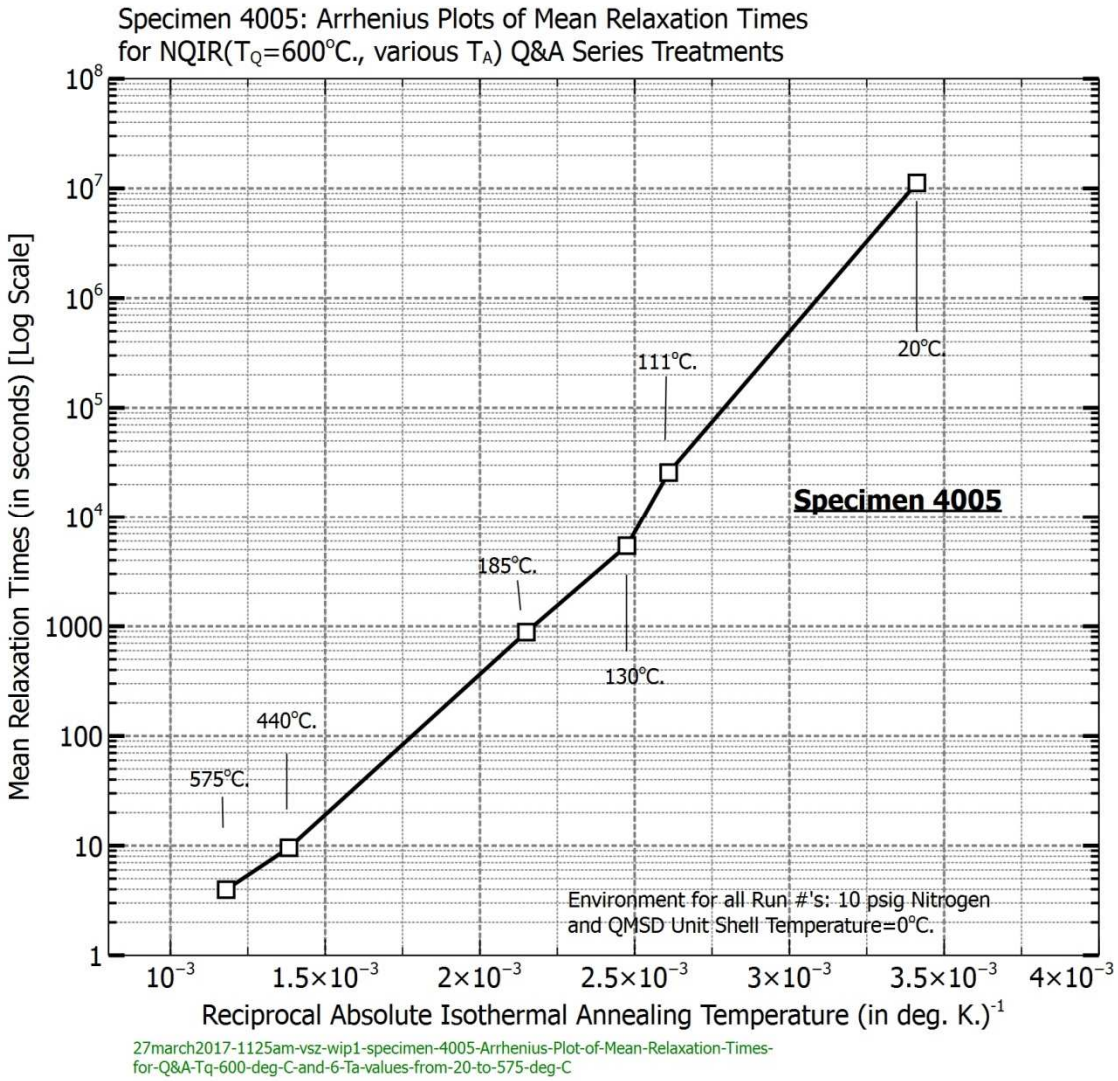

Figure 158. Specimen 4005: Arrhenius Plot of Mean Relaxation Time (t_{mean}) for various NQIR(600°C,T_A, Δt_A) Q&A Series Treatments

8.3.10.1.7 Specimens 3013, 4002, and 4005: Arrhenius Plots of Mean Relaxation Times (t_{mean}) for three independent sets of various NQIR(600°C,T_A, Δt_A) Q&A Series Treatments

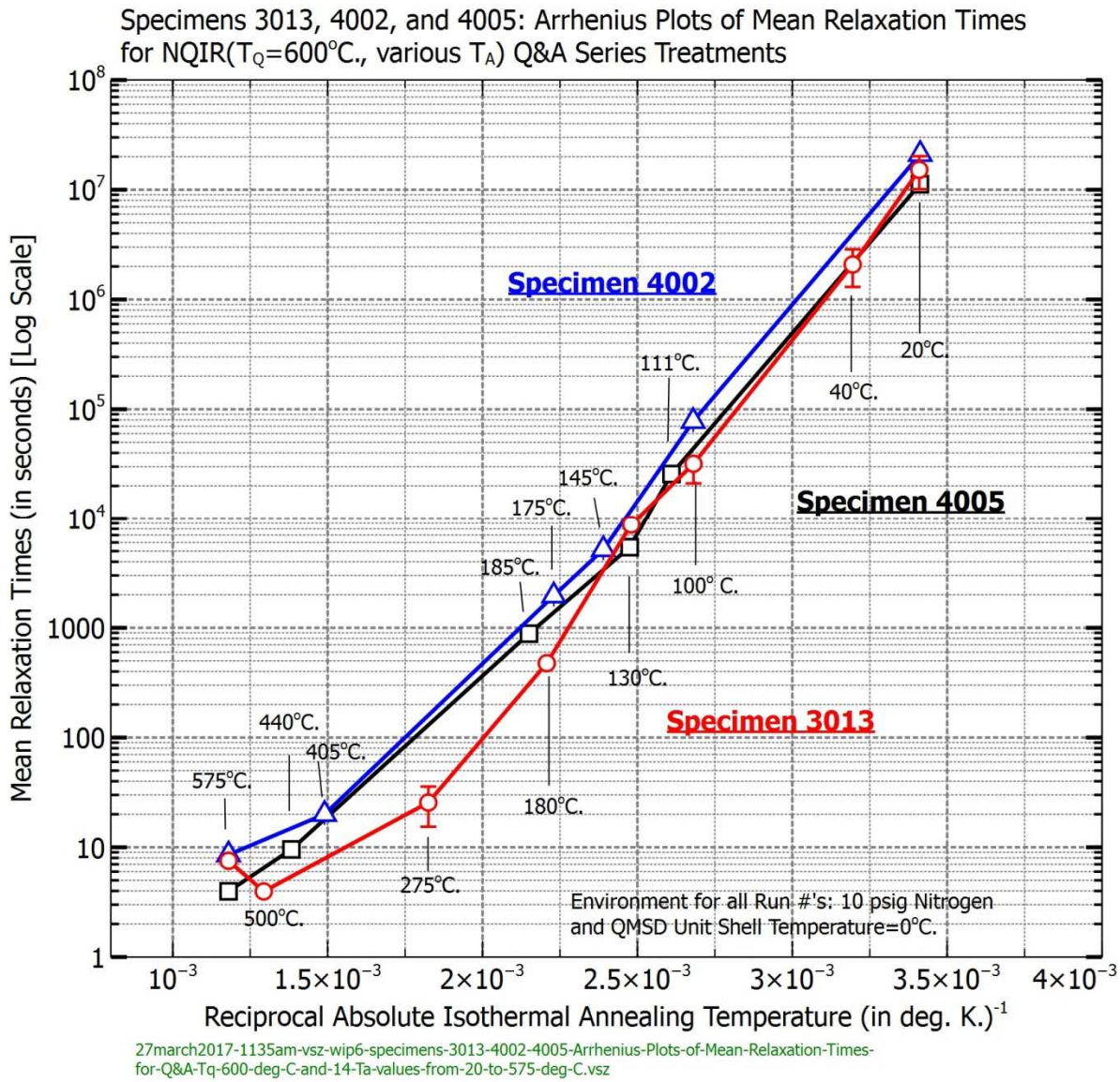

Figure 159. Specimens 3013, 4002, and 4005: Arrhenius Plots of Mean Relaxation Times (t_{mean}) for three independent sets of various NQIR(600°C,T_A, Δt_A) Q&A Series Treatments

8.3.10.1.8 Specimen 3013: Instantaneous Vacancy Activation Energy, $E^{M}_{V}(act)$, Determinations from an Arrhenius plot of Mean Relaxation Times (t_{mean}) for various NQIR(600°C,T_A, Δt_A) Q&A Series Treatments

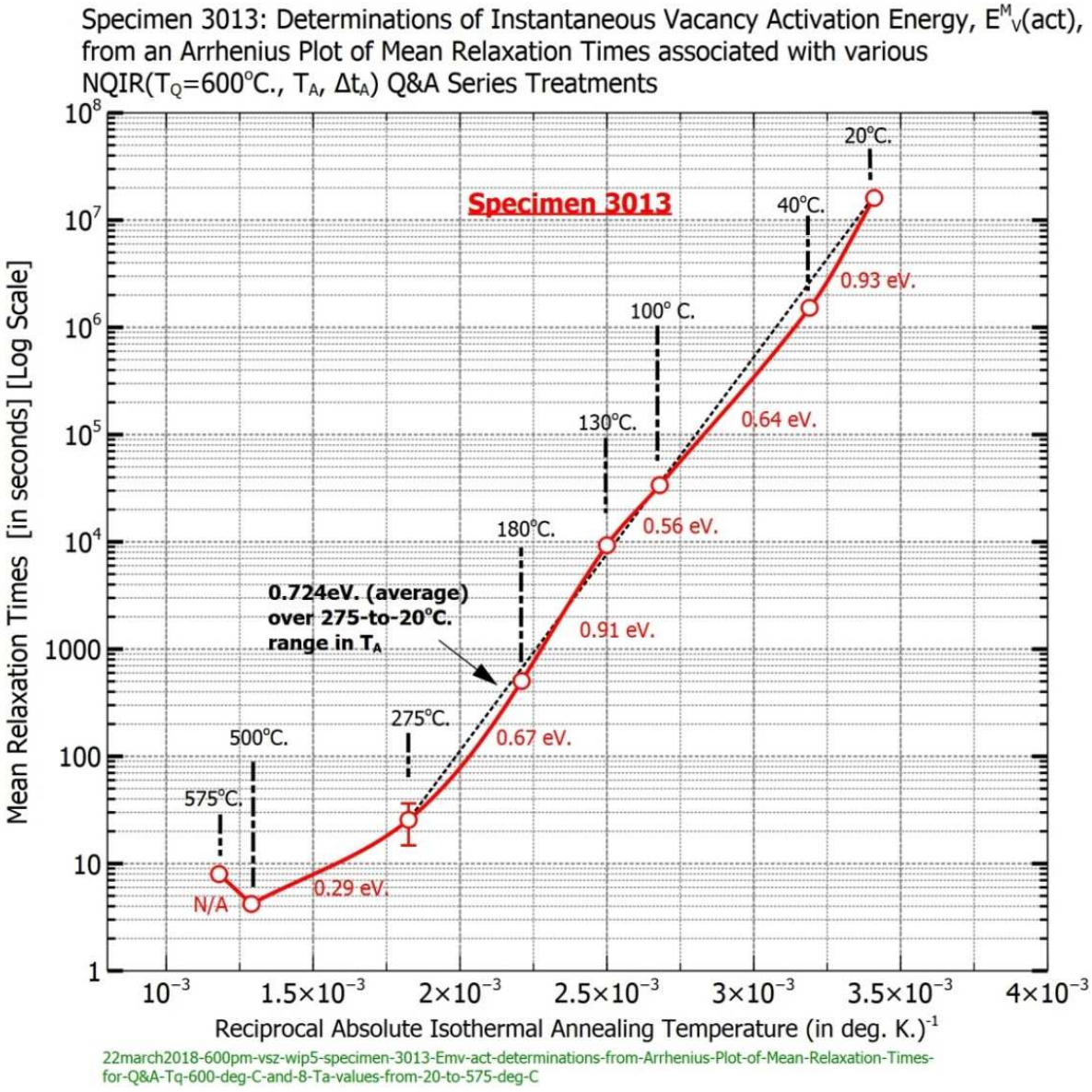

Figure 160. Specimen 3013: Instantaneous Vacancy Activation Energy, $E^{M}_{V}(act)$, Determinations from an Arrhenius plot of Mean Relaxation Times (t_{mean}) for various NQIR(600°C,T_A, Δt_A) Q&A Series Treatments

8.3.10.1.9 Specimen 4002: Instantaneous Vacancy Activation Energy, $E^{M}_{V}(act)$, Determinations from an Arrhenius plot of Mean Relaxation Times (t_{mean}) for various NQIR(600°C,T_A, Δt_A) Q&A Series Treatments

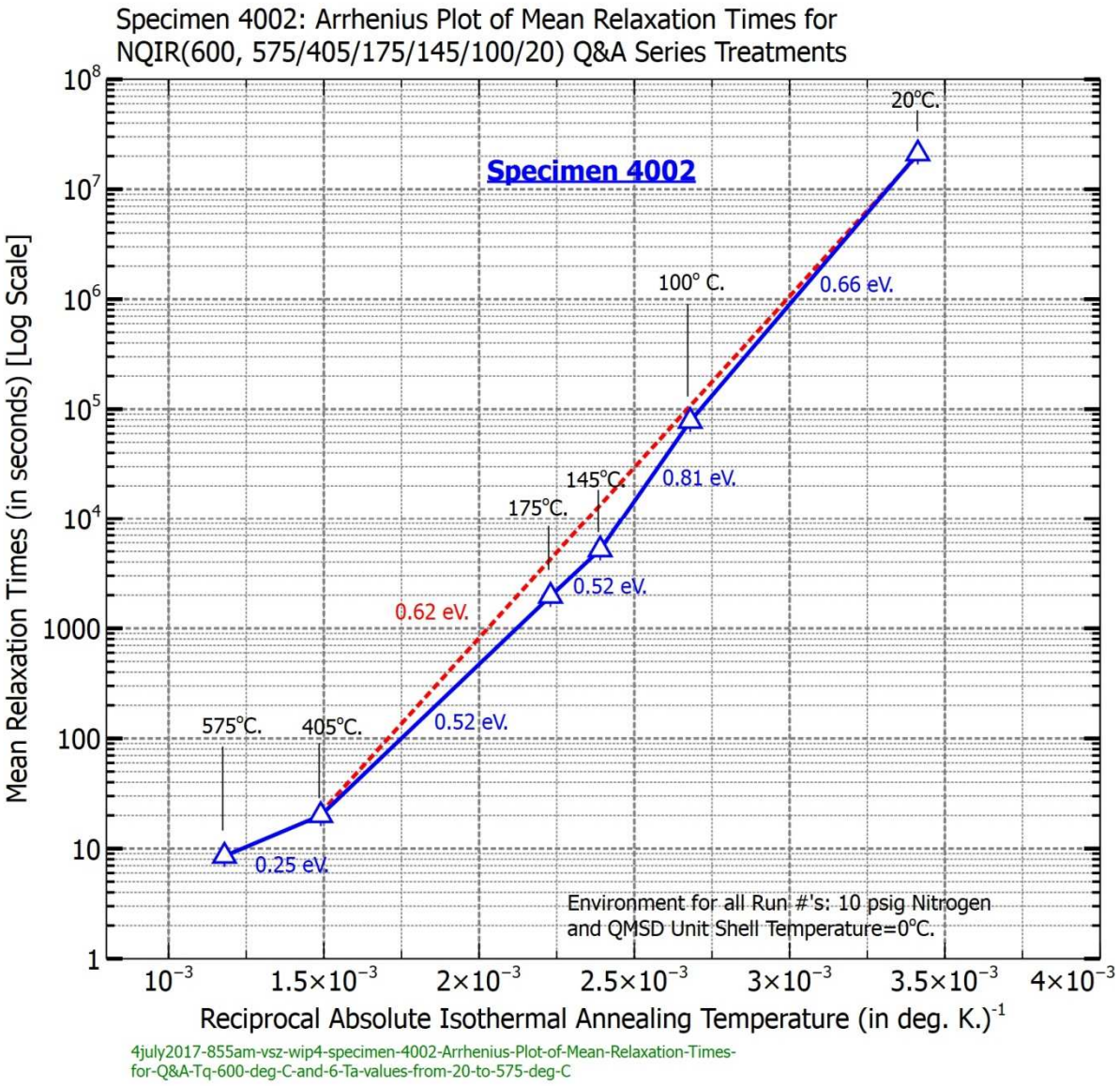

Figure 161. Specimen 4002: Instantaneous Vacancy Activation Energy, $E^{M}_{V}(act)$, Determinations from an Arrhenius plot of Mean Relaxation Times (t_{mean}) for various NQIR(600°C,T_A, Δt_A) Q&A Series Treatments

8.3.10.1.10 Specimen 4005: Instantaneous Vacancy Activation Energy, $E^{M}_{V}(act)$, Determinations from an Arrhenius plot of Mean Relaxation Times (t_{mean}) for an NQIR(600,T_A, Δt_A) Q&A Series Treatment

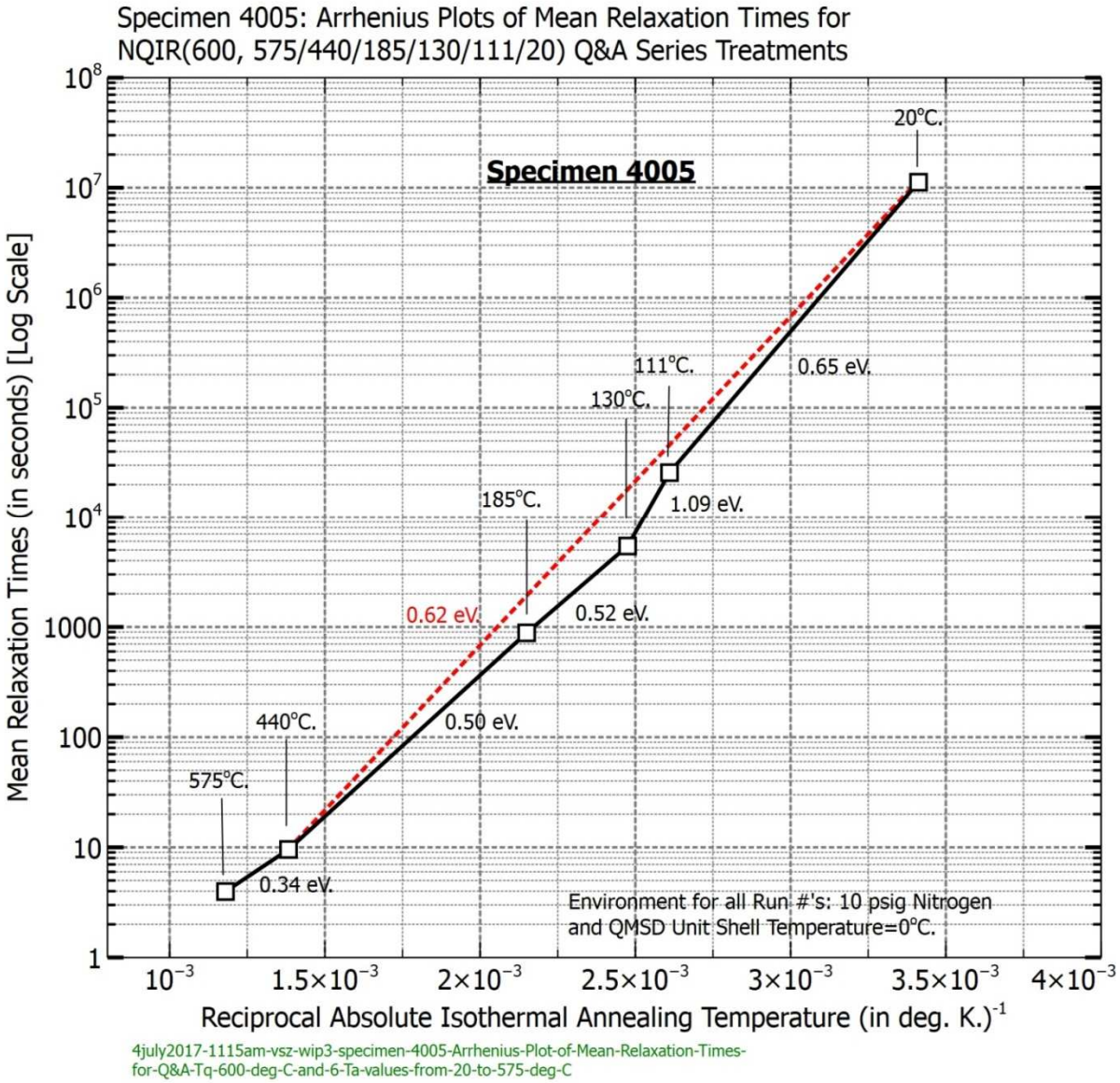

Figure 162. Specimen 4005: Arrhenius plot of Mean Relaxation Times (t_{mean}) for various NQIR(600°C,T_A, Δt_A) Q&A Series Treatments and calculated Instantaneous Vacancy Activation Energy, $E^{M}_{V}(act)$, values obtained from the respective slopes between data points

8.3.10.1.11 Plot of Instantaneous Vacancy Activation Energy, $E^{M}_{V}(act)$, for (600, T_A, Δt_A) Q&A Series Treatments vs. Vacancy Defect Chemical Potential (μ_V)

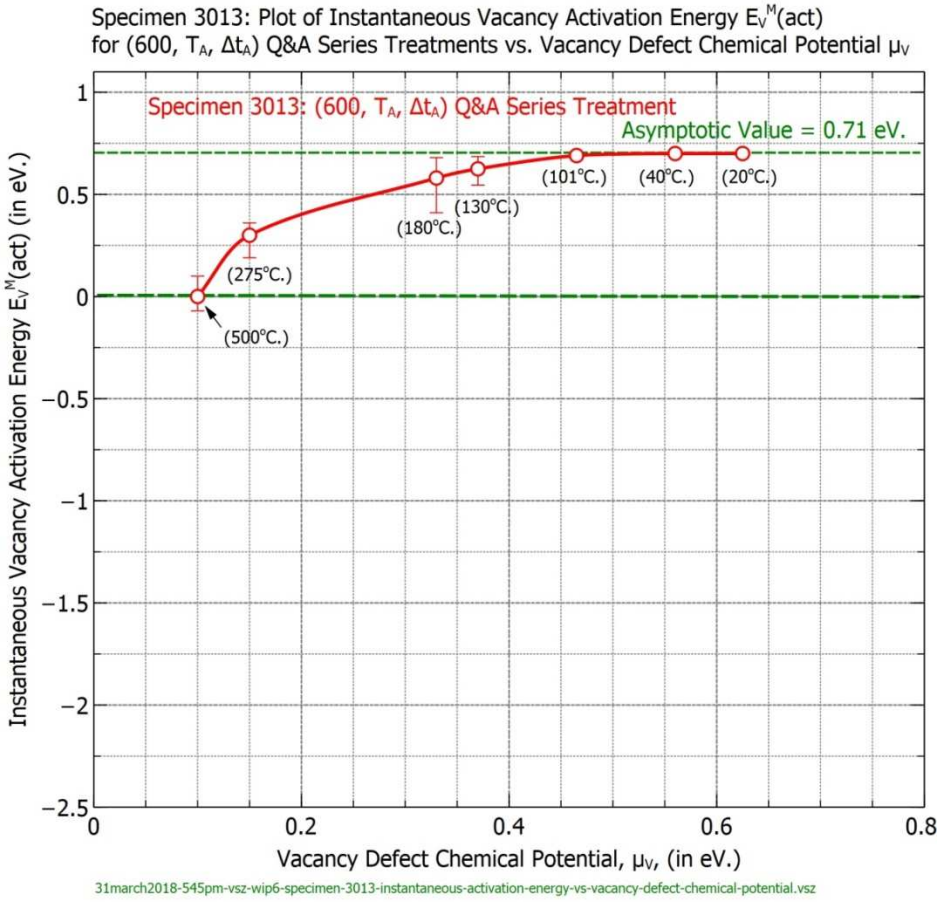

Figure 163. Specimen 3013: Dependency of Instantaneous Vacancy Activation Energy, $E^{M}_{V}(act)$, upon Vacancy Defect Chemical Potential (μ_V) during a (600, T_A, Δt_A) Q&A Series Treatment

Figure 163 shows how the instantaneous vacancy activation energy, $E^{M}_{V}(act)$, values (based on the slopes obtained from Figure 160 presented in sub-section 8.3.10.1.8) are influenced by vacancy defect chemical potential (μ_V).

8.3.10.1.12 Example of Influence of Vacancy Defect Chemical Potential on Absolute Macroscopic Sink Efficiency

The influence of vacancy defect chemical potential upon absolute macroscopic sink efficiency was assessed by comparing actual initial annealing rates with extrapolated (assuming unity efficiency associated for annealing temperatures below 200^{o}C) initial annealing rate values obtained for specimen 3013.

Figure 164 provides one example that illustrates the influence of vacancy defect chemical potential upon absolute macroscopic sink efficiency.

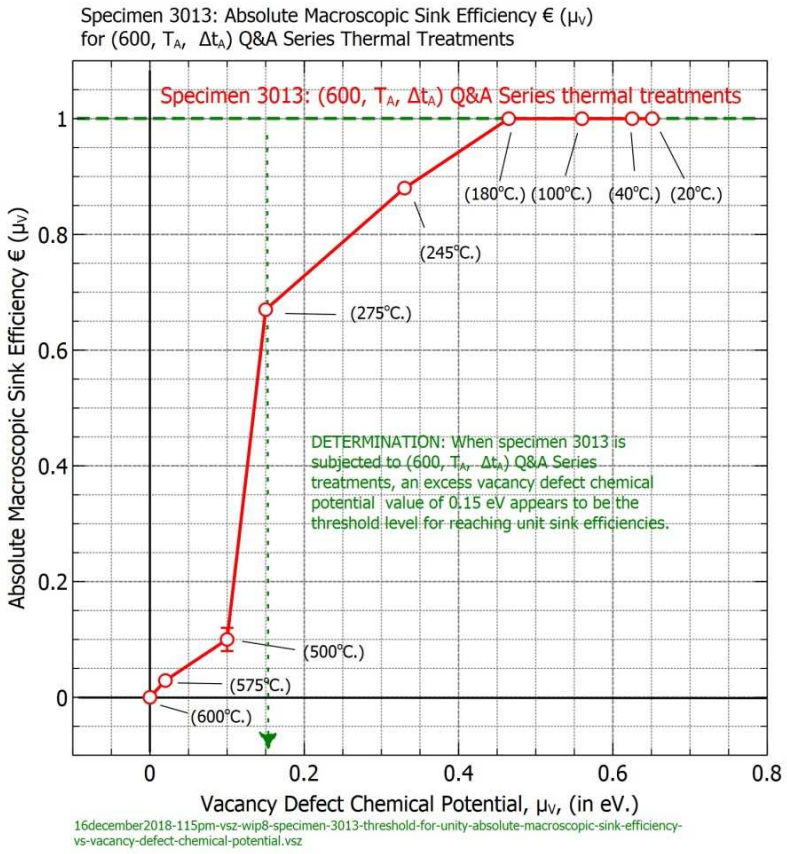

Figure 164. Specimen 3013: Influence of Vacancy Defect Chemical Potential μ_V upon Absolute Macroscopic Sink Efficiency €

8.3.10.2 NQIR(700, T_A, Δt_A) Q&A Series Treatments Results and Analyses

Figures 165 through 168 illustrate the respective Arrhenius plots.

8.3.10.2.1 Specimens 3013, 4002, and 4005: Arrhenius Plots of Initial Annealing Rates for an NQIR(700,T_A, Δt_A) Q&A Series Treatment and Instantaneous Vacancy Activation Energy, E^M_V(act), Values

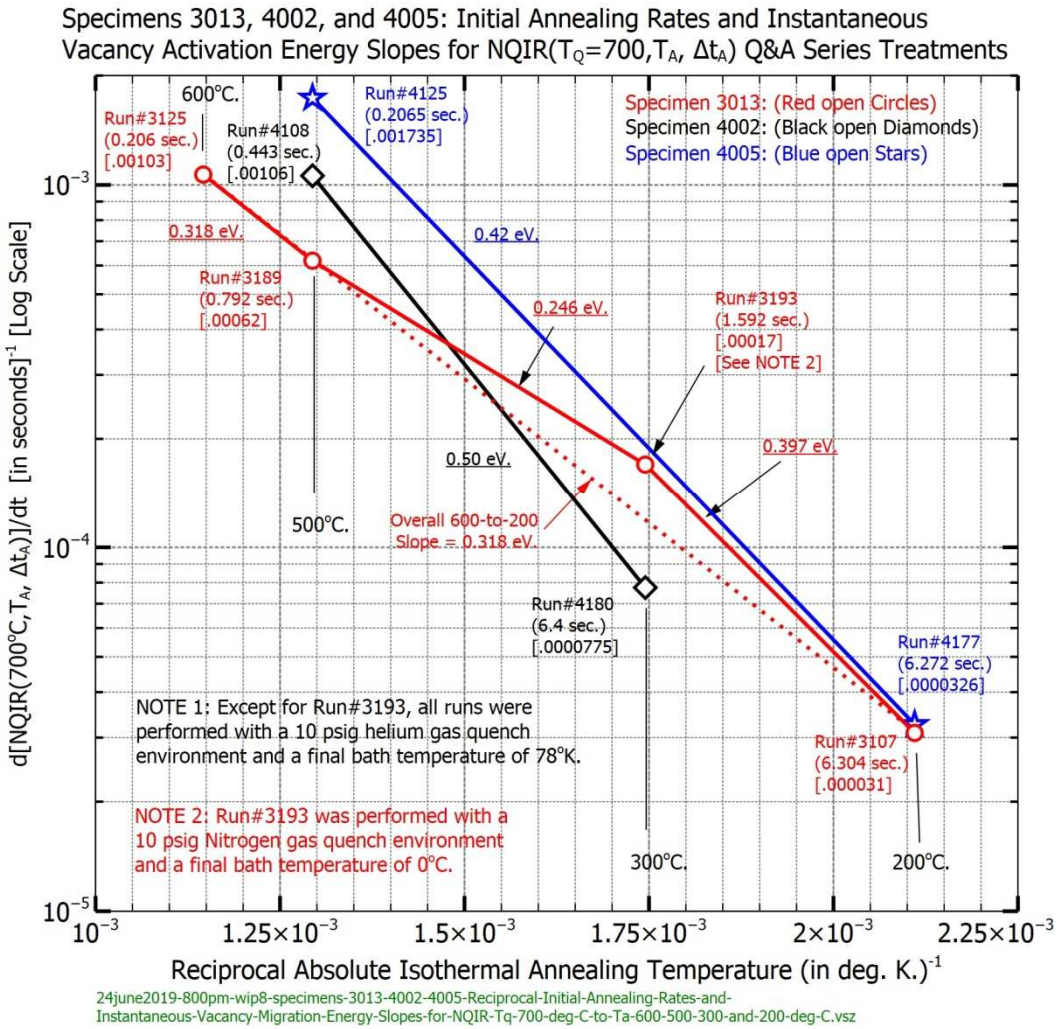

Figure 165. Specimens 3013, 4002, and 4005: Arrhenius Plots of Initial Annealing Rates for an NQIR(700,T_A, Δt_A) Q&A Series Treatment and Instantaneous Vacancy Activation Energy, E^M_V(act), Values obtained from the respective slopes between data points

8.3.10.2.2 Specimen 3013: Arrhenius Plots of Initial Annealing Rates for an NQIR(700-to-600/500/300/23, Δt_A) Q&A Series Treatments and Instantaneous Vacancy Activation Energy, E^M_V(act), Values

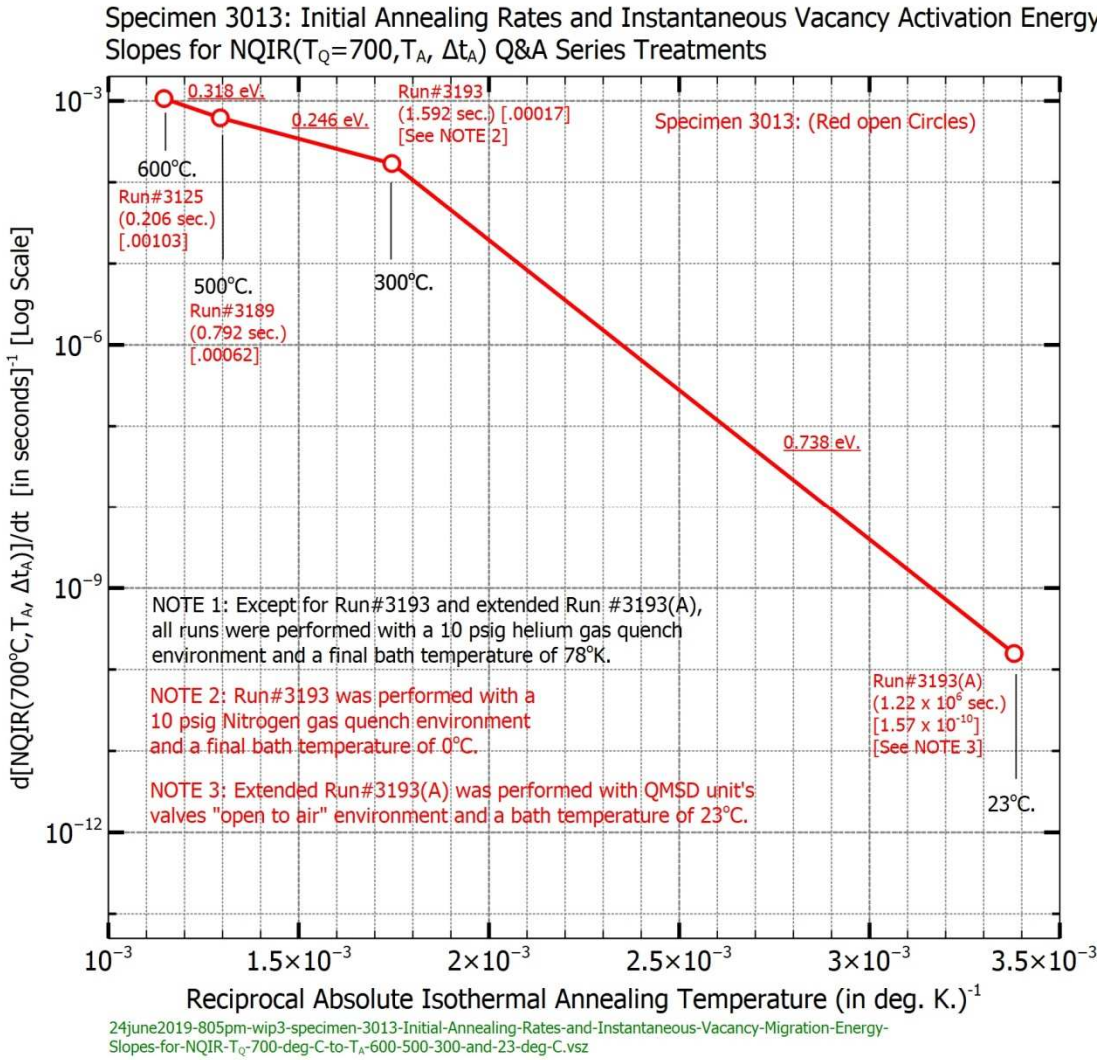

Figure 166. Specimen 3013: Arrhenius Plots of Initial Annealing Rates for an NQIR(700-to-600/500/300/23, Δt_A) Q&A Series Treatments and Instantaneous Vacancy Activation Energy, E^M_V(act), Values obtained from the respective slopes between data points

8.3.10.2.3 Specimens 3013 and 4005: Instantaneous Vacancy Activation Energy Determinations, E^{M}_{V}(act), from Arrhenius Plots of Mean Relaxation Times (t_{mean}) for NQIR(700-to-600/500/300/200, Δt_A) Q&A Series Treatments

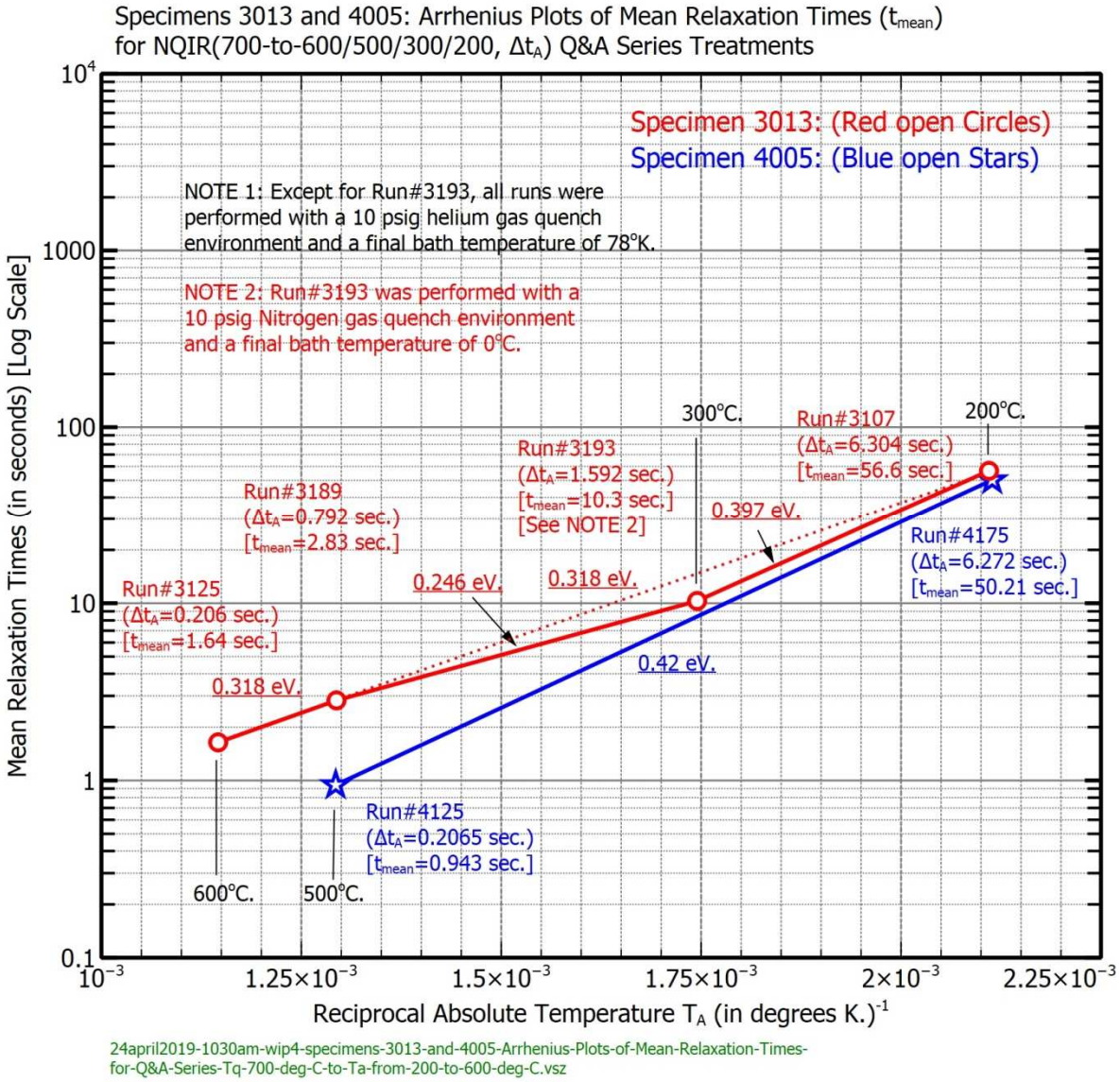

Figure 167. Specimens 3013 and 4005: Instantaneous Vacancy Activation Energy Determinations, E^{M}_{V}(act), from Arrhenius Plots of Mean Relaxation Times (t_{mean}) for NQIR(700-to-600/500/300/200, Δt_A) Q&A Series Treatments

8.3.10.2.4 Specimen 3013: Instantaneous Vacancy Activation Energy Determinations, $E^{M}_{V}(act)$, from Arrhenius Plots of Extended Mean Relaxation Times (t_{mean}) for NQIR(700-to-600/500/300/23, Δt_A) Q&A Series Treatments

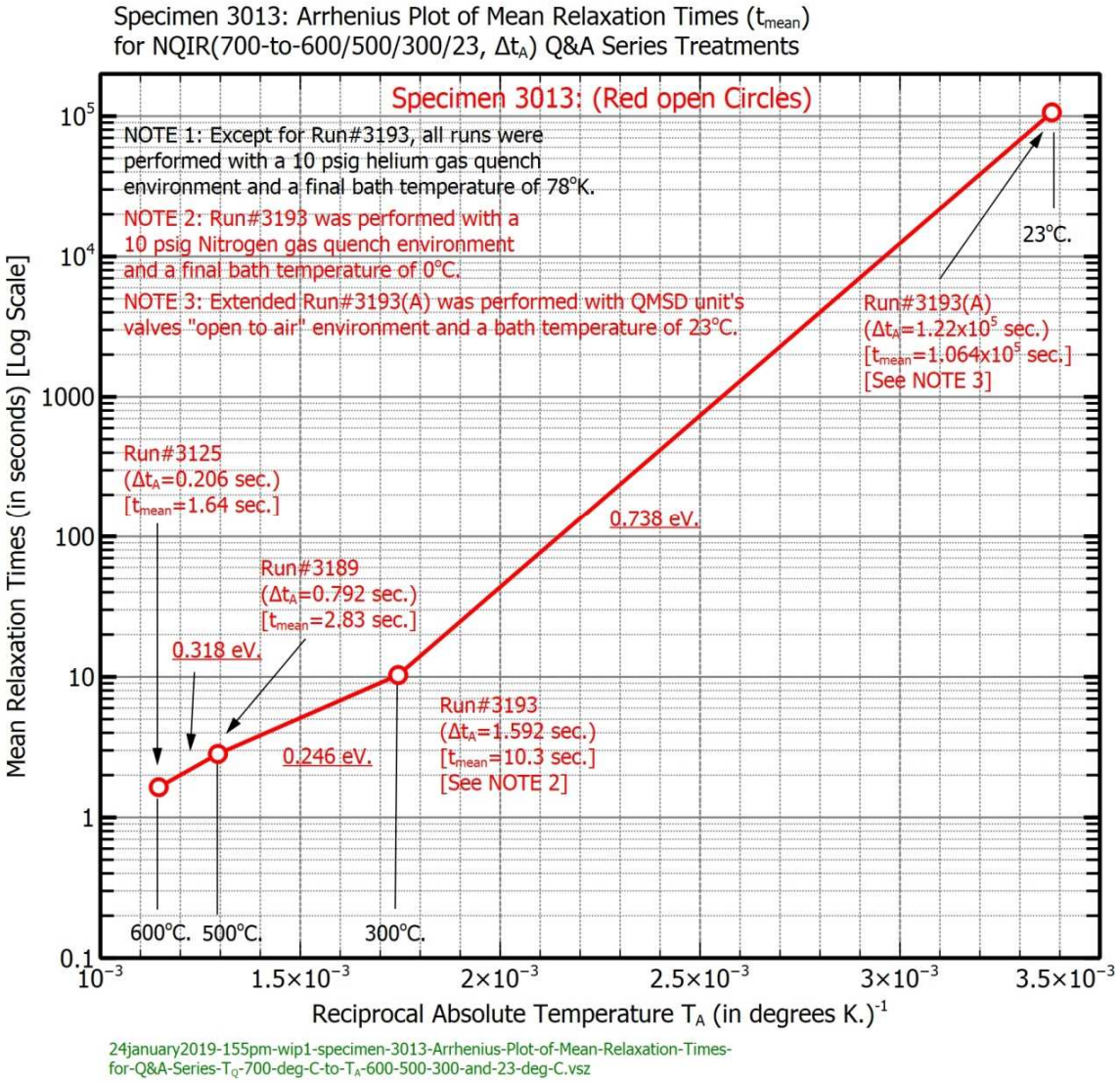

Figure 168. Specimen 3013: Instantaneous Vacancy Activation Energy Determinations, $E^{M}_{V}(act)$, from Arrhenius Plots of Extended Mean Relaxation Times (t_{mean}) for NQIR(700-to-600/500/300/23, Δt_A) Q&A Series Treatments

NQIR(900/800/700, T_A, Δt_A) Q&A Series treatments are covered next.

8.3.10.3 NQIR(900/800/700, T_A, Δt_A) Q&A Series Treatments Results and Analyses

Figures 169 through 172 illustrate the respective Arrhenius plots.

8.3.10.3.1 Specimen 4002: Instantaneous Vacancy Activation Energy, E^M_V(act), Determinations from Arrhenius Plots of Initial Annealing Rates for NQIR(900-to-700/500/400/300, Δt_A); NQIR(800-to-600/500/300, Δt_A); and NQIR(700-to-500/300, Δt_A) Q&A Series Treatments

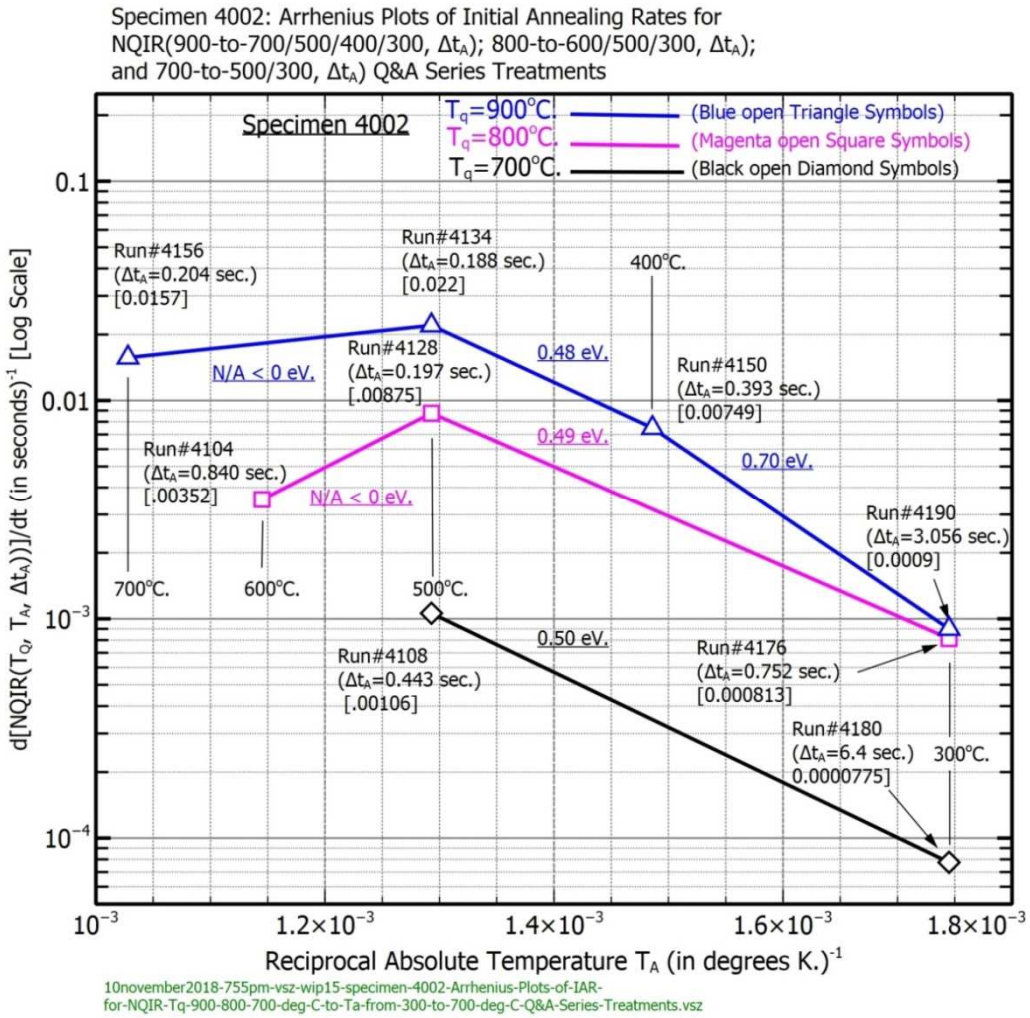

Figure 169. Specimen 4002: Instantaneous Vacancy Activation Energy, E^M_V(act), Determinations from Arrhenius Plots of Initial Annealing Rates for NQIR(900-to-700/500/400/300, Δt_A); NQIR(800-to-600/500/300, Δt_A); and NQIR(700-to-500/300, Δt_A) Q&A Series Treatments

8.3.10.3.2 Specimen 4005: Instantaneous Vacancy Activation Energy, $E^{M}_{V}(act)$, Determinations from Arrhenius Plots of Initial Annealing Rates for NQIR(900-to-700/500/200/20, Δt_A); NQIR(800-to-500/200, Δt_A); and NQIR(700-to-500/200, Δt_A) Q&A Series Treatments

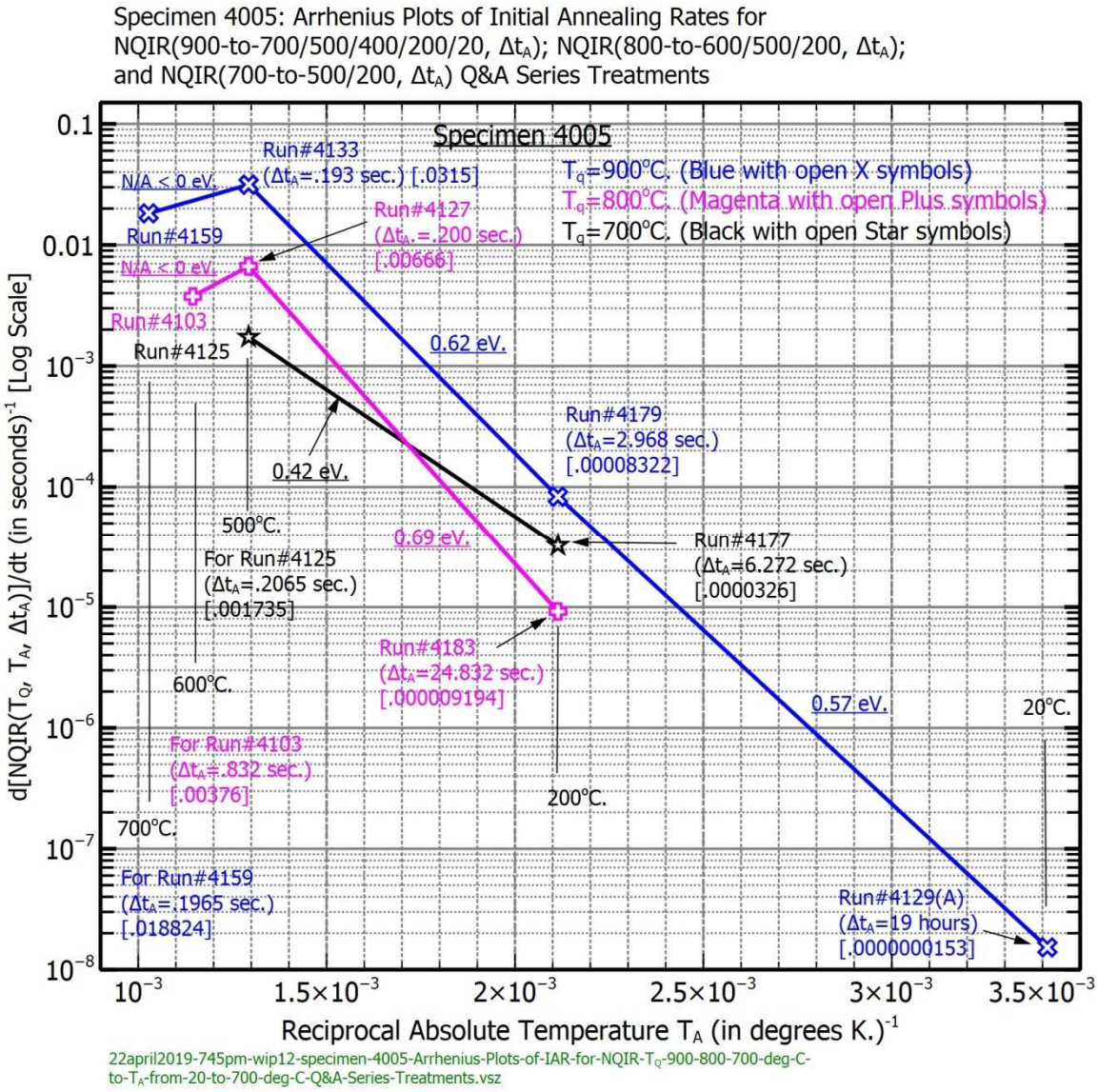

Figure 170. Specimen 4005: Instantaneous Vacancy Activation Energy, $E^{M}_{V}(act)$, Determinations from Arrhenius Plots of Initial Annealing Rates for NQIR(900-to-700/500/200/20, Δt_A); NQIR(800-to-600/500/200, Δt_A); and NQIR(700-to-500/200, Δt_A) Q&A Series Treatments

8.3.10.3.3 Specimen 4002: Instantaneous Vacancy Activation Energy Determinations, $E^{M}_{V}(act)$, from Arrhenius Plots of Mean Relaxation Times (t_{mean}) for NQIR(900-to-700/500/400/300, Δt_A); NQIR(800-to-600/500/300, Δt_A); and NQIR(700-to-500/300, Δt_A) Q&A Series Treatments

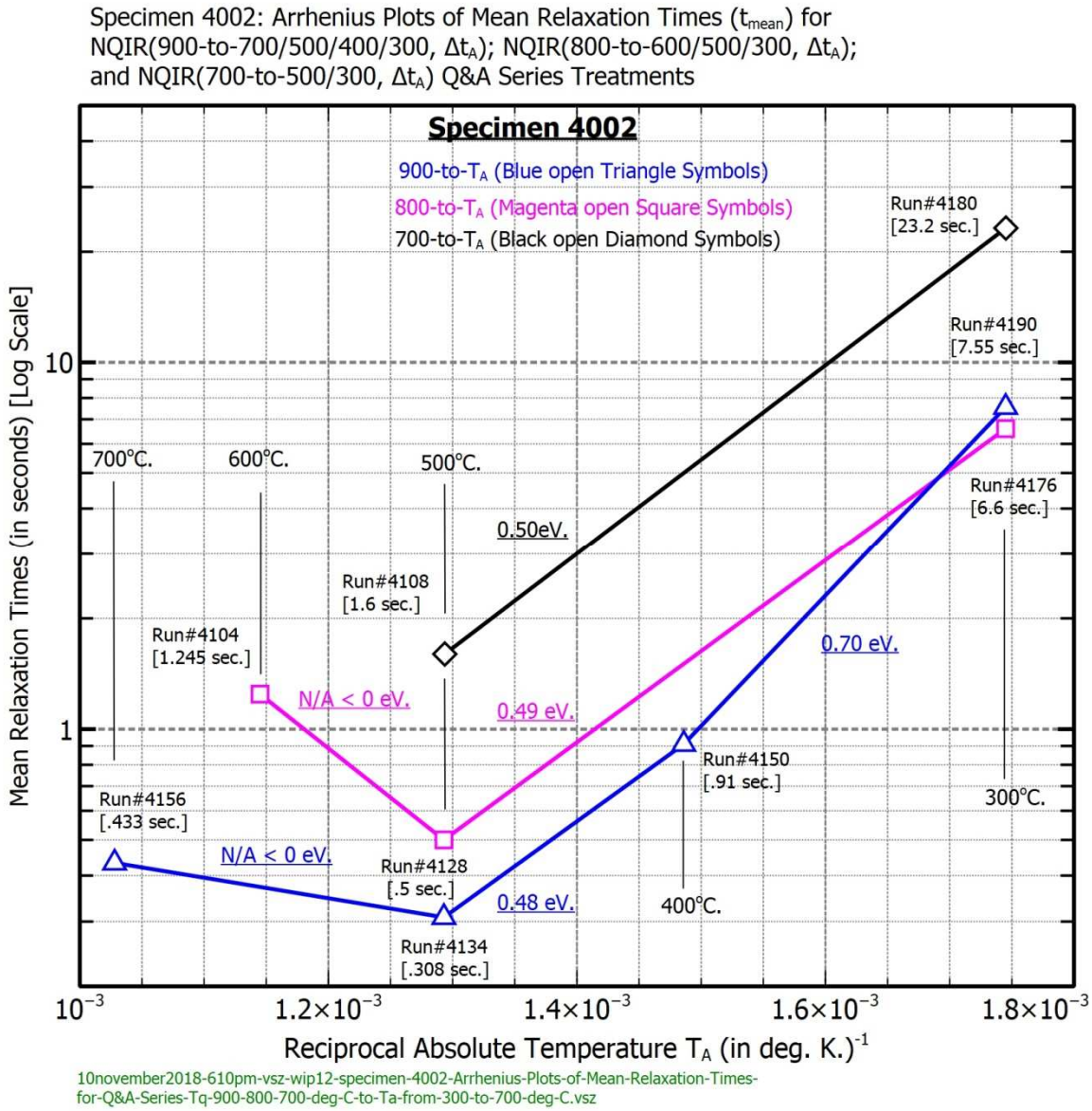

Figure 171. Specimen 4002: Instantaneous Vacancy Activation Energy Determinations from Arrhenius Plots of Mean Relaxation Times (t_{mean}) for NQIR(900-to-700/500/400/300, Δt_A); NQIR(800-to-600/500/300, Δt_A); and NQIR(700-to-500/300, Δt_A) Q&A Series Treatments

8.3.10.3.4 Specimen 4005: Instantaneous Vacancy Activation Energy Determinations, $E^{M}_{V}(act)$, from Arrhenius Plots of Mean Relaxation Times (t_{mean}) for NQIR(900-to-700/500/400/200/20, Δt_A); NQIR(800-to-500/200, Δt_A); NQIR(700-to-500/200, Δt_A) Q&A Series Treatments

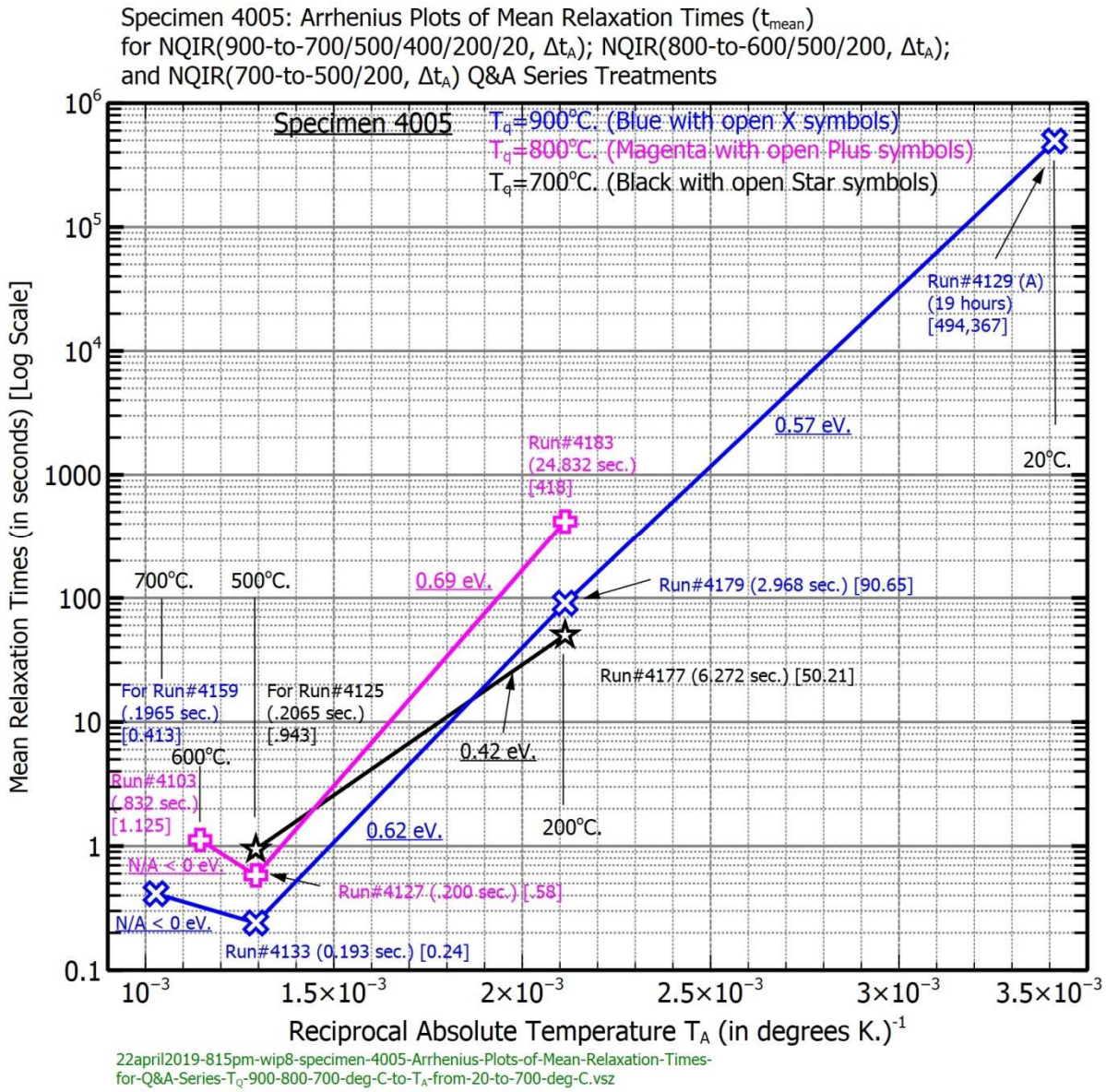

Figure 172. Specimen 4005: Instantaneous Vacancy Activation Energy, $E^{M}_{V}(act)$, Determinations from Arrhenius Plots of Mean Relaxation Times (t_{mean}) for NQIR(900-to-700/500/400/200/20, Δt_A); NQIR(800-to-600/500/200, Δt_A); and NQIR(700-to-500/200, Δt_A) Q&A Series Treatments

8.3.10.4 Summaries of Data Analyses of NQIR(600, T_A, Δt_A) Q&A Series Treatments

8.3.10.4.1 Summaries of Results

Quantitatively, Figure 153 shows for specimen 3013 the following:

1) a total of ten runs (with coinciding data points for two pairs of runs) obtained for isothermal annealing temperatures ranging from 20^{o}C to 575^{o}C,

2) a nearly constant slope from 20^{o}C through 275^{o}C,

3) a reduced slope between 275^{o}C and 500^{o}C,

4) a negative slope (labeled N/A) between 500^{o}C and 575^{o}C, and

5) a range in initial annealing rates of nearly seven orders of magnitude.

Figure 154 is a modification of Figure 153 in that use is made of the normalized initial annealing rate (NIAR), a parameter that eliminates specimen geometrical considerations which thereby allows collective comparisons to be made among multiple specimens.

Figure 155 illustrates the usefulness of NIAR values for revealing characteristics for independent specimens 3013, 4002, and 4005 for NQIR(600, T_A, Δt_A), Q&A Series treatments that clearly involved differing sets of T_A values.

Figures 156, 157, and 158 illustrate Arrhenius plots of Mean Relaxation Time (t_{mean}) for specimens 3013, 4002, and 4005 for NQIR(600, T_A, Δt_A), Q&A Series treatments, and Figure 159 collectively shows the respective sets of Mean Relaxation Times for all three specimens.

Figures 160 through 162 show Arrhenius plots of the Mean Relaxation Time (t_{mean}) for various NQIR(600^{o}C,T_A, Δt_A) Q&A series treatments, along with labeled

values of the instantaneous vacancy activation energy $E^M_V(act)$, calculated from the slopes of the respective segments of each overall curve.

Figure 163 shows how the instantaneous vacancy activation energy, $E^M_V(act)$, values (based on the slopes obtained from Figure 160 presented in sub-section 8.3.10.1.8) are influenced by vacancy defect chemical potential (μ_V).

As described in sub-section 8.3.10.1.12, Figure 164 provides an example that illustrates how absolute macroscopic sink efficiency varies with the magnitude of the associated vacancy defect chemical potential.

8.3.10.4.2 Discussion of $E^M_V(act)$ Magnitudes for NQIR(600, T_A, Δt_A) Q&A Series Treatments

Comparisons of the values for the instantaneous vacancy activation energy, $E^M_V(act)$, for specimens 3013, 4002, and 4005 as indicated in Figures 160 through 162, respectively, reveal three specific characteristics.

1). Reasonable agreement for the average values for $E^M_V(act)$ of 0.724 eV, 0.62 eV, and 0.62 eV, respectively, over the ranges in annealing temperatures from 20^{o}C to 275^{o}C for specimen 3013, from 20^{o}C to 405^{o}C for specimen 4002, and from 20^{o}C to 440^{o}C for specimen 4005.

2) Reduced values for $E^M_V(act)$ of 0.29 eV, 0.25 eV, and 0.34 eV are noted to occur over the ranges in elevated isothermal annealing temperatures a) from 275^{o}C to 500^{o}C for specimen 3013, b) from 405^{o}C to 575^{o}C for specimen 4002, and c) from 440^{o}C to 575^{o}C for specimen 4005, respectively,

3) Only for specimen 3013 over the temperature range between 500^{o}C and 575^{o}C is a negative slope (labeled N/A) noted to occur.

8.3.10.5 Summaries of Data Analyses of NQIR(700, T_A, Δt_A) Q&A Series Treatments

8.3.10.5.1 Four Plots involving Specimens 3013

8.3.10.5.1.1 Figures 165 through 168

Figure 165 is an Arrhenius plot of Initial Annealing Rate (IAR) that illustrates determinations of instantaneous vacancy activation energy, E^M_V(act), values associated with the slopes for the three labeled plots for NQIR(700,T_A, Δt_A) Q&A series treatments performed on specimens 3013, 4002, and 4005. The respective slopes are labeled with the associated values for E^M_V(act) for each specimen. Note that the dashed slope line for specimen 3013 indicates a value of 0.318 eV[111] applies over the 600-to-200 annealing temperature range. Run #3193 involved a slower quench rate environmental condition, namely nitrogen gas and a higher bath temperature, and its inclusion in Figure 165 resulted in the two slopes of 0.246 eV and 0.397 eV over the 500-to-300 and 300-to-200 segments, respectively.

Figure 166 contains an extended anneal data point labeled Run #3193(A) in which an NQIR(700, 23, Δt_A) Q&A series treatment involving specimen 3013 was performed with a water bath temperature maintained at 23^{o}C and the QMSD Unit's valve kept open to the air undertaken immediately following completion of Run #3193's an NQIR(700, 300, Δt_A) Q&A series treatment. The Run #3193(A) data point was obtained following a contiguous extended isothermal anneal (see NOTE 3 in Figure 166) lasting for two weeks and three hours. Graphical extension of the Run #3193 data point to the Run #3193(A) data point resulted in the additional segment

[111] In sub-section 8.4.4.1.1 of this document further discussion is made of the values obtained for specimen 3013's slopes that are shown in Figure 165.

with a slope that yielded a calculated value for E^{M}_{V}(act) of 0.738 eV for the 23^{o}C-to-300^{o}C segment of the overall plot.

8.3.10.5.1.2 Figures 167 and 168

Arrhenius plots of mean relaxation times for specimen 3013 are shown in Figures 167 and 168. They were established upon conversion of the respective sets of IAR values presented in Figures 165 and 166 by calculations made using the definition for t_{mean} =

$NQIR(T_Q, T_A, t_A = 0) / \{[NQIR(T_Q, T_A, t_A = 0) - NQIR(T_Q, T_A, \Delta t_{A(initial)})] / \Delta t_{A(initial)} \}$.

The Arrhenius plots made using Mean Relaxation Time as the dependent parameter illustrate determinations of instantaneous vacancy activation energy, E^{M}_{V}(act), values associated with each of the labeled NQIR(700,T_A, Δt_A) Q&A series treatments for specimens 3013 and 4005 (see Figure 167) and for specimen 3013's extended anneal treatment.

8.3.10.5.2 One Plot involving Specimen 4002

Figure 165 reveals for specimen 4002 a 500-to-300 segment whose slope yielded a value for E^{M}_{V}(act) of 0.50 eV.

8.3.10.5.3 One Plot involving Specimen 4005

Figure 165 reveals for specimen 4005 a 500-to-200 segment whose slope yielded a value for E^{M}_{V}(act) of 0.42 eV which, and this is only slightly greater than the 0.397 eV value calculated for specimen 3013's 300-to-200 segment.

8.3.10.5.4 Discussion of Variations in E^M_V(act) Magnitudes for NQIR(700, T_A, Δt_A) Q&A Series Treatments

8.3.10.5.4.1 Specimen 3013

Quantitatively, Figure 165 shows the following:

1) a total of eight runs involving three specimens for Q&A series treatments quenches from 700^{o}C and isothermal annealing temperatures ranging from 200^{o}C to 600^{o}C,

2) six segments labeled with calculated values of instantaneous vacancy activation energy, E^M_V(act),

3) for specimen 3013 E^M_V(act) magnitudes of 0.318 eV for both the 200^{o}C to 500^{o}C and 500^{o}C to 600^{o}C segments; 0.246 eV for the 300^{o}C to 500^{o}C segment; and 0.397 eV for the 200^{o}C to 300^{o}C segment,

4) an E^M_V(act) magnitude for specimen 4002 of 0.50 eV for the 300^{o}C to 500^{o}C segment,

5) an E^M_V(act) magnitude for specimen 4005 of 0.42 eV for the 200^{o}C to 500^{o}C segment, and

6) an overall range in initial annealing rates spanning almost two orders of magnitude.

Figures 167 and 168 provide a calculated value for E^M_V(act) of 0.738 eV for the isothermal annealing temperature range from 23^{o}C to 300^{o}C that involved performing an extended anneal (labeled by the data point Run#3193(A) that lasted for two weeks and three hours. Figure 168 reveals that the range in mean relaxation times spans five orders of magnitude.

8.3.10.5.4.2 Specimen 4002

Figure 165 reveals for specimen 4002 a 500-to-300 segment whose slope yielded a value for E^{M}_{V}(act) of 0.50 eV.

8.3.10.5.4.3 Specimen 4005

Figure 165 reveals for specimen 4005 a 500-to-200 segment whose slope yielded a value for E^{M}_{V}(act) of 0.42 eV which, and this is only slightly greater than the 0.397 eV value calculated for specimen 3013's 300-to-200 segment

8.3.10.6 Summaries of Data Analyses of NQIR(900/800/700, T_A, Δt_A) Q&A Series Treatments

8.3.10.6.1 Two Plots involving Specimens 4002: Figures 169 and 171

Quantitatively, Figure 169 shows for specimen 4002 the following:

1) A total of nine runs: a) four for NQIR(900, T_A, Δt_A) Q&A series treatments obtained over isothermal annealing temperatures ranging from 300^{o}C to 700^{o}C; b) three for NQIR(800, T_A, Δt_A) Q&A series treatments obtained for isothermal annealing temperatures ranging from 300^{o}C to 600^{o}C; and c) two for NQIR(700, T_A, Δt_A) Q&A series treatments obtained for isothermal annealing temperatures ranging from 300^{o}C to 500^{o}C;

2) over the isothermal temperature range between 300^{o}C and 500^{o}C, calculated values for E^{M}_{V}(act) were: a) 0.50 eV when T_Q=700^{o}C; b) 0.49 eV when T_Q=800^{o}C; c) and when T_Q=900^{o}C, E^{M}_{V}(act) was equal to 0.70 eV for the segment from 300^{o}C to 400^{o}C and 0.48 eV for the segment from 400^{o}C to 500^{o}C;

3) two negative slopes (labeled N/A) occurred; one for the segment from 500^{o}C to 600^{o}C when T_Q=800^{o}C, and the second for the segment from 500^{o}C to 700^{o}C when T_Q=900^{o}C;

4) an overall range in initial annealing rates of two orders of magnitude.

Figure 171 is the corresponding plot of mean relaxation time (t_{mean}) defined herein as being equal to NQIR(T_Q, T_A, t_A = 0) / {[NQIR(T_Q, T_A, t_A = 0) - NQIR(T_Q, T_A, $\Delta t_{A(initial)}$)] / $\Delta t_{A(initial)}$)} which is equal to the reciprocal of the Normalized Initial Annealing Rate NIAR.

8.3.10.6.2 Two Plots involving Specimens 4005: Figures 170 and 172

Figure 170 shows for specimen 4005 the following:

1) a total of nine runs: a) four for NQIR(900, T_A, Δt_A) Q&A series treatments obtained over isothermal annealing temperatures ranging from 20^{o}C to 700^{o}C; b) three for NQIR(800, T_A, Δt_A) Q&A series treatments obtained for isothermal annealing temperatures ranging from 200^{o}C to 600^{o}C; and c) two for NQIR(700, T_A, Δt_A) Q&A series treatments obtained for isothermal annealing temperatures ranging from 200^{o}C to 500^{o}C;

2) Over the isothermal temperature range between 200^{o}C and 500^{o}C the calculated values for E^{M}_{V}(act) were a) 0.42 eV when T_Q=700^{o}C; b) 0.69 eV when T_Q=800^{o}C; and c) 0.62 eV when T_Q=900^{o}C;

3) Over the isothermal temperature range from 20^{o}C to 500^{o}C the calculated value for E^{M}_{V}(act) was 0.57 eV;

4) two negative (N/A) slopes when $T_A \geq$ 500^{o}C for 900^{o}C$\leq T_Q \geq$800^{o}C, and

5) an overall range in IAR values of more than five orders of magnitude.

Figure 172 is the corresponding plot of mean relaxation time (t_{mean}) defined herein as being equal to NQIR(T_Q, T_A, $t_A = 0$) / {[NQIR(T_Q, T_A, $t_A = 0$) - NQIR(T_Q, T_A, $\Delta t_{A(initial)}$)] / $\Delta t_{A(initial)}$)} which is equal to the reciprocal of the Normalized Initial Annealing Rate NIAR.

8.3.10.6.3 Discussion of E^M_V(act) Magnitudes for NQIR(900/800/700, T_A, Δt_A) Q&A Series Treatments

8.3.10.6.3.1 Specimen 4002

Quantitatively, Figure 169 shows for specimen 4002 the following:

1) a total of nine runs for Q&A series treatments involving quenches from 900^{o}C, 800^{o}C, and 700^{o}C and isothermal annealing temperatures ranging from 300^{o}C to 500^{o}C,

2) four segments labeled with calculated values of instantaneous vacancy activation energy, E^M_V(act),

3) an E^M_V(act) magnitude of 0.50 eV for the 300^{o}C to 500^{o}C segment when T_Q=700^{o}C;

4) an E^M_V(act) magnitude of 0.49 eV for the 300^{o}C to 500^{o}C segment when T_Q=800^{o}C;

5) an E^M_V(act) magnitude of 0.70 eV for the 300^{o}C to 400^{o}C segment when T_Q=900^{o}C;

6) an E^M_V(act) magnitude of 0.48 eV for the 400^{o}C to 500^{o}C segment when T_Q=900^{o}C;

7) two negative (labeled N/A) slopes are noted to occur for quenches from 800^{o}C and 900^{o}C that involve isothermal annealing temperatures above 500^{o}C; and

8) an overall range in initial annealing rates spanning more than two orders of magnitude.

8.3.10.6.3.2 Specimen 4005

Quantitatively, Figure 170 shows for specimen 4005 the following:

1) A total of nine runs: a) four for NQIR(900, T_A, Δt_A) Q&A series treatments obtained over isothermal annealing temperatures ranging from 20^{o}C to 700^{o}C; b) three for NQIR(800, T_A, Δt_A) Q&A series treatments obtained for isothermal annealing temperatures ranging from 200^{o}C to 600^{o}C; and c) two for NQIR(700, T_A, Δt_A) Q&A series treatments obtained for isothermal annealing temperatures ranging from 200^{o}C to 500^{o}C;

2) four segments labeled with calculated values of instantaneous vacancy activation energy, E^M_V(act),

3) an E^M_V(act) magnitude of 0.42 eV for the 200^{o}C to 500^{o}C segment when T_Q=700^{o}C;

4) an E^M_V(act) magnitude of 0.69 eV for the 200^{o}C to 500^{o}C segment when T_Q=800^{o}C;

5) an E^M_V(act) magnitude of 0.62 eV for the 200^{o}C to 500^{o}C segment when T_Q=900^{o}C;

6) Over the isothermal temperature range between 20^{o}C and 200^{o}C the calculated value for E^M_V(act) was 0.57 eV that followed performing an extended anneal (labeled by the data point Run#4129(A) that lasted for nineteen hours;

7) two negative (labeled N/A) slopes are noted to occur for quenches from 800^{o}C and 900^{o}C that involve isothermal annealing temperatures above 500^{o}C; and

8) an overall range in initial annealing rates of more than six orders of magnitude.

8.3.10.6.4 Discussions of Slope Reversal Occurrences in Arrhenius Plots

8.3.10.6.4.1 Present Research Findings

Arrhenius plots of NQIR(900/800/700, T_A, Δt_A) Q&A series treatments involving specimens 4002 and 4005 of calculated values for initial annealing rates (IARs) to determine instantaneous vacancy activation energy, E^M_V(act), values each clearly exhibited two negative slope segments – 1) for $600^oC \leq T_A \geq 500^oC$ when $T_Q = 800^oC$ and 2) for $700^oC \leq T_A \geq 500^oC$ when $T_Q = 900^oC$.

Notably, the same hypothesis proposed in sub-section 8.3.9.1 that might account for negative slope occurrences in Arrhenius plots of half-time annealing kinetics seems reasonable to propose as applicable to account for such observed negative slopes occurring during initial annealing kinetics situations.

Specifically, as excess vacancy defect chemical potentials diminish to levels ≤ 0.2 eV whenever $T_A \rightarrow T_Q$ conditions are encountered, significant reductions in absolute macroscopic sink efficiency **€** are likely. When that occurs, either a diminished slope in that segment would occur or a negative slope segment would be manifested if the mean relaxation time proves to be higher than that associated with the adjacent (lower T_A) segment.

8.3.10.6.4.2 Other Researchers' Findings

Three specific examples of occurrences of slope reversals involving alloys are summarized below:

1. Feder, et al. [see Figure 8 in Reference 220] includes a series of data points for Cu_3Au that were obtained by Weisberg and Quimby [237] who performed Young's modulus experiments that used lattice parameter measurements to obtain values for the rate constant as a function of temperature. The Arrhenius plot clearly revealed slope reversal over the higher temperature range.
2. Noble and Crook [see Figure 15 in Reference 238] illustrated for an Mg-3 wt.% Th alloy two transformation curves of precipitation kinetics each of which exhibited a slope reversal for higher ageing temperatures and were also noted to occur independently of each other.
3. Uwe Köster [see Figure 4 in Reference 239] provided a precipitation diagram obtained from electrical resistivity measurements for an aluminum-1.3% germanium alloy material following five stated specimen treatments which resulted in slope reversals in three instances.

8.3.11 Extensive Sets of Log-Log TEV Plots of Time Exponent (m) Behaviors

Based on the cumulative Q&A series treatment data sets presented in prior sub-sections of this document, this sub-section provides extensive sets of Time Exponent Variation (TEV) plots that will illustrate the dynamic behavior of what is generally referred to as the time exponent **m** that is cited as an indicator of the nature of the overall precipitation kinetics for excess vacancies associated with specimens that have been subjected to quench and anneal treatments involving elevated temperatures and extended ranges in isothermal annealing times.

In this empirically-driven research investigation, use is made of the formula $\mathbf{f_r}$ = NQIR(T_Q, T_A, t_A)]/NQIR(T_Q, T_A, t_A=0) throughout the sub-sections that follow [112]. The various sets of log-log plots of ln($\mathbf{f_r}$)$^{-1}$ vs. isothermal annealing time t_A obtained for each specimen and various sets of NQIR(T_Q, T_A, t_A) Q&A series thermal treatments are graphically analyzed to obtain directly from the dynamic slopes associated with each Time Exponent Variation (TEV) plot the associated values for the dynamic time exponent **m**.

Specifically, eighteen sub-sections are presented that contain such data sets of Time Exponent Variation (TEV) plots of ln($\mathbf{f_r}^{-1}$) values corresponding to the excess fraction remaining ($\mathbf{f_r}$) vs. annealing time obtained for many specimens and for the indicated NQIR(T_Q, T_A, t_A) Q&A series thermal treatments.

Table 16 lists magnitudes of ln($\mathbf{f_r}^{-1}$) values corresponding to the indicated excess fraction remaining ($\mathbf{f_r}$) data sets obtained from Q&A series treatments and subsequently applied to generate numerous combinations of TEV plots, and Figure 173 illustrates this information graphically.

[112] In its more accurate representation, $\mathbf{f_r}$ would be expressed as {NQIR(T_Q, T_A, t_A) – "No Loss" NQIR(T_A)}]/NQIR(T_Q, T_A, t_A=0). However, when T_Q is more than several hundred degrees higher than T_A, the above stated definition is sufficiently accurate and will be used here wherever it proves applicable.

Table 16. Excess Fraction Remaining ($\mathbf{f_r}$) Values associated with TEV Plots of $\ln[(\mathbf{f_r})^{-1}]$ vs. Isothermal Annealing Times for Q&A Series Thermal Treatments

Excess Fraction Remaining ($\mathbf{f_r}$) = $NQIR(T_Q, T_A, t_A)]/NQIR(T_Q, T_A, t_A=0)$	$\ln[(\mathbf{f_r})^{-1}]$
0.99	0.01
0.98	0.02
0.95	0.05
0.90	0.11
0.85	0.16
0.80	0.22
0.75	0.29
0.66	0.42
0.50	0.69
0.31	1.17
0.2	1.61
0.10	2.30
0.05	2.99
0.04	3.22
0.03	3.51
0.02	3.91
0.01	4.61

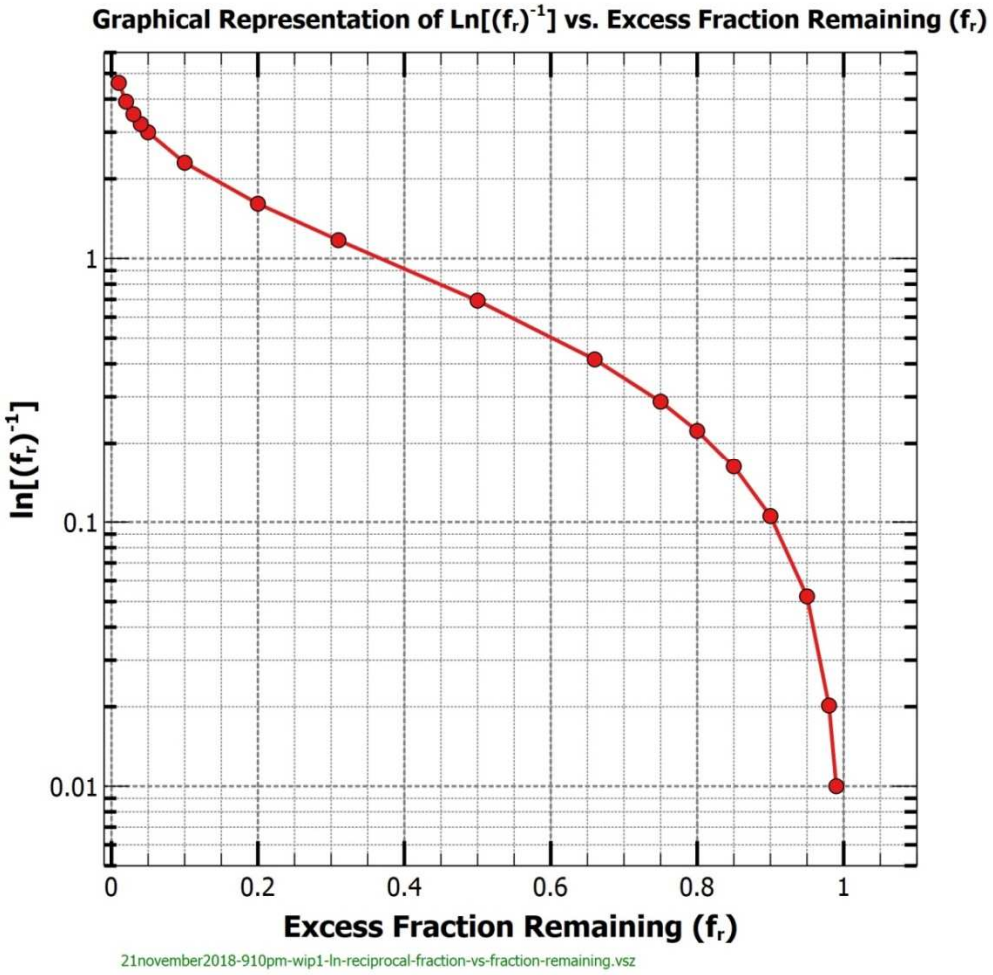

Figure 173. Plot of Ln[$(\mathbf{f_r})^{-1}$] vs. Excess Fraction Remaining ($\mathbf{f_r}$).

Log-log TEV plots of time exponent (m) behaviors for several specimens and specific Q&A series treatments are shown in Figures 174 through 191.

Many of these TEV plots also include data points associated with annealing times that extend well beyond the maximum plotted values of isothermal annealing times used in many of the Q&A series treatment plots presented in earlier sub-sections.

The principal objective sought from this data acquisition activity was to analyze TEV plots to be able to establish what is the overall dynamic behavior -- graphically established through determinations of the slopes associated with the respective plots of isothermal annealing kinetics -- of the time exponent **m** for each specimen and its associated sets of Q&A series thermal treatments.

As a visual aid to help in estimating values for the time exponent **m**, a number of slope line indicators are provided within most TEV plots. In general, the values found to represent the time exponent **m** will a) perhaps be as high as 2 (depending on the Q&A series treatment) for very short annealing times, b) exhibit for intermediate ranges in annealing times slope values of 1, 2/3, or 1/2 over major portions of each respective TEV plot, and c) will approach a slope of zero for extended anneal times.

Most of the Figures that follow provide at least four slope lines (for m=0, 1/2, 2/3, and 1), and some Figures are supplemented with a second axis on the right side of the plots to indicate approximate values for fraction remaining values for NQIR(T_Q, T_A, t_A) Q&A series treatments [113] that were performed on the indicated specimens.

In Figure 174, it is readily noted that specimen 4005 has greater losses than those for specimen 4002, nearly identical MRR levels (around 3%) following extended anneals, and exhibit slopes of 2/3 for both specimens over the major portion of isothermal annealing times. Noteworthy, however, is the fact that examination of the same data as plotted in Figure 110 does not reveal these specific details. For this reason, the use of TEV plots proves critical to adopt in order to make such slope-specific determinations in a most straightforward manner.

---

[113] Refer to Table 16 for calculated estimations for the corresponding values.

8.3.11.1 TEV Comparison Plots for Specimens 4002 and 4005 for (900, 400) Q&A Treatments

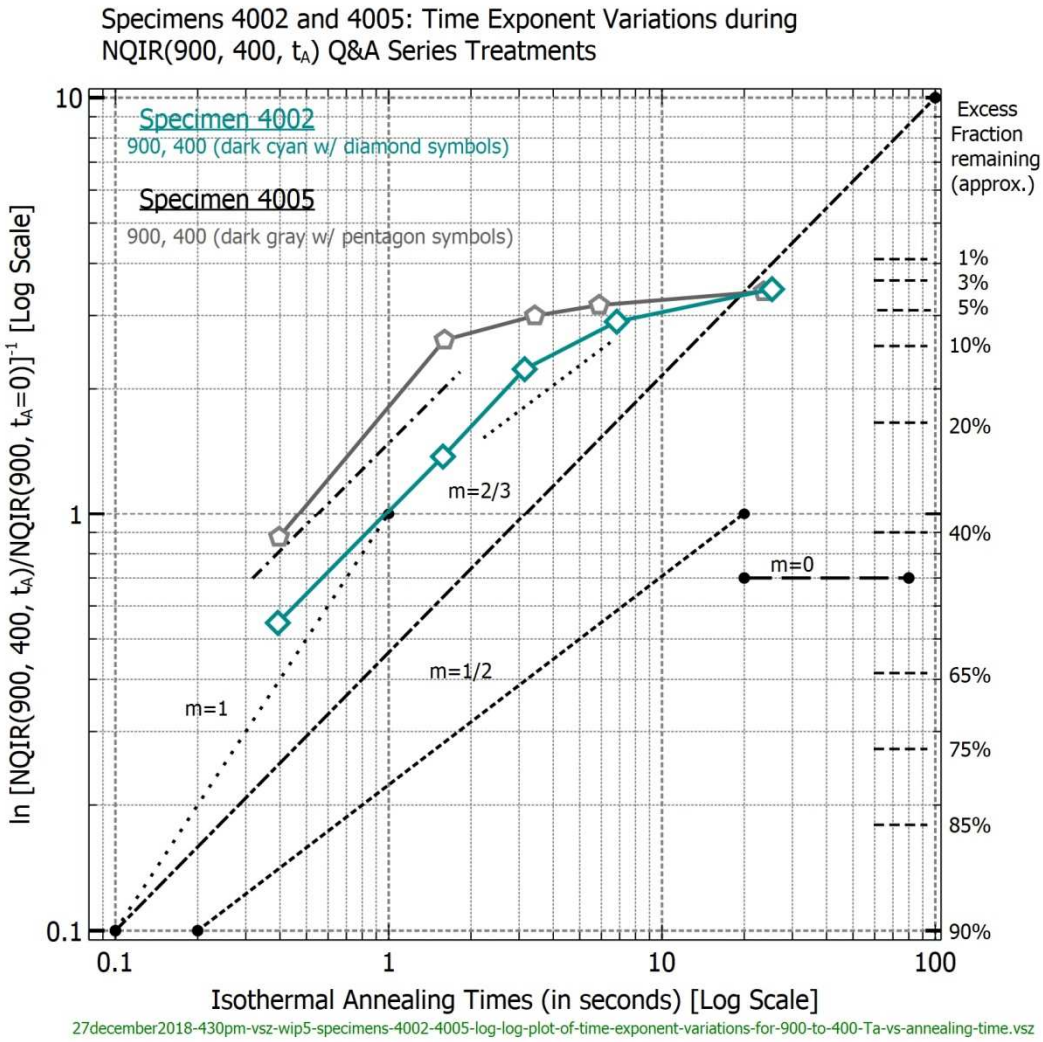

Figure 174. Specimens 4002 and 4005: Two-Axes Log-Log Plots of Time Exponent (m) Variations for two NQIR(900, 400, t_A) during Q&A Series Treatments vs. Annealing Times of less than 30 seconds

Refer to Figure 110 for the NQIR(900, 400, t_A) fractional remaining plots for specimens 4002 and 4005, along with their respective annealing half time values.

8.3.11.2 TEV Plots for Specimens 3016, 4002, and 4005 for (900/700, 700/400) Q&A Treatments

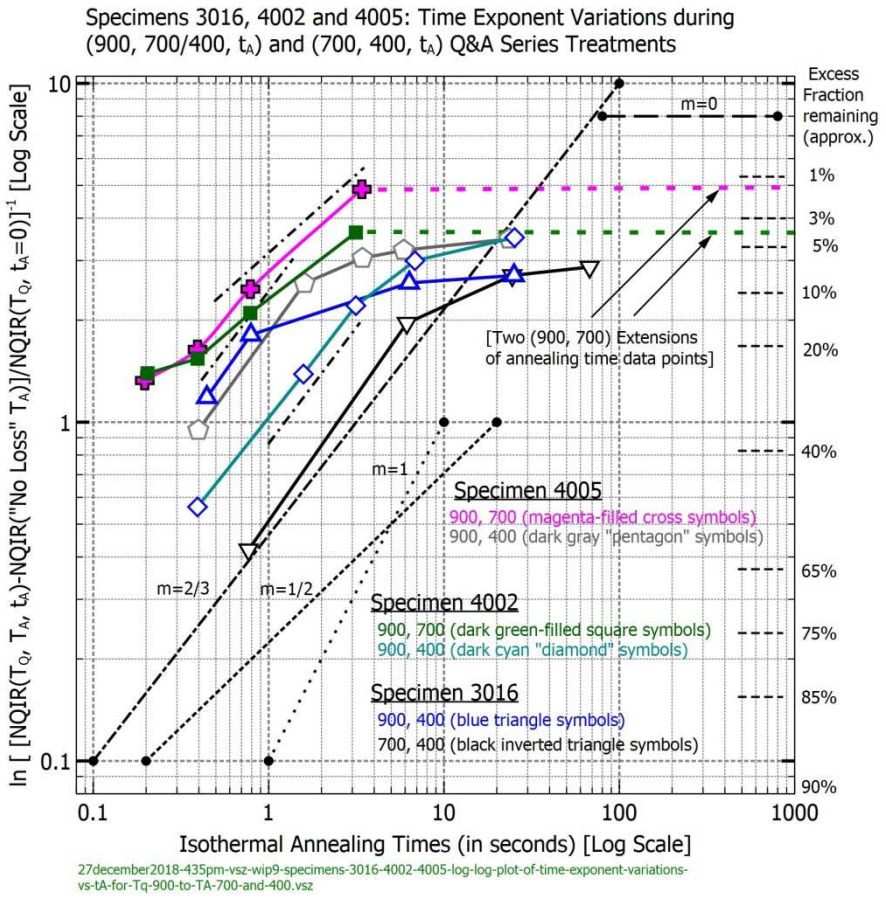

Figure 175. Specimens 3016, 4002 and 4005: Two-Axes Log-Log Plots of Time Exponent (m) Variations for two NQIR(900, 700, t_A), three NQIR(900, 400, t_A), and one NQIR(700, 400, t_A) Q&A Series Treatments vs. Annealing Times of less than 70 seconds

In Figure 175, time exponent slopes close to 2/3 appear for four of the six data sets. However, the slopes for the (900, 700) treatments performed on specimens 4002 and 4005 exhibit initial values for **m** much less than 2/3, and this could possibly be related directly to the slope reversals that were revealed in Figures 171 and 172.

8.3.11.3 TEV Plots for Specimens 4002 and 4005 for (900/800/700, 500, t_A) Q&A Treatments

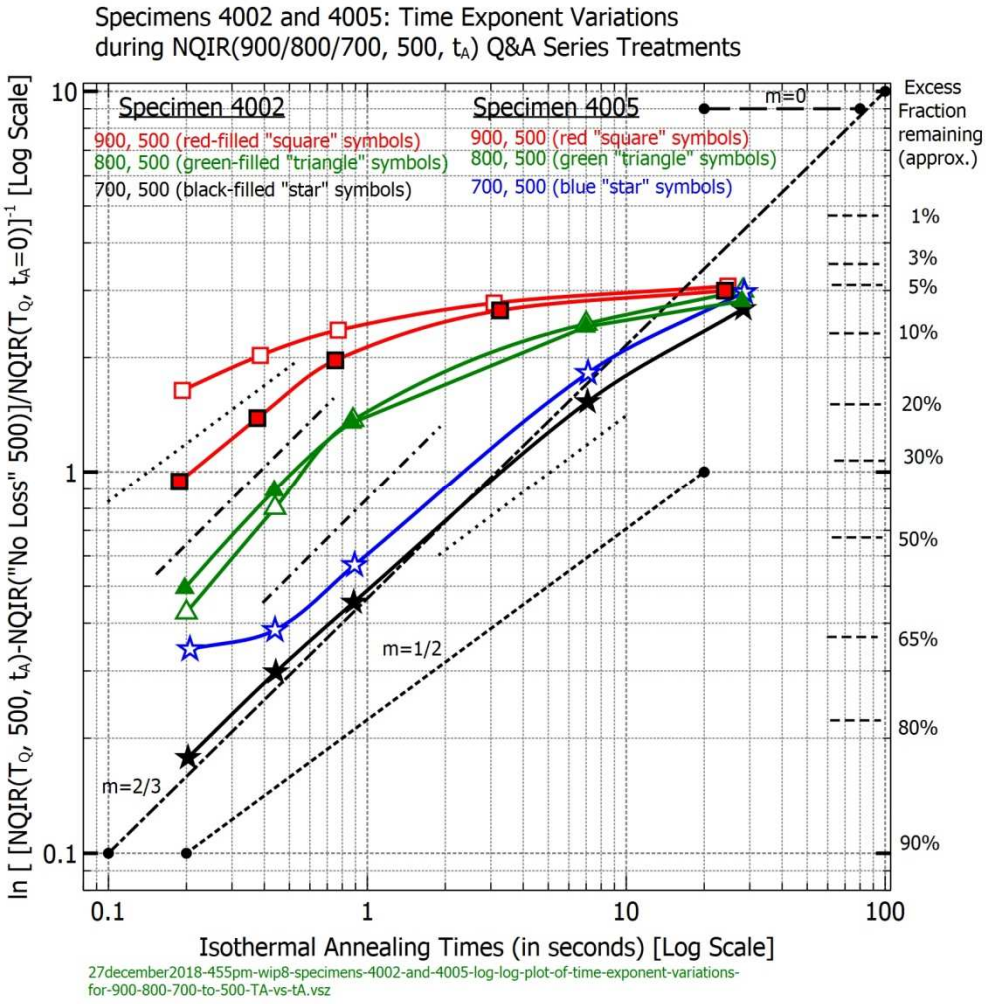

Figure 176. Specimens 4002 and 4005: Two-Axes Log-Log Plots of Time Exponent (m) Variations for NQIR(900/800/700, 500, t_A) Q&A Series Treatments vs. Annealing Times of less than 30 seconds

In Figure 176 the dominant value for time exponent **m** remains close to 2/3 over the major portions of annealing for four of the six NQIR(900/800/700, 500, t_A) Q&A series treatments.

Note that featuring six sets of Q&A series treatments in a single Figure conveniently allows for direct comparisons between the respective behaviors obtained for wholly independent specimens 4002 and 4005. Moreover, the plotted curves do appear to support comparable results both in nature and magnitudes for the six sets of NQIR(900/800/700, 500, t_A) Q&A series treatments.

Additionally, the corresponding MMR values associated with each respective Q&A series treatment do tend to support convergence as the longest annealing times are approached.

8.3.11.4 TEV Plots for Specimen 4005 for (900/800/700, 500/400) Q&A Treatments

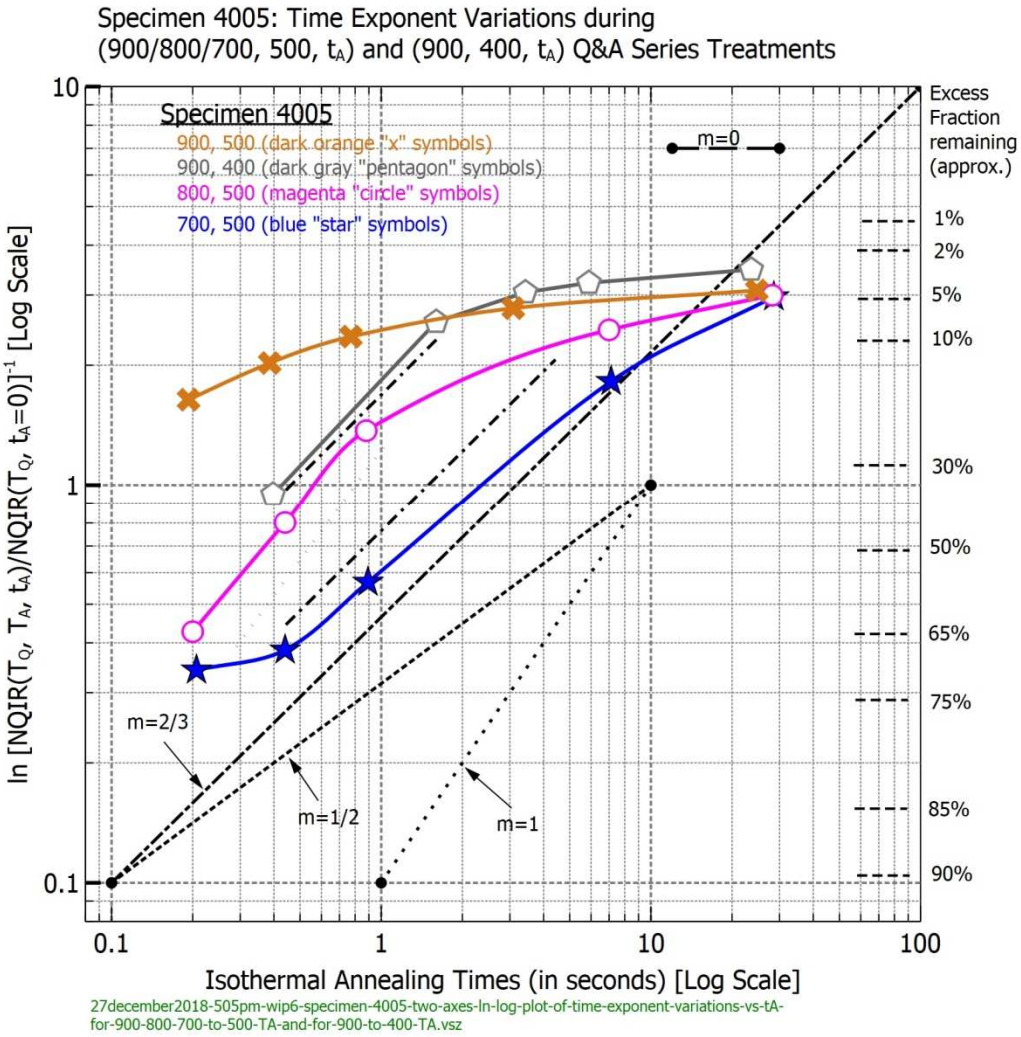

Figure 177. Specimen 4005: Two-Axes Log-Log Plots of Time Exponent (m) Variations for NQIR(900/800/700, 500, t_A) and NQIR(900, 400, t_A) during Q&A Series Treatments vs. Annealing Times of less than 30 seconds

Major portions of all but the 900, 500 TEV plot do appear to follow $t_A^{2/3}$ slopes.

8.3.11.5 TEV Comparison Plots for Specimens 4002 and 4005 during various NQIR(900, T_A, t_A) Q&A Treatments

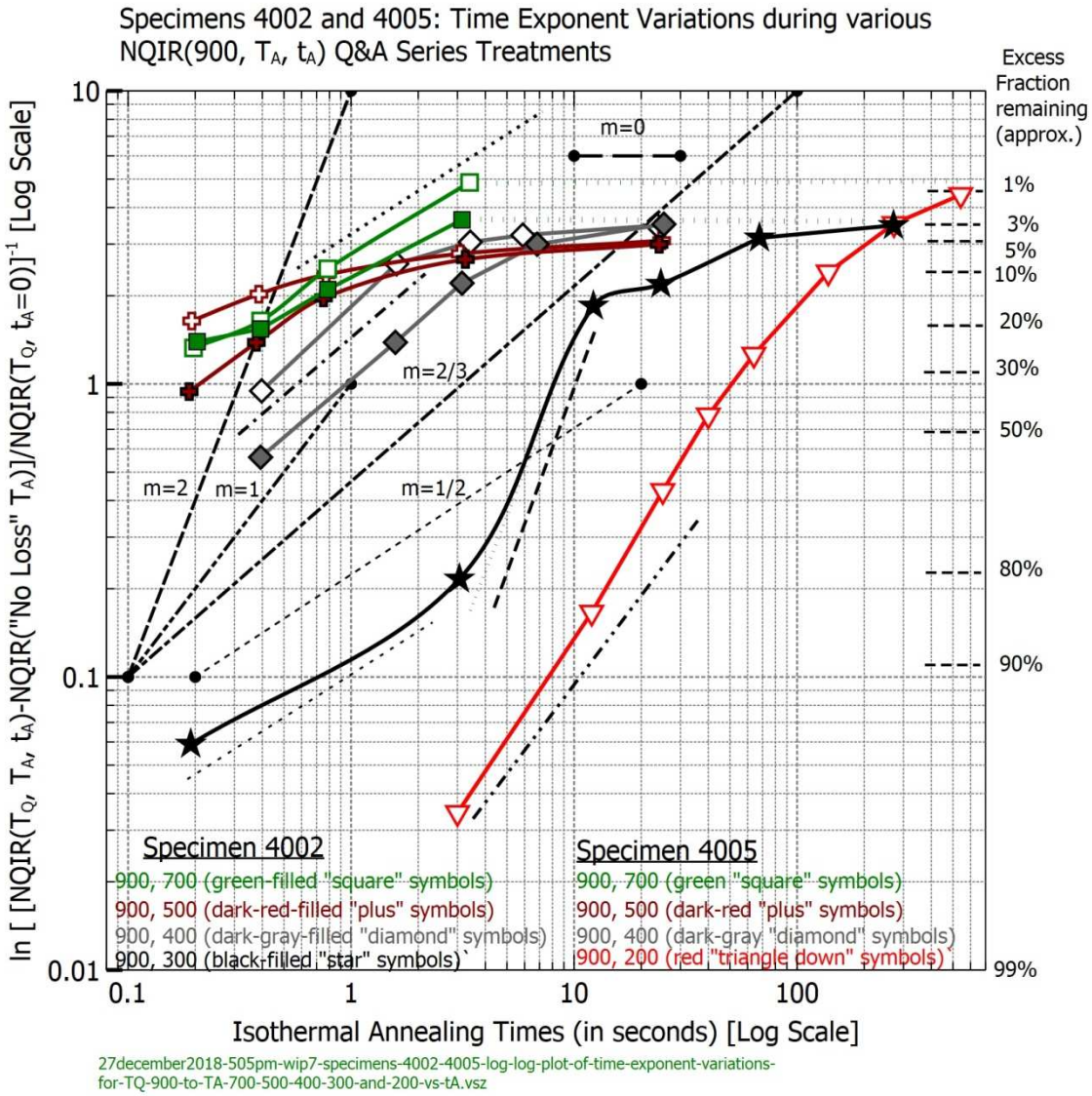

Figure 178. Specimens 4002 and 4005: Two-Axes Log-Log Plots of Time Exponent (m) Variations during various NQIR(900, T_A, t_A) Q&A Series Treatments vs. Annealing Time

Figure 178 reveals slopes of less than 1/2 to as high as 2 for 8 sets of

NQIR(900, T_A, t_A) Q&A Series Treatments performed on specimens 4002 and 4005.

8.3.11.6 TEV Plots for Specimen 4002 for NQIR(900, 700/500/400/300, t_A) Q&A Series Treatments

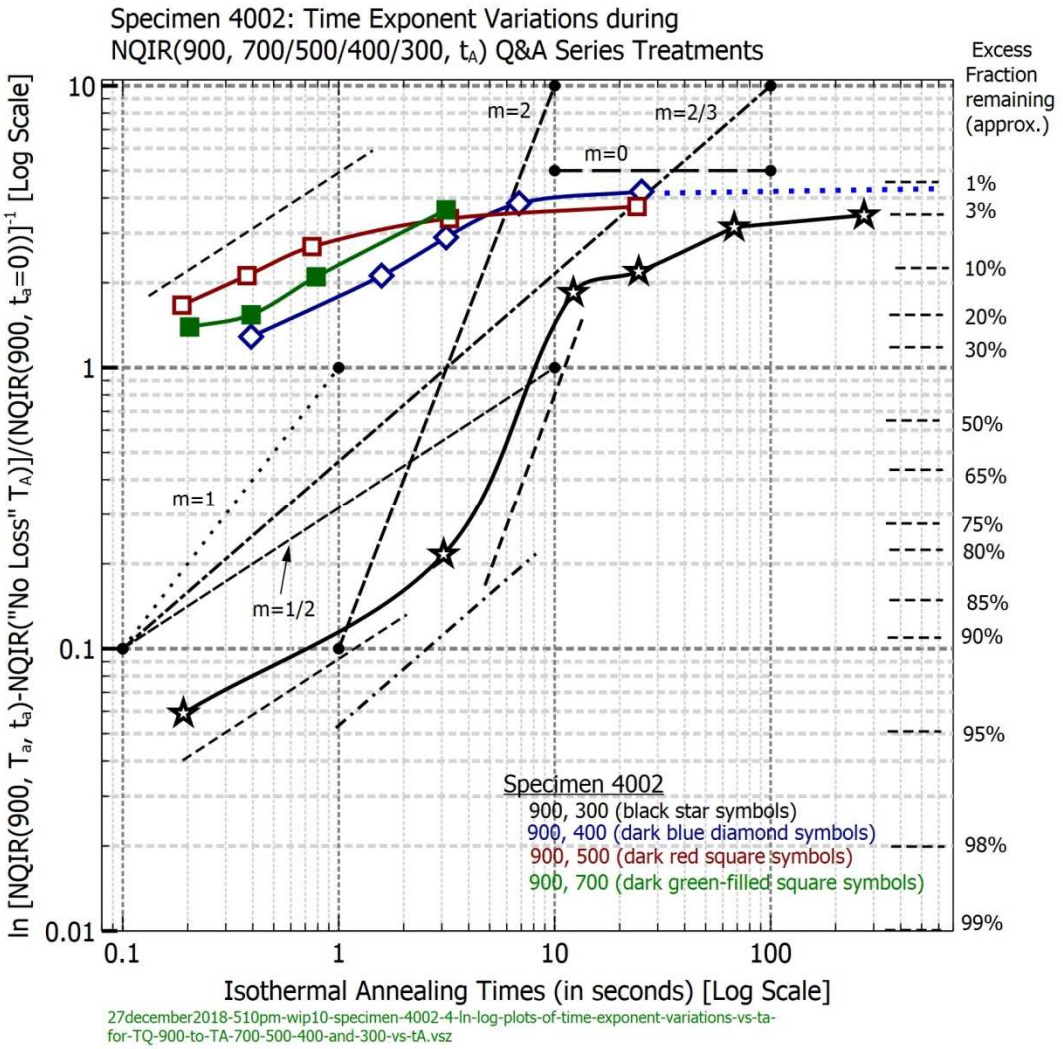

Figure 179. Specimen 4002: Log-Log Plot of Time Exponent (m) Variations for NQIR(900, 700/500/400/300, t_A) during Q&A Series Treatments vs. Annealing Times approaching 300 seconds

Figure 179 shows for specimen 4002 subjected to four sets of NQIR(900, 700/500/400/300, t_A) Q&A Series Treatments that slopes ranging from less than 1/2 to as high as 2 are revealed.

8.3.11.7 TEV Comparison Plots for Specimens 3013 and 4002 for (800, 300) Q&A Treatments

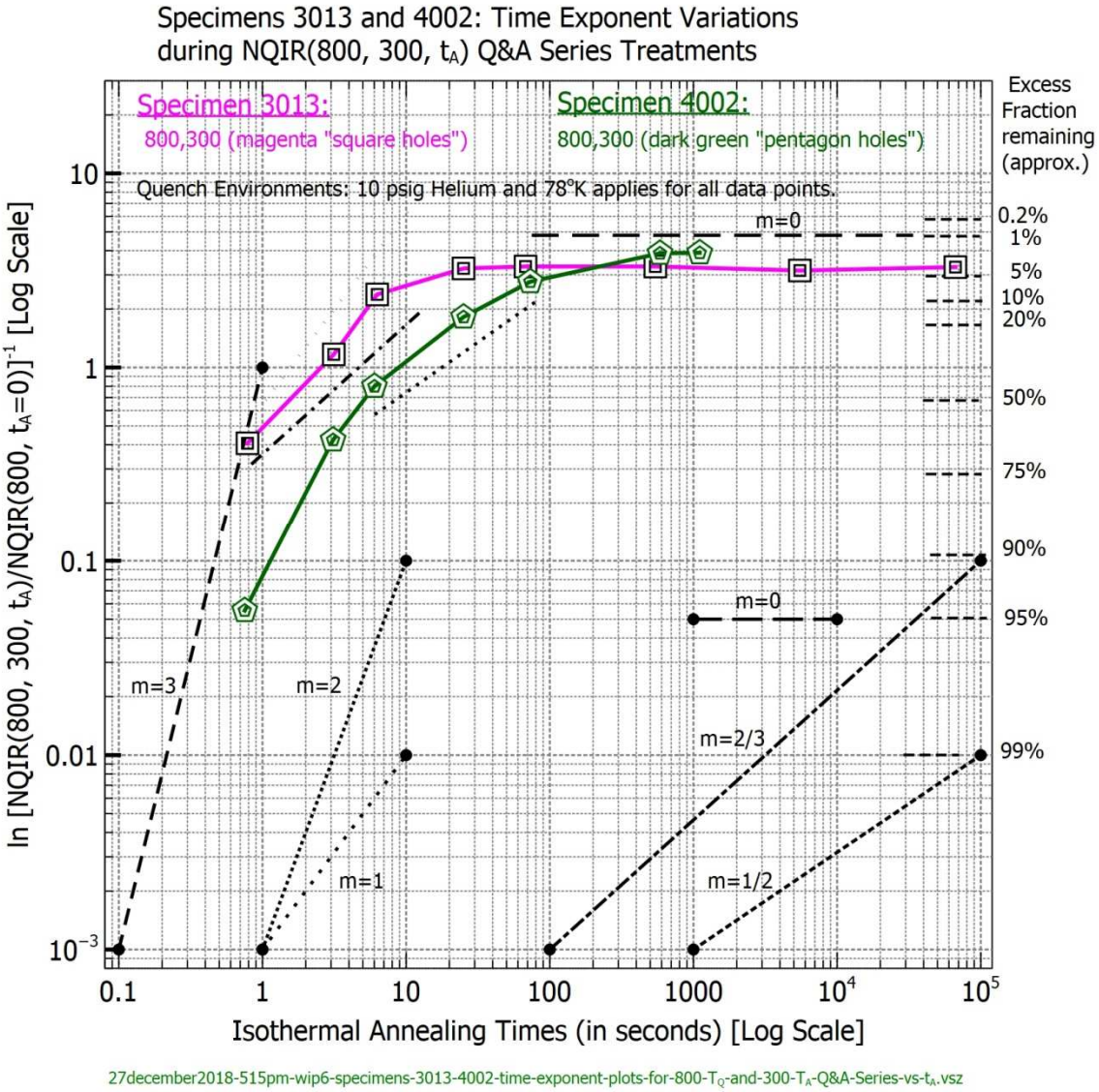

Figure 180. Specimens 3013 and 4002: Log-Log Plots of Time Exponent (m) Variations for 2 Sets of NQIR(800, 300, t_A) during Q&A Series Treatments vs. Annealing Times to more than 60,000 seconds

In Figure 180 two sets of NQIR(800, 300, t_A) Q&A series treatments exhibit initial slope values near 2 that gradually level off to zero slopes.

8.3.11.8 TEV Plots for Specimen 3013 for (900/800/700, 300) Q&A Treatments

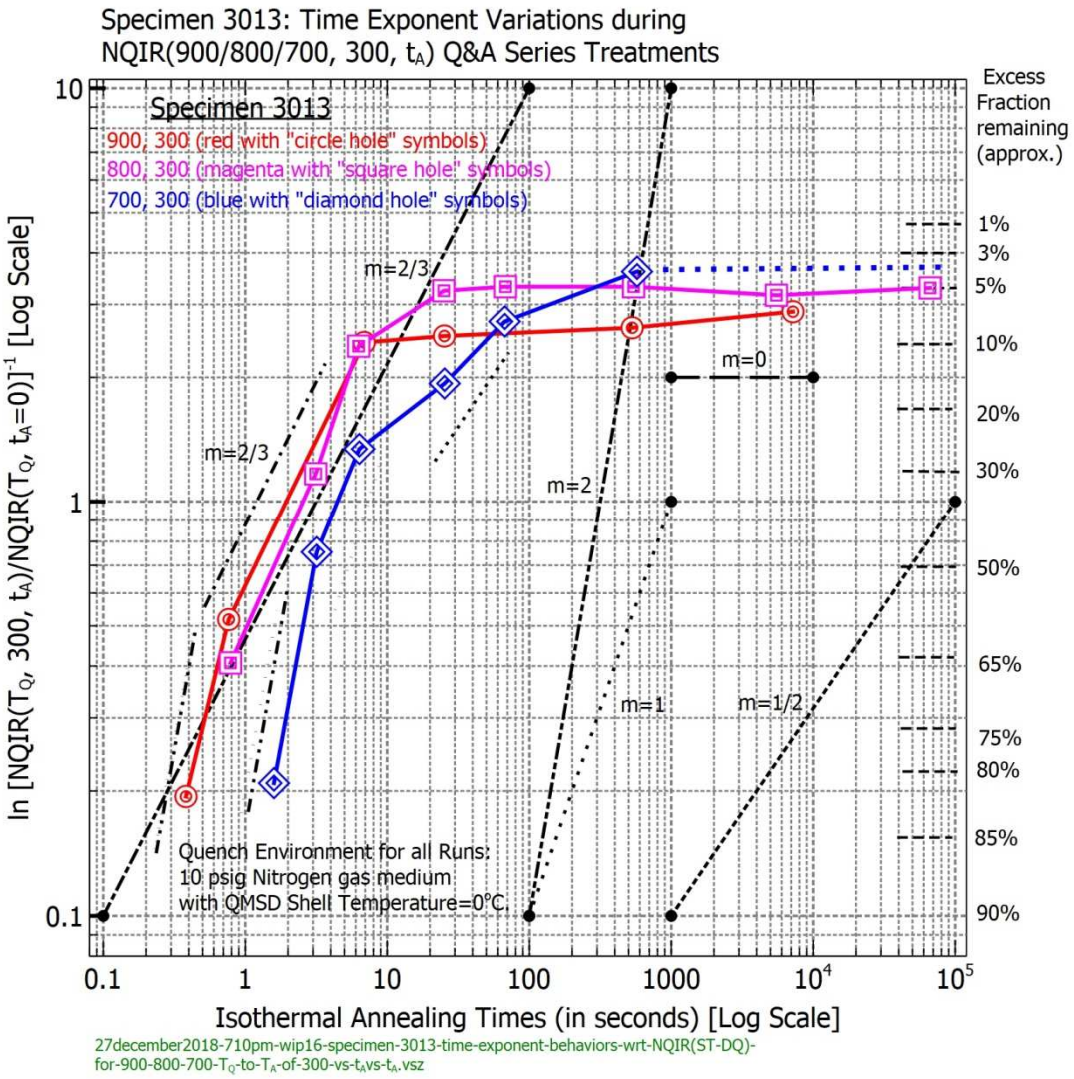

Figure 181. Specimen 3013: Log-Log Plots of Time Exponent (m) Variations for 3 Sets of Q&A Series Treatments: (900/800/700, 300, t_A) vs. Annealing Times approaching 10,000 seconds

The (900/700, 300, t_A) TEV plots in Figure 181 exhibit common segments having slopes equal to two, 2/3, and eventually approach zero. Specimen 3013's (800, 300, t_A) TEV plot has an initial slope is 1, changes rather abruptly to zero, and clearly demonstrates the fact that a stable MRR level had been reached.

8.3.11.9 TEV Comparison Plots for Specimens 3013, 4002, and 4005 for Six Sets of (700, T_A) Q&A Treatments

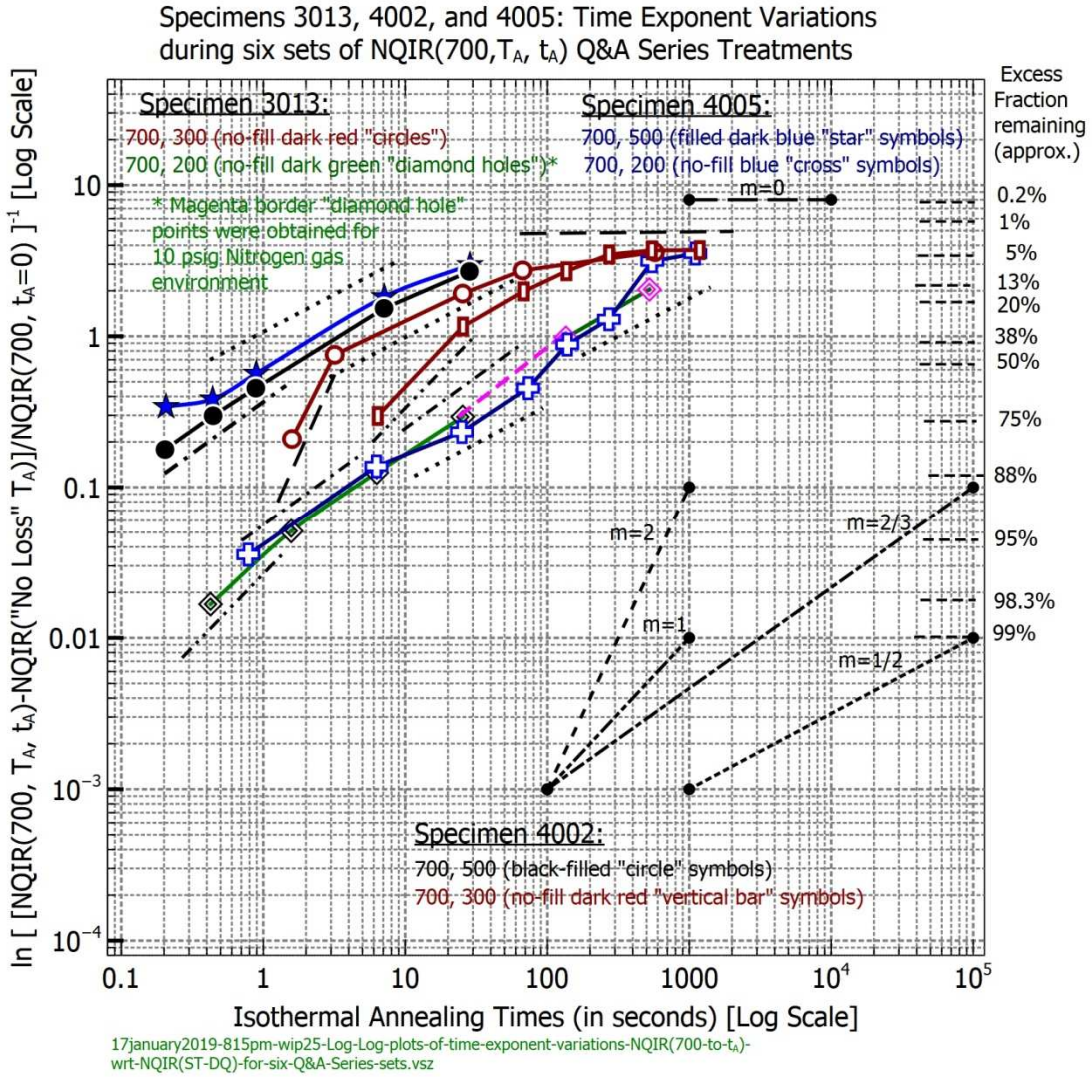

Figure 182. Specimens 3013, 4002, and 4005: Log-Log Plots of Time Exponent (m) Variations for six NQIR(700, 500/300/200, t_A) during Q&A Series Treatments vs. Annealing Times exceeding 1000 seconds

Specimen 4005's initial slope of slightly above zero for its NQIR(700, 500, t_A)

Q&A series treatment may be an indication of reduced sink efficiency associated with

a low u_V situation. This is followed by an intermediate slope of 2/3, whereas specimen 4002's initial slope of 2/3 extends over most of the overall plot.

8.3.11.10 TEV Comparison Plots for Specimens 3013, 4002, and 4005 for additional Sets of (700, T_A) Q&A Treatments

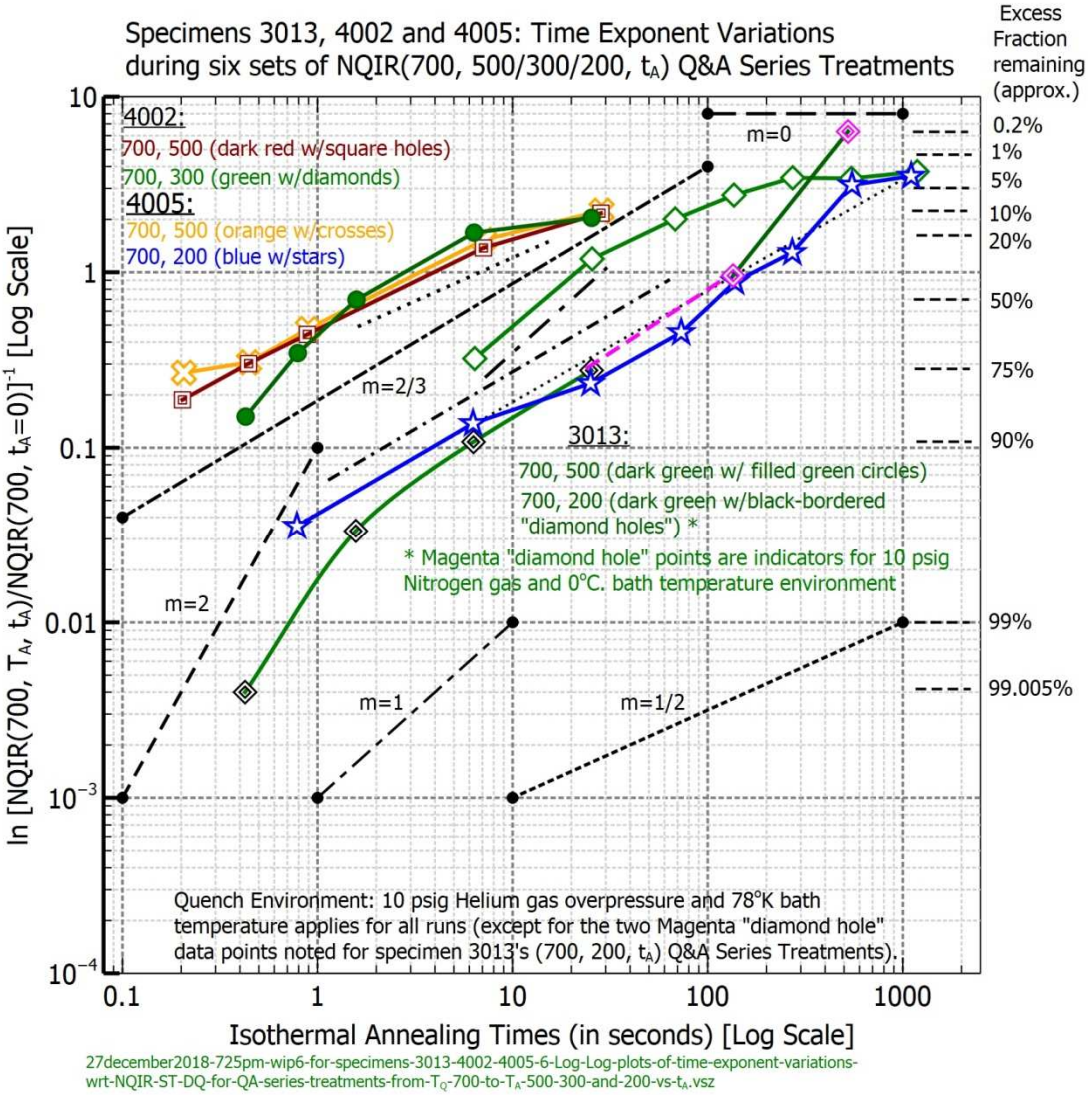

Figure 183. Specimens 3013, 4002, and 4005: Log-Log Plots of Time Exponent (m) Variations for six NQIR(700, 500/300/200, t_A) Q&A Series Treatments vs. Annealing Times of up to 1100 seconds

Figure 183 shows that slopes ranged from 1/2, 2/3, 1, and 2.

8.3.11.11 TEV Comparison Plots for Specimens 3012 (Post-Direct Deformation Treatment) and 3013 for (700, 200, t_A) Q&A Series Treatments

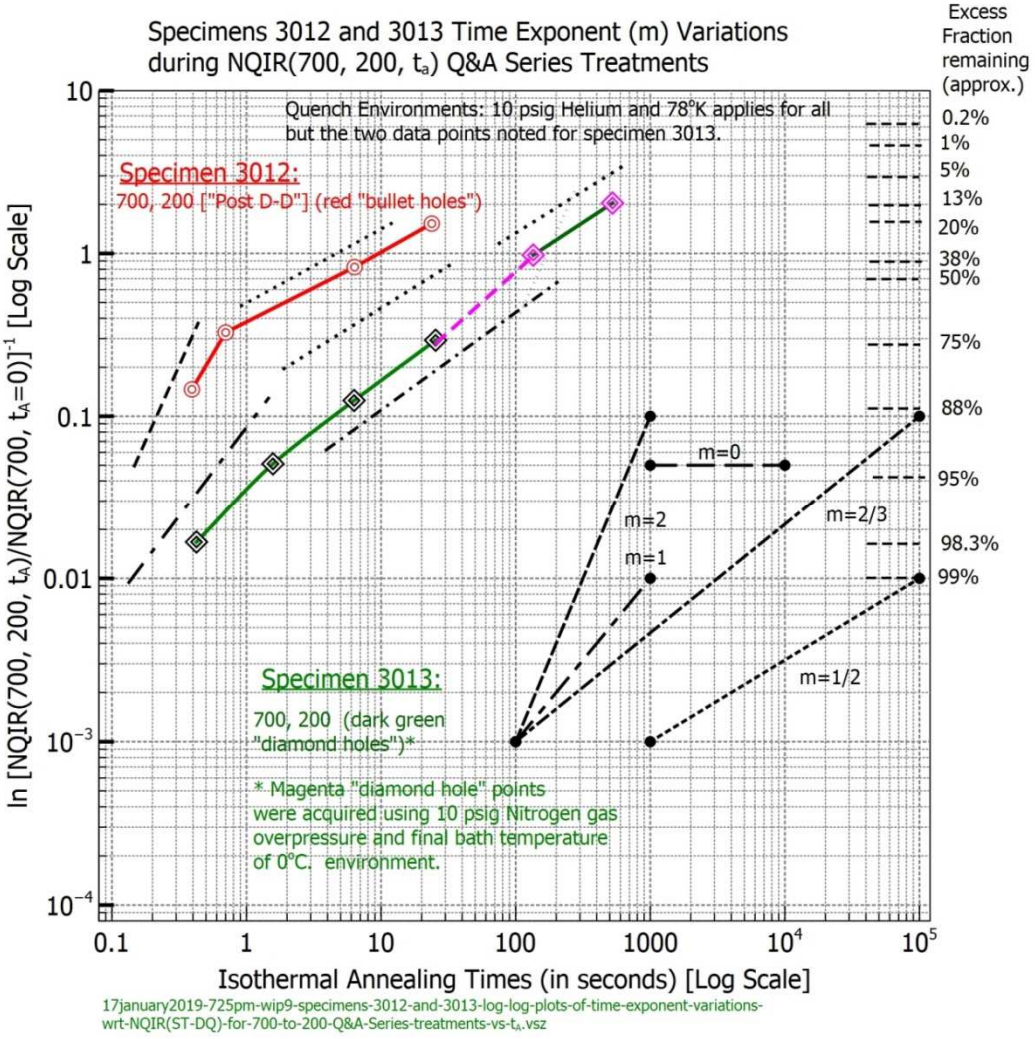

Figure 184. Specimens 3012 (Post-Direct Deformation Treatment) and 3013: Log-Log Plots of Time Exponent (m) Variations for two sets of (700, 200, t_A) Q&A Series Treatments

Specimen 3012's (700, 200, t_A) treatment exhibited an initial slope of 2 followed by a subsequent slope of 1/2 for the remainder of its annealing times. Specimen 3013's (700, 200, t_A) treatment exhibited over its range in annealing times an average slope of 2/3.

It is important to point out that immediate examinations of Figure 184 reveal slope-related information that is not readily discernible from examinations of the respective Arrhenius plots provided in Figure 127 (see sub-section 8.3.4.13).

Table 17 lists how the NQIR(700, 200, t_A) data for specimens 3012 and 3013 for the two curves of isothermal annealing kinetics were transformed into **ln $(f_r)^{-1}$** values that led to generation of the two sets of TEV data points shown in Figure 184.

Table 17. Tabulated Examples of Determinations of TEV Data Points

Specimen Number	t_A (sec.)	ST DQ or Q&A	T_Q (^oC)	T_A (^oC)	NQIR	**f_r**	**$(f_r)^{-1}$**	**Ln $(f_r)^{-1}$**
3012	0	ST DQ	700	N/A	5.44×10^{-4}	1.0	1.0	0
	0.393	Q&A	700	200	4.7×10^{-4}	0.864	1.157	0.1462
	1.7	Q&A	700	200	3.924×10^{-4}	0.721	1.386	0.327
	6.35	Q&A	700	200	2.383×10^{-4}	0.721	2.28	0.8257
	23.81	Q&A	700	200	1.184×10^{-4}	0.218	4.595	1.52
3013	0	ST DQ	700	N/A	1.81×10^{-3}	1.0	1.0	0
	0.425	Q&A	700	200	1.78×10^{-3}	0.9834	1.017	1.67×10^{-2}
	1.57	Q&A	700	200	1.72×10^{-3}	0.9503	1.052	5.1×10^{-2}
	6.30	Q&A	700	200	1.597×10^{-3}	0.8823	1.133	0.125
	25.41	Q&A	700	200	1.35×10^{-3}	0.7548	1.341	0.293
	135	Q&A	700	200	6.774×10^{-4}	0.3743	2.672	0.983
	524	Q&A	700	200	2.357×10^{-4}	0.1302	7.679	2.04

8.3.11.12 TEV Comparison Plots for Specimens 3012, 3013, and 4005 for (700, 200, t_A) Q&A Treatments

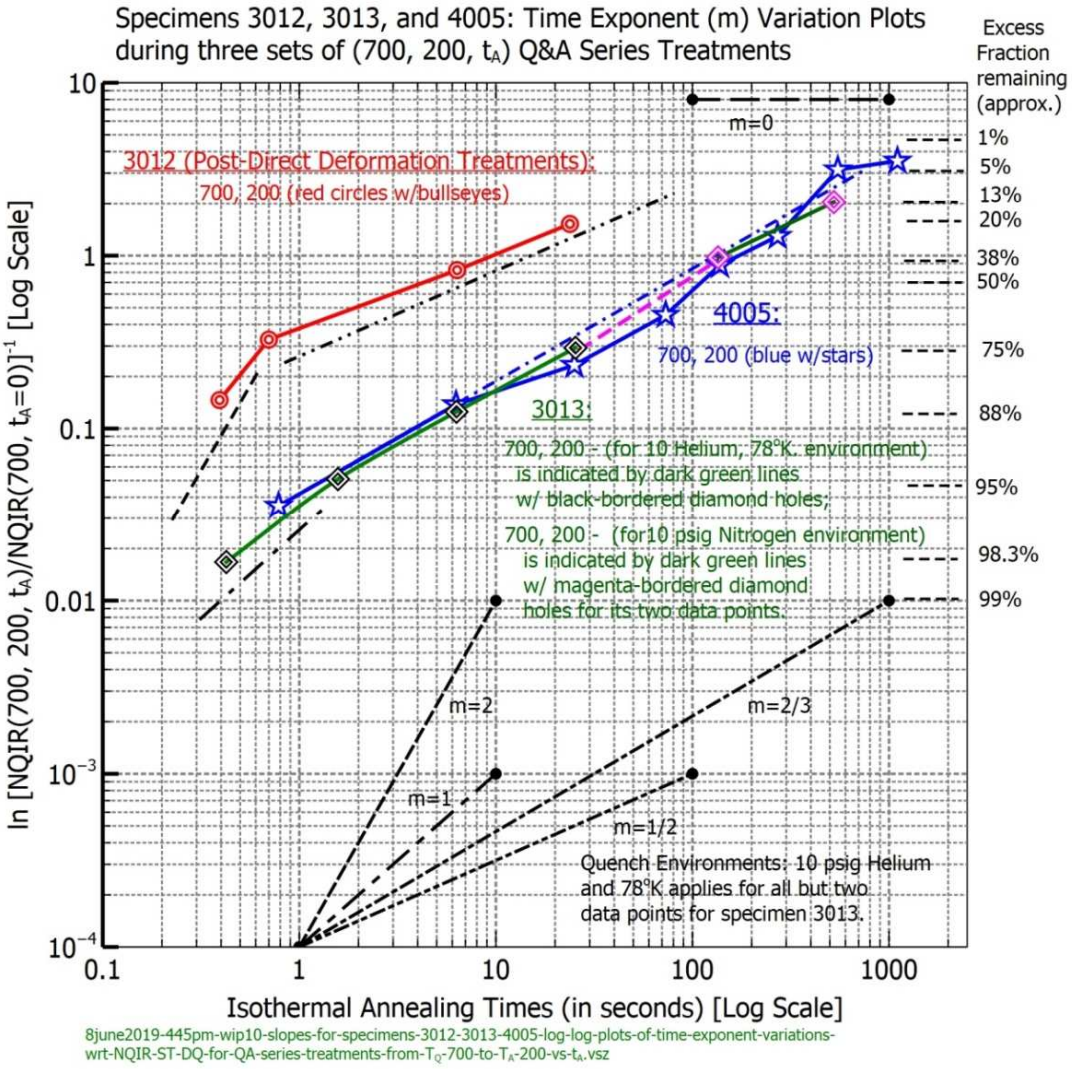

Figure 185. Specimens 3012 (Post-Direct Deformation treatment), 3013, and 4005: Overall Log-Log Plots of Time Exponent (m) Variations during NQIR(700, 200, t_A) Q&A Series Treatments

Figure 185 adds in specimen 4005's (700, 200, t_A) Q&A series treatment and reveals an average slope of 2/3 over nearly the entire range in annealing times. Such direct quantification of slope values is readily discernible from TEV plots and serves as a testament to their practicality in assessing precipitation annealing kinetics, whereas an examination of the log-log plot of Figure 102 (see sub-section 8.3.3.5), and specimen 3013's average slope is 2/3.

Moreover, it should be noted that specimen 3012's 700, 200 Q&A series treatment exhibited an initial slope of 2 followed by a subsequent slope of 1/2.

Note the significant differences in fractions remaining for specimen 3013 and that for the post-direct deformation specimen 3012 for the same (700, 200, t_A) Q&A series treatments.

In Figure 186 an overall slope of zero was exhibited for the post-direct deformation specimen 3012 and an initial slope of zero for specimen 3013 for their 700, 600 Q&A series treatments. By comparison, initial slopes of 2 are exhibited for specimen 3012's 700, 200 Q&A series treatment and specimen 3013's 700, 600 Q&A series treatment. For the remainder of annealing times, an average slope of 1/2 is revealed for specimen 3012's 700, 200 Q&A series treatment and for specimen 3013's 700, 600 Q&A series treatment. Specimen 3013's 700, 500 Q&A series treatment displays a series of gradual transitions from an initial slope near 2, then a slope of 1, then a slope of 2/3, and ending with a slope of nearly zero.

8.3.11.13 TEV Comparison Plots for Specimens 3012 and 3013 for (700, TA) Q&A Treatments

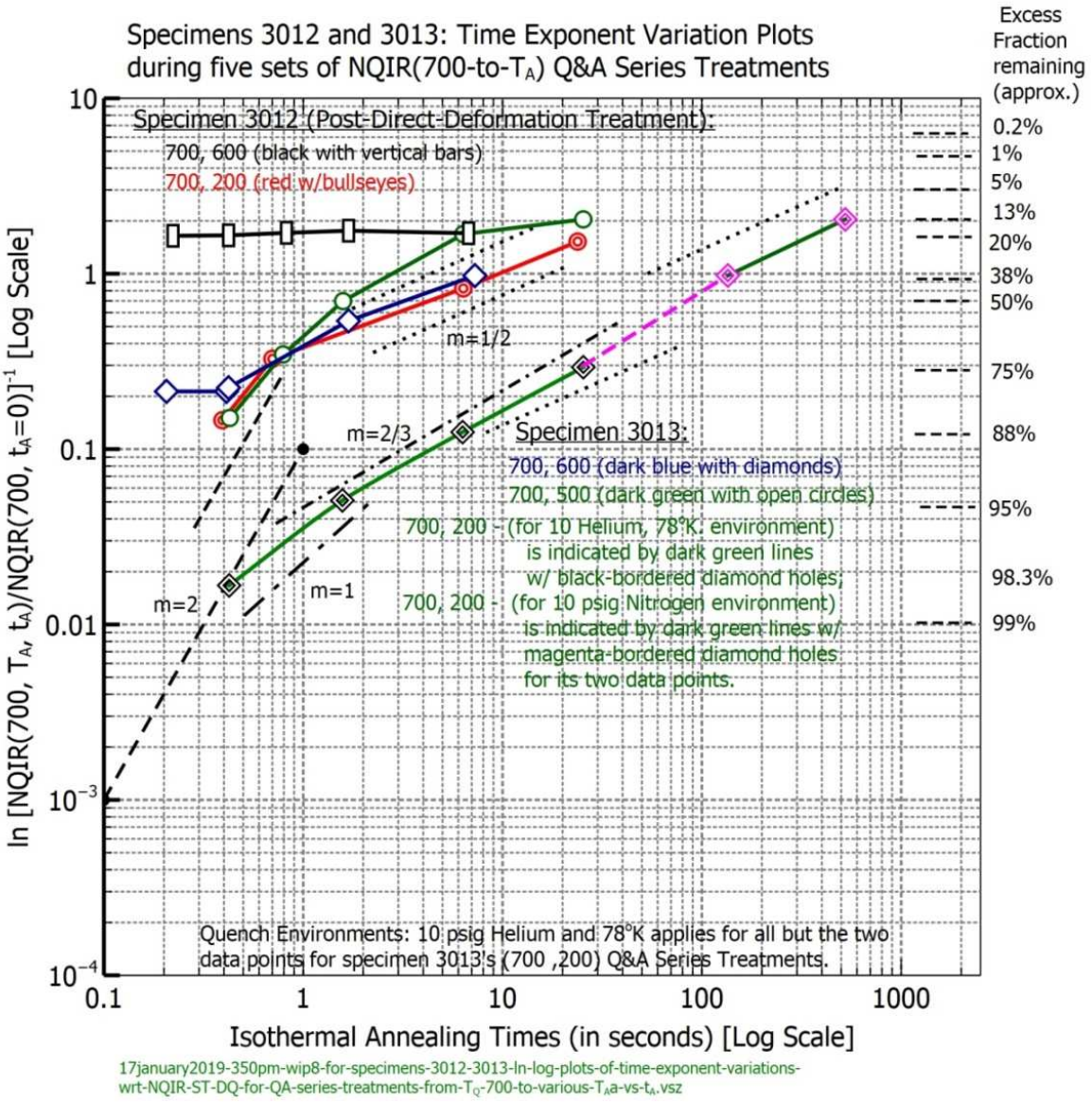

Figure 186. Specimens 3012 and 3013: Log-Log Plots of Time Exponent (m) Variations during five NQIR(700, 600/500/200, t_A) Q&A Series Treatment Combinations vs. Annealing Times up to 500 seconds

8.3.11.14 TEV Comparison Plots for Specimens 3012, 3013, 4002, and 4005 for (700, T_A) Q&A Treatments

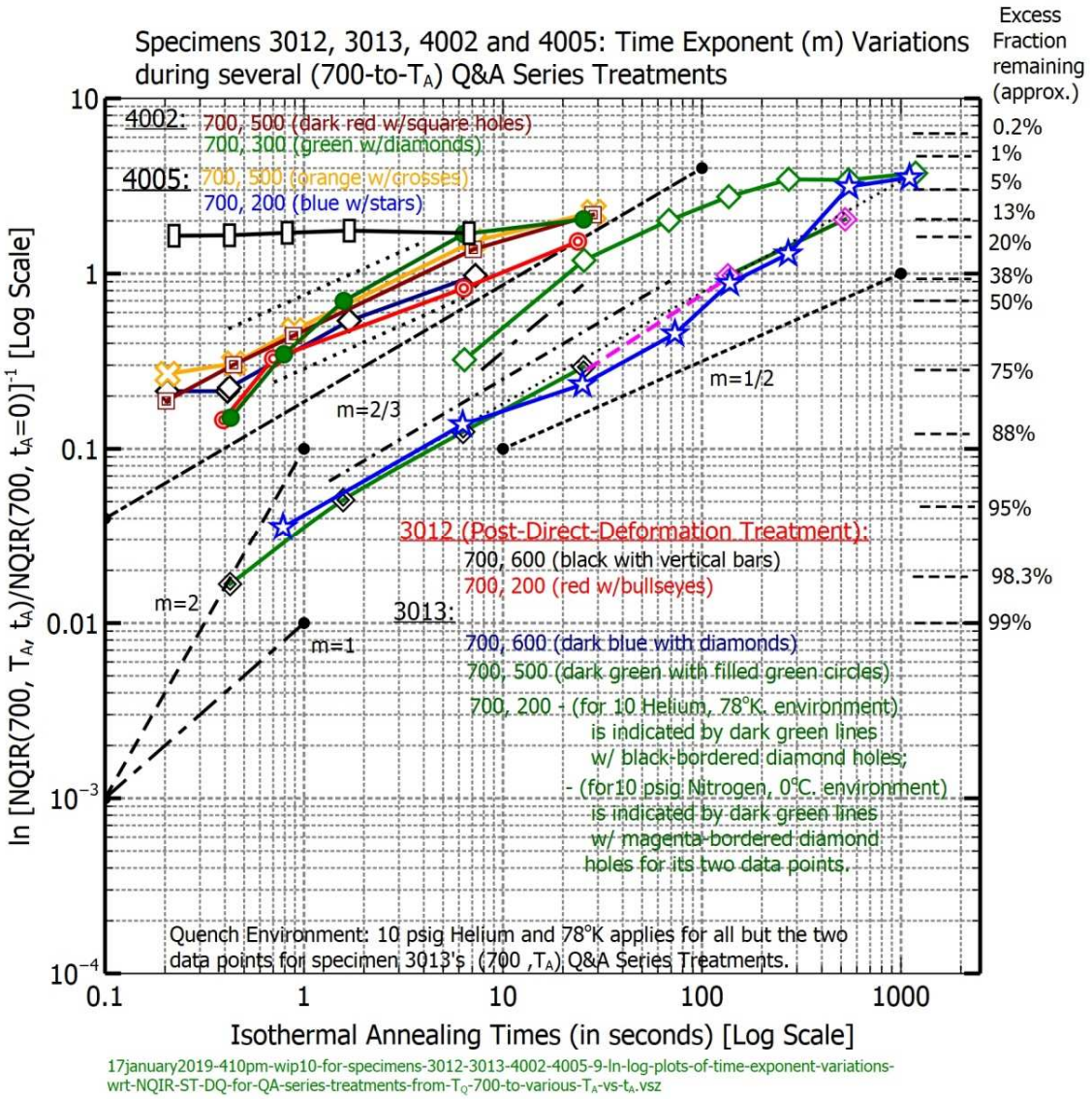

Figure 187. Specimens 3012, 3013, 4002, and 4005: Overall Log-Log Plots of Time Exponent (m) Variations during nine NQIR(700, 600/500/300/200, t_A) Q&A Series Treatment Combinations

Figure 187 shows nine sets of Log-Log plots of the Time Exponent (m) Variations associated with (700, 600/500/300/200, t_A) Q&A series treatments involving four specimens (3012, 3013, 4002, and 4005). Specimen 4005's 700, 500 Q&A series treatment begins with an initial slope that is close to zero followed by a slope of 1/2, and ending with a slope that approaches zero. Specimen 4002's 700, 300 Q&A series treatment exhibits an initial slope close to 2, then 1, then 2/3, and ends with a slope that approaches zero.

Figure 188 illustrates TEV plots of NQIR(700, 200, t_A), NQIR(700, 300, t_A), and NQIR(500, 150, t_A) Q&A series treatments. Specimen 3013's 700, 300 initial slope is 2, specimen 4002's initial slope is 2/3, and specimen 4002's 500, 150 Q&A series treatment reveals an average slope of 1/2.

8.3.11.15 TEV Comparison Plots for Specimens 3013 and 4002 for one NQIR(700, 200, t_A), two NQIR(700, 300, t_A), and one NQIR(500, 150, t_A) Q&A Treatments

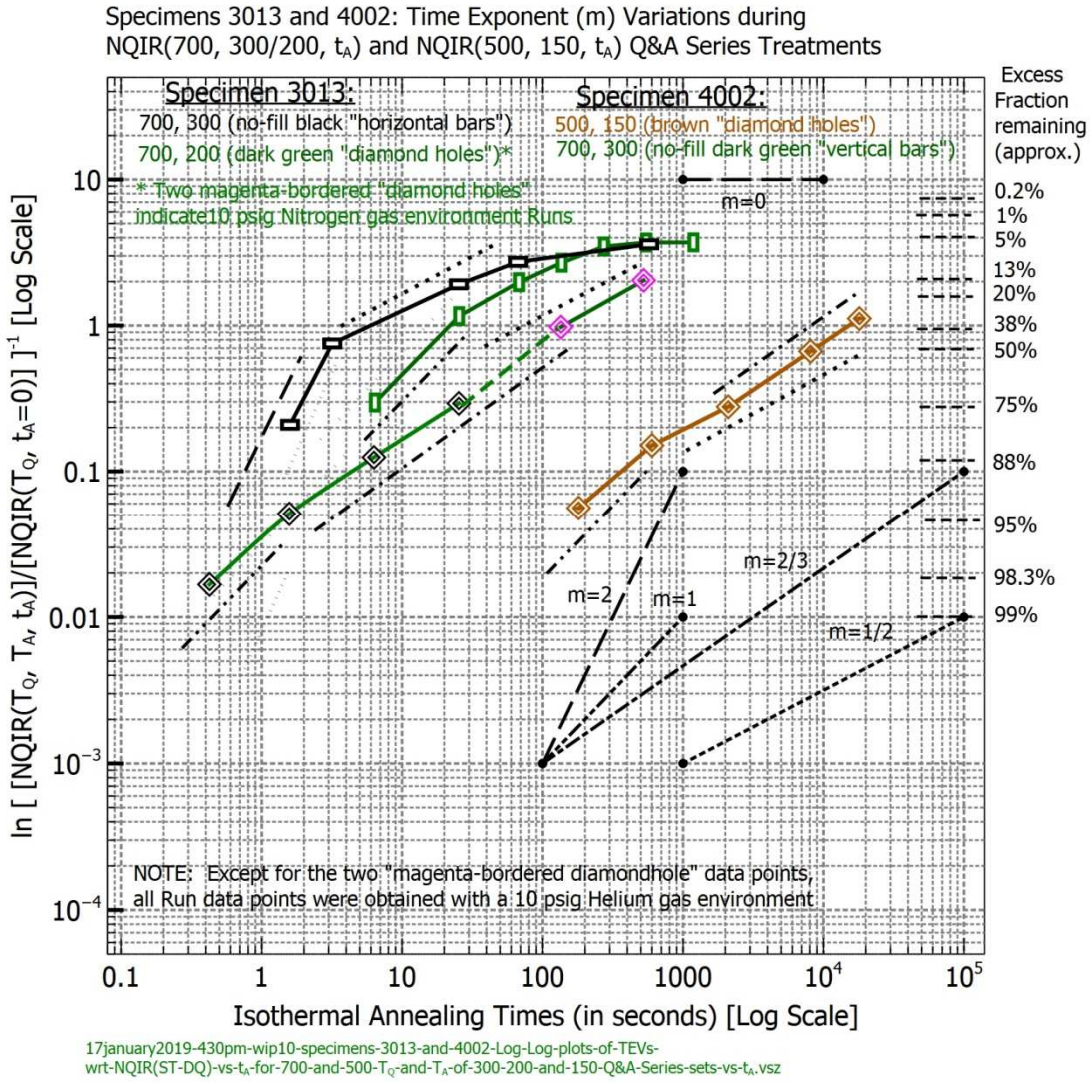

Figure 188. Specimens 3013 and 4002: Overall Log-Log Plots of Time Exponent (m) Variations for one NQIR(700, 200, t_A), two NQIR(700, 300, t_A), and one NQIR(500, 150, t_A) Q&A Series Treatments

8.3.11.16 TEV Plot for Specimen 4002 for an NQIR(500, 150, tA) Q&A Treatment

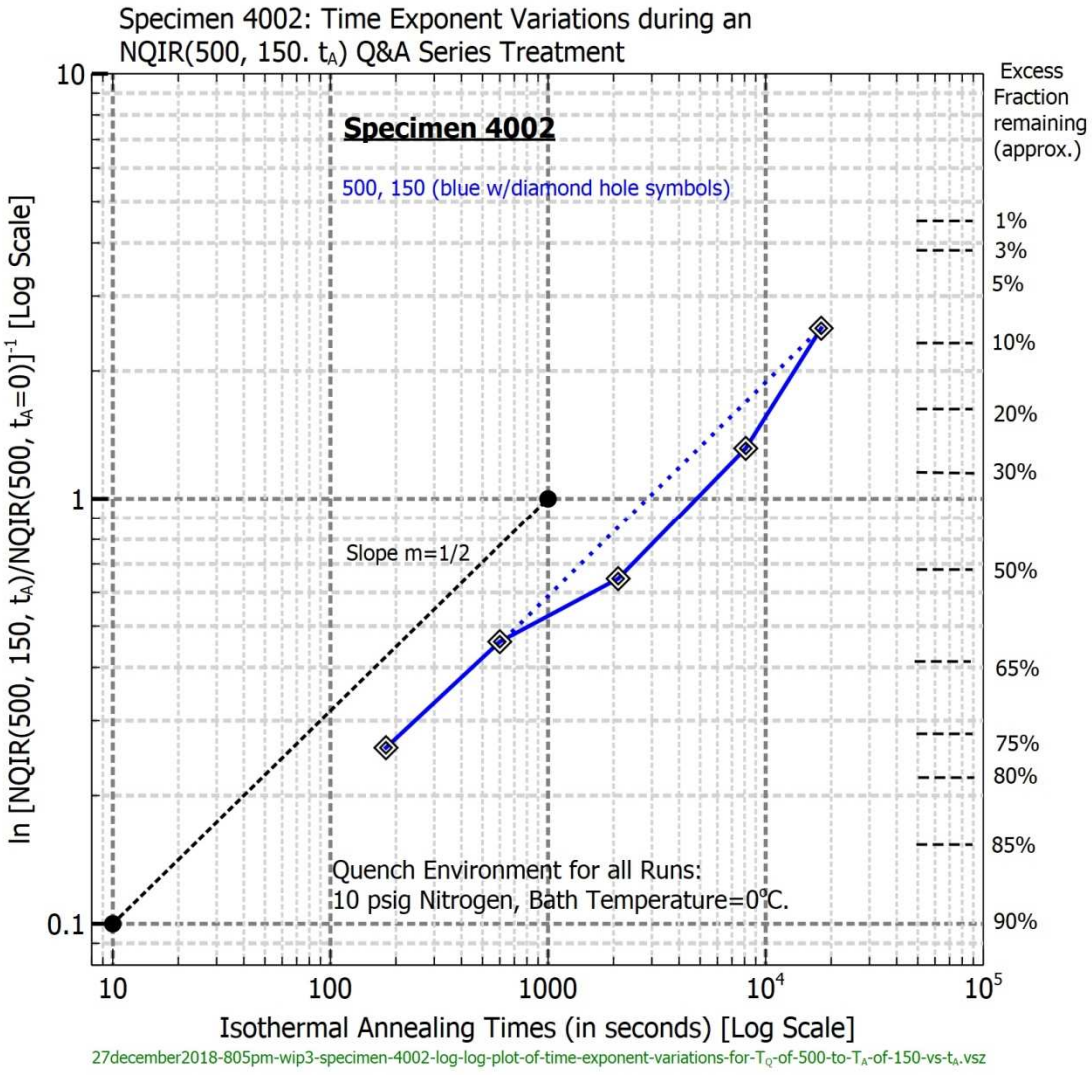

Figure 189. Specimen 4002: Time Exponent Variation exhibited via Log-Log Plot of ln{[NQIR(500, 150, t_A)] / [NQIR(500,'t_a=0)] }$^{-1}$ vs. Annealing Time up to nearly 20,000 seconds

Figure 189 provides a more clearly distinguished slope of 1/2 compared with the multiple sets of various slope lines that are included in Figure 188.

8.3.11.17 TEV Comparison Plots for Specimens 3013 and 4002 for NQIR(500, 300/150, t_A) Q&A Treatments

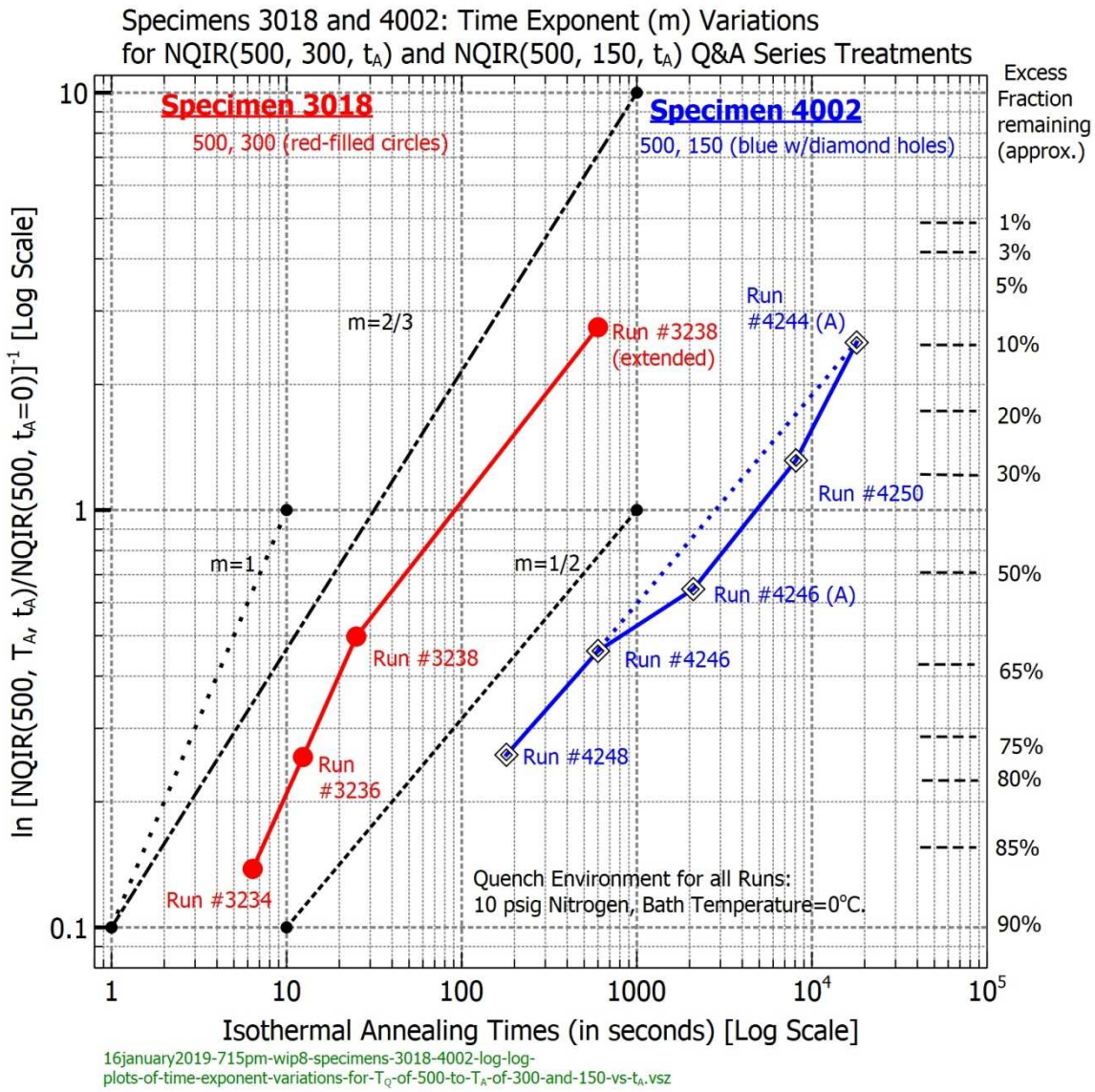

Figure 190. Specimens 3018 and 4002: Log-Log Plots of Time Exponent (m) Variations for NQIR(500, 300, t_A) and NQIR(500, 150, t_A) during Q&A Series Treatments vs. Annealing Times to nearly 20,000 seconds

Figure 190 clearly shows for specimen 3018's 500, 300 Q&A series treatment an initial slope of 1 and a subsequent slope of 1/2.

8.3.11.18 TEV Comparison Plots for Specimens 3013, 4002, and 4005 for 14 sets of NQIR(T_Q, T_A, t_A) Q&A Treatments

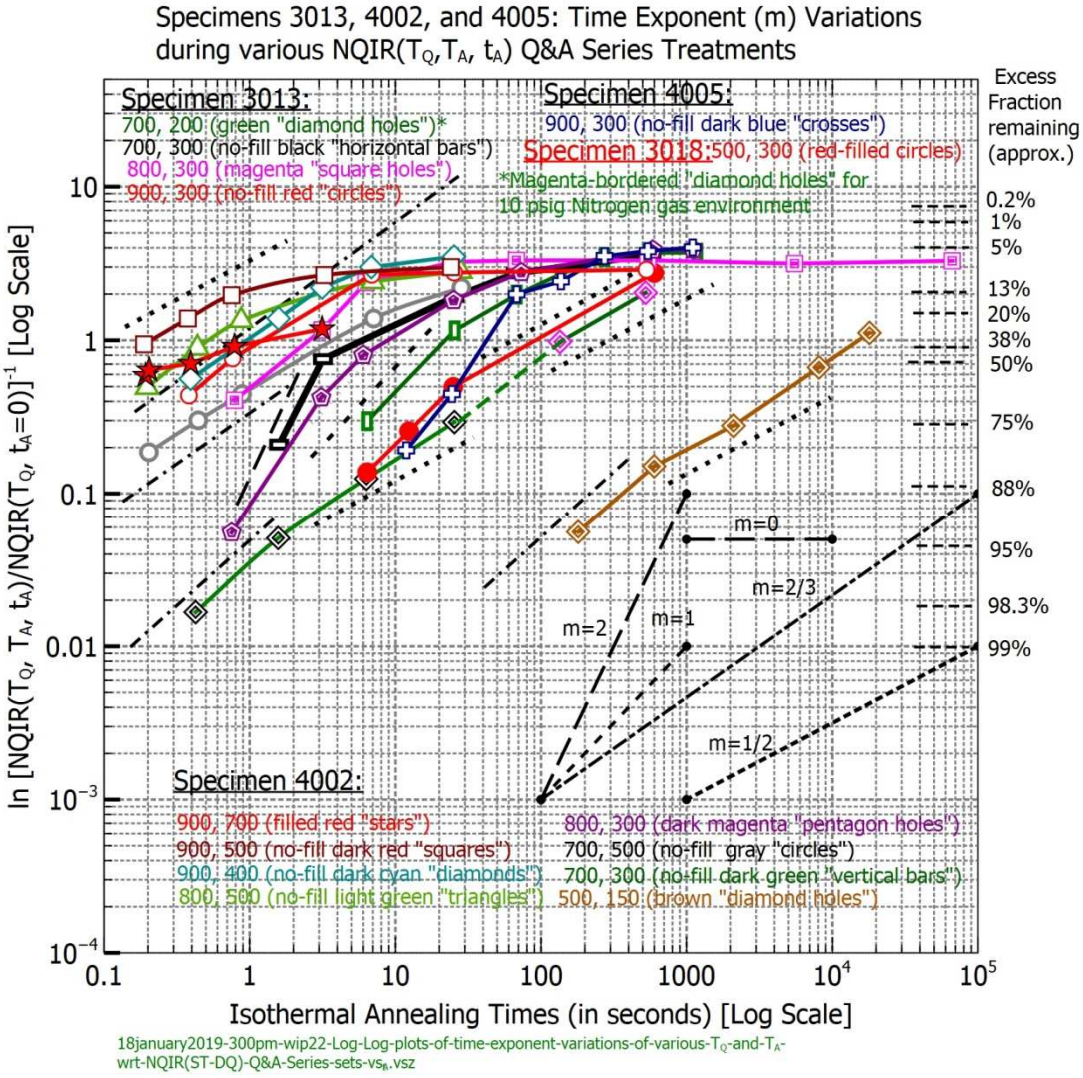

Figure 191. Specimens 3013, 4002, and 4005: Log-Log Plots of Time Exponent (m) Variations vs. Annealing Time for 14 Sets of Q&A Series Treatments: (900/800/700, 500/300, t_A), (900, 700/400, t_A), (700, 200, t_A), and (500, 150, t_A).

Figure 191 provides an overlay of slopes for 14 sets of NQIR(T_Q, T_A, t_A) Q&A series treatments involving specimens 3013, 4002, and 4005.

8.3.12 Observations of Metastable Residual Resistance (MRR) Levels for various Q&A Series Treatments

Figures 174 through 191 cited earlier and Figures 192 through 196 presented in this sub-section each have for the associated Q&A series treatments either 1) a second axis which provides MRR level magnitudes expressed as percentage of excess fraction remaining NQIR(T_Q,T_A, t_A)/NQIR("No-Loss" T_A), or 2) includes labeled dashed horizontal lines to indicate the associated Q&A series treatment's NQIR("No-Loss" T_A) values established from B.E.T. analyses presented in section 7.4, or 3) include both 1) and 2) in the plot.

Figure 195 is included for the purpose of illustrating how monitored NQIR values do prove to be especially sensitive to specific Q&A series treatments. Here, a "Hybrid Run" measurement was performed following "insertion" of an isothermal anneal at 400^{o}C for 22.5 hours, and an NQIR that had been nearly constant was significantly reduced as a consequence of that immediately prior specific Q&A treatment.

Moreover, looking back, MRR-related indicators have been included in many plots presented in earlier Q&A series treatment sub-sections of this document. The specific indicators included dashed line NQIR("No-Loss" T_A) markers with associated numerical values and/or right-hand-side axes indicating associated remaining supersaturation ratios calculated from NQIR(T_Q, T_A, t_A)/["No Loss" NQIR(T_A)] values. See, for example, Figures 81, 83 - 88, 90, 92 - 97, 102, 105, 115, 116, 119 - 122, and 124 - 129.

8.3.12.1 Specimen 3016: Metastable Residual Resistance Levels illustrated in Two-Axes Comparison Log-Log Plots of NQIR(900/800/700, 400, t_A) Q&A Series Treatments

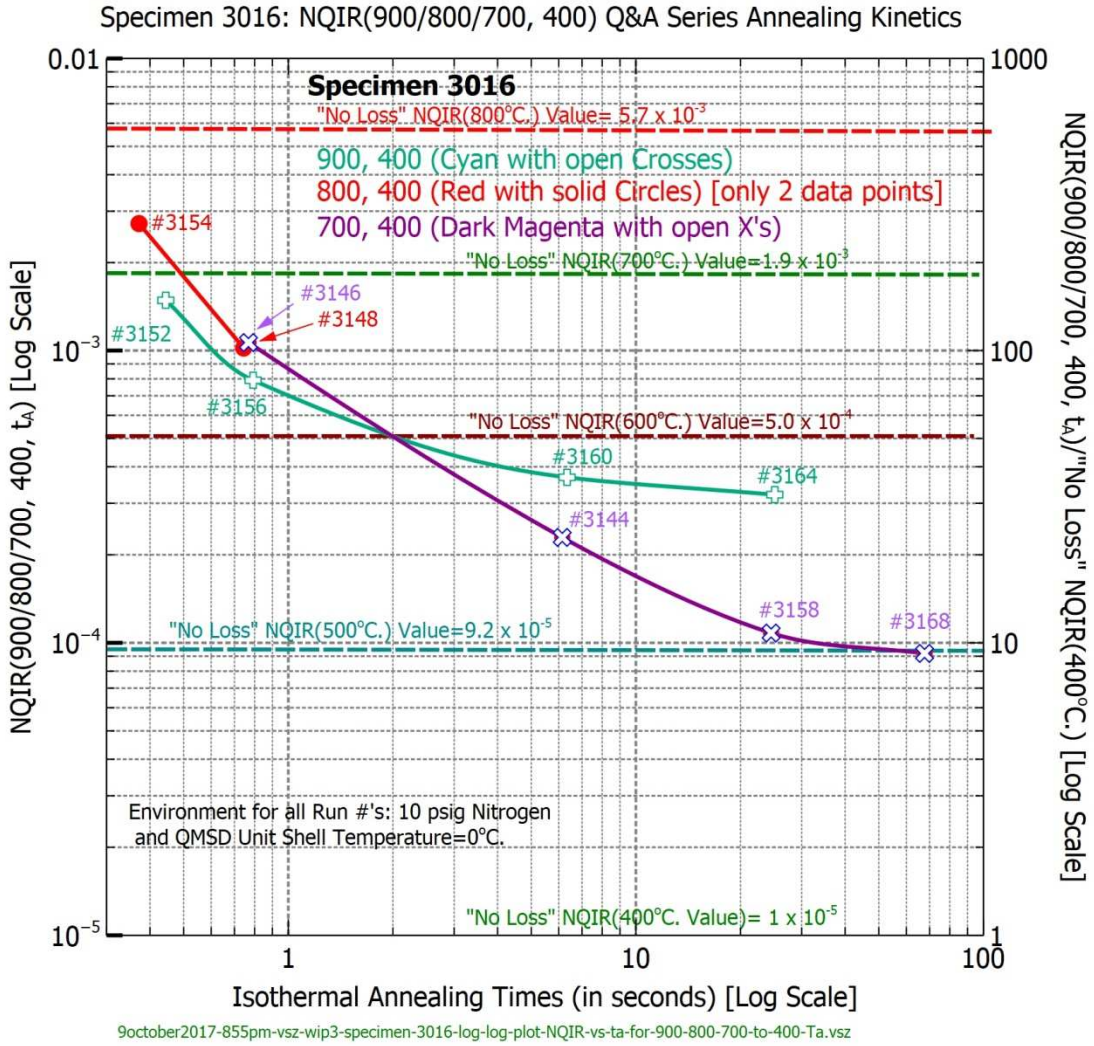

Figure 192. Specimen 3016: Metastable Residual Resistance Levels illustrated in Two-Axes Comparison Log-Log Plots of NQIR(900/800/700, 400, t_A) Q&A Series Treatments vs. Annealing Times up to 70 seconds

8.3.12.2 Specimens 4002 and 4005: Metastable Residual Resistance Levels illustrated in Two-Axes Comparison Log-Log Plots of NQIR(900/800/700, 500, t_A) Q&A Series Treatments

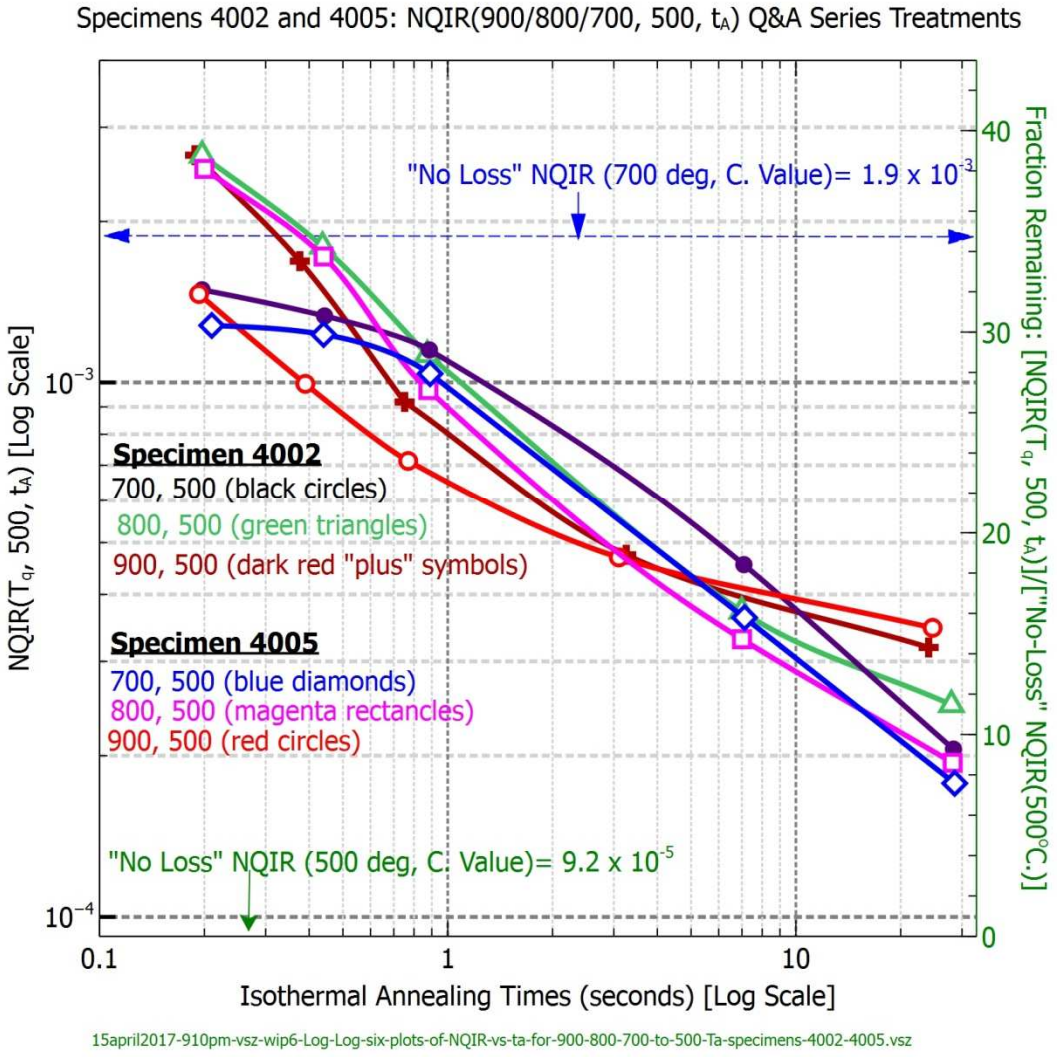

Figure 193. Specimens 4002 and 4005: Metastable Residual Resistance Levels illustrated in Two-Axes Comparison Log-Log Plots of NQIR(900/800/700, 500, t_A) Q&A Series Treatments vs. Annealing Times up to 30 seconds

In Figure 193, the MRR levels range from eight to 16 times the "No-Loss" NQIR(500) value, and MRR values are noted to become larger with increasing T_Q.

8.3.12.3 Specimen 3013: Metastable Residual Resistance Levels illustrated in Plots of NQIR(900/800/700, 300, t_A) Q&A Series Treatments

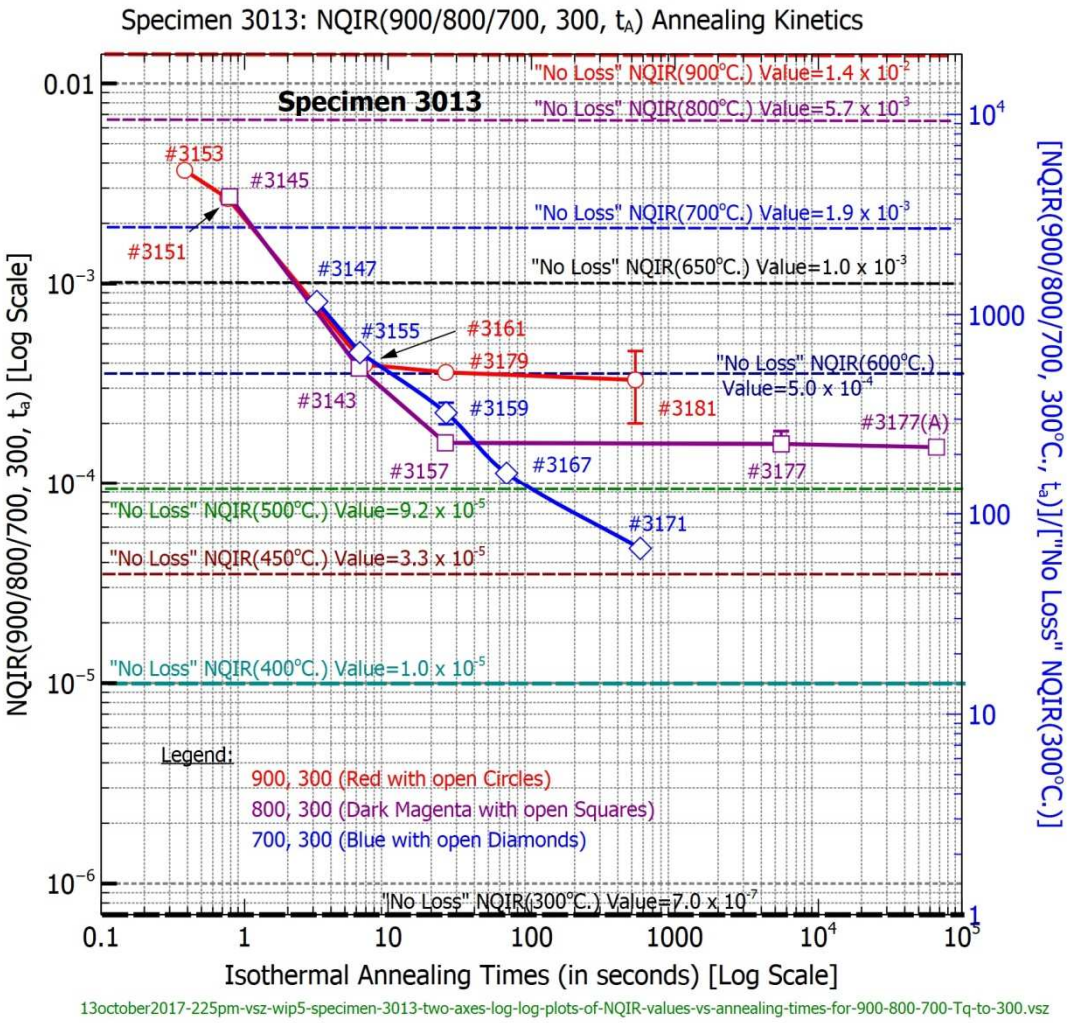

Figure 194. Specimen 3013: Metastable Residual Resistance Levels illustrated in Plots of NQIR(900/800/700, 300, t_A) Q&A Series Treatments vs. Annealing Times up to 26 seconds

8.3.12.4 Specimen 3013: Metastable Residual Resistance Levels illustrated in Log-Log Plot of NQIR Values for (900, 300, t_A) a Q&A Series Treatment (with a "Hybrid Run" Data Point included)

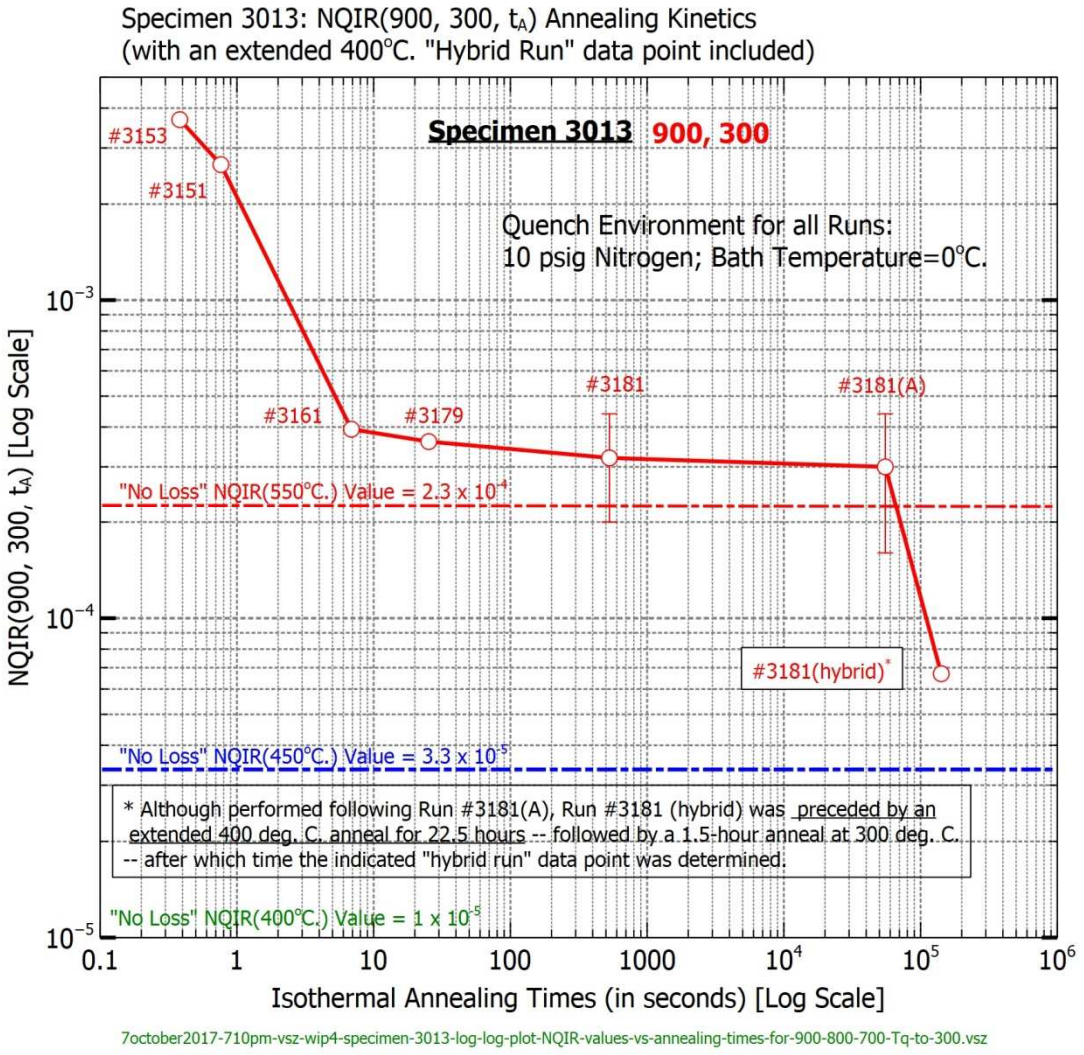

Figure 195. Specimen 3013: Metastable Residual Resistance Levels illustrated in Log-Log Plot of NQIR Values for (900, 300, t_A) a Q&A Series Treatment (with a "Hybrid Run" Data Point included) vs. Annealing Times extending beyond 100,000 seconds

8.3.12.5 Specimen 4002: Metastable Residual Resistance Levels illustrated in Two-Axes Log-log Plot of an NQIR(500, 150, t_A) Q&A Series Treatment vs. Annealing Times up to 300 minutes

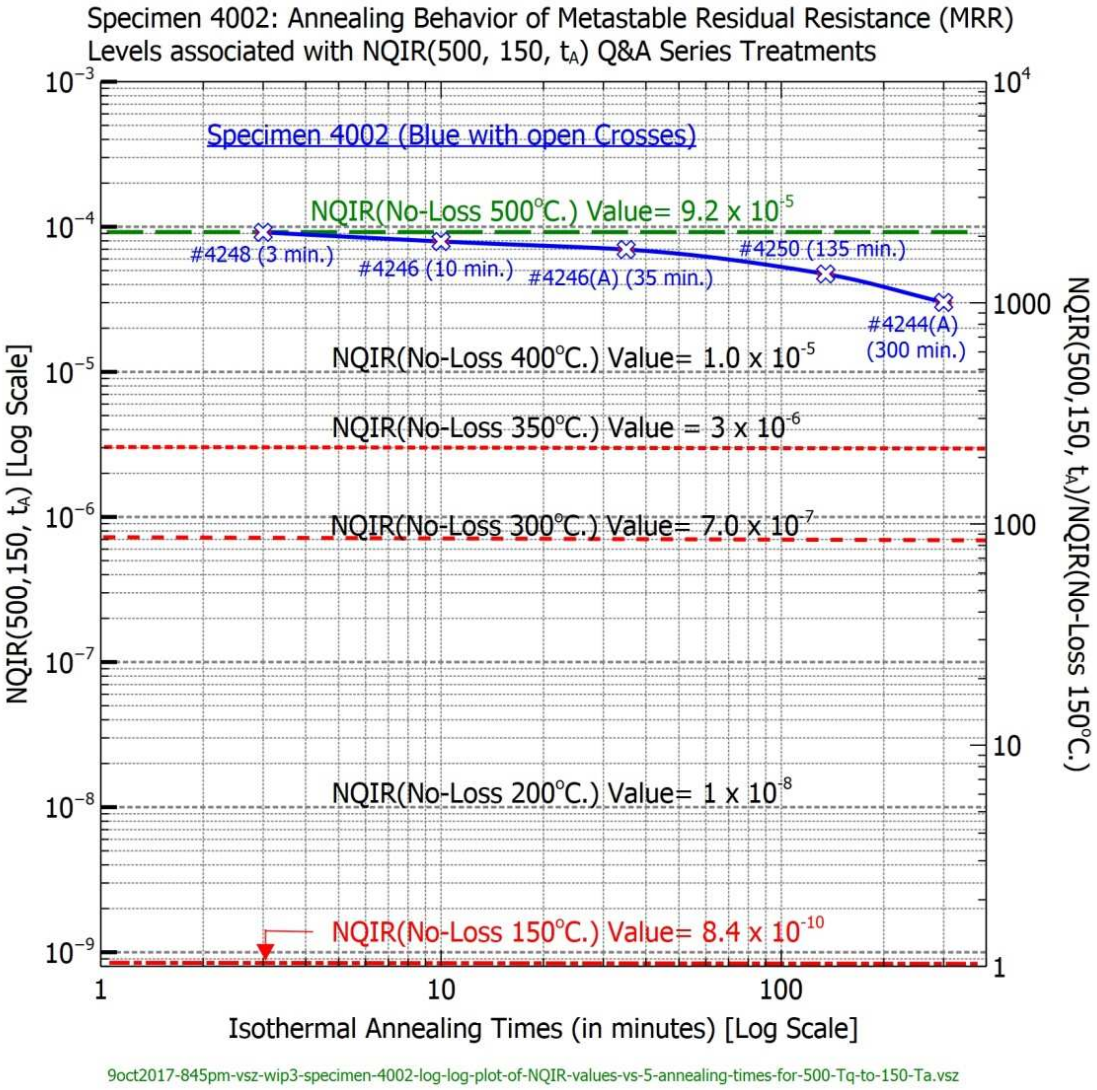

Figure 196. Specimen 4002: Metastable Residual Resistance Levels illustrated in Two-Axes Log-log Plot of an NQIR(500, 150, t_A) Q&A Series Treatment vs. Annealing Times up to 300 minutes.

Sub-section 8.4.3 will discuss extended region Q&A annealing kinetics and provide quantitative assessments for MRR levels that are clearly evident in many Q&A series treatment plots.

8.3.13 High-Level Summary of Assessments obtained from Specific Categories of Plots of NQIR(T_Q, T_A, t_A) Q&A Series Treatments

Through analyses of the acquired NQIR(T_Q, T_A, t_A) Q&A series treatments data using several graphical approaches, quantitative assessments were obtained of annealing half-times (see Figures 115 through 130), associated order of annealing kinetics (see Figures 101, 102, and 131), effective vacancy migration energies E^M_V(eff) from Arrhenius plots of half-times (see Figures 132 through 136), NQIR supersaturation ratios vs. annealing time (see Figures 137 and 138), vacancy defect chemical potential (μ_v) profiles (see Figures 139 through 142), extended (700/500. 65. t_A) Q&A series treatment anneals (Figures 143 through 145), a plot for specimen 4002 of an NQIR(500, 150, t_A) Q&A Series Treatment vs. Square Root of Annealing Time (see Figure 146), fraction remaining values of NQIR(T_Q, T_A, t_A) vs. reduced annealing time variable $t_A/t_{1/2}$ (see Figures 147 through 152), initial annealing rates (see Figures 153 and 167), normalized initial annealing rates (see Figures 154 and 155), mean relaxation times (see Figures 156 through 159), determinations of instantaneous vacancy activation energies E^M_V(act) from Arrhenius plots of mean relaxation times (see Figures 160 through 162, and Figures 167-168, 171 and 172) and from Arrhenius plots of initial annealing rates (see Figures 165-166, 169, and 170), influence of vacancy defect chemical potential upon instantaneous vacancy activation energy (see Figure 163) and upon Absolute Macroscopic Sink Efficiency **€**

(see Figure 164), log-log plots of time exponent m variations (see Figures 174 through 191), and magnitudes of Metastable Residual Resistance (MRR) levels resulting from specific Q&A Series treatments (see Figures 192 through 196).

8.4 CATEGORIZED DISCUSSIONS OF ANNEALING KINETICS DATA

8.4.1 Segmentation of Data Analyses into Regions

Various categorized sets of plots of annealing kinetics data acquired from numerous specific Q&A series treatments performed during this overall research investigation were described in sub-sections 8.3.2 through 8.3.12 and the associated analyses were covered in each respective sub-section.

In sub-sections 8.4.2 through 8.4.5, the discussions of Q&A annealing kinetics are separated into four regions: half-time; extended anneal time; initial decay, and overall behavior. Lastly, sub-section 8.4.6 provides highlights garnered regarding specific parameters determined from analyses of eight distinct sets of Q&A annealing kinetics plots.

Figure 8 serves to illustrate a detailed summary of the respective analyses that were made from these four regions of Q&A kinetics. Interconnections are included to exemplify interrelated observations among these four distinct regions.

8.4.2 Half-time Region Q&A Annealing Kinetics

Data analyses of the half-time region of Q&A series treatments involve detailed examinations of the plots already presented in sub-section 8.3.4.

8.4.2.1 Observations made from Plots of Fraction Remaining Values of NQIR(T_Q, T_A, t_A) vs. Reduced Annealing Time Variable $t_A/t_{1/2}$.

Figure 147 reveals for a given specimen and Q&A series treatment a) the strong dependencies of the annealing kinetics upon vacancy supersaturation levels even before values of t_A extend much beyond the respective $t_{1/2}$ values and b) the resulting MMR levels that become evident for values of t_A that approach five times the respective $t_{1/2}$ values.

Figure 148 reveals a) the close proximities of the various curves when t_A is less than the respective $t_{1/2}$ values, b) the manifestation of MRR levels that become obvious when Q&A series treatments are conducted for annealing times extended substantially beyond the associated annealing half-times for any given specimen, and c) the revelation of the underlying influence of excess vacancy defect chemical potential (μ_V) upon the eventual MRR levels associated with the (T_Q, T_A, t_A) Q&A series thermal treatments presented in Figure 148.

Figure 149 reveals in these semi-log plots three things associated with the eleven sets of Q&A series treatments: a) the obvious “loss’ levels that are easily noted when ST DQ data points having t_A values equal to zero would be "off scale" when a logarithmic axis is used, so a starting abscissa value of 0.02 was chosen as the initial value for graphing of the reduced annealing time variable parameter; b) the generally non-sigmoidal shapes that illustrate the majority of behaviors; and c) the trend among the various "end-point" MRR values being higher when Q&A treatments involving both higher T_Q and higher T_A are compared.

Figure 150 reveals for the five T_Q equal to 700^{o}C Q&A series treatments that a) only specimen 3013’s (700, 300, t_A) plot exhibits a sigmoidal shape, b) the

magnitudes for the MRR levels begin to exhibit a leveling off when the respective annealing times approach five times the magnitude of the reduced annealing time variable, and c) the magnitudes of the MRR levels are higher for higher annealing temperatures.

Figure 151 reveals for the two T_Q equal to 800^{o}C Q&A series treatments that the pair of curves: a) happen to closely follow each other while the reduced annealing time variable is less than 2, b) begin to differ in magnitude as an MRR level starts to set in as annealing times extend beyond twice the reduced annealing time variable's magnitude, and c) reveal a magnitude of MRR level that is higher for the higher annealing temperature Q&A series treatment.

Figure 152 reveals for the four T_Q equal to 900^{o}C Q&A series treatments that a) both of the (900, 700, t_A) Q&A series treatments exhibit nearly identical annealing kinetics for reduced annealing variable values ranging from zero to just under one, b) both the (900, 400, t_A) and the (900, 200, t_A) Q&A series treatments exhibit nearly identical annealing kinetics for reduced annealing variable values ranging from zero to just under two, c) the initial annealing rates for the two (900, 700, t_A) Q&A series treatments are higher than either the (900, 400, t_A) or the (900, 200) Q&A series treatments, and d) the magnitudes of the MRR levels for the two (900, 700, t_A) Q&A series treatments are noticeably higher than those resulting from the (900, 400, t_A) and (900, 200, t_A) Q&A series treatments.

8.4.2.2 Discussion and Comparisons of Results

8.4.2.2.1 Reduced Time Variable Results

Some basic comparisons are made at this time with the results of others who chose the reduced time variable $t/t_{1/2}$ [114] as the independent parameter to apply to their annealing kinetics data obtained for only a single annealing temperature of 40^oC.

8.4.2.2.1.1 De Jong and Koehler

M. de Jong and J. S. Koehler (see Figures 2 and 3 in [25]) obtained results that they referred to as universal S-shaped curves when the fraction of the resistivity increment remaining at time t was plotted against reduced time $t/t_{1/2}$ for quenches ranging between 800^oC and 1000^oC followed by anneals at 40^oC. They noted that some deviations did appear especially at long times for quenches around 1000^oC, and these values were higher than the resistivity at infinite annealing times that were obtained for lower quench temperatures.

8.4.2.2.1.2 R. W. Siegel

Similarly, R. W. Siegel (see Figure 3 in [56]) presented the results involving nine specimens of varying purity [115] subjected to quenches from 900^oC and annealing at 40^oC using the fraction of the resistivity increment remaining at time t plotted against reduced time $t/t_{1/2}$ and also obtained a single universal S-shaped curve and concluded that this result implies that a unique process was responsible for the

---

[114] NOTE: The variable $t/t_{1/2}$ equates to the parameter $t_A/t_{1/2}$ employed throughout this document.

[115] The reported residual resistivity values of the nine specimens ranged from 0.385 to 1.925 x 10^{-9} ohm-cm. These values for $\Delta\rho_V(T)$ resistivity (see Table 10) correspond to elevated temperatures of approximately 500^oC and 650^oC, respectively, and may be indicative of MRR levels rather than true residual resistivity determinations.

observed annealing in all of these specimens. This universality was noted to occur even though the sets of resistivity annealing curves among the various specimens clearly exhibited dependencies upon specimen purity (see Figures 1 and 2 in [56]).

In contrast to the above, this research revealed no discernible indications of any effects of specimen purity -- such as might be inferred from the monitored LTA chronologies documented as generally gradual increases in $R(40^oC)/R_{LTA}(4.2^oK)$ ratios that were noted to occur during extensive sets of thermal treatments involving many specimens -- upon any of the numerous data analyses reported herein.

8.4.2.2.2 E^M_V(eff)-related Results

8.4.2.2.2.1 Yttherus, Siegel, and Balluffi

Yttherus, et al. [67] studied the effects of defect concentration, annealing temperature, and specimen purity upon values obtained for the effective migration energy E^M_V(eff) and reported, respectively, the following:

1) diminishing of E^M_V(eff) values as vacancy resistivity $\Delta\rho_V$ or vacancy concentration C_V values increase;

2) no detectable effect of annealing temperature upon E^M_V(eff) values;

3) no effect of specimen purity upon E^M_V(eff) values, and

4) their reporting of the influence of the degree of prequench annealing (see Figure 4 in Ref. 18) upon the annealing curves for specimens with considerably different resistance ratios, $R(24^oC)/R(4.2^oK)$, both quenched from 900^oC and annealed at 30^oC and 40^oC.

8.4.2.2.2.2 Kino and Koehler

Kino and Koehler (see Ref. [42]) also noted a diminishing of E^M_V(eff) values as vacancy resistivity $\Delta\rho_V$ or vacancy concentration C_V values increased.

8.4.2.2.2.3 Sahu, Jain, and Siegel

Sahu, Jain, and Siegel (see Ref. [101]) reported on the vacancy properties in gold that resulted from their detailed, multi-parameter analysis performed on experimental data that was available for self-diffusion, equilibrium vacancy concentrations and effective migration energies, obtained from direct observations of vacancy precipitation after quenching.

For a mono-, di-, tri-vacancy model that was used for the analysis of the E^M_V(eff) data to fit the combined data with the physical model required that the trivacancy must be more mobile that the divacancy (i.e., $E^M_{3V} < E^M_{2V}$ for all allowed parameter sets).

Using computer simulation of the quench and annealing, their results led to the conclusion that "… while the vacancy system was indeed not in exact local equilibrium during the post-quench annealing, it was nevertheless sufficiently close to local equilibrium that such an assumption was not an unreasonable one to facilitate the E^M_V(eff) fitting analysis."

Their check on the validity of this assumption led to an excellent agreement (see their Figure 12 in Ref. [101]) between calculated values of E^M_V(eff) with experimental results that had been reported by researchers Wang, et al. [63], De Jong and Koehler [24], Y&B [65], Siegel [56], B&L [11], MMK [230], K&M [39], and DHMA [222].

8.4.2.2.3 Computer Simulation of Point Defect Annealing Kinetics

It may prove instructive to compare the results presented in Figure 100 (see sub-section 8.3.3.3) with what Mehrer [236] obtained when he applied Monte Carlo simulation to random walks and annealing processes of point defects in cubic lattices. He chose the simulation method as a means to account for the geometric restrictions imposed on defect jumps in a lattice that cannot be incorporated in the interpretation of annealing kinetics of point defects in crystals either in terms of rate equations or in terms of diffusion equations with suitable boundaries.

Among his key findings were the following: 1) Annealing of monovacancies at an unfillable sink obey first-order kinetics, 2) annealing of mono- and divacancies will obey second-order kinetics when divacancies diffuse much faster than monovacancies, e.g. when the lifetime ratios are less than 0.01, divacancies compared to monovacancies and 3) when the kinetics are more complicated, such that the monovacancy contribution to the diffusion current is no longer negligible (due to higher monovacancy mobility), Mehrer's simulation [see Figure 5 on page 650] results in quadratic plus linear decay precipitation kinetics.

It may be that what is shown for specimens 3013, 4002, and 4005 in Figure 100 relates to Mehrer's simulation findings in the following ways: 1) The straight line segments that were obtained for the three (700, 600) Q&A series treatments agree with the second-order annealing kinetics simulation results, and 2) the changeovers from straight line segments to the more complex annealing curves associated with the (900/800, 500) Q&A series treatments may be indicative of quadratic (or even higher-order) plus linear decay precipitation kinetics.

8.4.2.3 Conclusions drawn from Analyses of Half-time Annealing Kinetics

In sharp contrast to the restricted span of data cited by these researchers, further insights can be made from examinations of Figures 147 through 152, each of which has been presented in preceding sub-sections. Some concluding points, however, are enumerated below.

1. Given that quench temperatures of 900, 800, and 700^{o}C and annealing temperatures of 700, 500, 400, 300 and 200^{o}C were employed, segmentation of plotted data into three ranges in reduced annealing time variable parameter allowed for specific insights to be garnered and presented here.
2. The observed annealing kinetics in the regions surrounding the respective annealing half-times, generally exhibited reasonable agreement among a diverse range of Q&A treatments involving numerous specimens and over a wide range in both quench and anneal temperatures.
3. Metastable residual resistance (MRR) levels were clearly established as being present for essentially all Q&A series treatments, and these MRR levels were noted to increase both for higher T_Q and higher T_A temperatures.
4. Figure 150 was the only plot of fraction remaining of NQIR vs. $t_A/t_{1/2}$ which suggested that an S-shaped curve might apply, namely for specimen 3013's (700, 300, t_A) Q&A treatment.

8.4.3 Extended Anneal Region Annealing Kinetics and Resulting MRR Levels

Plots presented in sub-sections 8.3.12 and 8.3.13 included indicators of MRR levels, and those results are further analyzed and discussed here because they form

the principal topic under extended anneal region annealing kinetics as indicated in the flowchart of Figure 8.

8.4.3.1 Observations and Quantitative Determinations from calculated MRR Levels

For each respective isothermal annealing temperature T_A, examinations of the plotted values of ΔR_{QAN} associated with nearly all of the elevated temperature Q&A series involving extended isothermal annealing times (see Figures 82, 84, 87 - 91, 93 - 95, 97- 99, 101, and 109 and Figures 180 through 191) revealed ΔR_{QAN} values that are significantly higher [116] than "No Loss" NQIR(T_A, $t_A \rightarrow \infty$).

The MRR levels indicated in Figures 178 through 183 were usually just a few percent. However, based on calculations that were made as indicated in Table 18 which lists the MRR levels and temperature values for specimens 3013, 3016, 4002, and 4005 for each of the indicated sets of Q&A series thermal treatments associated with the cited Figures, quantitative assessments of the listed sets of data revealed the fact that all of the MRR levels clearly corresponded to values associated with elevated temperatures that ranged between 430^{o}C and 575^{o}C with the associated values for the listed quantity MRR/[“No Loss” NQIR(T_A)] ranging from 1.9 to 23,600. These collective observations provide reasonable evidence for confirming that metastable residual resistance (MRR) levels are not only present, but the MRR levels

---

[116] Typically, the metastable residual resistance levels (see Table 18 for examples) proved to be several orders of magnitude larger than what would be indicated for “No Loss” NQIR(T_A, t_A --> ∞) for the respective isothermal annealing temperature equilibrium values calculated using data contained in Table 9.

are, in most instances, substantially above the reference level "No Loss" NQIR(T_A) data values for the associated isothermal annealing temperatures cited in Table 18.

Table 18. Metastable Residual Resistance (MRR) Tabulations

Specimen Number	Figure #	T_Q (^oC)	T_A (^oC)	NQIR (MRR Level)	"No Loss" NQIR(T_Q)	"No Loss" NQIR(T_A)	MRR ÷ "No Loss" NQIR(T_A)	Approximate NQIR(T) (^oC) [117]
3013	81	900	300	3.3×10^{-4}	1.4×10^{-2}	7×10^{-7}	471	570
		800	300	1.5×10^{-4}	5.7×10^{-3}	7×10^{-7}	214	525
		700	300	4.7×10^{-5}	1.9×10^{-3}	7×10^{-7}	67	465
	94	700	200	2.36×10^{-4}	1.9×10^{-3}	1×10^{-8}	23600	550
3016	85	900	400	3.21×10^{-4}	1.4×10^{-2}	1×10^{-5}	32	570
		700	400	9.2×10^{-5}	1.9×10^{-3}	1×10^{-5}	9.2	500
4002	96	900	500	3.2×10^{-4}	1.4×10^{-2}	9.2×10^{-5}	3.5	450
		800	500	2.5×10^{-4}	5.7×10^{-3}	9.2×10^{-5}	2.7	435
		700	500	2.1×10^{-4}	1.9×10^{-3}	9.2×10^{-5}	2.3	430
	86	900	400	2.1×10^{-4}	1.4×10^{-2}	1×10^{-5}	21	545
	87	900	300	2.0×10^{-4}	1.4×10^{-2}	7×10^{-7}	285	545
	90	800	300	8.5×10^{-5}	5.7×10^{-3}	7×10^{-7}	121	490
4005	96	900	500	3.5×10^{-4}	1.4×10^{-2}	9.2×10^{-5}	3.8	575
		800	500	1.94×10^{-4}	5.7×10^{-3}	9.2×10^{-5}	2.1	545
		700	500	1.78×10^{-4}	1.9×10^{-3}	9.2×10^{-5}	1.9	535
	95	900	200	1.36×10^{-4}	1.4×10^{-2}	1×10^{-8}	13600	520
		800	200	1.48×10^{-5}	5.7×10^{-3}	1×10^{-8}	1480	525
		700	200	4.8×10^{-5}	1.9×10^{-3}	1×10^{-8}	4800	470

[117] Refer to Table 9 in sub-section 7.4.7.1 for various temperatures from which these values were interpolated.

8.4.3.2 Conclusions Regarding MRR Levels

The findings presented herein regarding MRR levels associated with extended annealing times for elevated temperature Q&A series treatments empirically support many of the observations that have been reported by other researchers that resulted from their investigations involving precipitation, nucleation, clustering, and TEM determinations involving metals and alloys.

8.4.4 Initial Decay Region Q&A Annealing Kinetics

Data analyses of the initial decay region of Q&A series treatments involve detailed examinations of the plots that have been presented in sub-section 8.3.10.

8.4.4.1 Data Analyses of NQIR(600, T_A, Δt_A) Q&A Series Treatments

8.4.4.1.1 Specimen 3013

Figure 156 illustrates an Arrhenius plot of Mean Relaxation Times (t_{mean}) for an NQIR(600^{o}C,T_A, Δt_A) Q&A series treatment for specimen 3013, and Figure 160 includes the associated values for the instantaneous vacancy activation energy, E^M_V(act), for each of the six respective slopes between the indicated segments.

For specimen 3013, the labeled values for E^M_V(act) are as follows: 0.93, 0.64, 0.56, 0.91, 0.67, and 0.29 eV, and the average slope over the 275-to-20^{o}C range in T_A has a calculated value of 0.724 eV. Notably, the final segment between the 575-to-500^{o}C range in T_A is labeled N/A due to its negative slope.

8.4.4.1.2 Specimen 4002

Figure 157 illustrates an Arrhenius plot of Mean Relaxation Times (t_{mean}) for an NQIR(600^{o}C,T_A, Δt_A) Q&A series treatment for specimen 4002, and Figure 161

includes the associated values for the instantaneous vacancy activation energy, E^{M}_{V} (act), for each of the five respective slopes between the indicated segments.

For specimen 4002, the labeled values for E^{M}_{V}(act) are as follows: 0.66, 0.81, 0.52, 0.52, and 0.25 eV, and the average slope over the 405-to-20^{o}C range in T_A has a calculated value of 0.62 eV.

8.4.4.1.3 Specimen 4005

Figure 158 illustrates an Arrhenius plot of Mean Relaxation Times (t_{mean}) for an NQIR(600^{o}C,T_A, Δt_A) Q&A series treatment for specimen 4005 and Figure 162 includes the associated values for the instantaneous vacancy activation energy, E^{M}_{V}(act), which are as follows: 0.65, 1.09, 0.52, 0.50, and 0.34 eV, and the average slope over the 440-to-20^{o}C range in T_A has a calculated value of 0.62 eV.

8.4.4.2 Data Analyses of NQIR(700, T_A, Δt_A) Q&A Series Treatments

8.4.4.2.1 Specimen 3013

Figures 167 and 168 illustrate Arrhenius plots of mean relaxation times (t_{mean}) that provide a means for estimating instantaneous activation energy magnitudes when specimen 3013 has been subjected to (700, T_A = 600/500/300/200, Δt_A) and (700, T_A = 600/500/300/23, Δt_A) Q&A series treatments, respectively.

The slope of the dashed line [118] in Figure 167 for specimen 3013 reveals the overall activation energy, labeled as instantaneous vacancy activation energy,

[118] As NOTE 2 indicates, the single data point associated with Run #3193 involved use of nitrogen gas and a different final bath temperature. Its value illustrates that higher losses do occur when a slower initial quench rate is associated with a change in environmental conditions.

E^{M}_{V}(act), to be 0.318 eV for the isothermal annealing temperature range from 600^{o}C down to 200^{o}C.

Notably, this value turns out to be in reasonable agreement with the rate of nucleation value of 0.28 ± 0.03 eV measured and reported by Quader and Dodd [52] in their TEM study of the kinetics of vacancy clusters for zone-refined gold in which they established that secondary defects formed as a result of vacancy condensation included stacking fault tetrahedra, faulted Frank loops, and a few prismatic loops. They concluded that, in general, several precipitate types were observed to occur in zone-refined gold during the course of their investigation.

The slope of the extended line segment shown in Figure 168 for the isothermal annealing temperature range from 300^{o}C down to 23^{o}C reveals an instantaneous vacancy activation energy, E^{M}_{V}(act), equal to 0.738 eV which might be attributable either to vacancies or divacancies given the uncertainty associated with interpreting such limited data.

8.4.4.2.2 Specimen 4005

Figure 167 also illustrates for specimen 4005 an Arrhenius plot that provides a means for estimating an instantaneous activation energy magnitude for (700, T_A = 500/200, Δt_A) Q&A series treatments. The slope of the line for specimen 4005 in Figure 167 indicates an instantaneous vacancy activation energy, E^{M}_{V}(act), of 0.42 eV over the isothermal annealing temperature range from 500^{o}C down to 200^{o}C.

Notably, Chik [12] pointed out that for vacancy annealing at high vacancy concentrations, the value for $E^M_V(act)$[119] would equate to $E^M_{2V} - E^B_{2V}$ (the difference between divacancy migration and binding energies) based on analyses using a mono-divacancy model. So, a value of 0.42 eV for $E^M_V(act)$ in gold would be expected to fall somewhere within that range.

8.4.4.3 Data Analyses of NQIR(900/800/700, T_A, Δt_A) Q&A Series Treatments

8.4.4.3.1 Specimen 4002

Figures 169 and 171 illustrate the Arrhenius plots of Initial Annealing Rate (IAR) and Mean Relaxation Time (t_{mean}) for specimen 4002.

Segments (700, 500/300, Δt_A), (800, 500/300, Δt_A), and (900, 500/400, Δt_A) exhibit nearly identical slopes that fall within the range of 0.49±0.01 eV, which might equate to $E^M_{2V} - E^B_{2V}$ (the difference between divacancy migration and binding energies) based on analyses using a mono-divacancy model, and the slope for the (700, 400/300, Δt_A) segment is 0.70 eV which might be indicative of the instantaneous migration energy for divacancies for that particular instance.

Both the (900, 700, Δt_A) and (800, 600, Δt_A) segments exhibited N/A slopes, and these observations were cited in sub-section 8.3.10.6.3.1.

8.4.4.3.2 Specimen 4005

Figures 170 and 172 illustrate the Arrhenius plots of Initial Annealing Rate (IAR) and Mean Relaxation Time (t_{mean}) for specimen 4005.

---

[119] Note that Chik labeled this parameter $E^M_V(eff)$ rather than $E^M_V(act)$ as is used here.

For the (900/800, 500/300, Δt_A) segments the slopes of 0.62 and 0.69 eV are indicated, and for the (900, 200/20, Δt_A) segment a slope of 0.57 eV is indicated and might be indicative of the instantaneous migration energy for divacancies for that particular instance. For the (700, 500/200, Δt_A) segment a slope of 0.42 eV is indicated, which might equate to $E^M_{2V} - E^B_{2V}$ (the difference between divacancy migration and binding energies) based on analyses using a mono-divacancy model.

The (900, 700/500, Δt_A) and the (800, 600/500, Δt_A) segments exhibited N/A slopes, and these observations were cited in sub-section 8.3.10.6.3.2.

8.4.4.4 Observations of Crossovers in Q&A Series Annealing Kinetics

Occurrences of crossovers during annealing kinetics were commonly observed. Figures 81, 84, 95, 96, 97, 98, and 99 illustrate, respectively, seven specific examples of the occurrences of crossovers revealed in the NQIR(T_Q, T_A, t_A) annealing kinetics, namely during:

1) Q&A series treatments (900/800/700, 300) for specimen 3013;

2) Q&A series treatments (900, 400) and (700, 400) for specimen 3016;

3) Q&A series treatments (900/800/700, 500) for specimen 4005;

4) Q&A series treatments (900/800/700, 200) for specimen 4005;

5) Q&A series treatments (900/800/700, 500) for specimens 4002 and 4005;

6) Q&A series treatments (900/700, 400) for specimen 3016; and

7) Q&A series treatments (700, 200) for specimens 3012, 3013, and 4005.

Similar occurrences of such crossovers have been reported by other researchers for gold [see Figure 9 in Reference 8 and Figure 4 in Reference 84], other metals [copper: See Figure 2 on page 49 in Reference 18; aluminum: see

Figure 4 in Reference 110], alloys [Cu_3Au: see Figure 1 in Reference 99 and Figure 1 in Reference 220; Fe_3Al: see Figures 3 and 4 in Reference 113], and for internal friction measurements for gold [see Figure 1 in Reference 37] and for β brass [see Figure 2 in Reference 111].

More specifically, Kamel [37] performed internal friction measurements on gold strips quenched into cold water from four temperatures (800, 700, 600, and 500), then immediately brought to the experimental measuring position. Room temperature internal friction measurements followed immediately. The typical quenched-in internal friction decay curves (see Figure 1 in Reference [37]) in the initial annealing period exhibited similar crossovers for 800^{o}C, 700^{o}C, and 600^{o}C quenches, and the energy of formation of vacancies was found to be 0.96 eV.

8.4.4.5 Instantaneous Activation Energy Determinations

8.4.4.5.1 Results reported by Other Researchers

8.4.4.5.1.1 Chik et al. and Quader and Dodd

The parameter that has been labeled in sub-section 8.3.10 as instantaneous vacancy activation energy, $E^M_V(act)$, has been determined by other researchers [6, 11, 35, 37, 82, 92] from analyses of defect nucleation kinetics.

This parameter was also reported as the nucleation process activation energy for stacking fault tetrahedra (SFT) in gold by Chik [12-15] [120] and as the activation energy for nucleation of tetrahedra by Quader and Dodd [52] for gold, gold-cadmium, and gold-zinc alloys.

8.4.4.5.1.2 Burton and Lazarus

Also notable is the research of Burton and Lazarus [10, 11] that revealed two well-defined activation energies for quenched defects in gold. In their computer-generated data, one was defined as the instantaneous activation energy which is characteristic of the defect-annihilating step, and the second was defined as the apparent activation energy which was characteristic of the rate-limiting annealing step[121].

In their resistance measuring technique used to study the annealing of quenched gold Burton and Lazarus [10, 11] obtained an instantaneous activation energy of 0.52 ± 0.03 eV and identified it as the divacancy motion energy in gold. For their evaluation of what they referred to as the apparent activation energy determined by the rate-controlling annealing step, values were found to be between 0.70 and 0.95 eV.

Notable also were their reported determinations of activation energies obtained from slope-change data. Their analysis involved graphing of the time derivative

---

[120] NOTE: In Chik's references, the physical quantity $E^{M}_{1V} + E^{B}_{2V} - E^{M}_{2V}$ is equated to the independently determined value of 0.26 eV made from his electron microscope observations and which is pointed out to not be an effective migrating energy. Chik also cites comparable values for this same quantity ranging from 0.26 to 0.34 eV were obtained from data presented in Figure 9 of the work performed by Emrick [102] using isothermal recovery of quenched-in resistivity in gold after low-temperature (around 700^{o}C) quenches involving anneal temperatures between 61 and 90^{o}C.

[121] A similar conclusion for pure silver was described in the work of Doyama and Koehler [78].

$d\Delta R/dt$ that was obtained by differentiating and smoothing of the defect resistance ΔR divided by the sample resistance for a sample quenched from 975^oC and annealed at 37^oC until only 15% of the quenched-in defect resistance remained. At that time, the annealing temperature was changed from T_1 = 37^oC to T_2 = 40^oC, and the annealing curve $\Delta R(t)$ at T_2 was smoothed and differentiated to obtain $d\Delta R/dt(T_2, t_0)$ at the time of the temperature change by extrapolating $d\Delta R/dt$ backwards from large times.

Results for a slope-change run wherein the annealing temperature was changed from T_1 = 37^oC to T_2 = 40^oC (see Figures 10(a) and 10(b) in [Ref. 11]) revealed [in Figure 10(b)] a sharply reduced and nearly flat slope for annealing times below 15 minutes.

8.4.4.5.2 Current Investigation Results for E^M_V(act)

By comparison, results from the current research investigation revealed similar magnitudes for E^M_V(act) were found that were dependent upon the associated quench temperatures and ranged in values, e.g., 0.246, 0.318, 0.397, 0.42, 0.48, 0.49, 0.50, and 0.62 eV in several instances (see specimen 3013's Figure 168) involving annealing temperature ranges between 300^oC and 600^oC and a value of 0.738 eV (see specimen 3013's Figure 167) for the extended annealing temperature range between 23^oC and 300^oC. Somewhat similar results were obtained for specimens 4002 and 4005 for annealing temperatures up to 500^oC (see Figures 169 through 172).

Quite possibly, the occurrence of an abrupt and nearly flat slope for shorter annealing times as reported in the Burton and Lazarus reference [11] might

correspond to the observations of decreasing and even negative slopes that were observed to occur during this research investigation.

The same argument presented in sub-section 8.3.9.1 for half-time segments exhibiting negative slope instances would seem appropriate to suggest here, namely, when vacancy supersaturation conditions result in vacancy defect chemical potentials that are diminished to a point whereby reduced associated absolute vacancy sink efficiencies take effect and result in increased values for the mean relaxation times.

8.4.5 Additional Observations and Findings made from TEV Plots

Data analyses of the overall behavior of Q&A series treatments involved detailed examinations of TEV plots that have been presented in sub-section 8.3.11.

8.4.5.1 Overall Behaviors revealed by TEV Plots

Examinations of Figures 174 through 191 reveal the nature of the variations in time exponent **m** when collectively plotted to include annealing times whose durations ranged anywhere from a few tenths of a second to hundreds of hours for multiple specimens each involving various combinations of quench and isothermal annealing temperatures.

The dynamic behavior of the values determined for the time exponent **m** was found to range from values as high as two at the onset of isothermal annealing followed by gradual reductions that tend to approach zero-slope values. The MRR levels associated with the zero-slope values for **m** ranged in magnitude from a few percent of the equilibrium value associated with the annealing temperature T_A to

several orders of magnitude larger than that, depending upon the specific Q&A series treatment and specimen [122].

8.4.5.2 Impact of Direct Deformation Treatments on TEV Plots

Examination of Figure 185 with its three sets of plots of NQIR(700, 200, t_A) during Q&A series treatments involving specimens 3012 and 3013 reveals several points in particular that are worth noting, namely:

1) When visually compared with that for specimen 3013, substantially higher losses of excess vacancies are easily noted by the fraction remaining magnitudes shown in such TEV plots and this result is, of course, attributable to the fact that the NQIR(700, 200, t_A) Q&A series treatment was performed on the post-direct deformation specimen 3012.

2) Except for the initial portions of annealing, the respective plots for the three specimens do appear to exhibit nearly parallel time exponent slopes of 2/3 over much of the annealing time ranges. This strongly supports dislocations as being dominant sinks for excess vacancies following the initial annealing (under one second).

3) That specimen 3012 exhibits an initial time exponent slope of two could be interpreted as an indication of second-order annealing kinetics as occurring for annealing times less than one second, and such slopes may be indicative of di-vacancies and tri-vacancies being active contributors during the earliest stages of annealing for whatever particular Q&A series treatments exhibit slope values close or equal to 2.

---

[122] See Table 18 in sub-section 8.4.3.1 for some specific examples.

4) Examinations of Figures 174 through 191 also reveal the nature of the variations in time exponent **m** when collectively plotted to include annealing times whose durations ranged anywhere from a few tenths of a second to hundreds of hours for multiple specimens each involving various combinations of quench and isothermal annealing temperatures.

5) The leveling off of fraction remaining values can be taken as an indication as to what magnitudes of MRR levels are associated with each specific Q&A thermal treatment for a given specimen. See sub-section 8.3.12 for further details regarding this topic.

8.4.5.3 Time Exponent Behavior Findings

Figures 174 through 191 illustrate another graphical technique for ascertaining the best time-dependent relationship for fractional annealing as well as to indicate order of annealing assessments.

Such plots of Time Exponent (m) Variations illustrate sets of collective Q&A data obtained for several specimens with differing sink densities subjected to numerous quench-and-anneal temperature combinations. These types of plots reveal for all such data several common behaviors, particularly regarding slopes and metastable residual resistance levels that might not otherwise prove to be so readily discernable.

The time exponent plots of Figures 174 through 191 also illustrate the influence of temperature of quench upon the respective MRR values associated with extended isothermal annealing times.

The time exponent plot of Figure 184 clearly reveals 1) the significant differences between specimen 3013 and that for post-direct deformation specimen

3012 in "loss" values for fraction remaining for NQIR(700, 200) Q&A Series treatment as a function of annealing times, and 2) the associated slopes appearing to be nearly the same for much of the range in annealing times.

8.4.5.4 Time Exponent Behaviors Reported by Other Researchers

8.4.5.4.1 Ikeuchi, et al.

Similar results were reported in the work of Ikeuchi, et al. [139-141], namely:

1) Dependencies upon dislocation sink density and associated values for the exponent **m** were found not to be constant but varied with dislocation density. For specimens which had been subjected to strains ≥ 5.5%, m was expressed as:

$$m = 0.5 + a \exp(-b \Delta\rho_d) \qquad \text{Eqn. (8-2)}$$

where constants a and b are 0.12 and 0.57 x 10^{11} $(\text{ohm m})^{-1}$, respectively, and $\Delta\rho_d$ is the resistivity increment due to dislocations introduced by the deformation;

2) In specimens having low dislocation density (tensile strain ≤ 3%) the whole annealing process is described by a single (constant) exponent **m** (see Figure 5 in Ref. [139]). However, in specimens of high dislocation density (tensile strain ≥ 5.5%), the early stage of annealing is expressed by an exponent **m'** which is larger than **m** (see Figures 6 and 7 in Ref. [139]), whereas the substantial part of the annealing process is described by exponent **m** given by equation (8-4); and

3) Regardless of the amount of strain (see Figure 9 in Reference [139]), the effective activation energy for the annealing process was 0.70 ±. 0.02 eV.

These researchers concluded that results 1) and 2) are incompatible with Harper's analysis (see Ref. [186] for an example) that the value of exponent **m** is

uniquely defined by the form of the vacancy-dislocation interaction potential, They cited several factors that might account for the experimental results, among which were (a) vacancy flow due to the concentration gradient, (b) vacancy flow due to the vacancy-dislocation interaction force, and (c) the sink efficiency of dislocations.

Ikeuchi, et al. performed a computer simulation in which they state the following: “The simulation of the annihilation of vacancies to dislocations in a simple cubic lattice under the elastic interaction is made by means of a Monte Carlo simulation with particular reference to the dislocation density and the sink efficiency. The sink efficiency is taken into account by assuming that a vacancy at a nearest neighbor site of a dislocation must overcome an additional energy barrier ΔE for the annihilation. Three types of the sink efficiency are assumed: (a) the perfect sink where ΔE = 0; (b) the limited (fixed) sink efficiency in which ΔE is unchanged during the annealing; and (c) the variable sink efficiency in which ΔE is an increasing function of the number of vacancies N_a.”

What Ikeuchi, et al. determined (see Figure 2 in reference [139] for the three relevant diagrams (a), (b), and (c) and associated formulas) was that the simulation showed that the experimental results can qualitatively be explained only by the model with the variable sink efficiency, but not with either the perfect sink or the fixed sink efficiency. References [140] and [141] include additional plots of experimental results as well as a detailed flowchart for the computer simulation.

8.4.5.4.2 Kamel

Based on the assumption that the disappearance of vacancies is mainly responsible for the observed decay in the quenched-in internal friction, Kamel [37] calculated vacancy precipitation curves for different quenches using the formula:

$$f(t) = 1 - \exp[-(t/\tau)^n]$$

where f(t) is the fraction of vacancies precipitated after time t.

Precipitation curves of vacancies after different quenches (see Figure 2 in Reference [37]) exhibited the following slope values[123] for five quenching temperatures, namely: n=2.3 and n=0.61 for T_Q = 800^{o}C; n=1.6 and n=0.53 for T_Q = 700^{o}C; n=1.1 for both T_Q = 600^{o}C and for T_Q = 500^{o}C; and n=1.14 for T_Q = 400^{o}C.

Kamel goes on to state the following: "For quenches from temperatures higher than 700^{o}C, the precipitation curves show two distinct stages, indicating two different modes of vacancy precipitation. The high decay rate characterizing the first stage may be attributed to the high concentration of vacancies which generate their own dislocation sinks, namely the Frank sessile rings, by the collapse of vacancy clusters condensed on the (111) planes. In the second stage the slopes of the precipitation lines yielded a value of about 0.6 which is less than that obtained in the case of low-temperature quenching. This observed difference in the behaviour of the vacancy precipitation process in the two cases may be attributed to the fact that at the end of the first stage (where T_A > 700^{o}C) the crystal becomes enriched with stacking faults

[123] Slopes were calculated using the formula $f(t) = 1 - \exp[-(t/\tau)^n]$ and confirmed by plotting the rate of decay of internal friction, dQ^{-1}/dt, vs. annealing time t which resulted in a linear relationship.

which possibly interact with the remaining vacancies to cause the observed delay in decay rate."

8.4.5.4.3 Folweiler and Brotzen

Folweiler and Brotzen [164] investigated the effect of quenched-in vacancies on the elastic modulus of aluminum and observed that the time relation of vacancy concentration was analogous to that determined by electrical resistivity measurements. One of their plots (labeled as Figure 5 in their publication) exhibits a time exponent behavior value that starts out initially with a slope during the first 0.7 seconds of perhaps as high as 1 that becomes a least-squares fit value of 0.51 throughout the subsequent three seconds of annealing times.

Such an occurrence in the dynamic behavior in the time exponent **m** is in agreement with higher slopes for the shortest annealing times that are illustrated in many of the TEV plots presented in this research investigation.

8.4.5.5 Discussions of Obtained Time Exponent Behaviors

Presented in this section are some possible explanations that might be able to account for the magnitudes of the slopes indicated in various sets of TEV plots.

8.4.5.5.1 Characterizations of Precipitation Modes based on Slope Magnitudes

Kamel [37] related that according to the theory of Ham [187] on diffusion-limited precipitation from supersaturated solid solutions, the slope of the precipitation curve was found to be unity only when the majority of sinks were in the form of long thin cylinders. In Kamel's Figure 2, straight line segments of slopes of magnitudes 1.11, 1.11, and 1.14 were obtained for quenches from 600^{o}C, 500^{o}C, and 400^{o}C, respectively, that he states, "By analogy, it might be envisaged here that stray

dislocation lines originally present in the gold matrix form the predominating sinks for vacancies in the case of quenches from below 700^{o}C."

In this research investigation, segmented slopes associated with TEV plots generally ranged from a high of 2 followed by typical subsequent slopes of 1, 2/3, 1/2, and eventually zero (indicative of when MRR levels were asymptotically reached). Each of these slopes could possibly be associated with one or more particular modes of precipitation as was outlined in Kamel's publication [37]. However, an alternative approach that might also be considered is presented next.

8.4.5.5.2 Hypothesis for an Empirical Dynamic Slope Parameter

A hypothesis is proposed here that the dynamic behaviors of the time exponent **m** as a function of annealing time that are revealed in each of the TEV plots established during this research investigation might be accounted for by defining an empirical dynamic slope parameter **m(obs)** Ξ **m** * [**€** (**μ**$_{v}$)] wherein the graphically estimated slope values gradually diminish in part because the associated magnitudes for the absolute macroscopic sink efficiency **€** undergo transitions from initial values that may be at or near unity and eventually approach zero as the remaining excess vacancy defect concentration becomes sufficiently reduced to the point where the associated vacancy defect chemical potential (**μ**$_{v}$) approaches zero [124].

Accordingly, the gradual reductions observed to occur in magnitudes for the dynamic time exponent **m(obs)** would thereby be accounted for over the entire range

[124] Figure 164 in sub-section 8.3.10.1.12 is one such illustration of the nearly step function nature for such a dependency that was revealed when vacancy supersaturation ratios (and hence excess vacancy defect chemical potentials) diminish toward zero during Q&A series treatments.

in isothermal annealing times for the Q&A series treatments, including those instances for which **m(obs)** diminishes from values as high as two down to zero.

Such a hypothesis would align with the conclusion (cited in the last paragraph of sub-section 8.4.5.4.1 above) of Ikeuchi, et al. [Reference 139] determined from their simulation that the experimental results can qualitatively be explained only by a model with variable sink efficiency.

8.4.5.6 Conclusions from Analyses of TEV Plots of Annealing Kinetics

1. Time Exponent Variation (TEV) plots provide convenient graphical representations of the overall annealing kinetics associated with Q&A series thermal treatments involving wide ranges in elevated quench-and-isothermal-anneal temperatures and isothermal annealing times.
2. TEV plots illustrate the dynamic behavior of the time exponent **m** which serves as an indicator of the nature of the overall precipitation kinetics for excess vacancies.
3. Dynamic values for time exponents are obtained directly from the slopes associated with each TEV plot.
4. In general, the values found to represent the time exponent **m** for extended anneal times approach zero, may initially be as high as 2 (depending on the Q&A series treatment) for very short annealing times, and for intermediate ranges in annealing times generally exhibit slope values of 1, 2/3, or 1/2 over major portions of each respective TEV plot.

5. For specimens subjected to identical Q&A series treatments the respective time exponent behaviors, losses, and MRR levels can be discerned by direct visual comparisons of the associated TEV plots.
6. A wide variability in time exponent behaviors may be discerned when several Q&A series thermal treatments involving a single quench temperature and a wide range in isothermal annealing temperatures are performed on a given specimen. See Figure 179 for one such example.
7. Understandably, for whatever specimens that have high straight downquench losses associated with elevated quench temperatures, TEV plots will exhibit curves having slopes that are close or equal to zero and will not contribute much in the way of information regarding the associated annealing kinetics for Q&A series treatments that involve values of T_Q where such high losses occur.
8. Slope-related information that may not be discernible from the respective Arrhenius plots (e.g., see Figures 127 and 128) is easily noted in the associated TEV plots (e.g., see Figures 184 and 185).

8.4.6 Highlights from Various Sets of Graphical Plots

Discussions based on examinations of each of eight categories of plots are presented in this sub-section.

8.4.6.1 NQIR(T_Q, T_A, t_A) Annealing Kinetics

Figures 80 through 103 illustrate plots made from the obtained ΔR_{QAN} [a shorthand notation for NQIR(T_Q, T_A, t_A)] data for various combinations of quench temperature T_Q and annealing temperature T_A. The independent variable is time t_A

indicating the duration of the isothermal anneals for the particular data points shown. When included, the value of ΔR_{QAN} (T_Q, T_A, t_A=0) represents the magnitude of ΔR_{QN} obtained for a straight downquench from temperature T_Q for the same sets of quench environment conditions.

The effects of using differing quench temperatures but the same annealing temperature are shown in Figures 95 through 97, and Figures 100 through 103 reveals similar NQIR(T_Q, T_A, t_A) behaviors for specimens 4002 and 4005 associated with (900/800/700, 500) Q&A Series treatments.

8.4.6.2 Fraction Remaining NQIR(T_Q, T_A, t_A) Plots

Figures 98, 99, and 104 through 114 permit ready comparison of retained fraction ΔR_{QAN} / ΔR_{QN} or excess fraction remaining f_r which in TEV plots is plotted as the function $\ln(\mathbf{f_r}^{-1})$.

Figure 105 illustrates for specimens 3013 and 4002 the influence of differing sink densities upon ΔR_{QAN} magnitudes and upon annealing kinetics for 800-to-300 Q&A series treatments for annealing times approaching 70,000 seconds.

8.4.6.3 Annealing Half-times and E^M_V(eff) Determinations

Plots were made from various NQIR(T_Q, T_A, t_A) Q&A series treatments to establish annealing half-times. Figures 115 through 130 illustrate specific instances that led to quantitative annealing half-time values established from these data sets.

Determinations of effective vacancy migration energies were made from the 13 sets of Arrhenius plots of half-times (as collectively shown in Figure 131). The various effective vacancy migration energy values are indicated in Figures 132 through 135 and are collectively indicated in Figure 136.

8.4.6.4 Initial Annealing Rates and E^{M}_{V}(act) Determinations

Determinations from Arrhenius plots of initial annealing rates (IARs) of instantaneous vacancy activation energy, E^{M}_{V}(act), values were made and are indicated in Figures 160 through 162 for NQIR(600, T_A, Δt_A) Q&A series treatments, Figures 165 and 166 for NQIR(700, T_A, Δt_A) Q&A series treatments, and in Figures 169 and170 for NQIR(900/800, T_A, Δt_A) Q&A series treatments.

8.4.6.5 Normalized Initial Annealing Rates and E^{M}_{V}(act) Determinations

Normalized initial annealing rates (NIARs) are presented in Figures 154 and 155 and were used to assess the instantaneous vacancy activation energy, E^{M}_{V}(act), values associated with the initial decay portions of each respective specimen and quench-and-isothermal anneal history.

8.4.6.6 Mean Relaxation Times (t_{mean}) and E^{M}_{V}(act) Determinations

Instantaneous vacancy activation energy, E^{M}_{V}(act), determinations made from Arrhenius plots of mean relaxation times (see Figures 156 through 159) are indicated in Figures 160-162, 165 through168, and Figures 171 and 172.

Figure 171 shows mean relaxation times determined for specimen 4002 upon subjection to three Q&A series treatments, namely: (T_Q=900: T_A= 700, 500, 400, and 300), (T_Q=800: T_A= 600, 500, 300), and (T_Q=700: T_A= 600, 500, 300).

Examination of the respective slopes of each curve in Figure 171 when T_A is below 500^{o}C suggests values for instantaneous vacancy activation energy, E^{M}_{V}(act), that are virtually identical (0.48 and 0.49 eV) for the region between 500^{o}C and 400^{o}C for the (900, T_A) and (800, T_A) plots.

However, the respective slopes decrease as the associated isothermal annealing temperature approaches the initial quench temperature T_Q becoming negative when $T_A \geq 500^oC$ is associated with $T_Q \geq 800^oC$.

Figure 172 shows mean relaxation times determined for specimen 4005 upon subjection to three Q&A series treatments, namely: (T_Q=900: T_A= 700, 500, 200, and 20), (T_Q=800: T_A= 500, 200), and (T_Q=700: T_A=500, 200).

Examination of the respective slope of the (900, 700/500) segment in Figure 172 when T_A is above 500^oC suggests a negative value for instantaneous vacancy activation energy, E^M_V(act), which demands further discussion.

For comparison purposes, data for specimen 3013 when subjected to a (600, T_A) Q&A series treatment are revealed in Figure 154. In this graphical representation, a gradual reduction in the value for the effective vacancy migration energy occurs for $180^oC \leq T_A \leq 500^oC$ [125] and exhibits a reversal in slope when $500^oC \leq T_A \leq 575^oC$.

8.4.6.7 Vacancy Defect Chemical Potential Determinations

Moreover, through use of the concept of vacancy defect chemical potential as a key factor in influencing the instantaneous vacancy activation energy (see Figure 163 for a specific example), occurrences of reversal-of-slope in Arrhenius plots may be accounted for in a rather straightforward manner.

Figure 163 shows for specimen 3013 the manner in which a vacancy defect chemical potential value of 0.1 eV is associated with the instantaneous vacancy

[125] This occurs when the associated vacancy defect chemical potential values of $\boldsymbol{\mu}_V$ fall below 0.15 eV (see Figure 163 in sub-section 8.3.10.1.11).

activation energy corresponding to the zero slope point in the Arrhenius plots of Figures 153, 154, 155, 156, 159, and 160 (presented in sub-section 8.3.10.1.8).

Associated values for vacancy defect chemical potential can be expressed as

$$\mu_v(T_Q, T_A, t_A) = kT_A \ln[1 + VSR(T_Q, T_A, t_A)] \quad \text{Eqn. (8-3)}$$

Based on the assumption of a straightforward conversion factor between vacancy concentration and NQIR values, the vacancy defect chemical potential $\mu_v(T_Q, T_A, t_A)$ associated with a Q&A series treatment for a quench from temperature T_Q to an isothermal temperature T_A and for annealing time t_A using NQIR data leads to the slightly modified[126] equation

$$\mu_v(T_Q, T_A, \Delta t_A) =$$

$$kT_A \ln \{ 1 + [NQIR(T_Q,T_A, \Delta t_A) - ["No\ Loss"\ NQIR(T_A)]] / [NQIR(T_A, t_A \rightarrow \infty)] \}$$

Eqn. (8-4)

where the phrase "No Loss" infers the equilibrium value that would be reached for the annealing temperature T_A.

In this manner Eqn. (8-4) provides a direct means for using the respective NQIR data sets to establish and assess vacancy defect chemical potential characteristics and parametric dependencies for any given Q&A series treatment. Examples are provided in Figures 139 through 142.

8.4.6.8 Metastable Residual Resistance (MRR) Determinations

Figures 103 through 107 and Figures 180 through 191 are among the numerous examples of Q&A series treatments that include data involving extended isothermal annealing times. Each of these Figures provides strong evidence for the presence of metastable residual resistance levels (wherein the respective $NQIR(T_Q, T_A, t_A)$ values

[126] This re-definition for VSR is made necessary based on analyses of results obtained for Q&A series treatments that revealed significant MRR levels do remain even after long annealing times. As a consequence, the value for $NQIR(T_A, t_A \rightarrow \infty)$ proves to remain larger than what would occur in the ideal situation of complete annealing, namely values equal to "No Loss" $NQIR(T_A)$. See Table 18 in sub-section 8.4.3.1 for examples of such calculations.

remain noticeably above the anticipated respective "No Loss" equilibrium NQIR(T_A) values. Sub-section 8.3.4 provided further discussion of MRR levels and led to conducting supplementary TEM experiments (detailed in Chapter 10) to further explore the possible source(s) for MRR levels.

8.4.7 Need for TEM-based Investigations

The desire to find out more about what might account for the occurrence of these metastable residual resistance levels led to the decision to perform supplementary Transmission Electron Microscopy studies (detailed in Chapter 10) using one-half mil 6N (99.9999 weight percent) pure gold ribbon foils some of which would be subjected to similar extended time Q&A treatments and additional foils subjected to LTA treatments for the purpose of serving as control specimens that would allow for critical comparisons among the two sets of results so obtained.

8.4.8 Conclusions from Data Analyses of Q&A Series Treatments

The principal conclusions listed below are drawn from the results and analyses of various sets of graphical plots involving Q&A series treatments.

1. Both effective vacancy migration energy values and instantaneous vacancy activation energy values were found to diminish when increasing quench temperatures are associated with Arrhenius plots of isothermal annealing kinetics.
2. Quantitative assessments either of effective vacancy migration energy values or instantaneous vacancy activation energy values cannot be made when negative slope conditions are found to be associated with segments of Arrhenius plots of annealing kinetics for NQIR(T_Q, T_A, t_A) and NQIR(T_Q,T_A,

Δt_A) Q&A series treatments. For this reason, all negative slope segments have been labeled N/A to indicate such non-applicability situations.

3. Vacancy clustering at elevated temperatures is noted to occur even after extended annealing times as evidenced by the manifestation of metastable residual resistance levels (typically equivalent to straight downquenches from 500^{o}C or higher).
4. TEV plots of precipitation annealing kinetics exhibited time exponent behavior values that ranged from as high as two and gradually diminishing toward zero. Generally, time exponent values of 1, 2/3, and 1/2 were most often exhibited over significant ranges in annealing kinetics for nearly all Q&A series treatments.

9 SUPPLEMENTARY THERMAL-MECHANICAL TREATMENTS

9.1 INTRODUCTION

This chapter presents the results and analyses of thermal-mechanical treatments that involved performing direct deformation (DD) within a specimen's gauge length followed either by thermal treatments, such as ST DQ and Q&A, or Thermal Cycling (TC) and/or High Temperature Annealing (HTA) extended thermal treatments which are defined in subsequent sub-sections of this chapter. Figure 9 provides a flowchart of LTA, TC, HTA, and DD treatments and analyses.

All of these additional treatments were conducted with the objective of gaining additional insights into lattice defect properties in high-purity gold, and detailed descriptions of and conceptual justifications for HTA and TC extended thermal treatments are covered in various sub-sections of this chapter.

9.2 DIRECT DEFORMATION AND COLD-WORKING

A number of investigators have employed electron microscopy [13-15, 57] methods to reveal various dislocation structures in metals. Subsequent annealing may result in formation of tangled dislocation networks or subgrain boundaries which are often found to be thermally stable following extended annealing.

Application of substantial additional cold-working of a thermally stable deformation structure may result in the formation of a stable polygonized structure [93, 152, 153].

Given that annealing encourages polygonization, further annealing would tend to encourage subgrain boundary formation which may result in a reduction in the average dislocation density.

9.3 THERMAL-MECHANICAL (DD + HTA/TC) TREATMENTS

When some degree of mechanical deformation is performed on a previously in-situ-only-history specimen and any extended thermal treatment is performed, this combination is referred to as a thermal-mechanical treatment.

Thermal-mechanical treatments involved Direct Deformation (DD) actions on specific specimens followed by one or more types of thermal treatments (ST DQ, Q&A, TC, or HTA). In all cases, the objective sought was to ascertain what would be the effects (if any) of each treatment upon NQIR(ST DQ and/or Q&A) losses and the associated annealing kinetics for each specimen.

9.3.1 Direct Deformation (DD) Treatments

Throughout this research investigation, the influence of mechanical deformation (that is, direct deformation within a specimen's gauge length) was examined for ST DQ, Q&A, prolonged HTA, and TC thermal treatments.

9.3.1.1 Objectives of DD Treatments

Insights as to the nature of the induced sink structure, its stability relative to degree of deformation [127], and some means for obtaining an estimate for the associated sink structure recovery activation energy were sought.

[127] Throughout prior sections of this document where ST DQ and Q&A series treatments have been presented, relevant comments as to observations, results, and conclusions about the impact on specimens subjected to mild, moderate, or severe direct deformation have been made.

9.3.1.2 Direct Deformation Procedure

After completion of many ST DQ thermal treatments performed on an in-situ-only-history specimen 3012, an intentional direct deformation (DD) within that specimen's gauge length was performed. The change in specimen resistance due to the direct deformation was measured, and a calculation of the induced sink density was established. These actions were followed by a repetition of the several ST DQ thermal treatments, and two more direct deformations that followed with the same sequence of actions as just stated for the initial direct deformation procedure.

9.3.1.3 Influence of Direct Deformation upon NQIR(ST DQ) Values

An investigation was conducted to attempt to discern what the influence of "mild or moderate[128]" and "severe[129]" direct deformations within a specimen's gauge length might have upon QIR(T_Q)/R40 values for ST DQ series treatments compared with prior (pre-deformation) values. Figure 197 indicates the influence of direct deformation for specimen 3012 for both in situ and direct deformation cases. Examination of the resulting sets of data revealed several significant observations.

---

128 Specimen 3012 was used for this investigation. For ST DQs from 800^{o}C, the associated losses were 3% for pre-deformation, 60% for an initial "mild" deformation, and 97% for the second "moderate" deformation within its gauge length.

129 "Severe" direct deformation is defined here as cold-working (flexing as much as 11 times) the specimen's gauge length region prior to initiating the sintering of potential leads operation of the specimen which thereby defines the specimen's actual gauge length for all subsequent in situ thermal treatments.

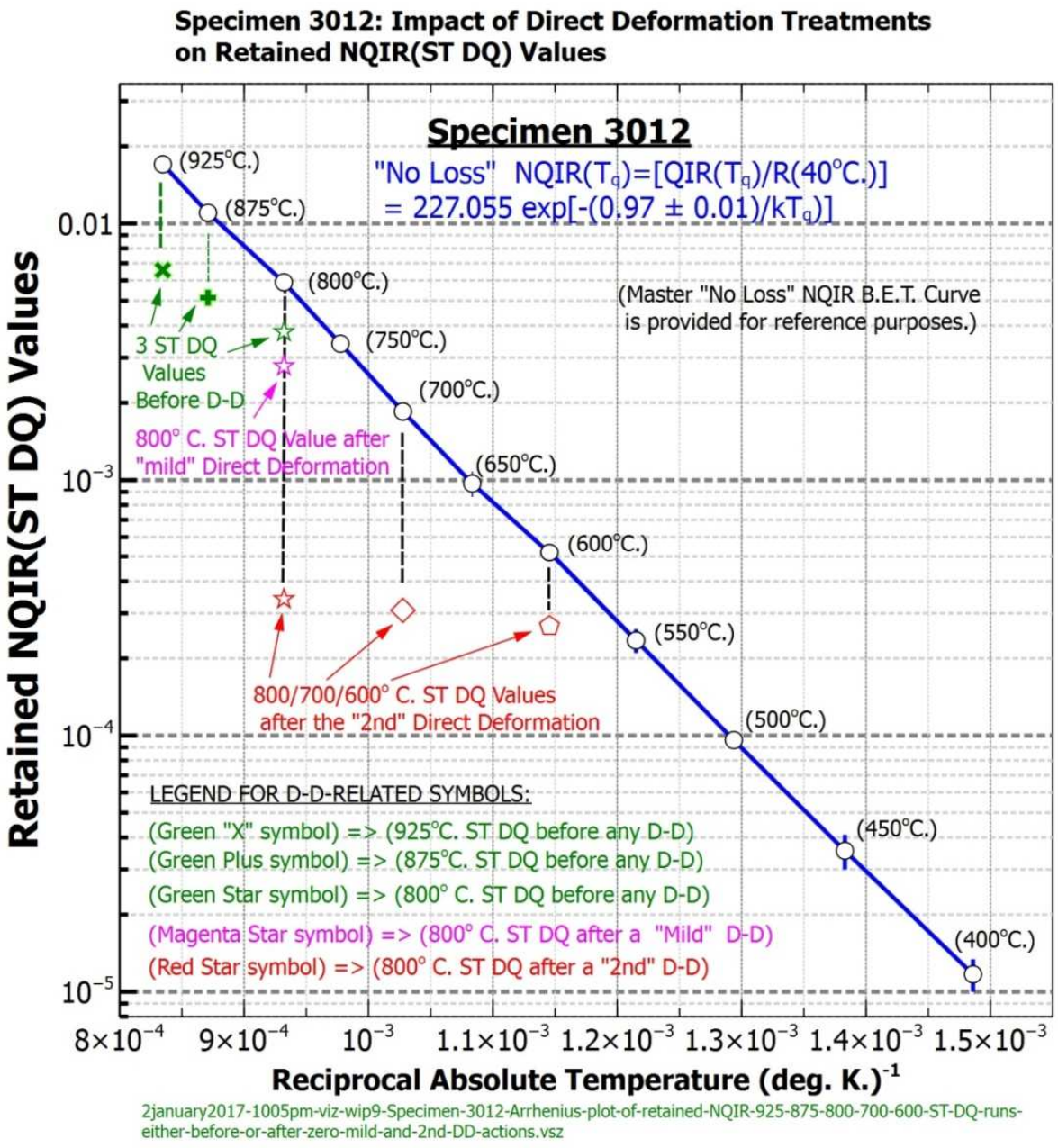

Figure 197. Specimen 3012: Influence of Direct Deformation on Resulting NQIR(T_Q) Values

1. Data associated with three in situ (pre-direct deformation) ST DQ treatments from 925^{o}C, 875^{o}C, and 800^{o}C are included as initial reference points.
2. Following a "mild" direct deformation -- uniformly changing the radius of curvature within the gauge length -- resulted in a modest reduction in QIR(T_Q)/R40 values for a subsequently performed ST DQ treatment from 800^{o}C.
3. Data points associated with a second moderate" direct deformation for ST DQ treatments from 800^{o}C, 700^{o}C, and 600^{o}C are also included.

9.3.1.4 Estimates of Dislocation Sink Densities induced by Direct Deformations

Using a conversion formula $\Delta N_D = \Delta\rho / (2.6 \times 10^{-19})$, where a dislocation scattering resistivity value of 2.6 x 10^{-19} ohm-cm^3 (see page 426 in reference [234]) is chosen, conversions of the associated changes in measured resistivity for the initial "mild" and the second "moderate" direct deformations yielded estimated values of 3.1 x 10^8 and 1.53 x 10^9 cm^{-2} for the induced dislocation sink densities that are associated with the respective ST DQ data points shown in Figure 197.

9.3.2 Post-direct deformation Thermal Treatments and Objectives

Two specific thermal treatments (labeled HTA and TC) were implemented in order to investigate 1) what, if any, changes might be discerned in specimen quenched-in and residual resistance values following execution of these treatments, and 2) to attempt to obtain possible insights into the nature of the induced sink structure(s), such as dislocations, or precipitates, such as vacancy clusters.

9.3.2.1 Definition and Objectives of HTA Treatments

An HTA treatment is defined here as a prolonged isothermal anneal at a temperature near 950^{o}C for a number of hours for any given specimen.

The purpose of an HTA treatment was to encourage grain growth [77] within the specimen and to provide a method for encouraging sink density reduction, particularly for those specimens subjected intentionally to either severe cold-working or some form of direct deformation during their respective lifetimes.

In addition, HTA thermal treatments were incorporated into this research in an attempt to discern any long-term effects of ST DQ and Q&A treatments upon specimen sink structures and densities.

In essence, the idea behind an HTA thermal treatment on a given specimen was to attempt to obtain some indication as to the nature of its pre-existing sink structures. This might be discerned, for example, by analyses of recovery of quenched-in resistance associated with straight downquenches performed prior to and following an HTA treatment from a chosen quench temperature of 800^{o}C as a function of hours of annealing at 950^{o}C between such ST DQ treatments with their attendant QIR determinations made at liquid helium temperatures. In concept at least, it might prove possible to estimate the activation energy for sink structure recovery using analyses for the effective migration energy of vacancies at elevated temperatures as a reference value.

9.3.2.2 Influence of HTA Treatments upon NQIR Values after performing Direct Deformation Treatments on a Specimen

An investigation was conducted to attempt to discern what the influence upon the induced sink structure(s) recovery upon subjection to HTA treatments from examinations of the resulting sets of data (see Figures 198 and 199) revealed several a number of noteworthy observations.

1. For specimen 3012 which had initially been subjected to a "mild" deformation, about four hours annealing at 950^{o}C was noted as being required to restore the original QIR(T_Q)/R40 value (see Figure 198).

2. For specimen 3011 which had initially been subjected to "severe" deformation, little to no noticeable recovery was noted to occur even after tens of hours of High Temperature Annealing (HTA) annealing (see Figure 198).

9.3.2.2.1 Results of HTA Treatments

In this sub-section the effects of prolonged high-temperature annealing on both quenched-in and residual resistances of several specimens are examined.

HTA treatments of several specimens were performed to ascertain whether or not specimen sink density could be reduced in either specimens maintained in situ or after being subjected to direct deformation after extensive sets of in situ straight downquench and quench-and-isothermal anneal treatments.

Abrupt increases in a specimen's R_{LTA} residual resistance values (obtained by performing an LTA treatment) after potentiometric measurements of QIR_{TOTAL} were made immediately following an HTA treatment. Such dramatic increases were in

sharp contrast to the gradual increases noted in all specimens subjected to ST DQ and Q&A series treatments throughout their respective lifetimes.

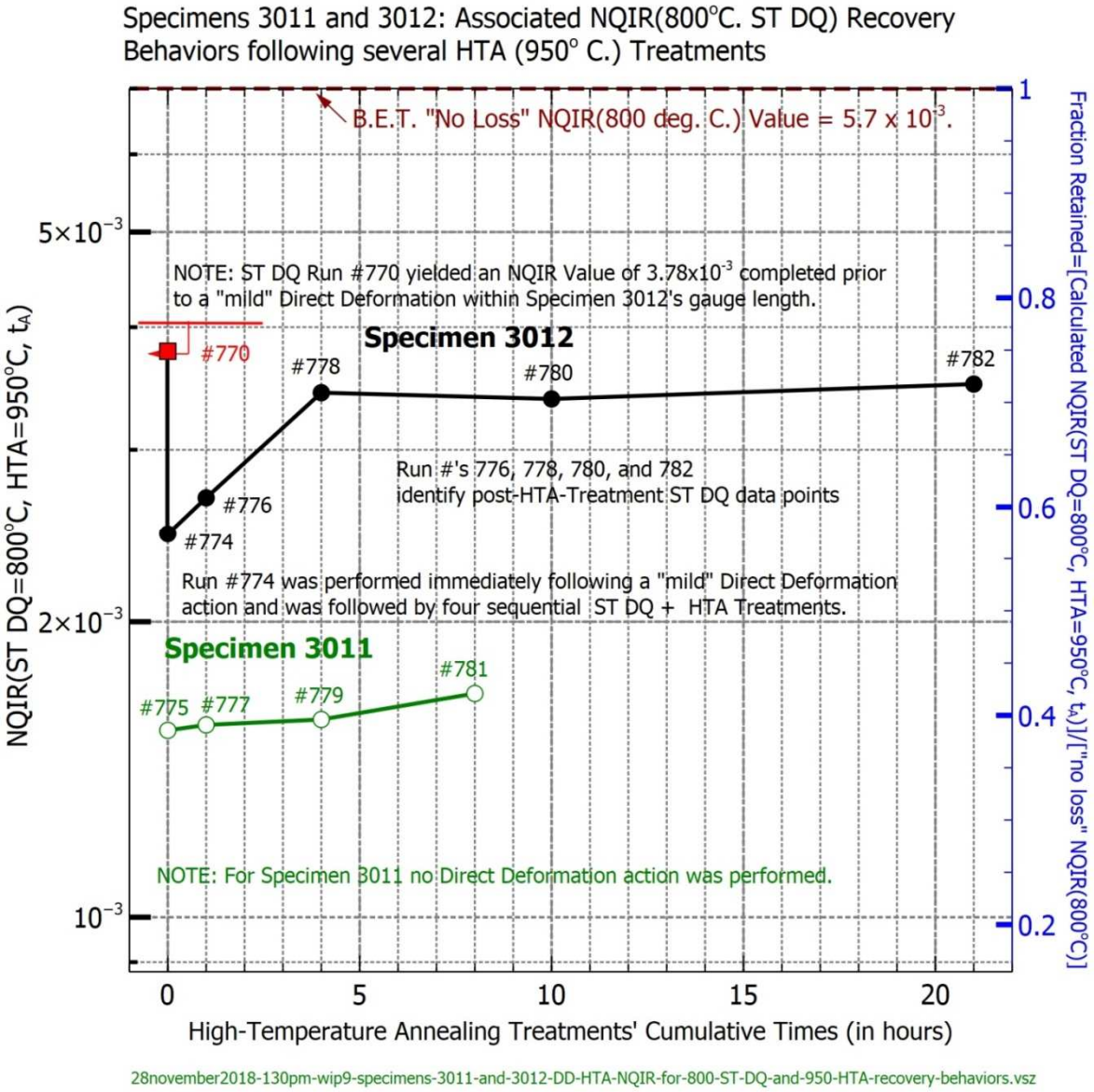

Figure 198. Specimens 3011 and 3012: Two-Axes Plots of Influence of a Series of HTA(950°C) Treatments upon Specimen Sink Structure based on associated NQIR(800°C ST DQ) Recovery Behaviors

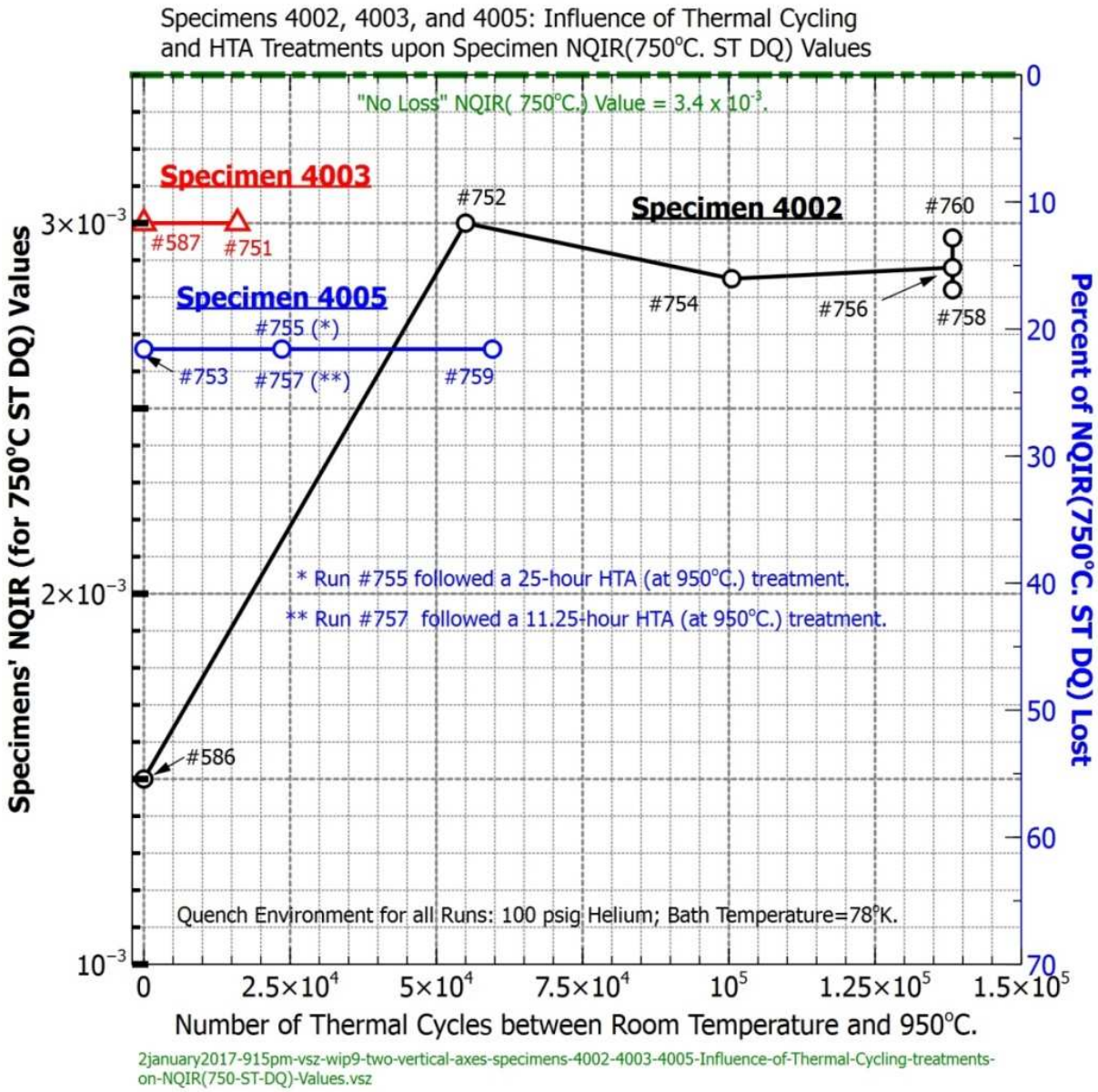

Figure 199. Specimens 4002, 4003, and 4005: Two-Axes Plot of Influence of Thermal Cycling and HTA Treatments upon specimen NQIR(750°C ST DQ) Values

9.3.2.2.2 Discussion of HTA Treatment Findings

A hypothesis of grain boundary growth is forwarded as one possible explanation that might account for the noted abrupt increases in specimen residual resistances immediately following an HTA treatment.

Moreover, the associated quenched-in resistance values obtained for a given thermal history performed following HTA treatments always proved to be highly reproducible for each specimen. Also, given the fact that the specimens used did span a wide range in pre-existing sink densities, it seems reasonable to conclude that grain boundary structures did not serve as dominant sinks for excess vacancies during elevated temperature Q&A series treatments.

9.3.2.2.3 Comparisons of Results involving HTA Treatments

Investigations by Prekel and Lawley [180] involving elevated temperature annealing treatments of molybdenum at 1900^{o}C in hydrogen for periods up to eight hours resulted in 1) a lowering of dislocation density from ~6 x 10^{7} cm^{-2} to ~10^{6} cm^{-2} which were directly correlated to TEM observations of changes in etch-pit densities and 2) re-arrangement of dislocations into sub-grain boundaries, leaving the interior of the sub-grains relatively free of dislocations.

Particularly noteworthy in their published work is Figure 11 on page 556 of Ref. 180 which shows a Curve 2 illustrating etch-pit density as a function of annealing time at 1900^{o}C. Curve 2 is of complementary (inverted as expected) nature to the NQIR(800^{o}C ST DQ) behavior vs. HTA(950^{o}C) annealing time that is shown in Figure 198 in sub-section 9.3.2.3.1 of this document.

9.3.2.2.4 Conclusions from HTA Treatments

Prolonged high temperature annealing does not appear to alter quenched-in resistance values even though concomitant increases in specimen residual resistance were observed to occur following any HTA treatment.

Furthermore, reproducibility of quenched-in resistance values following high-temperature annealing suggests that a constant dominant sink density is maintained.

9.3.2.3 Definition and Objectives of TC Treatments

One approach selected to attempt to observe the long-term effects of thermal quenching upon specimen sink density.

Thermal cycling (TC) is defined here as the repetitive cycling of a given specimen for thousands of cycles between an elevated quench temperature T_Q and a final bath temperature T_F.

The purpose for performing a TC treatment was to establish what might be the consequences, if any, of such thermal cycling treatments upon specimen sink densities and on the reproducibility of quenched-in resistance values for a chosen ST DQ thermal treatment.

Because large vacancy supersaturations can be produced by rapid downquenches from elevated temperatures [5, 8, 9, 11-13, 17, 18, 24, 25, 28, 34, 35, 37-39, 41-43, 48-50, 55, 56, 63, 65-67, 69, 76, 91, 118, 122, 128, 129], sink density reductions are thereby encouraged, for example by dislocation line climb [45, 73, 124-126]. If sink density reductions were to occur to any significant extent, subsequent determinations of quenched-in resistance for a given specimen and straight downquench history would likely be reflected in reduced vacancy losses.

Alternatively, if a reduction in retained quenched-in resistance values were instead observed, this would infer that an increase in specimen sink density had been produced by the thermal cycling treatment. If such an observation were found to be true, this would suggest that thermal strains associated with the quench rates associated with the straight downquench portion of the overall thermal cycling process were sufficient to introduce plastic deformation within the specimen.

Thus, a straightforward monitoring of the normalized quenched-in resistance (NQIR) values as a function of the number of associated thermal cycles for a given straight downquench should reveal whether either of these two behaviors is manifested [130], or possibly that there will be little to no discernible effect associated with such thermal cycling treatments upon retained quenched-in resistance values.

If reproducible QIR values were to be obtained after performing a significant number of thermal cycling treatments, a constant sink density could be inferred. This would certainly be the most desirable outcome, for it would endorse strongly the conclusion that constant sink density for excess vacancies can be associated with both of the adopted Quench/Measurement/System/Design (QMSD) units [131] used for all primary research investigations.

It should be noted here that thermal cycling treatments were performed only following completion of an extensive set of in situ straight downquench and quench-and-isothermal experiments involving several specimens.

---

[130] Refer to Figure 20 to see how selection of 5-mil diameter gold wires satisfies this concern.
[131] Refer to sub-section 11.2.2 for specifics.

Thermal cycling treatments were performed in an attempt to observe the long-term effects of thermal quenching upon specimen sink density. Specimens 4002, 4003, and 4005 were chosen for these TC treatments in which they were subjected to tens of thousands of cycles [**132**] of quenches [**133**] followed by a conventional ST DQ from a selected elevated temperature.

9.3.2.3.1 Results and Observations of Combined DD + HTA + TC Treatments upon NQIR Values

By monitoring specimen quenched-in resistance (for a selected thermal history and quench temperature) as a function of annealing time at 950^{o}C, it becomes possible to examine the recovery kinetics associated with pre-existing sink structures.

Figure 198 shows the results of such a study on two specimens, one (specimen 3011) having been heavily cold-worked prior to its creation and subjection to any thermal treatment and the other (specimen 3012) directly deformed after having been subjected to numerous ST DQ and Q&A series treatments. Quenched-in resistance values (prior to or following the prolonged High Temperature Anneal (HTA) treatments [134] at 950^{o}C) involved execution of straight downquenches from 800^{o}C.

Figure 198 provides several interesting observations.

First, for a cold-worked (flexed a number of times prior to final shaping and before sintering of potential leads that would then define the specimen's gauge length), specimen 3011, the recovery is negligible. A high-loss QIR/R40 plateau was

---

132 A non-concentric cam driven by a 25-rpm motor activated a micro-switch connected to the solid-state-controller circuitry was used to achieve the indicated thermal cycling activity.

133 It should be noted that the associated thermal cycling initial quench rates were generally less than 10^{4} ^{o}C per second.

134 Refer to Section 9.2 for details about HTA treatments.

noted to remain even after subjecting specimen 3011 to HTA annealing at 950°C treatments for as many as 10 hours.

Second, for a ”lightly deformed" [135] specimen (3012) significant recovery was noted to occur after several hours of HTA treatment, and the recovery times were noted to be many orders of magnitude longer (3.6×10^4 seconds) than would be associated with in situ isothermal annealing of quenched-in vacancies (10^{-3} seconds).

Thirdly, the asymptotic QIR/R40 value associated with the lightly deformed specimen remains below the in situ value even after tens of hours of HTA annealing at 950°C.

The slow sink structure recovery requiring hours of annealing even to be discerned supports the high degree of reproducibility of experimental data involving not only a considerable number of straight downquench experiments from temperatures as high as 925°C as well as wide-ranging and numerous isothermal annealing investigations involving annealing temperatures as high as 700°C with no significant changes occurring in vacancy sink density within any of the numerous specimens that were used. This was most especially noted to hold for those specimens quenched in situ and pre-quench annealed at elevated temperatures to stabilize each specimen's microstructure.

As an example, the ability to accumulate over one hundred reproducible data points of quenched-in resistance with specimen 4002 prior to conducting the thermal cycling and constant High Temperature Anneal (HTA) studies (see Figure 198) which

---

[135] “Lightly deformed” is defined here as a strain of less than one percent induced by direct deformation within that specimen's gauge length.

did reduce the sink density indicates the noteworthy reliability of the adopted system design and ST DQ and Q&A series treatments and related procedures.

9.3.2.3.2 TC Treatment Results, Observations, and Conclusions

The results for three specimens are shown in Figure 199.

Examination of the results obtained for specimen 4002 provides confirmation of the possibility for reducing specimen pre-existing sink density via Thermal Cycling treatments. For specimens 4003 and 4005, no discernible changes in NQIR(750^{o}C) ST DQ treatments occurred even after many thousands of such thermal cycling actions had been performed on each of these specimens.

From Figure 199 it can be concluded that thermal cycling treatments of five-mil diameter wires involving initial quench rates generally less than 10^{4} ^{o}C/sec. do not introduce additional sinks for excess vacancies into the specimens [**136**].

On the contrary, if anything, a reduction in sink density is the consequence of such a treatment as is clearly supported by the plot for specimen 4002 wherein the quenched-in resistance values increased by a factor of approximately two following the initial 55,500 thermal cycles between room temperature and 950^{o}C.

Moreover, the overall results depicted in Figure 199 endorse what had been hypothesized by several workers in theoretical discussions on quenching rate [40], thermal strain vacancies [13], and plastic deformation [20], namely, five-mil diameter gold wires can be repeatedly quenched at quench rates approaching 10^{5} degrees C per second without undergoing stresses that result in plastic deformation. Thus, no

---

136 This experimental observation is in agreement with theoretical calculations of Jackson [33], Takamura [60], and Van Bueren [61], among others.

strain vacancies or new dislocations are produced for the selected in situ gas quench technique adopted for these research investigations involving several distinct types of thermal treatments.

That thermal cycling does not result in increased losses associated with a selected thermal history leads to the conclusion that no significant thermal strain occurs within the five-mil gold wire specimens, even for quenches from temperatures as high as 950°C having associated initial quench rates in excess of 10^3 degrees Celsius per second. Furthermore, since the magnitude of quenched-in resistance is observed to either remain constant or increase upon repeating a specific thermal history, thermal cycling in excess of 10^5 times does not appear to create additional sinks for excess vacancies.

Conversely, the observed increases in quenched-in resistance values suggest not only that the repetitively-produced vacancy supersaturation conditions promote a reduction of pre-existing sink density but at the same time do not result in any significant increase in vacancy self-sink density.

Specimens subjected to thermal cycling treatments exhibited either an increase or constancy in quenched-in resistance when a ST DQ treatment was subsequently performed and its NQIR value was compared with a prior ST DQ having a comparable thermal history associated with it.

9.3.2.3.3 Interpretations of Results for Specimens 4002 and 4005

The influence of thermal cycling is clearly demonstrated in Figure 199 wherein specimen sink densities can be inferred to either remain constant or decrease upon subjection to thermal cycling treatments described here.

Figure 199 illustrates the influence of thermal cycling on measured ST DQ QIR/R40 values for several specimens as a function of the number of thermal cycles between 950^{o}C and room temperature.

The data points are associated with straight downquenches from 800^{o}C performed at the indicated number of thermal cycles. Thus, the monitoring of defect electrical resistance is considered as being a ready means to ascertain long-term, or cumulative, effects on specimen pre-existing sink density of such multiple quenching.

Specifically, it is to be noted that $\Delta R_{QN}(800^{o}C.)$ values either remain constant or increase for any five-mil diameter gold wire specimen subjected to quenches having initial quench rates of approximately 10^{3} degrees Celsius per second. Thus, magnitudes of thermal strain associated with the quench rates used can be considered as insufficient to produce plastic deformation in any of the selected specimens [40].

To examine what occurs to specimen quenched-in resistance and residual resistance following protracted exposure to quenching and to high temperature annealing, Thermal Cycling and High Temperature Anneal treatments were performed (see Figure 199).

Figure 199 illustrates the behavior of $QIR(T_Q)/R40$ for specimens 4002; 4003; and 4005. From these data, it is concluded that in situ gas quenching does not introduce any detectable thermal strain in five-mil gold wires for initial quench rates as high as 10^{5} degrees C per second (determined from associated thermal histories). This is in agreement with published work of Jackson [20], Takamura [60], and Van Bueren [61].

Furthermore, extensive numbers of thermal cycling, e.g. tens of thousands of times may, for some cases, result in a reduction in pre-existing sink density, as manifested for specimen 4002. If the dominant sinks are dislocations, this would suggest that dislocation climb is encouraged by the creation of large vacancy supersaturations via downquenching from 950^{o}C.

9.3.2.3.4 Influence of TC and HTA Treatments on QIR/R40 Values

The influences of thermal cycling and HTA treatments upon quenched-resistance are illustrated by the three plots shown in Figure 199[137].

Specimen 4002 yielded especially interesting results. Although this specimen had been annealed for more than eighteen hours at or above 940^{o}C and had been subjected to over 100 straight downquenches prior to subjection to thermal cycling, the improvement (nearly two-fold) in quenched-in resistance after 55,500 cycles from 950^{o}C down to room temperature and back is noteworthy.

Apparently, the repetitive creation of vacancy supersaturations somehow encouraged the pre-existing sink structure(s) to decrease in density, whereas a series of prolonged HTA treatments did not result in any reduction in the sink densities for the two previously cold-worked specimens 4003 and 4005.

For specimen 4002, thirty-seven additional hours of constant high temperature annealing following completion of 138,750 thermal cycles did not alter the quenched-in resistance magnitude, and this observation strongly suggests that a stable vacancy sink structure had been attained.

---

[137] The influence of TC and HTA thermal treatments on R_{LTA} values is covered in section 11.2.2 of this document.

Specimen 4003, previously annealed for six hours at 937^{o}C and subjected to over 100 straight downquenches, did not undergo any detectable change in vacancy sink structure -- as evidenced by quenched-in resistance reproducibility even after subjection to 15,900 thermal cycles.

Unfortunately, because of specimen 4003's burnout during subsequent heating, no further tests could be conducted on it.

9.3.2.4 Overall Observations made from Results of TC and HTA Treatments

Five observations are to be noted from the results of thermal cycling and prolonged high temperature annealing treatments of in situ specimens:

1) Thermal cycling rather than prolonged high temperature annealing is more likely to reduce pre-existing sink density magnitudes for any given specimen.

2) Although HTA treatments may not significantly alter the magnitude of quenched-in resistances for given quench temperatures and thermal histories (see Figure 199), a significant increase in residual resistance values do appear to be manifested following such prolonged HTA treatments (see Figure 32).

3) Thermal cycling treatments do not appear to contribute to an increase in specimen residual resistance values throughout a given specimen's lifetime.

4) Low sink density specimens [138] do not exhibit sink density reductions following either TC or HTA treatments.

5) No indications of any increases in specimen sink density were manifested as a consequence of TC treatments.

---

[138] Defined here as exhibiting T* values within a few percent of the respective "no loss" T_Q value for the associated ST DQ treatment (usually at or above 700^{o}C).

9.3.2.5 Range in Sink Density Attributable to Specimen Creation and Handling

Even though careful mechanical handling and shaping was intended for the majority of specimens prepared for these series of in situ straight downquench treatments, a few specimens were purposely flexed a number of times prior to attaching and sintering the two-mil 5N-pure gold wires that would serve to define the specimen's gauge length.

As a consequence, magnitudes of normalized quenched- in resistance for a given ST DQ or Q&A thermal treatment were observed to differ appreciably among the specimens. These results are typified by sets of data that are plotted in Figure 40. It can thus be concluded from that a range of specimen sink densities was achieved among the various five-mil diameter gold wire specimens used for this research investigation.

NQIR(T_Q, T_A, t_A) magnitudes for a given quench temperature and initial quench rate combination selection are strongly dependent upon mechanical treatment prior to in situ gas quenching. That direct deformation increases specimen sink density can be inferred from substantial reductions in $\Delta R_Q/R40$ values obtained upon repeating a given thermal history on the directly deformed specimen.

Figure 198 shows the recovery characteristics for specimen 3011 (heavily cold-worked during creation) and specimen 3012 (first lightly deformed; later more severely deformed both before and after each of several in situ elevated temperature runs).

9.3.2.6 Sink Structure Recovery Activation Energy Investigations

Comparison of straight downquench annealing kinetics for an in situ (albeit a high-loss) specimen with the observed kinetics associated with a directly deformed specimen may possibly suggest whether dislocation lines (or simple networks), such as are created by such mechanical treatments, are dominants sinks for excess vacancies in both specimens.

9.3.2.7 Estimation of Sink Structure Recovery Activation Energy

Figure 198 illustrates the recovery kinetics associated with an HTA treatment at 950^{o}C monitored by performing a ST DQ from 800^{o}C to determine the respective NQIR(800^{o}C, t_A=0) values following completion of each HTA treatment.

An estimate for the underlying sink structure's recovery activation energy was made as follows:

1) A plot was made (see Figure 200) that extended the Q&A (900, T_A) series thermal treatment's slope for an effective vacancy migration energy value of 0.67 eV (refer to the 400-to-200 range slope labeled in Figure 135 for specimen 4005) to arrive at an estimated value of 1 msec. for the associated time to reach 99% annealing for an isothermal annealing temperature of 950^{o}C;

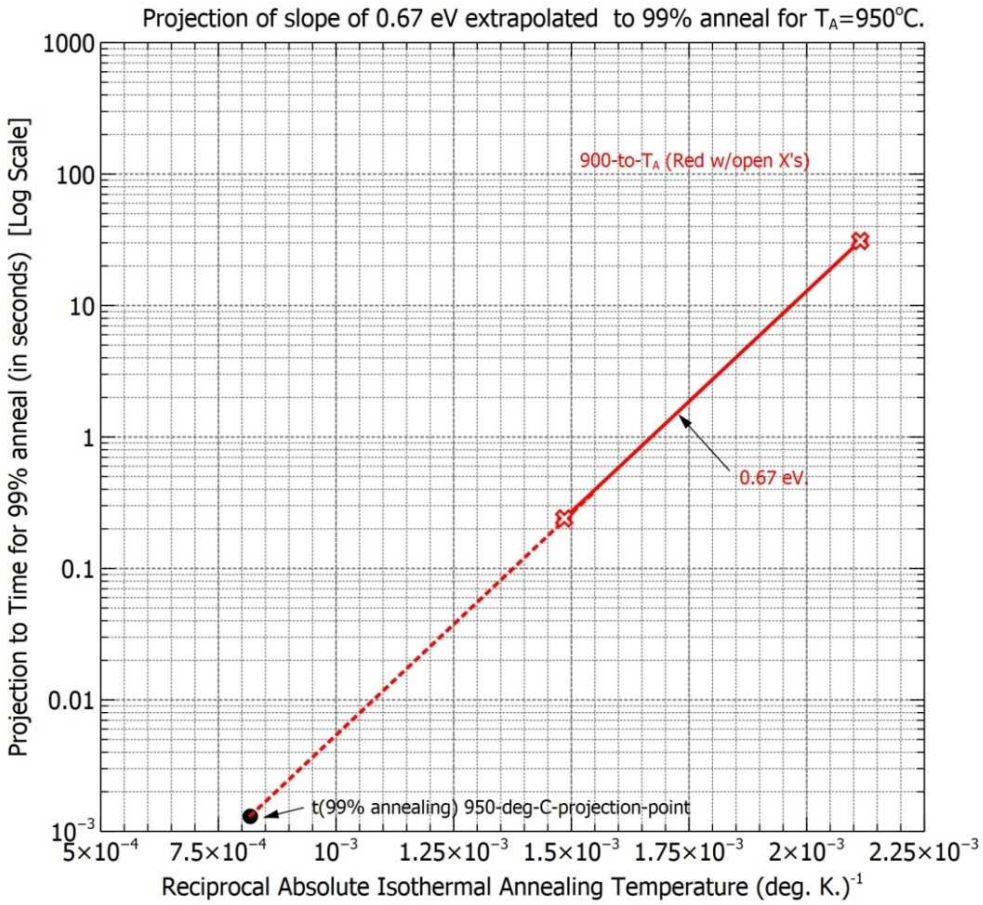

Figure 200. Projection of slope of 0.67 eV to 99% anneal time for T_A=950°C.

2) For what was judged to be a corresponding 99% recovery time of about four hours [139] as discerned from examination of the plot for specimen 3012 shown in Figure 198, a proposed 1/e time associated with an exponential sink structure recovery of four hours would suggest 48 minutes as an associated recovery time (labeled perhaps $\boldsymbol{\tau_{recovery}}$(950°C);

[139] Run #778's result appears to equate to the 99% recovery level in Figure 198.

3) Using the ratio of these two relaxation times, (assuming a thermally-activated process having a vacancy migration energy of 0.67 eV was responsible for the observed recovery characteristics resulting from the series of HTA treatments at 950^{o}C) leads to the following estimate for the activation energy for sink structure recovery:

E(sink recovery activation) = [kT_A ln(48x60/0.001) + 0.67] eV

= 8.6167x10^{-5} x (950+273)ln(2880000) + 0.67= 0.1055 x 14.873 + 0.67= 2.24 eV.

This activation energy for sink structure recovery value is approximately 0.5 eV above the vacancy self-diffusion energy value of 1.82 ± 0.04 eV established for gold by other researchers [46], and the differential value might be associated, for example, with the formation of jogs associated with dislocation climb [45].

Since additional dislocation lines are acknowledged to be produced by direct deformation [77, 85, 97], this calculated value of 2.24 eV may be suggestive of annealing out of partial dislocation lines by a vacancy climb process.

9.3.2.8 Conclusions regarding Sink Structure Recovery Findings

The associated sink recovery activation energy for specimen 3012 was calculated to be 2.24 eV. This determination was based upon use of an estimated mean relaxation time of one millisecond for excess vacancies that was based on projection of a plot having a slope of 0.67 eV for (900, 400/200) Q&A treatments, and an observed sink recovery activation time constant defined as 1/5 (4 hours) = 48 minutes.

Certainly, little more can be concluded from this particular set of experimental data other than 1) the induced sink structure appears to be a dominant sink structure

for excess vacancies during the associated quenches from 800^{o}C and 2) the sink structure's calculated recovery activation energy of 2.24 eV strongly endorses the likelihood of a dislocation-type sink structure as being responsible for the associated losses.

9.3.2.9 Sink Structure Investigations

Although numerous experimental measurements of incremental changes in defect electrical resistance have been reported in the literature on quenched metals, controversy still exists both as to the nature and constancy of the types of sinks for excess vacancies associated with either straight downquench or quench-and-isothermal anneal treatments [18, 77, 88, 95, 96, 97].

For specimens initially cold-worked or directly deformed a number of times once subjected to elevated temperatures sink density reduction by prolonged high temperature annealing at 950°C is observed to be negligible. For a specimen possessing an initially, low pre-existing sink density such annealing following a mild direct deformation can result in some degree of reduction in the induced sink density. These observations can be qualitatively explained as follows.

9.3.2.10 Influence of High Temperature Annealing on Vacancy Sinks

Exposure to elevated temperatures is known to result in grain and subgrain boundary growth. Moreover, dislocation line arrays attempt to polygonize to lower the strain field energy within the crystal [93,152, 153]. Once polygonized, the dislocation lines are arranged in metastable microstructures.

For mild direct deformations, the number and distribution of dislocation lines introduced are apparently such that some degree of annealing out of these dislocations can occur upon exposure to an HTA treatment.

However, for severe deformations or cold-worked specimens the dislocation lines likely form complex arrays that are effectively unable to anneal out but remain effective sinks for excess vacancies created during straight downquenches or Q&A treatments.

9.3.2.11 Minimal QIR/R40 Recovery suggests Stable Sink Structures

By inference, specimens that exhibited minimal improvement in quenched-in resistance after subjection to either thermal cycling or constant high temperature annealing can be considered to have stable sink structures. These stable structures may, perhaps, be attributed to either severe cold-working or deformation produced after initial sintering of potential leads had taken place.

9.3.3 Conclusions from Results of Thermal-Mechanical Treatments

Two generalizations can be made from examinations of Figure 199:

1) Severely cold-worked specimens exposed to high temperature annealing (HTA) annealing treatments -- even for a short period of time -- form stable micro-structures that prove to be efficient sinks for vacancies during subsequent quenches from elevated temperatures, and

2) Specimens that have not been cold-worked but have subsequently subjected to mild deformation are more likely to undergo at least some reduction in vacancy sink structure -- manifested by increased NQIR(T_Q)/R(40^oC) values for a subsequent ST DQ treatment -- as a consequence of subjection to prolonged HTA treatments.

3) Examination of Figure 198 also suggests that severe cold-working (specimen 3011) results in a stable microstructure. Even eight hours of annealing at 950°C does not noticeably result in any significant increases in the quenched-in resistance associated with a subsequent straight downquench from 800°C.

4) By comparison, prior to when direct deformation (mildly deformed << one percent strain) had been performed after in situ quenching specimen 3012 a) had a lower sink density and b) did exhibit a recovery time of four hours to reach a plateau level. One might conclude from this sole observation that specimens directly mounted after proper shaping without subsequent direct deformation are likely to attain stable sink structures within four hours annealing at 950^{o}C.

5) To summarize, with the introduction of a mild direct deformation and an increase in dislocation density as a consequence, greater losses are noted to occur for a given elevated temperature quench as compared to the in situ magnitude. In some cases, several hours annealing may aid in reducing the additional sink density produced by the direct deformation. The fact that direct deformation of a severe nature followed by even long periods of annealing at high temperatures did not result in any significant increase in QIR(T_Q)/R40 values suggests that dislocation lines or networks are acting as efficient sinks and that no substantial number of individual dislocations are climbing out of the crystal structure.

6) It is important to point out that a specimen such as 3011, an "undeformed after mounting" specimen, exhibited high losses attributed to possessing a pre-existing high sink density. For example, the QIR(T_Q)/R40 for the control specimen

cited in Figure 199 is significantly lower than that for the mildly deformed specimen 3012 even for the initial annealing time measurement.

7) The reason underlying the high sink density of specimen 3011 was the fact that it had been purposely flexed nearly ten times before final shaping. The results shown in Figure 198 tend to suggest two things: 1) that a large sink density (probably attributable to severe cold-working) was introduced due to "substantial" work hardening of the microstructures created and 2) the sink structures once created are neither significantly reduced nor removed even after prolonged high-temperature annealing treatments even when the ratio $T_A/T_{melt} = 0.9$.

10 SUPPLEMENTARY TEM EXPERIMENTS

This chapter is comprised of the following five sections:

- Introduction
- Pre-TEM treatments performed on gold ribbon foils
- TEM results following LTA and Q&A series thermal treatments
- Discussion
- Conclusions

10.1 INTRODUCTION

One specific limitation of macroscopic electrical resistivity-based investigations is that neither spatial nor population distributions among the types of lattice defects present after thermal quenching can be clearly demonstrated. Fortunately, transmission electron microscopy (TEM) complements the electrical resistance method by providing information at the submicroscopic level about defect densities, geometries, and distributions present.

Recall that in sub-section 8.3.12 of this document, it was established that significant specimen metastable residual resistance (MRR) levels (see Table 18) were associated with almost all Q&A series treatments. Notably, even after prolonged isothermal anneals of several hours, the fractions remaining generally ranged between one and 15 per cent of the associated initial quenched-in resistance.

As an attempt to more convincingly interpret what might be the root cause for what underlies these MRR levels, an additional experimental study was conducted using Transmission Electron Microscopy (TEM) methods. The treatments, results,

and conclusions drawn from this specific investigation are detailed in sections 10.2 through 10.5.

10.2 PRE-TEM TREATMENTS PERFORMED ON GOLD RIBBON FOILS

Use was made of one-half mil thick 6N (99.9999 weight percent) pure gold ribbon foils to create four distinct specimens (two for subjection to LTA treatments and two for elevated Q&A series treatments) that would be followed by subsequent TEM examinations using a GEM 1 MEV Electron microscope.

10.2.1 LTA Treatment Control Specimens #3 and #6

Two of these ribbon foils (referred to as specimens #3 and #6) were subjected to a modified LTA treatment that started at 800^{o}C to improve the likelihood for breaking upon of pre-existing vacancy clusters but otherwise following the adopted LTA treatment already described in sub-section 6.4.1 of this document.

Subsequent preparations were made to prepare these two control specimens for TEM examinations with the intention of observing what has been referred to herein as "vacancy-free" conditions.

10.2.2 Q&A Series Treatments on Specimens #3015 and #3020

In order to examine what might on a submicroscopic level account for the metastable residual resistance levels discussed in sub-section 8.4.3 of this document, a supplementary investigation employing Transmission Electron Microscopy was conducted using 0.5-mil 6N (99.9999 weight percent) pure gold ribbon foils.

Two specimens (identified as #3015 and #3020) were subjected to differing Q&A treatments to seek to discern any meaningful differences in the resulting TEM observations and how well those observations correlated with the respective specimen's potentiometrically determined macroscopic resistance values.

Specimen 3015 was subjected to an (800, 385, t_A= one hour) Q&A treatment, and specimen 3020 was subjected to a (900, 340, t_A= one hour) Q&A treatment [140] after which potentiometric resistance measurements were made to establish the respective metastable residual resistance (MRR) values retained [141].

Following these determinations, a subsequent aging treatment near 100^{o}C for several hours was performed after which the specimens were prepared for TEM examinations.

10.3 TEM RESULTS FOLLOWING LTA AND Q&A SERIES TREATMENTS

TEM examinations (see Figures 201 through 205) revealed the following:

1). Neither control specimen (referred to as specimens #3 and #6) exhibited significant evidence for the presence of secondary defects (see Figures 201 and 202);

2). Specimen #3015 which had been subjected to an (800, 385, t_A= one hour) Q&A series treatment prior to TEM examination exhibited black spot defects having an estimated density of 7.5 x 10^{14} cm^{-3} and diameters of approximately 80 Angstroms (see Figure 203). Specimen 3015's dislocation sink density was estimated to be 3 x

[140] A 10 psig nitrogen gas environment was associated with both of these Q&A Series treatments.

[141] For specimen 3015, the MMR level corresponded to an NQIR equal to 6.95 x 10^{-4} [equivalent to 50% of the obtained NQIR(800, 385, t_A=0) value]. For specimen 3020, the MMR level corresponded to an NQIR equal to 1.522 x10^{-3} [equivalent to 10% of the obtained NQIR(900, 340, t_A=0) value].

10^7 lines per cm^2. Notably, no black spots were observed in the immediate vicinity of dislocation lines or structures.

3). Specimen 3020 which had been subjected to an (900, 340^{o}C, t_A= one hour) Q&A series treatment prior to TEM examination exhibited severely jogged dislocations with a lesser density of black spot defects (see Figures 204 and 205) in comparison with specimen 3015's (800,385, t_A= one hour) Q&A series treatment. These TEM photos lend support to a hypothesis of greater sink efficiency for dislocation climb as long as larger defect chemical potentials (due to the higher vacancy supersaturation ratios) are present.

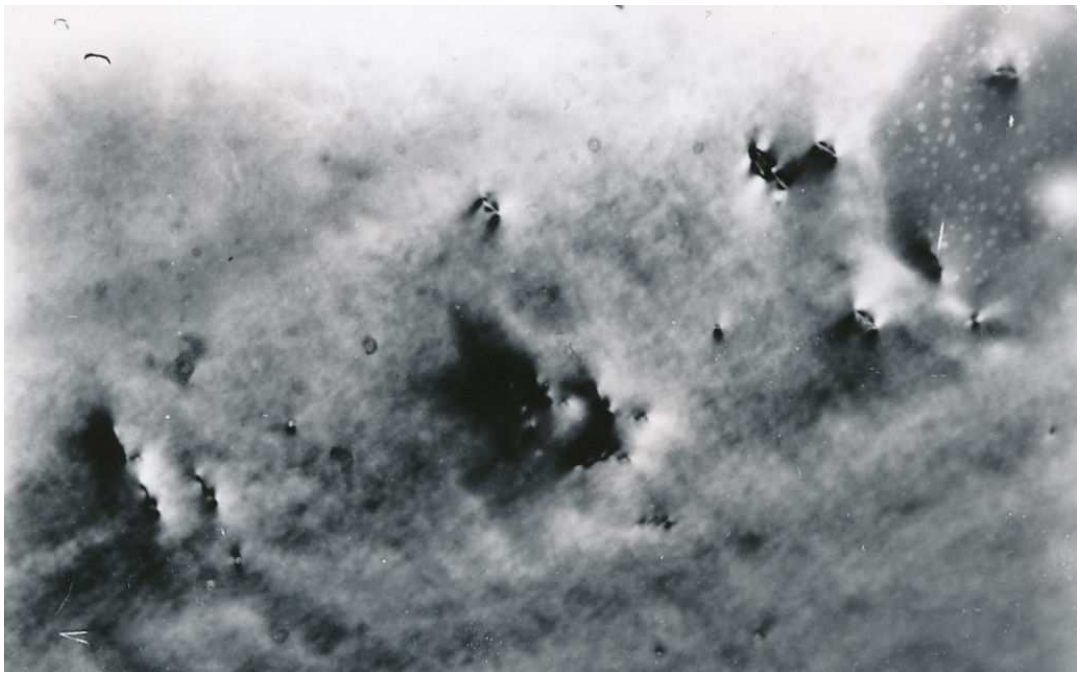

Figure 201. TEM Photo of Gold Ribbon Foil Control Specimen #3 following an LTA Treatment.

4). The overall conclusion reached based on the above observations is that the metastable residual resistance (MRR) levels found to occur for extended isothermal annealing times for elevated temperature Q&A treatments are hypothesized as being

attributable to secondary defect structures that form in the bulk of the material at some distance from pre-existing sink structures, such as dislocation lines and grain boundaries.

Figure 202. TEM Photo of Gold Ribbon Foil Control Specimen #6 following an LTA Treatment.

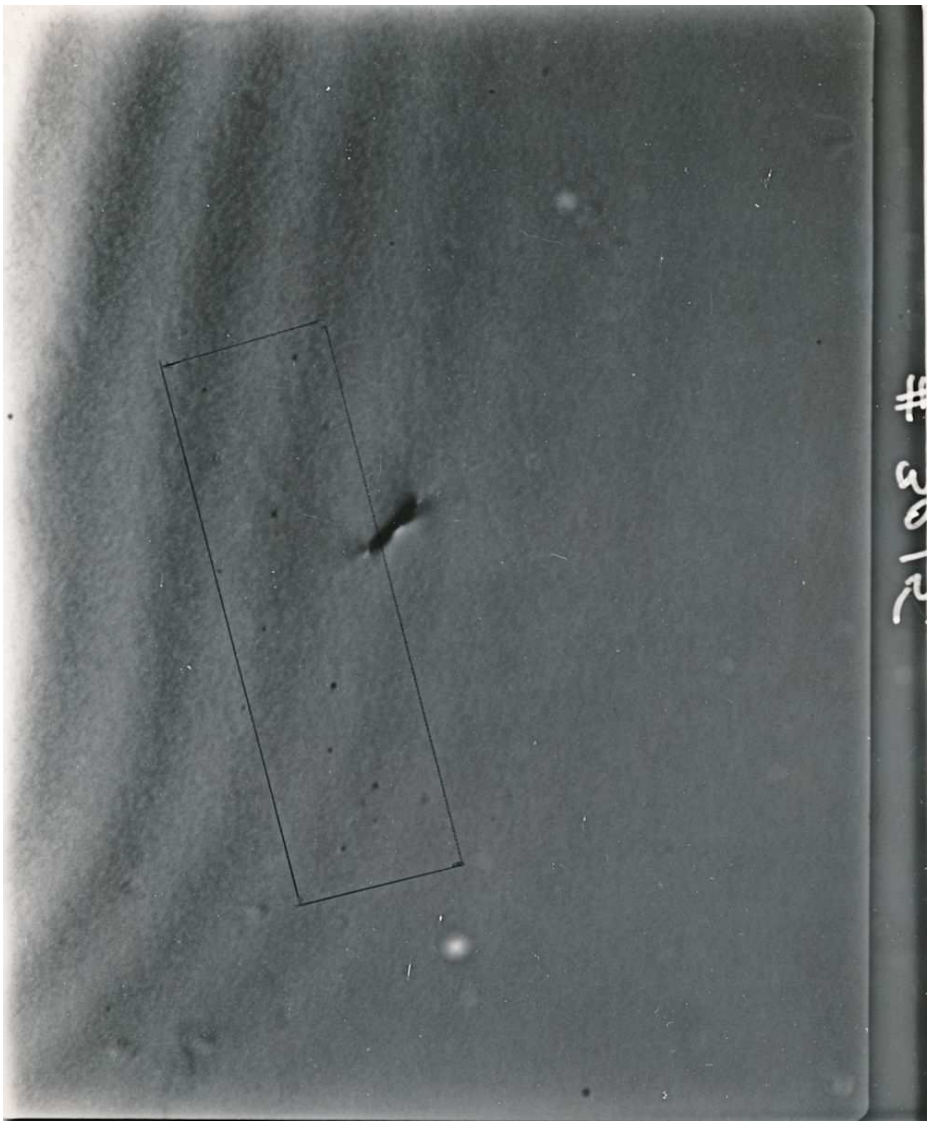

Figure 203. TEM Photo of Gold Ribbon Foil Specimen 3015 following an (800, 385, t_A= 1 hour) Q&A Series Treatment. Calculated dislocation sink density = 3 x 10^{7} cm^{-2}. Estimated Black Spot defect density = 7.5 x 10^{14} cm^{-3} of 50 to 80 Angstroms diameter.

Figure 204. TEM Photo of Gold Ribbon Foil Specimen 3020 following an (900, 340, t_A= 1 hour) Q&A Series Treatment. Note tangled subgrain boundary wall of dislocations and the presence of black spot secondary defects in regions away from various dislocation structures.

Figure 205. TEM Photo of Gold Ribbon Foil Specimen 3020 following an (900, 340, t_A= 1 hour) Q&A Series Treatment. Calculated dislocation sink density = 2 x 10^8 cm^{-2}.

10.3.1 TEM Observations obtained for Control Specimens #3 and #6

Following subjection to an LTA treatment intended to serve for establishing "vacancy-free" control specimens for TEM-based comparison purposes, control

specimens #3 and #6 exhibited no significant evidence for the presence of secondary defects (see Figures 201 and 202).

10.3.2 TEM Observations obtained for Specimen 3015

For specimen #3015 which had been subjected to an (800, 385, t_A= 1 hour) Q&A series treatment. The associated specimen dislocation density was calculated to be approximately 3 x 10^7 cm^{-2}, and 'black spot secondary defects' of approximately 50 to 80 Angstroms in diameter were observed to be present (see Figure 203). Notably, however, the region immediately surrounding dislocation lines or networks appeared devoid of secondary defects.

This observation represents strong evidence that secondary defects might in fact account for the potentiometrically-determined metastable residual resistance (MRR) levels that were found to remain within specimens following such elevated temperature annealing treatments.

By comparison, each of the two control specimens (#3 and #6) that were slowly cooled from 800^{o}C in a manner analogous to a long-term anneal (LTA) did not show evidence of 'black spot' secondary defects.

These contrasting observations would appear to support a reasonable assertion that the 'black spot secondary defects' detected for specimen 3015 were formed from clustering of excess vacancies. The estimated black spot defect concentration for quench-and-annealed specimen 3015 was calculated to be approximately 7.5 x 10^{14} cm^{-3}.

Endorsement of such an interpretation is supported also by the fact that the estimated atomic fraction of vacancies (a value of 5 x 10^{-6}) as calculated from the

estimated size and density of black spot defects observed in specimen 3015 converts to an NQIR of 3.17×10^{-4} which proves to be only slightly less than 50% of the value of $\Delta R_{QA}/R40 = 6.95 \times 10^{-4}$ calculated from the normalized quenched-in resistance that had been determined from potentiometric measurements that were conducted at liquid helium temperatures immediately following the Q&A(800, 385, t_A = 1 hour) treatment which, of course, was performed prior to this subsequent TEM treatment.

10.3.3 TEM Observations obtained for Specimen 3020

Specimen 3020 had an estimated sink density of 2×10^{8} cm^{-2} and had been subjected to a (900°C, 340°C, t_A= one hour) Q&A treatment. Subsequent TEM examinations revealed (see Figures 204 and 205) the presence of severely jogged dislocation lines (some of which were part of a grain boundary), as well as formation of some black spot secondary defects in regions removed from these dislocation line sink structures.

For specimen 3020, TEM observations were made that revealed the presence of severely jogged dislocation lines, some dislocation loops, and some black spots in regions away from pre-existing sinks. Heavily jogged dislocation lines were present in some portions of the TEM photos. Also noted was some tangling of dislocations within a grain boundary 'edge' view.

10.4 DISCUSSION

The consistencies garnered from the findings obtained by two independent techniques, namely electrical resistance measurements and TEM observations, support a hypothesis of a significant degree of vacancy clustering occurring for

contiguous Q&A treatments involving extended anneals even at elevated isothermal annealing temperatures. Moreover, the observed metastable residual resistance (MRR) levels were generally found to range in magnitude from a few per cent to more than 20 per cent of the associated NQIR(T_Q, T_A, t_A=0) magnitudes, depending on such factors as the specific specimen's pre-existing sink density, quench and isothermal annealing temperatures, isothermal annealing times, and initial quench rates.

10.5 CONCLUSIONS

The above-noted results and observations made as a result of this supplementary TEM investigation do tend to lend reasonable support for the following conclusions to be drawn:

1. LTA treatments do appear to be endorsed as a means for attaining what appear to be "vacancy-free" conditions that are achieved as a result of such a treatment.

2. The interpretation of the occurrence of significant MRR levels even following many hours of isothermal annealing following quenches initiated from quench temperatures above 800^{o}C as being attributable to the formation of stable vacancy clusters for annealing temperatures approaching 400^{o}C is supported by the presence of 'black spot secondary defects' having calculated concentrations that fall within a factor of two of what was established involving the macroscopic resistometric measurements data for comparable Q&A series treatments using five-mil diameter 6N-pure gold wires.

11 LTA TREATMENTS

Three sub-sections are covered within this chapter:

- Tie-in to pre-quench anneal (PQA) treatments
- LTA chronologies
- Observations of Changes in Specimen Surface Morphologies

Details presented here are based on analyses of extensive sets of LTA data acquired for a number of specimens and involving hundreds of thermal treatments (ST DQ and Q&A), TC, and HTA treatments, and thermal-mechanical (Direct Deformation followed by TC and/or HTA) treatments.

11.1 TIE-IN TO PRE-QUENCH ANNEAL (PQA) TREATMENTS

11.1.1 Reasoning for Establishing a Reliable PQA Cleansing Procedure

What is referred to as a reliable pre-cleansing anneal procedure associated with elevated temperature lattice defect resistance treatments has been cited in the literature **[142]** as an elusive but highly desired objective.

11.1.2 Influence of PQA Treatments upon Annealing Kinetics

Research has been reported by others that illustrates the influence of selected pre-quench anneal treatments on specimen residual resistivity levels and annealing curves can be found in the literature. See Ytterhus, et al. [66] and Ytterhus, et al. [67][143]. Such findings emphasized the need for performing further investigations that would establish pre-quench "cleansing" anneal treatments that would result in

---

[142] In Reference [18], on page 640 is the statement, "We have not been able to find details in the literature of any adequate cleansing procedure.' - Flynn, Bass, and Lazarus article [28].

[143] See pages 680 - 685 in LDQM [18] for a specific example regarding annealing of quenched-in vacancies in gold.

achieving more accurate residual level NQIR determinations and reproducible Q&A series annealing kinetics.

11.1.3 Tie-in between PQA and LTA Treatments

The investigations and subsequent findings that are presented and discussed in this chapter were in large part attributable to the efforts expended from the outset of this research investigation toward establishing a reliable Long-Term Anneal (LTA) treatment as an essential component for achieving reliable data acquisition via potentiometric measurements involving elevated temperature treatments of high-purity gold wire specimens.

11.2 LTA CHRONOLOGIES

Details presented here are based on analyses of extensive sets of LTA data [144] acquired for a number of specimens which may have involved tens or even more than one hundred combinations of various thermal treatments, namely: (ST DQ and Q&A), TC, and HTA treatments, and thermal-mechanical (Direct Deformation followed by TC and/or HTA) treatments.

11.2.1 Results and Overall Observations

Table 19 and Table 20 list the R_{LTA} chronological sequence of combined thermal cycling and constant high temperature annealing for specimens 4002 and 4003,

[144] LTA Count #'s are associated with each specimen. They are wholly independent for each specimen. Thus, the LTA #'s in Tables 19 and 20 are not to be interpreted as having been concurrently performed but rather as indicators of a record for the number of LTA treatments performed for that specific specimen and are so used for representation purposes in Tables and Figures provided within this document.

including when and for what durations HTA treatments were performed, and how many cumulative runs were made prior to each specimen's particular LTA treatment.

Figure 32 (already presented in sub-section 6.4.1.3) illustrates LTA chronologies for three specimens 4002, 4003, and 4005 **[145]** (which later replaced 4003) from among many that were used for a large number of both ST DQ and Q&A treatments. For several specimens R_{LTA} values were obtained over as many as one hundred or more ST DQ, Q&A, or other thermal treatments. An especially important general observation to be made is that the $R_{LTA}(4.2^{o}K)/R(40^{o}C)$ ratios determinations do -- over a large number of ST DQ and/or Q&A thermal treatments -- endorse and clearly reflect well on the criticality of adopting and adhering to a truly reliable step-annealing sequence.

Figure 32 also reveals the notable reproducibility of each specimen's residual resistance values throughout ST DQ and Q&A thermal treatments **[146]**, thereby confirming the overall reliability of the specific R_{LTA} treatment adopted during this research investigation.

---

[145] NOTE: LTA chronologies for specimen 4005 are presented in Figure 32.

[146] Abrupt drops between several $R(40^{o}C)/R_{LTA}$ values were noted to result following High-Temperature Anneal (HTA) treatments (see Figure 32) performed just prior to each subsequent specific LTA treatment followed immediately by the usual potentiometric measurements performed at liquid helium temperatures.

Table 19. Specimens 4002 and 4003: R_{LTA} Chronologies (LTA #'s 1 through 22)

Cumulative Count of LTA Treatments	Cumulative # of Runs (ST DQ or Q&A) for Spec. #4002	R_{LTA} Values for Specimen 4002 (µohms)	R_{LTA} Values for Specimen 4003 (µohms)	*Associated Comments*
1	0	12.66	7.65	*Newly-created specimens*
2	3	15.35	7.92	*HTA treatment for 8 hours @ 943°C for specimen 4002 yielded increased R_{LTA} value after HTA; no HTA was performed for specimen 4003.*
3	5	14.82	8.23	
4	9	15.32	9.29	
5	12	15.15	9.40	
6	15	15.435	9.80	
7	18	15.565	10.26	
8	21	15.778	10.465	
9	24	15.845	10.425	
10	28	16.53	10.58	
11	31	17.04	10.94	
12	35	17.20	11.045	
13	35	23.515	18.60	*HTA treatments: 10 hours @ 939°C for specimen 4002; 6.5 hours @ 937°C for specimen 4003.* *Note that both RLTA values increased after HTA treatments.*
14	39	23.578	18.612	
15	43	23.455	18.53	
16	46	23.575	18.60	
17	53	23.64	18.68	
18	59	23.76	18.815	
19	66	23.83	18.89	
20	72	23.93	19.025	
21	76	24.02	19.17	
22	81	24.115	19.26	

Table 20. Specimens 4002 and 4003: R_{LTA} Chronologies (LTA #'s 23 through 37)

Cumulative Count of LTA Treatments	Cumulative # of Runs (ST DQ or Q&A) for Spec. #4002	R_{LTA} Values for Specimen 4002 (µohms)	R_{LTA} Values for Specimen 4003 (µohms)	*Associated Comments*
23	86	24.185	19.365	
24	91	24.465	19.55	
25	96	24.66	19.895	
26	100	24.81	20.04	
27	106	25.135	20.42	
28	110	25.20	20.46	
29	112	28.66	27.225	*TC treatments:* *55,500 cycles for specimen 4002;* *15,900 cycles for specimen 4003;* *Note that both R_{LTA} values increased after TC.*
30	112	28.75	----	*TC treatments:* *100,500 cycles for specimen 4002;* *138,750 cycles for specimen 4003;* *HTA treatments:* *12 hours @ 942^{o}C for specimen 4002; Specimen 4003 burned out during HTA.* *R_{LTA} value increased slightly following HTA.*
31	115	28.80	----	
32	119	28.03	----	*HTA treatments:* *25 hours @ 942^{o}C for specimen 4002; R_{LTA} value decreased only slightly after HTA.*
33	127	28.03	----	*R_{LTA} value remained unchanged.*
34	143	28.35	----	
35	151	28.365	----	
36	160	28.61	----	
37	177	29.60	----	
----	183	----	----	*No more LTA's were performed.*

11.2.2 Influence of TC and HTA Treatments on R_{LTA} Values

Examinations of these sets of R_{LTA} chronologies (see Figure 32) revealed close reproducibility of a specimen's residual resistance values throughout many thermal treatments and thereby confirmed the overall reliability of the adopted R_{LTA} treatment.

However, Figure 32 is annotated to point out the fact that abrupt increases in a specimen's R_{LTA} residual resistance values (obtained by performing an LTA treatment) after potentiometric measurements of QIR_{TOTAL} were made immediately following an HTA treatment. Such dramatic increases were in sharp contrast to the gradual increases noted in all specimens subjected to ST DQ and Q&A series treatments throughout their respective lifetimes.

11.2.3 Conclusions

Gradual increases in R_{LTA} values were noted to occur throughout each specimen's lifetime.

In contrast to this, abrupt increases in specimen residual resistance were noted to occur following exposure to an HTA treatment, and this is clearly reflected in Figure 32 by the subsequently calculated values for $R(40^oC)/RLTA(4.2^oK)$ values following HTA treatments. These increases are suspected to most likely be attributable to grain or subgrain boundary growth, a phenomenon readily associated with such high temperature annealing for prolonged times that is associated with recrystallization in metals [93, 152, 153].

Moreover, the fact that reproducibility of $QIR(T_Q)/R40$ values is nonetheless exhibited - even when substantial increases in R_{LTA} have occurred - infers that grain

and/or subgrain boundaries do not appear to be dominant sinks for excess vacancies during straight downquenches.

11.3 OBSERVATIONS OF SPECIMEN SURFACE MORPHOLOGIES

Physical changes in the appearances of the surfaces of several specimens were obtained to document each specimen's morphologies that were noted to occur (see Figures 206 through 209 for specific examples) as the various types of thermal treatments (ST DQ, Q&A, TC, and HTA) were performed for the indicated specimens.

Figure 206. Specimen 3013: Morphology after 10 Runs (X150 magnification).

Figure 207. Specimen 3016: Morphology after 27 Runs (X150 Magnification).

Figure 208. Specimen 4002: Morphology after more than 100 Runs (x50).

Figure 209. Specimen 4005: Morphology after more than 100 Runs (X50).

All specimens displayed "bamboo-type" structures within portions of their gauge lengths during the early stages of data acquisition. See Figure 206 for specimen 3013 and Figure 207 for specimen 3016. Over many runs, including Thermal Cycling and prolonged High-Temperature Anneal (HTA) treatments, much more obvious changes in morphologies became evident. See Figure 208 for specimen 4002, and Figure 209 for specimen 4005.

For comparison purposes, specimens 4002 and 4005 had been subjected to several hundred runs and/or hundreds of thermal cycles and/or many hours of HTA treatments during their lifetimes, whereas specimens 3013 and 3016 had but limited exposure for long times at high temperatures.

Over their respective elevated temperature run histories, the average grain size of the 5-mil 6N-pure gold wire specimens was between two and five mils (see Figure 208 for specimen 4002 and Figure 209 for specimen 4005). Moreover, specimen 4005 exhibited obvious grain boundary sliding within its gauge length sufficient to increase its R(40^{o}C) value by approximately one percent.

Notably, specimens that were not subjected to prolonged HTA treatments did not exhibit such significant alterations in their surface morphologies or shapes.

12 SUMMARY OF RESEARCH INVESTIGATION FINDINGS

Four sub-sections are covered within this chapter:

- Adopted assumptions
- Summary of B.E.T. studies
- Summary of Q&A series treatment studies
- Summary of parameter determinations

Extensive sets of data involving five-mil diameter pure (6N) gold wires maintained in situ during subjection to thermal treatments and subsequent lattice defect electrical resistance determinations at liquid helium temperatures have been analyzed. As a consequence of these studies, quantitative estimates for numerous lattice defect parameters were made possible, and insights into the interrelationships among many of these parameters were revealed.

12.1 ADOPTED ASSUMPTIONS

Enumerated below are several assumptions that were made regarding various data acquired and subsequent interpretations of these data:

1. Monitored quenched-in electrical resistance magnitudes are considered to be directly proportional to the mean vacancy concentration retained within a specimen's gauge length and attributed to the associated thermal history immediately prior to the potentiometric measurement at liquid helium temperatures ($4.2^{o}K$).

2. Pre-quench annealing treatments are sufficient to break up any vacancy defect structures which may have been produced by or after a straight downquench or a quench-and-isothermal-anneal treatment. This assumption is endorsed as being a reasonable one when and if before initiation of any quench temperature series an

LTA treatment (see sub-section 6.4.1.2) is performed both to establish a reliable residual resistance magnitude for each specimen subjected to it and also to assure the removal of any significant concentration of secondary defects which might have been created as a result of prior thermal treatments.

3. Annealing kinetics were presumed to reflect submicroscopic annealing phenomena even though the actual observations are monitored using macroscopic electrical resistance techniques.

4. A direct proportionality is assumed between changes in a specimen's macroscopic defect electrical resistance (measured at $4.2^{o}K$) and the induced dislocation density as a result of intentional direct deformation. This assumption applies only for those experiments wherein no elevated temperature thermal treatment immediately followed direct deformation within a given specimen's gauge length.

12.2 SUMMARY OF B.E.T. STUDIES

An experimental study to independently determine the effective energy of vacancy formation in pure gold over the temperature range from $400^{o}C$ through $925^{o}C$ has been completed.

High-speed, high-accuracy data acquisition and recording equipment provided a tangible record of thermal histories. Each specimen constituted its own resistance thermometer during elevated temperature treatments. Quench temperatures were controlled to within ± 0.1°C in nearly every case, and data samplings time intervals down to 200 milliseconds were obtained during the quench. In situ five-mil gold wires were gas quenched at selectable initial quench rates of from one thousand to more

than twenty thousand degrees Celsius per second. Nitrogen or helium gas served as the gas quench medium for any particular quench.

A reliable pre-quench cleansing anneal procedure (referred to as a Long-Term Anneal treatment) was established that served to achieve "vacancy-free" residual resistance levels obtained from subsequent potentiometric measurements conducted at liquid helium temperatures.

Standard potentiometric techniques were employed for excess vacancy resistance determinations. An Arrhenius plot of normalized quenched-in resistance values extrapolated to no-loss conditions (reciprocal initial quench rate equal to zero) permitted determination of the effective vacancy formation energy. The technique of back extrapolation was applied, and it is demonstrated to be experimentally self-consistent with results obtained by other researchers who have applied this same methodology.

A value of 0.97±0.01 eV was found to represent the least squares best fit slope to an Arrhenius Master B.E.T. Plot so obtained. The vacancy formation entropy is also estimated to be equal to 1.1×10^{-4} eV ^{o}K.

Moreover, the Master B.E.T. plot of quenched-in resistance ratios as a function of reciprocal absolute quench temperature proves to be sink density independent (based on the good agreement of extrapolated data for each ST DQ series involving use of a number of independent specimens having significantly different losses for the same ST DQ series treatments).

As should be expected for a state function property, the obtained B.E.T. values did not exhibit dependencies upon either specimen pre-existing sink densities, purity ratios, or any kinetics-related parameters.

Therefore, a Master B.E.T. plot provides a reference for which thermodynamic models can be proposed to account for the obtained results even if no single set of parameters can be assured to uniquely fit the acquired data which led to the establishment of a Master B.E.T. plot.

A definitive study to establish $C_V(T_Q)$ in gold over a wide range in quench temperature T_Q and performed under closely-controlled conditions has been completed.

Such a study served to provide temperature-dependent boundary conditions for use in modeling of controlled-anneal experiments, especially quench-and-isothermal anneals that ranged widely in quench temperatures (T_Q), isothermal annealing temperatures (T_A), and isothermal annealing times (t_A).

For specimens with low pre-existing sink densities such that minimal losses occur during the transition from T_Q to T_A, these experiments could contribute substantially to increased accuracy in determinations of both effective vacancy migration energy and annealing kinetics. Moreover, when a contiguous quench-and-anneal thermal history is employed, the likelihood for formation of complex structures, such as secondary defects, vacancy clusters or whatever, would likely be minimized compared to a quench followed by an up-quench to temperature T_A and subsequent annealing for time t_A before initiating a quench from temperature T_A down to a final bath temperature T_F.

Based upon analyses of sets of data that involved helium and nitrogen gas quench environments and quench temperatures over the range from 400^{o}C to 550^{o}C, evidence led to the hypothesis that helium is soluble in pure gold wherein the heat of solution of helium was calculated to be 0.357 ± 0.003 eV.

12.3 SUMMARY OF Q&A SERIES TREATMENTS STUDIES

Analyses of Q&A annealing kinetics for each region led to several findings and underlying hypotheses, including the following:

1. Elevated temperature Q&A series annealing kinetics can range from 1st, 2nd, and possibly approaching 3rd order, depending upon the particular T_Q and T_A combinations that are involved.

2. Dislocations become more dominant sinks for excess vacancies as absolute macroscopic sink efficiency approaches unity.

3. Dislocations do serve as the dominant sinks for excess vacancies during elevated temperature Q&A treatments provided that the associated vacancy defect chemical potential remains somewhat higher than 0.15 eV in order for the absolute macroscopic sink efficiency to approach or to remain close to unity.

4. Vacancy clustering occurs in nearly all cases of elevated temperature Q&A treatments even after prolonged isothermal annealing times and results in metastable residual resistance levels as the annealing kinetics approach constant levels.

5. Clustering of defects is one possible contributor to and explanation for the occurrence of metastable residual resistance (MRR) levels [147] when extended isothermal annealing times are involved (see sub-section 8.4.3).

TEM photos (see Figures 201 through 205) revealed visual evidence as to what defect types and structures might account for these metastable residual resistance levels. Two gold ribbon foil specimens (referred to simply as Specimen #3 and Specimen #6) that had been subjected to the adopted LTA treatment described earlier served as "vacancy-free" controls for TEM-based comparison purposes and were found to exhibit a clean morphology.

6. Values determined for pure gold for both the effective vacancy migration energy for vacancies, E^M_V(eff), and for the instantaneous vacancy activation energy, E^M_V(act), were found to diminish as the vacancy supersaturation ratio decreases (e.g., as T_A approaches T_Q) and/or as the associated vacancy defect chemical potential approaches zero. See Table 15 for some calculated VSR(T_Q, T_A) and vacancy defect chemical potential combinations, many of which apply to Q&A series treatments that were performed.

12.4 SUMMARY OF PARAMETER DETERMINATIONS

12.4.1 A Consolidated Listing

From analyses of data associated with the treatments described above, quantitative estimates for the following parameters were made:

---

[147] MRR levels are defined herein as those detectable occurrences of NQIR(T_Q, T_A, t_A) levels that remain significantly above NQIR(T_A, t_A --> ∞) values associated with the isothermal annealing temperatures. These MRR levels were subsequently revealed via a separate TEM investigation to be associated with secondary defects, such as "black spots." Refer to Chapter 10 for more details.

1. Establishment of the melting point resistance ratio R(1063^{o}C)/R(40^{o}C) for gold equal to 5.57 ± 0.01.
2. Establishment of a temperature-time profile[148] defined as a Long-Term Anneal (LTA) treatment that assure reaching "vacancy-free" residual resistance levels for potentiometric resistance measurements conducted at 4.2^{o}K.
3. "No Loss" Normalized Quenched-In Resistance NQIR(T) Ξ QIR(T)/R(40^{o}C)
4. "No Loss" Vacancy resistivity $\Delta\rho_V(T)$
5. "No Loss" equilibrium vacancy concentration $C_V(T)$ [**149**]
6. Vacancy formation energy (E^F_V)
7. Vacancy formation entropy (S^F_V)
8. Heat of solution of helium in pure gold
9. Effective vacancy migration energy E^M_V(eff)
10. Remaining Vacancy Supersaturation Ratios VSR(T_Q, T_A, t_A) defined as

    $[C_v(T_Q,T_A, t_A) - C_v(T_A, t_A)]/C_v(T_A, t_A \rightarrow \infty)$
11. Vacancy defect chemical potential $\mu_v(T_Q, T_A, t_A)$
12. Absolute macroscopic sink efficiency (€)
13. Variations in time exponent (m) during various sets of Q&A series treatments
14. Metastable Residual Resistance (MRR) Levels for Q&A series treatments

---

[148] An LTA treatment incorporates a “pre-cleansing annealing” treatment (see sub-section 6.4.2 for details) that is intended to serve as a means to remove entirely or at least minimize whatever lattice defect “histories” that might be present that were associated with prior thermal treatments.

[149] Calculated by converting "No Loss" NQIR(T) Ξ QIR(T)/R(40^{o}C) values using a scattering cross-section for vacancies of 1.5 micro-ohms per one atomic percent vacancies [1, 36, 63].

15. Initial annealing rates (IARs) defined as

    {[NQIR(T_Q, T_A, $t_A = 0$) - NQIR(T_Q, T_A, $\Delta t_{A(initial)}$)] / ($\Delta t_{A(initial)}$) }, wherein $\Delta t_{A(initial)}$ is the duration time of the shortest isothermal anneal (hence the added descriptor *initial*) for the overall NQIR(T_Q, T_A, Δt_A) series treatment.

16. Mean relaxation times t_{mean} defined as

    NQIR(T_Q, T_A, $t_A = 0$) / {[NQIR(T_Q, T_A, $t_A = 0$) - NQIR(T_Q, T_A, $\Delta t_{A(initial)}$)] / $\Delta t_{A(initial)}$ }

17. Instantaneous Vacancy Activation energy E^M_V(act)

18. Post-direct deformation sink structure recovery activation energy

12.4.2 Energy Values Estimates

12.4.2.1 Vacancy Formation Energy

The "no-loss" equilibrium vacancy concentration over the temperature range 400^{o}C to 925^{o}C was found to be well represented by Eqn. (12-1):

$$C_V(T_Q) = 3.583 \exp\{-(0.97 \pm 0.01)/kT\} \qquad \text{Eqn. (12-1)}$$

where the vacancy formation energy E^F_V value is based upon a least-squares fit to the composite sets of no-loss ΔR_{QN} magnitudes.

12.4.2.2 Heat of Solution of Helium in Gold

A value of 0.357 ± 0.003 eV (see Figure 48) is proposed to represent the heat of solution of helium in pure gold as determined from data analyzed from ST DQ series made over the quench temperature range from 400^{o}C to 550^{o}C.

12.4.2.3 Effective Vacancy Migration Energy E^M_V(eff) Determinations

The wide range in values for effective vacancy migration energy determined for specimens 3012, 3013, 4002, and 4005 from Arrhenius plots of annealing half-times are clearly illustrated in Figure 136 (see sub-section 8.3.5.5).

12.4.3 Annealing Kinetics

12.4.3.1 Instantaneous Vacancy Activation Energy Determinations and Dependencies

Values for E^{M}_{V}(act) were found to vary greatly because of the dependencies upon vacancy defect chemical potential associated with any given Q&A series treatment. See Figure 163 for one such illustration of this dependency.

A composite value of 0.67 +/- 0.05 eV appears to represent the instantaneous vacancy activation energy, E^{M}_{V}(act), associated with excess vacancies for Q&A treatments involving three independent specimens and a quench temperature of 600^{o}C and annealing temperatures ranging from 20^{o}C to nearly 200^{o}C.

12.4.3.1.1 Instantaneous Vacancy Activation Energy Dependencies upon Vacancy Defect Chemical Potential

Moreover, for some specific specimens and associated quench-and-isothermal anneal treatments the values for E^{M}_{V}(act) were noted to diminish as the selected annealing temperatures approached the associated quench temperature for specific Q&A series treatments. See Figures 133 through 136 for examples that demonstrate these statements.

12.4.3.1.2 Instantaneous Vacancy Activation Energy Dependencies upon Absolute Macroscopic Sink Efficiency

Moreover, some values for E^{M}_{V}(act) were noted to diminish as selected annealing temperatures from a given quench-and-isothermal anneal series treatment approached the quench temperature. That E^{M}_{V}(act) could become negative (i.e., slope inversion was observed to occur in Arrhenius-type decay rate plots for some Q&A series treatments) as the chosen annealing temperatures closely approached

the Q&A series quench temperature could possibly be attributed to a diminution in absolute macroscopic sink efficiency € with decreased initial vacancy supersaturation conditions [9, 70]. See Figure 164 for an example of the dependency of absolute macroscopic sink efficiency € upon vacancy defect chemical potential μ_V.

Graphs of instantaneous vacancy activation energy and absolute macroscopic sink efficiency dependencies upon vacancy defect chemical potential are presented in support of this hypothesis. Refer to Figures 163 and 164.

It is important to stress that estimates for instantaneous vacancy activation energy, E^M_V(act), or for effective vacancy migration energy E^M_V(eff) for vacancy defects using the slope exhibited in the respective Arrhenius plots involving elevated temperatures should only be considered as a reliable technique provided that the magnitude of the absolute macroscopic sink efficiency for a given set of experimental conditions is close to unity or is in some manner taken into account when low vacancy supersaturation conditions apply.

12.4.3.1.3 Instantaneous Vacancy Activation Energy, E^M_V(act), Determinations and Dependencies

From Arrhenius plots of mean relaxation times associated with Q&A series treatments involving a quench temperature of 600^{o}C and three independent specimens, the following magnitudes for instantaneous vacancy activation energy, E^M_V(act), for excess vacancies, were calculated:

1) For specimen 3013 (see Figure 154), an average value of 0.724 eV for the temperature range spanning 20^{o}C to 275^{o}C; 0.29 eV for the temperature range from 275 to 500^{o}C; and for the temperature range from 500 to 575^{o}C an N/A value

indicative of non-applicability of slope-related techniques for such a determination is assigned.

2) For specimen 4002 (see Figure 152), a value of 0.62 eV for the temperature range spanning 20^{o}C to 405^{o}C; 0.25 eV for the temperature range from 405^{o}C and 575^{o}C.

3) For specimen 4005 (see Figure 153), a value of 0.62 eV for the temperature range spanning 20^{o}C to 440^{o}C; and 0.34 eV for the temperature range from 440^{o}C and 575^{o}C.

12.4.3.2 During Isothermal Annealing

Fractional losses are generally proportional to $t_A^{2/3}$ over the major portion of annealing ($1 \leq f_{QA} \geq 0.1$) for nearly all Q&A profiles involving $T_Q \geq 700^{o}$C. However, metastable residual levels are noted to result for these Q&A treatments when conducted for extended annealing times (typically, $t_A >$ one hour).

12.4.4 Activation Energy for Sink Structure Recovery

A value of 2.24 eV was estimated for the activation energy for sink structure recovery at 950^{o}C. The dominant sink structure was introduced by direct deformation within the gauge length of a given specimen, and sink structure recovery was monitored using the same macroscopic resistance measurement techniques heretofore associated only with low-to-moderate pre-existing sink density specimens as reflected in calculable vacancy concentration losses for highly reproducible thermal histories.

12.4.5 Discussion of Possible Sink Structures

12.4.5.1 Pre-existing Sinks for Vacancies

When quench temperature above 500^{o}C are employed or when direct deformation has been performed on any specimen following its creation, sinks of dislocation-line nature appear to be dominant sinks for excess vacancies during both straight downquench and quench-and-isothermal anneal treatments. This statement is based upon respective annealing kinetics, wherein an effective time of quench loss dependency for ST DQ and an annealing time $t_A^{2/3}$ loss relationship for Q&A are observed. Both observations suggest annealing to line sinks as a dominant mechanism that might account for the macroscopically discerned annealing kinetics.

12.4.5.2 Influence of Vacancy Defect Chemical Potential upon Sink Efficiencies

The influence of vacancy defect chemical potential upon absolute macroscopic sink efficiency is assessed. This is done by comparing actual initial annealing rates with extrapolated (assuming unity efficiency associated for annealing temperatures below 100^{o}C [150]) initial annealing rate values. Figure 164 provides one example that illustrates the influence of vacancy defect chemical potential upon absolute macroscopic sink efficiency.

12.4.5.3 Vacancy Clustering into Secondary Defects

Self-sinks. Vacancy agglomeration is proposed to account for metastable residual resistance levels observed to remain when prolonged quench-and-

[150] This assumption is made based on noting in Figure 155 of nearly parallel slopes for specimens 3013, 4002, and 4005 over the temperature range of 20^{o}C and 100^{o}C.

isothermal anneal treatments incorporating quench temperatures ≥ 700^{o}C and annealing temperatures as high as 500^{o}C are involved.

Observations of secondary defects, namely black spots, via supplementary TEM investigations of 0.5 mil gold ribbon foils subjected to similar Q&A treatments as the five-mil diameter gold wires and involving annealing temperatures near 400^{o}C strongly support this hypothesis.

Figures 201 through 205 illustrate the results obtained from TEM investigations using 0.5 mil 6N-pure gold ribbon foils some of which had been subjected to elevated temperature Q&A treatments and other control specimens that had been subjected to LTA treatments.

12.4.6 Need for Further and More Advanced Experimentation

Even though many empirical investigations have been conducted and reported on in this document, further experiments always seem to be necessary to address issues that cannot truly be discerned using electrical resistivity measurements alone.

Technologies and research tools that are beyond the capabilities of present day methodologies continue to evolve, and these advances can contribute uniquely toward addressing current limitations in what has been presented in this research investigation.

Hopefully, what has been presented in this document will serve to provide future researchers with insights that will prove to be of some assistance in helping them to delve ever more deeply into the subject of lattice defect properties in high-purity gold.

REFERENCES

1. Abeles F., Comptes Rendus Acad. Sci. Vol. **237**, No. 15, p. 796 (1953).
2. Asdente, M. W. and Friedel, J, *Calcul de la résistivité des cavités sphériques dans le cuivre*, J. Phys. Chem. Solids, Vol. **11**, p. 115 (1959).
3. Balluffi, R.W., *Vacancy Defect Mobilities and Binding Energies obtained from Annealing Studies*, Journal of Nuclear Materials, Vols. **69-70**, pp. 240-263 (1978).
4. Balluffi, R. W. and Seidman, D. N., *Annealing Kinetics of Vacancies to Dislocations*, Phil. Mag., Vol. **17**, Issue 148, pp. 843-848 (1968).
5. Balluffi, R. W., Lie, K. H., Seidman, D. N., and Siegel, R. W., *Determinations of Concentrations and Formation Energies and Entropies of Vacancy Defects From Quenching Experiments*, in Ref. 53, pp. 125-167.
6. Bass, J., Ph.D. Thesis, University of Illinois (1964).
7. Bass, J., *Quenched Resistance in Dilute Gold-Tin and Gold-Silver Alloys*, Phys. Rev., Vol. **137**, p. A765 (1965).
8. Bauerle, J. E. and Koehler, J. S. *Quenched-in Lattice Defects in Gold*. Phys. Rev., Vol. **107**, pp. 1493–1498 (1957).
9. Bradshaw, F. J. and Pearson, S., *Quenching Vacancies in Gold*, Phil. Mag., Series 8, Vol. **2**, Issue 15, pp. 379-383 (1957).
10. Burton, J. J. and Lazarus, D., *Divacancy Motion Energy in Gold*, Appl. Phys. Letters, Vol. **16**, No. 3, p. 131 (1970).
11. Burton, J. J. and Lazarus, D., *Annealing of Quenched Defects in Gold*, Phys. Rev., B, Vol. **2**, No. 4, pp. 787-798 (1970).
12. Chik, K. P., *Annealing and Clustering of Quenched-in Vacancies in F.C.C. Metals*, in Ref. 53, pp. 183-212.
13. Chik, K. P., *Electron Diffraction Contrast of Small Stacking Fault Tetrahedra with Applications to Quenched Gold*, Physica Status Solidi, Vol. **16**, 685 (1966).
14. Chik, K. P., *Elektronenmikroskopische Untersuchungen der Bildung von Leerstellenagglomeraten in abgeschrecktem Gold*, Physica Status Solidi, Vol. **10**, pp. 659-674 (1965).
15. Chik, K. P., *Ein Modell für die Keimbildung dere Stapelfehlertetraeder in abgeschrecktem Gold*, Physica Status Solidi, Vol. **10**, pp. 675-688 (1965).
16. Chik, K. P., D. Schumacher, and A. Seeger, *Binding Energies and Entropies of Multiple Vacancies in FCC Metals*, pp. 449-467 in Phase

Stability in Metals and Alloys, ed. by P. S. Rudman, et al.(McGraw-Hill Book Co., New York, 1967).

17. Clarebrough, L. M., Segall, R. L., Loretto, M. H., and Hargreaves, M. E., *The Annealing of Vacancies and Vacancy Aggregates in Quenched Gold, Silver and Copper*, Phil. Mag., Series 8, Vol. **9**, Issue 99, pp. 377-400 (1964).
18. Lattice Defects in Quenched Metals [LDQM], edited by Cotterill, R. M. J., Doyama, M., Jackson, J. J., and Meshii, M., (Academic Press, New York, 1965).
19. Cotterill, R. M. J., *Vacancy Clusters in Pure and Impure FCC Metals*, in Ref. 18, pp. 97-162.
20. Cotterill, R. M. J., in Ref. 18, pp. 133-134, provides a description of temperature T*, along with a graphic illustration for a mono-divacancy model.
21. Cotterill, R. M. J., Ph. D. Dissertation, Cambridge University, 1962 and *An Experimental Determination of the Electrical Resistivity of Stacking Faults and Lattice Vacancies in Gold*, Phil. Mag., Vol. **6**, Issue 71, pp. 1351-1362 (1961).
22. Damask, A. C. and Dienes, G. J., Point Defects in Metals, (Gordon and Breach, New York and London, 1963).
23. Damask, A. C. and Dienes, G. J., *Theory of Vacancy Annealing in Impure Metals*, Phys. Rev., **120**, No. 1, p. 99 (1960).
24. de Jong, M. and Koehler, J. S., *Diffusion of Single Vacancies and Divacancies in Quenched Gold*, Phys. Rev., Vol. **129**, 1, pp. 40-49 (1963).
25. de Jong, M. and Koehler, J. S., *Annealing of Pure Gold Quenched from above 800^{o}C*, Phys. Rev., Vol. **129**, No. 1, pp. 49-62 (1963).
26. Dexter, D. L., *Scattering of electrons from point singularities in metals*, Phys. Rev., Vol. **87**, p. 768 (1952).
27. Duhl, D., Hirano, K., and Cohen, M., *Diffusion of iron, cobalt and nickel in gold*, Acta Met. Vol. **11**, Issue 1, pp. 1-6 (1963).
28. Flynn, C. P., Bass, J., and Lazarus, D., *Vacancy Migration to Sinks during Quenches*, in Ref. 18, pp. 639-652.
29. Flynn, C. P., Bass, J., and Lazarus, D., *The Vacancy Formation and Motion Energies in Gold*, Phil. Mag., Vol. **11**, Issue 111, pp. 521-538, March 1965.
30. Gilder, H. M. and Lazarus. D, *Self-diffusion in gold*, J. Phys. Chem. Solids Vol. **26**, pp. 2081-2082 (1965).

31. Hirsch, P. B., Silcox, J., Smallman, R. E., and Westmacott, K. H., *Dislocation loops in quenched aluminum*, Phil. Mag., Series 8, Vol. **3**, Issue 32, pp. 897-908 (1958).

32. Schűle, W., Seeger, A., Schumacher, D., and King, K., *Point Defects in Gold*, Physica Status Solidi, Vol. **2**, pp. 1199-1220 (1962).

33. Jackson, J. *Strains in Quenched Metals*, in Ref. 18, pp. 479-513.

34. Jeannotte, D. and Machlin, E. S., *Quenching-in and Annealing-out of Point Defects in Degassed Gold held in Clean and Dirty Atmospheres*, Phil. Mag., Series 8, Vol. **8**, Issue 95, p. 1835 (1963).

35. Johnston, I. A., Dobson, P. S., and Smallman, R. E., *The Heterogeneous nucleation of tetrahedra in quenched gold*, Proc. Roy. Soc. Lond. A, Vol. **315**, Issue 1521, pp. 231-238 (1970).

36. Jongenburger, P., *The Extra-Resistivity Owing to Vacancies in Copper*, Phys. Rev., **90**, p. 710 (1953); Appl. Sci. Res. Vol. **B3**, p. 237 (1953).

37. Kamel, R., *Vacancy Precipitation in Quenched Gold from Internal Friction Measurements*, Acta Met. Vol. **7**, Issue 6, p. 680 (1959).

38. Kauffman, J. W. and Koehler, J. S., *The quenching-in of lattice vacancies in pure gold*, Phys. Rev., Vol. **88**, p. 149 (1952); ibid. **97**, p. 555 (1955).

39. Kauffman, J. W. and Meshii, M., *The Annealing Out of Lattice Vacancies in Gold During and Following Rapid Quenching*, in Ref. 18, pp. 77-95.

40. Kimura, H., Madden, R., and Kuhlmann-Wilsdorf, D., *Quenched-In Vacancies in Noble Metals -- I: Theory of Decay*, Acta Met. Vol. **7**, pp. 145-153 (1959).

41. Kimura, H., Madden, R., and Kuhlmann-Wilsdorf, D., *Quenched-In Vacancies in Noble Metals -- II: Mechanism of Quench Hardening*, Acta Met. Vol. **7**, Issue 6, pp. 154-162 (1959).

42. Kino, T. and Koehler, J. S., *Vacancies and Divacancies in Quenched Gold*. Phys. Rev., Vol. **162**, pp. 632–648 (1967).

43. Koehler, J. S., Seitz, F. and Bauerle, J. E. *Interpretation of the Quenching Experiments on Gold*. Phys. Rev., Vol. **107**, pp. 1499–1505 (1957).

44. Lazarev, B. G. and Ovcharenko, O. N. *The Energy of Formation and Migration of Vacancies in Gold and Platinum*. Soviet Physics JETP. Vol. **36** (9), No. 1, pp. 42-47, July 1959.

45. Lothe, J., *Theory of Dislocation Climb in Metals*, J. Appl. Phys. Vol. **11**, No. 6, pp. 1077-1087 (1960).

46. Makin, S.M., Rowe, A. H., and LeClaire, A.D., *Self-Diffusion in Gold*, Proceedings of the Physical Society, Section B, Vol. **70**, No. 6, p. 545 (1957).

47. Meechan, C. J. and R. R. Eggleston, R. R., *Formation Energies of Vacancies in Copper and Gold*, Acta Met. Vol. **2**, p. 680 (1954).

48. Meshii, M., Mori, T., and Kauffman, J. W., *Recovery of Electrical Resistivity in Gold Quenched from Below 700^{o}C*, Phys. Rev., Vol. **125**, No. 4, pp. 1239-1243 (1962).

49. Mori, T., Meshii, M., and Kauffman, J. W., *Quenching Rate and Quenched-In Lattice Vacancies in Gold*, J. Appl. Phys. Vol. **33**, 9, pp. 2776-2780 (1962).

50. Perry, A. J., *Vacancy Annealing Kinetics during Quenching*, Phil Mag. Vol. **21**, No. 2, pp.743-753, January 1970.

51. Perry, A. J. and Hofelich, F. A., *Vacancy Annealing Kinetics during Non-Isothermal Ageing*, Phil Mag. Vol. **22**, 179, pp.1039-1047, November 1970.

52. Quader, M. A. and Dodd, R. A., *The Structure of Quenched and Aged Gold, Gold-Cadmium, and Gold-Zinc Alloys*, Phil. Mag., Series 8, Vol. **17**, Issue 147, pp. 575-593 (1968).

53. Seeger, A., et al. (eds.), Vacancies and Interstitials in Metals [VIM], North-Holland, Amsterdam, (1970).

54. Bross, H. J. and Seeger, A. *Elektronentheoretische studies of defects in metals-VI: The electrical resistance of double spaces in single-valued metals*, Phys. Chem. Solids, Vol. **6**, Issue 4, pp. 324-334 (1958).

55. Seeger, A. and Schumacher, D., *Quenching of Noble Metals and Nickel*: Table 1 in Ref. 18, p. 27.

56. Siegel, R. W., *An Investigation of the Vacancy Annealing Kinetics and Precipitate Structure in Quenched Gold*, Phil. Mag., Series 8, Vol. **13**,. Issue 122, pp. 337-358, February 1966.

57. Silcox, J. and Hirsch, P. B., *Direct Observations of Defects in Quenched Gold*, Phil. Mag., Series 8, Vol. **4**, Issue 37, pp. 72-89 (1959).

58. Simmons, R. O. and Balluffi, R. W., *Measurement of Equilibrium Concentrations of Lattice Vacancies in Gold*, Phys. Rev., Vol. **125**, p. 862 (1962).

59. Sondheimer, E. H., *The Mean Free Path of Electrons in Metals*, Adv. In Physics, Vol. **1**, p. 1 (1952).

60. Takamura, J., *Quenched-in Vacancies and Quenching Strains in Gold*, Acta Met. Vol. **9**, pp. 547-557 (1961).

61. Van Bueren, H. G., Imperfections in Crystals, p. 276. North-Holland Publ. Co., Amsterdam, 1960.

62. Wang, C. G., PhD. Thesis (1967).

63. Wang, C. G., Seidman, D. N., and Balluffi, R. W., *Annealing Kinetics of Vacancy Defects in Quenched Gold at Elevated Temperatures*, Phys. Rev., Vol. **169**, No. 3, p. 553-569, 15 May 1968.

64. Wenzl, H., *Physical Properties of Point Defects in Cubic Metals*, in Ref. 53, pp. 363-423.

65. Ytterhus. J. A. and Balluffi, R. W., *On the Annealing of Quenched-In Vacancies in Gold*, Phil. Mag., Vol. **11**, Issue 112, pp. 707-727, April 1965.

66. Ytterhus, J. A., Balluffi, R. W., Koehler, J. S., and Siegel, R. W., *Comments on Recent Work on the Annealing of Vacancy Defects in Gold Quenched in Different Atmospheres*, Phil. Mag., Series 8, Vol. **10**, Issue 103, pp. 169-172, (1964).

67. Ytterhus. J. A., Siegel, R. W., and Balluffi, R. W., I. *An Investigation of the Annealing of Quenched-In Vacancies in Gold*, in Ref. 18, pp. 679-691 (1965). (Refer to Figure 6 on p. 687.)

68. Koehler, J. S., *Electrical Resistivity Measurements of Vacancy Annealing*, in Ref. 53, pp. 169-182.

69. Meshii, M. and Kauffman, J. W., *Recovery of Quenched-in Resistivity at High Temperatures in Gold*, Phil. Mag., Series 8, Vol. **5**, Issue 55, pp. 687-690 (1960).

70. Balluffi, R. W., *The Supersaturation and Precipitation of Vacancies during Diffusion*, Acta Met. Vol. **2**, pp. 194-202, (1965).

71. Elbaum, C., *On Dislocations Formed by the Collapse of Vacancy Discs*, Phil. Mag, Vol. **5**, Issue 55, pp. 669-674 (1960).

72. Bass, J., *Quenched Resistance in Dilute Gold-Tin and Gold-Silver Alloys*, Phys. Rev., Vol. **137**, Issue 3A, pp. A765-A782 (1965).

73. Silcox, J. and Whelan, M.J., *Direct Observations of the Annealing of Prismatic Dislocation Loops and of Climb of Dislocations in Quenched Aluminium*, Phil. Mag., Series 8, Vol. **5**, Issue 49, pp. 1-23 (1960).

74. Barnes, R. S., *The Generation of Vacancies in Metals*, Phil. Mag., Vol. **5**, Issue 54, pp. 635-646 (1960).

75. Barnes, R. S., *The Observation of Vacancy Sources in Metals*, Phil. Mag., Vol. **3**, Issue 25, pp. 97-99 (1958).

76. Balluffi, R. W. and Siegel, R. W., II. *On Problems associated with the Analysis of Complex Annealing Kinetics in Quenched Metals: Annealing Model for Quenched Gold*, in Ref. 18, pp. 693-712.

77. Balluffi, R. W., Koehler, J. S., and Simmons, R. O., *Present Knowledge About Point Defects in Deformed Face-Centered-Cubic Metals*, in Ref. 93, pp. 1-62.

78. Doyama, M. and Koehler, J. S., *Quenching and Annealing of Lattice Vacancies in Pure Silver*, Phys. Rev., Vol. **127**, Issue 1 (1962).

79. Gripshover, R. J., Khoshnevisan, M., Zetts, J. S., and Bass, J. *A Study of Vacancies in Tungsten Wires Quenched in Superfluid Helium*, Phil. Mag., Vol. **22**, Issue 178, pp. 757-777 (1970).

80. Nowick, A. S. and Roswell, A. E., *Kinetics of vacancy precipitation in a silver-zinc solid solution*, Acta Vol. Met. **7**, pp. 433-436 (1959).

81. Burke, J., *The Kinetics of the Growth of Precipitates from Solid Solutions*, Phil. Mag., Vol. **5**, Issue 50, pp. 176-185 (1960).

82. Burke, J., *The Kinetics of Precipitation from Solid Solutions by Nucleation and Diffusion Controlled Growth Processes*, Phil. Mag., Vol. **6**, Issue 72, pp. 1439-1447 (1961).

83. Thomas, G. and Whelan, M. J., *Observations of Precipitation in Thin Foils of Aluminium + 4% Copper Alloy,* Phil. Mag., Vol. **6**, Issue 69, pp. 1103-1114 (1961).

84. Panseri, C., Gatto, F., and Federighi, T., *The Quenching of Vacancies in Aluminum*, Acta Met. Vol. **5**, pp. 50-52 (1957).

85. Meshii, M. and Kauffman, J. W., *Migration energies in quenched and deformed gold*, Acta Met. Vol. **8**, pp. 815-816 (1960).

86. Flynn, C. P., *Monodefect Annealing Kinetics*, Phys. Rev., Vol. **133**, Issue 2A, pp. A587-A595 (1964).

87. Flynn, C. P., *Thermal Equilibrium Kinetics of Interacting Point Defects*, Phys. Rev., Vol. **134**, 1A, pp. A241-A246 (1964).

88. Yoshida, S. and Koehler, J. S., *Influence of Plastic Deformation on the Annealing of Quenched Gold*, Acta Met. Vol. **8**, pp. 878-881 (1960).

89. Siegel, R. W., *A Measurement of the Electrical Resistivity of Lattice Vacancies and Stacking Faults in Gold,* Phil. Mag., Vol. **13**, Issue 122, pp. 359-366, February 1966.

90. Weibull, W., *A Statistical Distribution Function of Wide Applicability*, Journal of Applied Mechanics, pp. 293-297 (1952).

91. Doyama, M. *"Methods of Quenching"*; *"Divacancies in Pure Metals"*; and *"Effects of Impurity Atoms on Quenching and Annealing Experiments"*, in Ref. 18, pp. 163-216.

92. Westdorp, W., Kimura, H., and Maddin, R. *Nucleation and Growth of Stacking Fault Tetrahedra in Gold*", Acta Met. Vol. **12**, pp. 495-500 (1964).

93. Himmel, L. (Editor), Recovery and Recrystallization of Metals [RRM], Interscience Publishers, New York and London (1963).

94. Cotterill, R. M. J. and Segall, R. L., *"The Effect of Quenching History, Quenching Temperature and Trace Impurities on Vacancy Clusters in Aluminium and Gold"*, Phil. Mag., Vol. **8**, pp. 1105-1125 (1963).

95. Takamura, J., Furukawa, K., Miura, S., and Shingu, P. H., *Production of Point Defects due to Plastic Deformation in Gold,* J. Phys. Soc. of Japan, Vol. **18**, Supplement III, pp. 7-16 (1963).

96. Kiritani, M., Sato, A., Sawai, K., and Yoshida, S. *Influence of Plastic Deformation on the Clustering of Vacancies in Quenched Gold*, J. Phys. Soc. Japan, Vol. **24**, No. 3, pp 461-467 (1968).

97. Seidman, D. N. and Balluffi, R. W., *Vacancy Annealing in Quenched and Deformed Gold: Tetrahedron Formation at Vacancy Type Dislocation Debris Along <110> Directions*, Phil. Mag., Vol. **110**, Issue 108, pp. 1067-1074 (1964).

98. Kernforshungsanlage Jülich, Germany, International Conference on Vacancies and Interstitials in Metals, Vols. **I** and **II**, September 23-28, 1968. Preprint of Conference Papers.

99. Brinkman, J.A., Dixon, C.E., and Meechan, C.J., *Interstitial and Vacancy Migration in Cu_3Au and Copper*, Acta Met. Vol. **2**, pp. 38-48 (1954).

100. Franklin, D. H. and H. K. Birnbaum, *An anelastic study of quenched gold*, Acta Met. Vol. **19**, Issue 9, pp. 965-971 (1971).

101. Sahu, R. P., Jain, K. C., and Siegel, R. W., *Vacancy properties in gold*, Journal of Nuclear Materials, Vols. **69-70**, pp. 264-276 (1978).

102. Emrick, R. M., *Pressure Effect on Vacancy Migration Rate in Gold*, Phys. Rev., Vol. **122**, pp. 1720-1733 (1961).

103. Siegel, R. W., Jain, K. C. Schober, T., Balluffi, R. W., and Thomas, L. E., *A Measurement of the Vacancy Sink Efficiency of Stacking-Fault Tetrahedra in Quenched Gold*, Crystal Lattice Defects, Vol. **1**, pp. 31-36 (1969).

104. Jain, K. C. and Siegel, R. W., *Temperature Dependence of the Vacancy Sink Efficiency of Stacking Fault Tetrahedra in Quenched Gold*, College of Engineering Report #185, SUNY, L. I., New York, December 1970.

105. Ham, Frank S., *Theory of Diffusion-Limited Precipitation*, J. Phys. Chem. Solids, Vol. **6**, Pergamon Press, pp. 335-351 (1958).

106. Ham, Frank S., *Diffusion-Limited Growth of Precipitate Particles*, J. Appl. Phys., Vol. **30**, Number 10, pp. 1518-1525 (1959).

107. Federighi, T., *A possible determination of the activation energy for self-diffusion in aluminium*, Phil. Mag., Vol. **4**, pp. 502-510 (1959).

108. Johnson, R. A., *Kinetic Study of Vacancy Clustering and Annealing in Metals*, Phys. Rev., Vol. **174**, 1, pp. 684-690 (1968).

109. Siegel, R. W., *Defects in Metals [Positron Annihilation Spectroscopy]*, Argonne National Lab., IL (USA), Report # CONF-820274-1, June 1982.

110. Kabemoto, Satoru, *Quenched-in Vacancies in Zone-Refined Aluminum*, Japanese Journal of Applied Physics, Vol. **4**, No. 11, pp. 896-905, (1965).

111. Clarebrough, L. M., *Internal Friction of β Brass*, Acta Met. Vol. **5**, pp. 413-426 (1957).

112. Panseri, C. and Federighi, T., *Isochronal Annealing of Vacancies in Aluminum*, Phil. Mag., Vol. **3**, pp. 1223-1240, Issue 35 (1958).

113. Feder, R. and Cahn, R. W., *Kinetics of Ordering in Fe_3Al*, Phil. Mag., Vol. **5**, Issue 52, pp. 343-353 (1960).

114. Loretto, M. H., Clarebrough, L. M., and Segall, R. L., *Annealing of Defects in Quenched Copper, Silver, and Gold*, International Conference on Electron Diffraction and Crystal Defects, Melbourne, **II**, G-3 (1965).

115. Kiritani, M., *Nucleation and Growth of Secondary Defects in Quenched Face-Centered Cubic Metals*, J. Phys. Soc. Japan, Vol. **20** (10): pp. 1834-1853 (1965).

116. Kiritani, M., *Formation of Voids and Dislocation Loops in Quenched Aluminum*, J. Phys. Soc. Japan, Vol. **19** (5): 618-631 (1965).

117. Johnson, R. A., *Kinetic Study of Vacancy and Interstitial Annealing in Metals*, Phys. Rev., B., Vol. **1**, No. 10, pp. 3956-3962 (1968).

118. Yoshinaka, A., Shimomura, Y., Kiritani, M., and Yoshida, S., *Nature of Black Spot Defects in Quenched Gold*, Japanese Journal of Applied Physics, Vol. **7**, No. 7, pp. 709-714 (1968).

119. Hasiguti, R. R. (editor), Lattice Defects and Their Interactions, Gordon and Breach Science Publishers (1967).

120. Yoshida, A. and Kiritani, M., *The Role of Small Vacancy Clusters in Quenched Face-Centered Cubic Metals*, in Ref. 119, pp. 457-476.

121. Kauffman, J. W. and Dienes, G. J., *Effective Migration Energies Associated with Vacancies, Divacancies and Impurities*, Acta Met. Vol. **13**, pp. 1049-1055 (1965).

122. Yoshida, S. and Kiritani, M., *Voids in Quenched Gold*, J. Phys. Soc. Japan, Vol. **10**, pp. 628-629 (1965).

123. Bokshtein, B. S., Bokshtein, S. Z., Zhukhovitskii, A. A., Kishkin, S. I., Kornelyuk, L. G., and Nechaev, Yu. S., *Transient Period of Equilibrium Concentration of Vacancies*, Soviet Physics – Doklady, Vol. **13**, No. 12, pp. 1231-1233 (1969).

124. Balluffi, R. W., *Mechanisms of Dislocation Climb*, Physica Status Solidi, Vol. **31**, Issue 2, pp. 443-463 (1969).

125. Seidman, D. N. and Balluffi, R. W., *On the Efficiency of Dislocation Climb in Gold*, Physica Status Solidi (b), Vol. **17**, Issue 2, pp. 531-541 (1966).

126. Turunen, M. J. and Lindroos, V. K., *Model for dislocation climb by a pipe diffusion mechanism*, Phil. Mag., Vol. **29**, Issue 4, pp. 701-708 (1974).

127. Yokota, M. J. and Washburn, J., *Annealing of stacking-fault tetrahedra in gold*, Phil. Mag., Vol. **16**, Issue 141, pp. 459-466 (1967).

128. Emrick, R. M., *High-Temperature Anneals of Quenched Gold*, Phys. Rev., Ltrs., Vol. **12**, Number 26, pp. 724-725 (1964).

129. Mancini, N. A., *Quenching Rate and Defect Clusters in Gold*, Phil. Mag., Vol. **21**, Issue 173, pp. 1081-1085 (1970).

130. Camanzi, A., *A Transmission Electron Microscopy Study of the Effect of Quenched-in Vacancies on Long and Short-range Order in Cu_3Au Alloy*, Phil. Mag., Vol. **21**, Issue 172, pp. 649-657 (1970).

131. Galligan, J. and Washburn, J., *Effect of Vacancy Clusters on Yielding and Strain Hardening of Copper*, Phil. Mag., Vol. **8**, Issue 93, pp. 1455-1466 (1963).

132. Chik, K., Seeger, A., and Rühle, M., *Vacancy Clusters in Quenched Copper*, Fifth International Conference for Electron Microscopy, Section J-11 (1962).

133. Cotterill, R. M. J. and Segall, R. L., *The Influence of Impurities on the Clustering of Vacancies in Quenched Metals*, Fifth International Conference for Electron Microscopy, Section J-12 (1962).

134. Uefuji, T., Shimomura, Y. and Kino, T., *Formation of Vacancy Clusters in Quenched Pure Gold and Gold Dilute Alloys*, Japanese Journal of Applied Physics, Vol. **16**, Issue 6, p. 909 (1977).

135. Lengeler, B., *Quenching of high quality gold single crystals*, Phil. Mag., Vol. **34**, Issue 2, pp. 259-264 (1976).

136. Triftshäuser, W. and McGervey, J. D., *Monovacancy formation energy in copper, silver, and gold by positron annihilation*, Applied Physics, Vol. **6**, Issue 2, pp. 177-180 (1975).

137. Herman, H. and Cohen, J. B., *Resistivity Changes due to Formation of GP Zones (Clusters rich in Solute)*, Nature, Vol. **191**, pp. 63-64 (1961).

138. Matyas, Z., *Change of electrical resistance of alloys during ageing*, Phil. Mag., Series 7, Vol. **40**, Issue 302, pp. 324-327 (1949).

139. Ikeuchi, K., Furukawa, K., and Takamura, J., *Annealing Kinetics of Vacancies in Deformed Metals*, Journal of Nuclear Materials, Vols. **69-70**, pp. 676-677 (1978).

140. Ikeuchi, K., Furukawa, K., and Takamura, J., *Annealing Kinetics of Vacancies in Deformed Metals*, J. Japan Inst. Metals, Vol. **44**, No. 6, pp. 630-636 (1980).

141. Ikeuchi, K., Furukawa, K., and Takamura, J., *Computer Simulation of Vacancy Annihilation to Dislocations*, J. Japan Inst. Metals, Vols. **44**, No. 6, pp. 637-644 (1980).

142. Siegel, R. W., *Atomic Defects and Diffusion in Metals*, Argonne National Lab., IL (USA), Report # CONF-811150--17, 11 pages, November 1981.

143. Goland, A. N., *Recent studies of point defects in metals: selected topics*, Brookhaven National Lab., NY (USA), Report # BNL-19243, 223 pages, July 1974.

144. Yoshida, S., Kiritani, M., and Shimomura, Y., *Dislocation Loops with Stacking Fault in Quenched Aluminum*, J. Phys. Soc. Japan, Vol. **18**, (2): 175-183, (1963).

145. Kiritani, M., Sato, A., and Yoshida, S., *Nucleation and Growth of Voids in Quenched Aluminum*, J. Phys. Soc. Japan, Vol. **21,** (11), pp. 2291-2299 (1966).

146. Doyama, M. and Koehler, J. S., *Quenching and Annealing of Zone-Refined Aluminum*, Phys. Rev., Vol. **134**, pp. A522-A529 (1964).

147. Reiss, H., *Diffusion-Controlled Reactions in Solids*, J. Appl. Physics, Vol. **30**, 10, pp. 1141-1151 (1959).

148. Kuhlman-Wilsdorf, D., *The Growth and Annealing of Stacking Fault Tetrahedra in FCC Metals*, International Conference on Electron Diffraction and Crystal Defects, Melbourne, **II**, G-2, (1965).

149. Yang, Z., Sakaguchi, N., Watanabe, S. and Kawai, M., *Dislocation Loop Formation and Growth under In Situ Laser and/or Electron Irradiation*, Sci. Rep. **1**, 190; DOI:10: 1038/srep00190 (2011).

150. Panseri, C. and Federighi, T., *A Resistometric Study of Pre-Precipitation in Al-10% Zn*, Acta Met. Vol. **8**, pp. 217-238 (1960).

151. Turnbull, D., Rosenbaum, H.S., and Treaftis, H. N., *Kinetics of Clustering in Some Aluminum Alloys*, Acta Met. Vol. **8**, pp. 277-295 (1960).

152. Doo, V. Y., *Polygonization of 31% Alpha-Brass*, Acta Met. Vol. **8**, Issue 4, Issue 2, pp. 106-111 (1960).

153. Doo, V.Y. and Balluffi, R. W., *Structural Changes in Single Crystal Copper-Alpha Brass Diffusion Couples*, Acta Met. Vol. **6**, Issue 6, pp. 428-438 (1958).

154. Stoebe, T. G. and Dawson, H.IA., *Analysis of Self-Diffusion and Quenching Studies in Aluminum and Gold*, Phys. Rev., Vol. **166**, No. 3, pp. 621-625 (1968).

155. Federighi, T. and Passari, L., *Anomalous increase of resistivity during ageing of aluminum-silver alloys*, Acta Met. Vol. **7**, Issue 6, pp. 422-424 (1959).

156. Fraikor, F. J. Ph.D. Thesis, *Vacancy Concentration and Precipitation in Quenched Pure Gold and Gold-Silver Alloys*, Ohio State University (1965).

157. Schoeck, G. and Tiller, W. A., *On Dislocation Formation by Vacancy Condensation*, Phil. Mag., Vol. **5**, Issue 93, pp. 43-63 (1960).

158. Jackson, K. A. *The Nucleation of Dislocation Loops from Vacancies*, Phil. Mag., Vol. **7**, Issue 79, pp. 1117-1127 (1962).

159. Siegel, R. W., Chang, S. M., and Balluffi, R. W., *Vacancy Loss at Grain Boundaries in Quenched Polycrystalline Gold*, Acta Met. Vol. **28**, Issue 3, pp. 249-257 (1980).

160. Panseri, C. and Federighi, T., *A Resistometric Study of Pre-precipitation in Al-10% Zn*, Acta Met. Vol. **8**, Issue 4, pp. 249-257 (1960).

161. Hiraki, A., *Experimental Determination of Diffusion and Formation Energies of Thermal Vacancies in Germanium*, J. Phys. Soc. Japan, Vol. **21**, (1), pp. 34-41 (1966).

162. De Jong, M., *The Diffusion of Supersaturated Concentrations of Vacancies in Dilute F.C.C. Alloys*, Phil. Mag., Vol. **11**, Issue 114, pp. 1189-1206 (1965).

163. Wintenberger, M. *Elimination des lacunes les aluminiums tres purs*, Acta Met. Vol. **7**, Issue 8, pp. 549-555 (1959).

164. Folweiler, R. C. and Brotzen, F. R., *The Effect of Quenched-in Vacancies on the Elastic Modulus of Aluminum*, Acta Met. Vol. **7**, Issue 11, pp. 718-721 (1959).

165. Baggerly, R. G. and Dawson, H. I., *Lattice Defects in Fatigued Gold*, Scripta Met. Vol. **5**, Issue 4, pp. 319-324 (1971).

166. Seidman, D. N. and Balluffi, R. W., *Dislocations as Sources and Sinks for Point Defects in Metals*, in Ref. 119, pp. 911-960.

167. Balluffi R. W., Seidman, D. N., and Siegel, R. W., *On the Identification and Properties of the Vacancy Defects in Quenched and Annealed Gold*, Report #886, NYO-3504-18, Cornell University (1968).

168. Balluffi, R.W., Siegel, R. W., Lie, K. H., and Seidman, D. N., *Determination of Concentrations and Formation Energies and Entropies*

of Vacancy Defects from Quenching Experiments, College of Engineering Report #125, SUNY, L. I., New York, January 1969.

169. Berger, A. S., Seidman, D. N., and Balluffi, R. W., *A Quantitative Study of Vacancy Defects in Quenched Platinum by Field Ion Microscopy and Electrical Resistivity—I. Experimental Results*. Acta Met. Vol. **21**, pp. 123-135 (1973).

170. Berger, A. S., Seidman, D. N., and Balluffi, R. W., *A Quantitative Study of Vacancy Defects in Quenched Platinum by Field Ion Microscopy and Electrical Resistivity—II. Experimental Results*. Acta Met. Vol. **21**, pp. 13-137-147 (1973).

171. Hasiguti, R. R., *Internal Friction of Metal Crystals due to Vacancy Pairs*, J. Phys. Soc. Japan, Vol. **8**, page 798 (1953).

172. Okuda, S. and Hasiguti, R. R., *Internal Friction Peak in Quenched Gold*, J. Phys. Soc. Japan, Vol. **19**, pp. 242-243 (1964)

173. Mori T., Meshii, M, and Kauffman, J. W., *Quench-hardening for relatively low vacancy concentrations*, Acta Met. Vol. **29**, p. 71 (1961).

174. Mori, T. and Meshii, M., *On the nucleation of vacancy clusters in gold*, Acta Met. Vol. **12**, pp. 104-106 (1964).

175. Korevaar, B. M., *The resistivity of ordered Au_3Cu*, Physica, Vol. **25**, Issues 7-12, pp. 1021-1032 (1958).

176. Korevaar, B. M., *The formation of short range order in quenched gold-copper alloys*, Acta Met. Vol. **9**, Issue 4, pp. 297-303 (1961).

177. Korevaar, B. M., *The influence of lattice defects on the electrical resistivity of a gold-copper alloy (7 at. % Cu)*, Acta Met. Vol. **6**, Issue 9, pp. 572-579 (1961).

178. Kamel, R., *Microcreep relaxation of pinned dislocations in gold*, Acta Met. Vol. **9**, Issue 1, pp. 65-68 (1961).

179. Veljkovic, S. R., *The Annealing Kinetics of Recoil Atoms in Solids*, Phil. Mag., Vol. **21**, Issue 171, pp. 627-631 (1970).

180. Prekel, H. L. and Lawley, A., *The Direct Observation of Etch-pits at Dislocations in Molybdenum*, Phil. Mag., Vol. **14**, Issue 129, pp. 545-561 (1966).

181. Kovacs, I. and El Sayed, H., *Point Defects in Metals*, Journal of Mat. Sci., Vol. **11**, Issue 3, pp. 529-559 (1976).

182. Herman, H., Cohen, J. B., and Fine, E. *Formation and reversion of Guinier-Preston zones in Al-5.3 at. % Zn*, Acta Met. Vol. **11**, Issue 1, pp. 43-56 (1963).

183. Ascoli, A., Asdente, M., Germagnoli, E. and Manara, A., *Activation Energies for the Production and Migration of Vacancies in Platinum*, J. Phys. Chem. Solids, Vol. **6**, Pergamon Press, pp. 59-64 (1958).

184. DeSorbo, W., *Calorimetric Studies on Annealing Quenched-In Defects in Gold*, Phys. Rev., Vol. **117**, p. 444 (1960).

185. Seeger, A. and Chik, K. P., *Vacancies and Vacancy Agglomerates in F.C.C. Metals*, International Conference on Electron Diffraction and Crystal Defects, Melbourne, **II**, H-2, (1965).

186. Harper, S., *Precipitation of Carbon and Nitrogen in Cold-Worked Alpha-Iron*, Phys. Rev., Vol. **83**, Issue 4, pp. 709-712 (1951).

187. Ham, F. S., *Stress-Assisted Precipitation on Dislocations, Journal of Applied Physics*, Vol. **30**, Number 6, p. 915 (1959).

188. Bullough, R. and Newman, R. C., *The kinetics of migration of point defects to dislocations*, Reports on Progress in Physics, Vol. **33**, Number 1, pp. 101-148 (1970).

189. Christian, J. W. and Vitek, V., *Dislocations and Stacking Faults,* Reports on Progress in Physics, Vol. **33**, Number 1, p. 307 (1970).

190. Ehrhart, P., Carstanjen, H. D., Fattah, A. M., and Roberto, J. B., *Diffuse-scattering study of vacancies in quenched gold*, Phil. Mag., Vol. **40**, Issue 6, pp. 843-858 (1979).

191. Bullough, R. and Newman, R. C., The growth of impurity atmospheres round dislocations, Proc. Royal Soc. Vol. **266**, Issue 1325, pp. 198-208 (1962).

192. Bullough, R. and Newman, R. C., *The Distribution of Vacancies and Hard Impurity Atoms around an Edge Dislocation*, J. Physical Soc. of Japan, Vol. **18**, Supplement III, pp. 27-29 (1963).

193. Cottrell, A. H. and Bilby, B. A., *Dislocation Theory of Yielding and Strain Ageing of Iron*, Proc. Phys. Soc, **A**, pp. 49-62 (1949).

194. Waite, T. R., *Diffusion-Limited Annealing of Radiation Damage in Germanium*, Phys.Rev. Vol. **107**, No. 2, pp. 471-478 (1957).

195. Hussein, A. A. and Dodd, R. A., *Nucleation of Secondary Defects in Quenched Gold and Zinc-Doped Gold*, Phil. Mag., Vol. **24**, Issue 192, pp. 1441-1458 (1971).

196. Hussein, A. A., *The Critical Nucleation Temperature of Stacking Fault Tetrahedra in Gold*, Metallurgical Transactions A, Vol. **8A**, Issue 11, pp. 1745-1747 (1977).

197. Bapna, M. S., Meshii, M., and Mori, T., *Initial Hardening in Quenched Gold*, Physica Status Solidi (b) **40** (2): pp. 725-736 (2006).

198. Meshii, M. and Kauffman, J. W., *Quenching Studies on Mechanical Properties of Pure Gold*, Acta Met. Vol. **7**, pp. 180-186 (1959).

199. Meshii, M. and Kauffman, J. W., *The Mechanism of Quench-hardening and its Recovery in Gold*, Phil. Mag., Vol. **51**, Issue 57, pp. 939-946 (1960).

200. Kiritani, M., Murakami, H., Yoshinaka, A., Sato, A., and Yoshida, S., *Second Order Electrical Resistivity Decay in Quenched Aluminum*, J. Phys. Soc. of Japan, Vol. **29**, No. 6, pp. 1494-1499 (1970).

201. Cost, J. R., *Zener Relaxation Studies of Vacancy Annealing in Quenched Alloys*, in Ref. 18, pp. 443-466.

202. Nihoul, J. and Stals, L., *On the Reaction Order of Bimolecular Recovery Processes in Solids*, Physica Status Solidi (b), Vol. **17**, Issue 1, pp. 295-305 (1966).

203. Szkopiak, Z. C. and Pouzet, B., *Effect of Oxygen on "Stage III" Recovery in Cold Worked Niobium*, in Ref. 98, Vol. **II**, pp. 709-723.

204. Laakmann, J., Jung, P., and Uelhoff, W., *Solubility of helium in gold*, Acta Met. Vol. **35**, Issue 8, pp. 2063-2069 (1987).

205. Nihoul, J., *Body-centred Cubic Transition Metals*, in Ref. 53, pp. 835-887.

206. Williams, J. M., Brundage, W. E., and Stanley, J. T., *Effect of Oxygen on "Stage III" Annealing in Neutron-Irradiated Niobium*, Metal Science Journal, Vol. **2**, Issue 1, pp. 100-104 (1968).

207. Stals, L. and Nihoul, J., *The recovery of cold-worked molybdenum*, Physica, Vol. **42**, Issue 2, pp. 165-178 (1969).

208. Waite, T. R., *Theoretical Treatment of the Kinetics of Diffusion-Limited Reactions*, Phys.Rev. Vol. **107**, No. 2, pp. 463-470 (1957).

209. Yoshida, S., Kiritani, M., and Shimomura, Y., *Voids in Quenched Face-centered Cubic Metals*, International Conference on Electron Diffraction and Crystal Defects, Melbourne, **II**, G-4, (1965).

210. Hirth, J. P. and Lothe, J., Theory of Dislocations, McGraw-Hill Book Company (1968).

211. Roswell, A. E. and Nowick, A. S., *Quench Hardening of Pure Gold as Observed by Internal Friction Methods*, Acta Vol. Met. Vol. **5**, pp. 228-235 (1957).

212. Simmons, R. O., *Properties of Vacancies in the Noble Metals,* J. Phys. Soc. of Japan, Vol. **18**, Supplement II, pp. 172-178 (1963).

213. Simmons, R. O. and Balluffi, R. W., *Measurement of Equilibrium Concentrations of Vacancies in Copper*, Phys. Rev., Vol. **129**, No. 4, pp. 1533-1544 (1963).

214. Sharma, R. K., *The Production and Annealing of Point Defects Produced by Quenching and by Tensile Deformation in Pure Gold and Silver*, Ph. D. Thesis, University of Illinois (1968).

215. Khellaf, A., Seeger, A., and Emrick, R. M., *Quenching Studies of Lattice Vacancies in High-Purity Aluminum*, Materials Transactions, Vol. **43**, No. 2, pp. 186-198 (2002).

216. Lazarus, D., *Diffusion Studies of vacancies and impurities*, J. Phys. Radium, Vol. **23**, (10), pp. 772-778 (1962).

217. Chaieb, Z., Ouarda, O. M., Raho, A. A., and Kadi-Hanifi, M., *Effect of Fe and Si impurities on the precipitation kinetics of the GPB zones in the Al-3wt%Cu-1wt%Mg alloy*, AIMS Materials Science, Vol. **3**, Issue 4, pp. 1443-1455 (2016).

218. Damask, A. C., Dienes, G. J., and Weizer, V. G., *Calculation of Migration and Binding Energies of Mono-, Di-, and Trivacancies in Copper with the Use of a Morse Function*, Phys. Rev., Vol. **113**, Issue 3, p. 781 (1959).

219. Dienes, G. J. and Damask, A. C., *Theory of annealing of vacancies and divacancies in pure metals*, Discussions of the Faraday Society, Vol. **31**, pp. 29-37 (1961).

220. Feder, R., Mooney, M., and Nowick, A. S., *Ordering Kinetics in Long-Range Ordered Cu_3Au*, Acta Met. Vol. **6**, pp. 266-277 (1958).

221. Nowick, A. S. and Weisberg, L. R., *A Simple Treatment of Ordering Kinetics*, Acta Met. Vol. **6**, pp. 260-265 (1958).

222. Bullough, R. and Newman, R. C., *The Interaction of Vacancies with Dislocations*, Phil. Mag., Vol. **7**, Issue 75, pp. 529-531 (1962).

223. Johnson, R. A., *Empirical potentials and their use in the calculation of energies of point defects in metals*, Journal of Physics: Metal Physics Vol. **3**, No. 2, p. 295 (1973).

224. Wilde, J., Cerezo, A., and Smith, G. D. W., *Three-Dimensional Atomic-Scale Mapping of a Cottrell Atmosphere around a Dislocation in Iron*, Scripta mater. **43**, pp. 39-48 (2000).

225. Johnson, R. A., *Kinetic Study of Vacancy Clustering and Annealing in Metals*, Phys. Rev., Vol. **174**, Issue 3, p. 684 (1968).

226. Berry, B. S., *Review of internal friction due to point defects*, Acta Met. Vol **10**, Issue 4, pp. 271-280 (1962).

227. Fujita, F. E., *On the Kinetics of Precipitation in Alloys*, Journal of the Physical Society of Japan, Vol. **19**, No. 5, pp. 640-651 (1964).

228. Siegel, R.W., *Vacancy concentrations in metals*, Journal of Nuclear Materials, Vols. **69-70**, pp. 117-146 (1978).

229. De Laplace, J, Hillairet, J, Mairy, C., and Adda, Y., *Contributions to the Study of Vacancies in Gold*, Mem. Sci. Rev. Met. Vol. **63**, p. 282 (1966)

230. Mori, T., Meshii, M., and Kauffman, J. W., *Quench-hardening for relatively low vacancy concentrations*, Acta Met. Vol. **9**, pp.71-72 (1961)

231. Corbett, J. W. and Peak, D., *Theory of Reaction Kinetics*, SUNY (Albany, NY) Final Report C00-3478-14, 37 pages.

232. M. J. Laubitz, *Transport properties of pure metals at high temperatures. II. Silver and gold*, Canadian Journal of Physics, Vol. **47** (23), pp. 2633-2644 (1969).

233. Shockley, W., Holloman, J. H., Maurer, R., and Seitz, F. (Editorial Committee), Imperfections in Nearly Perfect Crystals, John Wiley & Sons, Inc., New York (1950).

234. Friedel, J., Dislocations, Addison-Wesley Publishing Company, Inc., (1964).

235. Seeger, A. and Mehrer, H., *Analysis of Self-Diffusion and Equilibrium Measurements*, in Ref. 53, pp. 1-58.

236. Mehrer, H., *Computer Simulation of Point Defect Annealing Kinetics*, in Ref. 98, pp. 643-658.

237. Weisberg, L. R. and Quimby, S. L., *Ordering and Disordering Processes in Cu_3Au – I*, Phys. Rev., Vol. **110**, Number 2, April 1958, pp. 338-348.

238. Noble, B. and Crook, A., *A Kinetic and Electron-Microscope Study of Precipitation in Magnesium-Thorium Alloys*, Journal of the Institute of Metals, Vol. **98**, 1970, pp. 375-380.

239. Köster, Uwe, *Precipitation of germanium from aluminium*, Mater. Sci. Eng., Vol. **5** (1969/70), pp. 174-176.